frontiers | Research Topics

Optimization and data-driven approaches for energy storage-based demand response to achieve power system flexibility

Edited by
Yue Xiang, Yingjun Wu, Luhao Wang, Zixuan Wang and Chenghong Gu

Published in
Frontiers in Energy Research

ISSN 1664-8714
ISBN 978-2-8325-6497-4
DOI 10.3389/978-2-8325-6497-4

Generative AI statement
Any alternative text (Alt text) provided alongside figures in the articles in this ebook has been generated by Frontiers with the support of artificial intelligence and reasonable efforts have been made to ensure accuracy, including review by the authors wherever possible. If you identify any issues, please contact us.

About Frontiers

Frontiers is more than just an open access publisher of scholarly articles: it is a pioneering approach to the world of academia, radically improving the way scholarly research is managed. The grand vision of Frontiers is a world where all people have an equal opportunity to seek, share and generate knowledge. Frontiers provides immediate and permanent online open access to all its publications, but this alone is not enough to realize our grand goals.

Frontiers journal series

The Frontiers journal series is a multi-tier and interdisciplinary set of open-access, online journals, promising a paradigm shift from the current review, selection and dissemination processes in academic publishing. All Frontiers journals are driven by researchers for researchers; therefore, they constitute a service to the scholarly community. At the same time, the *Frontiers journal series* operates on a revolutionary invention, the tiered publishing system, initially addressing specific communities of scholars, and gradually climbing up to broader public understanding, thus serving the interests of the lay society, too.

Dedication to quality

Each Frontiers article is a landmark of the highest quality, thanks to genuinely collaborative interactions between authors and review editors, who include some of the world's best academicians. Research must be certified by peers before entering a stream of knowledge that may eventually reach the public - and shape society; therefore, Frontiers only applies the most rigorous and unbiased reviews. Frontiers revolutionizes research publishing by freely delivering the most outstanding research, evaluated with no bias from both the academic and social point of view. By applying the most advanced information technologies, Frontiers is catapulting scholarly publishing into a new generation.

What are Frontiers Research Topics?

Frontiers Research Topics are very popular trademarks of the *Frontiers journals series*: they are collections of at least ten articles, all centered on a particular subject. With their unique mix of varied contributions from Original Research to Review Articles, Frontiers Research Topics unify the most influential researchers, the latest key findings and historical advances in a hot research area.

Find out more on how to host your own Frontiers Research Topic or contribute to one as an author by contacting the Frontiers editorial office: frontiersin.org/about/contact

Optimization and data-driven approaches for energy storage-based demand response to achieve power system flexibility

Topic editors

Yue Xiang — Sichuan University, China
Yingjun Wu — Hohai University, China
Luhao Wang — University of Jinan, China
Zixuan Wang — North China Electric Power University, China
Chenghong Gu — University of Bath, United Kingdom

Citation

Xiang, Y., Wu, Y., Wang, L., Wang, Z., Gu, C., eds. (2025). *Optimization and data-driven approaches for energy storage-based demand response to achieve power system flexibility*. Lausanne: Frontiers Media SA. doi: 10.3389/978-2-8325-6497-4

Table of contents

frontiers | Frontiers in Energy Research

TYPE Editorial
PUBLISHED 11 June 2025
DOI 10.3389/fenrg.2025.1618235

OPEN ACCESS

EDITED AND REVIEWED BY
Kui Jiao,
Tianjin University, China

*CORRESPONDENCE
Yingjun Wu,
ywu_ee@vip.163.com

RECEIVED 25 April 2025
ACCEPTED 06 June 2025
PUBLISHED 11 June 2025

CITATION
Wang Z, Xiang Y, Wu Y, Wang L and Gu C (2025) Editorial: Optimization and data-driven approaches for energy storage-based demand response to achieve power system flexibility.
Front. Energy Res. 13:1618235.
doi: 10.3389/fenrg.2025.1618235

Editorial: Optimization and data-driven approaches for energy storage-based demand response to achieve power system flexibility

Zixuan Wang[1], Yue Xiang[2], Yingjun Wu[3]*, Luhao Wang[4] and Chenghong Gu[5]

[1]School of Electrical and Electronic Engineering, North China Electric Power University, Baoding, China, [2]College of Electrical Engineering, Sichuan University, Chengdu, China, [3]School of Energy and Electrical Engineering, Hohai University, Nanjing, China, [4]School of Electrical Engineering, University of Jinan, Jinan, China, [5]Department of Electronic and Electrical Engineering, University of Bath, Bath, United Kingdom

KEYWORDS

energy storage, demand response, renewable energy, new power system, optimization and data-driven

Editorial on the Research Topic
Editorial: Optimization and data-driven approaches for energy storage-based demand response to achieve power system flexibility

Introduction

In recent years, with the widespread adoption of distributed renewable energy and electric vehicles, the power grid faces new challenges in ensuring stable and sustainable development. Concurrently, insufficient local consumption resulting from distributed generation also impacts the power grid's safe operation. In this context, energy storage, electric vehicles and demand response play an important role by promoting flexible grid operation and low-carbon transition. In comparison to traditional loads, flexible loads can be efficiently managed through demand response to optimize consumption patterns to meet grid needs. Therefore, the collaborative dispatching of multi-modal energy storage integration technologies, such as batteries, pumped hydro storage, hydrogen storage, and distributed generators, alongside diverse demand-side flexible resources like flexible loads and electric vehicles, holds significant importance. The coordinated optimization of these distributed resources can effectively address the intermittency of variable renewable energies (VERs), encourage the adoption of flexible loads, and enhance the overall adaptability and carbon emission reduction efforts of the power system.

This Research Topic cover latest research in the areas of energy storage system optimization and control, demand response and load management, new power system scheduling, power system security defense and restoration, energy market and trading,

and application of machine learning. A summary of the contribution of this research is presented as follows.

For energy storage system optimization and control, Yixi et al. Focus on the lack of flexibility of energy-intensive industrial and mining loads in stand-alone microgrids. This study quantifies the regulation potential of lithium mining loads, combines the regulation boundaries of photovoltaics, gas turbines and energy storage, and constructs a capacity optimization model for industrial and mining loads and energy storage (ES), which improves the capacity of new energy consumption while guaranteeing the balance of power and the electricity demand of energy-intensive loads. On this basis, Wang et al. further deepen the energy storage optimization problem, focusing on considering the coupling effect of storage life and charging/discharging strategy, using the rainflow counting method to establish a life loss model for lithium iron phosphate batteries, to realize the accurate configuration of multi-user shared storage. To address the dynamic stability challenges of grid-connected renewable energy, Yang et al. developed a synergistic control strategy for the power density virtual energy storage (PDVES) model and the energy density virtual energy storage (EDVES) model. The strategy equates wind power, photovoltaic (PV) and electric vehicle (EV) as virtual energy storage units, and constructs a microgrid energy regulation framework to improve the energy regulation and dynamic stability control performance of microgrids.

For demand response and load management, a number of studies focus on demand response modelling, scheduling and optimization strategies. Zhou et al. study the load characteristics of urban grids through IoT technology. On this basis, they comprehensively analyze the impact of IoT-based load control technologies and market maturity differences on load control, providing technical support for relevant carbon emission scenarios. Qian et al. build a demand response model for fused magnesium load (FML), combining principal component analysis and clustering algorithms to generate a set of low-conservative scenarios with spatial and temporal correlation uncertainty. Afterwards, they develop a two-stage robust optimization framework to reduce the cost of day-ahead scheduling and enhance the capacity of renewable energy consumption. Feng et al. optimize the energy storage allocation and grid expansion scenarios by decomposing and reconstructing the model, and assess the impact of the demand response credibility on the planning of a low-carbon power system to optimize the economy and carbon emissions. On the user side, Yang et al. consider the demand-side controllable loads as dispatchable resources, propose a tiered pricing mechanism, and reduce the punitive cost by constructing a stackelberg game model, which improves the user's participation in demand response. Wang et al. model the energy interaction problem between distribution system protocols as a Nash bargaining problem and combine it with the augmented ADMM algorithm to protect privacy. This approach reduces regional operating costs and facilitates the integration of renewable energy sources. Xing et al. select an integrated load model using PMU voltage data as input and refine the initialization process based on good point sets to mitigate the effect of local maxima. By using an improved dung beetle optimization algorithm, this method improves the accuracy of load model parameter identification.

For new power system scheduling, Gong et al. propose an active optimization scheduling model for the distribution network by considering the regulation capacity, and a fast solution method is designed herein to formulate the priority control order of the adjustable units. In view of the dual uncertainty of renewable energy output and demand response, Zhang et al. design a multi-source uncertainty quantification framework based on cloud modelling theory, taking into account both the uncertainty of renewable energy and demand response, and its effectiveness and superiority is verified in a typical case of IEEE 33 nodes. To extend the multi-energy synergy scenario, Zhou et al. proposed a distributed optimization method for electro-thermal-hydrogen systems based on the alternating direction multiplier method (ADMM). The method accurately models the power-to-hydrogen (P2H) conversion process in an electrolyzer, and comprehensively investigates the impact of microgrid connection topology on the total operating cost. Finally, Tan et al. focus on the key challenges in the field of large-scale scheduling of heterogeneous elastic resources, and propose a two-layer asynchronous optimization model, which reduces the computational complexity through the decomposition-coordination mechanism, and provides theoretical support for real-time co-optimization of multiple types of energy storage and loads.

For power system security defense and restoration, the following three studies propose innovative solutions from different perspectives. Wang et al. focus on building a hardware-in-the-loop co-simulation platform based on RT-LAB and OPNET. This research verifies the effectiveness of the platform in analyzing the impact of network attacks on the power system in real time through DDOS attack and intermediate node attack scenarios in the communication network, which provides an experimental basis for the formulation of smart grid security strategies. Wang et al. propose a defense strategy that combines Petri net modelling with mobile energy storage pre-layout. This method first assesses system vulnerability by integrating historical attack data, and then simulates and verifies the effectiveness of the proposed planning strategy in a 33-node system using the Columns and Constraints Generation (C&CG) algorithm. Zhang et al., on the other hand, address the uncertainties introduced by renewable energy sources and controllable loads by designing a Deep Reinforcement Learning (DRL)-based Soft Actor-Critic algorithm (Soft Actor-Critic, SAC). Based on this, combined with an improved Markov decision process model, it achieves fast recovery of system frequency and minimization of dispatch cost of controllable loads, and effectively solves the source load uncertainty problem exacerbated by faulty power shortage.

For energy market and trading, Li et al. propose an integrated energy system model to address the existing deficiencies in the coupled electricity-carbon market. Combined with the baseline carbon emission quota allocation method and the actual emission data of gas equipment, an improved carbon trading mechanism is designed to achieve the low-carbon operation of the system, and the numerical case verifies its effectiveness in reducing carbon emissions and improving energy efficiency. Yan et al. on the other hand, put forward a two-tier gaming framework, by integrating the carbon emission flow theory to construct a comprehensive energy carbon pricing mechanism, which encourages virtual power plants (VPPs) to dynamically adjust their trading strategies in a multi-energy system. Case studies show that this strategy can effectively promote multi-initiative co-optimization for emission reductions and the economics of energy trading. Moreover, in response to the irregular relationship between the dynamic service scope of charging

stations (CSs) and the real-time charging price, Yang et al. propose a dynamic service field strength (SFS) model to optimize charging station service range delineation and real-time pricing, and validate its effectiveness in reducing the regional power bias and improving the operator's revenue.

For application of machine learning, Xiong et al. embed Kalman filtering and sparse self-encoder into the Transformer framework, which is capable of realizing dynamic noise suppression and multidimensional feature extraction, providing a new solution for battery state prediction in high volatility scenarios. Wang et al. correct the numerical weather prediction (NWP) wind speed error through ResNet-GRU network and optimize the parameters of CNN-LSTM model by combining with Keplerian Optimization Algorithm (KOA), which effectively improves the accuracy of short-term wind power prediction. Aiming at the PV uncertainty modelling, Deng et al. propose a StyleGAN framework incorporating meteorological physical constraints to generate diversified year-round weather scenarios with spatio-temporal correlation. This study provides a high-fidelity experimental data base for PV planning and risk assessment under extreme weather. Moreover, Wang et al. and Zhang et al. also introduce machine learning methods into power system security defense and restoration, and Zhao et al. focus on the financial management and leverage the advantages of deep learning to capture complex patterns and dependencies in financial time series data.

In addition to the above topics, Chen et al. propose a control strategy with a current hysteresis loop to address the issues of high inductance current ripple in photovoltaic systems and achieve real-time duty cycle regulation, which provides reference for the follow-up studies on the control of renewable energy and energy storage.

In summary, due to the limit of time, there could be many related works that could not be collected in this Research Topic. We look forward to keep following Frontiers in Energy Research, especially with a focus on the Research Topic of energy storage-based demand response.

Author contributions

ZW: Writing – original draft. Yue Xiang: Writing – review and editing. Yingjun Wu: Writing – review and editing. LW: Writing – review and editing. CG: Writing – review and editing.

Funding

The author(s) declare that financial support was received for the research and/or publication of this article. This work was supported in part by the Natural Science Foundation of Hebei Province (E2024502063) and in part by the Fundamental Research Funds for the Central Universities (2024MS102).

Acknowledgments

The team of Guest Editors would like to express their gratitude to all the authors who provided their high-quality papers. Meanwhile, the reviewers who put effort into ensuring a high level of scientific publications also deserve recognition. We are very grateful to all the Research Topic editors for their support in this Research Topic.

Conflict of interest

The authors declare that the research was conducted in the absence of any commercial or financial relationships that could be construed as a potential conflict of interest.

Generative AI statement

The author(s) declare that no Generative AI was used in the creation of this manuscript.

Publisher's note

frontiers | Frontiers in Energy Research

TYPE Original Research
PUBLISHED 22 April 2024
DOI 10.3389/fenrg.2024.1378016

OPEN ACCESS

EDITED BY
Yitong Shang,
Hong Kong University of Science and Technology, Hong Kong SAR, China

REVIEWED BY
Youjun Deng,
Southwest Petroleum University, China
Haoasn Yang,
Hong Kong Polytechnic University, Hong Kong SAR, China
Wenlong Liao,
Swiss Federal Institute of Technology Lausanne, Switzerland

*CORRESPONDENCE
Xiafei Tang,
xiafei.tang@csust.edu.cn

RECEIVED 29 January 2024
ACCEPTED 20 March 2024
PUBLISHED 22 April 2024

CITATION
Yang X, Tang X, Chen Y, Wu J and Tan Y (2024), Charging station service scope division and real-time pricing strategy based on the strongest occupation method.
Front. Energy Res. 12:1378016.
doi: 10.3389/fenrg.2024.1378016

Charging station service scope division and real-time pricing strategy based on the strongest occupation method

Xian Yang[1,2], Xiafei Tang[1]*, Yuxiang Chen[1], Jialong Wu[1] and Yudong Tan[3]

[1]School of Electrical and Information Engineering, Changsha University of Science and Technology, Changsha, China, [2]Hunan Key Laboratory of Energy Perception and Edge Computing, Hunan City University, Yiyang, China, [3]State Grid Hunan Electric Power Company Limited Economic, Technical Research Institute, Changsha, Hunan, China

With the rapid construction of charging stations (CSs), charging station operators need to enhance their core competitiveness by precisely planning their service areas and formulating reasonable and effective pricing strategies. However, the regional competition among multiple charging station operators is generally ignored. In the traditional model, the service scope of CSs appears as regular circles, which is inconsistent with the market distribution law. In response to the irregular relationship between the dynamic service scope of CSs and the real-time charging price, a charging station service scope (CSSS) model is proposed by introducing the variable service field strength (SFS). First, the competitiveness of CSs is evaluated quantitatively, and the SFS of CSs is defined to describe the service scope of CSs by the strongest occupation method. Second, the impact of the charging price on the charging demand is analyzed based on the CSSS division model. In addition, the revenue of charging station operators and the stability of the power grid are considered to establish a real-time pricing optimization model. Finally, the numerical simulation is operated in Furong District of Changsha. It is shown that the proposed method effectively achieves more profits for charging stations and decreases the average power deviation of the whole region.

KEYWORDS

charging stations, service field strength, service scope, real-time pricing strategy, strongest occupation method

1 Introduction

The electric vehicle (EV) market has experienced rapid growth since the latter half of 2020. The global sales of EVs exceeded 10 million units in 2022, and it is expected to exceed 70 million units by 2030. EVs have a penetration rate of up to 79.3% in Norway, ranking first in the world. Sweden ranks second globally, with EVs accounting for 32.1%. In addition, China ranks third in the world, with EVs accounting for 19.9% (ITF, 2022; Liu, 2022). As the public infrastructure of power supply, charging facilities play a critical role in the promotion of EVs. The China Electric Vehicle Charging Infrastructure Promotion Alliance (EVCIPA) released that the charging infrastructure increased up to 2.593 million units in 2022, increasing by 225.5% year-on-year (China News Network, 2023), which reflects the fierce competition in the charging station (CS) industry. In addition, the service scope could be

expanded by various parameters, such as advanced charging piles, large contracts, and low-cost charging prices (CPs) (Liu et al., 2019; Yang et al., 2022; Zhou et al., 2023a). Thus, it is necessary to propose the precise division of service scope and reasonable pricing strategies to enhance the core competence among charging station operators.

The service scope of CSs reflects the market competitiveness of CSs directly, which is important for its operators to analyze the market situation (Chen et al., 2019a; Wang et al., 2019). However, recent works seldom discuss the service scope of CSs. Their service scope research is mainly in target with airports (Anna et al., 2019), logistics parks (Wu et al., 2016), and urban economic zones (Dai, 2018). Notably, an inevitable market competition exists among multiple CSs in the region (Li et al., 2023a), and this competition also leads to an uneven market distribution. At present, most present facility planning methods are based on the Wilson model or breaking point theory by the regularized circle or the weighted Voronoi diagram (Chen et al., 2017; Li et al., 2023b), which can only divide the market area within a fixed range. Unfortunately, the symmetrically distributed shape cannot precisely describe the service scope of CSs in terms of practical reality (Zhou et al., 2023b). Thus, a reasonable service scope of the charging station is inevitably irregular and varies with the relevant parameters. Furthermore, the Isard method, i.e., the strongest occupation method (Wilson, 1972), is used to quantify the attraction strength of CSs and further recognize the service scope in this paper.

The real-time charging price has a great influence on the charging habits of EV users (Chen et al., 2019b; Gong et al., 2020), which further affects the service scope of CSs. An effective charging pricing strategy should aim to achieve four objectives, namely, guiding EV users to charge in an orderly manner, increasing the profits of operators, improving the utilization rate of charging piles, and reducing the load peak–valley difference (Yang et al., 2021; Zhou et al., 2022). Considering the willingness of the users (CA et al., 2022; Khan et al., 2022), the demand-side response (Shinde and Shanti, 2018; Lai et al., 2023), and the complex time-varying relationship between the charging price and charging demand (Wang et al., 2021; Yang et al., 2023), various models have been proposed to formulate a real-time pricing strategy. However, the existing literature often neglects the impact of a dynamic charging price on the market division, resulting in no changes in service scope.

On the basis of the abovementioned work, this paper studies the service scope division and real-time pricing strategy of CSs based on the Isard method. First, an evaluation index system is established to quantitatively evaluate the comprehensive strength of CSs. Then, the charging station service scope (CSSS) model with the service field strength of CSs is built based on the Isard method. Second, the impact of the charging price on the charging demand is analyzed based on the initial CSSS division. Third, a dynamic charging price strategy is proposed considering the profit of the CSs and the auxiliary service of the power grid. Finally, the relationship between the charging price and the service scope is analyzed in a real-world scenario to provide reasonable pricing suggestions for CS operators. It is significant for enhancing the operational efficiency of CSs and promoting the healthy development of charging infrastructure. The contributions of this paper are as follows.

1) The CSSS division model is built to describe the dynamic service scope of CSs.
2) The impact of the charging price on the charging demand is analyzed based on the charging station service scope.
3) The real-time charging price is formulated via multi-objective optimization with the goals of increasing operator revenue and decreasing power deviation to modify the charging station service scope.

The rest of this paper is organized as follows: Section 2 defines the service field strength (SFS) and builds the CSSS division model based on the Isard method; Section 3 shows the impact of the charging price on the charging demand; Section 4 establishes a real-time pricing optimization model with multi-objectives including the power deviation rate and the operator profitability; the case study and conclusion are presented in Section 5 and 6, respectively.

2 SFS and CSSS division model based on the strongest occupation method

2.1 Comprehensive strength of CSs

The CSSS is closely related to its comprehensive strength. The evaluation index system for the comprehensive strength of CSs is shown in Figure 1, mainly including the contract capacity of CSs, the number of fast/slow charging piles, service fees, and charging prices.

In Figure 1, the contract capacity and the number of fast/slow charging piles are positive factors. The higher the value of these factors, the stronger the comprehensive strength C_n of CSs. It also indicates a stronger attraction to the surrounding demand area, where more users are willing to go to CS_n for charging, resulting in a larger service scope S_n. Conversely, the charging price and service fees are negative factors. The higher the value, the smaller the CSSS.

The evaluation indicators are standardized by the extreme value method as follows. The positive and negative indicators are standardized, as shown in Eqs 1, 2, respectively:

$$T_{n,i} = \frac{T_{n,i} - T_{\min,i}}{T_{\max,i} - T_{\min,i}}, \tag{1}$$

$$T_{n,i} = \frac{T_{\min,i} - T_{\mathrm{n},i}}{T_{\max,i} - T_{\min,i}}, \tag{2}$$

where $T_{n.i}$ is the original value of index i of CS_n and $T_{\max.i}$ and $T_{\min.i}$ represent the maximum and minimum values of index i, respectively.

The contribution of CS_n is calculated with index i, as shown in Eq. 3:

$$p_{n,i} = \frac{T_{n,i}}{\sum_{i=1}^{N} T_{n,i}}, \tag{3}$$

where $p_{n.i}$ is the contribution of CS_n with index i and N is the number of CSs.

The entropy of index i is calculated as shown in Eq. 4:

$$e_i = -\frac{1}{\ln N} \sum_{i=1}^{N} p_{n,i} \ln\left(p_{n,i}\right). \tag{4}$$

The evaluation index weight of CSs could be obtained as shown in Eq. 5:

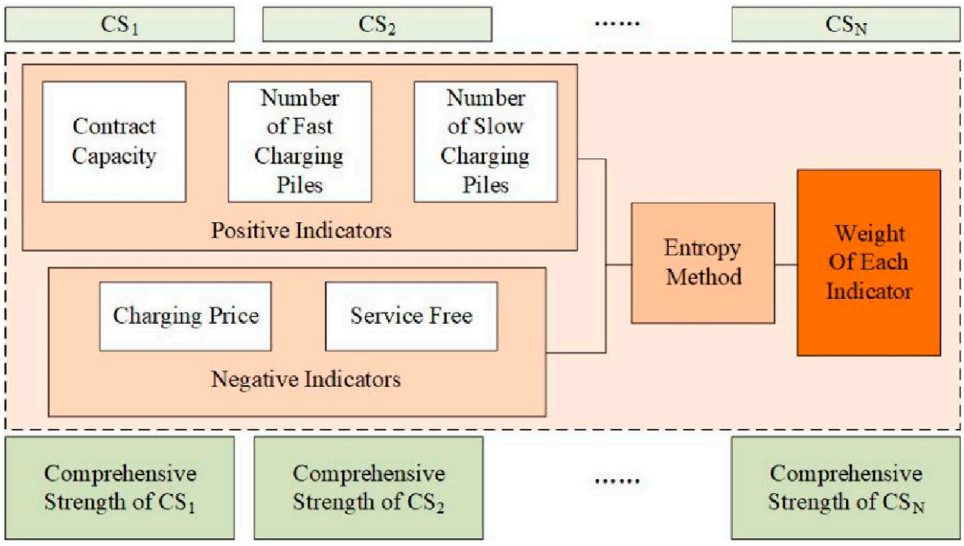

FIGURE 1
Charging station evaluation index system.

$$\gamma_i = \frac{g_i}{\sum_{i=1}^{N} g_i}, \tag{5}$$

$$g_i = 1 - e_i, \tag{6}$$

where γ_i is the weight of index i and g_i and e_i are the coefficients of difference and entropy, respectively.

Then, the comprehensive strength of CS_n could be quantified as shown in Eq. 7:

$$C_n = \sum_{i=1}^{5} c_i \gamma_i \frac{T_{n.i}}{T_{\max.i}}, \tag{7}$$

where C_n represents the comprehensive strength of CS_n and c_i indicates the correlation coefficient. $c_i = 1$ when γ_i is positive, and $c_i = -1$ if γ_i is negative.

2.2 Definition of SFS

The formula of the point charge field strength is obtained by Eq. 8:

$$E_e = k_e \frac{q_e}{r_e^2}, \tag{8}$$

where E_e represents the point charging field strength, k_e is the electrostatic force constant with the unit $N{\cdot}m^2/C^2$, q_e is the charge electric quantity, and r_e indicates the distance between the center and charge.

Analogous to the electrostatic field generated by a point charge, the attraction of CSs to the surrounding area will not change abruptly, in accordance with the characteristics of the typical non-rotating scattered field. According to the Helmholtz theorem, the function of the non-rotating scattered field is always inversely proportional to the distance vector R^2. Therefore, the SFS of the CSSS, akin to the electric field strength of a point charge, is defined to quantify the attraction strength of CSs to the surrounding charging demand areas (CDAs).

It is assumed that a certain area is divided into K small grid areas with a certain precision, which is defined as CDAs. Taking CS_n as the center, SFS $E_{n.k}$ of CS_n for CDA_k is defined considerating the average distance and the comprehensive strength, which is obtained by Eq. 9:

$$E_{n.k} = k_c \frac{C_n}{r_{n.k}^2}, \tag{9}$$

where k_c is the service constant and $r_{n.k}$ represents the distance between CS_n and CAD_k, which can be calculated by the longitude and latitude.

The Wilson model is appropriate for studying spatial interactions (Zhang et al., 2010). Thus, the charging service capacity ratio of CS_n to CDA_k can be described as shown in Eq. 10:

$$T_{n.k} = KC_nD_ke^{-\beta r_{n.k}}, \tag{10}$$

where K represents the normalization factor, describing the regional difference of the CSs and the demand area. $K = 1$ when the regional difference is ignored. D_k indicates the total charging demand in CDA_k. β is the attenuation factor, determining the speed of service attenuation.

Combined with the electrostatic force constant k_e, and assuming each CS has the same service constant, k_c is derived as follows:

$$k_c = \frac{KC_{ave}D_{ave}e^{-\beta r_{ave}}r_{ave}^2}{C_{ave}^2}, \tag{11}$$

$$\beta = \sqrt{\frac{2N}{t_{\max}S_{ave\_n}}}, \tag{12}$$

where C_{ave} is the average comprehensive strength of all CSs, D_{ave} represents the average demand of all demand areas, and r_{ave} is the average distance between the CSs and demand areas. Calculated

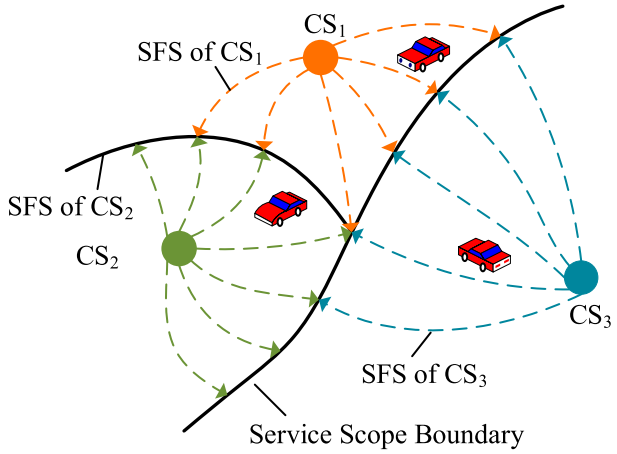

FIGURE 2
Charging station service scope diagram.

using Statistical Product and Service Solutions (SPSS) software, $t_{\max}$ represents the number of CSs with a comprehensive score greater than 0. S_{ave_n} represents the average area of each CS served.

2.3 CSSS division model

In the two-dimensional space, a facility or an enterprise is attractive to the users within a certain range of its surroundings, catering to their needs and preferences. Similarly, as the charging service provider, the CSs act as the central hub, offering charging service to electric vehicle users in their vicinity. Then, CSSS, defined as the geographical spatial distribution range of electric vehicle users who receive charging services from that CS, is usually of an irregular shape, as shown in Figure 2. Notably, the dotted line represents the SFS emitted by CSs, and the CSs are attractive to EVs at the same time.

Any CS_n will attract the CDAs, resulting in a CSSS that is constrained by the parameters of the surrounding CS and itself. According to the strongest occupation method proposed by Isard, if SFS $E_{n.k}$ of CS_n to the demand area k is larger than SFS $E_{m.k}$ of other CS_m, the demand area k is identified as the CSSS of CS_n, as shown in Eq. 13:

$$S_n = \{S \mid E_{n.k} \geq E_{m.k}, m = 1, ..., N\,(m \neq n)\}, \tag{13}$$

where S_n represents the CSSS of CS_n and the demand area k is defined as the market demand area. Eq. 13 indicates that among all CSs, CS_n has the greatest attraction to the demand area k, and the demand area k belongs to the CSSS of CS_n.

3 CSSS-based charging demand

The initial CSSS $S^* = (S^*_1, S^*_2, \ldots, S^*_N)$ is obtained from Eq. 13. Ignoring the difference between areas, the initial charging demand proportion is determined by the CSSS. In addition, the initial charging demand proportion is shown in Eq. 14.

$$\lambda_{n.t} = \frac{S^*_n}{\sum_{n=1}^{N} S^*_n}. \tag{14}$$

The charging demand of CS_n is jointly affected by its own charging price and the price of other CSs, as shown in Eq. 15. The charging demand is a negative correlation function of its own price. As the charging price increases, the charging demand for CS_n decreases and shifts to other CSs in the area, which results in the CSSS reduction in CS_n and the CSSS increase in other CSs.

$$q_{n.t} = \lambda_{n.t} q_{ev.t} - k_{p.n}\left(\frac{P_{n.t} - P_{r.t}}{P_{r.t}}\right) + k_{av.n}\frac{\left(\sum_{\substack{m=1 \\ m \neq n}}^{N-1} C^*_m P_{m.t}\right) - P_{r.t}}{P_{r.t}}, \tag{15}$$

where $q_{ev.t}$ represents the predicted value of the day-ahead charging load at time t. $k_{p.n}$ is the influence parameter of the policy price difference between the CS price and policy price on the charging demand. In addition, $k_{av.n}$ indicates the influence parameter of the charging price difference between CS_n and other CSs. $P_{n,t}$ represents the charging price of CS_n at time t, and $P_{r.t}$ represents the policy electricity price at time t, satisfying the peak–valley–flat electricity price. C_m* is the ratio of the comprehensive strength of CS_m to the sum of all CSs.

The income of CSs in a day is shown in Eq. 16.

$$E_n = \sum_{t=1}^{96} P_{n.t} \cdot q_{n,t}, \tag{16}$$

where E_n is the income of CS_n in a day.

The proof of the existence and uniqueness of the Nash equilibrium of the proposed model is given in Appendix A.

4 CSSS-based real-time pricing optimization model

4.1 Pricing optimization model

In a scenario of a perfectly competitive market, it is assumed there are N CSs with different sizes, which belong to H different operators, $H \leq N$. All charging loads are evenly distributed throughout the area; users will only choose one of the N CSs to charge when needed.

A multi-objective real-time pricing model is established considering the profit rate and power deviation rate. The objective is optimized by maximizing the total profit rate of all CSs and minimizing the power deviation rate, as shown in Eq. 17.

$$\max E = \max\left(\omega_n E_{p\_lr} + \omega_{bc} E_{p\_pc}\right), \tag{17}$$

$$E_{p\_lr} = \sum_{t=1}^{T}\sum_{n=1}^{N} \frac{P_{n.t} - (P_e + P_{n.w})}{P_{r.t}}, \tag{18}$$

$$E_{p\_pc} = \sum_{t=1}^{T} \frac{\Delta P_t - \left(\sum_{n=1}^{N} q_{n.t} - q_{ev.t}\right)}{\Delta P_t}, \tag{19a}$$

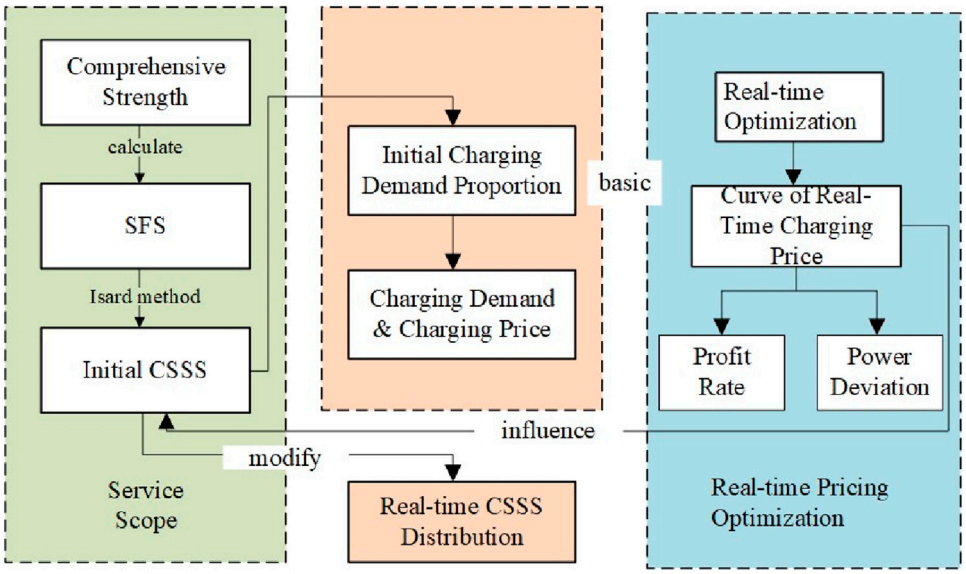

FIGURE 3
Real-time pricing optimization model based on charging station service scope (CSSS) and solution flowchart.

$$\Delta P_t = P_{W.t} + P_{L.t} - P_{w.t} - P_{l.t}, \tag{20a}$$

where E_{p_lr} and E_{p_pc} represent the profit rates of the CS and the reduced power deviation rate, respectively. ω_n and ω_{ab} represent the weights of the above two, respectively. P_e and $P_{n.w}$ are the electricity purchasing cost and the operation and maintenance cost of the CS, respectively. ΔP_t is the power deviation between the real-time output of renewable energy and the day-ahead forecast. $P_{W.t}$ and $P_{w.t}$ are the real-time and day-ahead wind power output, respectively. $P_{L.t}$ and $P_{l.t}$ are the real-time and day-ahead photovoltaic outputs, respectively. If $\Delta P_t > 0$, indicating that the real-time output of wind power and photovoltaic at time t is greater than the predicted output, it is necessary to guide users to charge and increase the charging load to absorb the excess wind and photovoltaic power. Otherwise, if $\Delta P_t < 0$, indicating that the real-time output of wind and photovoltaic power at time t is less than the day-ahead predicted output, users need to be encouraged to reduce the charging load.

The constraints of optimization model are as follows:

Market demand constraint

$$0 < q_{n.t} < q_{ev.t}. \tag{21}$$

Eq. 21 implies that the charging demand of the CS does not exceed the predicted charging load.

Charging load constraint

$$\xi_l q_{ev.t} \le \sum_{n=1}^{N} q_{n.t} \le \xi_h q_{ev.t}, \tag{19b}$$

where ξ_l and ξ_h represent the lower and upper limit coefficients, respectively, which means that the sum of the charging demand should not exceed a certain range of the day-ahead charging load.

Charging price constraint

$$P_{r.n}(1 - \varphi_l) \le P_{n.t} \le P_{r.n}(1 + \varphi_h), \tag{20b}$$

where φ_l and φ_h represent lower and upper limits of the charging price, respectively.

4.2 Relationship between CSSS and real-time pricing

The basic idea of a real-time pricing optimization model based on CSSS is shown in Figure 3. First, the initial CSSS was obtained by the strongest occupation method. Then, based on the pricing optimization model, the charging station operator obtains the real-time charging price of charging stations, which affects the initial CSSS, and further develops into the real-time CSSS.

The detailed steps of real-time pricing optimization based on CSSS are designed as follows:

Step 1: The CSSS is calculated

1) Based on the basic data on CSs and the day-ahead wind power and photovoltaic predicted data, the weight of each index was calculated according to the entropy method, and the real-time output data of wind power and photovoltaic were obtained by adding the power deviation.
2) The comprehensive strength of CSs was quantitatively evaluated according to Eq. 7, and then SFS $E_{n.k}$ of each CS was calculated according to Eq. 9.
3) According to Eq. 13, the initial CSSS S^*_n based on the strongest occupation method proposed by Isard was obtained.
4) The initial charging demand proportion λ was calculated, as shown in Eq. 14.
5) The relationship between the charging price and charging demand was established, and the CS income model was built, as shown in Eqs 15, 16.

Step 2: The real-time price is optimized

TABLE 1 Basic data on charging stations (CSs).

	Contract capacity (kWh)	Number of fast-charging piles	Number of slow-charging piles	Service fee (yuan)	Longitude (°)	Latitude (°)
CS1	1,000	23	0	0.29	112.98879	28.202264
CS2	1,000	18	5	0.3	113.08703	28.202149
CS3	1,830	15	10	0.4	113.0064	28.19503
CS4	715	10	15	0.4	113.02054	28.21223
CS5	1,000	15	8	0.29	113.06240	28.20092
CS6	1,250	13	15	0.8	113.04103	28.19882
CS7	45,880	0	20	0.4	113.08266	28.18040
CS8	630	4	6	0.62	113.03552	28.20279

1) The multi-objective real-time pricing model with the profit rate and power deviation was built.
2) A day was divided into 96 time points at a resolution of 15 min, taking 1 h as the operation cycle and optimizing the pricing model using CPLEX. Then, the dynamic charging price of CSs at 96 time points, as well as the optimized profit rate and power deviation rate of each CS, was obtained.
3) With the real-time change in the dynamic charging price, the comprehensive strength and the SFS of the CS will also change. Finally, the real-time dynamic CSSS at each time was simulated and obtained

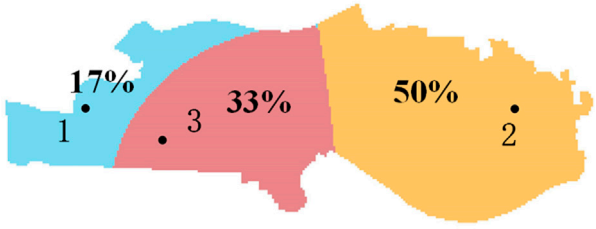

FIGURE 4
Initial service scope of three charging stations.

5 Case study

5.1 Basic data

Furong District in Changsha is taken as an example for simulation, and the data on CSs are all obtained from Hunan Economic and Technological Research Institute of the State Grid. Notably, the output data of wind power and photovoltaic are for the total province. First, the map of Furong District is divided into 16,288 market areas with latitude and longitude accuracy of 0.0005 using ArcGIS drawing software. Then, the first three representative CSs are selected from Furong District for calculation as examples. The basic data of these three CSs are shown in Table 1. Based on the evaluation index system, the weight of each index of the CS is obtained by the entropy method. The weight of the contract capacity, the number of fast/slow-charging piles, the service fee, and the charging price are 0.221, 0.486, 0.201, 0.051, and 0.041 yuan/kWh, respectively. Afterward, SPSS is employed for the factor analysis. A total of 143 CSs have a comprehensive score greater than 0.

For the load of the three charging stations $q_{1,t}$, $q_{2,t}$, and $q_{3,t}$, its boundary is given by setting $\xi_l = 0.8$ and $\xi_h = 1.2$ in Eq. 19a and $\varphi_l = \varphi_h = 0.1$ in Eq. 20a. In addition, according to the related policy issued by the Comprehensive Department of the National Energy Administration, the electricity purchasing price in Hunan Province is 0.46244 yuan/kWh. The daily maintenance cost of each CS is $P_{1.w}$ = 600 yuan, $P_{2.w}$ = 550 yuan, and $P_{3.w}$ = 500 yuan. Based on the project data, the day-ahead wind power and photovoltaic output data of a typical day are shown in Supplementary Figure AB1. It is assumed that the wind power and photovoltaic prediction error is 10%, and the real-time output meets the normal distribution.

5.2 Analysis of the charging price

Without considering the interaction of the charging price, the initial CSSS and occupancy of each CS are calculated based on the strongest occupation method, as shown in Figure 4.

As shown in Figure 4, the CSSS of CS_2 is the largest without considering the influence of the charging price. It is noted that CS_2 has the largest number of fast charging piles, and also, no other competing CS is present in the surrounding area. Thus, its CSSS occupies half of Furong District. As shown in Table 2, the comprehensive strength of CS_1 is the strongest. However, due to the remote location and the competition from CS_3, the CSSS of CS_1 only occupied 17% of the market share and is smallest among the three CSs. In addition, from the shape of the CSSS of CS_1 and CS_3, the boundary presents an inward curved arc, which indicates that the further away from the two CSs, the more area belongs to CS_1. That is, compared to CS_3, the distance from one point to CS_1 is larger, but it is still attracted by CS_1. Therefore, it can be concluded that the SFS of CS_1 is greater than that of CS_3. The average peak–valley–flat charging price of CSs is then calculated by the real-time pricing optimization model mentioned in Section 4, as shown in Table 2.

TABLE 2 Comprehensive strength and average charging price of three charging stations (CSs).

	Comprehensive strength	Valley period (yuan/kW)	Flat period (yuan/kW)	Peak period (yuan/kW)	Optimized profit rate %	Profit rate of policy price %
CS1	0.4480	0.3842	0.9958	1.5979	61.74	59.92
CS2	0.3557	0.3923	0.9929	1.5957	62.68	61.92
CS3	0.3039	0.4021	1.0235	1.6137	63.27	61.58
Policy price	\	0.4	1.0	1.6	\	\

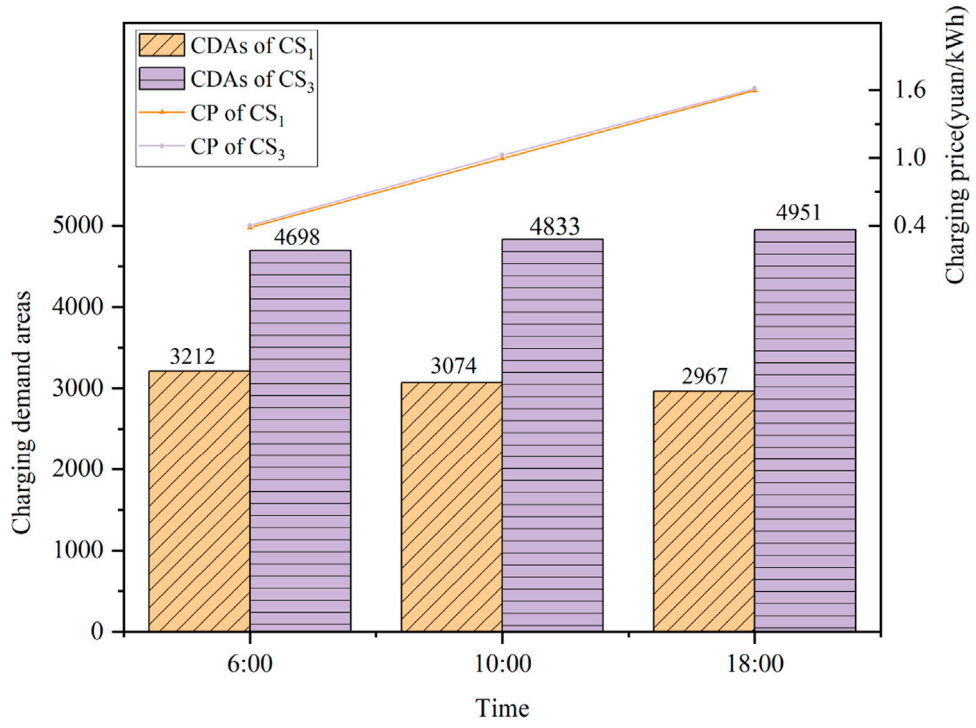

FIGURE 5
Number of charging demand areas and charging price of three charging stations.

Table 2 shows that the charging prices of CS_1 and CS_2 are lower than the policy price, while the charging price of CS_3 is higher than the policy price. Due to the higher comprehensive strength of CS_1 and CS_2, the electric vehicle users will pay more attention and be more sensitive to price changes. Accordingly, the influence parameter of the policy price difference $k_{p.n}$ in Eq. 16 is also larger, indicating that charging prices can increase the charging demand and profit if they are lower than the policy price. In comparison, the comprehensive strength of CS_3 is the smallest, and users pay the least attention to its price change. Thus, CS_3 will maintain its income by setting a higher price than the policy price, increasing by 0.0137 yuan/kWh during the peak period and 0.0235 yuan/kWh during the flat period.

Then, the change in CDAs is analyzed for the peak, valley, and flat periods, and three time points of 6:00, 10:00, and 18:00 are selected. The number of CDAs occupied by each CS at these time points is shown in Supplementary Figure AB2. It is observed that there is no significant change in the CSSS of CS_2 due to the small competitive pressure. On the contrary, the CSSS changed with the charging price mainly for CS_1 and CS_3. Therefore, the CSSS changes for CS_1 and CS_3 are discussed as primary. The number of CDAs occupied by CS_1 and CS_3 and their CP changes are shown in Figure 5.

Afterward, the real-time charging price is taken into consideration. Since charge station 1 has a higher comprehensive strength and a small charging price difference of 0.02 yuan, the market share increases from 17% in Figure 4 to 20% (the number of CDAs is 3,212 at 6:00). Correspondingly, CS_3, which is closer to CS_1, lost part of its CSSS due to its smaller comprehensive strength, and its market share decreased from 33% to 29%.

With the increase in the charging price, the number of CDAs occupied by CS_1 decreased by 245 from 6:00 to 18:00. At the same time, the number of CDAs occupied by CS_3 increased by 253. This can be attributed to the fact that CS_1 has stronger comprehensive strength, and users are more responsive to its charging price changes. Thus, as the charging price of charge

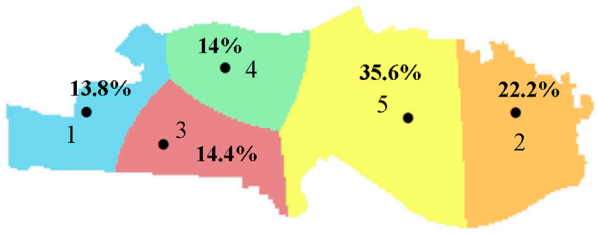

FIGURE 6
Initial service scope of five charging stations.

station 1 increases, the number of users of CS_1 decreases faster than those of CS_3, resulting in a more significant change in the CSSS of CS_1.

It can be seen that the charging price and CSSS are affected by many factors, such as comprehensive strength, geographical location, and number of competitors around.

5.3 Analysis of the number of charging stations

The impacts of the number of CSs on the CSSS, power deviation rate, and profit margin are analyzed to verify the relevant conclusions given in Section 5.2. Taking five CSs and eight CSs as examples, the data of CSs are shown in Table 1.

5.3.1 Analysis of five CSs

Without considering the interaction of the real-time charging price, the initial CSSS and the market share of five CSs are shown in Figure 6. It was notes that the density of CSs in the western region is relatively high. CS_1, CS_3, and CS_4, due to their close distribution and fierce market competition, have a limited CSSS, and their market share is 13.8%, 14.4%, and 14%, respectively. However, only CS_2 and CS_5 exist in the eastern region, and they are located far from the CSs in the west, resulting in less competition. Therefore, the CSSS of CS_2 and CS_5 is relatively large, and their market share is 22.2% and 35.6%, respectively.

The charging price and comprehensive strength of five CSs are calculated and shown in Table 3. It is found that CS_4, with smaller comprehensive strength, has higher charging prices than the other CSs in each period. It can gain more profits by setting a higher charging price than the policy price. However, with higher comprehensive strength, CS_1 and CS_2 can obtain more charging demand and profit with a lower charging price.

Similarly, three time points of 6:00, 10:00, and 18:00 are selected for simulation, and the number of CDAs occupied by each CS is shown in Figure 7. It is observed that the CSSS of CS_3 increases 89 CDAs and the CSSS of CS_4 decreases 207 CDAs with the increase in the charging price. The reason for such a great change is that CS_3 and CS_4 have weak comprehensive strength, and they are in the center of a region surrounded by many CSs.

5.3.2 Analysis of eight CSs

The initial CSSS of eight CSs is calculated, as shown in Figure 8. It can be seen that, interestingly, due to the strong comprehensive strength and the remote location, the market share of the CS_1 is unchanged compared to the condition of the five charging stations. However, CS_8 has the smallest comprehensive strength and is close to the other CSs, making the CDAs less competitive than other CSs, resulting in a very small CSSS, and its market share is only 0.2%.

The charging price and comprehensive strength of eight CSs are shown in Table 4. Due to higher user attention, CSs with larger comprehensive strength have lower real-time charging prices than policy electricity prices. However, CSs with smaller comprehensive strength will set higher real-time charging prices to ensure profits.

The number of CDAs occupied by eight CSs is shown in Figure 9. With the increase in the number of CSs, market competition becomes increasingly fierce. Furthermore, the reduction in the distance between stations results in little difference in the CSSS, and CS_5, with the largest CSSS, does not account for more than 4,000 CDAs. Meanwhile, due to the weak market competitiveness of CS_7 and CS_8, the CDAs of CS_2, CS_5, and CS_6 account for more than half (58%). Compared to the scenario of five CSs, due to the addition of CS_6, the number of CDAs of CS_3 and CS_4 has decreased, while CS_1, with the strongest market competitiveness, has not been affected, and the CSSS has not changed. With the increase in the charging price, it is observed that the CSSS of CS_4, CS_7, and CS_8 decreased due to the weak market competitiveness, and the CSSS of CS_1, CS_2, and CS_5 increased due to the strong market competitiveness. In addition, the insignificant change in CSSS of CS_3 and CS_4 is mainly because they are in the center of a region surrounded by other CSs.

Table 5 presents the profit rate and power deviation rate of different CSs. It is noted that the profits obtained by the policy electricity price will decrease gradually with the increase in

TABLE 3 Comprehensive strength and average charging price of five charging stations (CSs).

	Comprehensive strength	Valley period (yuan/kW)	Flat period (yuan/kW)	Peak period (yuan/kW)	Optimized profit rate %
CS1	0.4756	0.3852	0.9865	1.5768	65.65
CS2	0.3834	0.3901	0.9909	1.589	65.35
CS3	0.3329	0.3953	0.9972	1.5921	64.32
CS4	0.2359	0.4196	1.0413	1.6592	66.07
CS5	0.3290	0.4056	1.0237	1.6264	64.41

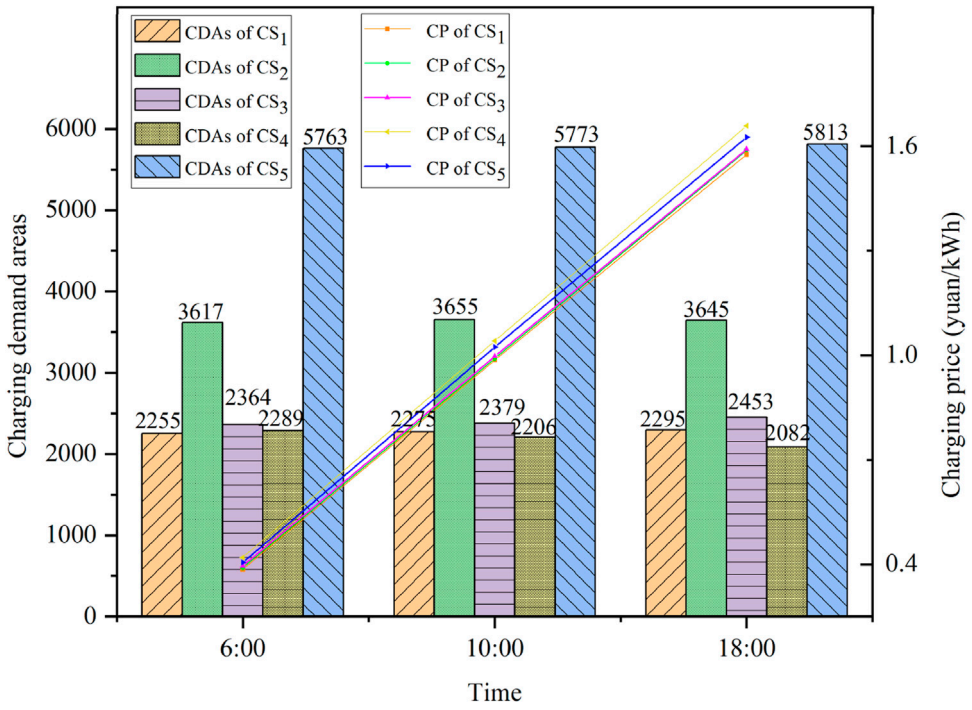

FIGURE 7
Number of charging demand areas and charging price of five charging stations.

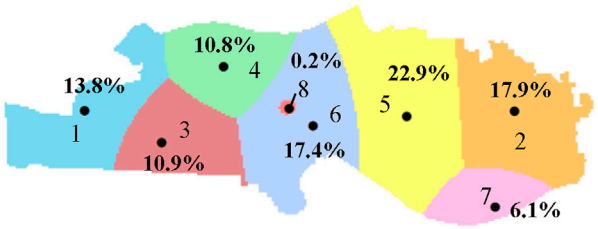

FIGURE 8
Initial service scope of eight charging stations.

competitive CSs. Furthermore, when the number of CSs involved in real-time pricing optimization increases from 3 to 5 and 8, the profit margin increases by 2.60% and 4.05%, respectively; meanwhile, the power deviation decreases by 764 kW and 1,309 kW, respectively. That is because the increase in CSs expands the optimize adjustment space. Consequently, the total charging demand participating in optimization increases, and the profit distribution between CSs becomes more reasonable, which improves the CS profit rate significantly and reduces the power deviation of wind and photovoltaic power. However, for this case, the adjustment effect of power deviation is not obvious for all of Hunan Province because of the small number of CSs.

TABLE 4 Comprehensive strength and average charging price of eight charging stations (CSs).

	Comprehensive strength	Valley period (yuan/kW)	Flat period (yuan/kW)	Peak period (yuan/kW)	Optimized profit rate %
CS1	0.4756	0.3965	0.9623	1.5725	66.62
CS2	0.3834	0.3962	0.9689	1.5766	65.89
CS3	0.3329	0.397	0.9717	1.5839	65.53
CS4	0.2359	0.4012	1.033	1.6377	66.47
CS5	0.3290	0.3974	0.9779	1.5912	65.21
CS6	0.2812	0.3981	0.9896	1.5987	65.05
CS7	0.2566	0.4023	1.0586	1.6531	67.08
CS8	0.0724	0.4132	1.0886	1.7	68.46

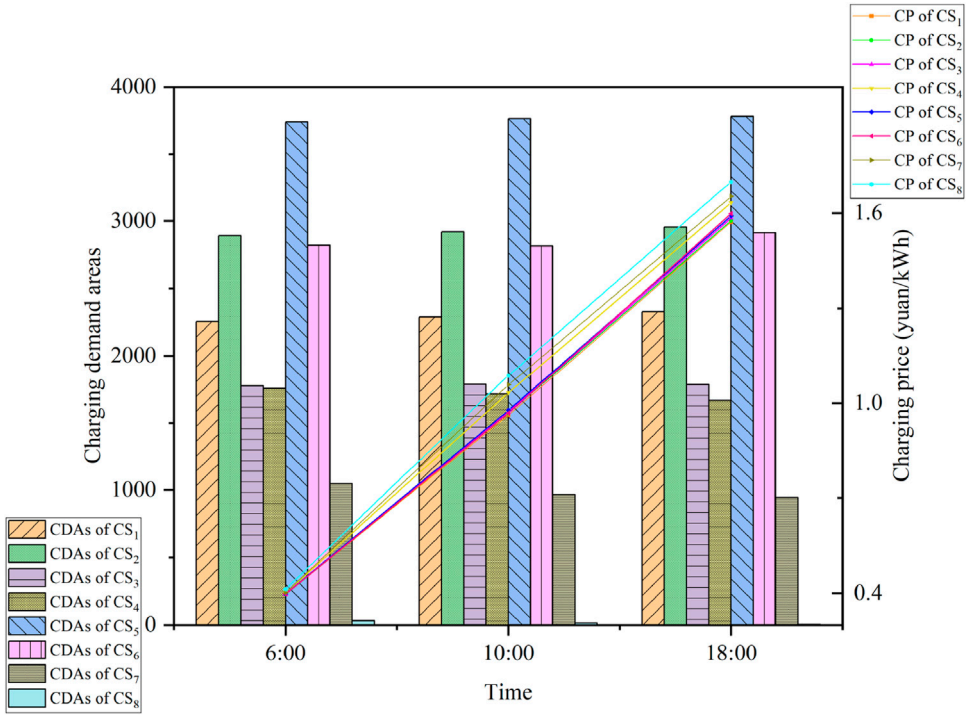

FIGURE 9
Number of charging demand areas and charging price of eight charging stations.

TABLE 5 Profit rate and power deviation rate of different charging stations (CSs).

Number of CSs	Average optimized profit rate %	Average profit rate of policy price %	Average power deviation (10,000 kW)
Three CSs	62.56	61.14	36.3536
Five CSs	65.16	60.21	36.2808
Eight CSs	66.28	58.20	36.2263

6 Conclusion

A dynamic CSSS division model is proposed based on the strongest occupation method and pricing strategy in this paper. Notably, the variation in the CSSS is well simulated by the dynamic optimization of the charging price. Then, the relationship among the comprehensive strength, the charging price, and the charging demand is well reflected. Furong District of Changsha is simulated as an example, and the following conclusions are obtained:

1) Charging stations with greater comprehensive strength attract more attention from electric vehicle users, and users are more sensitive to the fluctuation of their charging price. Therefore, the charging station can obtain more profits by setting a lower charging price than the policy price.
2) The competition is more intense for areas with dense charging stations, and the CSSS change caused by charging price fluctuation is also more obvious. On the contrary, the CSSS is more stable with sparse charging stations, and the charging price fluctuation has less impact on the CSSS. It provides a reference for the construction of future charging facilities for operators.
3) With the increase in charging stations participating in the market competition, the profit based on the policy price will gradually decrease. Thus, the profit of charging stations should be improved by setting a real-time charging price based on the CSSS.

It should also be pointed out that the CSSS model should comprehensively consider the influence of regional differences, such as traffic conditions and geographic information, to improve the accuracy and authenticity of simulation results. Thus, the establishment of a complete CSSS model with the regional evaluation index system will be the next topic in future research.

Data availability statement

The original contributions presented in the study are included in the article/Supplementary Material; further inquiries can be directed to the corresponding author.

Author contributions

XY: Formal analysis, Writing–original draft. XT: Methodology, Writing–review and editing. YC: Validation, Writing–review and editing. JW: Data curation, Software, and Writing–original draft. YT: Visualization and writing–review and editing

Funding

The author(s) declare that financial support was received for the research, authorship, and/or publication of this article. This research was funded by the National Natural Science Foundation of China (grant numbers 52277076 and 52307081). Hunan Provincial Nature Science General Project (grant number S2024JJMSXM1107). Excellent Youth Program of Hunan Provincial Department of Education (grant number 23B0334)

Conflict of interest

Author YT was employed by State Grid Hunan Electric Power Company Limited.

The remaining authors declare that the research was conducted in the absence of any commercial or financial relationships that could be construed as a potential conflict of interest.

Publisher's note

Supplementary material

The Supplementary Material for this article can be found online at: https://www.frontiersin.org/articles/10.3389/fenrg.2024.1378016/full#supplementary-material

References

Anna, B., Maurizio, C., and Davide, V. (2019). Scale and (quasi) scope economies in airport technology. An application to UK airports. *Transp. Res. Part A Policy and Pract.* 125 (C), 150–164. doi:10.1016/j.tra.2019.05.013

Ca, M. M., Grzanic, M., Pavic, I., Pandžić, H., and Capuder, T. (2022). The effects of household automation and dynamic electricity pricing on consumers and suppliers. *Sustain. Energy, Grids Netw.* 32, 100931. doi:10.1016/j.segan.2022.100931

Chen, C. S., Xiao, L. L., Duan, S. X., and Chen, J. (2019a). Cooperative optimization of electric vehicles in microgrids considering across- time- and- space energy transmission. *IEEE Trans. Industrial Electron.* 66 (2), 1532–1542. doi:10.1109/tie.2017.2784410

Chen, J., Huang, X. Q., Tian, S. M., Cao, Y., Huang, B., Luo, X., et al. (2019b). Electric vehicle charging schedule considering user's charging selection from economics. *IET Generation, Transm. Distribution* 13 (15), 3388–3396. doi:10.1049/iet-gtd.2019.0154

Chen, Y. T., Zeng, X. Z., and Wang, J. X. (2017). Airport service scope research based on improved Wilson model. *J. East China Jiaot. Univ.* 34 (05), 56–64. doi:10.16749/j.cnki.jecjtu.2017.05.009

China News Network (2023). China electric vehicle charging infrastructure promotion alliance: rapid growth of China's charging infrastructure. http://www.ce.cn/xwzx/gnsz/gdxw/202301/12/t20230112_38343857.shtml.

Dai, D. (2018). Selection of central cities and influence area of Yangzi River city cluster based on gravitational model. *Sci. Technol. Perspect.* (28), 290–292.

Gong, L. L., Cao, W., Liu, K. L., and Zhao, J. (2020). Optimal charging strategy for electric vehicles in residential charging station under dynamic spike pricing policy. *Sustain. Cities Soc.* 63 (0), 102474. doi:10.1016/j.scs.2020.102474

ITF Comprehensive electrification and global cooperation under the vision of carbon neutrality. World new energy vehicle congress, Hainan and virtual, August, 2022, 2022,

Khan, K., Sayed, I. E., and Arboleya, P. (2022). Multi-issue negotiation evs charging mechanism in highly congested distribution networks. *IEEE Trans. Veh. Technol.* 71 (6), 5743–5754. doi:10.1109/tvt.2022.3175266

Lai, S. Y., Qiu, J., Tao, Y. C., and Zhao, J. (2023). Pricing for electric vehicle charging stations based on the responsiveness of demand. *IEEE Trans. Smart Grid* 14 (1), 530–544. doi:10.1109/tsg.2022.3188832

Li, Y. B., Wang, J. N., Wang, W. Y., and Liu, C. (2023a). Dynamic pricing based electric vehicle charging station location strategy using reinforcement learning. *Energy* 281, 128284. doi:10.1016/j.energy.2023.128284

Li, Z., Liu, L., Ding, L., Wang, J. Y., Zhang, S. H., Chen, X. X., et al. (2023b). Scenario-based charging infrastructure planning based on tyson' s multilateral graph. *Power Syst. Clean Energy* 39 (3), 131–135.

Liu, H. C. (2022). World new energy vehicle conference: faster, farther, and smarter. *Product. Reliab. Rep.* 2022, 08. (in Chinese).

Liu, S. Q., Cui, W., and Zhang, L. (2019). Research on enterprise bidding mode selection and control strategy. *Clust. Comput.* 22 (6), 14269–14276. doi:10.1007/s10586-018-2285-x

Shinde, P., and Shanti, S. K. (2018). Stackelberg game-based demand response in multiple utility environments for electric vehicle charging. *IET Electr. Syst. Transp.* 8 (3), 167–174. doi:10.1049/iet-est.2017.0046

Wang, J. Y., Bharati, G. R., Paudyal, S., Ceylan, O., Bhattarai, B. P., and Myers, K. S. (2019). Coordinated electric vehicle charging with reactive power support to distribution grids. *IEEE Trans. Industrial Electron.* 15 (1), 54–63. doi:10.1109/tii.2018.2829710

Wang, S. Y., Bi, S. Z., and Zhang, Y. J. (2021). Reinforcement learning for real-time pricing and scheduling control in ev charging stations. *IEEE Trans. Industrial Inf.* 17 (2), 849–859. doi:10.1109/tii.2019.2950809

Wilson, A. G. (1972). Entropy in urban and regional modeling [J]. *Economic Geography* 48 (4), 364–394.

Wu, J. Q., He, R., Li, X., and Gao, T. (2016). Research on the radiation range of logistics park based on improved breakpoint model. *Logist. Eng. Manag.* 38 (11), 13–16+31.

Yang, H. R., Xu, Y. L., and Guo, Q. L. (2023). Dynamic incentive pricing on charging stations for real-time congestion management in distribution network: an adaptive model-based safe deep reinforcement learning method. *IEEE Transaction Sustain. Energy* 10, 1–13. doi:10.1109/tste.2023.3327986

Yang, X. L., Niu, D. X., Sun, L. J., Ji, Z., Zhou, J., Wang, K., et al. (2021). A bi-level optimization model for electric vehicle charging strategy based on regional grid load following. *J. Clean. Prod.* 325, 129313. doi:10.1016/j.jclepro.2021.129313

Yang, X. Y., Guo, X. P., Li, Y., and Yang, K. (2022). The sequential construction research of regional public electric vehicle charging facilities based on data-driven analysis—empirical analysis of Shanxi Province. *J. Clean. Prod.* 380 (1), 134948. doi:10.1016/j.jclepro.2022.134948

Zhang, X. M., Hong, R. Y., Wang, R. J., and Wei, N. (2010). Research on the service capacity of regional logistics parks based on Wilson model. *Logist. Technol.* 29 (Z1), 41–43.

Zhou, Z., Liu, Z. T., Su, H., and Zhang, L. (2023a). Planning of static and dynamic charging facilities for electric vehicles in electrified transportation networks. *Energy* 263, 126073. doi:10.1016/j.energy.2022.126073

Zhou, Z., Liu, Z. T., Su, H. Y., and Zhang, L. (2022). Integrated pricing strategy for coordinating load levels in coupled power and transportation networks. *Appl. Energy* 307, 118100. doi:10.1016/j.apenergy.2021.118100

Zhou, Z., Liu, Z. T., Su, H. Y., and Zhang, L. (2023b). Planning of static and dynamic charging facilities for electric vehicles in electrified transportation networks. *Energy* 263, 126073. doi:10.1016/j.energy.2022.126073

frontiers | Frontiers in Energy Research

TYPE Brief Research Report
PUBLISHED 06 May 2024
DOI 10.3389/fenrg.2024.1391692

OPEN ACCESS

EDITED BY
Yitong Shang,
Hong Kong University of Science and Technology, China

REVIEWED BY
Yikui Liu,
Stevens Institute of Technology, United States
Can Wang,
China Three Gorges University, China

*CORRESPONDENCE
Guangzheng Yu,
powerygz@shiep.edu.cn

RECEIVED 26 February 2024
ACCEPTED 09 April 2024
PUBLISHED 06 May 2024

CITATION
Wang S, Liu H and Yu G (2024), Short-term wind power combination forecasting method based on wind speed correction of numerical weather prediction.
Front. Energy Res. 12:1391692.
doi: 10.3389/fenrg.2024.1391692

Short-term wind power combination forecasting method based on wind speed correction of numerical weather prediction

Siyuan Wang[1], Haiguang Liu[2] and Guangzheng Yu[3]*

[1]Power Dispatching Control Center of State Grid Shaanxi Electric Power Co., Ltd., Xi'an, China, [2]Electric Power Research Institute of State Grid Hubei Electric Power Co., Ltd., Wuhan, China, [3]School of Electrical Engineering, Shanghai University of Electric Power, Shanghai, China

The temporal variation of wind power is primarily influenced by wind speed, exhibiting high levels of randomness and fluctuation. The accuracy of short-term wind power forecasts is greatly affected by the quality of Numerical Weather Prediction (NWP) data. However, the prediction error of NWP is common, and posing challenges to the precision of wind power prediction. To address this issue, the paper proposes a NWP wind speed error correction model based on Residual Network-Gated Recurrent Unit (ResNet-GRU). The model corrects the forecasted wind speeds at different heights to provide reliable data foundation for subsequent predictions. Furthermore, in order to overcome the difficulty of selecting network parameters for the combined prediction model, we integrate the Kepler Optimization Algorithm (KOA) intelligent algorithm to achieve optimal parameter selection for the model. We propose a Convolutional Neural Network-Long and Short-Term Memory Network (CNN-LSTM) based on Attention Mechanism for short-term wind power prediction. Finally, the proposed methods are validated using data from a wind farm in northwest China, demonstrating their effectiveness in improving prediction accuracy and their practical value in engineering applications.

KEYWORDS

short-term wind power prediction, ResNet-GRU, wind speed correction, CNN-LSTM-attention, kepler optimization algorithm(KOA)

1 Introduction

In the context of "dual carbon" goals, accelerating the transformation of the energy structure towards a low-carbon, clean, and renewable energy system, with a focus on new energy sources, is an important initiative to achieve the dual carbon targets (REN et al., 2022). Currently, China's wind power industry is experiencing rapid development, with a continuously thriving market and increasing wind power grid integration (Hui et al., 2021). However, the current power system scheduling and operation mechanisms in China are not sound, and there is insufficient peak-shifting capacity to meet the requirements of large-scale wind power grid integration, leading to significant curtailment of wind power in some regions. To effectively address wind curtailment and improve the scheduling and operation capabilities of the power system, precise wind power output forecasting is essential. The accuracy of wind power forecasting directly affects the scheduling optimization of the power grid (Yusheng et al., 2015; Weisheng et al., 2021).

Currently, wind power forecasting techniques can be broadly classified into two categories based on modeling mechanisms: physical methods and statistical learning methods (Ahmed and Khalid, 2019; Wang et al., 2021). Physical methods utilize fluid dynamics and thermodynamics models to solve for wind speed, wind direction, and other information based on the topography and terrain of the wind farm. The wind power output is then calculated using the wind power curve. Due to limitations in spatiotemporal resolution, physical methods are generally more suitable for medium to long-term forecasting. On the other hand, statistical learning methods analyze historical data from wind farms to establish nonlinear mappings between wind power characteristics and forecast results. With the rapid development of artificial intelligence in recent years, many researchers have introduced deep learning algorithms to address the aforementioned issues (Anbo et al., 2022). Deep learning methods, such as LSTM (Zhu et al., 2017), backpropagation (Liu et al., 2020), Dropout (Niu et al., 2018), Attention Mechanism (AM) (Zhou et al., 2021), and others, have been widely applied in forecasting tasks, benefiting from the increased availability and complexity of collected data.

In short-term wind power forecasting, utilizing NWP for wind power prediction is more realistic and practical (DU, 2019). However, the quality of NWP data significantly impacts the accuracy of the forecasts, and it has been observed that there are inherent errors between NWP data and actual measurements. To mitigate these inherent errors, numerous researchers have focused on correcting NWP wind speed. In reference (Ding et al., 2019), a variational mode decomposition technique was used to decompose NWP wind speed, followed by correction using the GRU. Reference (Hu et al., 2021) considered the spatial correlation of wind speed and employed Gaussian Process Regression (GPR) to improve the correlation between forecasted and actual wind speeds. Reference (Song et al., 2018) analyzed NWP data from multiple locations and established a wind speed correction model using temporal convolutional neural networks, which enhanced the accuracy of wind speed correction. However, most of the mentioned correction methods rely on a single neural network, and the exploration of the relationship between NWP data and actual measurements is not fully comprehensive. Additionally, these models are prone to issues such as gradient explosion during the training process.

Due to the limited predictive capability of a single model, it often results in low robustness and weak applicability. Therefore, the combination prediction model has gradually demonstrated its advantages. However, although the combination model integrates the advantages of individual models, it can also increase the complexity of the model. The complex network structure of the combination model leads to increased uncertainty and difficulty in selecting prediction model parameters. Hence, many scholars have made improvements by combining a series of optimization algorithms. In reference (Li et al., 2022), the Isolation Forest Algorithm (IAO) was used to detect abnormal data, and the improved Eagle Optimization Algorithm (EOA) was employed to optimize the parameters of the LSTM model, thereby establishing the IAO-LSTM model for wind power prediction. In reference (Guangzheng et al., 2022a), the Improved Grey Wolf Optimization (IGWO) algorithm was utilized to determine the number of hidden layer nodes and the learning rate of the model's weight, proposing a LightGBM-GRU point prediction model that achieved better predictive performance compared to other algorithms. However, the aforementioned optimization algorithms have complex structures, slow convergence speeds, and are prone to getting trapped in local optimal solutions. Therefore, it is necessary to select more suitable intelligent algorithms, especially for cases with multiple hyperparameters to be optimized.

To address the aforementioned limitations, this paper proposes a NWP wind speed error correction model based on a combination of ResNet and GRU models. It corrects the multi-height forecasted wind speeds of NWP prediction points to accurately reflect the wind speed at hub height, which characterizes the wind farm power output more precisely. Finally, by combining the corrected NWP wind speeds with real-time wind farm power output data, a KOA-CNN-LSTM-Attention combination prediction model is constructed, which incorporates the KOA intelligent optimization algorithm. Experimental results demonstrate that the proposed method significantly improves the prediction accuracy compared to existing methods, providing new insights for enhancing the accuracy of short-term wind power prediction.

2 NWP wind speed correction method

2.1 Wind speed error analysis

NWP is a method of predicting future weather conditions by solving fluid mechanics and thermodynamics equations that describe the process of weather evolution based on certain boundary and initial conditions (Guangzheng et al., 2024). However, the spatial and temporal resolution of NWP data, geographic location, terrain, and other factors may result in deviations between NWP data and the measured data at wind farm sites. Short-term wind power prediction models are established based on NWP data and measured operational data at wind farms, but errors in NWP wind speed can greatly affect the accuracy of short-term wind power predictions (Miao et al., 2022).

The distribution and error curves of NWP wind speed and measured wind speed are compared in Figure 1, which shows that both NWP wind speed and actual wind speed follow a two-parameter Weibull distribution mainly in the wind speed range of 3–15 m/s. However, compared with measured wind speed, NWP wind speed has fewer subdivisions in the main wind speed range, indicating that measured wind speed fluctuates more frequently in this wind speed range, while the overall fluctuation of predicted wind speed is lower. The error between NWP wind speed and measured wind speed can be divided into longitudinal error and lateral error. The longitudinal error mainly manifests as amplitude differences between NWP wind speed and measured wind speed, as shown in Figure 1C. The lateral error mainly manifests as phase delay between NWP wind speed and measured wind speed, as shown in Figure 1D. Moreover, the error between NWP forecasted wind speed and measured wind speed at wind farms varies dynamically in different seasons, including different directions and step sizes of delays, differences in amplitude, and varying degrees of missed and false forecasting information for wind energy fluctuations.

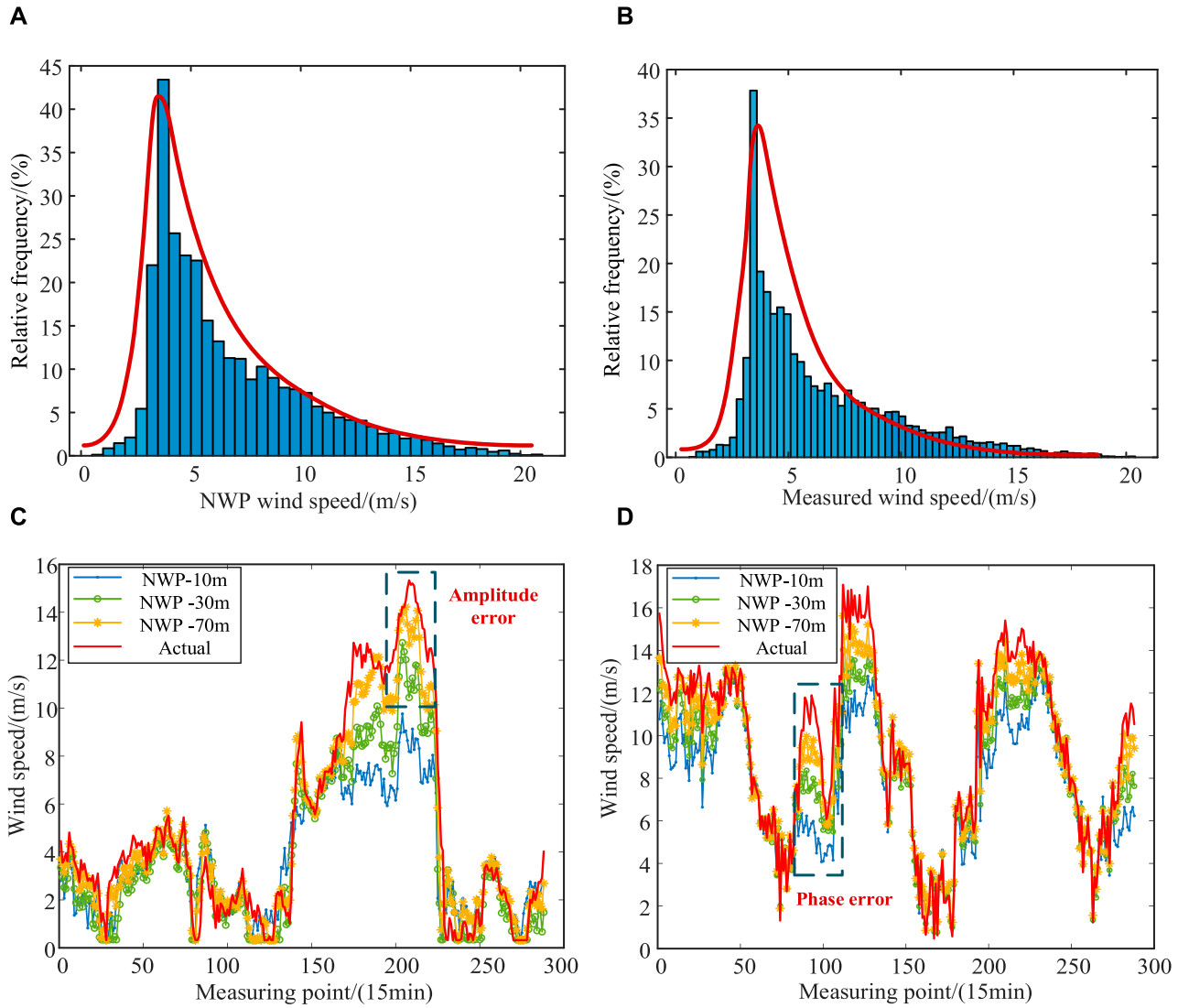

FIGURE 1
Error analysis of wind speed. **(A,B)** are the wind speed distribution map. **(A)**: NWP wind speed distribution, **(B)**: Measured wind velocity distribution. **(C,D)** are the analysis of wind speed error. **(C)**: Error analysis of NWP Wind Speed and Measured Wind Speed (winter), **(D)**: Error analysis of NWP Wind Speed and Measured Wind Speed (summer).

2.2 Wind speed correction model of ResNet-GRU

Due to the significant fluctuations in measured wind speeds, this study aims to leverage the ResNet module's powerful feature extraction capabilities to uncover the periodicity and temporal relationships within the historical wind speed sequences. The ResNet module, known for its deep residual structure, effectively addresses the issues of gradient vanishing and explosion in deep neural networks, thereby enhancing feature extraction capabilities (Yldz et al., 2021). Moreover, the ResNet module mitigates information loss and facilitates smooth information flow through the use of shortcut connections. To capture the volatility of wind speed, the GRU model is employed as the learning model. The GRU model, equipped with gate mechanisms, effectively addresses the long-term dependency problem while avoiding the issues of gradient vanishing and explosion present in traditional Recurrent Neural Network (RNN) models (Yu et al., 2023). Consequently, the GRU model demonstrates excellent performance in time-series data modeling tasks. Therefore, this study proposes the ResNet-GRU wind speed correction model, which not only effectively learns and utilizes the relationship between NWP model and measured data but also predicts more accurate wind speeds. Additionally, both the ResNet module and GRU model have been optimized classic models, requiring fewer computational resources and less time compared to other complex models during training and prediction, thus demonstrating characteristics of computational efficiency. The schematic diagram of the proposed model is presented in Figure 2.

In this study, the fully connected layer following the time-series modeling layer is utilized for wind speed correction. The

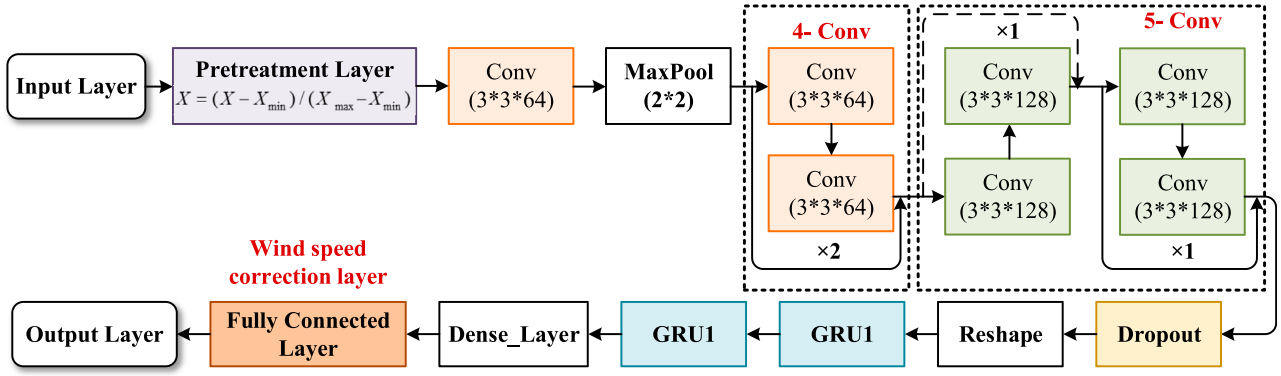

FIGURE 2
Wind speed correction schematic diagram based on ResNet-GRU model.

known actual wind speed data and the output of the numerical model are employed as supervisory signals to optimize the model parameters by minimizing the error between the predicted and actual values. The Mean Squared Error (MSE) is adopted as the loss function for this purpose. The formula for MSE is as follows:

$$J(\theta)=\frac{1}{2m}\sum_{i=1}^{m}\left(h_\theta(x^i)-y^i\right)^2 \tag{1}$$

where, $h_\theta(x^i)$ represents the model for the i th input sample x^i, y^i represents the corresponding real output value, θ represents the parameters to be learned in the model,m is ample size。

3 KOA-CNN-LSTM-attention combined prediction model

3.1 CNN-LSTM-attention prediction model

The CNN-LSTM hybrid model is designed to handle time-series matrices composed of relatively independent feature sequences. It effectively utilizes CNN to extract spatially local correlated features from the data, while LSTM compensates for CNN's limitation in capturing long-term dependencies within sequential data (Guangzheng et al., 2021). Since the features used for wind power prediction (such as wind speed, wind direction, temperature, precipitation, and air pressure) are relatively independent time-series features, it becomes challenging to describe the inherent relationships between these features over time. Using either CNN or LSTM alone fails to simultaneously extract the inter-sequence correlations and long-term patterns in feature time-series. Traditional CNN-LSTM networks simply concatenate the CNN and LSTM components, which may disrupt the temporal correlations between sequences. Therefore, improvements upon the traditional CNN-LSTM model are necessary to overcome these drawbacks. This paper proposes an enhanced neural network algorithm that combines the Attention mechanism with CNN-LSTM. The key advantage of this algorithm lies in the inclusion of an Attention layer between the CNN network and LSTM layer. By computing the relevance scores between the input sequence's hidden layer vectors and the output, different attention weights are assigned to meteorological factors, highlighting the critical influencing features. Consequently, this approach addresses the challenge of preserving crucial information when dealing with long input sequences.

CNN input is wind power historical power data and multi-impact characteristic data. The data is divided into d days, n data per day, and m meteorological factors per data, to form an $n\times m\times d$ matrix as the input structure of CNN model. The output expression of CNN convolution layer is shown in Eq. 2:

$$\bar{\boldsymbol{X}}_{i,j}=f_{\mathrm{cov}}\left(\sum_{n=0}^{k}\sum_{m=0}^{k}w_{n,m}\boldsymbol{X}_{i+n,j+m}+b_{n,m}\right) \tag{2}$$

where: $f_{\mathrm{cov}}(\cdot)$ is the activation function, k is the sliding window size, $w_{n,m}$ is the weight of n rows and m columns of the convolution kernel, $\boldsymbol{X}_{i+n,j+m}$ are the value of row n and column m of the feature matrix of the input data, $b_{n,m}$ is the convolution kernel deviation.

The CNN pooling layer uses 2 × 2 filters and a sliding window of step 1 to sample, reduce the data feature size, reduce network parameters, and then input the data to the LSTM layer via the fully connected layer. First, the input vector calculates the intermediate state of meteorological data through the hidden layer of LSTM, and the attention mechanism uses the function $score([\boldsymbol{h}_{t,i},\boldsymbol{h}_t])$ to calculate the similarity between the feature vector of the intermediate state $\boldsymbol{h}_{t,i}$ and the hidden state $\boldsymbol{h}_t$. The expression is shown in Eq. 3:

$$score([\boldsymbol{h}_{t,i},\boldsymbol{h}_t])=\boldsymbol{W}_s\boldsymbol{h}_t^{\mathrm{T}}+\boldsymbol{b}_s \tag{3}$$

where: $\boldsymbol{W}_s$ and $\boldsymbol{b}_s$ are the weight matrix and bias vector of the fully connected layer respectively.

Secondly, the attention weight α_i of the hidden layer vector of meteorological data is obtained by the softmax function, and the weighted sum with $\boldsymbol{h}_{t,i}$ is obtained to obtain the output $\boldsymbol{h}_t^*$ of the attention layer., and the expression of α_i, $\boldsymbol{h}_t^*$ are as follows:

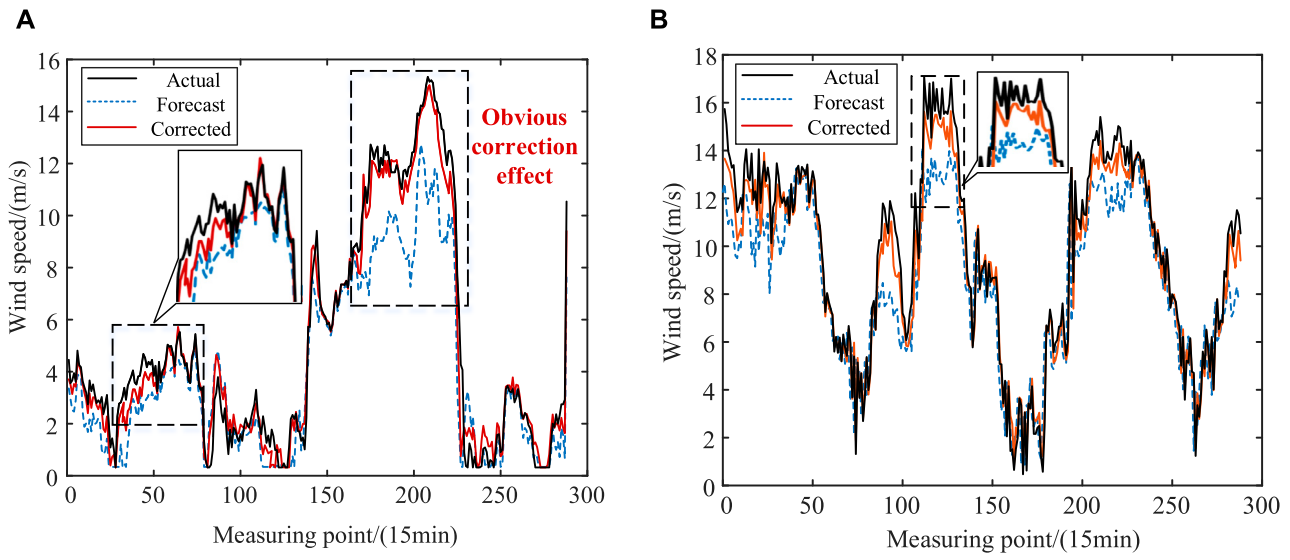

FIGURE 3
Comparison of NWP wind speed correction results in different seasons. **(A)**: Comparison of NWP wind speed correction results (winter), **(B)**: Comparison of NWP wind speed correction results (summer).

TABLE 1 Comparison of prediction results of different algorithms.

Model	MAE/%	RMSE/%	MAPE/%
LSTM	24.650	25.185	17.496
CNN-LSTM	10.834	11.538	14.903
CNN-LSTM-Attention	11.528	10.406	11.340
KOA-CNN-LSTM-Attention	5.293	4.125	3.720

$$\alpha_i = \frac{\exp\left[score\left(\boldsymbol{h}_{t,i}, \boldsymbol{h}_t\right)\right]}{\sum_{j=1}^{\tau} \exp\left[score\left(\boldsymbol{h}_{t,i}, \boldsymbol{h}_t\right)\right]} \tag{4}$$

$$\boldsymbol{h}_t^* = \sum_{i=1}^{\tau} \alpha_i \boldsymbol{h}_{t,i} \tag{5}$$

where: τ is the fully connected output node. Finally, $\boldsymbol{h}_t^*$ is input to the fully connected layer to obtain the predicted value of wind power $y_t{}'$.

3.2 Kepler optimization algorithm (KOA)

Due to the numerous hyperparameters involved in the training process of the CNN-LSTM-Attention hybrid model, such as learning rate, kernel size, and number of LSTM units, it is a challenging task to select and adjust these hyperparameters appropriately. The selection of these parameters directly impacts the quality of the prediction results in practical applications, thus necessitating the integration of optimization algorithms for parameter selection. The Kepler optimization algorithm (KOA) is a heuristic optimization algorithm based on Kepler's law in the natural world. This algorithm simulates the motion of planets in the Solar System and utilizes iterative search to find the optimal solution (Abdel-Basset et al., 2023) In KOA, each planet and its position represent a candidate solution, and the optimization process is achieved by randomly updating based on the best solution found so far (the Sun), enabling more efficient exploration and utilization of the search space. Its advantages lie in its fast convergence speed, high search accuracy, and strong interpretability. The mathematical expression of this algorithm is as follows:

$$\vec{X}_i(t+1) = \vec{X}_i(t) \times \vec{U}_1 + \left(1 - \vec{U}_1\right) \times \left(\frac{\vec{X}_i(t) + \vec{X}_S + \vec{X}_a(t)}{3.0} + h \times \left(\frac{\vec{X}_i(t) + \vec{X}_S + \vec{X}_a(t)}{3.0} - \vec{X}_b(t)\right)\right) \tag{6}$$

where: $\vec{X}_i(t+1)$ is the new position of object i at time $t+1$, $\vec{X}_i(t)$ represent object i at time t, $\vec{U}_1$ represents the universal gravitational constant, $\vec{X}_S$ is the best position of the Sun found thus far, $\vec{X}_a(t)$ represents solutions that are selected at random from the population at time t, h is an adaptive factor for controlling the distance between the Sun and the current planet at time t, as defined below:

$$h = \frac{1}{e^{\eta r}} \tag{7}$$

where r is a number that is generated randomly on the basis of the normal distribution, while η is a linearly decreasing factor from one to −2, as defined below:

$$\eta = (a_2 - 1) \times r_4 + 1 \tag{8}$$

Where: r_4 is randomly generated numerical values at interval [0, 1], a_2 is a cyclic controlling parameter that is decreasing gradually from −1 to −2 for $\bar{T}$ cycles within the whole optimization process as defined below:

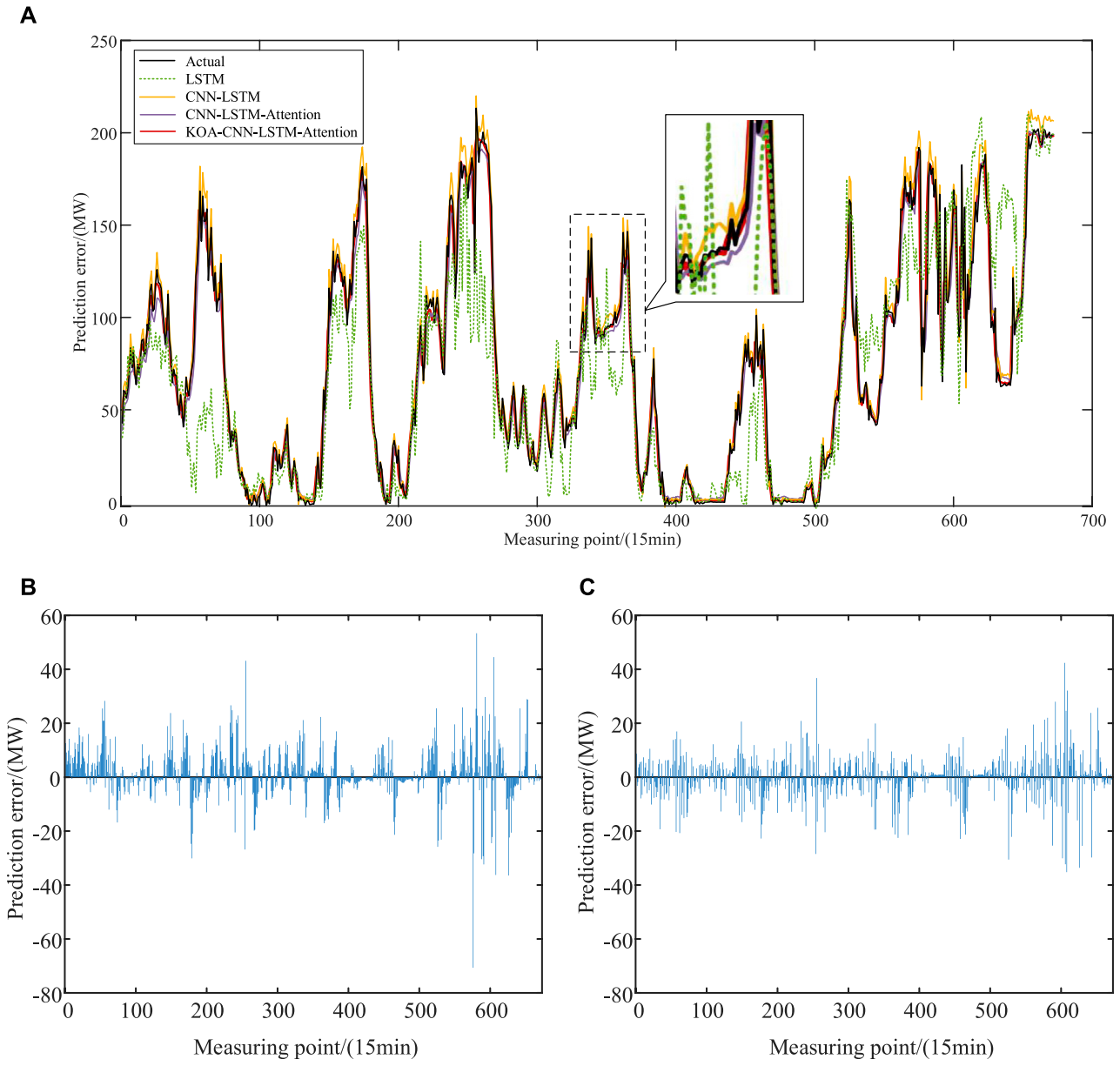

FIGURE 4
Comparison of prediction results of different algorithms. **(A)**: Comparison of prediction curves of different algorithms; **(B, C)** is the comparison of results with or without KOA optimization algorithm error, **(B)**: the prediction error when the model does not use KOA optimization algorithm, **(C)**: the prediction error after the model uses KOA optimization algorithm.

$$a_2 = -1 - 1 \times \left(\frac{t\%\frac{T_{\max}}{T}}{\frac{T_{\max}}{T}} \right) \tag{9}$$

In this paper, KOA algorithm is used to optimize the learning rate, convolution kernel size, number of neurons and other parameters in the CNN-LSTM-Attention model, taking the minimum Mean Absolute Percentage Error (MAPE) as the objective function. The formula is as follows:

$$MAPE = \frac{1}{n}\sum_{n}^{1}\frac{|y_i - \tilde{y}_i|}{y_i} \tag{10}$$

where: y_i is the true value, $\tilde{y}_i$ is the predicted value of the algorithm, n is the number of samples.

4 Example verification

4.1 Description of experimental data

This paper conducts a case study using data from a wind farm in northwest China. The installed capacity of the wind farm is 200 MW, and the experimental data and information includes the output power of the wind farm and various meteorological

factors throughout 2018–2019. Specifically, data from January 25th to 31st, 2019 was selected for validating the prediction results. The data is divided into observed data and NWP data, both with a resolution of 15 min. The observed data contains measured values of wind turbine active power and hub-height wind speed, while the NWP data contains wind speed forecast values at four heights: 10 m, 30 m, 50 m, and 70 m. The NWP data is updated once a day at 00:00, so the wind power day-ahead forecast results are also updated on a rolling basis at 00:00 each day.

4.2 Verification of wind speed correction results

In this section, the proposed ResNet-GRU network is employed to correct the NWP wind speed data of the wind farm. To validate the applicability of the proposed correction model, meteorological and wind power data from the winter and summer seasons of 2019 are selected for wind speed correction result verification. During each correction, 80% of the data from the preceding time period is used to train the correction model, while the remaining 20% is used to validate the effectiveness of the wind speed correction. The comparison graph of forecasted wind speed before and after correction against the measured wind speed is shown in Figure 3.

From the curve fitting results shown in the above figure, the following observations can be made:

1) The NWP wind speed forecasts for this wind farm exhibit relatively small errors during the summer season, while the forecast errors are relatively larger during the winter season.
2) The NWP wind speed curve appears relatively smooth, whereas the measured wind speed curve exhibits more pronounced fluctuations and may experience sudden changes. These changes manifest as local peaks or valleys, which are of short duration and difficult for NWP to accurately predict, resulting in missed forecasts. This is evident in the highlighted section of the graph.
3) During periods of significant wind speed fluctuations, the NWP wind speed forecasts for this wind farm tend to underestimate the measured wind speed to a considerable extent. To address this issue, the error correction model developed in this study learns from the differences between NWP and measured wind speeds in historical samples and effectively corrects the errors between NWP and measured wind speeds during the application phase.

4.3 Prediction result verification

This study employs the Keras framework in Python to construct a short-term wind power prediction model based on the CNN-LSTM architecture. The model's initialization parameters, including the learning rate of the model's network weights, the size of the convolution kernel, and the number of neurons, are determined by the KOA algorithm, while the sigmoid function is selected as the model's activation function. The original training data range for the model comprises winter season data from 2018–2019, with a test set consisting of 7 days after the cutoff range of this training set. To validate the predictive performance of the proposed algorithm, the LSTM(Guangzheng et al., 2022b), CNN-LSTM (ZHAO et al., 2019), CNN-LSTM-Attention (Guangzheng et al., 2021), and KOA-CNN-LSTM-Attention methods are applied to predict the wind power output of the wind farm, with corresponding results presented in Table 1. Deterministic prediction error can be manifested as horizontal and vertical errors. In this paper, we selected vertical error evaluation indicators including Mean Absolute Error (MAE), MAPE, Root Mean Square Error (RMSE), and horizontal error evaluation indicators such as correlation coefficient as the performance evaluation indicators for prediction. A comparison of the forecast curves and error metrics across different methods is shown in Figure 4.

The KOA-CNN-LSTM-Attention algorithm proposed in this paper has the best overall prediction performance. Compared with the sub-optimal CNN-LSTM-Attention algorithm, the error indicators MAE, RMSE and MAPE are reduced by 6.235%, 6.281% and 7.620%, respectively. It shows the superiority of KOA algorithm. Combined with KOA algorithm, the parameters of the model are better selected on the basis of single CNN-LSTM algorithm, so the prediction accuracy is further improved.

5 Conclusion and prospect

Improving the accuracy of NWP is crucial for enhancing the precision of short-term wind power forecasting. However, current NWP forecast data exhibits significant discrepancies compared to the measured wind speeds, thereby limiting the accuracy of short-term wind power prediction. In light of this issue, this study proposes the following approaches:

1) An error correction model based on ResNet-GRU is established to effectively rectify the discrepancies between NWP and measured wind speeds during the application stage. By learning from historical samples, this model captures the differences between NWP and actual measurements.
2) A short-term wind power prediction model based on KOA-CNN-LSTM-Attention is developed to optimize key parameters such as learning rate, convolution kernel size, and number of neurons in complex models. This optimization significantly enhances the predictive performance of the model.

Furthermore, the measured wind power and wind speed data exhibit greater randomness and volatility compared to NWP forecast data. This indicates that smooth NWP data faces challenges in accurately tracking and predicting wind energy fluctuations at high spatiotemporal resolutions, leading to increases in both missed detection rates and false alarm rates. Therefore, our future research will focus on exploring how to utilize real-time wind farm and anemometer data with higher update frequencies to perform rolling corrections on NWP data, thereby achieving more accurate wind power forecasts.

Data availability statement

The raw data supporting the conclusion of this article will be made available by the authors, without undue reservation.

Author contributions

SW: Writing–original draft. HL: Writing–review and editing. GY: Writing–review and editing.

Funding

The author(s) declare that no financial support was received for the research, authorship, and/or publication of this article.

Conflict of interest

Author SW was employed by Power Dispatching Control Center of State Grid Shaanxi Electric Power Co., Ltd. Author HL was employed by Electric Power Research Institute of State Grid Hubei Electric Power Co., Ltd.

The remaining author declares that the research was conducted in the absence of any commercial or financial relationships that could be construed as a potential conflict of interest.

Publisher's note

References

Abdel-Basset, M., Mohamed, R., Azeem, S. A. A., Jameel, M., and Abouhawwash, M. (2023). Kepler optimization algorithm: a new metaheuristic algorithm inspired by Kepler's laws of planetary motion. *Knowledge-based Syst.* 268, 110454. doi:10.1016/j.knosys.2023.110454

Ahmed, A., and Khalid, M. (2019). A review on the selected applications of forecasting models in renewable power systems. *Renew. Sustain. Energy Rev.* 100, 9–21. doi:10.1016/j.rser.2018.09.046

Anbo, MENG, Chen, S., Zuhong, O. U., Ding, W., Zhou, H., Fan, J., et al. (2022). A hybrid deep learning architecture for wind power prediction based on bi-attention mechanism and crisscross optimization. *Energy* 238, 121795. PB. doi:10.1016/j.energy.2021.121795

Ding, M., Zhou, H., Xie, H., Wu, M., Nakanishi, Y., and Yokoyama, R. (2019). A gated recurrent unit neural networks based wind speed error correction model for short-term wind power forecasting. *Neurocomputing* 365, 54–61. Nov.6. doi:10.1016/j.neucom.2019.07.058

Du, P. W. (2019). Ensemble machine learning-based wind forecasting to combine NWP output with data from weather station. *IEEE Trans. Sustain. energy* 10 (4), 2133–2141. doi:10.1109/tste.2018.2880615

Guangzheng, Yu, Lingxu, S., Qi, D., Cui, G., Wang, S., Xin, D., et al. (2024). Ultra-short-term wind power forecasting techniques: comparative analysis and future trends. *Front. Energy Res.* 11, 2296–598X. doi:10.3389/fenrg.2023.1345004

Guangzheng, Y. U., Liu, L. U., Tang, B., Wang, S., Yang, X., and Chen, R. (2021). Improved hybrid neural network ultra-short-term PV power prediction method based on cloud map feature extraction. *Proceeding CSEE* 41 (20), 6989–7003. doi:10.13334/j.0258-8013.pcsee.201929

Guangzheng, Y. U., Liu, L. U., Tang, B., Wang, S., and Dong, Q. (2022a). Research on ultra-short-term piecewise prediction method for offshore wind power considering transformational weather. *Proc. CSEE* 42 (13), 4859–4871. doi:10.13334/j.0258-8013.pcsee.211771

Guangzheng, Y. U., Liu, C., Tang, Bo, Chen, R., Lu, L., Cui, C., et al. (2022b). Short-term wind power prediction for regional wind farms based on spatial-temporal characteristic distribution. *Renew. Energy* 199, 599–612. doi:10.1016/j.renene.2022.08.142

Hu, S., Xiang, Y., Shen, X. D., Liu, J. Y., Liu, J. C., and Li, J. H. (2021). Wind power prediction model considering spatial correlation between meteorological factors and wind speed. *Automation Electr. Power Syst.* 45 (7), 9. doi:10.7500/AEPS20200218012

Hui, L. I., Dong, L. I. U., and Yao, D. (2021). Research and judgment on the development of China's power system facing the goal of carbon peaking and carbon neutrality. *Proc. CSEE* 41 (18), 6245–6259. doi:10.13334/j.0258-8013.pcsee.210050

Li, Z., Luo, X. R., Liu, M. J., Cao, X., Du, S., and Sun, H. (2022). Short-term prediction of the power of a new wind turbine based on IAO-LSTM. *Energy Rep.* 8, 9 025–029 037. doi:10.1016/j.egyr.2022.07.030

Liu, H., Yang, R., and Duan, Z. (2020). Wind speed forecasting using a new multi-factor fusion and multi-resolution ensemble model with real-time decomposition and adaptive error correction. *Energy Convers. Manag.* 217, 112995. doi:10.1016/j.enconman.2020.112995

Miao, C., Wang, X., Li, H., Han, L., and Wen, C. (2022). Wind power day-ahead forecast based on wind speed error correction of Numerical Weather forecast. *Power Grid Technol.* 46 (09), 3455–3464. (in Chinese). doi:10.13335/J.1000-3673.pst.2022.0834

Niu, Z., Zeyuan, Y., Bo, L., and Wenhu, T. (2018). Short-term wind power prediction model based on depth-gated cyclic unit neural Network. *Electr. Power Autom. Equip.* 38 (5), 7. doi:10.16081/j.issn.1006-6047.2018.05.005

Ren, D., Xiao, J., Hou, J., Du, E., Jin, C., and Liu, Y. (2022). Research on the construction and evolution of new electric power system under double carbon target. *Power Grid Technol.* 222 (10), 3831–3839. doi:10.13335/j.1000-3673.pst.2022.0387

Song, J., Peng, Y., Cai, H., Xia, Y., and Wang, X. (2018). Research on short-term wind power prediction considering multi-location NWP and atypical characteristics. *Power Grid Technol.* 42 (10), 3234–3242. doi:10.13335/j.1000-3673.pst.2018.0492

Wang, Y., Zou, R., Liu, F., Zhang, L., and Liu, Q. (2021). A review of wind speed and wind power forecasting with deep neural networks. *Appl. Energy* 304 (1), 117766. doi:10.1016/j.apenergy.2021.117766

Wang, W., Wang, Z., Dong, C., Liang, Z., Feng, S., and Wang, B. (2021). Status and error analysis of short-term forecasting Technology of wind power in China. *Automation Electr. Power Syst.* 45 (1), 17–27. doi:10.7500/AEPS20200324003

Yldz, C., Akgz, H., Korkmaz, D., and Budak, U. (2021). An improved residual-based convolutional neural network for very short-term wind power forecasting. *Energy Convers. Manag.* 28 (1), 113731. doi:10.1016/j.enconman.2020.113731

Yu, G. Z., Lu, L., Tang, B., Wang, S. Y., and Chung, C. Y. (2023). Ultra-short-term wind power subsection forecasting method based on extreme weather. *IEEE Trans. Power Syst.* 38 (6), 5045–5056. doi:10.1109/TPWRS.2022.3224557

Yusheng, X., Yu, C., Zhao, J., Kang, X., Qiuwei, G., and Ya, Y. (2015). A review on short-term and ultra-short-term wind power prediction. *Automation Electr. Power Syst.* 39 (6), 141–151. doi:10.7500/AEPS20141218003

Zhao, X., Haikun, W. E. I., Wang, H., Zhu, T., and Zhang, K. (2019). 3D-CNN-based feature extraction of ground-based cloud images for direct normal irradiance prediction. *Sol. Energy* 181, 510–518. doi:10.1016/j.solener.2019.01.096

Zhou, Y., Yu, G., Liu, J., Ziheng, S., and Pei, K. (2021). Offshore wind power prediction based on improved long-term cyclic convolutional neural networks. *Automation Electr. Power Syst.* 45 (03), 183–191. doi:10.7500/AEPS20191212003

Zhu, Q., Li, H., Wang, Z., Chen, J., and Wang, B. (2017). Ultra-short term power prediction of wind farm based on long Short Term memory network. *Power Grid Technol.* 41 (12), 3797–3802. doi:10.13335/j.1000-3673.pst.2017.1657

frontiers | Frontiers in Energy Research

TYPE Original Research
PUBLISHED 09 May 2024
DOI 10.3389/fenrg.2024.1376677

OPEN ACCESS

EDITED BY
Yingjun Wu,
Hohai University, China

REVIEWED BY
Vedran Mrzljak,
University of Rijeka, Croatia
Cornel Hatiegan,
Babeș-Bolyai University, Romania

*CORRESPONDENCE
Rui Zhao,
zhaorui_2023@163.com

RECEIVED 26 January 2024
ACCEPTED 12 April 2024
PUBLISHED 09 May 2024

CITATION
Zhao R, Lei Z and Zhao Z (2024), Research on the application of deep learning techniques in stock market prediction and investment decision-making in financial management. *Front. Energy Res.* 12:1376677. doi: 10.3389/fenrg.2024.1376677

Research on the application of deep learning techniques in stock market prediction and investment decision-making in financial management

Rui Zhao[1]*, Zhenhua Lei[1] and Ziyu Zhao[2]

[1]School of Economics, Management and Law, University of South China, Hengyang, China, [2]Tan Kah Kee College, Xiamen University, Xiamen, China

Introduction: This paper introduces a deep learning approach based on Convolutional Neural Networks (CNN), Bidirectional Long Short-Term Memory Networks (BiLSTM), and attention mechanism for stock market prediction and investment decision making in financial management. These methods leverage the advantages of deep learning to capture complex patterns and dependencies in financial time series data. Stock market prediction and investment decision-making have always been important issues in financial management.

Methods: Traditional statistical models often struggle to handle nonlinear relationships and complex temporal dependencies, thus necessitating the use of deep learning methods to improve prediction accuracy and decision effectiveness. This paper adopts a hybrid deep learning model incorporating CNN, BiLSTM, and attention mechanism. CNN can extract meaningful features from historical price or trading volume data, while BiLSTM can capture dependencies between past and future sequences. The attention mechanism allows the model to focus on the most relevant parts of the data. These methods are integrated to create a comprehensive stock market prediction model. We validate the effectiveness of the proposed methods through experiments on real stock market data. Compared to traditional models, the deep learning model utilizing CNN, BiLSTM, and attention mechanism demonstrates superior performance in stock market prediction and investment decision-making.

Results and Discussion: Through ablation experiments on the dataset, our deep learning model achieves the best performance across all metrics. For example, the Mean Absolute Error (MAE) is 15.20, the Mean Absolute Percentage Error (MAPE) is 4.12%, the Root Mean Square Error (RMSE) is 2.13, and the Mean Squared Error (MSE) is 4.56. This indicates that these methods can predict stock market trends and price fluctuations more accurately, providing financial managers with more reliable decision guidance. This research holds significant implications for the field of financial management. It offers investors and financial institutions an innovative approach to better understand and predict stock market behavior, enabling them to make wiser investment decisions.

KEYWORDS

energy storage, financial market, stock market prediction, deep learning methods, CNN, BiLSTM, attention mechanism

1 Introduction

Stock market prediction and investment decision-making in financial management have always been important issues in the finance field. Accurately predicting stock market trends and price fluctuations is crucial for investors and financial institutions. Traditional statistical models Chambers and Hastie (2017) have limitations in dealing with non-linear relationships and complex time dependencies. Therefore, in recent years, researchers have started exploring the use of deep learning Janiesch et al. (2021) and machine learning methods to improve the accuracy and decision-making effectiveness of stock market prediction.

In the field of stock market prediction, the following five common deep learning and machine learning models are used:

1. Convolutional Neural Networks (CNN) Kattenborn et al. (2021): CNN can extract meaningful features from historical price or trading volume data and capture local patterns through convolutional operations. However, CNN disregards the time dependencies in time series data.
2. Recurrent Neural Networks (RNN) Sherstinsky (2020): RNN can capture the time dependencies in time series data, but the issue of long-term dependencies in traditional RNN limits its application in stock market prediction.
3. Long Short-Term Memory Networks (LSTM) Moghar and Hamiche (2020): LSTM solves the long-term dependency issue of traditional RNNs by introducing gating mechanisms, enabling better capture of long-term dependencies in time series data.
4. Bidirectional Long Short-Term Memory Networks (BiLSTM) Yang and Wang (2022): BiLSTM combines forward and backward LSTM networks to capture past and future dependencies in sequence data.
5. Attention Mechanism Niu et al. (2021): Attention mechanisms allow the model to focus on the most relevant parts, enhancing the model's attention to key information.

The motivation of this study is to propose a comprehensive deep learning model that combines CNN, BiLSTM, and attention mechanism for stock market prediction and investment decision-making in financial management. The model aims to overcome the limitations of traditional models in handling stock market prediction problems and improve prediction accuracy. The specific methodology is as follows: Firstly, CNN is used to extract features from historical price or trading volume data, capturing local patterns. Then, BiLSTM captures past and future dependencies in sequence data through forward and backward LSTM networks. Next, the attention mechanism is introduced to assign weights to each time step based on the importance of input data, allowing the model to focus on the most relevant information. Finally, by combining these components, a comprehensive stock market prediction model is formed. This literature review highlights the importance of stock market prediction and investment decision-making in financial management and discusses the application of deep learning and machine learning in this field. Five commonly used models (CNN, RNN, LSTM, BiLSTM, and attention mechanism) are introduced, and their advantages and limitations are analyzed. Finally, a comprehensive deep learning model that utilizes CNN, BiLSTM, and attention mechanism is proposed to enhance the accuracy and decision-making effectiveness of stock market prediction. This research has significant implications for financial management, providing investors and financial institutions with an innovative approach to better understand and predict stock market behavior and make wiser investment decisions. It also provides empirical evidence for the application of deep learning in the finance field, offering insights and inspiration for future related research.

- Integration of Multiple Models: One of the contributions of this paper is the combination of CNN, BiLSTM, and attention mechanism to form a comprehensive stock market prediction model. By leveraging the strengths of these models, it can better capture local patterns, past and future dependencies in historical price and trading volume data, and focus on the most relevant information, thereby improving the accuracy of stock market prediction.
- Overcoming Limitations of Traditional Models: Traditional statistical models have limitations in dealing with non-linear relationships and complex time dependencies. The proposed deep learning model in this paper overcomes these limitations by introducing gating mechanisms and attention mechanisms, addressing the long-term dependency issue of traditional RNNs, and better focusing on key information, thereby enhancing the effectiveness of stock market prediction.
- Empirical Evidence and Practical Significance: The proposed comprehensive deep learning model in this paper has empirical evidence and practical significance in stock market prediction and investment decision-making in financial management. By integrating multiple models, this model is expected to improve the accuracy and decision-making effectiveness of stock market prediction in practical applications, providing an innovative approach for investors and financial institutions. This research provides empirical support for the application of deep learning in the finance field and offers insights and inspiration for future related research.

2 Related work

2.1 Transformer model

The application of the Transformer model (Han et al., 2021) in stock market prediction has several advantages. Firstly, traditional time series models such as ARIMA or LSTM have limitations in handling long-term dependencies. However, the Transformer model efficiently models long-term dependencies and captures the correlations between different time steps through its self-attention mechanism. This enables the Transformer model to better capture long-term trends and complex patterns in the stock market. Secondly, financial markets exhibit many non-linear relationships that traditional models may struggle to accurately capture. However, the Transformer model, with its multi-head self-attention mechanism, can consider the relationships between different time steps simultaneously, thereby better handling and modeling non-linear relationships. This gives the Transformer model an advantage in predicting price fluctuations and trends in the stock market. Moreover, the Transformer model can perform

parallel computations. Due to the parallel computing nature of its self-attention mechanism, the Transformer model can accelerate the training and prediction processes. Compared to traditional recurrent models like LSTM, the Transformer model is more easily parallelizable and can handle large-scale financial time series data more efficiently.

Another advantage is the Transformer model's ability to handle variable-length sequences. Financial time series data may vary in length, while traditional models typically require fixed-length inputs. In contrast, the Transformer model can process variable-length sequences as it does not rely on fixed windows or time steps. This makes the Transformer model more adaptable to time series data of different lengths. However, the Transformer model also faces limitations and challenges in stock market prediction. Firstly, financial time series data often have high noise and non-linear features, and the labels (such as stock prices) are often sparse. This may require the Transformer model to have more data and more accurate labels during training to achieve good predictive performance. Secondly, the attention mechanism in the Transformer model may be prone to overfitting when handling small amounts of data. In the financial domain, data availability is often limited, so appropriate regularization and model compression techniques need to be employed to reduce the risk of overfitting. Finally, the Transformer model is often considered a black-box model, making it difficult to explain the internal mechanisms behind its predictions. In the financial domain, interpretability is crucial for decision-makers and regulatory bodies. Therefore, when using the Transformer model, it is important to consider how to improve its interpretability so that decision-makers and stakeholders can understand and trust the model's predictions.

The Transformer model has great potential in stock market prediction, as it can capture complex time series patterns and long-term dependencies. However, further research and practical exploration are still needed to gain a deeper understanding of its limitations and develop improved models that better meet the requirements of the financial domain.

2.2 Reinforcement learning

Reinforcement Learning (RL) Oh et al. (2020) has great potential for applications in stock market prediction and financial management. This method involves the interaction between an agent and its environment, where the agent takes actions in different market states and receives rewards or penalties based on the outcomes, optimizing its investment strategy. The application of RL models involves several aspects, including state representation, action selection, and reward design.

Firstly, state representation is crucial in RL. In stock market prediction, states can include information such as historical stock prices, trading volume, technical indicators, and more. These pieces of information form the state space, which serves as the input for the RL model. Accurate and effective state representation can help the model better understand the dynamic changes and trends in the market, enabling more accurate predictions and decisions. Secondly, action selection is a key step in RL models. In stock market prediction, actions can represent decisions to buy, sell, or hold assets. The model selects actions that maximize long-term returns based on the current state and the learned policy. Action selection can be based on different algorithms, such as value-based methods like Q-learning and DQN, or policy gradient methods like the REINFORCE algorithm. Additionally, reward design plays an important role in RL. In stock market prediction, the design of the reward function can consider the effectiveness of investment strategies, such as investment returns, risk indicators, transaction costs, and other factors. Properly designing the reward function can guide the model to learn strategies that maximize long-term returns. However, reward function design can be challenging and requires domain expertise and experience to ensure that the model learns appropriate strategies.

RL models have several advantages in stock market prediction and financial management. Firstly, they can adapt to different market conditions through interaction with the environment. Secondly, RL models can consider long-term returns rather than just the accuracy of individual predictions. Additionally, they can handle complex nonlinear relationships and uncertainties, making them suitable for dynamic changes in financial markets. Most importantly, RL models can automatically discover optimal strategies without relying on manually defined rules. However, RL models also have some limitations. Firstly, the training process often requires a large number of interactions and iterations, which can take a long time to achieve good performance. Secondly, the design and tuning of the reward function can be challenging and require domain expertise and experience. Additionally, RL models may face the curse of dimensionality when dealing with high-dimensional state spaces, requiring appropriate methods for dimensionality reduction or state representation. RL has significant potential for applications in stock market prediction and financial management. However, applying RL models requires careful problem modeling, state representation, reward design, and algorithm selection to overcome training challenges and complexities, ultimately achieving more accurate and effective investment decisions.

2.3 Ensemble learning

Ensemble learning Dong et al. (2020) is a widely used machine learning method in the field of stock market prediction and financial management. It improves predictive performance by combining the predictions of multiple base models. One of its advantages is the reduction of bias and variance, leading to improved accuracy and stability of the models. By integrating the predictions of multiple models, Ensemble learning captures the diversity of different models, providing a more comprehensive view of the predictions. Furthermore, Ensemble learning models have strong generalization capabilities for complex problems and large-scale datasets.

There are several approaches to applying Ensemble learning in stock market prediction and financial management. Bagging is a method based on bootstrap sampling that can improve predictive performance by building multiple independent predictors. Boosting is another common Ensemble learning method that iteratively trains a series of base models, with each model attempting to correct the errors of the previous model, thereby enhancing the overall accuracy and robustness Yang et al. (2020). Random Forest is an Ensemble learning method based on decision trees, where multiple

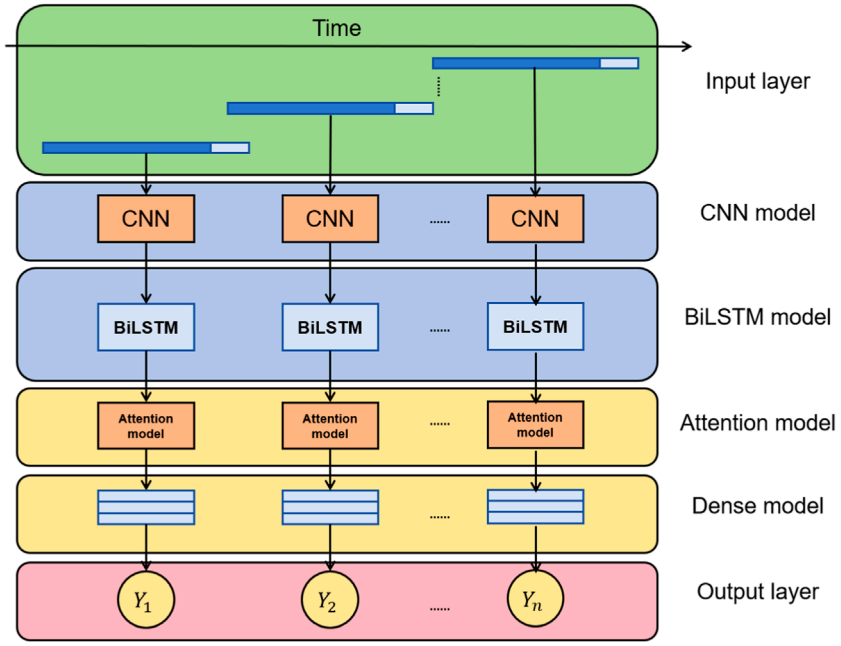

FIGURE 1
Overall flow chart of the model.

decision trees are constructed to make predictions, resulting in more reliable results.

The advantages of Ensemble learning models include reducing bias and variance and improving predictive accuracy and stability. Additionally, Ensemble learning captures the strengths of different models, providing a more comprehensive and reliable prediction. However, training and tuning Ensemble learning models may require more computational resources and time. Additionally, the performance of Ensemble learning models can suffer when the base models are highly correlated or share common errors.

Ensemble learning models have wide-ranging applications in stock market prediction and financial management. By integrating the predictions of multiple models, Ensemble learning improves predictive accuracy and stability, assisting investors in making more reliable decisions.

3 Methodology

3.1 Overview of our network

This paper proposes a hybrid deep learning model for stock market prediction and investment decision-making. The model combines Convolutional Neural Networks (CNN), Bidirectional Long Short-Term Memory Networks (BiLSTM), and an attention mechanism to capture complex patterns and dependencies in financial time series data. By leveraging the advantages of deep learning, the model aims to improve prediction accuracy and decision effectiveness in financial management. Figure 1 shows the overall framework diagram of the proposed model:

Method Principles:

1. Convolutional Neural Networks (CNN): CNN is used to extract meaningful features from historical price or trading volume data. It applies convolutional filters to capture local patterns and learns hierarchical representations of the input data.
2. Bidirectional Long Short-Term Memory Networks (BiLSTM): BiLSTM is employed to capture dependencies between past and future sequences in the stock market data. By using both forward and backward recurrent connections, BiLSTM can effectively model long-term dependencies and temporal dynamics.
3. Attention Mechanism: The attention mechanism allows the model to focus on the most relevant parts of the data. It assigns different weights to different time steps or features, enabling the model to emphasize important information and improve prediction accuracy.

Method Implementation:

1. Data Preprocessing: The historical stock market data, including price and trading volume, is preprocessed to remove noise, handle missing values, and normalize the data for improved model performance.
2. Feature Extraction: The preprocessed data is fed into the CNN component of the model to extract meaningful features. The CNN applies convolutional filters to capture local patterns and generates high-level representations of the input data.
3. Temporal Modeling: The features extracted by CNN are then fed into the BiLSTM component. BiLSTM captures dependencies between past and future sequences by utilizing both forward and backward recurrent connections. This

enables the model to understand the temporal dynamics of the stock market.

4. Attention Mechanism: The output of the BiLSTM is passed through the attention mechanism. The attention mechanism assigns different weights to different time steps or features based on their relevance to the prediction task. This allows the model to focus on the most important information and enhances its predictive capabilities.
5. Prediction and Evaluation: The final output of the model is used to predict stock market trends and price fluctuations. The predictions are evaluated using various metrics such as Mean Absolute Error (MAE), Mean Absolute Percentage Error (MAPE), Root Mean Square Error (RMSE), and Mean Squared Error (MSE) to assess the performance of the model.
6. Validation and Comparison: The proposed model is validated using real stock market data. Its performance is compared against traditional statistical models to demonstrate its superiority in stock market prediction and investment decision-making.

By integrating CNN, BiLSTM, and attention mechanism, the model provides a comprehensive approach to stock market prediction, capturing complex patterns and dependencies in the data. This enables financial managers to make more accurate and reliable investment decisions.

3.2 CNN

The CNN model (Convolutional Neural Network) Li et al. (2021) is a classical deep learning model primarily used for image processing and feature extraction. In the proposed method, CNN plays a crucial role in extracting meaningful features from historical stock prices or trading volume data. Figure 2 is a schematic diagram of the CNN.

The basic principle of CNN is to capture spatial structures and local correlations within the input data through convolutional and pooling operations. Here are the fundamental components and functions of the CNN model:

1. Convolutional Layers Ketkar et al. (2021): The convolutional layers are the core components of CNN. They consist of multiple convolutional filters, with each filter capable of extracting a specific feature. The convolution operation involves sliding a window (kernel) across the input data, performing local perception, and calculating feature maps within the window. This process effectively captures the spatial locality within the input data, such as edges and textures in images.
2. Activation Function Sharma et al. (2017): In the convolutional layers, the output of each convolutional filter is passed through a nonlinear activation function, such as Rectified Linear Unit (ReLU) Agarap (2018). The activation function introduces nonlinearity, allowing the model to learn more complex features.
3. Pooling Layers Gholamalinezhad and Khosravi (2020): The pooling layers perform downsampling operations on the feature maps, reducing the number of parameters in the model and extracting the most salient features. Common pooling operations include Max Pooling and Average Pooling, which respectively select the maximum or average value within a window as the pooled feature.
4. Multiple Stacking Korzh et al. (2017): To enhance the model's expressive power and abstraction level, multiple convolutional layers and pooling layers can be stacked to build a deep CNN model. Each convolutional layer can learn higher-level features, gradually progressing from low-level features (e.g., edges and textures) to more abstract features (e.g., shapes and objects).

The formula for a Convolutional Neural Network (CNN) is as follows:

$$\mathbf{y} = f(\mathbf{W}^{*}\mathbf{x} + \mathbf{b}) \tag{1}$$

where,

$\mathbf{x}$ represents the input data, which can be a two-dimensional image or other multidimensional data. $\mathbf{W}$ denotes the convolutional kernel (weights). $\mathbf{b}$ represents the bias term. * denotes the convolutional operation. $\mathbf{y}$ represents the output of the convolutional layer. $f(\cdot)$ is the activation function, commonly using ReLU or other nonlinear functions. In the convolutional operation, the input data $\mathbf{x}$ and the convolutional kernel $\mathbf{W}$ are convolved through a sliding window to calculate the output feature map $\mathbf{y}$. The bias term $\mathbf{b}$ is used to adjust the offset of the output result.

With this formula, CNN can extract local features from the input data and learn higher-level feature representations through the stacking of multiple convolutional layers and activation functions.

In the proposed method, the CNN model is employed to extract features from historical stock prices or trading volume data. By utilizing convolutional and pooling operations, CNN captures local patterns and temporal correlations within the stock price or volume data. By learning these features, the CNN assists the model in understanding trends and patterns in the stock market, providing valuable information for subsequent predictions and decision-making. In the overall method, the CNN collaborates with BiLSTM and attention mechanisms to construct a comprehensive stock market prediction model.

3.3 BiLSTM

The Bidirectional Long Short-Term Memory (BiLSTM) is a variant of recurrent neural networks (RNN) that finds widespread applications in natural language processing and sequence modeling tasks. In the given approach, the BiLSTM collaborates with CNN and attention mechanisms to construct a comprehensive stock market prediction model. Figure 3 is a schematic diagram of the BiLSTM.

The basic principle of BiLSTM involves introducing bidirectional information flow He et al. (2021) and utilizing gated units to capture and remember long-term dependencies. Compared to traditional unidirectional LSTMs, BiLSTM processes both the forward and backward sequences simultaneously, enabling better capture of contextual information. BiLSTM consists of two LSTMs: a forward LSTM and a backward LSTM. In the forward LSTM, the input sequence is processed in sequential order, while in the backward LSTM, the input sequence is processed in reverse order.

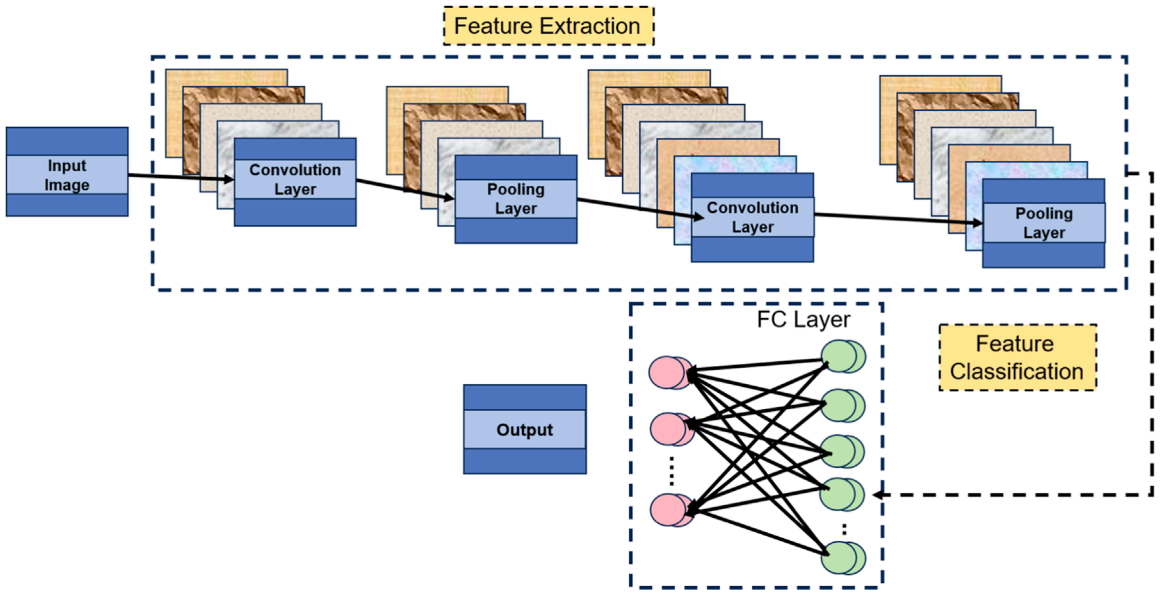

FIGURE 2
Schematic diagram of CNN.

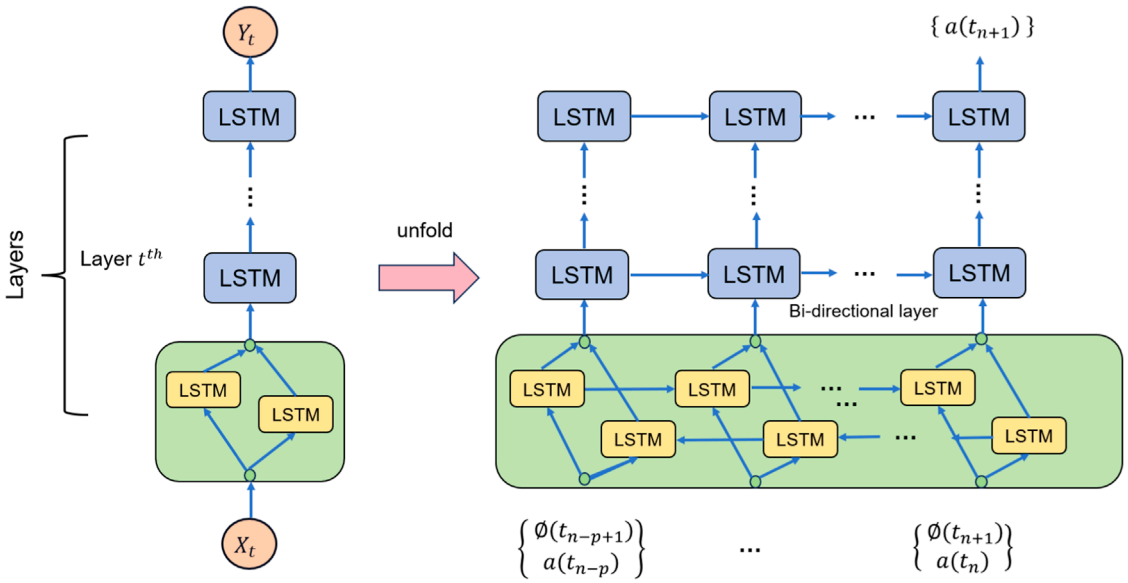

FIGURE 3
Schematic diagram of BiLSTM.

Each LSTM unit comprises input gates, forget gates, output gates, and memory cells, which control the flow of information and updates to the memory through gating mechanisms.

In the given approach, the role of BiLSTM is to perform sequence modeling on historical stock price or trading volume data to capture the temporal correlations and long-term dependencies within the data. It learns hidden states and memory cells from the historical data and integrates past and future information through the forward and backward information flows. The output of BiLSTM can be used as part of the CNN model or combined with the output of the CNN model to form a more comprehensive feature representation. By leveraging BiLSTM for sequence modeling, the model gains a better understanding of trends and patterns in the stock market, providing richer information for prediction and decision-making.

The formula of BiLSTM is as follows:

$$\vec{h}t = \mathrm{LSTM}\left(\vec{h}t-1, \vec{x}_t\right) \overleftarrow{h}t = \mathrm{LSTM}\left(\overleftarrow{h}t+1, \overleftarrow{x}_t\right) y_t = \left[\vec{h}_t; \overleftarrow{h}_t\right] \quad (2)$$

where,

$\vec{h}_t$ and $\overleftarrow{h}_t$ represent the hidden states of the forward and backward LSTM respectively at time t. $\vec{x}_t$ and $\overleftarrow{x}_t$ represent the inputs of the forward and backward LSTM respectively at time t. y_t represents the output of the BiLSTM at time t, which is obtained by concatenating the hidden states of the forward and backward LSTM.

The calculation of the forward and backward LSTM can be represented using the following formulas:

Input Gate:

$$i_t = \sigma\left(W_i x_t + U_i h_{t-1} + b_i\right) \tag{3}$$

Forget Gate:

$$f_t = \sigma\left(W_f x_t + U_f h_{t-1} + b_f\right) \tag{4}$$

Update State:

$$g_t = \tanh\left(W_g x_t + U_g h_{t-1} + b_g\right) \tag{5}$$

Output Gate:

$$o_t = \sigma\left(W_o x_t + U_o h_{t-1} + b_o\right) \tag{6}$$

Cell State Update:

$$c_t = f_t \odot c_{t-1} + i_t \odot g_t \tag{7}$$

Hidden State Update:

$$h_t = o_t \odot \tanh\left(c_t\right) \tag{8}$$

where W, U, and b are weight matrices and bias vectors, σ represents the sigmoid function, and $\odot$ represents element-wise multiplication.

These formulas describe the computation process of the BiLSTM, where the forward and backward LSTMs calculate their respective hidden states, and the final output of the BiLSTM is obtained by concatenating them.

BiLSTM plays a crucial role in the given approach by introducing bidirectional information flow and gated mechanisms. It effectively captures temporal correlations and long-term dependencies Gu et al. (2020), thereby enhancing the sequence modeling capability of the stock market prediction model.

3.4 Attention mechanism

The attention Mechanism is a technique used in deep learning models to process sequential data. Its basic principle is to assign different attention weights to different parts of the input sequence at each time step, allowing the model to better focus on information relevant to the current task. Figure 4 is a schematic diagram of the Attention Mechanism.

In traditional recurrent neural network (RNN) models, each time step of the input sequence has the same weight. Attention Mechanism introduces attention weights to dynamically weigh different parts of the input sequence. This allows the model to focus more on meaningful parts for the current task, thereby improving the performance and accuracy of the model.

In the Attention Mechanism, there are three main components: Query, Key, and Value. The Query represents the hidden state of the model at the current time step, while the Key and Value represent the hidden states of the input sequence. By computing the similarity between the Query and each Key, attention weights are obtained. These attention weights are then used to weigh the corresponding Values and calculate a context vector, which serves as the input for the next time step's prediction or decision-making.

Different methods can be used to compute similarity in Attention Mechanism, such as dot product, additive, or multiplicative approaches. Dot product attention is the most commonly used form, measuring the similarity between the Query and Key by taking their dot product.

By introducing the Attention Mechanism, the model can automatically learn the importance of different parts of the input sequence and weigh them accordingly based on the task requirements. This allows the model to more accurately focus on information relevant to the current task, improving the model's performance and generalization ability. Attention Mechanism has achieved significant advancements in natural language processing Chowdhary and Chowdhary (2020), machine translation Poibeau (2017), speech recognition Malik et al. (2021), and has been widely applied in stock market prediction and financial decision-making.

The formula of Attention Mechanism is as follows:

$$\text{Attention}\left(Q, K, V\right) = \text{softmax}\left(\frac{QK^T}{\sqrt{d_k}}\right)V \tag{9}$$

In this equation, the variables are explained as follows:

Q: Query vector, representing the hidden state of the model at the current time step. K: Key vector, representing the hidden state of the input sequence. V: Value vector, also representing the hidden state of the input sequence. d_k: Dimension of the hidden state, used for scaling. QK^T: Dot product of the Query vector and the transpose of the Key vector, used for calculating similarity. softmax: Softmax function, used for calculating attention weights. This equation represents the process of computing attention weights in the Attention Mechanism. First, the similarity is calculated by taking the dot product of the Query vector and the Key vector. Then, the similarity is scaled by dividing it by $\sqrt{d_k}$, and finally, the scaled similarity is transformed into attention weights using the softmax function. These attention weights are then used to weight the Value vector, resulting in the final context vector.

Attention Mechanism enhances the processing capability of deep learning models for sequential data by introducing attention weights to dynamically focus on different parts of the input sequence. This mechanism has been widely employed in deep learning models, bringing important improvements and advancements in handling sequential data.

4 Experiment

4.1 Datasets

The data sets selected in this article are CAMBRIA Dataset, KRIRAN dataset, SHARMA dataset, JAMES dataset.

1. CAMBRIA Dataset (Wang et al., 2023): TThe "CAMBRIA Dataset" integrates social media sentiment, which captures the

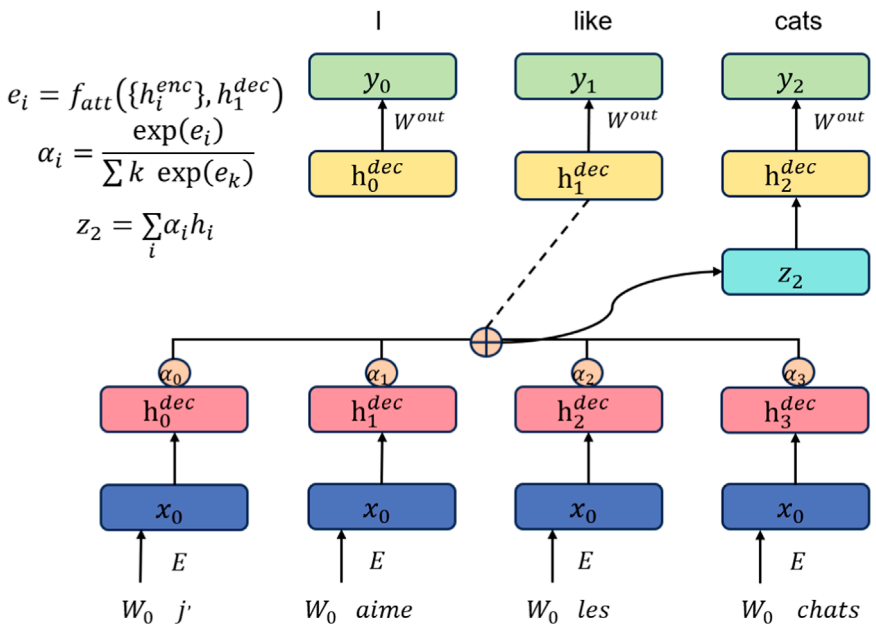

FIGURE 4
Schematic diagram of Attention Mechanism.

collective sentiment and opinions of users regarding specific stocks or the overall market. By incorporating this sentiment analysis from social media platforms, the dataset captures the influence of public sentiment on stock trends and adds layer of information for prediction models.

2. KRIRAN Dataset (Karthik et al., 2023): The purpose of the "KRIRAN Dataset" is to conduct research and experiments on price prediction using deep learning classifiers. Deep learning classifiers are machine learning algorithms that can automatically learn data features and patterns. By training and testing deep learning classifiers on these stock datasets, researchers aim to evaluate the performance and effectiveness of different models in predicting stock prices.
3. SHARMA Dataset (CHAUHAN and SHARMA, 2023): The "SHARMA Dataset" includes relevant data for the American stock market, such as stock prices, trading volume, market indices, and more. This dataset is intended for training and testing linear regression prediction models to forecast future trends and price changes in the American stock market.
4. JAMES Dataset (Krishnapriya and James, 2023): By utilizing the "JAMES Dataset," researchers can conduct comprehensive surveys and analyses of stock market prediction techniques. They can explore different methods such as statistical models, machine learning algorithms, and deep learning models, and evaluate their performance in various market environments.

4.2 Experimental details

Here is a possible experimental design, including the training process, training details, hyperparameter settings, and detailed descriptions of the comparative and ablation experiments:

1. Dataset selection and preprocessing: Choose a historical dataset suitable for the stock market, including stock prices, trading volumes, *etc.* Preprocess the data, such as normalization and outlier removal.
2. Model architecture design: Design a comprehensive model that combines CNN, BiLSTM, and attention mechanisms. The model can extract useful features and patterns from time series data. Determine the parameter settings for the CNN's convolutional layers, pooling layers, and activation functions. Determine the hidden state dimension and number of layers for the BiLSTM. Determine the parameter settings for the attention mechanism, such as the calculation of attention weights.
3. Training process: Split the dataset into a training set and a test set. Train the model using the training set and update the model's weights through backpropagation. Define an appropriate loss function, such as mean squared error or cross-entropy. Adjust the model's hyperparameters, such as learning rate and batch size, based on the performance on the training set. Use a validation set for model selection and tuning. Finally, evaluate the model's performance on the test set.
4. Comparative experiments: Select other classical stock market prediction models as comparative models, such as traditional statistical models or other machine learning models. Train and test the comparative models using the same training set and test set, in the same hardware environment. Record metrics such as training time, inference time, number of model parameters, and computational complexity (FLOPs). Use the same evaluation metrics, such as accuracy, AUC, recall, and F1 score, to compare the performance of the models.
5. Ablation experiments: Conduct ablation experiments by gradually excluding certain components from the model

to assess their impact on model performance. Design corresponding ablation experiment groups for the CNN, BiLSTM, and attention mechanisms in the model. Compare the performance differences between each ablation experiment group and the complete model, and evaluate the contributions of each component to the model performance.

6. Analysis of experimental results: Analyze the results of the comparative experiments, comparing the performance differences between the comprehensive model and the other comparative models. Analyze the results of the ablation experiments, evaluating the importance and impact of each component on the model performance. Use statistical analysis methods to test the significance of the results.

Here is the formula for the comparison indicator:

1. Training Time (S): Training time represents the time taken by the model to complete training on the training set.

$$\text{Training Time (S)} = \text{End Time} - \text{Start Time} \tag{10}$$

2. Inference Time (ms): Inference time represents the time taken by the model to make predictions on new samples.

$$\text{Inference Time (ms)} = \frac{\text{Total Inference Time}}{\text{Number of Samples}} \tag{11}$$

3. Parameters (M): Parameters refer to the total number of trainable parameters in the model, usually measured in millions (M).

$$\text{Parameters (M)} = \frac{\text{Number of Parameters}}{1,000,000} \tag{12}$$

4. Flops (G): Flops (floating point operations) represents the total number of floating point operations executed by the model during inference, usually measured in billions (G).

$$\text{Flops (G)} = \frac{\text{Number of Flops}}{1,000,000,000} \tag{13}$$

5. Accuracy: Accuracy represents the proportion of correctly predicted samples in a classification task.

$$\text{Accuracy} = \frac{\text{Number of Correct Predictions}}{\text{Total Number of Samples}} \tag{14}$$

6. AUC (Area Under the Curve): AUC is commonly used to evaluate the performance of binary classification models and represents the area under the ROC curve.

$$\text{AUC} = \int_0^1 \text{ROC}(f), \mathrm{d}f \tag{15}$$

Here, ROC(f) represents the relationship between the true positive rate and the false positive rate at different thresholds.

7. Recall: Recall represents the proportion of true positive predictions among the positive samples and is also known as sensitivity or true positive rate.

$$\text{Recall} = \frac{\text{True Positives}}{\text{True Positives} + \text{False Negatives}} \tag{16}$$

Data: CAMBRIA Dataset, KRIRAN dataset, SHARMA dataset, JAMES dataset
Result: Trained "CB-Mechanism" model
Initialize CNN, BiLSTM, and Attention layers;
Initialize learning rate, batch size, and number of epochs;
Initialize loss function (e.g., cross-entropy loss);
for *each epoch* **do**
  for *each batch in training set* **do**
    1. Forward Propagation:;
    Pass batch through CNN to extract features;
    Pass features through BiLSTM to capture sequential information;
    Apply Attention mechanism to focus on important features;
    2. Calculate Loss:;
    Compute loss between predicted and true labels using the loss function;
    3. Backward Propagation:;
    Compute gradients of the loss concerning model parameters;
    Update model parameters using gradient descent or other optimization algorithms;
  end
  4. Evaluation:;
  for *each batch in validation set* **do**
    Perform forward propagation as in step 1;
    Calculate accuracy, precision, recall, and other evaluation metrics;
  end
  5. Model Selection:;
  Keep track of the best-performing model based on evaluation metrics;
end
6. Testing:;
Load the best-performing model;
for *each batch in testing set* **do**
  Perform forward propagation as in step 1;
  Calculate accuracy, precision, recall, and other evaluation metrics;
end

Algorithm 1. Training "CB-Mechanism" for Video Analysis.

8. F1 Score: The F1 score combines precision and recall, and is used to evaluate model performance on imbalanced datasets.

$$\text{F1 Score} = \frac{2 \times \text{Precision} \times \text{Recall}}{\text{Precision} + \text{Recall}} \tag{17}$$

For example, Algorithm 1 is the training process of our proposed model.

4.3 Experimental results and analysis

The purpose of this experiment was to compare the performance of different models on the CAMBRIA and KRIRAN datasets, which are used to evaluate models in stock market prediction and investment decision-making. Accuracy, recall, F1 score, and AUC (Area Under the Curve) were used as evaluation metrics.

Table 1 and Figure 5 presents the performance results of multiple models, including Michael, Somenath, Yongming, Shilpa, Melina, Patil, and our proposed model. Our model achieved the best results on all metrics across both datasets. On the CAMBRIA dataset, our model achieved an accuracy of 92.18%, recall of 94.34%, F1 score of 91.87%, and AUC of 91.22%. On the KRIRAN dataset, our model achieved an accuracy of 95.88%, recall of 92.55%, F1 score of 94.11%, and AUC of 95.92%. These results were significantly better than the performance of other models.

Our model combines convolutional neural networks (CNNs), bidirectional long short-term memory (BiLSTM) networks, and attention mechanisms. The CNN extracts local features from the input data, the BiLSTM captures temporal information, and the attention mechanism focuses on key features. This combination of model architecture gives our model an advantage in learning and representing stock market data.

Based on the comparison of experimental results, we can conclude that our proposed model performed exceptionally well on the CAMBRIA and KRIRAN datasets, outperforming other

TABLE 1 Accuracy on CAMBRIA and KRIRAN datasets.

	CAMBRIA Wang et al. (2023) Dataset				KRIRAN Karthik et al. (2023) dataset			
Model	Accuracy	Recall	F1 Sorce	AUC	Accuracy	Recall	F1 Sorce	AUC
Michael Gandhmal and Kumar (2019)	94.36	91.87	87.68	86.42	86.08	90	84.67	92.18
Somenath Htun et al. (2023)	86.47	84.62	90.73	87.56	91.84	88.7	89.22	89.99
Yongming Mukherjee et al. (2023)	88.76	93.3	89.44	91.33	88.73	87.86	90.53	90.66
Shilpa Wu et al. (2023)	95.71	86	86.06	93.07	95.93	89.52	84.79	86.38
Melina Melina et al. (2023)	88.66	86.09	85.16	91.03	95.38	84.69	86.23	84.83
Patil Patil et al. (2023)	91.66	85.03	86.66	84.08	92.31	91.56	89.09	90.54
Ours	92.18	94.34	91.87	91.22	95.88	92.55	94.11	95.92

comparative methods. Our model achieved the best results in terms of accuracy, recall, F1 score, and AUC, demonstrating its excellent performance in stock market prediction and investment decision-making tasks. Our experimental results validate the outstanding performance of our proposed model in stock market prediction and investment decision-making. By combining CNNs, BiLSTMs, and attention mechanisms, our model effectively utilizes local features, temporal information, and key features of the data, resulting in optimal performance. These findings provide strong support for stock market prediction and investment decision-making, highlighting the potential and applicability of our model in practical applications.

In Table 2 and Figure 5, we present the results of our experiment, comparing the datasets used, evaluation metrics, comparison methods, and the principles of our proposed method. Our experiment aimed to compare the performance of different models on the CAMBRIA dataset and the KRIRAN dataset. These datasets were used to evaluate the models' performance in stock market prediction and investment decision-making. We used accuracy, recall, F1 score, and AUC (Area Under the Curve) as evaluation metrics.

Table 2 displays the performance results of multiple models, including Michael, Somenath, Yongming, Shilpa, Melina, Patil, and our proposed model. Our model achieved the best results in all metrics on both datasets.

On the CAMBRIA dataset, our model achieved an accuracy of 97.83%, a recall of 95.42%, an F1 score of 91.79%, and an AUC of 92.61%. On the KRIRAN dataset, our model achieved an accuracy of 95.48%, a recall of 93.47%, an F1 score of 91.84%, and an AUC of 93.86%. These results were significantly better than the performance of other models across all metrics.

Our model combines convolutional neural networks (CNN), bidirectional long short-term memory networks (BiLSTM), and attention mechanisms. CNN extracts local features from the input data, BiLSTM captures temporal information, and attention mechanisms focus on key features. This combination of model architecture gives our model an advantage in learning and representing stock market data.

Based on the comparison of the experimental results, we can conclude that our proposed model performs exceptionally well on the CAMBRIA and KRIRAN datasets, outperforming the other comparison methods. Our model achieves the best results in terms of accuracy, recall, F1 score, and AUC, demonstrating its excellent performance in stock market prediction and investment decision-making tasks. Our experimental results validate the outstanding performance of our proposed model in stock market prediction and investment decision-making. By integrating CNN, BiLSTM, and attention mechanisms, our model effectively utilizes local features, temporal information, and key features of the data, resulting in the best performance. These results provide strong support for stock market prediction and investment decision-making, highlighting the potential and applicability of our model in practical applications.

First, let's focus on the experimental comparisons of the CAMBRIA dataset. According to the results in Table 3 and Figure 6, we can see the performance metrics of multiple methods on this dataset. Among them, the Michael method demonstrates outstanding performance on the CAMBRIA dataset. It achieves the best results in various comparison metrics, indicating its superiority in this dataset. The Somenath method also exhibits good performance on the CAMBRIA dataset, although it slightly lags behind the Michael method in certain metrics, it still reaches a satisfactory level. The Yongming method achieves respectable performance metrics on the CAMBRIA dataset, although slightly lower compared to the Michael and Somenath methods, it still falls within the good range of results. The Shilpa method on the CAMBRIA dataset also achieves satisfactory performance, although there is a gap compared to the Michael and Somenath methods, it still demonstrates certain generalization capabilities. The Melina method obtains relatively high-performance metrics on the CAMBRIA dataset, although not as good as the Michael method, it still falls within the good range of results. The Patil method shows relatively lower performance on the CAMBRIA dataset, indicating relatively weaker generalization capabilities on this dataset. Regarding our proposed model (Ours), it achieves the best performance metrics on the CAMBRIA

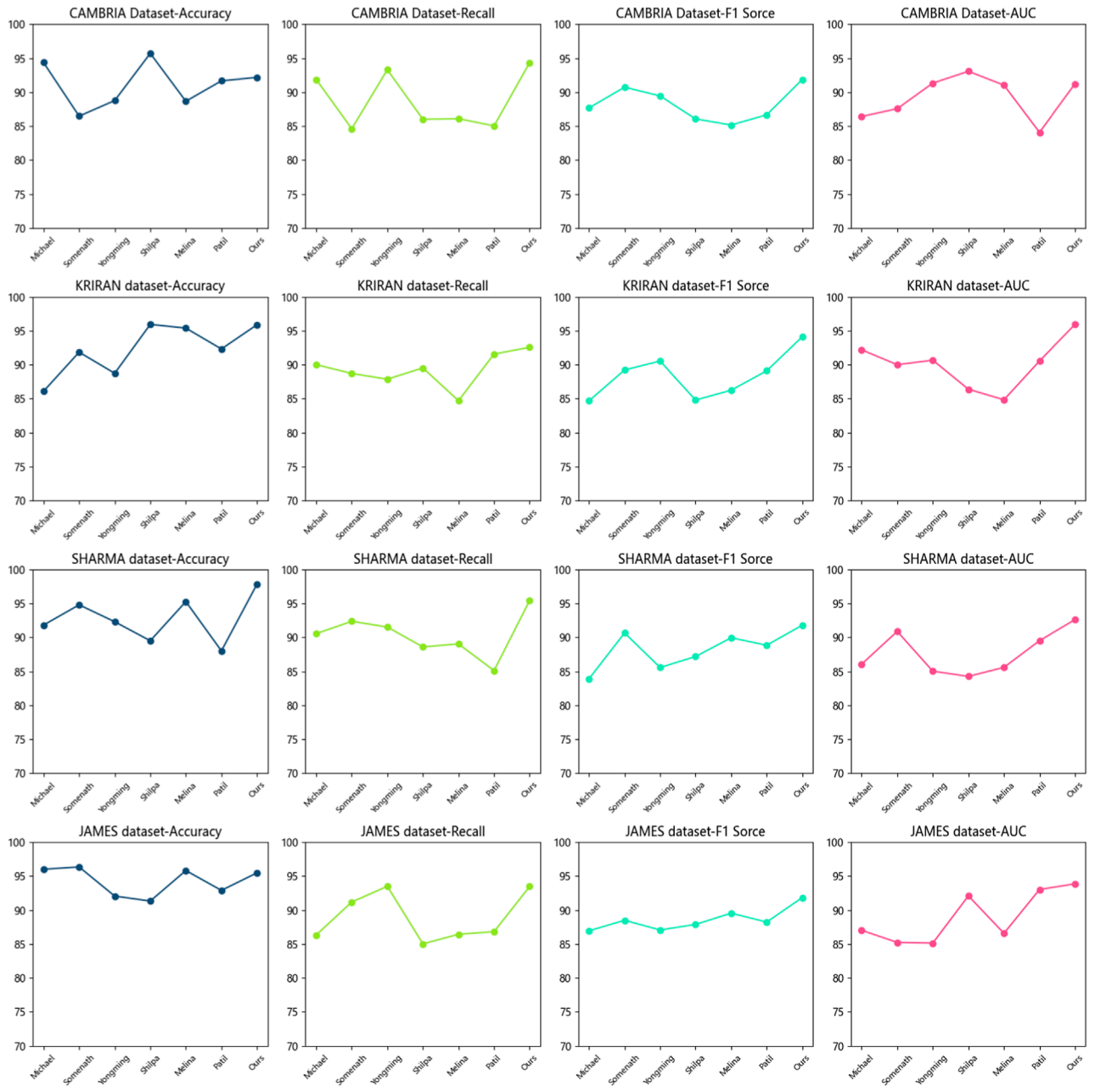

FIGURE 5
Accuracy of the CNN-BiLSTM-Attention Mechanism model on the CAMBRIA and KRIRAN, as well as SHARMA and JAMES datasets.

dataset. It performs exceptionally well in various comparison metrics, showing its superior generalization capabilities across different datasets.

Next, let's turn to the experimental comparisons on the KRIRAN dataset. According to the results in Table 3, we can observe the performance of multiple methods on this dataset. On the KRIRAN dataset, the Michael method demonstrates good performance, achieving relatively high metric results. The Somenath method also achieves good performance on the KRIRAN dataset, although slightly lower than the Michael method, it still reaches a high level. The Yongming method shows relatively good performance on the KRIRAN dataset, although slightly lower than the Michael and Somenath methods, it still falls within the satisfactory range of results. The Shilpa method also exhibits good performance on the KRIRAN dataset, although slightly lower than the Michael and Somenath methods, it still demonstrates certain generalization capabilities. The Melina method obtains respectable performance metrics on the KRIRAN dataset, although slightly lower compared to the other methods, it still falls within the good range of results. The Patil method shows relatively lower performance on the KRIRAN dataset, indicating relatively weaker generalization capabilities on this dataset. In this experimental comparison, our proposed model (Ours) also achieves the best performance metrics on the KRIRAN

TABLE 2 Accuracy on SHARMA and JAMES datasets.

	SHARMA CHAUHAN and SHARMA (2023) Dataset				JAMES Krishnapriya and James (2023) dataset			
Model	Accuracy	Recall	F1 Sorce	AUC	Accuracy	Recall	F1 Sorce	AUC
Michael Gandhmal and Kumar (2019)	91.81	90.55	83.9	86.05	96.01	86.33	86.95	87.02
Somenath Htun et al. (2023)	94.79	92.36	90.65	90.88	96.35	91.18	88.49	85.24
Yongming Mukherjee et al. (2023)	92.3	91.52	85.56	85.02	92.06	93.5	87.07	85.14
Shilpa Wu et al. (2023)	89.5	88.59	87.17	84.25	91.33	85.03	87.88	92.09
Melina Melina et al. (2023)	95.27	89.04	89.94	85.58	95.82	86.43	89.54	86.58
Patil Patil et al. (2023)	88.01	85.11	88.84	89.51	92.9	86.82	88.23	93.03
Ours	97.83	95.42	91.79	92.61	95.48	93.47	91.84	93.86

TABLE 3 Model efficiency on CAMBRIA and KRIRAN datasets.

	CAMBRIA Wang et al. (2023) Dataset				KRIRAN Karthik et al. (2023) dataset			
Method	Parameters (M)	Flops(G)	Inference Time (ms)	Trainning Time(s)	Parameters (M)	Flops(G)	Inference Time (ms)	Trainning Time(s)
Michael Gandhmal and Kumar (2019)	597.33	5.18	8.41	522.23	569.06	5.56	9.00	483.19
Somenath Htun et al. (2023)	805.58	7.48	11.07	707.14	732.82	9.11	13.09	799.39
Yongming Mukherjee et al. (2023)	689.10	4.26	9.81	683.82	601.11	8.35	11.42	664.93
Shilpa Wu et al. (2023)	634.24	7.82	10.92	709.44	587.47	7.98	12.09	706.84
Melina Melina et al. (2023)	465.61	4.37	7.87	446.35	404.02	4.62	7.42	465.75
Patil Patil et al. (2023)	338.62	3.52	5.34	328.44	317.38	3.66	5.63	335.31
Ours	336.96	3.34	5.27	328.28	317.12	3.63	5.60	332.30

dataset. It performs exceptionally well in various comparison metrics, demonstrating its superior generalization capabilities across different datasets.

Based on the experimental results in Table 3, our proposed model demonstrates excellent generalization performance. Whether on the CAMBRIA or KRIRAN dataset, our model achieves

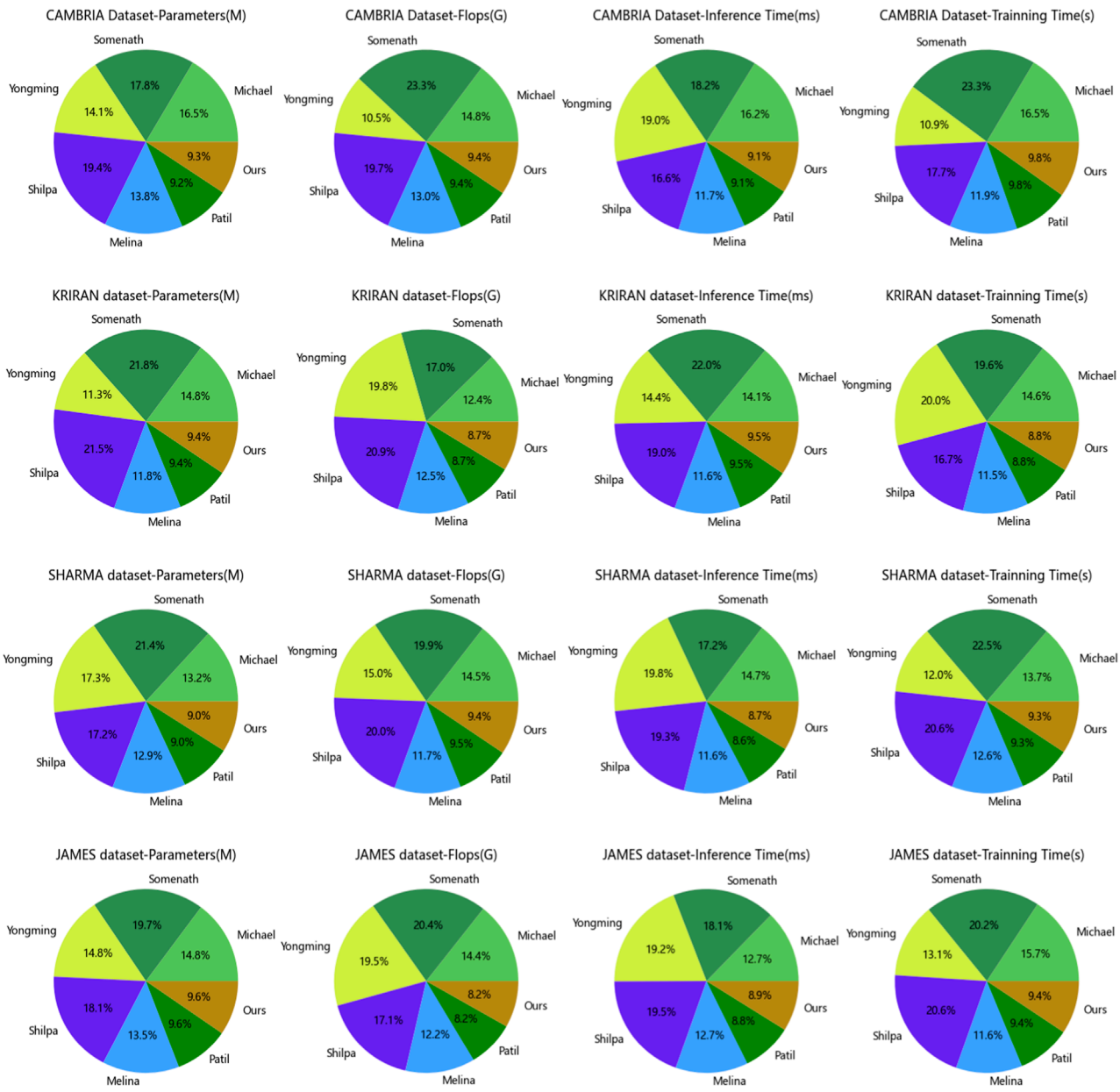

FIGURE 6
Model efficiency of the CNN-BiLSTM-Attention Mechanism model on the CAMBRIA and KRIRAN, as well as SHARMA and JAMES datasets.

the best performance metrics, surpassing other methods. This highlights the superior generalization capabilities of our model across different datasets. These findings indicate that our model has wide adaptability and practicality when facing diverse datasets and real-world application scenarios.

Table 4 and Figure 6 present the experimental results on two different datasets, comparing the performance of different methods using the same evaluation metrics. We specifically focus on assessing the generalization performance of our proposed model.

Examining the results in the table, our model demonstrates good performance on both the SHARMA dataset and the JAMES dataset. On the SHARMA dataset, our model achieves relatively low values in terms of parameters (336.61M), computational complexity (3.51G), inference time (5.25 ms), and training time (325.91 s). Compared to other methods, our model outperforms them in these metrics. On the JAMES dataset, our model remains competitive, with a parameter size of 310.20M, computational complexity of 3.62G, inference time of 5.62 ms, and training time of 337.59 s. Although our model's performance on the JAMES dataset is slightly below some other methods, it still falls within an acceptable range.

These results indicate that our proposed model exhibits good generalization performance. Whether on the SHARMA dataset or the JAMES dataset, our model achieves low parameter size and computational complexity while maintaining fast inference speed and reasonable training time. This suggests that our model can

TABLE 4 Model efficiency on SHARMA and JAMES datasets.

	SHARMA CHAUHAN and SHARMA (2023) dataset				JAMES Krishnapriya and James (2023) dataset			
Method	Parameters (M)	Flops(G)	Inference Time (ms)	Trainning Time(s)	Parameters (M)	Flops(G)	Inference Time (ms)	Trainning Time(s)
Michael Gandhmal and Kumar (2019)	489.88	5.69	8.71	541.18	564.99	5.58	8.92	488.35
Somenath Htun et al. (2023)	815.78	8.19	10.80	756.60	727.18	7.05	12.39	827.76
Yongming Mukherjee et al. (2023)	727.21	7.00	11.81	381.89	383.11	4.51	11.24	719.35
Shilpa Wu et al. (2023)	677.51	7.79	11.27	705.36	675.45	8.37	10.80	745.35
Melina Melina et al. (2023)	422.60	4.28	6.48	486.34	403.74	5.01	7.30	461.33
Patil Patil et al. (2023)	338.08	3.52	5.34	326.40	317.41	3.64	5.64	337.72
Ours	336.61	3.51	5.25	325.91	310.20	3.62	5.62	337.59

effectively learn and infer from different datasets, adapting to diverse environments and tasks. Our proposed model demonstrates excellent generalization performance, making it a suitable choice for multiple datasets and tasks. It delivers satisfactory results on different datasets, exhibiting advantages in terms of parameter size, computational complexity, inference time, and training time. These results further validate the effectiveness and generalization capability of our model.

Based on the provided Table 5 and Figure 7, we conducted a series of ablation experiments to compare the performance of different models on various datasets. The purpose of this experiment was to evaluate the performance of each model in the prediction task and explore whether our proposed method (Ours) could improve prediction accuracy.

Firstly, let's consider the datasets used. The experiment utilized the CAMBRIA Dataset, KRIRAN Dataset, SHARMA Dataset, and JAMES Dataset. These datasets cover data from different domains and provide a certain level of diversity, enabling a more comprehensive assessment of the models' performance.

In terms of comparison, we selected several commonly used evaluation metrics, including Mean Absolute Error (MAE), Mean Absolute Percentage Error (MAPE), Root Mean Squared Error (RMSE), and Mean Squared Error (MSE). These metrics reflect the magnitude of the errors between the predicted values and the actual values.

Next, we will analyze the models and their results one by one.

Firstly, the CNN model. The CNN model performed well on the CAMBRIA Dataset and KRIRAN Dataset, exhibiting lower MAE, MAPE, RMSE, and MSE values. However, its performance was relatively poor on the other datasets, which may be attributed to the limited feature extraction capability of the model for specific datasets.

Secondly, the BiLSTM model. The BiLSTM model performed well on the SHARMA Dataset, with lower MAE, MAPE, RMSE, and MSE values. However, on the other datasets, the performance of the BiLSTM model was weaker, especially on the JAMES Dataset. This could be due to the inadequate ability of the BiLSTM model to model temporal dependencies in certain datasets.

Next, the Attention Mechanism model. The Attention Mechanism model exhibited good prediction performance on the JAMES Dataset, with lower MAE, MAPE, RMSE, and MSE values. However, its performance was average on the other datasets. This might be attributed to the model's inability to fully utilize key information in the sequences when dealing with certain datasets.

Moving on to the CNN + BiLSTM and CNN + Attention Mechanism models. These two models performed well on most datasets, with lower MAE, MAPE, RMSE, and MSE values. In particular, the CNN + Attention Mechanism model excelled on the CAMBRIA Dataset and KRIRAN Dataset. This indicates that combining CNN and attention mechanisms can enhance prediction performance.

Lastly, the BiLSTM + Attention Mechanism model. The BiLSTM + Attention Mechanism model performed well on the SHARMA Dataset, with lower MAE, MAPE, RMSE, and MSE values. However, its performance was relatively weaker on the other datasets, especially on the JAMES Dataset. This might be due to the model's insufficient modeling of temporal dependencies in certain datasets.

10.3389/fenrg.2024.1376677

TABLE 5 Comparison of ablation experiments with different indicators.

	CAMBRIA Wang et al. (2023) Dataset				KRIRAN Karthik et al. (2023) dataset				SHARMA CHAUHAN and SHARMA (2023) dataset				JAMES Krishnapriya and James (2023) dataset			
Model	MAE	MAPE (%)	RMSE	MSE	MAE	MAPE (%)	RMSE	MSE	MAE	MAPE (%)	RMSE	MSE	MAE	MAPE (%)	RMSE	MSE
CNN	33.79	9.01	8.13	25.25	31.01	10.27	7.57	26.30	29.23	14.63	5.86	13.82	27.63	13.30	8.44	12.67
BiLSTM	45.29	8.77	5.28	14.59	50.14	11.69	4.26	22.56	34.67	11.48	5.38	18.58	24.31	9.16	7.53	28.12
Attention Mechanism	27.69	14.62	7.20	28.50	49.97	12.09	8.50	21.43	31.71	10.32	7.75	21.92	37.31	9.80	7.52	15.15
CNN + BiLSTM	32.04	12.48	4.92	15.11	25.69	9.59	7.40	26.43	22.24	15.16	4.68	20.64	25.67	11.40	6.10	30.17
CNN + Attention Mechanism	23.77	13.46	4.65	26.06	47.31	12.20	7.22	12.27	23.64	13.72	6.19	19.46	31.33	9.11	4.53	15.84
BiLSTM + Attention Mechanism	43.68	13.65	7.04	19.23	39.86	14.82	4.42	25.99	38.94	12.56	5.37	24.12	32.86	10.53	7.62	14.57
Ours	15.20	4.12	2.13	4.56	15.20	4.12	2.13	4.56	15.20	4.12	2.13	4.56	15.20	4.12	2.13	4.56

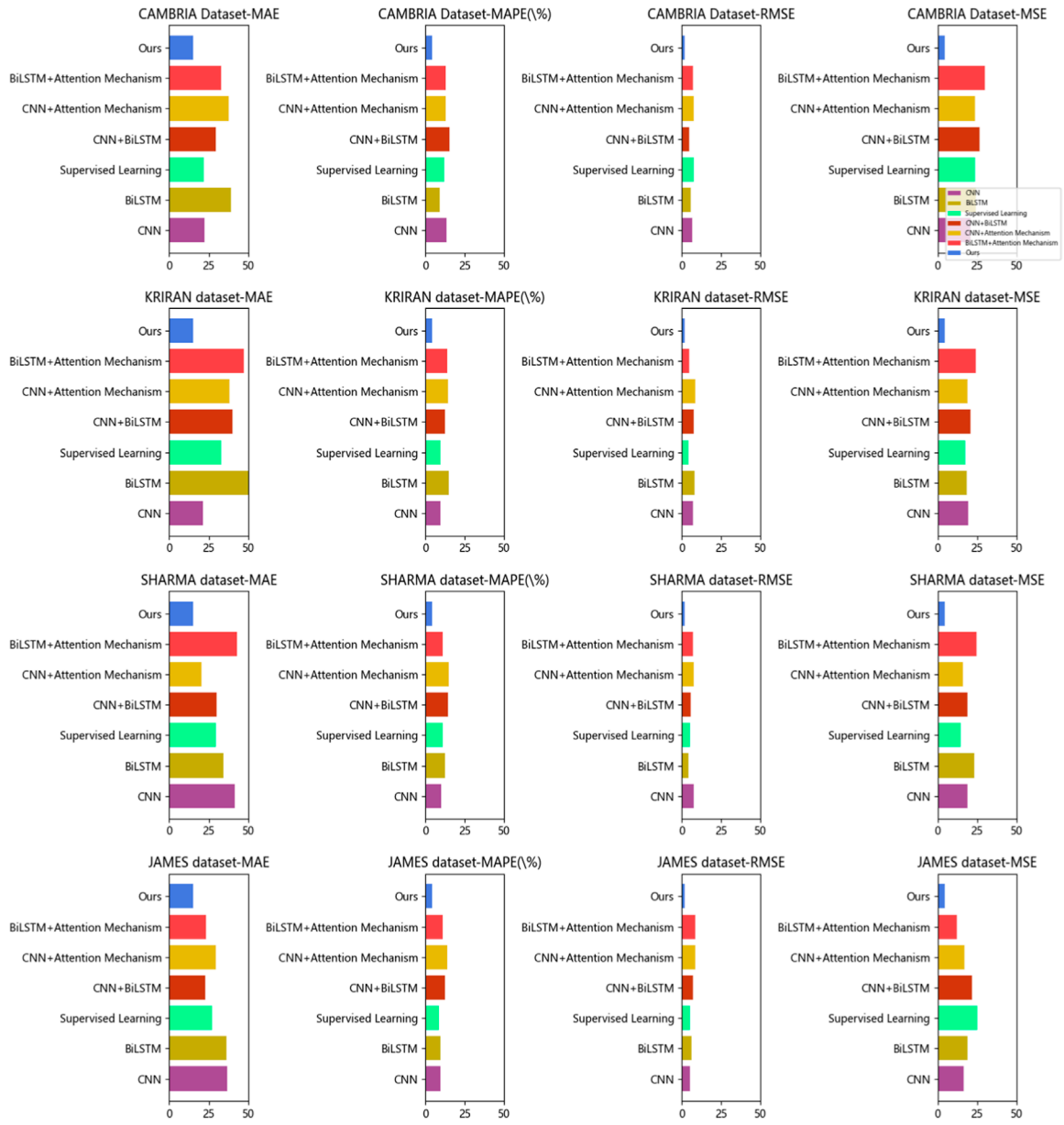

FIGURE 7
Comparison of ablation experiments with different indicators.

Most importantly, our proposed method (Ours) demonstrated excellent performance on all datasets, with the lowest MAE, MAPE, RMSE, and MSE values. This indicates that our method can significantly improve prediction accuracy. Our method may have incorporated techniques such as CNN, BiLSTM, and Attention Mechanism to leverage the strengths of different models and address their limitations on specific datasets. Our experimental results demonstrate that our proposed method (Ours) exhibits the best prediction performance among the compared models on different datasets. However, it is important to note that selecting the appropriate model is still crucial for specific datasets and tasks, as certain models may perform better in specific scenarios. Therefore, we encourage further research and experimentation to gain a deeper understanding of the performance of each model under different conditions and choose the most suitable model based on practical needs.

5 Conclusion and discussion

The study proposes a deep learning model based on CNN, BiLSTM, and attention mechanism to address the challenges of stock market prediction and financial management. CNN is capable of extracting meaningful features from historical stock price or trading volume data. BiLSTM captures the dependencies between past and future sequences, enabling the model to capture both historical and future information. The

attention mechanism allows the model to focus on the most relevant parts of the data, giving higher weights to important features. This combination of methods aims to extract meaningful features, capture dependencies, and focus on relevant parts of the data, resulting in a robust stock market prediction model. Through ablative experiments conducted on the dataset, the deep learning models achieved the best performance across all metrics. For example, the average absolute error (MAE) is 15.20, the mean absolute percentage error (MAPE) is 4.12%, the root mean square error (RMSE) is 2.13, and the mean square error (MSE) is 4.56. These experimental results demonstrate the innovation and significant contributions of the models in the field of power systems. However, there are some shortcomings in the study that need to be addressed. One of them is the issue of data quality and reliability. Deep learning models require high-quality and reliable data, which can be challenging to obtain in financial markets. Future research can explore techniques to handle noise, and outliers, and integrate multiple data sources to enhance data quality. Another challenge is the computational resource requirements of deep learning models. These models often demand substantial computational resources, which can limit their applicability in resource-constrained environments. Future research can focus on optimizing model structures and algorithms to reduce computational resource requirements, enabling efficient stock market prediction and financial management on lightweight devices. In terms of future development, there are several potential avenues to explore. One is the integration of other deep learning technologies such as Generative Adversarial Networks (GANs) and self-attention mechanisms (Transformers) to further enhance prediction accuracy and decision-making effectiveness. Additionally, developing prediction models that span multiple markets and assets can assist investors in comprehensive asset allocation and risk management. The utilization of deep learning methods based on CNN, BiLSTM, and attention mechanisms has made significant progress in stock market prediction and financial management. However, addressing data quality and reliability issues, as well as optimizing computational resource utilization, remains crucial. Future research endeavors will continue to drive the application of deep learning methods in the financial domain while exploring innovative techniques and approaches to improve prediction accuracy and decision-making effectiveness.

Data availability statement

The original contributions presented in the study are included in the article/supplementary materials, further inquiries can be directed to the corresponding author.

Author contributions

RZ: Conceptualization, Data curation, Formal Analysis, Funding acquisition, Investigation, Methodology, Project administration, Resources, Software, Supervision, Validation, Visualization, Writing–original draft, Writing–review and editing. ZL: Conceptualization, Formal Analysis, Investigation, Methodology, Project administration, Resources, Supervision, Visualization, Writing–review and editing. ZZ: Conceptualization, Data curation, Investigation, Methodology, Project administration, Resources, Validation, Visualization, Writing–original draft.

Funding

The author(s) declare that no financial support was received for the research, authorship, and/or publication of this article.

Conflict of interest

The authors declare that the research was conducted in the absence of any commercial or financial relationships that could be construed as a potential conflict of interest.

Publisher's note

All claims expressed in this article are solely those of the authors and do not necessarily represent those of their affiliated organizations, or those of the publisher, the editors and the reviewers. Any product that may be evaluated in this article, or claim that may be made by its manufacturer, is not guaranteed or endorsed by the publisher.

References

Agarap, A. F. (2018). Deep learning using rectified linear units (relu). arXiv preprint arXiv:1803.08375

Chambers, J. M., and Hastie, T. J. (2017). "Statistical models," in *Statistical models in S* (Routledge), 13–44. Available at: https://www.taylorfrancis.com/chapters/edit/10.1201/9780203738535-2/statistical-models-john-chambers-trevor-hastie.

Chauhan, K., and Sharma, N. (2023). "Study of linear regression prediction model for american stock market prediction," in Recent Developments in Electronics and Communication Systems: Proceedings of the First International Conference on Recent Developments in Electronics and Communication Systems (RDECS-2022) (IOS Press), 406.

Chowdhary, K., and Chowdhary, K. (2020). Natural language processing. *Fundam. Artif. Intell.*, 603–649. doi:10.1007/978-81-322-3972-7_19

Dong, X., Yu, Z., Cao, W., Shi, Y., and Ma, Q. (2020). A survey on ensemble learning. *Front. Comput. Sci.* 14, 241–258. doi:10.1007/s11704-019-8208-z

Gandhmal, D. P., and Kumar, K. (2019). Systematic analysis and review of stock market prediction techniques. *Comput. Sci. Rev.* 34, 100190. doi:10.1016/j.cosrev.2019.08.001

Gholamalinezhad, H., and Khosravi, H. (2020). Pooling methods in deep neural networks, a review. arXiv preprint arXiv:2009.*07485*.

Gu, A., Gulcehre, C., Paine, T., Hoffman, M., and Pascanu, R. (2020). "Improving the gating mechanism of recurrent neural networks," in International Conference on Machine Learning (PMLR), 3800–3809.

Han, K., Xiao, A., Wu, E., Guo, J., Xu, C., and Wang, Y. (2021). Transformer in transformer. *Adv. Neural Inf. Process. Syst.* 34, 15908–15919. Available at: https://proceedings.neurips.cc/paper/2021/hash/854d9fca60b4bd07f9bb215d59ef5561-Abstract.html.

He, Y., Huang, H., Fan, H., Chen, Q., and Sun, J. (2021). "Ffb6d: a full flow bidirectional fusion network for 6d pose estimation," in Proceedings

of the IEEE/CVF Conference on Computer Vision and Pattern Recognition, 3003–3013.

Htun, H. H., Biehl, M., and Petkov, N. (2023). Survey of feature selection and extraction techniques for stock market prediction. *Financ. Innov.* 9, 26. doi:10.1186/s40854-022-00441-7

Janiesch, C., Zschech, P., and Heinrich, K. (2021). Machine learning and deep learning. *Electron. Mark.* 31, 685–695. doi:10.1007/s12525-021-00475-2

Karthik, K., Ranjithkumar, V., Kp, S. K., and Ps, S. K. (2023). "A survey of price prediction using deep learning classifier for multiple stock datasets," in 2023 Second International Conference on Electronics and Renewable Systems (ICEARS) (IEEE), 1268–1275.

Kattenborn, T., Leitloff, J., Schiefer, F., and Hinz, S. (2021). Review on convolutional neural networks (cnn) in vegetation remote sensing. *ISPRS J. photogrammetry remote Sens.* 173, 24–49. doi:10.1016/j.isprsjprs.2020.12.010

Ketkar, N., Moolayil, J., Ketkar, N., and Moolayil, J. (2021). "Convolutional neural networks," in *Deep learning with Python: learn best practices of deep learning models with PyTorch*, 197–242.

Korzh, O., Cook, G., Andersen, T., and Serra, E. (2017). "Stacking approach for cnn transfer learning ensemble for remote sensing imagery," in 2017 Intelligent Systems Conference (IntelliSys) (IEEE), 599–608.

Krishnapriya, C., and James, A. (2023). "A survey on stock market prediction techniques," in 2023 International Conference on Power, Instrumentation, Control and Computing (PICC) (IEEE), 1–6.

Li, Z., Liu, F., Yang, W., Peng, S., and Zhou, J. (2021). A survey of convolutional neural networks: analysis, applications, and prospects. *IEEE Trans. neural Netw. Learn. Syst.* 33, 6999–7019. doi:10.1109/tnnls.2021.3084827

Malik, M., Malik, M. K., Mehmood, K., and Makhdoom, I. (2021). Automatic speech recognition: a survey. *Multimedia Tools Appl.* 80, 9411–9457. doi:10.1007/s11042-020-10073-7

Melina, S., Napitupulu, H., and Mohamed, N. (2023). A conceptual model of investment-risk prediction in the stock market using extreme value theory with machine learning: a semisystematic literature review. *Risks* 11, 60. doi:10.3390/risks11030060

Moghar, A., and Hamiche, M. (2020). Stock market prediction using lstm recurrent neural network. *Procedia Comput. Sci.* 170, 1168–1173. doi:10.1016/j.procs.2020.03.049

Mukherjee, S., Sadhukhan, B., Sarkar, N., Roy, D., and De, S. (2023). Stock market prediction using deep learning algorithms. *CAAI Trans. Intell. Technol.* 8, 82–94. doi:10.1049/cit2.12059

Niu, Z., Zhong, G., and Yu, H. (2021). A review on the attention mechanism of deep learning. *Neurocomputing* 452, 48–62. doi:10.1016/j.neucom.2021.03.091

Oh, J., Hessel, M., Czarnecki, W. M., Xu, Z., van Hasselt, H. P., Singh, S., et al. (2020). Discovering reinforcement learning algorithms. *Adv. Neural Inf. Process. Syst.* 33, 1060–1070.

Patil, P. R., Parasar, D., and Charhate, S. (2023). Wrapper-based feature selection and optimization-enabled hybrid deep learning framework for stock market prediction. *Int. J. Inf. Technol. Decis. Mak.* 23, 475–500. doi:10.1142/s0219622023500116

Poibeau, T. (2017). *Machine translation*. MIT Press.

Sharma, S., Sharma, S., and Athaiya, A. (2017). Activation functions in neural networks. *Towards Data Sci.* 6, 310–316. doi:10.33564/ijeast.2020.v04i12.054

Sherstinsky, A. (2020). Fundamentals of recurrent neural network (rnn) and long short-term memory (lstm) network. *Phys. D. Nonlinear Phenom.* 404, 132306. doi:10.1016/j.physd.2019.132306

Wang, Z., Hu, Z., Li, F., Ho, S.-B., and Cambria, E. (2023). Learning-based stock trending prediction by incorporating technical indicators and social media sentiment. *Cogn. Comput.* 15, 1092–1102. doi:10.1007/s12559-023-10125-8

Wu, Y., Fu, Z., Liu, X., and Bing, Y. (2023). A hybrid stock market prediction model based on gng and reinforcement learning. *Expert Syst. Appl.* 228, 120474. doi:10.1016/j.eswa.2023.120474

Yang, M., and Wang, J. (2022). Adaptability of financial time series prediction based on bilstm. *Procedia Comput. Sci.* 199, 18–25. doi:10.1016/j.procs.2022.01.003

Yang, Y.-Y., Rashtchian, C., Zhang, H., Salakhutdinov, R. R., and Chaudhuri, K. (2020). A closer look at accuracy vs. robustness. *Adv. neural Inf. Process. Syst.* 33, 8588–8601.

frontiers | Frontiers in Energy Research

TYPE Opinion
PUBLISHED 21 May 2024
DOI 10.3389/fenrg.2024.1402840

OPEN ACCESS

EDITED BY
Yitong Shang,
Hong Kong University of Science and Technology, Hong Kong SAR, China

REVIEWED BY
Zhang Hongwei,
China University of Mining and Technology, China
Xiaodong Zheng,
South China University of Technology, China
Xiurong Zhang,
China Agricultural University, China

*CORRESPONDENCE
Jing Zhang,
16601148530@163.com

RECEIVED 18 March 2024
ACCEPTED 23 April 2024
PUBLISHED 21 May 2024

CITATION
Deng J and Zhang J (2024), Opinion on enhancing diversity in photovoltaic scenario generation using weather data simulating by style-based generative adversarial networks. *Front. Energy Res.* 12:1402840. doi: 10.3389/fenrg.2024.1402840

Opinion on enhancing diversity in photovoltaic scenario generation using weather data simulating by style-based generative adversarial networks

Jianbin Deng and Jing Zhang*

Guangzhou Power Supply Bureau, Guangdong Power Grid Co., Ltd., Guangzhou, China

KEYWORDS

photovoltaic, scenario generation, weather scenario, generative adversarial network, uncertainty

1 Introduction

In 2023, the global installed capacity of photovoltaic (PV) power generation broke another record. The International Energy Agency recently released the 2023 annual report shows that last year, the global PV power generation new installed capacity of about 375 GW, an increase of more than 30 per cent (Szalóczy et al., 2024). Among them, China is the world's largest PV market and product supplier (Fu et al., 2024). However, the inherent intermittency and volatility of distributed PV power generation introduce considerable uncertainty, necessitating the modeling of PV scenarios to mitigate this uncertainty and support the growth of the PV industry. Among the various factors influencing PV output, weather conditions play a significant role in causing fluctuations and uncertainties in PV generation. However, the vast majority of the current PV scenario generation literature generates PV scenarios directly, which can overlook the important impact of weather on PV (Cai et al., 2023). To account for weather-related uncertainties and impose stricter physical constraints on PV power generation models, the PV scenario is modeled by simulating weather scenarios, enabling both specificity and generality in the models. Consequently, the development of a stochastic simulation model for year-round weather scenarios becomes essential to provide accurate weather information for PV power generation modeling (Rohani et al., 2014).

Current weather generation models mainly rely on mathematical approaches involving probabilistic calculations. The most common approach is to directly fit the distribution of weather data with probability distributions, such as sunlight intensity following a Beta distribution (Rathore et al., 2023) and wind speed following a Weibull distribution (Hussain et al., 2023). Li et la. proposed a two-stage scheme. In the first stage, weather sequences are simulated from a single-site multivariate weather generator, and in the second stage, the empirical Copula method is used to reproduce the inter-variable and inter-site dependencies as well as the temporal structure (Li et al., 2019). Richardson proposed WGEN based on a dynamic two-parameter Gamma distribution model and a two-parameter Beta distribution model (Richardson, 2018). WGEN is currently one of the widely used weather generator models, and many other weather generator models are developed based on improvements and extensions of WGEN, such as CLIGEN developed by the United States Department of Agriculture Agricultural Research Service. Sparks et al. proposed a novel method by transforming partial time series into an inferred linear function model, considering weather variables as Gaussian variables with temporal behavior (Sparks

et al., 2018). Sun et al. utilized Copula for simulating multivariate joint distributions between observed and predicted weather variables, alongside Bayesian theory to derive conditional probability density functions for specific weather forecast scenarios, facilitating large-scale weather scenario generation (Sun et al., 2020). However, these probabilistic model-based approaches fail to fully capture the complexity of weather data.

In recent years, with the rapid advancements in artificial intelligence, deep learning has emerged as a pivotal technology in various domains, including electricity and agriculture (Fu and Zhou, 2023). Currently, several deep generative models tailored for time-series data have emerged to inform weather scenario generation. Yang et al. combined LSTM and Generative Adversarial Networks (GAN) to generate health time series data (Yang Z. et al., 2023). Li et al. fused transformer and GAN to ensure temporal consistency in generating time-series data (Li et al., 2022). Yi et al. utilized a diffusion model based on U-net with attention mechanism to generate time-series data, preserving frequency features (Yi et al., 2023). In PV scenario generation, Li et al. used a time series correlation evaluation mechanism and a GAN-based generator-assisted updating mechanism to generate PV scenarios with long and short time scale time series correlation (Li et al., 2023). Xu et al. used Deep Convolutional GAN (DCGAN) to generate high-accuracy PV scenario (Xu et al., 2023). Zhang et al. used Spectral Normalization GAN (SNGAN) to improve the training stability and generate PV scenarios with probabilistic characteristics. However, these methods primarily focus on preserving the temporal characteristics and uncertainty of the generated data, neglecting the diversity aspect. We believe that diverse weather data is crucial for generating PV scenarios and analyzing uncertainty in PV systems, enabling comprehensive performance simulation across various environmental conditions. This aids in optimizing the design and operational strategies of PV systems, enhancing their stability and reliability under diverse climate conditions. Hence, generating diverse weather data remains pivotal for weather generation in the context of power applications.

In recent years, style-based GAN (StyleGAN) has become a research and application hotspot due to its ability to ensure diversity in generated image data (Karras et al., 2020). Sauer et al. utilized StyleGAN to meet the specific requirements of large-scale text-to-image synthesis (Sauer et al., 2023). Xiong et al. utilized StyleGAN to achieve fast generation of high-quality 3D digital humans (Xiong et al., 2023). Yang et al. utilized StyleGAN to implement flipping and editing operations on real face images (Yang S. et al., 2023). StyleGAN excels at disentangling images, separating different image features in a hierarchical manner to generate images with diverse and realistic styles. In the context of weather scenario, we utilize style-based learning to enhance the level of refinement and granularity in weather simulations. Style-based learning enables the separation of various levels of image features (Karras et al., 2019). We believe that, in the case of weather data, it allows the matching of overall trend features and local random features, respectively. This allows for the generation of weather scenarios that capture the accurate overall trend while incorporating nuanced variations. However, style-based learning relies on convolutional neural networks (CNNs) for data processing, which may limit StyleGAN's ability to learn temporal features from weather data. To address this limitation, replacing the 2-dimensional CNNs in StyleGAN with 1-dimensional CNNs could better model the temporal characteristics of weather data.

2 Model for weather simulation

As shown in Figure 1, we present a novel stochastic simulation approach for generating year-round PV scenarios utilizing weather scenarios generated on Conditional Style-based Generative Adversarial Networks (C-StyleGAN). The weather scenarios consist of three variables, temperature, direct radiation and diffuse radiation, which are placed side by side during the training of the model to facilitate the neural network to learn the correlation between the variables. An increase in temperature causes a decrease in the power generation efficiency of the PV panels because high temperatures increase the resistance to electron flow within the PV panels. Direct radiation is the main source of energy for PV panels, while diffuse radiation affects the propagation path of light and indirectly affects the amount of radiant energy received by the PV panels. This method leverages real weather data as a foundation for simulating weather scenarios. The weather data generated using C-StyleGAN exhibits comprehensive diversity and effectively captures temporal correlations through active learning. The proposed method employs a Conditional Generative Adversarial Network (CGAN) as the primary framework, and the underlying neural network architecture is an enhanced version of the style-based Generative Adversarial Network (StyleGAN2). In Sections 2.1, 2.2, we will introduce the CGAN and the improved StyleGAN2, respectively. The generated PV scenarios can be obtained by inputting the temperature, direct radiation and diffuse radiation generated by C-StyleGAN into the PV model (Yano et al., 2009).

2.1 CGAN using weather features as labels

CGAN is the main framework of this model and provides the overall idea for the training and optimization of the model (Zhang et al., 2021).

In a GAN framework, the primary components are the generator and the discriminator. The objective of generator is to learn the underlying distribution $P_{ori}(w)$ of the real data by randomly sampling from real data. It takes a random noise $P_z(z)$ as input and converts it into a synthesized data $P_{gen}(\hat{w}: \theta)$ using a network parameter θ. The primary objective of the generator is to produce weather data samples that closely resemble real data, with the intention of deceiving the discriminator. On the other hand, the discriminator is a binary model responsible for distinguishing between the data samples. Its role is to classify the weather data samples, with the objective of labeling the generated weather data samples $P_{gen}(\hat{w}: \theta)$ by the generator as "false" and the real weather data samples $P_{ori}(w)$ as "true" to the best of its ability. In the training process, both the discriminator and the generator are trained using an adversarial approach. The generator's primary objective is to enhance its generation performance in order to deceive the discriminator, while the discriminator aims to improve its discrimination ability to accurately classify the weather data samples.

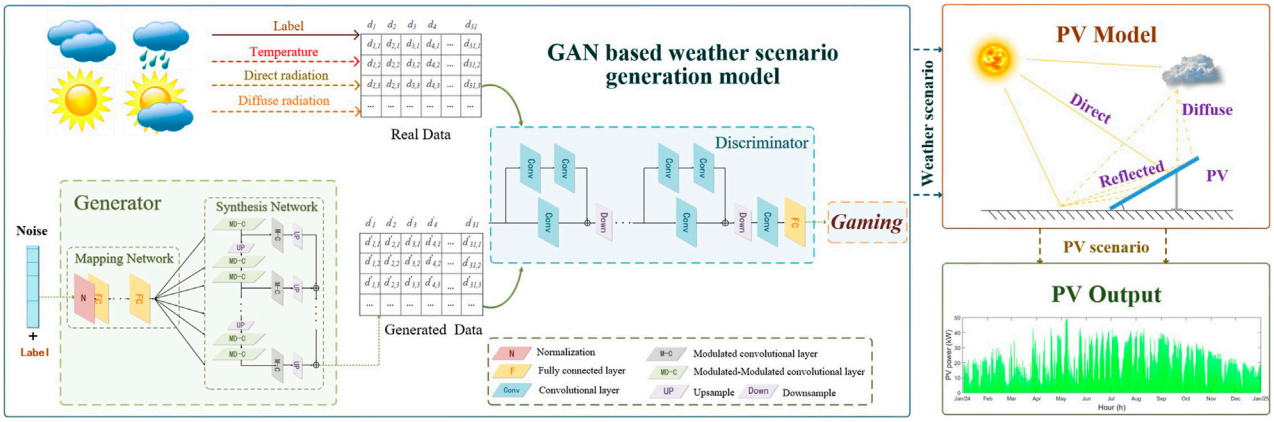

FIGURE 1
Conditional style-based generative adversarial networks model for weather simulation of PV scenario.

The training process of a GAN can be characterized as a minimax game, which is formulated as a value function $V(D,G)$ by Eq. 1. In this game, the objective is to maximize $V(D,G)$ with respect to the generator G, while minimizing the value function V with respect to the discriminator D. This minmax game provides a clear understanding of the GAN training process.

$$\min_G \max_D V(D,G) = \mathrm{E}_{x \sim P_{ori}}(x)\left[\log D(P_{ori}(w))\right] + \mathrm{E}_{x \sim P_{gen}(x:\theta)}\left[\log\left(1 - D\left(P_{gen}(\hat{w}:\theta)\right)\right)\right] \quad (1)$$

However, the data generated by GAN is inherently random and lacks control over specific output. To address this limitation, the concept of Conditional GAN (CGAN) has been proposed, incorporating the principles of supervised learning into GAN. The fundamental idea behind CGAN is to introduce conditional information into both the generator and discriminator. In our model, we utilize weather features as conditional labels, such as sunny, cloudy, overcast, and rainy/snowy, to steer and facilitate the training. This approach enables us to generate weather data sequences that align with specific desired features. The objective function of our model (Eq. 2) is derived by adapting Eq. 1.

$$\min_G \max_D V(D,G) = \mathrm{E}_{x \sim P_{ori}(w)}\left[\log D\left(P_{ori}(w)|y\right)\right] + \mathrm{E}_{x \sim P_{gen}(\hat{w}:\theta)}\left[\log\left(1 - D\left(P_{gen}(\hat{w}:\theta)|y\right)\right)\right] \quad (2)$$

where, y denotes the condition and corresponds to the weather features.

2.2 Style-based learning model

We draw inspiration from StyleGAN2, which leverages the concept of style migration to learn from image data. The style-based learning generator incorporates two main parts, namely the Mapping network and the Synthesis network, to facilitate its functionality. The Mapping network plays a crucial role in decoupling complex features that are coupled together. On the other hand, the Synthesis network incorporates two important components for data processing: modulation-demodulation convolutional layers (MD-C) and modulation convolutional (M-C) layers. Eqs 3–6 (Karras et al., 2019) illustrate the functioning of MD-C network blocks, while for M-C the operation of Eq. 5 is omitted. y incorporating style-based learning from StyleGAN2, we are able to enhance the fidelity and realism of weather simulations. This approach enables us to capture not only the overall global trends but also the localized variations in the generated weather scenarios.

$$\boldsymbol{s} = \boldsymbol{\omega}^{\mathrm{f}} \cdot w + \boldsymbol{b}^{\mathrm{f}} \quad (3)$$

$$\boldsymbol{\omega}^{\mathrm{c}'} = \left[s_i \cdot \omega^{\mathrm{c}}_{ijmn}\right] \quad (4)$$

$$\boldsymbol{\omega}^{\mathrm{c}''} = \left[\frac{\omega^{\mathrm{c}'}_{ijmn}}{\sqrt{\sum_{i,m,n}\left(\omega^{\mathrm{c}'}_{imn}\right)^2 + \epsilon}}\right] \quad (5)$$

$$\hat{w} = \boldsymbol{\omega}^{\mathrm{c}''} * \boldsymbol{x}^{\mathrm{c}} + \boldsymbol{b}^{\mathrm{c}} \quad (6)$$

where, the w decoupled by the Mapping Network is first passed through a fully connected layer with a weight of $\boldsymbol{\omega}^{\mathrm{f}}$ and a deviation of $\boldsymbol{b}^{\mathrm{f}}$ to obtain the style information $\boldsymbol{s}$. The resulting $\boldsymbol{s}$ is then multiplied element-wise with the convolution kernel ω^{c}, producing modulation weights $\boldsymbol{\omega}^{\mathrm{c}'}$. Subsequently, a demodulation weight $\boldsymbol{\omega}^{\mathrm{c}''}$ is computed using a root mean square operation, incorporating an infinitesimal constant ϵ. Utilizing $\boldsymbol{\omega}^{\mathrm{c}''}$ and the convolutional bias $\boldsymbol{b}^{\mathrm{c}}$, a convolutional operation is performed on $\boldsymbol{x}^{\mathrm{c}}$ which is the original input. This operation enables the extraction of complicated features from weather scenario.

The discriminator is predominantly implemented using a residual Convolutional Neural Network (CNN). This choice of architecture enables the discriminator to effectively identify abstract features and uncover hidden invariant structures within the weather data sequence. Within each residual block, average pooling down-sampling is employed to reduce the temporal resolution of the samples by half. Pattern collapse, a common issue in GAN structures where only a subset of data patterns are captured, is addressed by incorporating a small batch standard difference layer into the network structure. This addition aims to increase the diversity of reproducible samples generated, mitigating

the problem. Towards the end of the discriminator, two fully connected layers are applied to adjust the output shape. The discriminator's discriminant results being closer to 1 indicate a more realistic weather scenario. These discriminant results are then utilized to construct loss functions for both the generator network and the discriminator network, as described by Eqs 7, 8. The purpose of computing these losses is to optimize the parameters of each component in the neural network using backpropagation, thereby continuously improving the realism of the weather data generated by the generator.

$$LossG = \mathrm{Relu}\left(1 - D\left(G\left(z \mid y\right)\right)\right) \tag{7}$$

$$LossD = \mathrm{Relu}\left(1 + D\left(G\left(z \mid y\right)\right)\right) + \mathrm{Relu}\left(D\left(w \mid y\right)\right) \tag{8}$$

where the function denoted as Relu is represented by $\mathrm{Relu}(x) = \max\{0, x\}$ and has the capability to be smoothed.

3 Discussion

Currently, almost all GAN-based PV scenario generation models are directly based on renewable energy generation data such as PV data or wind power data, and the proposed model is also theoretically applicable to the direct modelling of the PV scenario and the wind power scenario, as they are both essentially time series data. However, these approaches often overlook the crucial factor of weather scenarios. Weather conditions significantly impact PV power generation, and PV power models rely on factors such as direct radiation, diffuse radiation, and temperature to simulate PV power output. Solar radiation levels and temperature directly influence the performance of PV modules, and the uncertainty in weather scenarios contributes greatly to the uncertainty in PV power generation. Therefore, solely relying on direct PV data simulation neglects the physical constraints imposed by weather scenarios on PV power generation, limiting the generalizability of PV scenario modeling approaches. To address this limitation, we propose a weather-based PV generation scenario simulation that first models weather scenarios to accurately capture their realism. By incorporating weather-based simulations, we can enforce strict physical constraints on PV scenarios, thus ensuring a higher level of generality in PV scenario simulation models.

Traditional methods for modeling weather scenarios primarily rely on explicit methods based on probabilistic statistical approaches. These explicit methods require formulating probability distribution functions for PV generation data, leading to limitations such as small capacity, poor generalization capability, and difficulties in handling high-dimensional data. With the advancements in artificial intelligence algorithms, deep learning methods, particularly unsupervised learning methods based on GAN, have gained prominence. GAN-based models do not necessitate explicit specification of probability distribution functions for scenario data, nor do they require explicit likelihood estimation. GAN is capable of capturing complex data distributions due to its data-driven approach. GAN has the flexibility to generate realistic weather simulations while effectively capturing spatial and temporal dependencies. In addition, GANs have the ability to generate high-resolution simulations and estimate uncertainty, providing a powerful tool for weather prediction and climate research. However, one limitation of GANs is the lack of control over the generated data, as it is random and unpredictable. CGAN enable GANs to transition from unsupervised to supervised learning, allowing better control over the network's output. In our proposed model, we utilize weather features as labels, such as sunny, cloudy, overcast, and rainy/snowy, to generate weather scenarios based on specified weather conditions. By incorporating weather features as labels, we can generate weather scenarios according to our specific requirements. To achieve better control over the overall probabilistic, temporal, and correlation characteristics of weather scenario data, as well as the diversity represented by local differences, we propose a style-based weather data simulation algorithm. This algorithm enables us to learn the trend characteristics and local uncertainty random variation characteristics of weather data, representing high and low image characteristics, respectively. By separating these characteristics, we can generate weather scenarios with consistent trends but diverse variations.

4 Conclusion

For PV scenario modeling, generating weather data sequences with specific features is crucial. We propose a conditional style-based generative adversarial network for stochastic weather scenario simulation.

In conclusion, two key points stand out. Firstly, methods based on weather data for generating PV scenarios can comprehensively consider weather's impact on PV system performance, enhancing simulation accuracy. This aids in understanding PV system behavior under various conditions and supports system design and operation. Secondly, current time-series data generation models and PV scenario generation models often lack scenario diversity consideration. StyleGAN, an advanced image generation technology, holds significant potential for weather data generation. Leveraging its hierarchical feature control and continuous latent space, StyleGAN can generate richer, more diverse, and realistic weather scenarios. This increases data diversity and enhances simulation realism.

Moreover, AI advancements, like ChatGPT, are promising for weather scenario generation. It can automate dataset annotations, improve data quality, and analyze discrepancies between generated and real data, aiding GAN training and refining generated results. This opens avenues for processing higher-dimensional and larger-scale weather data.

Author contributions

JD: Conceptualization, Data curation, Investigation, Writing–original draft. JZ: Funding acquisition, Investigation, Visualization, Writing–review and editing.

Funding

The author(s) declare that financial support was received for the research, authorship, and/or publication of this article. This study is supported by the science and technology program of Guangzhou

Power Supply Bureau, Guangdong Power Grid Co., Ltd. (030109KK52222003).

Conflict of interest

Authors JD and JZ were employed by Guangzhou Power Supply Bureau of Guangdong Power Grid Co., Ltd.

The authors declare that this study received funding from the science and technology program of Guangzhou Power Supply Bureau of Guangdong Power Grid Co., Ltd. (030109KK52222003). The funder had the following involvement in the study: Data collection.

Publisher's note

All claims expressed in this article are solely those of the authors and do not necessarily represent those of their affiliated organizations, or those of the publisher, the editors and the reviewers. Any product that may be evaluated in this article, or claim that may be made by its manufacturer, is not guaranteed or endorsed by the publisher.

References

Cai, C., Li, Y., He, Y., and Guo, L. (2023). Two-tier coordinated optimal scheduling of wind/PV/hydropower and storage systems based on generative adversarial network scene generation. *Front. Energy Res.* 11. doi:10.3389/fenrg.2023.1266079

Fu, X., Wei, Z., Sun, H., and Zhang, Y. (2024). Agri-energy-environment synergy-based distributed energy planning in rural areas. *IEEE Trans. Smart Grid*, 1. doi:10.1109/TSG.2024.3364182

Fu, X., and Zhou, Y. (2023). Collaborative optimization of PV greenhouses and clean energy systems in rural areas. *IEEE Trans. Sustain. Energy* 14, 642–656. doi:10.1109/TSTE.2022.3223684

Hussain, I., Haider, A., Ullah, Z., Russo, M., Casolino, G. M., and Azeem, B. (2023). Comparative analysis of eight numerical methods using Weibull distribution to estimate wind power density for coastal areas in Pakistan. *Energies* 16, 1515. doi:10.3390/en16031515

Karras, T., Laine, S., Aittala, M., Hellsten, J., Lehtinen, J., and Aila, T. (2020). "Analyzing and improving the image quality of StyleGAN," in 2020 IEEE/CVF Conference on Computer Vision and Pattern Recognition (CVPR), Seattle, WA, USA, June 13 2020 to June 19 2020, 8107–8116.

Li, P., Huang, W., Liang, L., Dai, Z., Cao, S., Zhang, H., et al. (2023). Power system data-driven dispatch using improved scenario generation considering time-series correlations. *Front. Energy Res.* 11. doi:10.3389/fenrg.2023.1267713

Li, X., and Babovic, V. (2019). A new scheme for multivariate, multisite weather generator with inter-variable, inter-site dependence and inter-annual variability based on empirical copula approach. *Clim. Dyn.* 52, 2247–2267. doi:10.1007/s00382-018-4249-5

Li, X., Metsis, V., Wang, H., and Ngu, A. H. (2022). "TTS-GAN: a transformer-based time-series generative adversarial network," in Conference on Artificial Intelligence in Medicine in Europe, Halifax, Canada, June 14-17 2022, 133–143.

Rathore, A., Kumar, A., and Patidar, N. P. (2023). Techno-socio-economic and sensitivity analysis of standalone micro-grid located in central India. *Int. J. Ambient Energy* 44, 1490–1511. doi:10.1080/01430750.2023.2176922

Richardson, C. W. (2018) *Wgen: a model for generating daily weather variables*.

Rohani, G., and Nour, M. (2014). Techno-economical analysis of stand-alone hybrid renewable power system for Ras Musherib in United Arab Emirates. *Energy* 64, 828–841. doi:10.1016/j.energy.2013.10.065

Sauer, A., Karras, T., Laine, S., Geiger, A., and Aila, T. (2023). "StyleGAN-T: unlocking the power of GANs for fast large-scale text-to-image synthesis," in International Conference on Machine Learning, Honolulu; HI; United States, 23-29 July 2023.

Sparks, N. J., Hardwick, S. R., Schmid, M., and Toumi, R. (2018). IMAGE: a multivariate multi-site stochastic weather generator for European weather and climate. *Stoch. Environ. Res. Risk Assess.* 32, 771–784. doi:10.1007/s00477-017-1433-9

Sun, M., Feng, C., and Zhang, J. (2020). Probabilistic solar power forecasting based on weather scenario generation. *Appl. Energy* 266, 114823. doi:10.1016/j.apenergy.2020.114823

Szalóczy, Z., Gelencsér, A., Rostási, Á., and Abonyi, J. (2024) *The economic growth paradigm must Be abandoned in the transition to green energy*. Available at SSRN 4735910.

Xiong, Z., Kang, D., Jin, D., Chen, W., Bao, L., Han, X., et al. (2023). "Get3DHuman: lifting StyleGAN-human into a 3D generative model using pixel-aligned reconstruction priors," in 2023 IEEE/CVF International Conference on Computer Vision (ICCV), Paris, France, October 2-3, 2023, 9253–9263.

Xu, J., Ji, Z., Liu, X., Bao, Y., Zhang, S., Wang, W., et al. (2023). Two-stage scheduling of integrated energy systems based on a two-step DCGAN-based scenario prediction approach. *Front. Energy Res.* 10. doi:10.3389/fenrg.2022.1012367

Yang, S., Jiang, L., Liu, Z., and Loy, C. C. (2023b). "StyleGANEX: StyleGAN-based manipulation beyond cropped aligned faces," in 2023 IEEE/CVF International Conference on Computer Vision (ICCV), Paris, France, October 2-3, 2023, 20943–20953.

Yang, Z., Li, Y., and Zhou, G. (2023a). TS-GAN: time-series GAN for sensor-based health data augmentation. *ACM Trans. Comput. Healthc.* 4, 1–21. doi:10.1145/3583593

Yano, A., Furue, A., Kadowaki, M., Tanaka, T., Hiraki, E., Miyamoto, M., et al. (2009). Electrical energy generated by photovoltaic modules mounted inside the roof of a north-south oriented greenhouse. *Biosyst. Eng.* 103, 228–238. doi:10.1016/j.biosystemseng.2009.02.020

Yi, H., Hou, L., Jin, Y., and Saeed, N. A. (2023). Time series diffusion method: a denoising diffusion probabilistic model for vibration signal generation. Available at: https://arxiv.org/abs/2312.07981.

Zhang, Q., Ferdowsi, A., Saad, W., and Bennis, M. (2021). Distributed conditional generative adversarial networks (GANs) for data-driven millimeter wave communications in UAV networks. *IEEE Trans. Wirel. Commun.* 21, 1438–1452. doi:10.1109/TWC.2021.3103971

Zhang, X., Fan, S., and Li, D. (2024). Spectral normalization generative adversarial networks for photovoltaic power scenario generation. *IET Renew. Power Gener*. doi:10.1049/rpg2.12978

frontiers | Frontiers in Energy Research

TYPE Original Research
PUBLISHED 21 May 2024
DOI 10.3389/fenrg.2024.1401080

OPEN ACCESS

EDITED BY
Yingjun Wu,
Hohai University, China

REVIEWED BY
Shuai Yao,
Cardiff University, United Kingdom
Sufan Jiang,
The University of Tennessee, Knoxville, United States
Shuxin Tian,
Shanghai University of Electric Power, China

*CORRESPONDENCE
Lili Hao,
lili_hao@163.com

RECEIVED 14 March 2024
ACCEPTED 24 April 2024
PUBLISHED 21 May 2024

CITATION
Qian J, Cai J, Hao L and Meng Z (2024), Improved typical scenario-based distributionally robust co-dispatch of energy and reserve for renewable power systems considering the demand response of fused magnesium load.
Front. Energy Res. 12:1401080.
doi: 10.3389/fenrg.2024.1401080

Improved typical scenario-based distributionally robust co-dispatch of energy and reserve for renewable power systems considering the demand response of fused magnesium load

Junchen Qian, Jilin Cai, Lili Hao* and Zhixiang Meng

College of Electrical Engineering and Control Science, Nanjing Tech University, Nanjing, China

In recent years, the penetration of solar and wind power has rapidly increased to construct renewable energy-dominated power systems (RPSs). On this basis, the forecasting errors of renewable generation power have negative effects on the operation of the power system. However, traditional scheduling methods are overly dependent on the generation-side dispatchable resources and lack uncertainty modeling strategies, so they are inadequate to tackle this problem. In this case, it is necessary to enhance the flexibility of the RPS by both mining the load-side dispatchable resources and improving the decision-making model under uncertainty during the energy and reserve co-dispatch. In this paper, due to the great potential in facilitating the RPS regulation, the demand response (DR) model of fused magnesium load (FML) is first established to enable the deeper interaction between the load side and the whole RPS. Then, based on the principal component analysis and clustering algorithm, an improved typical scenario set generation method is proposed to obtain a much less conservative model of the spatiotemporally correlated uncertainty. On this basis, a two-stage distributionally robust optimization model of the energy and reserve co-dispatch is developed for the RPS considering the DR of FML. Finally, the proposed method is validated by numerical tests. The results show that the costs of day-ahead dispatch and re-dispatch are significantly decreased by using the improved typical scenario set and considering the DR of FML in regulation, which enhances the operation economy while maintaining the high reliability and safety of the RPS.

KEYWORDS

distributionally robust optimization, demand response, fused magnesium load, optimal dispatch, typical scenario generation

1 Introduction

Under the background of increasingly serious environmental problems and accelerated depletion of resources, renewable energy-dominated power systems (RPSs) are developing rapidly (Cai et al., 2022; Liu et al., 2023). The novelty of RPSs is reflected by two main characteristics: environmentally friendly and highly flexible. Being environmentally friendly requires the large-scale application of renewable energy sources (RESs) in generation, but

the complex uncertainty of RESs poses a great challenge to power system scheduling and dispatch. Therefore, the RPS must have an abundance of dispatchable resources and effective optimal dispatch methods, which means that the RPS needs to be highly flexible (Cheng et al., 2023; Trojani et al., 2023).

In the traditional power system, dispatchable resources mainly refer to thermal power, hydropower, and other conventional units on the generation side, so the dispatch mode is generation-follow-load. However, with the progress of carbon peaking and carbon neutrality, thermal power units in the RPS will inevitably be replaced by RES generation on a large scale, causing a paradoxical situation of increasing system uncertainty and decreasing generation-side regulation capability. In this case, the demand response (DR) mechanism, as a method to exploit the potential of load-side participation in system scheduling, has gained wide attention in recent years (Xie et al., 2023; Yang et al., 2024).

Currently, most related studies focus on the DR modeling of residential loads and commercial loads (Chen et al., 2022; de Chalendar et al., 2023). Compared with residential and commercial loads, industrial loads account for a higher proportion in the whole power system. In particular, the energy-consuming industrial loads have the advantages of complete infrastructures, large capacities, and strong willingness to participate in DR, so they have huge dispatch potential. However, the relevant research studies are still insufficient at present.

As typical energy-consuming industrial loads, there have been reports about the participation of iron/steel loads and fused magnesium loads (FMLs) in DR and RPS dispatch. Boldrini et al. (2024) investigated the potential of participation in DR for the electric arc furnace (EAF) technology using hydrogen as the reductant of iron. Wang et al. (2023) considered the production plans of the steel refining process to be adjustable, so that the ladle furnaces are treated as cuttable loads and modeled as DR resources. FML was reported to participate in the primary frequency control market, and the corresponding declared capacity optimization method was proposed by Guo et al. (2023). In summary, it is the heat storage processes of the iron/steel loads and FMLs using EAFs that can be regarded as DR resources. EAFs melt raw materials with electric heating technology to manufacture products, which is simple and less sensitive to power fluctuations, making them highly flexible during RPS dispatch. In addition, EAFs typically have large capacities, so rational production arrangements for enterprises using such equipment can provide significant dispatchable capacity for the power system. Hence, it is necessary to construct DR models for these energy-consuming industrial loads, so that their flexibility can contribute to the RPS. Different from FMLs, iron/steel loads have many consecutive processes such as refining and rolling. Due to the limited amount of equipment in each process, it is necessary to consider their coordination in the DR model, which is relatively complex. Therefore, to focus on the DR potential exploitation, FMLs are taken as the representative of the energy-consuming industrial loads.

To fully utilize the flexible resources of both generation and load sides, effective dispatch decision methods are also needed to enhance the ability of the power system to cope with the uncertainty of RESs. According to decision conservativeness, commonly used methods are usually classified into two categories: scenario-based stochastic optimization (SO) and robust optimization (RO) (Mazidi et al., 2019; Tan et al., 2019; Cheng et al., 2024).

For example, a stochastic scenario-based optimization model was proposed by Derakhshandeh et al. (2017) to optimize the generation scheduling of microgrids integrated with plug-in electric vehicles. A stochastic and affinely adjustable robust optimization method was constructed by Huang et al. (2019) for the co-dispatch of energy and reserve of the RPS. However, the two methods have their drawbacks.

The SO methods rely on the uncertainty sets generated by parameterized probability distribution functions. However, it is difficult to guarantee the validity of the chosen parameterized function. In addition, the obtained uncertainty sets are less capable of considering the extreme scenarios, so the dispatch results tend to be over-optimistic and insufficiently reliable. The RO methods only consider the extreme scenarios corresponding to the uncertainty space boundaries, some of which are completely impossible in reality, so the derived dispatch schemes are overly conservative. Both methods lack the capability to deal with the spatiotemporal correlation between uncertainty variables.

To combine SO and RO to achieve complementary effects, the distributionally robust optimization (DRO) theory is proposed and gradually promoted for use, which is also convenient for taking into account the spatiotemporal correlation of uncertainty variables (Shui et al., 2019; Gao et al., 2020; Liu et al., 2022).

The balance between the economy and reliability of the decision using DRO is closely related to the way of selecting the typical scenarios of uncertainty. The space enclosed by the typical scenarios is required to contain as many samples in the historical data as possible and to contain as little redundant area where no sample is located as possible. For example, the historical samples were directly used to derive an empirical probability distribution by Wang et al. (2020), where the interval centers of the distribution were adopted as the typical scenarios to construct a DRO dispatch model for the distribution network. The Wasserstein metric-based uncertainty set construction methods are also popular choices but need to consider large numbers of historical scenarios when solving the DRO model, which causes computational burden (Saberi et al., 2021; Feizi et al., 2022; Zheng et al., 2023). In recent years, minimum volume enclosing ellipsoid (MVEE)-based uncertainty set construction methods have achieved better results in typical scenario selection. Zhang et al. (2022) first obtained the MVEE that covers all the historical samples with an iteration algorithm, and then the vertices on each symmetry axis of the MVEE are regarded as the typical scenarios. However, the space enclosed by these vertices is the inscribed polyhedron of the MVEE and is not guaranteed to cover all the historical samples. To solve this problem, an expansion method of the inscribed polyhedron was proposed by Zhang et al. (2021) to obtain the vertices of its corresponding circumscribed polyhedron. Unfortunately, although all samples are covered after such treatment, the redundant scenarios in the polyhedral space increase significantly, some of which even exceed the upper and lower bounds of the uncertainty variables. These impossible scenarios result in great conservativeness of the decision scheme, which makes the DRO lose advantages. It can be observed that directly using the vertices of the inscribed and circumscribed polyhedron as typical scenarios for DRO is inappropriate.

According to the above analysis, the RPS still has deficiencies in both flexible resource mining and dispatch capability enhancement, so this paper focuses on the relevant works shown as follows:

1) FML is taken as the representative of energy-consuming industrial loads, and its lean DR model integrated with time-coupled constraints is established to further exploit the regulation potential of the RPS load side.
2) An improved typical scenario generation method is proposed by uniting the boundary points with cluster centers of the historical samples and then adjusting the impossible points. Then, an improved typical scenario-based DRO (ITSDRO) dispatch model for the RPS is established to lower the conservativeness and achieve a better balance between reliability and economy.

The rest of the paper is organized as follows: in Section 2, the two-stage DRO model is constructed for the co-dispatch of energy and reserve for the RPS considering the DR of FML; Section 3 details the improved typical scenario set generation method, and it is integrated into the model established in Section 2; then, the solving algorithm of the proposed DRO model is given in Section 4; numerical tests are carried out and discussed in Section 5; and the conclusion is summarized in Section 6.

2 DRO co-dispatch of energy and reserve for the RPS considering the DR of FML

In this section, the two-stage DRO co-dispatch model of energy and reserve for the RPS is established considering the participation of the FML in the DR. Although only the DR of the FML is integrated into the model, DR models of other types of loads can be added conveniently.

2.1 DR model of the FML

The FML utilizes EAFs to prepare electrically fused magnesia as its product, whose main component is MgO. The production process is to use the electric arc to heat the raw materials containing MgO until they are melted in the EAF. The molten raw materials are cooled naturally, and magnesite crystals grown from the molten material are ground to obtain the magnesium sand. In this process, the EAF can lift or lower the electrode to control the current, so it can regulate its power consumption. Since the rated power of a single EAF can reach the MW class, the participation of the FML in the DR project provides considerable flexible capacity for the RPS dispatch.

However, as one type of high energy-consuming industrial load, the pre-requisite for the participation of the FML in the DR is to ensure its production safety and the achievability of production tasks. Hence, it is necessary to construct the DR model of a single EAF based on the constraints in the production process and then to form the DR model of the FML accordingly.

2.1.1 Regulation capacity constraints of the EAF

$$P_{m,t}^{\mathrm{M}} = P_{m,t}^{\mathrm{M,base}} + P_{m,t}^{\mathrm{M,u}} - P_{m,t}^{\mathrm{M,d}}, \tag{1}$$

$$.0 \le P_{m,t}^{\mathrm{M,u}} \le s_{m,t}^{\mathrm{u}} P_{\max,m}^{\mathrm{u}}, 0 \le P_{m,t}^{\mathrm{M,d}} \le s_{m,t}^{\mathrm{d}} P_{\max,m}^{\mathrm{d}}, \tag{2}$$

$$s_{m,t}^{\mathrm{u}} + s_{m,t}^{\mathrm{d}} = 1, \tag{3}$$

where t is the index of time. $P_{m,t}^{M}$ is the regulated power of the mth EAF. $P_{m,t}^{\mathrm{M,base}}$ is the base power of the mth EAF. $P_{m,t}^{\mathrm{M,u}}$ and $P_{m,t}^{\mathrm{M,d}}$ are the upward and downward regulated power of the mth EAF, respectively; $P_{\max,m}^{\mathrm{u}}$ and $P_{\max,m}^{\mathrm{d}}$ are the upper limits of $P_{m,t}^{\mathrm{M,u}}$ and $P_{m,t}^{\mathrm{M,d}}$ due to the safety consideration, respectively; and $s_{m,t}^{\mathrm{u}}$ and $s_{m,t}^{\mathrm{d}}$ are binary variables indicating the EAF to be in upward and downward regulation states, respectively.

2.1.2 Constraints of regulation times of the EAF

Within a day, the total upward and downward regulation times of an EAF should not exceed a scheduled maximum number. This avoids the overly frequent regulation of one EAF and ensures its productivity and product purity.

$$0 \le \sum_{t=2}^{T} \left| s_{m,t}^{\mathrm{u}} - s_{m,t-1}^{\mathrm{u}} \right| \le M, \tag{4}$$

where M is the scheduled maximum regulation number of one EAF in 1 day. T is the number of time slots in 1 day.

Upward and downward regulation times are both considered in (4), which is intuitively demonstrated by introducing binary auxiliary variables in Section 2.2.4.

2.1.3 Regulation duration constraints of the EAF

One EAF should not be in the upward regulation state for several consecutive periods; otherwise, the temperature of the molten liquid continues to increase, resulting in accidents such as furnace eruption. In addition, if the power of the EAF is continuously regulated downward for too long, the temperature in the furnace cannot meet the production requirements, which affects the purity of the products. Therefore, the upward and downward regulation duration constraints of the EAF are constructed as follows:

$$\begin{cases} s_{m,t}^{\mathrm{u}} \left(T_m^{\mathrm{u}} - \sum_{\tau=t-T_m^{\mathrm{u}}-1}^{t-1} s_{m,\tau}^{\mathrm{u}} \right) \ge 0 \\ s_{m,t}^{\mathrm{d}} \left(T_m^{\mathrm{d}} - \sum_{\tau=t-T_m^{\mathrm{d}}-1}^{t-1} s_{m,\tau}^{\mathrm{d}} \right) \ge 0 \end{cases}, \tag{5}$$

where T_m^{u} and T_m^{d} are the maximum duration of upward and downward power regulation of the EAF, respectively.

2.1.4 Constraints of the power and production of the FML

The power consumed by the FML is accumulated from all EAFs:

$$\sum_{m} P_{m,t}^{\mathrm{M}} = P_t^{\mathrm{FML}}, \tag{6}$$

where $P_{\mathrm{FML}}(t)$ is the total power of all the EAFs belonging to the FML at time t.

Then, the FML is modeled as a shiftable load in (7), which means that the energy consumed in 1 day should remain unchanged

whether FML participates in DR projects or not. This constraint ensures that production is not affected by the DR.

$$\sum_t \sum_m P_{m,t}^{\mathrm{M,base}} = \sum_t P_t^{\mathrm{FML}}. \tag{7}$$

2.2 Construction of the two-stage DRO co-dispatch model

To optimize the day-ahead energy and reserve strategy of the RPS, the DRO model constructed in this paper is composed of two stages. In the first stage, the base case of the day-ahead RES and load prediction is used to optimize the unit commitment and reserved capacity of conventional units. In the second stage, a prediction error scenario set is constructed and used to optimize the operation of flexible resources to ensure the RPS reliability considering the day-ahead RES and load prediction uncertainty.

By the interaction of decision variables of the two stages, the determined unit commitment and reserved capacity finally achieve a balance between reliability and economy.

2.2.1 Objective function

The overall objective of the proposed model is to minimize the total operation costs of the two stages, as shown in (8):

$$\min_{x} C_{\mathrm{op}}(\boldsymbol{x}) + \max_{p_k \in \Omega} \sum_{k=1}^{n_{\mathrm{sce}}} p_k \min_{y_k} C_{\mathrm{reg}}(\boldsymbol{x}, \boldsymbol{y}_k), \tag{8}$$

$$\begin{aligned} \boldsymbol{x} &= \left[I_{i,t}, P_{i,t}, \alpha_{i,t}^{\mathrm{u}}, \alpha_{i,t}^{\mathrm{d}}, R_{i,t}^{\mathrm{u}}, R_{i,t}^{\mathrm{d}}\right] \\ \boldsymbol{y}_k &= \left[P_{i,t,k}^{\mathrm{u}}, P_{i,t,k}^{\mathrm{d}}, W_{w,t,k}^{\mathrm{cur}}, L_{b,t,k}^{\mathrm{sh}}, P_{m,t,k}^{\mathrm{M,u}}, P_{m,t,k}^{\mathrm{M,d}}, s_{m,t,k}^{\mathrm{u}}, s_{m,t,k}^{\mathrm{d}}\right], \end{aligned} \tag{9}$$

where $\boldsymbol{x}$ and $C_{\mathrm{op}}(\boldsymbol{x})$ are the decision variables and objective function in the first stage, respectively. The values of $\boldsymbol{x}$ remain unchanged during the optimization of the second stage. n_{sce} is the number of prediction error scenarios employed in the second stage. k is the index of the scenarios. p_k is the occurrence of scenario k. Ω is the uncertainty space of the probability distribution $\{p_k | k = 1, \ldots, n_{\mathrm{sce}}\}$. $\boldsymbol{y}_k$ and $C_{\mathrm{reg}}(\boldsymbol{x}, \boldsymbol{y}_k)$ are the decision variables and objective function in the second stage, respectively.

According to (8), the two-stage dispatch model is established based on the DRO theory. The max–min structure in the second stage is used to search for the worst distribution of the prediction error scenarios within Ω, which ensures that the optimized strategy can adapt to this worst distribution, so that the reliability and economy are balanced.

The functions of $C_{\mathrm{op}}(\boldsymbol{x})$ and $C_{\mathrm{reg}}(\boldsymbol{x}, \boldsymbol{y}_k)$ are shown as (10) and (11), respectively:

$$C_{\mathrm{op}}(x) = \sum_t \left[\sum_i C_i^{\mathrm{fuel}} F_i(P_{i,t}) + \sum_i \left(S_i^{\mathrm{u}} \alpha_{i,t}^{\mathrm{u}} + S_i^{\mathrm{d}} \alpha_{i,t}^{\mathrm{d}} \right) + \sum_i \left(C_i^{\mathrm{u}} R_{i,t}^{\mathrm{u}} + C_i^{\mathrm{d}} R_{i,t}^{\mathrm{d}} \right) \right], \tag{10}$$

$$\begin{aligned} C_{\mathrm{reg}}(x, y_k) = \sum_t \Bigg[&\sum_i \left(Q_i^{\mathrm{u}} P_{i,t,k}^{\mathrm{u}} + Q_i^{\mathrm{d}} P_{i,t,k}^{\mathrm{d}} \right) + \sum_w C^{\mathrm{w}} W_{w,t,k}^{\mathrm{cur}} \\ &+ \sum_b C^{\mathrm{ld}} L_{b,t,k}^{\mathrm{cur}} | + \sum_m \left(C^{\mathrm{M,u}} s_{m,t,k}^{\mathrm{u}} + C^{\mathrm{M,d}} s_{m,t,k}^{\mathrm{d}} \right) \Bigg], \end{aligned} \tag{11}$$

where C_i^{fuel} is the fuel price of unit i. $F_i(\cdot)$ is the linearized function of the consumed fuel and the power output of unit i. $R_{i,t}^{\mathrm{u}}$ and $R_{i,t}^{\mathrm{d}}$ are upward and downward reserve capacity of unit i at time t, respectively. S_i^{u} and S_i^{d} are startup and shutdown costs of unit i, respectively. $\alpha_{i,t}^{\mathrm{u}}$ and $\alpha_{i,t}^{\mathrm{d}}$ are binary variables of unit i indicating the occurrence of startup and shutdown at time t, respectively. C_i^{u} and C_i^{d} are the up and down reserve prices of unit i, respectively. $P_{i,t,k}^{\mathrm{u}}$ and $P_{i,t,k}^{\mathrm{d}}$ are the upward and downward regulated powers of unit i at time t in scenario k, respectively. Q_i^{u} and Q_i^{d} are up and downregulation prices of unit i, respectively. $W_{w,t,k}^{\mathrm{cur}}$ and $L_{b,t,k}^{\mathrm{cur}}$ are the amount of curtailed power of RES station w and load shedding of bus b at time t in scenario k, respectively. C^{w} and C^{ld} are the penalty prices of RES curtailment and load shedding, respectively. $C^{\mathrm{M,u}}$ and $C^{\mathrm{M,d}}$ are the subsidized prices of upward and downward regulation of the FML, respectively.

2.2.2 Power system operation constraints

The constraints in the first stage correspond to the RES power prediction base case. The constraints in the second stage correspond to the RES power prediction error cases. The details are given below.

Constraints in the first stage:

(1) Minimum up/down time of conventional units:

$$\begin{cases} \left(\sum_{\tau=t-T_i^{\mathrm{on}}}^{t-1} I_{i,\tau} - T_i^{\mathrm{on}} \right) (I_{i,t-1} - I_{i,t}) \geq 0 \\ \left(\sum_{\tau=t-T_i^{\mathrm{off}}}^{t-1} (1 - I_{i,\tau}) - T_i^{\mathrm{off}} \right) (I_{i,t} - I_{i,t-1}) \geq 0 \end{cases}, \tag{12}$$

where T_i^{on} and T_i^{off} are the minimum duration of the on and off statuses of unit i, respectively. $I_{i,t}$ is a binary variable of unit i at time t, which takes 1 for the on status and 0 for the off status.

(2) Startup and shutdown limits of conventional units:

$$\begin{cases} \alpha_{i,t}^{\mathrm{u}} - \alpha_{i,t}^{\mathrm{d}} = I_{i,t} - I_{i,t-1} \\ \alpha_{i,t}^{\mathrm{u}} + \alpha_{i,t}^{\mathrm{d}} \leq 1 \end{cases}. \tag{13}$$

(3) Output power and ramp rate limits of conventional units:

$$\begin{cases} I_{i,t} P_{i,\min} \leq P_{i,t} \leq I_{i,t} P_{i,\max} \\ -DR_i \leq P_{i,t} - P_{i,t-1} \leq UR_i \end{cases}, \tag{14}$$

where $P_{i,\min}$ and $P_{i,\max}$ are the minimum and maximum output power of unit i, respectively. UR_i and DR_i are the maximum upward and downward ramp power of unit i, respectively.

(4) Limits of the unit reserve capacity and system reserve requirement:

$$\begin{cases} 0 \leq R_{i,t}^{\mathrm{u}} \leq \min\left(UR_i, I_{i,t} P_{i,\max} - P_{i,t}\right) \\ 0 \leq R_{i,t}^{\mathrm{d}} \leq \min\left(DR_i, P_{i,t} - I_{i,t} P_{i,\min}\right) \end{cases}, \tag{15}$$

$$\sum_i R_{i,t}^{\mathrm{u}} \geq R_t^{\mathrm{u}}, \sum_i R_{i,t}^{\mathrm{d}} \geq R_t^{\mathrm{d}}, \tag{16}$$

where R_t^{u} and R_t^{d} are the upward and downward reserve power requirements of the RPS at time t, respectively.

(5) Power balance limits:

$$\sum_i P_{i,t} + \sum_w \hat{W}_{w,t} = \sum_b L_{b,t} + \sum_m P_{m,t}^{\mathrm{M,base}}, \tag{17}$$

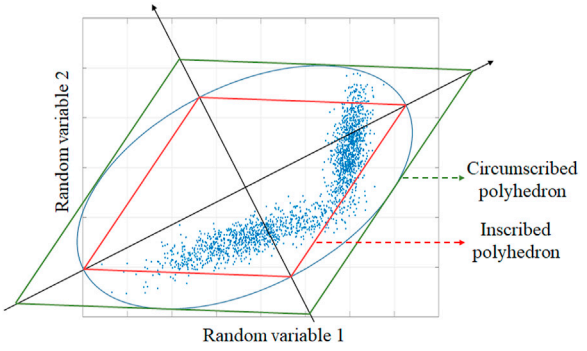

FIGURE 1
Typical scenario sets constructed by the circumscribed and inscribed polyhedra of the MVEE.

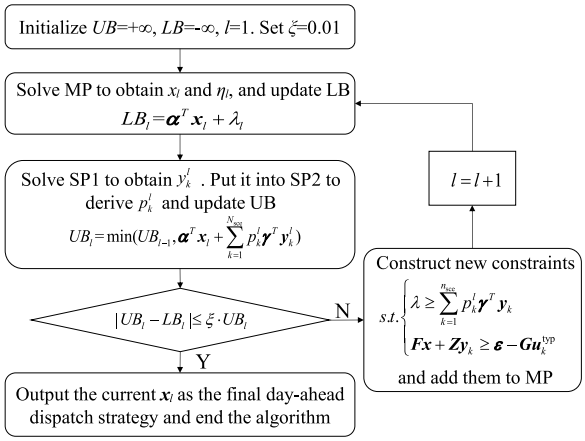

FIGURE 2
Flowchart of the solving algorithm for the two-stage RPS dispatch model.

where $\hat{W}_{w,t}$ is the predicted output power of RES station w at time t in the base case. $\hat{L}_{b,t}$ is the predicted load consumption of bus b at time t in the base case.

(6) Transmission capacity limits of power lines based on the DC power flow model:

$$\left|\sum_b k_{lb}\left(\sum_{i\in b}P_{i,t}+\sum_{w\in b}\hat{W}_{w,t}-\hat{L}_{b,t}-\sum_{m\in b}P_{m,t}^{\mathrm{M,base}}\right)\right|\le f_{l\max},\tag{18}$$

where k_{lb} is the power transfer distribution factor of bus b to line l, which represents the DC power flow model (Cai and Xu, 2021). $f_{l\max}$ is the maximum transmission power of line l.

Constraints in the second stage:

(1) Output power and ramp rate limits of conventional units:

$$\begin{cases}I_{i,t}P_{i,\min}\le P_{i,t}+P_{i,t,k}^{\mathrm{u}}-P_{i,t,k}^{\mathrm{d}}\le I_{i,t}P_{i,\max}\\ -DR_i\le P_{i,t}+P_{i,t,k}^{\mathrm{u}}-P_{i,t,k}^{\mathrm{d}}-\left(P_{i,t-1}+P_{i,t-1,k}^{\mathrm{u}}-P_{i,t-1,k}^{\mathrm{d}}\right)\le UR_i.\\ 0\le P_{i,t,k}^{\mathrm{u}}\le R_{i,t}^{\mathrm{u}}\\ 0\le P_{i,t,k}^{\mathrm{d}}\le R_{i,t}^{\mathrm{d}}\end{cases}\tag{19}$$

(2) Power balance limits:

$$\sum_i\left(P_{i,t}+P_{i,t,k}^{\mathrm{u}}-P_{i,t,k}^{\mathrm{d}}\right)+\sum_w\left(\hat{W}_{w,t}+\Delta W_{w,t,k}-W_{w,t,k}^{\mathrm{cur}}\right)=\sum_b\left(\hat{L}_{b,t}+\Delta L_{b,t,k}-L_{b,t,k}^{\mathrm{sh}}\right)+\sum_m P_{m,t}^{\mathrm{M}},\tag{20}$$

where $\Delta W_{w,t,k}$ and $\Delta L_{b,t,k}$ are the prediction error of RES station w and bus b at time t in scenario k, respectively.

(3) Transmission capacity limits of power lines based on the DC power flow model:

$$\left|\sum_b k_{lb}\left[\sum_{i\in b}\left(P_{i,t}+P_{i,t,k}^{\mathrm{u}}-P_{i,t,k}^{\mathrm{d}}\right)+\sum_{w\in b}\left(\hat{W}_{w,t}+\Delta W_{w,t,k}-W_{w,t,k}^{\mathrm{cur}}\right)-\left(\hat{L}_{b,t}+\Delta L_{b,t,k}-L_{b,t,k}^{\mathrm{sh}}\right)-\sum_{m\in b}P_{m,t}^{\mathrm{M}}\right]\right|\le f_{l\max}\tag{21}$$

(4) Wind curtailment and load shedding limits:

$$\begin{cases}0\le W_{w,t,k}^{\mathrm{cur}}\le\hat{W}_{w,t}+\Delta W_{w,t,k}\\ 0\le L_{b,t,k}^{\mathrm{sh}}\le\hat{L}_{b,t}+\Delta L_{b,t,k}\end{cases}.\tag{22}$$

(5) FML constraints

As indicated by (9), the DR of the FML is regarded as a flexible resource to cope with the prediction errors of the RES output. Therefore, (1–7) are treated as constraints in the second stage, where the FML decision variables should be included in y_k and the index k needs to be added to these variables.

2.2.3 Power prediction error probability distribution constraints

Using the norm-1 and norm-*inf*, the uncertainty space Ω in (8) can be constructed by the power prediction error probability distribution constraints below:

$$\Omega=\left\{p_k:\begin{array}{c}\sum_{k=1}^{N_{sce}}p_k=1,\ p_k\ge0\\ \sum_{k=1}^{N_{sce}}\left|p_k-p_{k0}\right|\le\theta_1\\ \max_{1\le k\le N_{sce}}\left|p_k-p_{k0}\right|\le\theta_\infty\end{array}\right\},\tag{23}$$

where p_{k0} is the initial probability of scenario k obtained by analyzing the historical samples. θ_1 and θ_∞ are the variation tolerance in the form of norm-1 and norm-*inf*, respectively, which can be calculated with the formula given by Wang et al. (2020).

The non-linear absolute term in (23) is linearized by introducing auxiliary variables. The constraints of these auxiliary variables are given below:

$$\begin{cases}z_{k+}+z_{k-}\le1\\ 0\le p_{k+}\le z_{k+}\theta_1,\quad 0\le p_{k-}\le z_{k-}\theta_1\\ 0\le p_{k+}\le z_{k+}\theta_\infty,\quad 0\le p_{k-}\le z_{k-}\theta_\infty\end{cases},\tag{24}$$

where z_{k+} and z_{k-} are binary auxiliary variables. p_{k+} and p_{k-} are real auxiliary variables.

The linearized form of (23) is shown as

$$\begin{cases} p_k = p_{k0} + p_{k+} - p_{k-} \\ \sum_{k=1}^{N_{sce}} (p_{k+} + p_{k-}) \le \theta_1 \\ p_{k+} + p_{k-} \le \theta_\infty \end{cases}. \tag{25}$$

2.2.4 Linearization of non-convex constraints

The constraints shown in (4), (5), (12), and (15) are non-convex, so the formulated model above cannot be directly solved by common commercial solvers. In this section, they are all linearized to obtain an equivalent convex form of the proposed DRO model.

For (4), binary auxiliary variables are introduced to derive its equivalent linearized form as shown below:

$$\begin{cases} z^{u}_{m,t} + z^{d}_{m,t} \le 1 \\ s^{u}_{m,t} - s^{u}_{m,t-1} = z^{u}_{m,t} - z^{d}_{m,t} \\ 0 \le \sum_{t=2}^{T} \left(z^{u}_{m,t} + z^{d}_{m,t} \right) \le M \end{cases}, \tag{26}$$

where $z^{u}_{m,t}$ and $z^{d}_{m,t}$ are the introduced pair of binary variables. $z^{u}_{m,t} = 1$ indicates that upward regulation happens in time t. Similarly, $z^{d}_{m,t}$ is the indicator of downward regulation.

For (5) and (12), both are the constraints of duration, so they have nearly the same structure. For such a structure, the linearized form is obtained by dividing T into three sections, which is given by Carrion and Arroyo (2006). For succinctness, the deduction is not repeated here.

For (15), the non-convexity of the two constraints is aroused by the nested min terms. Each of them can be replaced by two separated constraints to avoid the usage of the min terms, which is shown below:

$$\begin{cases} 0 \le R^{u}_{i,t} \le UR_i, & R^{u}_{i,t} \le I_{i,t} P_{i,\max} - P_{i,t} \\ 0 \le R^{d}_{i,t} \le DR_i, & R^{d}_{i,t} \le P_{i,t} - I_{i,t} P_{i,\min} \end{cases}. \tag{27}$$

3 Improved typical scenario set generation method

Whether the balance between economy and reliability can be achieved or not by DRO is closely related to the way how typical scenarios of prediction errors are selected. Previous DRO methods usually adopt the cluster centers of historical prediction errors as the typical scenarios, which are unable to test whether the determined day-ahead strategy can cope with the possible extreme prediction errors or not. Hence, these methods are too optimistic to consider the uncertainty in the day-ahead stage thoroughly. However, if the traditional box uncertainty set of RO is directly transferred to DRO, the spatiotemporal correlation between RES power outputs and loads is neglected, which results in an overconservative decision. In this case, to consider the spatiotemporal correlation, an MVEE containing all the historical prediction error samples is often constructed. The vertices of its inscribed and circumscribed polyhedra are used as the typical scenarios, which is shown by Figure 1 (Zhang et al., 2021; Zhang et al., 2022).

As shown in Figure 1, the inscribed polyhedron is unable to cover all the historical samples. In addition, for both the inscribed and circumscribed polyhedra, the coordinate values of the vertices may exceed the maximum or minimum values of the historical samples.

To solve this dilemma, an improved typical scenario set generation method is proposed based on the principal component analysis and K-means clustering algorithm, which unites the cluster centers and the extreme points of the historical prediction error samples to reduce decision conservativeness while maintaining reliability.

1) The prediction error vector is denoted by Eq. 28

$$\boldsymbol{u} = [\Delta \boldsymbol{W}, \Delta \boldsymbol{L}], \tag{28}$$

where $\Delta \boldsymbol{W}$ and $\Delta \boldsymbol{L}$ are the power prediction error vector of RES stations and load buses, respectively, which are detailed by Eq. 29

$$\begin{matrix} \Delta \boldsymbol{W} = \left[\Delta W_{1,1}, ..., \Delta W_{w,t}, ..., \Delta W_{N_W,T} \right] \\ \Delta \boldsymbol{L} = \left[\Delta L_{1,1}, ..., \Delta L_{b,t}, ..., \Delta L_{N_b,T} \right] \end{matrix}, \tag{29}$$

where N_W is the total number of RES stations. N_b is the total number of load buses.

2) The eigenvectors are computed, and the coordinates of the vertices along the direction of each eigenvector are obtained. Zhang et al. (2022); Zhang et al. (2021) used the iterative MVEE algorithm to obtain these coordinates, but the iteration will significantly decelerate when the area covered by historical samples lacks symmetry. Therefore, the iteration-free principal component analysis algorithm is chosen to obtain the abovementioned eigenvectors and vertices quickly and accurately. The process is detailed below.

The historical prediction error samples of the RES stations and load buses are denoted as matrix $\boldsymbol{U}$ in Eq. 30

$$\boldsymbol{U} = [\boldsymbol{u}_1, ..., \boldsymbol{u}_s, ..., \boldsymbol{u}_N]^T. \tag{30}$$

$\boldsymbol{U}$ is processed with the zero mean method as shown in Eq. 30:

$$\tilde{\boldsymbol{U}} = \boldsymbol{U} - 1_N \otimes \bar{\boldsymbol{u}}^T = [\tilde{\boldsymbol{u}}_1, ..., \tilde{\boldsymbol{u}}_s, ..., \tilde{\boldsymbol{u}}_N]^T, \tag{31}$$

where $\tilde{\boldsymbol{U}}$ is the version of $\boldsymbol{U}$ after the zero mean processing. $\bar{\boldsymbol{u}}$ is the mean vector of all historical samples. $\tilde{\boldsymbol{u}}_s$ is the sth sample after the zero mean processing. N is the number of historical samples.

The covariance matrix of $\tilde{\boldsymbol{U}}$ is obtained, and then, eigenvalue decomposition on the covariance matrix is performed by Eq. 32:

$$\begin{cases} \boldsymbol{S} = \frac{1}{N-1} \tilde{\boldsymbol{U}}^T \tilde{\boldsymbol{U}} \\ \boldsymbol{S} = \boldsymbol{Q} \boldsymbol{\Lambda} \boldsymbol{Q}^T \\ \boldsymbol{Q} = \left[\boldsymbol{q}_1, ..., \boldsymbol{q}_h, ..., \boldsymbol{q}_{(N_b+N_W)T} \right] \\ \boldsymbol{\Lambda} = diag\{\lambda_1, ..., \lambda_h, ..., \lambda_{(N_b+N_W)T}\} \end{cases}, \tag{32}$$

where $\boldsymbol{S}$ is the covariance matrix of $\tilde{\boldsymbol{U}}$. $\boldsymbol{q}_h$ is the hth eigenvector of $\boldsymbol{S}$. λ_h is the eigenvalue corresponding to $\boldsymbol{q}_h$. $\boldsymbol{\Lambda}$ is a diagonal matrix formed by all eigenvalues.

Each sample in $\tilde{\boldsymbol{U}}$ is transformed into a new coordinate system defined by the eigenvectors as shown in Eq. 33

$$\tilde{\boldsymbol{v}}_s = \boldsymbol{Q}^T \tilde{\boldsymbol{u}}_s = \left[\tilde{v}_{1,s}, \cdots, \tilde{v}_{h,s}, \cdots, \tilde{v}_{(N_b+N_W)T,s} \right]^T, \tag{33}$$

where $\tilde{\boldsymbol{v}}_s$ is the projection point of $\tilde{\boldsymbol{u}}_s$ in the eigenvector coordinate system. $\tilde{v}_{h,s}$ is the projection value of $\tilde{\boldsymbol{u}}_s$ in the direction of $\boldsymbol{q}_h$.

After all samples are projected, the coordinates of the two vertices are determined in the direction of each eigenvector by Eq. 34

$$\begin{cases} \tilde{\boldsymbol{v}}_h^{\min} = \min\{\tilde{v}_{h,1}, \cdots, \tilde{v}_{h,N}\} \cdot \boldsymbol{e}_h \\ \tilde{\boldsymbol{v}}_h^{\max} = \max\{\tilde{v}_{h,1}, \cdots, \tilde{v}_{h,N}\} \cdot \boldsymbol{e}_h \end{cases}, \tag{34}$$

where $\tilde{\boldsymbol{v}}_h{}^{\min}$ and $\tilde{\boldsymbol{v}}_h^{\max}$ are the coordinates of the two vertices in the direction of the hth eigenvector under the eigenvector coordinate system. $\boldsymbol{e}_h$ is a unit vector, with the hth element equal to 1.

3) All the vertices obtained above enclose the inscribed polyhedron. Then, the scaling factor η is introduced by Eqs 35 and 36 to expand it to the circumscribed polyhedron.

$$\min \sum_{s=1}^{N} \|\boldsymbol{\beta}_s\|_1$$
$$\text{s.t.} \begin{cases} \left[\tilde{\boldsymbol{v}}_1^{\min}, \cdots, \tilde{\boldsymbol{v}}_{(N_\mathrm{b}+N_\mathrm{W})T}^{\max}\right][\boldsymbol{\beta}_1, ..., \boldsymbol{\beta}_s, ..., \boldsymbol{\beta}_N] = [\tilde{\boldsymbol{v}}_1, ..., \tilde{\boldsymbol{v}}_s, ..., \tilde{\boldsymbol{v}}_N] \\ \boldsymbol{\beta}_s = \left[\beta_{1,s}, \cdots, \beta_{2(N_\mathrm{W}+N_\mathrm{b})T,s}\right]^T \end{cases}, \tag{35}$$

$$\eta = \max\left\{\|\boldsymbol{\beta}_1\|_1, \cdots, \|\boldsymbol{\beta}_N\|_1\right\}, \tag{36}$$

where $||\boldsymbol{\beta}_s||_1$ is the norm-1 of $\boldsymbol{\beta}_s$.

The vertices of the circumscribed polyhedron under the original coordinate system are calculated as

$$\begin{cases} \boldsymbol{u}_h^{\min} = \eta \boldsymbol{Q} \tilde{\boldsymbol{v}}_h^{\min} + \bar{\boldsymbol{u}} \\ \boldsymbol{u}_h^{\max} = \eta \boldsymbol{Q} \tilde{\boldsymbol{v}}_h^{\max} + \bar{\boldsymbol{u}} \end{cases}, \tag{37}$$

where $\boldsymbol{u}_h{}^{\min}$ and $\boldsymbol{u}_h{}^{\max}$ are the coordinates of two vertices in the direction of $\boldsymbol{q}_h$ under the original coordinate system.

As shown in Figure 1, some coordinate values of the vertices obtained by (37) may exceed the limits of the historical samples, which is impossible in the actual operation. Hence, adjustment is designed and imposed on these vertices by Eq. 38

$$u_{h,e}^{\min \text{ or } \max} = \begin{cases} \max\{u_{1,e}, \cdots, u_{N,e}\} & u_{h,e}^{\min \text{ or } \max} > \max\{u_{1,e}, \cdots, u_{N,e}\} \\ \min\{u_{1,e}, \cdots, u_{N,e}\} & u_{h,e}^{\min \text{ or } \max} < \min\{u_{1,e}, \cdots, u_{N,e}\} \\ u_{h,e}^{\min \text{ or } \max} & \text{otherwise} \end{cases}, \tag{38}$$

where $u_{h,e}^{\min \text{ or } \max}$ represents the eth element of $\boldsymbol{u}_h{}^{\min}$ or $\boldsymbol{u}_h{}^{\max}$.

The adjusted vertices of the circumscribed polyhedron are the extreme scenarios of the prediction errors. They are denoted as $\boldsymbol{u}^{\mathrm{vtx}}$, which contains $2(N_\mathrm{b} + N_\mathrm{w})T$ scenarios and shown in Eq. 39

$$\begin{aligned} \boldsymbol{u}^{\mathrm{vtx}} &= \left\{\boldsymbol{u}_h^{\min}, \boldsymbol{u}_h^{\max} \middle| h = 1, \cdots, (N_\mathrm{b} + N_\mathrm{W})T\right\} \\ &= \left\{\boldsymbol{u}_j^{\mathrm{vtx}} \middle| j = 1, \cdots, 2(N_\mathrm{b} + N_\mathrm{W})T\right\} \end{aligned}. \tag{39}$$

4) The attribution of each historical sample to every extreme scenario is analyzed.

First, the Euclidean distance between each extreme scenario in $\boldsymbol{u}^{\mathrm{vtx}}$ and every historical sample is computed by Eq. 40.

$$d_{s,j} = \left\|\boldsymbol{u}_s - \boldsymbol{u}_j^{\mathrm{vtx}}\right\|_2, \tag{40}$$

where $d_{s,j}$ is the Euclidean distance between the sth sample $\boldsymbol{u}_s$ and the jth extreme scenario $\boldsymbol{u}_j^{\mathrm{vtx}}$.

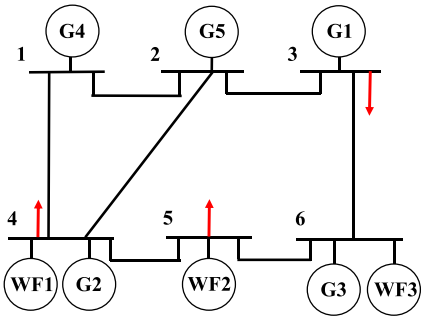

FIGURE 3
RPS structure.

Then, $\boldsymbol{u}_s$ is attributed to the nearest extreme scenario by Eq. 41.

$$\begin{cases} j = \arg\min_j d_{s,j} \\ n(j) = n(j) + 1 \end{cases}, \tag{41}$$

where the array n is a $2(N_\mathrm{b} + N_\mathrm{w})$-dimensional vector with all its components initialized to 0.

Every time a sample is attributed to the jth extreme scenario, the kth element of array n is incremented by 1. After this operation is performed for each sample, the final n is the one that reflects the attribution of samples to extreme scenarios.

5) The K-means algorithm is used to obtain the cluster centers of historical samples, which is denoted by $\boldsymbol{u}^{\mathrm{clu}}$. At the same time, the proportion of each cluster is derived and regarded as the occurrence of the corresponding cluster center, which is shown in Eq. 42.

$$\begin{aligned} \boldsymbol{u}^{\mathrm{clu}} &= \left\{\boldsymbol{u}_1^{\mathrm{clu}}, \cdots, \boldsymbol{u}_o^{\mathrm{clu}}, \cdots, \boldsymbol{u}_{n_{\mathrm{clu}}}^{\mathrm{clu}}\right\} \\ \boldsymbol{p}^{\mathrm{clu}} &= \left\{p_1^{\mathrm{clu}}, \cdots, p_o^{\mathrm{clu}}, \cdots, p_{n_{\mathrm{clu}}}^{\mathrm{clu}}\right\} \end{aligned}, \tag{42}$$

where $\boldsymbol{u}_o^{\mathrm{clu}}$ is the oth cluster center. p_o^{clu} is the occurrence of the oth cluster center. n_{clu} is the number of cluster centers, which can be adaptively determined by the contour coefficient, Calinski–Harabasz criterion, and so on (Balavand et al., 2018; Yuan and Yang, 2019; Karna and Gibert, 2022).

6) $\boldsymbol{u}^{\mathrm{clu}}$ and $\boldsymbol{u}^{\mathrm{vtx}}$ are incorporated to form the improved typical scenario set $\boldsymbol{u}^{\mathrm{typ}}$ by Eq. 43, whose scenario number is the value of n_{sce} in (8).

$$\boldsymbol{u}^{\mathrm{typ}} = \left\{\boldsymbol{u}^{\mathrm{vtx}}, \boldsymbol{u}^{\mathrm{clu}}\right\} = \left\{\boldsymbol{u}_k^{\mathrm{typ}} \middle| k = 1, \cdots, n_{\mathrm{sce}}\right\}. \tag{43}$$

Subsequently, the initial probability of each typical scenario in $\boldsymbol{u}^{\mathrm{typ}}$ is determined by (44).

$$p_{k0} = \begin{cases} \dfrac{n(j)}{N} \cdot \omega, & if\ \boldsymbol{u}_k^{\mathrm{typ}} = \boldsymbol{u}_j^{\mathrm{vtx}} \\ p_o^{\mathrm{clu}} \cdot (1 - \omega), & if\ \boldsymbol{u}_k^{\mathrm{typ}} = \boldsymbol{u}_o^{\mathrm{clu}} \end{cases}, \tag{44}$$

where p_{k0} is the initial probability of $\boldsymbol{u}_k^{\mathrm{typ}}$. ω is the weight of extreme scenarios in the typical scenario set, which is determined by the system operators according to the actual RPS structure and expected reliability level.

TABLE 1 Parameters of thermal units.

	G_1	G_2	G_3	G_4	G_5
P_{min}/MW	50	30	50	10	10
P_{max}/MW	200	80	220	80	20
Minimum up time/h	8	2	4	4	1
Minimum down time/h	8	2	4	4	1
Ramping rate/MW·h^{-1}	60	40	60	30	10
Initial status/h	10	−3	5	−4	2
a/MBtu·(MW^{2}h)$^{-1}$	4.4×10^{-3}	0.046	4×10^{-4}	1×10^{-3}	5×10^{-3}
b/MBtu·(MWh)$^{-1}$	13.29	15.47	13.51	32.63	17.7
c/MBtu·h^{-1}	39	74.33	176.95	129.97	137.41
Fuel price/$·MBtu^{-1}	1	1	1.4	1.4	1.4
Startup cost/$	1,500	100	1,000	500	120
Up and down reserve price/$·MW^{-1}	6	13	7.5	7.5	10
Up and downregulation price/$·MW^{-1}	12	27	15	15	20

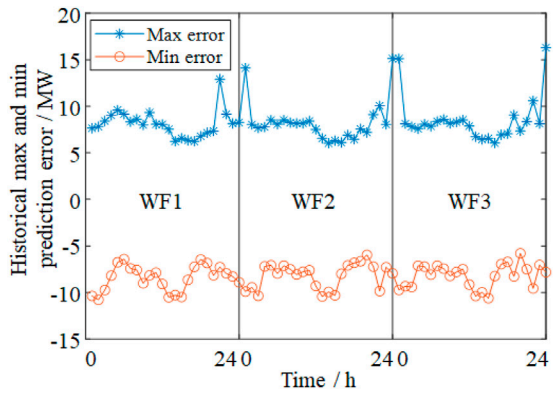

FIGURE 4
Maximum and minimum prediction errors at each hour of three wind farms in historical data.

Apparently, the improved typical scenario set $\boldsymbol{u}^{\text{typ}}$ includes both adjusted extreme scenarios and cluster centers, so the conservativeness is reduced.

4 Solution method

Combining Sections 2 and 3, the ITSDRO model for the co-dispatch of energy and reserve is finally established for the RPS. The objective function is composed of (8), (10)–(11), and the constraints are shown as (1)–(7), (12)–(22), and (24)–(27). For a given first-stage decision variable $\boldsymbol{x}$, if there exists a second-stage decision variable $\boldsymbol{y}$ that can ensure the steady operation of the RPS under all extreme scenarios, then $\boldsymbol{x}$ is a robust solution to the RPS dispatch problem.

The proposed two-stage tri-level model is a mixed-integer linear programming problem, so it can be rewritten as (45).

Original problem (OP):

$$\min_{\boldsymbol{x}} \ \boldsymbol{\alpha}^T\boldsymbol{x} + \max_{p_k} \sum_{k=1}^{n_{\text{sce}}} p_k \min_{\boldsymbol{y}_k} \boldsymbol{\gamma}^T\boldsymbol{y}_k$$
$$s.t. \begin{cases} \boldsymbol{A}\boldsymbol{x} \geq \boldsymbol{\theta} \\ \boldsymbol{Z}\boldsymbol{y}_k \geq \boldsymbol{\varepsilon} - \boldsymbol{F}\boldsymbol{x} - \boldsymbol{G}\boldsymbol{u}_k^{\text{typ}} \\ \boldsymbol{E}\boldsymbol{P} \geq \boldsymbol{\xi}, \quad \boldsymbol{P} = [p_1, \cdots, p_k, \cdots, p_{n_{\text{sce}}}] \end{cases}. \tag{45}$$

Then, the column and constraint generation algorithm is adopted to solve the model, of which the detailed procedures are given below.

1) (45) is decomposed into a master problem (MP) in Eq. 46 and two subproblems (SPs) shown by Eqs 47 and 48.

MP:

$$\min_{\boldsymbol{x}} \ \boldsymbol{\alpha}^T\boldsymbol{x} + \lambda$$
$$s.t. \begin{cases} \boldsymbol{A}\boldsymbol{x} \geq \boldsymbol{\theta} \\ \lambda \geq \sum_{k=1}^{n_{\text{sce}}} p_k^g \boldsymbol{\gamma}^T\boldsymbol{y}_k \\ \boldsymbol{F}\boldsymbol{x} + \boldsymbol{Z}\boldsymbol{y}_k \geq \boldsymbol{\varepsilon} - \boldsymbol{G}\boldsymbol{u}_k^{\text{typ}} \ \ g = 1, \cdots, l-1 \end{cases}, \tag{46}$$

where λ is an auxiliary real variable. p_k^g is the updated values of p_k in the gth iteration. l is the counter of iteration.

SP1:

$$\min_{\boldsymbol{y}_k} \ \boldsymbol{\gamma}^T\boldsymbol{y}_k$$
$$s.t. \ \boldsymbol{Z}\boldsymbol{y}_k \geq \boldsymbol{\varepsilon} - \boldsymbol{F}\boldsymbol{x} - \boldsymbol{G}\boldsymbol{u}_k^{\text{typ}}. \tag{47}$$

SP2:

$$\max_{p_k} \sum_{k=1}^{n_{\text{sce}}} p_k \boldsymbol{\gamma}^T\boldsymbol{y}_k^l$$
$$s.t. \ \boldsymbol{E}\boldsymbol{P} \geq \varphi. \tag{48}$$

10.3389/fenrg.2024.1401080

TABLE 2 Regulation parameters of the FML.

Rated power/MW	Maximum upregulation time/h	Maximum downregulation time/h	Maximum upregulation power/MW	Maximum downregulation power/MW	Up and downregulation price/$·h^{-1}
70	6	4	14	10.5	25.3

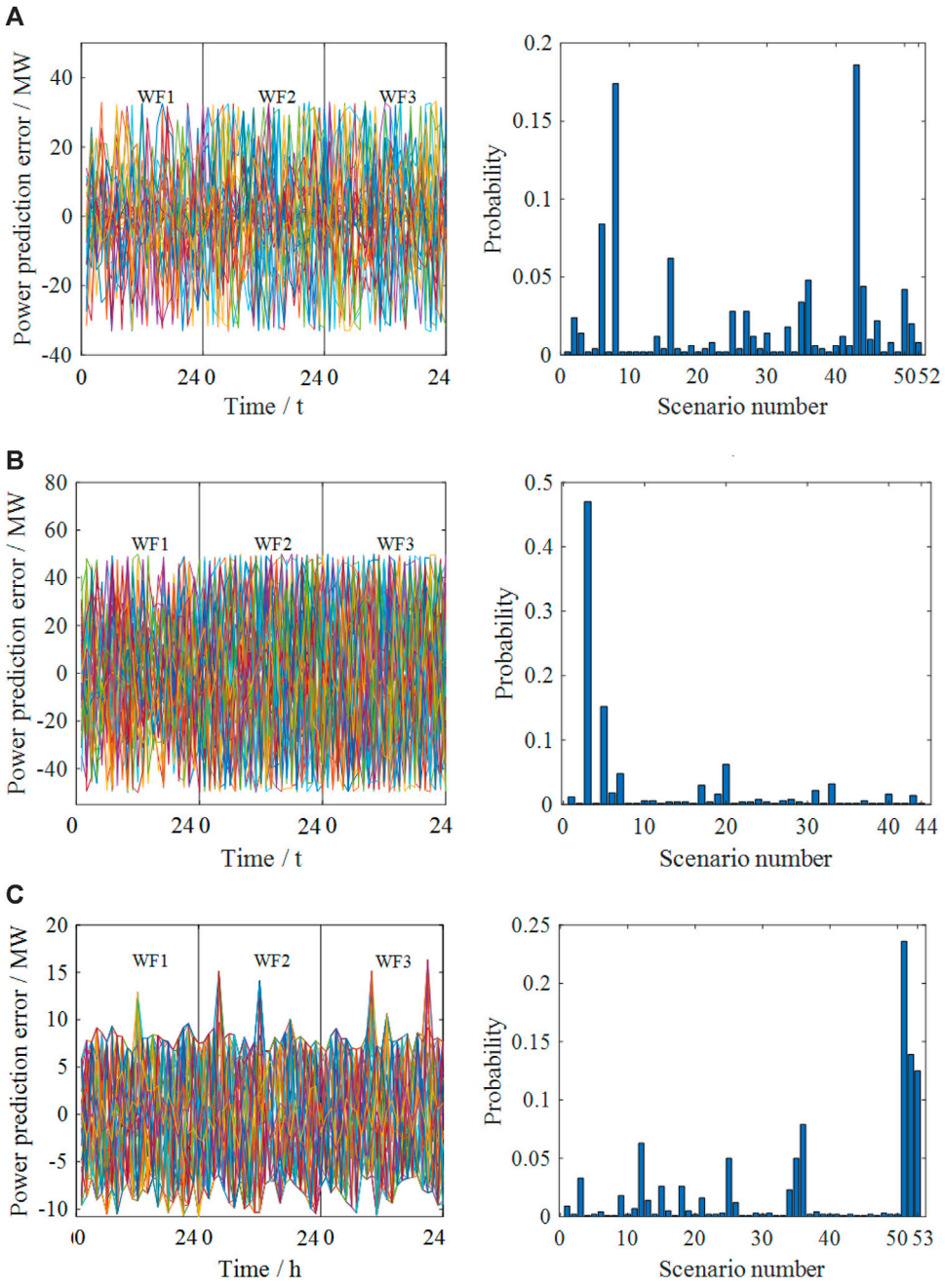

FIGURE 5
Comparison of the typical scenario sets of the three methods. **(A)** Typical scenarios and the corresponding probability of IPRO, **(B)** typical scenarios and the corresponding probability of CPDRO, and **(C)** typical scenarios and the corresponding probability of ITSDRO.

2) The lower and upper bounds of the objective of OP are denoted as LB and UB, respectively. The MP and two SPs are iteratively solved to update the *LB* and *UB*. Whether the difference between the *LB* and *UB* is small enough is determined. If so, the iteration ends; otherwise, the next iteration is run. The more specific procedures are given below.

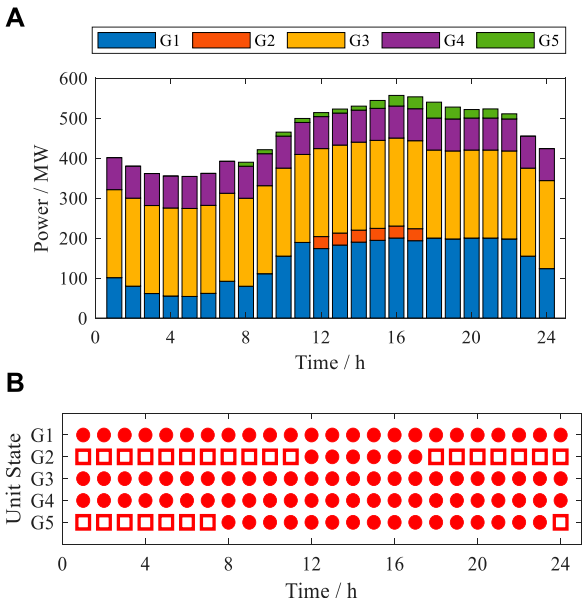

FIGURE 6
Day-ahead dispatch solution of the RPS by IPRO. **(A)** Scheduled power and **(B)** unit commitment.

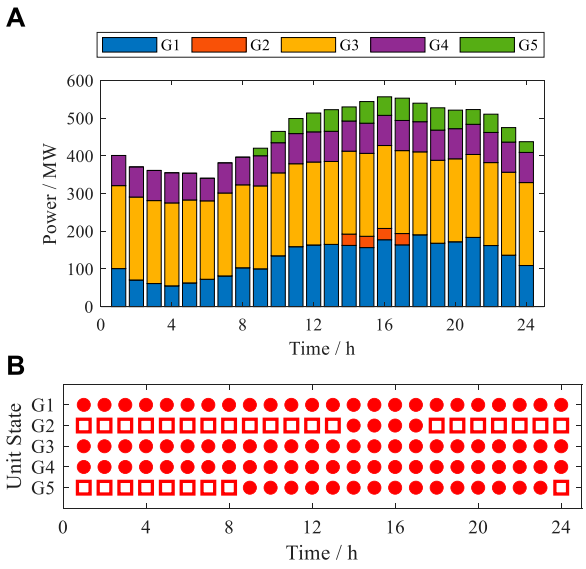

FIGURE 7
Day-ahead dispatch solution of the RPS by CPDRO. **(A)** Scheduled power and **(B)** unit commitment.

Step 1: UB_0 is initialized to $+\infty$ and LB_0 to $-\infty$. The counter l is set to 1, and the threshold coefficient ξ is set to 0.01.

Step 2: The lth iteration is entered. The MP is solved to update $\boldsymbol{x}$ and LB, shown as Eq. 49.

$$LB_l = \boldsymbol{\alpha}^T \boldsymbol{x}_l + \lambda_l. \tag{49}$$

Step 3: SP1 is solved to update $\boldsymbol{y}_k^l$ and taken into SP2 to update p_k^l. Based on $\boldsymbol{y}_k^l$ and p_k^l, UB is updated by Eq. 50

$$UB_l = \min\left(UB_{l-1}, \boldsymbol{\alpha}^T \boldsymbol{x}_l + \sum_{k=1}^{n_{scc}} p_k^l \boldsymbol{y}^T \boldsymbol{y}_k^l\right). \tag{50}$$

Step 4: Whether $|UB_l\text{-}LB_l| \leq \xi \cdot UB$ is true or not is identified. If true, the iteration ends and returns the current $\boldsymbol{x}$ as the final day-ahead dispatch decision scheme; otherwise, new constraints shown in (51) are added into the MP and run to the (l+1)th iteration:

$$s.t. \begin{cases} \lambda \geq \sum_{k=1}^{n_{scc}} p_k^l \boldsymbol{y}^T \boldsymbol{y}_k \\ \boldsymbol{F}\boldsymbol{x} + \boldsymbol{Z}\boldsymbol{y}_k \geq \boldsymbol{\varepsilon} - \boldsymbol{G}\boldsymbol{u}_k^{typ} \end{cases}. \tag{51}$$

The flowchart of the solving algorithm is shown in Figure 2.

5 Numerical tests

5.1 Basic settings

Numerical tests are carried out on a six-bus test system, the structure of which is shown in Figure 3. The parameters of the five thermal units are given in Table 1. The parameters of the seven transmission lines are given in the study by Jiang et al. (2012). Three wind farms, namely, WF1, WF2, and WF3, are connected to bus 4, bus 5, and bus 6, respectively. The predicted power curves of the total wind farm output and the system load excluding the FML are shown in Figure 3. Bus 3, bus 4, and bus 5 are load buses, peak load values of which are 196 MW, 98 MW, and 196 MW, respectively. The load buses are assumed to have a perfect positive correlation. The penalty prices of wind curtailment and load shedding are 100 \$/MW and 500 \$/MW, respectively.

The historical prediction error data are obtained from the study by Cai (2024). According to the historical data, the extreme power outputs of the three wind farms are computed and shown in Figure 4.

The FML is connected to bus 3, the regulation parameters of which are shown in Table 2.

The numerical tests are run on an Intel core i5-13500H personal computer with 32 GB RAM and solved using CPLEX 12.10 in MATLAB R2020b.

5.2 Comparison between ITSDRO with the existing RO and DRO methods

To demonstrate the performance of the ITSDRO method, the inscribed polyhedron-based RO (IPRO) in the study by Zhang et al. (2022) and the circumscribed polyhedron-based DRO (CPDRO) in the study by Zhang et al. (2021) are employed for comparison. All three methods are data-driven and need to construct the typical scenario set based on historical prediction error samples before formal optimization. For better presentation, only the typical scenarios in which the initial probability is non-zero are given in Figure 5.

Figures 4, 5 show that the typical scenarios of the three methods are not simply located at the maximum or minimum prediction errors of the wind farms because of the spatiotemporal correlation between the prediction errors. However, IPRO and CPDRO directly

10.3389/fenrg.2024.1401080

TABLE 3 Comparison of the dispatch costs optimized by the three methods.

	Cost/$	IPRO	CPDRO	ITSDRO
Day-ahead cost	Day-ahead generation cost	1.935×10^5	1.902×10^5	1.873×10^5
	Reserved capacity cost	1.498×10^4	1.416×10^4	1.240×10^4
	Unit startup cost	220	220	220
Maximum real-time cost	Maximum unit re-dispatch cost	7.570×10^3	1.940×10^4	9.601×10^3
	Maximum wind power curtailment cost	3.562×10^4	6.023×10^4	1.380×10^3
	Maximum load shedding cost	2.738×10^4	4.859×10^4	1.627×10^3
Average real-time cost	Average unit re-dispatch cost	—	5.310×10^3	5.342×10^3
	Average wind power curtailment cost	—	2.989×10^3	96.844
	Average load shedding cost	—	4.846×10^3	184.320
Total cost		2.791×10^5	2.178×10^5	2.055×10^5

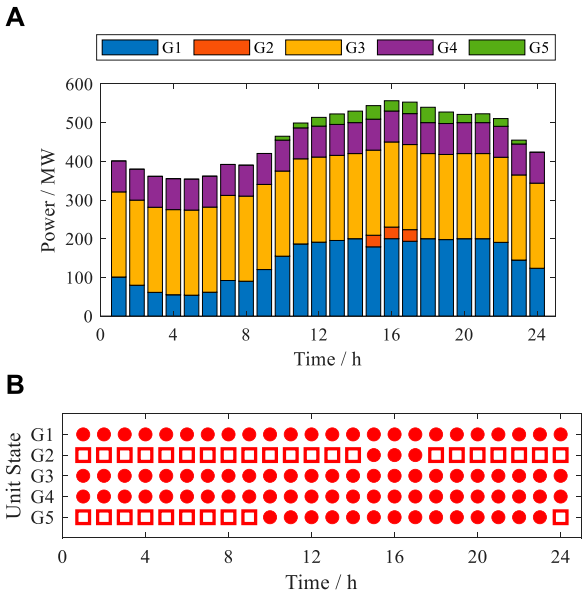

FIGURE 8
Day-ahead dispatch solution of the RPS by ITSDRO. **(A)** Scheduled power and **(B)** unit commitment.

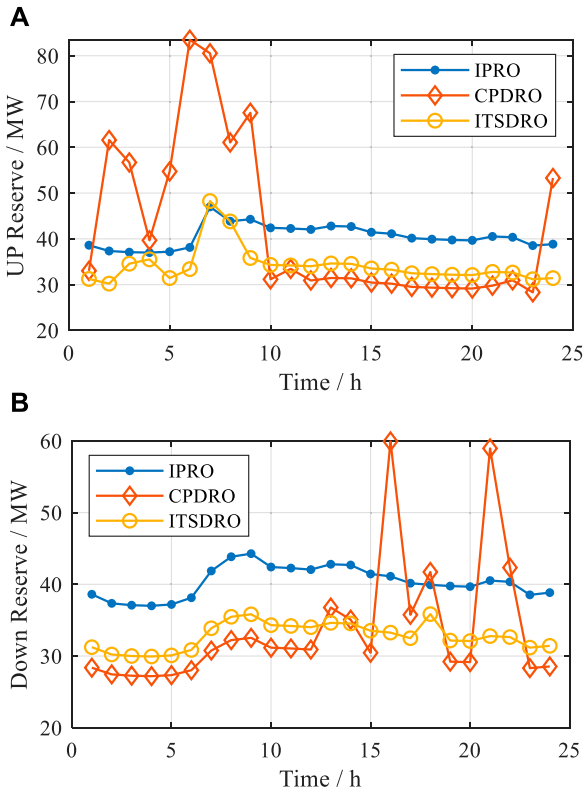

FIGURE 9
Total day-ahead reserved capacity of all units. **(A)** Up reserved capacity and **(B)** down reserved capacity.

adopt the vertices of the inscribed and circumscribed polyhedra of the MVEE as the typical scenario sets, respectively, in which some impossible scenarios exceed the limits of the prediction errors.

Then, the dispatch solutions of the three methods are shown in Figures 6–9. The corresponding dispatch costs of the test system optimized by the three methods are listed in Table 3.

Figures 6–9 and Table 3 show that

1) The solutions of the three methods can cope with all the uncertain scenarios they take into account, so they are all sufficiently robust.
2) The cost terms of the second stage are directly affected by the selected typical scenarios. IPRO and CPDRO only consider the extreme scenarios, while the uncertainty set of ITSDRO additionally contains the cluster centers. Since the re-dispatch costs of extreme scenarios are much higher than those of the cluster centers, the second-stage cost of ITSDRO is lower than that of the other two methods.
3) The cost terms of the first stage are indirectly affected by the selected typical scenarios. If only the extreme scenarios are taken into account in the DRO, the first-stage dispatch schemes will completely prepare for the extreme scenarios

10.3389/fenrg.2024.1401080

TABLE 4 Comparison of the dispatch results of case 1 and case 2.

	Case 1	Case 2
Maximum wind power curtailment/MW·h	15.39	13.80
Maximum load shedding/MW·h	3.754	2.252
Average wind power curtailment/MW·h	0.972	0.968
Average load shedding/MW·h	0.435	0.369
Day-ahead dispatch cost/$	2.043×10^5	1.999×10^5
Re-dispatch cost/$	5.651×10^3	5.623×10^3
Total dispatch cost/$	2.099×10^5	2.055×10^5

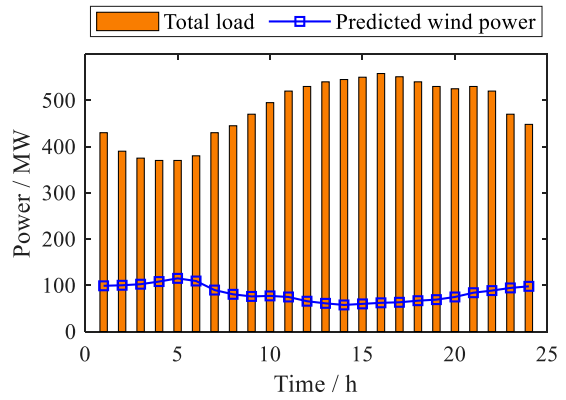

FIGURE 10
Predicted load and wind power.

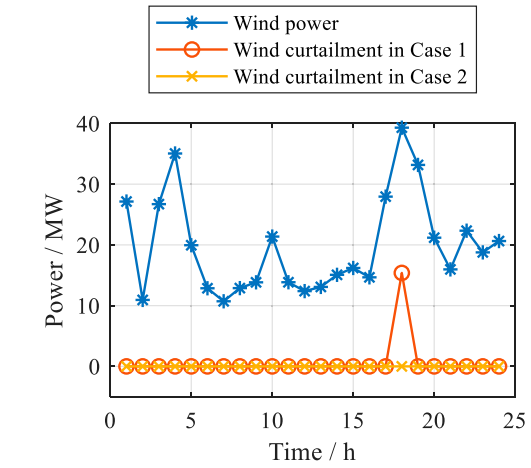

FIGURE 11
Wind curtailment in case 1 and case 2 under the worst scenario of wind curtailment.

with very low probabilities and arrange too much reserve capacity, as shown in Figure 9. In this case, unit commitment schemes are also forced to be in the relatively uneconomic region. As an example, IPRO and CPDRO start

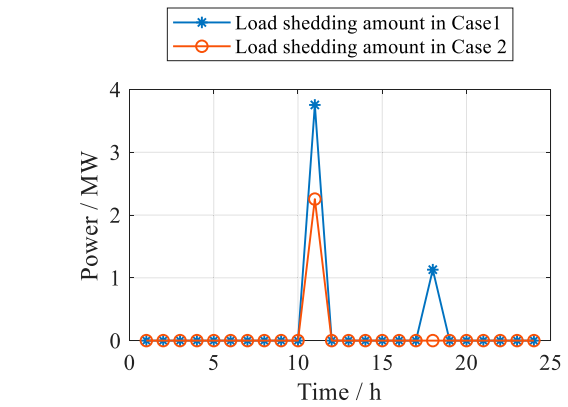

FIGURE 12
Load shedding amount in case 1 and case 2 under the worst scenario of load shedding.

up more units than ITSDRO in 8, 9, and 14 h, as shown in Figures 6–8.

4) In the absence of a targeted adjusting mechanism, these impossible scenarios of IPRO and CPDRO lead to conservative decisions and higher operation costs. As one of the RO methods, IPRO is more significantly affected because its solution is aimed at addressing the worst-case scenario. As one of the DRO methods, CPDRO is less affected because the initial probabilities of the impossible scenarios are much smaller than those of the other extreme scenarios.

The simulation results above are discussed below.

1) The second stage of a two-stage model is constructed to examine whether the RPS can sufficiently dispatch the flexible resources to cope with various scenarios including the extreme ones. However, most existing RO and DRO methods only consider extreme scenarios in the second stage, forcing the day-ahead dispatch to perform targeted preparation, which leads to redundancy in the flexible resource allocation and an increase in dispatch costs.
2) The proposed ITSDRO designs and employs an improved typical scenario set to reduce waste in the allocation of flexible resources without sacrificing the ability to cope with extreme scenarios. Therefore, the derived day-ahead dispatch scheme becomes more economical without the loss of robustness.

5.3 Validation of the DR of the FML

To validate the participation of the FML in the DR, two cases are designed for comparative analysis.

Case 1: Only conventional units are regarded as flexible resources in the second stage.

Case 2: Both conventional units and the DR of the FML participate in the re-dispatch in the second stage.

Based on the basic information given in Section 5.1, ITSDRO is performed to solve the two cases. The resulting dispatch costs are shown in Table 4, along with the amount of wind power curtailment and load shedding in the second stage.

Table 4 shows that, after the FML participates in DR projects, the maximum and average load shedding decrease by 13.32% and 15.17%, respectively, and the maximum and average wind power curtailment decrease by 10.33% and 0.41%, respectively. This indicates that the RPS becomes more flexible in coping with the power prediction error.

Figure 10 shows that the predicted wind power curve presents the anti-peak shaving characteristics. In load peak and valley periods, the FML can proactively decrease and increase its power consumption to reduce load shedding and wind curtailment amounts. From this perspective, since the DR of the FML plays the role of the regulation resource of RPS in the second stage, the reserved capacity in the first stage can be reduced accordingly. Therefore, the final total dispatch cost is decreased by 2.10%.

As shown in Figures 11 and 12, the wind curtailment is avoided and the load shedding amount is decreased even under the worst scenario, which verifies the effectiveness of the DR of the FML.

6 Conclusion

This paper focuses on establishing the ITSDRO method, which is a two-stage co-dispatch method of energy and reserve for the RPS considering the DR of the FML. First, the FML is regarded as a flexible regulation resource, and its constraints for participating in DR projects are constructed. Then, an improved typical scenario set generation method is proposed with the spatiotemporal correlation between the power prediction errors considered. Based on this typical scenario set and the DRO theory, the ITSDRO model is formed and then solved by the column and constraint generation algorithm. Numerical tests are designed to verify the correctness and effectiveness of ITSDRO. According to the simulation results, some conclusions are drawn below.

1) An impossible extreme scenario identification and adjustment mechanism is proposed to address the feasibility issue of the existing inscribed and circumscribed polyhedron-based methods. Then, the extreme scenarios are united with cluster centers of the historical prediction error samples to form an improved typical scenario set with much lower conservativeness.
2) The two-stage ITSDRO dispatch model and corresponding solution method are proposed to optimize the co-dispatch strategy of energy and reserve for the RPS. The simulation results indicate that because of the utilization of the improved typical scenario set, the day-ahead dispatch cost can be reduced while keeping a small amount of load shedding and RES power curtailment.
3) The DR model of the FML is constructed and integrated into the ITSDRO dispatch model. The simulation results indicate that, with the proactive participation of the FML in the DR, the amount of load shedding and RES power curtailment is significantly decreased even under large prediction errors. This means that the flexibility of the RPS to cope with uncertainty is enhanced due to the DR of the FML.

Data availability statement

Publicly available datasets were analyzed in this study. This data can be found here: https://dx.doi.org/10.13140/RG.2.2.20878.98888.

Author contributions

JQ: writing–original draft, conceptualization, data curation, methodology, validation, and visualization. JC: writing–original draft, funding acquisition, software, supervision, and writing–review and editing. LH: conceptualization, funding acquisition, investigation, project administration, supervision, and writing–review and editing. ZM: conceptualization, formal analysis, resources, validation, and writing–review and editing.

Funding

The author(s) declare that financial support was received for the research, authorship, and/or publication of this article. This study was supported by the Natural Science Foundation of Jiangsu Province of China (BK20220340).

Conflict of interest

The authors declare that the research was conducted in the absence of any commercial or financial relationships that could be construed as a potential conflict of interest.

Publisher's note

References

Balavand, A., Kashan, A. H., and Saghaei, A. (2018). Automatic clustering based on crow search algorithm-kmeans (CSA-Kmeans) and data envelopment analysis (DEA). *Int. J. Comput. Int. Sys* 11 (1), 1322–1337. doi:10.2991/ijcis.11.1.98

Boldrini, A., Koolen, D., Crijns-Graus, W., Worrell, E., and van den Broek, M. (2024). Flexibility options in a decarbonising iron and steel industry. *Renew. Sustain. Energy Rev.* 189, 113988. doi:10.1016/j.rser.2023.113988

Cai, J. Historical wind prediction error. Available at: https://dx.doi.org/10.13140/RG.2.2.20878.98888.2024; [Accessed 7 April 2024].

Cai, J., Hao, L., Xu, Q., and Zhang, K. (2022). Reliability assessment of renewable energy integrated power systems with an extendable Latin hypercube importance sampling method. *Sustain Energy Techn* 50, 101792. doi:10.1016/j.seta.2021.101792

Cai, J., and Xu, Q. (2021). Capacity credit evaluation of wind energy using a robust secant method incorporating improved importance sampling. *Sustain Energy Techn* 43, 100892. doi:10.1016/j.seta.2020.100892

Carrion, M., and Arroyo, J. M. (2006). A computationally efficient mixed-integer linear formulation for the thermal unit commitment problem. *Ieee T Power Syst.* 21 (3), 1371–1378. doi:10.1109/tpwrs.2006.876672

Chen, Z., Chen, Y., He, R., Liu, J., Gao, M., and Zhang, L. (2022). Multi-objective residential load scheduling approach for demand response in smart grid. *Sustain Cities Soc.* 76, 103530. doi:10.1016/j.scs.2021.103530

Cheng, L., Zang, H., Trivedi, A., Srinivasan, D., Wei, Z., and Sun, G. (2024). Mitigating the impact of photovoltaic power ramps on intraday economic dispatch using reinforcement forecasting. *Ieee T Sustain Energ* 15 (1), 3–12. doi:10.1109/tste.2023.3261444

Cheng, L., Zang, H., Wei, Z., and Sun, G. (2023). Secure multi-party household load scheduling framework for real-time demand-side management. *Ieee T Sustain Energ* 14 (1), 602–612. doi:10.1109/tste.2022.3221081

de Chalendar, J. A., McMahon, C., Fuentes Valenzuela, L., Glynn, P. W., and Benson, S. M. (2023). Unlocking demand response in commercial buildings: empirical response of commercial buildings to daily cooling set point adjustments. *Energ Build.* 278, 112599. doi:10.1016/j.enbuild.2022.112599

Derakhshandeh, S. Y., Hamedani Golshan, M. E., Ghazizadeh, M. S., and Sherkat Masoum, M. A. (2017). Stochastic scenario-based generation scheduling in industrial microgrids. *Int. T Electr. Energy* 27 (11), e2404. doi:10.1002/etep.2404

Feizi, M. R., Khodayar, M. E., and Li, J. (2022). Data-driven distributionally robust unbalanced operation of distribution networks with high penetration of photovoltaic generation and electric vehicles. *Electr. Pow. Syst. Res.* 210, 108001. doi:10.1016/j.epsr.2022.108001

Gao, H., Wang, R., Liu, Y., Wang, L., Xiang, Y., and Liu, J. (2020). Data-driven distributionally robust joint planning of distributed energy resources in active distribution network. *Iet Generation, Transm. Distribution* 14 (9), 1653–1662. doi:10.1049/iet-gtd.2019.1565

Guo, L., Wang, X., Li, Z., and Li, W. (2023). Optimization of declared capacity for electrical fused magnesia furnaces participating in primary frequency control. *Energy Rep.* 9, 687–694. doi:10.1016/j.egyr.2023.05.104

Huang, H., Zhou, M., Zhang, L., Li, G., and Sun, Y. (2019). Joint generation and reserve scheduling of wind-solar-pumped storage power systems under multiple uncertainties. *Int. T Electr. Energy.* 29 (7), e12003. doi:10.1002/2050-7038.12003

Jiang, R., Wang, J., and Guan, Y. (2012). Robust unit commitment with wind power and pumped storage hydro. *Ieee T Power Syst.* 27 (2), 800–810. doi:10.1109/tpwrs.2011.2169817

Karna, A., and Gibert, K. (2022). Automatic identification of the number of clusters in hierarchical clustering. *Neural Comput. Appl.* 34 (1), 119–134. doi:10.1007/s00521-021-05873-3

Liu, H., Qiu, J., and Zhao, J. (2022). A data-driven scheduling model of virtual power plant using Wasserstein distributionally robust optimization. *Int. J. Elec Power* 137, 107801. doi:10.1016/j.ijepes.2021.107801

Liu, J., Zang, H., Cheng, L., Ding, T., Wei, Z., and Sun, G. (2023). A Transformer-based multimodal-learning framework using sky images for ultra-short-term solar irradiance forecasting. *Appl. Energ* 342, 121160. doi:10.1016/j.apenergy.2023.121160

Mazidi, M., Rezaei, N., and Ghaderi, A. (2019). Simultaneous power and heat scheduling of microgrids considering operational uncertainties: a new stochastic p-robust optimization approach. *Energy (Oxford)* 185, 239–253. doi:10.1016/j.energy.2019.07.046

Saberi, H., Zhang, C., and Dong, Z. Y. (2021). Data-driven distributionally robust hierarchical coordination for home energy management. *Ieee T Smart Grid* 12 (5), 4090–4101. doi:10.1109/tsg.2021.3088433

Shui, Y., Gao, H., Wang, L., Wei, Z., and Liu, J. (2019). A data-driven distributionally robust coordinated dispatch model for integrated power and heating systems considering wind power uncertainties. *Int. J. Elec Power* 104, 255–258. doi:10.1016/j.ijepes.2018.07.008

Tan, W. S., Shaaban, M., and Ab Kadir, M. Z. A. (2019). Stochastic generation scheduling with variable renewable generation: methods, applications, and future trends. *Iet Generation, Transm. Distribution* 13 (9), 1467–1480. doi:10.1049/iet-gtd.2018.6331

Trojani, A. G., Moghaddam, M. S., and Baigi, J. M. (2023). Stochastic security-constrained unit commitment considering electric vehicles, energy storage systems, and flexible loads with renewable energy resources. *J. Mod. Power Syst. Cle.* 11 (5), 1405–1414. doi:10.35833/mpce.2022.000781

Wang, J., Wang, Q., and Sun, W. (2023). Quantifying flexibility provisions of the ladle furnace refining process as cuttable loads in the iron and steel industry. *Appl. Energ* 342, 121178. doi:10.1016/j.apenergy.2023.121178

Wang, L., Jiang, C., Gong, K., Si, R., Shao, H., and Liu, W. (2020). Data-driven distributionally robust economic dispatch for distribution network with multiple microgrids. *Iet Generation, Transm. Distribution* 14 (24), 5712–5719. doi:10.1049/iet-gtd.2020.0861

Xie, J., Ajagekar, A., and You, F. (2023). Multi-Agent attention-based deep reinforcement learning for demand response in grid-responsive buildings. *Appl. Energ* 342, 121162. doi:10.1016/j.apenergy.2023.121162

Yang, Q., Wang, J., Liang, J., and Wang, X. (2024). Chance-constrained coordinated generation and transmission expansion planning considering demand response and high penetration of renewable energy. *Int. J. Elec Power* 155, 109571. doi:10.1016/j.ijepes.2023.109571

Yuan, C., and Yang, H. (2019). Research on K-value selection method of K-means clustering algorithm. *J* 2 (2), 226–235. doi:10.3390/j2020016

Zhang, Y., Liu, Y., Shu, S., Zheng, F., and Huang, Z. (2021). A data-driven distributionally robust optimization model for multi-energy coupled system considering the temporal-spatial correlation and distribution uncertainty of renewable energy sources. *Energy* 216, 119171. doi:10.1016/j.energy.2020.119171

Zhang, Y., Yang, J., Pan, X., Zhu, X., Zhan, X., Li, G., et al. (2022). Data-driven robust dispatch for integrated electric-gas system considering the correlativity of wind-solar output. *Int. J. Elec Power* 134, 107454. doi:10.1016/j.ijepes.2021.107454

Zheng, X., Zhou, B., Wang, X., Zeng, B., Zhu, J., Chen, H., et al. (2023). Day-ahead network-constrained unit commitment considering distributional robustness and intraday discreteness: a sparse solution approach. *J. Mod. Power Syst. Cle* 11 (2), 489–501. doi:10.35833/mpce.2021.000413

Nomenclature

A. Indices

m	Index of EAFs
i	Index of units
k	Index of scenarios
t	Index of time
b	Index of buses
w	Index of RES stations
l	Index of transmission lines

B. Variables

$P^{\mathrm{M,u}}_{m,t}$ and $P^{\mathrm{M,d}}_{m,t}$	Upward and downward regulated power of the mth EAF, respectively
$s^{\mathrm{u}}_{m,t}$ and $s^{\mathrm{d}}_{m,t}$	Indicator of the EAF in upward and downward regulation states, respectively
x and y_k	Decision vectors in the first and second stage of the proposed DRO model, respectively
$\alpha^{\mathrm{u}}_{i,t}$ and $\alpha^{\mathrm{d}}_{i,t}$	Variables indicating the occurrence of startup and shutdown of unit i at time t, respectively
$R^{\mathrm{u}}_{i,t}$ and $R^{\mathrm{d}}_{i,t}$	Upward and downward reserve capacity of unit i at time t, respectively
$P^{\mathrm{u}}_{i,t,k}$ and $P^{\mathrm{d}}_{i,t,k}$	Upward and downward regulated power of unit i at time t in scenario k, respectively
$W^{\mathrm{cur}}_{w,t,k}$ and $L^{\mathrm{cur}}_{b,t,k}$	Amount of curtailed power of RES station w and load shedding of bus b at time t in scenario k, respectively
$I_{i,t}$	Status indicator of unit i at time t
p_k	Occurrence of scenario k

C. Constants and functions

M	Total number of EAFs
T	Number of time slots in 1 day
n_{sce}	Number of prediction error scenarios
N_{W}	Number of RES stations
N_{b}	Number of load buses
N	Number of historical prediction error samples
T^{u}_m and T^{d}_m	Maximum duration of upward and downward power regulation of the EAF, respectively
C^{fuel}_i	Fuel price of unit i
S^{u}_i and S^{d}_i	Startup and shutdown costs of unit i, respectively
C^{u}_i and C^{d}_i	Upward and downward reserve prices of unit i, respectively
Q^{u}_i and Q^{d}_i	Upward and downward regulation prices f unit i, respectively
C^{w} and C^{ld}	Penalty prices of RES curtailment and load shedding, respectively
$C^{\mathrm{M,u}}$ and $C^{\mathrm{M,d}}$	Subsidized prices of upward and downward regulation of the FML, respectively
T^{on}_i and T^{off}_i	Minimum duration of the on and off statuses of unit i, respectively
$P_{i,\min}$ and $P_{i,\max}$	Minimum and maximum output power of unit i, respectively
UR_i and DR_i	Maximum upward and downward ramp power of unit i, respectively
R^{u}_t and R^{d}_t	Upward and downward reserved power requirements of the RPS at time t, respectively
$\hat{W}_{w,t}$ and $\hat{L}_{b,t}$	Predicted power of RES station w and load bus b at time t in the base case, respectively
k_{lb}	Power transfer distribution factor of bus b to line l
$f_{l\max}$	Maximum transmission power of line l
$\Delta W_{w,t,k}$ and $\Delta L_{b,t,k}$	Prediction error of RES station w and bus b at time t in scenario k
Ω	Uncertainty space of the probability distribution
p_{k0}	Initial probability of scenario k
$C_{\mathrm{op}}(\cdot)$ and $C_{\mathrm{reg}}(\cdot)$	Objectives of the first and second stages of the proposed DRO model, respectively
$F_i(\cdot)$	Linearized function of the consumed fuel and the power output of unit i
U	Matrix composed of historical prediction error samples of the RES stations and load buses
$\tilde{U}$	Modified U after the zero mean processing
S	Covariance matrix of $\tilde{U}$
q_h	hth eigenvector of S
λ_h	Eigenvalue corresponding to q_h
Λ	Diagonal matrix formed by all λ_h
$\tilde{v}^{\min}_h$ and $\tilde{v}^{\max}_h$	Two vertices in the direction of q_h under the eigenvector coordinate system
$u^{\min}_h$ and $u^{\max}_h$	Two vertices in the direction of q_h under the original coordinate system
u^{vtx}	Adjusted vertices of the circumscribed polyhedron
u^{clu}	Cluster centers of historical samples
u^{typ}	Improved typical scenario set

D. Abbreviations

RPS	Renewable power system
FML	Fused magnesium load
EAF	Electric arc furnace
RES	Renewable energy source
DR	Demand response
SO	Stochastic optimization
RO	Robust optimization
DRO	Distributionally robust optimization
MVEE	Minimum volume enclosing ellipsoid
ITSDRO	Improved typical scenario-based DRO
IPRO	Inscribed polyhedron-based RO
CPDRO	Circumscribed polyhedron-based DRO

frontiers | Frontiers in Energy Research

TYPE Opinion
PUBLISHED 06 June 2024
DOI 10.3389/fenrg.2024.1411478

OPEN ACCESS

EDITED BY
Yue Xiang,
Sichuan University, China

REVIEWED BY
Junru Chen,
Xinjiang University, China
Manyun Huang,
Hohai University, China

*CORRESPONDENCE
Xiang Gao,
gaoxiang@szpu.edu.cn

RECEIVED 03 April 2024
ACCEPTED 15 May 2024
PUBLISHED 06 June 2024

CITATION
Tan M, Gao X and Liu Y (2024), Opinions on fast distributed optimization for large-scale scheduling of heterogeneous flexibility resources.
Front. Energy Res. 12:1411478.
doi: 10.3389/fenrg.2024.1411478

Opinions on fast distributed optimization for large-scale scheduling of heterogeneous flexibility resources

Man Tan[1], Xiang Gao[2]* and Yutong Liu[3]

[1]College of Electrical and Information Engineering, Hunan University, Changsha, China, [2]Industrial Training Centre, Shenzhen Polytechnic University, Shenzhen, China, [3]School of Mathematics, Shandong University, Jinan, China

KEYWORDS

asynchronous iteration, distribution networks, distributed optimization, flexibility resources, renewable energy

1 Introduction

With the high-proportion integration of distributed energy sources such as renewable energy and energy storage systems, the traditional distribution network has evolved from a passive power supply network to an active network with the bidirectional power flow (Sheng et al., 2021). The operation and scheduling of active distribution networks (ADNs) have undergone great challenges due to intrinsic intermittence and volatility from renewable energy resources (Xiang et al., 2017; Li et al., 2023). This has led to the necessity to fully utilize support and adjust the capability of flexibility resources such as distributed energy storage and electric vehicles for reliable power supply (Xu et al., 2022; Lu et al., 2023). Considering the properties of large quantities, decentralized locations, and diverse stakeholders for heterogeneous flexibility resources, the traditional centralized control strategy faces various challenges in the form of system reliability, mass communication, and information privacy (Hu et al., 2018). Hence, distributed optimization is proposed to purge the globally unified control of distribution networks that would enable the efficient management of flexibility resources through distributed clustering (Zhou B. et al., 2021; Fu et al., 2022; Zhong et al., 2023). However, conventional distributed algorithms have slow convergence properties, owing to the gradient-based update process and communication delays (Zhang et al., 2022), which cannot satisfy the fast real-time scheduling of ADNs. Therefore, this paper focuses on providing insightful perspectives and discussions on the fast distributed optimization for large-scale scheduling of heterogeneous flexibility resources.

The main contributions of this paper are two-fold: (1) a bi-level distributed scheduling model of large-scale heterogeneous flexibility resources is proposed to minimize the overall operational cost of ADNs and promote the accommodation of renewable energy resources and (2) a fast distributed asynchronous optimization method is presented to accelerate the convergence speed for the real-time scheduling of ADNs, and the correctness and superiority of the proposed method are demonstrated by case studies.

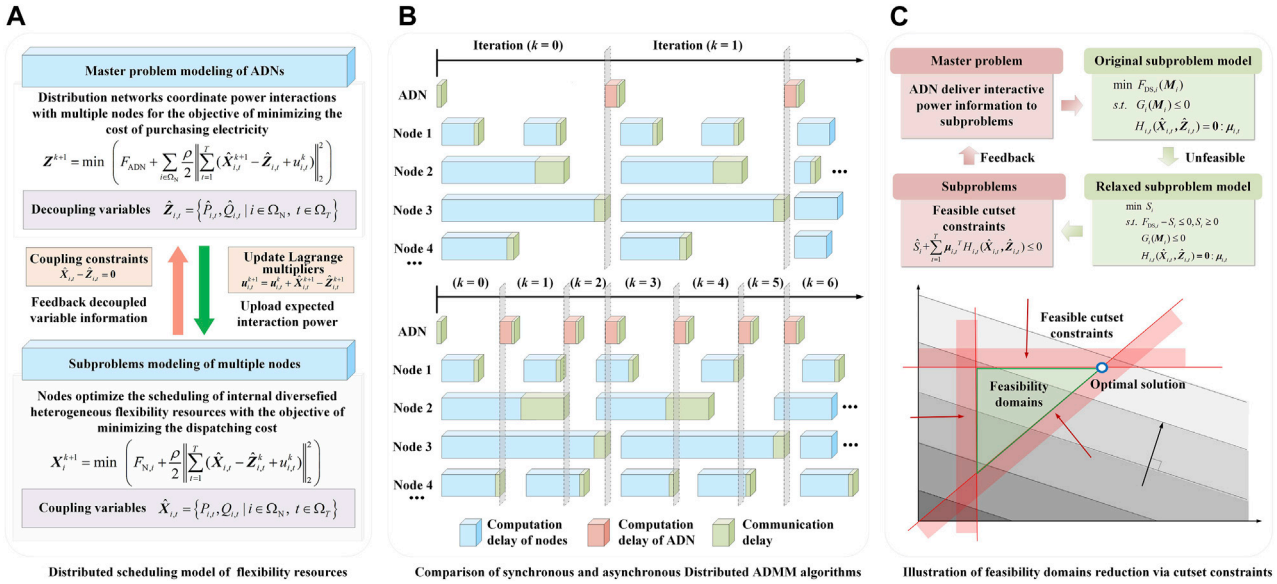

FIGURE 1
Distributed scheduling model and fast optimization method for active distribution networks (ADNs). **(A)** Distributed scheduling model of flexibility resources **(B)** Comparison of synchronous and asynchronous distributed ADMM algorithms **(C)** Illustration of feasibility domains reduction via cutset constraints.

2 Distributed scheduling model of large-scale heterogeneous flexibility resources

Optimized scheduling of ADNs needs to take into account potential benefits of different dispatching entities such as distribution networks and diversified flexibility resources for minimizing the overall operational costs while stimulating the incorporation of renewable energy. The objective function aims to minimize the costs associated with purchasing electricity, renewable energy curtailment, and dispatching flexibility resources for the purpose of economy enhancement as follows:

$$\min F = \sum_{t=1}^{T}\left[\lambda_t^{\text{buy}} P_t^{\text{buy}} + \sum_{i\in\Omega_{\text{RES}}} \lambda_{i,t}^{\text{RES.curt}} P_{i,t}^{\text{RES.curt}} + \sum_{i\in\Omega_{\text{DR}}} \lambda^{\text{DR}}\left|P_{i,t}^{\text{L.O}} - P_{i,t}^{\text{L}}\right| + \sum_{i\in\Omega_{\text{ESS}}} \lambda^{\text{ESS}}\left(\eta_i^{\text{c}} P_{i,t}^{\text{c}} + \frac{P_{i,t}^{\text{dc}}}{\eta_i^{\text{dc}}}\right)\right]\Delta t, \tag{1}$$

where T denotes the total number of scheduling periods; Δt denotes the duration of each scheduling period; λ_t^{buy}, $\lambda^{\text{RES.curt}}$, λ^{DR}, and λ^{ESS} represent the purchase price of electricity in time period t, the cost coefficient for the penalty of renewable energy curtailment, the unit dispatch cost of controllable loads, and the cost coefficient for the charging and discharging of the energy storage system, respectively; Ω_{RES}, Ω_{DR}, and Ω_{ESS} represent the set of renewable energy, demand response, and energy storage system in ADNs, respectively; P_t^{buy} denotes the purchased active power from the main grid in time period t; $P_{i,t}^{\text{RES.curt}}$ denotes the renewable energy curtailment at node i in time period t; $P_{i,t}^{\text{L}}$ and $P_{i,t}^{\text{L.O}}$ denote the actual dispatch power and original power of controllable load i in time period t, respectively; η_i^{c} and η_i^{dc} denote the charging and discharging efficiencies of energy storage unit i, respectively; and $P_{i,t}^{\text{c}}$ and $P_{i,t}^{\text{dc}}$ denote the charging and discharging power of energy storage unit i in time period t, respectively.

A bi-level distributed scheduling strategy is proposed to minimize the overall operational cost of ADNs, which is poised to meet the needs of individual economies and privacy preservation for agents with diverse flexible resources (Cao et al., 2024). At the upper level, the scheduling and control center of ADNs serves as a decision-maker to achieve synergies among multiple flexibility resources via information and energy exchange, thereby maximizing the overall economics of scheduling for distribution networks with high renewables. At the lower level, nodes integrated with controllable flexibility resources achieve autonomous operation through the full utilization of the inherent adjustment capacity. The proposed hierarchical optimization scheduling model can be solved by the alternating direction method of multipliers (ADMM) algorithm, which is a popular and efficient method to deal with distributed optimization problems with stable robustness and convergence (Gao et al., 2020; Qi et al., 2023). The distributed scheduling model of large-scale heterogeneous flexibility resources can be decomposed into the master problem of distribution networks at the upper level and subproblems of controllable flexibility resources at the lower level based on the ADMM, as shown in Figure 1A.

The objective function can be separated according to the bi-level distributed optimization scheduling strategy as follows:

$$F = F_{\text{ADN}} + \sum_{i\in\Omega_{\text{N}}} F_{\text{N},i}, \tag{2}$$

$$F_{\text{ADN}} = \sum_{t=1}^{T}\left(\lambda_t^{\text{buy}} P_t^{\text{buy}}\right)\Delta t, \tag{3}$$

$$F_{\text{N},i} = \sum_{t=1}^{T}\left(\lambda^{\text{RES.curt}} P_{i,t}^{\text{RES.curt}} + \lambda^{\text{DR}}\left|P_{i,t}^{\text{load.O}} - P_{i,t}^{\text{load}}\right| + \lambda^{\text{ESS}}\left|\eta_i^{\text{c}} P_{i,t}^{\text{c}} + \frac{P_{i,t}^{\text{dc}}}{\eta_i^{\text{dc}}}\right|\right)\Delta t, \tag{4}$$

where Ω_N denotes the set of nodes integrated with flexibility resources; F_{ADN} is the objective function of the master problem for the ADN; and $F_{N,i}$ is the objective function of subproblem for node i. The optimization variables for the master problem mainly comprise the power purchased from or sold to the main grid. The optimization variables for the subproblems include multiple heterogeneous flexibility resources dispatching power, which consist of the energy storage system, photovoltaic generation, wind turbine generation, micro-gas turbine, and demand response resources. Furthermore, there are coupling relationships between the nodes integrated with controllable flexibility resources and ADNs due to their energy interaction. Hence, the power injected to nodes integrated with controllable flexibility resources $\hat{\boldsymbol{X}}_{i,t} = \{P_{i,t}, Q_{i,t} | i \in \Omega_N\}$ is used as coupling variables, and the expected power from the distribution network to nodes $\hat{\boldsymbol{Z}}_{i,t} = \{\hat{P}_{i,t}, \hat{Q}_{i,t} | i \in \Omega_N\}$ is proposed as virtual decoupling variables to establish the consistency coupling constraints as follows (Zhou X. et al., 2021):

$$\hat{\boldsymbol{X}}_{i,t} - \hat{\boldsymbol{Z}}_{i,t} = \boldsymbol{0}. \tag{5}$$

The variables $\hat{\boldsymbol{X}}_{i,t}$ and $\hat{\boldsymbol{Z}}_{i,t}$ are solved separately at the upper and lower levels, respectively, and the optimization results are delivered iteratively between the two levels to solve the model. A Lagrange penalty function is added to the objective functions of the master problem and subproblems as follows:

$$\hat{\boldsymbol{X}}_i^{k+1} = \min \left(F_{N,i} + \frac{\rho}{2} \left\| \sum_{t=1}^{T} \left(\hat{\boldsymbol{X}}_{i,t} - \hat{\boldsymbol{Z}}_{i,t}^k + u_{i,t}^k \right) \right\|_2^2 \right), \tag{6}$$

$$\hat{\boldsymbol{Z}}^{k+1} = \min \left(F_{ADN} + \sum_{i \in \Omega_N} \frac{\rho}{2} \left\| \sum_{t=1}^{T} \left(\hat{\boldsymbol{X}}_{i,t}^{k+1} - \hat{\boldsymbol{Z}}_{i,t} + u_{i,t}^k \right) \right\|_2^2 \right), \tag{7}$$

where k denotes the iteration number; ρ is the penalty coefficient; and $u_{i,t}^j$ is the Lagrange multiplier. The proposed distributed scheduling model is solved by optimizing the coupling variables through continuous iterations between the master problem and subproblems. Relevant information about the expected interaction energy for ADNs and nodes integrated with controllable flexibility resources is delivered mutually at the two levels. The Lagrange multipliers will be updated after each iteration step as follows:

$$\boldsymbol{u}_{i,t}^{k+1} = \boldsymbol{u}_{i,t}^k + \hat{\boldsymbol{X}}_{i,t}^{k+1} - \hat{\boldsymbol{Z}}_{i,t}^{k+1}. \tag{8}$$

The primal residual r^k and dual residual s^k are introduced as convergence criteria (Xu et al., 2018), which are calculated after each iteration step as follows:

$$r^k = \sum_{i \in \Omega_N} \left\| \sum_{t=1}^{T} \left(\hat{\boldsymbol{X}}_{i,t}^k - \hat{\boldsymbol{Z}}_{i,t}^k \right) \right\|_2 \le \varepsilon_r, \tag{9}$$

$$s^k = \sum_{i \in \Omega_N} \rho \left\| \sum_{t=1}^{T} \left(\hat{\boldsymbol{X}}_{i,t}^k - \hat{\boldsymbol{X}}_{i,t}^{k-1} \right) \right\|_2 \le \varepsilon_s, \tag{10}$$

where ε_r and ε_s refer to the convergence threshold for the primal residual and dual residual, respectively. If the convergence criterion is not satisfied, the next iteration will continue with updated Lagrange multipliers along with the latest data on coupling and decoupling variables. Otherwise, the iteration process will be terminated to obtain the optimal scheduling determination of heterogeneous flexibility resources with minimal operational costs for ADNs.

3 Fast distributed asynchronous optimization for real-time scheduling of ADNs

Considering the time-varying nature of communication networks and the varied responsiveness of heterogeneous flexibility resources (Cao et al., 2024), traditional synchronized computation is insufficient to satisfy the fast real-time scheduling of ADNs, owing to the increased communication overhead and limited convergence speed. Specifically, under the synchronous protocol, the optimization model for the master problem is triggered at each iteration only if the scheduling center of ADNs receives the information from all nodes (Zheng et al., 2018). The master problem and computationally fast subproblems will remain idle most of the time, thereby impeding the full utilization of parallel computing resources. Hence, the distributed asynchronous optimization is adopted to improve the convergence efficiency, which allows the master problem to execute the next iterative updates without the reception of complete information from all nodes (Chang et al., 2016), as shown in Figure 1B. Initially, D_k is proposed to denote the index set of nodes from which the scheduling center receives coupling information during iteration k. The variable information of node i is uploaded to the scheduling center if $i \in D_k$. If a node fails to deliver information promptly due to communication delays or slow response speed, the data of the last iteration will be used instead to execute the next optimization updates for the master problem as follows:

$$\hat{\boldsymbol{X}}_{i,t}^k = \begin{cases} \hat{\boldsymbol{X}}_{i,t}^k, i \in D^k \\ \hat{\boldsymbol{X}}_{i,t}^{k-1}, i \notin D^k \end{cases}. \tag{11}$$

Two asynchronous constraints are set in the computation process to guarantee the convergence of the asynchronous optimization algorithm (Chang et al., 2016). On one hand, to ensure the efficacy of each iteration, the master problem proceeds to the next iteration only if the number of nodes in D_k is larger than the set threshold $\kappa \ge 1$. On the other hand, taking into account the hazard of unbounded delays on algorithm convergence (Chang et al., 2016; Bastianello et al., 2021), the inactive iteration of every node, as well as $i \notin D^k$, must be less than the set maximum tolerable delay τ. This means that the coupling variable information per node used by the center must be, at most, τ iterations old (Mohammadi and Kargarian, 2022). The variable d_i^k is introduced to count the delays of node i. If $i \in D_k$ at the current iteration k, then d_i^k is set to 0; otherwise, d_i^k is increased by 1 as follows:

$$d_i^k = \begin{cases} 0, i \in D^k \\ d_i^{k-1} + 1, i \notin D^k \end{cases}. \tag{12}$$

When both conditions cannot be satisfied simultaneously, the scheduling center must wait until the updated information from the unusual nodes is received. The master problem and subproblems, with smaller idle time, are frequently updated compared with the synchronous optimization. However, the benefit of the improved update frequency can outweigh the cost of the increased number of

TABLE 1 Comparison of the operational costs for active distribution networks (ADNs) and convergence properties.

Algorithm	Total cost/¥	Cost of ADNs/¥	Cost of flexibility resources/¥			Iteration	Time/s
		Electricity purchase	Energy storage system	Demand response	Renewable energy curtailment		
Centralized algorithm	27,903.4	24,216.3	1,950.6	432.6	1,303.9	-	204
General distributed algorithm	27,904.0	24,216.8	1,950.6	432.8	1,303.8	108	1,206
Fast distributed algorithm	27,904.0	24,216.8	1,950.6	432.8	1,303.8	83	967

iterations, enabling the asynchronous algorithm to converge in the shortest possible time (Bastianello et al., 2021).

In order to further accelerate convergence speed, this paper also proposes a method to curtail the feasibility domains of the master problem (Wu et al., 2018; Hua et al., 2023), as shown in Figure 1C. The feasibility of interactive power information delivered by the master problem is examined during the subproblem of nodes at the lower level. The optimization model of the subproblem for node i can be expressed as follows:

$$\begin{aligned} &\min\ F_{\mathrm{DS},i}(\boldsymbol{M}_i) \\ &s.t.\quad G_i(\boldsymbol{M}_i) \le 0 \\ &H_{i,t}\left(\hat{\boldsymbol{X}}_{i,t}, \hat{\boldsymbol{Z}}_{i,t}\right) = \boldsymbol{0} : \boldsymbol{\mu}_{i,t} \end{aligned}, \tag{13}$$

where $\boldsymbol{M}_i$ denotes the optimization variables for the subproblem of node i; $G_i(\boldsymbol{M}_i)$ denotes inequality constraints set for the subproblem of node i; $H_{i,t}(\hat{\boldsymbol{X}}_{i,t}, \hat{\boldsymbol{Z}}_{i,t})$ denotes the coupling equational constraints of the two levels; and $\boldsymbol{\mu}_{i,t}$ denotes the dual multipliers of coupling equational constraints. If the expected interaction power delivered by the scheduling center of the master problem is not feasible for the subproblem of node i, the relaxation factor S_i is introduced to transform the subproblem as follows:

$$\begin{aligned} &\min\ S_i \\ &s.t.\ F_{\mathrm{DS},i} - S_i \le 0, S_i \ge 0 \\ &G_i(\boldsymbol{M}_i) \le 0 \\ &H_{i,t}\left(\hat{\boldsymbol{X}}_{i,t}, \hat{\boldsymbol{Z}}_{i,t}\right) = \boldsymbol{0} : \boldsymbol{\mu}_{i,t} \end{aligned}. \tag{14}$$

With the optimization solution of the relaxed subproblem, the node i can provide feedback on feasible cutset constraints to the master problem as follows (Wu et al., 2022):

$$\hat{S}_i + \sum_{t=1}^{T} \boldsymbol{\mu}_{i,t}{}^T H_{i,t}\left(\hat{\boldsymbol{X}}_{i,t}, \hat{\boldsymbol{Z}}_{i,t}\right) \le 0, \tag{15}$$

where $\hat{S}_i$ denotes the optimal value of the objective function of the relaxed subproblem. Otherwise, no constraints are returned to the master problem if the subproblem is found to be feasible. Therefore, the objective function and constraint conditions are both restricted through the feedback of feasible cutset constraints after feasibility examination. Consequently, an improvement in the convergence speed was observed, owing to a reduction in the feasibility domains of the master problem.

4 Case studies

To validate the effectiveness of the proposed fast distributed optimization method for large-scale scheduling of heterogeneous flexibility resources in this paper, the IEEE33 bus distribution system is used as a specimen for case studies. The quantity of energy storage systems, photovoltaic generation, wind turbine generation, micro-gas turbine, and demand response resources in the distribution system is defined to be 2, 2, 1, 1, and 2, respectively. The proposed model is solved by the centralized algorithm, general synchronous distributed algorithm, and fast distributed asynchronous algorithm, respectively, to verify the preeminence of the presented method through comparative analysis. The comparison between the results of the operational costs for ADNs and convergence properties under different algorithms is shown in Table 1.

It can be seen that the operational cost results of ADNs obtained by centralized and distributed algorithms are almost the same, proving the correctness of the proposed method in this paper. Since the serial simulation is performed on a single computer, the distributed optimization time shall be the average optimization time of a single node integrated with controllable flexibility resources. Therefore, the average time used for one node by the general synchronous distributed algorithm and fast distributed asynchronous algorithm is 150.75 and 120.875 s, respectively. It shows that the fast asynchronous distributed methods have computational efficiency superior to the centralized and general synchronous distributed algorithms. The model convergence speed can be enhanced by 40.7% and 19.8% through asynchronous iteration and feasibility domain reduction via cutset constraints, respectively.

5 Discussion and conclusion

A fast distributed optimization method for the large-scale scheduling of heterogeneous flexibility resources is presented in the paper. The key conclusions can be summarized as follows: 1) the proposed bi-level distributed scheduling model coordinates multiple heterogeneous flexibility resources to enhance the operational economy of ADNs and facilitate the accommodation of renewable energy resources; 2) compared to the centralized and general synchronous distributed algorithm, the model convergence speed can be enhanced by 40.7% and 19.8%, respectively, through the proposed fast asynchronous distributed optimization method to

satisfy the fast real-time scheduling of ADNs; and 3) further research will focus on the distributed economic optimization of ADNs integrated with heterogeneous flexibility resources, considering the uncertainties of renewable energy resources and load demand.

Author contributions

MT: writing–original draft and writing–review and editing. XG: conceptualization, data curation, and writing–review and editing. YL: formal analysis, visualization, and writing–review and editing.

Funding

The author(s) declare that financial support was received for the research, authorship, and/or publication of this article. This work is sponsored by the Guangdong Basic and Applied Basic Research Foundation (2023A1515110105) and the Scientific Research Startup Fund for Shenzhen High-Caliber Personnel of SZPT (No. 6022310042k).

Conflict of interest

The authors declare that the research was conducted in the absence of any commercial or financial relationships that could be construed as a potential conflict of interest.

Publisher's note

References

Bastianello, N., Carli, R., Schenato, L., and Todescato, M. (2021). Asynchronous distributed optimization over lossy networks via relaxed ADMM: stability and linear convergence. *IEEE Trans. Automatic Control* 66, 2620–2635. doi:10.1109/TAC.2020.3011358

Cao, Y., Zhou, B., Chung, C. Y., Wu, T., Zheng, L., and Shuai, Z. (2024). A coordinated emergency response scheme for electricity and watershed networks considering spatio-temporal heterogeneity and volatility of rainstorm disasters. *IEEE Trans. Smart Grid*, 1. doi:10.1109/TSG.2024.3362344

Chang, T., Hong, M., Liao, W., and Wang, X. (2016). Asynchronous distributed ADMM for large-scale optimization—Part I: algorithm and convergence analysis. *IEEE Trans. Signal Process.* 64, 3118–3130. doi:10.1109/TSP.2016.2537271

Fu, X., Wu, X., Zhang, C., Fan, S., and Liu, N. (2022). Planning of distributed renewable energy systems under uncertainty based on statistical machine learning. *Prot. Control Mod. Power Syst.* 7, 41. doi:10.1186/s41601-022-00262-x

Gao, H., Wang, J., Liu, Y., Wang, L., and Liu, J. (2020). An improved ADMM-based distributed optimal operation model of AC/DC hybrid distribution network considering wind power uncertainties. *IEEE Syst. J.* 15, 2201–2211. doi:10.1109/JSYST.2020.2994336

Hu, J., Cong, H., and Wang, C. (2018). Coordinated scheduling model of power system with active distribution networks based on multi-agent system. *J. Mod. Power Syst. Clean Energy* 6, 521–531. doi:10.1007/s40565-017-0327-7

Hua, Z., Zhou, B., Or, S., Zhang, J., Li, C., and Wei, J. (2023). Robust emergency preparedness planning for resilience enhancement of energy-transportation nexus against extreme rainfalls. *IEEE Trans. Industry Appl.* 60, 1196–1207. doi:10.1109/TIA.2023.3274615

Li, P., Wu, Z., Zhang, C., Xu, Y., Dong, Z., and Hu, M. (2023). Multi-timescale affinely adjustable robust reactive power dispatch of distribution networks integrated with high penetration of PV. *J. Mod. Power Syst. Clean Energy* 11, 324–334. doi:10.35833/MPCE.2020.000624

Lu, Y., Xiang, Y., Huang, Y., Yu, B., Weng, L., and Liu, J. (2023). Deep reinforcement learning based optimal scheduling of active distribution system considering distributed generation, energy storage and flexible load. *Energy* 271, 127087. doi:10.1016/j.energy.2023.127087

Mohammadi, A., and Kargarian, A. (2022). Learning-aided asynchronous ADMM for optimal power flow. *IEEE Trans. Power Syst.* 37, 1671–1681. doi:10.1109/TPWRS.2021.3120260

Qi, J., Ma, D., Li, C., Pan, Y., Zhu, X., and Li, J. (2023). Multilevel optimization of economic dispatching in active distribution network based on ADMM. *Front. Energy Res.* 10. doi:10.3389/fenrg.2022.1088255

Sheng, H., Wang, C., Li, B., Liang, L., Yang, M., and Dong, Y. (2021). Multi-timescale active distribution network scheduling considering demand response and user comprehensive satisfaction. *IEEE Trans. Industry Appl.* 57, 1995–2005. doi:10.1109/TIA.2021.3057302

Wu, C., Gu, W., Zhou, S., and Chen, X. (2022). Coordinated optimal power flow for integrated active distribution network and virtual power plants using decentralized algorithm. *IEEE Trans. Power Syst.* 36, 3541–3551. doi:10.1109/TPWRS.2021.3049418

Wu, Z., Liu, Y., Gu, W., Zhou, J., Li, J., and Liu, P. (2018). Decomposition method for coordinated planning of distributed generation and distribution network. *IET Generation, Transm. Distribution* 12, 4482–4491. doi:10.1049/iet-gtd.2017.2050

Xiang, Y., Han, W., Zhang, J., Liu, J., and Liu, Y. (2017). Optimal sizing of energy storage system in active distribution networks using fourier–legendre series based state of energy function. *IEEE Trans. Power Syst.* 33, 2313–2315. doi:10.1109/TPWRS.2017.2779042

Xu, B., Zhang, G., Li, K., Li, B., Chi, H., Yao, Y., et al. (2022). Publisher Correction: reactive power optimization of a distribution network with high-penetration of wind and solar renewable energy and electric vehicles. *Prot. Control Mod. Power Syst.* 8, 21. doi:10.1186/s41601-023-00290-1

Xu, T., Wu, W., Zheng, W., Sun, H., and Wang, L. (2018). Fully distributed quasi-Newton multi-area dynamic economic dispatch method for active distribution networks. *IEEE Trans. Power Syst.* 33, 4253–4263. doi:10.1109/TPWRS.2017.2771950

Zhang, H., Liang, S., Liang, J., and Han, Y. (2022). Convergence analysis of a distributed gradient algorithm for economic dispatch in smart grids. *Int. J. Electr. Power Energy Syst.* 134, 107373. doi:10.1016/j.ijepes.2021.107373

Zheng, Y., Song, Y., Hill, D., and Zhang, Y. (2018). Multiagent system based microgrid energy management via asynchronous consensus ADMM. *IEEE Trans. Energy Convers.* 33, 886–888. doi:10.1109/TEC.2018.2799482

Zhong, J., Li, Y., Wu, Y., Cao, Y., Li, Z., Peng, Y., et al. (2023). Optimal operation of energy hub: an integrated model combined distributionally robust optimization method with stackelberg game. *IEEE Trans. Sustain. Energy* 14, 1835–1848. doi:10.1109/TSTE.2023.3252519

Zhou, B., Zou, J., Chi, Y., Wang, H., Liu, N., Voropai, N., et al. (2021a). Multi-microgrid energy management systems: architecture, communication, and scheduling strategies. *J. Mod. Power Syst. Clean Energy* 9, 463–476. doi:10.35833/MPCE.2019.000237

Zhou, X., Zou, S., Wang, P., and Ma, Z. (2021b). ADMM-based coordination of electric vehicles in constrained distribution networks considering fast charging and degradation. *IEEE Trans. Intelligent Transp. Syst.* 22, 565–578. doi:10.1109/TITS.2020.3015122

frontiers | Frontiers in Energy Research

TYPE Original Research
PUBLISHED 21 June 2024
DOI 10.3389/fenrg.2024.1424204

OPEN ACCESS

EDITED BY
Yitong Shang,
Hong Kong University of Science and Technology, Hong Kong SAR, China

REVIEWED BY
Ping Jiao,
Manchester Metropolitan University, United Kingdom
Lurui Fang,
Xi'an Jiaotong-Liverpool University, China

*CORRESPONDENCE
Cong Xu,
xu_cong@shu.edu.cn

RECEIVED 27 April 2024
ACCEPTED 31 May 2024
PUBLISHED 21 June 2024

CITATION
Xiong Y, Shi Q, Shen L, Chen C, Lu W and Xu C (2024), A hybrid neural network based on KF-SA-Transformer for SOC prediction of lithium-ion battery energy storage systems. *Front. Energy Res.* 12:1424204. doi: 10.3389/fenrg.2024.1424204

A hybrid neural network based on KF-SA-Transformer for SOC prediction of lithium-ion battery energy storage systems

Yifei Xiong[1], Qinglian Shi[1], Lingxu Shen[1], Chen Chen[2], Wu Lu[1] and Cong Xu[3]*

[1]College of Electrical Engineering, Shanghai University of Electric Power, Shanghai, China, [2]State Grid Xiongan New Area Electric Power Supply Company, Xiongan New Area, Hebei, China, [3]Intellectual Property Academy, Shanghai University, Shanghai, China

With the widespread application of energy storage stations, BMS has become an important subsystem in modern power systems, leading to an increasing demand for improving the accuracy of SOC prediction in lithium-ion battery energy storage systems. Currently, common methods for predicting battery SOC include the Ampere-hour integration method, open circuit voltage method, and model-based prediction techniques. However, these methods often have limitations such as single-variable research, complex model construction, and inability to capture real-time changes in SOC. In this paper, a novel prediction method based on the KF-SA-Transformer model is proposed by combining model-based prediction techniques with data-driven methods. By using temperature, voltage, and current as inputs, the limitations of single-variable studies in the Ampere-hour integration method and open circuit voltage method are overcome. The Transformer model can overcome the complex modeling process in model-based prediction techniques by implementing a non-linear mapping between inputs and SOC. The presence of the Kalman filter can eliminate noise and improve data accuracy. Additionally, a sparse autoencoder mechanism is integrated to optimize the position encoding embedding of input vectors, further improving the prediction process. To verify the effectiveness of the algorithm in predicting battery SOC, an open-source lithium-ion battery dataset was used as a case study in this paper. The results show that the proposed KF-SA-Transformer model has superiority in improving the accuracy and reliability of battery SOC prediction, playing an important role in the stability of the grid and efficient energy allocation.

KEYWORDS

state-of-charge, Transformer, Kalman filter, sparse autoencoder, lithium-ion battery

1 Introduction

With the transformation of the global energy structure and the increasing popularity of renewable energy, the integration of new energy generation into the power system has become an important aspect. However, due to the inherent randomness and instability of the output power of new energy sources, integrating them into the grid may impact power quality and reliability (Wang et al., 2019; Shi et al., 2022). Electrochemical batteries, as representatives of energy storage systems, provide a promising solution to mitigate the

instability and intermittency of new energy integration. They can assist in peak shaving and frequency regulation, thereby enhancing the security and flexibility of energy supply systems. The core of electrochemical energy storage is the Battery Management System (BMS), where the State of Charge (SOC) of the battery is a key parameter. However, due to the non-linear and time-varying electrochemical system inside batteries, SOC estimation can only be based on measurable parameters such as voltage and current, making accurate estimation of battery SOC a challenging task (Rivera-Barrera et al., 2017). Large errors in estimating battery SOC may damage battery capacity and service life, affect the economic operation of the grid, and even lead to catastrophic events such as combustion or explosion, posing a serious threat to grid safety (Zhou et al., 2021).

Currently, the common methods for predicting battery SOC mainly include the Ampere-hour integration method, open circuit voltage method, model-based prediction techniques, and data-driven methods. The Ampere-hour integration method, although simple, is prone to accumulating errors over time (Chang, 2013; Zhang et al., 2020). The accuracy of the open circuit voltage method is influenced by the battery's rest period. Model-based prediction techniques are based on specific operating conditions and may not be applicable to all conditions; accurate estimation of physical parameters in the model is very difficult, as these parameters change with battery aging and usage conditions, increasing model uncertainty and reducing prediction accuracy (How et al., 2019). Another method is the data-driven approach, which uses data training to identify the complex relationship between feature parameters and SOC, thereby avoiding the need for complex battery models. Typical data-driven methods usually utilize machine learning techniques such as Random Forest (Li et al., 2014) and Support Vector Machine (Song et al., 2020) to predict battery SOC. However, compared to traditional machine learning methods, deep learning methods based on neural networks demonstrate superior performance in extracting latent features and are widely used in SOC prediction, such as Long Short-Term Memory (LSTM) (Chen et al., 2023), Gated Recurrent Unit (GRU) (Dey and Salem, 2017), and Transformer series models (Han et al., 2021). The Transformer model, due to its inherent self-attention mechanism, can perform parallel computation and sequential data processing, making it more effective in handling time series data and providing a solution with higher accuracy and generalization capabilities for SOC prediction (Shen et al., 2022). (Hussein et al., 2024) conducted research on the SOC estimation of lithium-ion batteries using a self-supervised learning Transformer model, which demonstrated lower root mean square error (RMSE) and mean absolute error (MAE) under different ambient temperatures, indicating the potential of self-supervised learning in battery state estimation. However, this method has poor resistance to noise, which affects the robustness of the model in practical applications. (Chen et al., 2022) predicted the remaining useful life (RUL) of lithium-ion batteries based on the Transformer model, using a denoising autoencoder (DAE) to preprocess noisy battery capacity data, and then utilizing the Transformer network to capture temporal information and learn useful features. Eventually, by integrating the denoising and prediction tasks within a unified framework, the performance of RUL prediction was significantly improved. Despite this, the model by Chen et al. has some limitations. Although the DAE preprocessing step can remove noise, it may not fully preserve all the subtle features useful for prediction. To overcome these challenges, a Kalman filter can be added to the Transformer model. (Bao et al., 2024), in response to the limitations of existing methods in extracting time series features, proposed a time Transformer-based sequential network (TTSNet) for SOC estimation of lithium-ion batteries in electric vehicles. TTSNet effectively encodes features of the temporal dimension information through the time Transformer and introduces sliding time window technology and Kalman filtering as pre- and post-processing steps, which not only enhances the processing capability for long sequence data but also improves the accuracy and robustness of the estimation. In summary, these studies have made significant progress in the state monitoring and management of lithium-ion batteries, especially in improving prediction accuracy and handling long sequence data. However, the complexity of these models also brings significant computational costs. The Transformer model usually requires a large number of parameters and computational resources, which not only limits its application in resource-constrained environments but also increases the time cost for training and inference.

To overcome the limitations of the aforementioned methods, this paper introduces Sparse Autoencoder (SA) technology to improve the SA-Transformer model. The core idea of SA is to reduce the number of model parameters and computational complexity by learning the low-dimensional representation of data. It can significantly reduce the number of model parameters, thereby reducing memory usage and computational requirements, making the dimensionality-reduced model more lightweight, which can be trained and inferred more quickly. This is particularly important for application scenarios that require real-time responses. Since the sparse encoder encourages the model to learn more robust and discriminative feature representations, it can also improve the model's generalization capabilities.

To this end, this paper proposes a new model KF-SA-Transformer, which combines the advantages of the KF, SA, and Transformer. To enhance the model's resistance to noise and the smoothness of prediction, this paper introduces the KF module; to address the issue of model computational complexity, this paper uses the SA module to improve feature extraction capabilities by learning sparse representations of data, dimensionality reduction of large-scale sequence data, and reducing the input dimensions of the Transformer. The Transformer model is adept at capturing and learning long-term dependencies in the data, which enables the KF-SA-Transformer model to demonstrate higher prediction accuracy and stability in battery SOC prediction tasks. This three-in-one architecture aims to achieve more accurate SOC prediction, which can reduce the risk of overcharging and over-discharging the battery, thereby reducing the frequency of battery replacement and maintenance costs; it can also be used to develop intelligent charging strategies, improve charging efficiency, and reduce the impact on the power grid. In the field of new energy, such as wind and solar power generation, accurate SOC prediction of energy storage systems is of great importance for the stability of the power

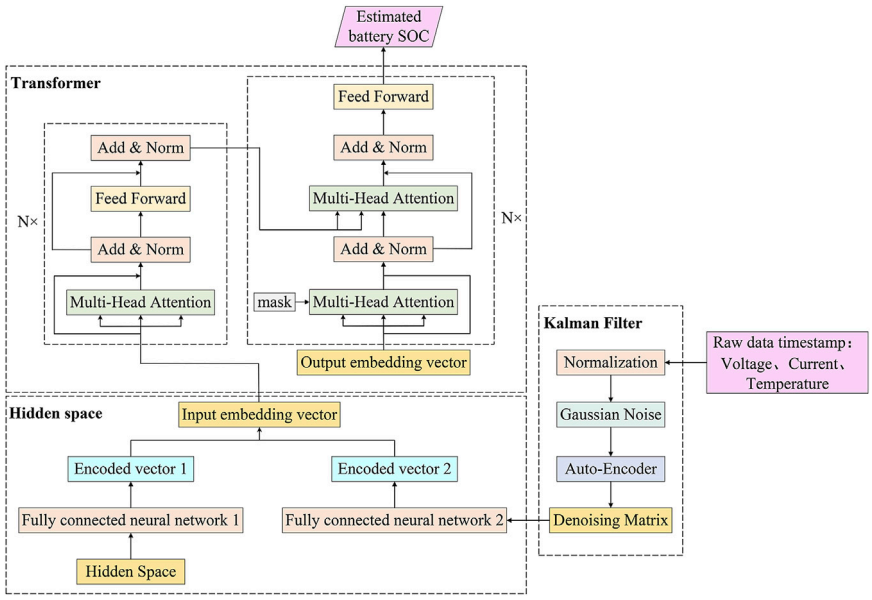

FIGURE 1
Overall model architecture.

grid and the effective distribution of energy (Schmietendorf et al.,2017; Yu G. et al., 2022a; Yu G. Z. et al., 2022b).

2 KF-SA-Transformer model for SOC prediction

2.1 Model architecture

The KF-SA-Transformer model is an innovative battery SOC prediction model that integrates three technologies: the Kalman filter, the sparse autoencoder, and the Transformer module. The input data of battery voltage, current, and temperature are filtered through the Kalman filter to eliminate noise interference and ensure data stability. The filtered data are then fed into the sparse autoencoder module, which extracts key features related to the battery SOC from the data through unsupervised learning, forming an embedding matrix that includes positional information. Finally, the embedding matrix is input into the Transformer module, which uses its unique self-attention mechanism to capture long-distance dependencies in the data, thereby accurately predicting the battery's SOC. The entire model achieves precise prediction from raw data to the battery SOC through this process, enhancing the accuracy and robustness of the prediction results. The overall architecture of the model is shown in Figure 1. This paper defines a feature input matrix X, with dimensions $m \times 3$, as shown in Eq. 1. Each row represents a sample, and each column represents a feature (current, voltage, or temperature).

$$X = \begin{bmatrix} X_{11}X_{12}X_{13} \\ X_{21}X_{22}X_{23} \\ \vdots \\ \vdots \\ X_{m1}X_{m2}X_{m3} \end{bmatrix} \quad (1)$$

Where: X_{ij} denotes the measurement value of the ith sample on the jth feature, and m is the total number of samples.

2.2 Kalman filter module

Using data-driven methods alone to predict battery SOC has significant limitations, as it requires high-precision battery data and may suffer from limited generalization capabilities. However, the integration of the Kalman filtering method can achieve optimal prediction of system states by minimizing the mean square error (MSE), effectively overcoming the inaccuracy of initial predictions. The Kalman filtering method treats estimated variables as system state variables and measured variables as observation variables. Through a recursive process, the Kalman filtering method can filter out noise and allocate different confidences to estimated and measured variables using Kalman gain until the estimated variables converge to more accurately reflect the actual variables (Peng, 2009). The state transition equation and observation equation are respectively, as shown in Eqs 2, 3:

$$X_k = AX_{k-1} + w(k) \quad (2)$$

$$Z_k = HX_k + v(k) \quad (3)$$

Where: X_k, Z_k are the system's state vector and observation vector at time k; u_{k-1} is the control input at time k-1; A, H, are the state transition matrix and observation matrix; $w(k)$, $v(k)$ are the system noise and observation noise.

The core of the Kalman filter lies in two main update steps: Prediction and Update. In the prediction step, the current state is predicted based on the previous moment's state estimate and process noise, as shown in Eqs 4, 5:

$$\hat{X}_k^- = A\hat{X}_k^- \quad (4)$$

$$P_k^- = AP_{k-1}A^T + Q \tag{5}$$

Where: $\hat{X}_k^-$ represents the predicted state vector, P_k^- is the predicted error covariance matrix, and Q is the process noise covariance matrix. To integrate predicted information with observational data, the concept of the Kalman gain is introduced. By utilizing the Kalman gain, it is possible to update the state estimate and the error covariance, as shown in Eqs 6–8:

$$K_K = P_k^- H^T \left(HP_k^- H^T + R\right)^{-1} \tag{6}$$

$$\hat{X}_k = \hat{X}_k^- + K_k\left(Z_k - H\hat{X}_k^-\right) \tag{7}$$

$$P_k = (I - K_k H)P_k^- \tag{8}$$

Where: K_k is the Kalman gain, $\hat{X}_k$ is the corrected state vector, Pk is the corrected error covariance matrix, and R is the observation noise covariance matrix. After processing by the Kalman filter, updated state estimates are obtained, which reflect the optimal estimated state of the battery system at each time step. These state estimates are integrated into a new matrix X_{KF}, which captures the evolution of the system state over time and filters out the effects of noise.

2.3 Sparse auto-encoder module

The Kalman filter, while effective in processing linear data, has limited capabilities when dealing with nonlinear data and complex relationships. To address this limitation, the integration of a sparse autoencoder into the data processing pipeline is proposed. This autoencoder effectively extracts features from the filtered data, reducing its dimensionality while preserving valuable feature information. This approach helps reduce data dimensionality and identify useful feature information, thereby enhancing the accuracy and performance of the prediction model.

SA introduces modifications to the embedding layer of the Transformer architecture, aiming to lighten the temporal positional encoding and enhance the modeling capabilities for temporal dependencies. As an unsupervised algorithm, SA adjusts its parameters adaptively by calculating the difference between the input and output of the autoencoding process, resulting in a trained final model. This algorithm finds widespread applications in information compression and feature extraction. Its goal is to reconstruct the input data using learned sparse representations.

The sparse autoencoder can sparsely represent battery input features, reduce the dimensionality of the original data, and improve computational efficiency. Its encoder input is the feature vector X_{KF} obtained after Kalman filtering, with the encoder output and decoder input in the hidden space, where the data is compressed into fewer dimensions while attempting to retain the most important information. The decoder output transforms the representation in the hidden space back to the original data space, attempting to reconstruct data as similar as possible to the input data, as shown in Eqs 9–11:

$$A_1 = sigmoid\left(W_1 X_{\mathrm{KF}} + b_1\right) \tag{9}$$

$$X_{\mathrm{SA}} = sigmoid\left(W_2 A_1 + b_2\right) \tag{10}$$

$$sigmoid\left(z\right) = \left(1 + e^{-z}\right)^{-1} \tag{11}$$

Where: z is any real number; W_1, W_2 are the weights of encoder and decoder; b_1, b_2 are the biases of encoder and decoder. The optimization objective is to minimize the reconstruction loss and approximate the probability density distribution, therefore, the network loss function is derived as shown in Eqs 12–14:

$$J\left(W_1, W_2, b_1, b_2\right) = \frac{1}{M}\sum_{i=1}^{M}\left\|x^{(i)} - \hat{x}^{(i)}\right\|^2 + \frac{\lambda}{2}\|W_1\| + \frac{\lambda}{2}\|W_2\| + \beta\sum_{j=1}^{d}\left[p \cdot \log_2\frac{p}{\hat{p}_j} + (1-p) \cdot \log_2\frac{(1-p)}{\left(1-\hat{p}_j\right)}\right] \tag{12}$$

$$\hat{p}_j = \frac{1}{M}\sum_{i=1}^{M} a_j^{(i)} \tag{13}$$

$$p = \frac{1}{M}\sum_{i=1}^{M} s_j^{(i)} \tag{14}$$

Where: $a_j^{(i)}$ is the *jth* neuron output value of the *ith* sample of the hidden space A_1; $s_j^{(i)}$ denotes the *j*th neuron input value of the *ith* sample of the encoder A_0; M is the total number of samples; β is the given sparsity constraint coefficient; λ is the given regularization coefficient. The encoder output of the sparse autoencoder results in a processed feature matrix, referred to as X_{SA}. This matrix encapsulates the salient characteristics of the input data, enabling the subsequent neural network to discern intricate relationships among the sequence elements.

2.4 Transformer module

Due to the inherent complexity and time-varying nature of chemical reaction processes within batteries, model-based prediction methods inherently carry the risk of errors. Enhancing model accuracy further complicates the task of parameter identification. To mitigate this challenge, the Transformer model is introduced, as it excels at capturing long-term dependencies and contextual information within sequence data, thereby enhancing the prediction accuracy of lithium battery SOC.

Transformer is a sequence-to-sequence (seq2seq) model based on the attention mechanism, which consists of two parts, Encoder and Decoder. The Transformer model consists of four parts, which are the self-attention mechanism, the multi-head attention mechanism, the positional encoding and the forward propagation network. As shown in Figure 2, the multi-head attention mechanism in the Transformer model allows the model to focus on different parts of the input sequence simultaneously, possessing the ability to globally perceive the input features, which improves the expressiveness of the model and better handles both local and global information. The forward propagation network is a fully-connected feedforward network consisting of two fully-connected layers.

The Transformer encoder comprises numerous identical sub-blocks, known as Transformer Blocks, stacked consecutively. The initial sub-layer within each block incorporates the multi-head attention mechanism, followed by a second sub-layer, a fully connected network. These two sub-layers are interconnected through residuals, which effectively prevent gradients from

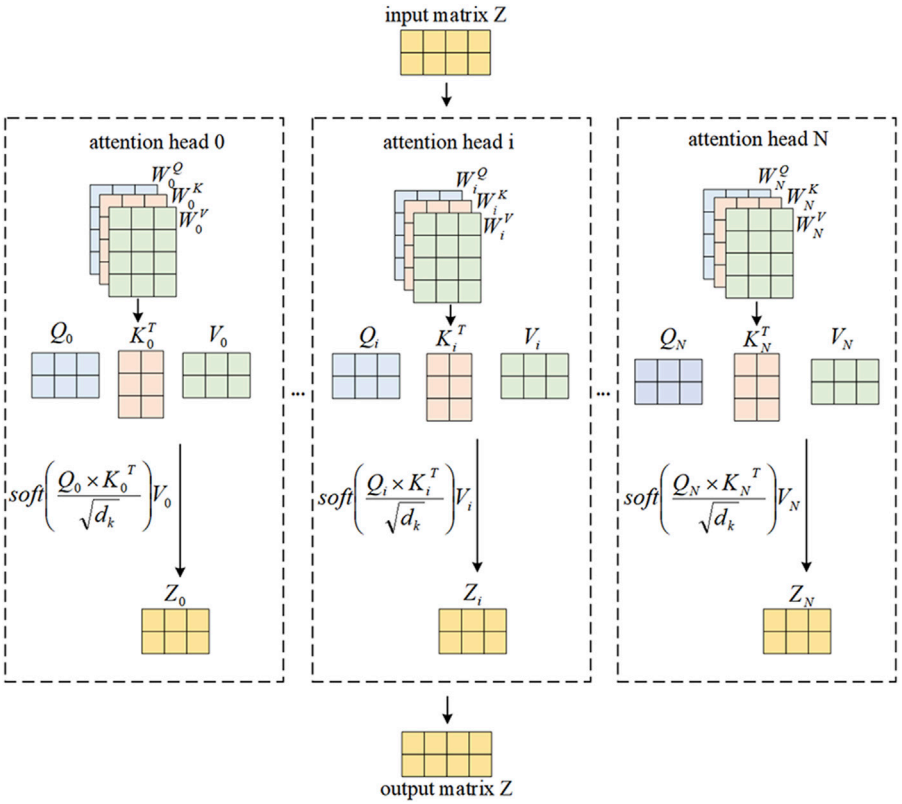

FIGURE 2
Multi-head attention structure.

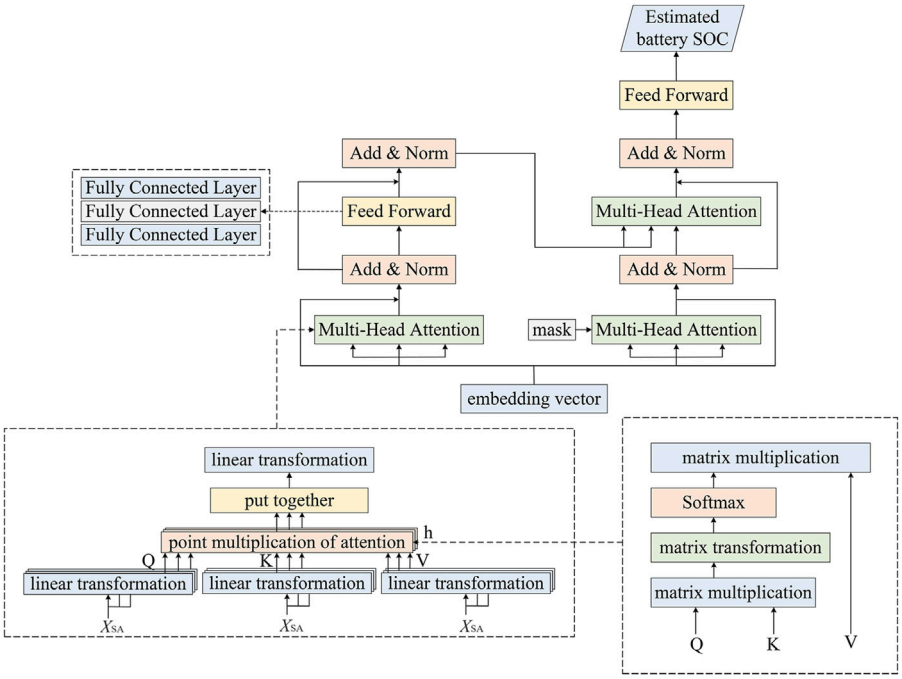

FIGURE 3
Transformer model.

vanishing and enhance the seamless flow of information between them. Additionally, a layer normalization operation is performed after the residuals are connected, further facilitating the algorithm's convergence. On the other hand, the decoder differs from the encoder in a crucial aspect: the resulting three vectors, along with an ordinal mask, are concurrently fed into the multi-head self-attention layer, as illustrated in Figure 3.

The Transformer leverages its unique structure to process the feature matrix X_{SA} refined by the sparse autoencoder, thereby achieving the prediction of the SOC for lithium batteries. The model first captures the interdependencies between sequence data in the input feature matrix through the self-attention mechanism, thereby understanding the long-term dependencies and contextual information within the sequence. And the multi-head attention mechanism allows the Transformer to focus on different parts of the input matrix simultaneously, globally perceiving the input features, which helps the model to better understand and process the input data. Positional encoding is used to provide positional information for each element in the sequence, which is crucial for understanding the sequential relationships. Finally, through the feed-forward neural network, the Transformer integrates this information and translates it into a prediction for the lithium battery SOC. This processing method makes the Transformer highly flexible and accurate when dealing with sequence data, enabling precise prediction of the lithium battery SOC.

3 Case analysis

3.1 Simulation platform and data

3.1.1 Simulation platform

The simulation platform is equipped with an Intel Core i7-7800X processor and an NVIDIA GeForce RTX 2080 Ti graphics card. It utilizes Python 3.8 as a programming language for algorithm development. The algorithmic model is built using TensorFlow, an open-source machine learning framework.

3.1.2 Data preparation

This paper utilized a publicly accessible lithium-ion battery dataset obtained by Dr. Phillip Kollmeyer at McMaster University in Hamilton, Ontario, Canada, to confirm the robustness of the studied model (Philip et al., 2020). This dataset was generated through various charge-discharge cycles on brand-new 3Ah LG 18650HG2 lithium-ion batteries following standard protocols. The collected data includes experiments conducted at six different temperatures ranging from −20°C to 40°C. This paper utilizes the driving condition data at 25°C as the dataset for validating the model's effectiveness. The dataset includes four standard drives (UDDS, HWFET, LA92, and US06) and eight driving cycles that are randomly combined from the four standard driving cycles.

The KF-SA-Transformer model used the terminal voltage, current, and temperature of the lithium battery as input variables to estimate the battery's SOC. However, the original data often exhibited significant fluctuations, which could introduce bias during the model parameter optimization process. Consequently, this might affect the effectiveness of the training process and the generalization capability of the model. Additionally, the variables were not uniformly scaled, which could lead to a contraction effect on the data size and range within the neurons of the deep learning model during parameter updates in the backpropagation phase. To address this issue, normalization of the data before prediction becomes imperative. This normalization process adjusts the data to be contained within the [0,1] interval, with the transformation function as show in Eq. 15:

$$X = \frac{X_0 - X_{\min}}{X_{\max} - X_{\min}} \tag{15}$$

Where: X represents the normalized sample data; X_0 represents the original sample data; $X_{\min}$ is the minimum value of the original sample data; $X_{\max}$ is the maximum value of the original sample data.

TABLE 1 Model parameter setting.

Parameters	Correlation coefficient
Encoder Layers	4
d_{model}	3
MLP hidden layer	4
Batch size	64
Learning rate	0.00001
Epochs	50

3.1.3 Assessment indicators

To appraise the precision of the model's predictive capabilities, this paper employs a suite of metrics: the MSE, MAE. These metrics collectively assess the model's performance in estimating the SOC of the battery. The specific calculation formula as shown in Eqs 16, 17:

$$MSE = \frac{1}{m}\sum_{i=1}^{m}(y_i - \hat{y}_i)^2 \tag{16}$$

$$MAE = \frac{1}{m}\sum_{i=1}^{m}\left|(y_i - \hat{y}_i)\right| \tag{17}$$

Where: m is the number of samples, i is the sample sequence number, y_i is the actual value of the *ith* sample, $\hat{y}_i$ is the predicted value of the *ith* sample, and d_i denotes the average of the real values. The above indicators are used to evaluate the error between the predicted value and the actual value, and the smaller the value is, the more accurate the prediction result is.

3.2 Model performance optimization strategies

3.2.1 Hyper-parameter settings

The accuracy of the neural network is influenced by hyper-parameters, which include, but are not limited to, the number of convolutional layers and the dimensions of the convolutional kernel. These hyper-parameters are pivotal in determining the SOC prediction outcomes. Commonly adopted methods for hyper-parameter optimization encompass grid search, random search,

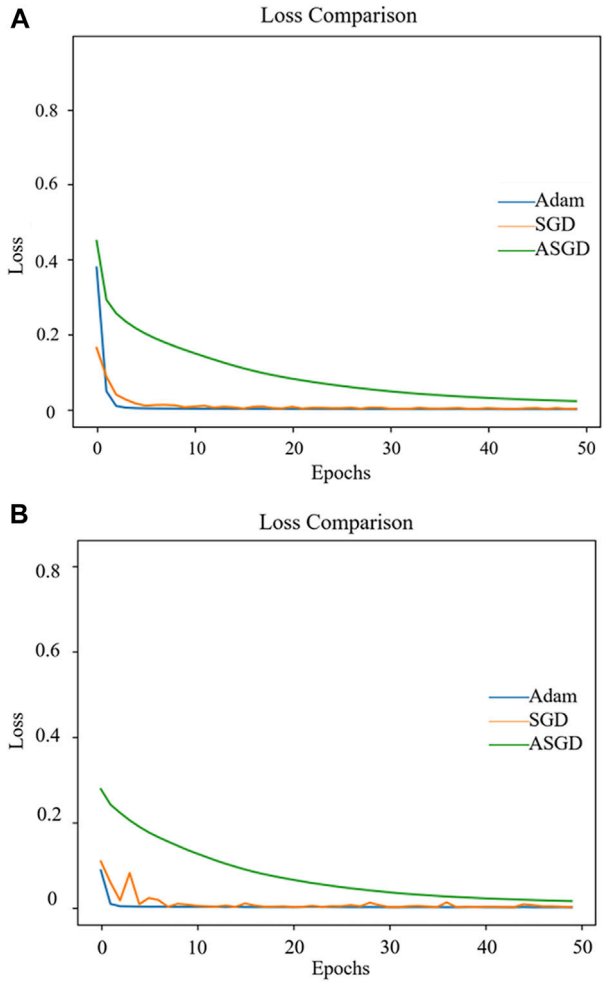

FIGURE 4
Loss profile based on KF-SA-Transformer model **(A)** training set **(B)** validation set.

and Bayesian optimization. While grid search is a straightforward approach, it can be computationally expensive and time-consuming. To achieve efficient hyper-parameter optimization within a reasonable timeframe, this paper opts for the Bayesian optimization algorithm. The underlying principle of Bayesian optimization involves the construction of a probabilistic model of the objective function. This model is iteratively refined by incorporating new sample points, thereby updating the posterior distribution of the objective function. The optimal hyperparameters selected in this paper are shown in Table 1.

3.2.2 Comparison of optimization algorithms

To further enhance the precision of the model's convergence value, reduce prediction errors, and improve generalization capabilities, it is necessary to introduce a parameter optimization algorithm into the KF-SA-Transformer model. This paper employs Stochastic Gradient Descent (SGD), Average Stochastic Gradient Descent (ASGD), and Adaptive Moment Estimation (Adam) to optimize the KF-SA-Transformer model. As shown in Figure 4, loss curves during iterative training on the training set and validation set for each algorithm are plotted. The analysis indicates that the Adam, SGD, and ASGD algorithms are all capable of achieving model convergence. However, the convergence rate of the ASGD optimization algorithm is relatively slow, failing to reach the convergence value of the other two algorithms even after 50 training epochs. In contrast, the SGD algorithm converges relatively quickly but exhibits significant fluctuations, especially in the loss curve on the validation set. Comparatively, the Adam optimization algorithm has the fastest convergence rate, with the loss value approaching zero and the smallest fluctuations after just 1-3 training epochs. Compared to SGD and ASGD, the Adam algorithm has significantly improved the predictive accuracy of the final model to a greater extent.

3.3 Results and discussion

3.3.1 Performance comparison of different models

To investigate the performance of the KF-SA-Transformer model, this paper compares it with the SA-Transformer and the Transformer models. Using the UDDS driving data as the test set, the SOC prediction results of these models were compared. Figure 5 illustrates the comparative analysis of the prediction data and the original data for the three models under the UDDS conditions, along with a comparison of their prediction errors.

Based on the thorough data analysis presented in Figure 5, the conclusions drawn are as follows: The KF-SA-Transformer model has exhibited remarkable predictive capabilities. It achieves a low MAE of 0.63% and an RMSE of 0.81% in SOC prediction, while its maximum error is contained within 3.08%. In contrast, the SA-Transformer model's SOC prediction performance is slightly inferior, with an MAE of 0.65%, an RMSE of 0.88%, and a maximum error of 3.59%. The traditional Transformer model, on the other hand, displays comparatively weaker performance, attaining an MAE of 1.3%, an RMSE of 1.72%, and a maximum error of 4.73%. These findings underscore the KF-SA-Transformer model's high degree of accuracy and stability in SOC prediction, highlighting its significant advantage over the other models.

3.3.2 Prediction performance under different conditions

To further explore the performance of the KF-SA-Transformer model in practical applications, this study selected the US06 driving data and a set of mixed driving cycles as the test set, thereby comprehensively evaluating the predictive capability of the KF-SA-Transformer model under variable operating conditions. The predicted results and errors are presented in Figures 6, 7.

Under the US06, a representative high-speed driving scenario, the KF-SA-Transformer model exhibited outstanding accuracy in predicting the battery's SOC. Notably, its predicted results achieved an MAE of merely 0.87%, along with an RMSE of 1.13%. Even at the peak of error, the deviation remained within a range of 3.48%. This data unequivocally demonstrates that the KF-SA-Transformer model maintains exceptional predictive accuracy under high-speed and high-load conditions.

In the more complex mixed driving cycles, which encompass a variety of driving speeds and load conditions, the KF-SA-

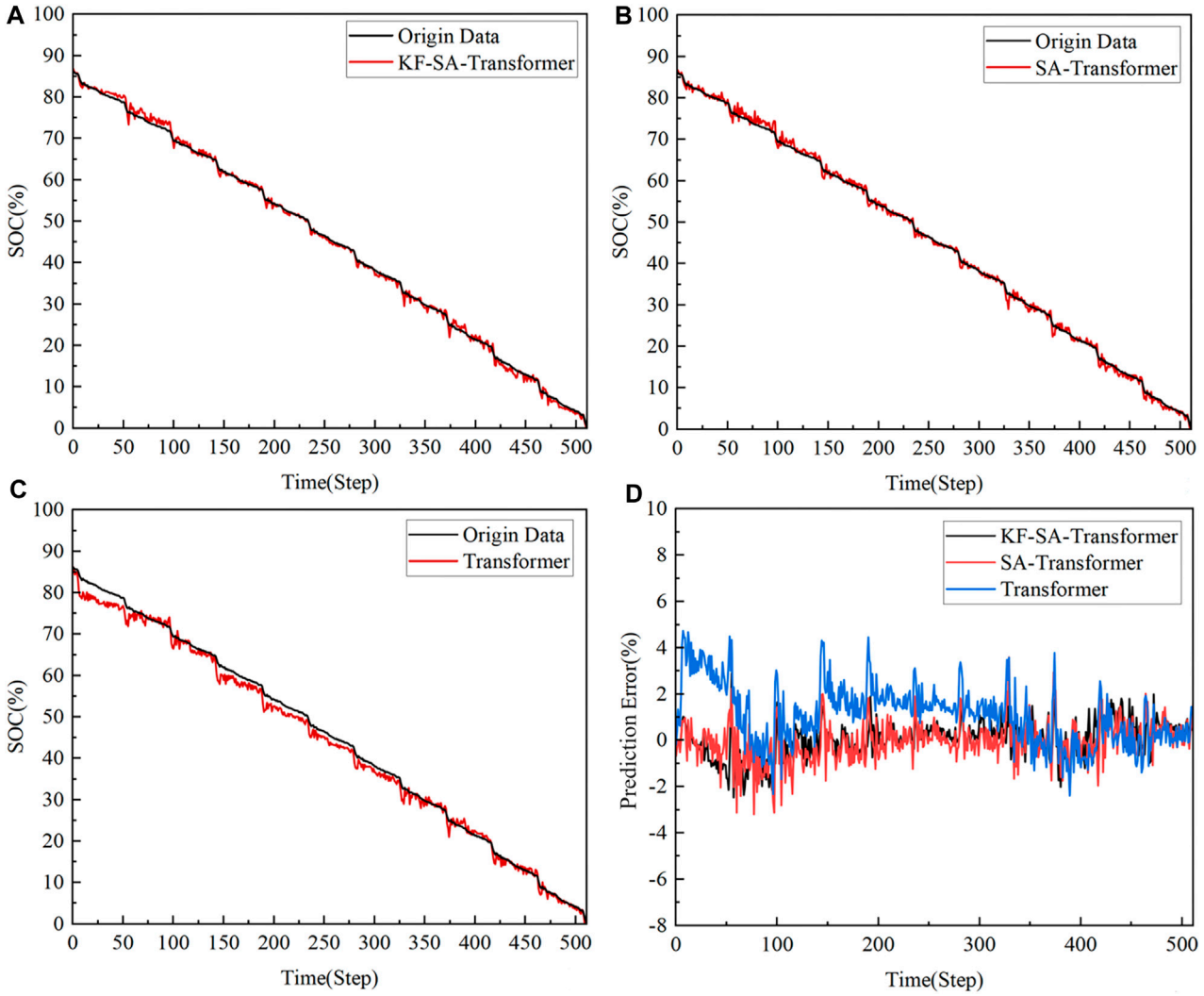

FIGURE 5
SOC prediction results **(A)** KF-SA-Transformer **(B)** SA-Transformer **(C)** Transformer **(D)** error comparison of each model.

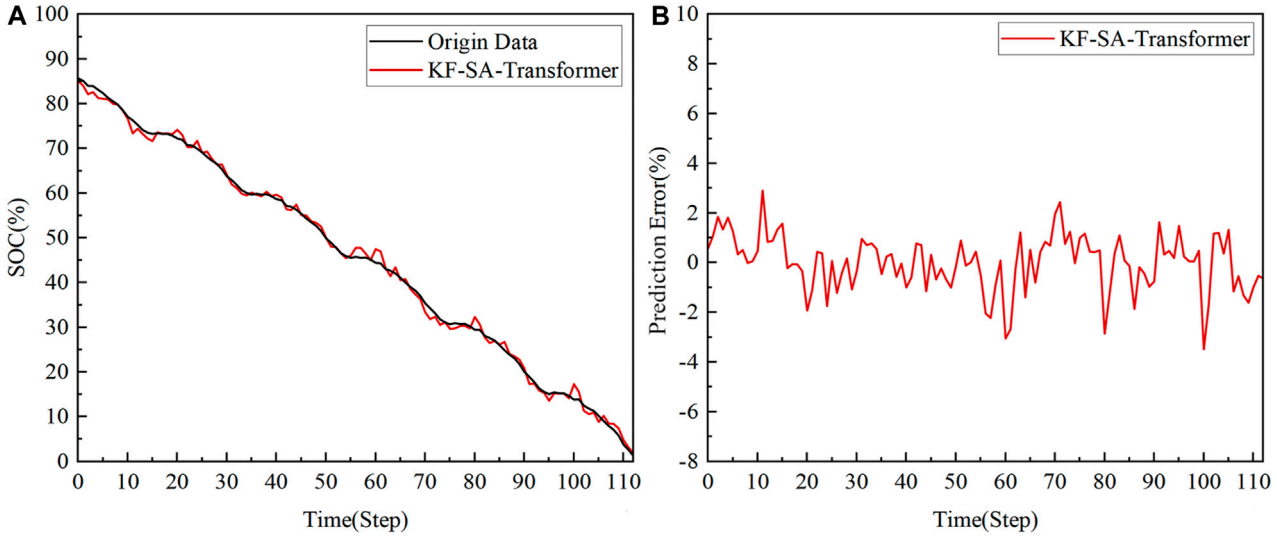

FIGURE 6
SOC prediction results of the US06 driving **(A)** prediction results **(B)** error curve.

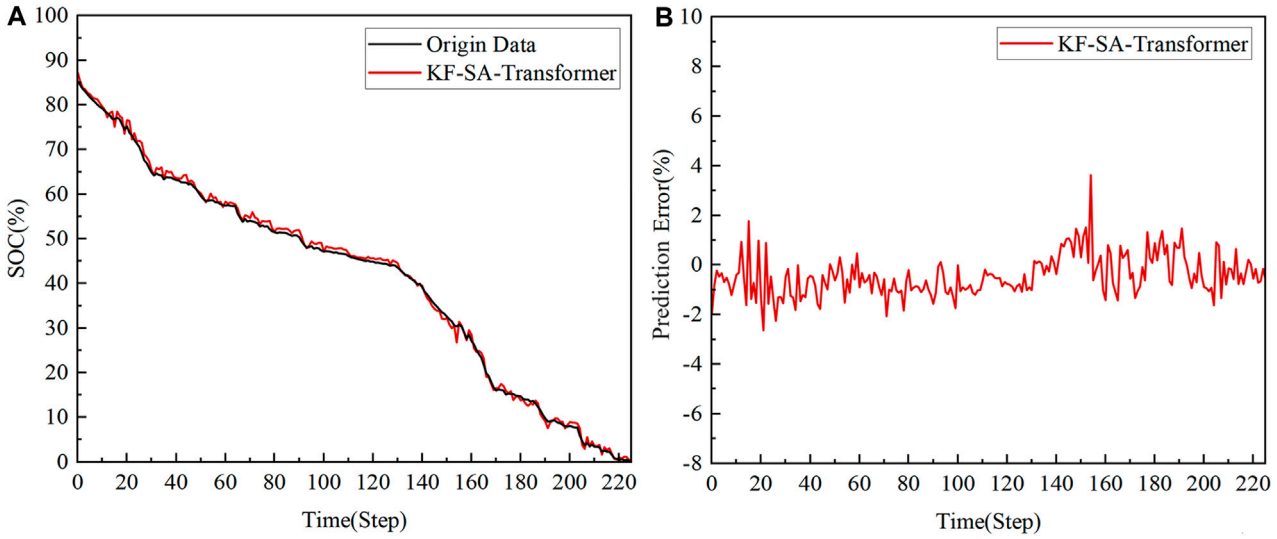

FIGURE 7
SOC prediction results of the mixed driving cycle **(A)** prediction results **(B)** error curve.

Transformer model's predictive performance remains equally remarkable. These conditions pose higher demands on the model's generalization capabilities. However, the KF-SA-Transformer model still demonstrated excellent performance, achieving an MAE of 0.79% and an RMSE of 0.94% for its SOC prediction results. The maximum error was only 3.63%. These data not only validate the model's adaptability under different operating conditions but also further reinforce the effectiveness of the KF-SA-Transformer model in the field of SOC prediction.

4 Conclusion

This paper introduces a method for predicting the SOC of lithium-ion battery energy storage systems using a hybrid neural network comprising the KF-SA-Transformer architecture. The approach takes current, voltage, and temperature data as inputs, first utilizes a Kalman filter for noise reduction, and then forwards the filtered data to a sparse autoencoder for feature extraction, effectively reducing the data dimensionality. Finally, the Transformer model leverages these low-dimensional features to establish a mapping relationship with the SOC, thereby significantly enhancing the accuracy and overall performance of SOC predictions.

Under identical driving cycle conditions, the KF-SA-Transformer model exhibits significant advantages compared to other models. Moreover, the application of the KF-SA-Transformer model has also yielded favorable results in various other driving cycle conditions. While the model performs exceptionally well on the selected lithium-ion battery dataset, its generalization capabilities to other battery types or varying operating conditions remain to be further validated. Therefore, future research could explore avenues such as enhancing dataset diversity, incorporating datasets from multiple battery models for model training, employing data augmentation techniques, or adopting an ensemble of multiple models to further improve the model's generalization abilities and foster wider applications and advancements in the field of SOC prediction.

Data availability statement

Publicly available datasets were analyzed in this study. This data can be found here: https://data.mendeley.com/datasets/cp3473x7xv/3.

Author contributions

YX: Data curation, Formal Analysis, Methodology, Writing–original draft. QS: Validation, Visualization, Writing–original draft. LS: Software, Writing–review and editing. CC: Writing–review and editing, Resources. WL: Writing–review and editing, Conceptualization. CX: Writing–review and editing, Supervision.

Funding

The author(s) declare that financial support was received for the research, authorship, and/or publication of this article. This study received funding from the Chenguang Program of the Shanghai Education Development Foundation and Shanghai Municipal Education Commission (Grant No. 21CGA63). The funder was not involved in the study design, collection, analysis, interpretation of data, the writing of this article or the decision to submit it for publication. All authors declare no other competing interests.

Conflict of interest

Author CC was employed by State Grid Xiongan New Area Electric Power Supply Company.

The remaining authors declare that the research was conducted in the absence of any commercial or financial relationships that could be construed as a potential conflict of interest.

Publisher's note

References

Bao, Z., Nie, J., Lin, H., Gao, K., He, Z., and Gao, M. (2024). TTSNet: state-of-charge estimation of Li-ion battery in electrical vehicles with temporal transformer-based sequence network. *IEEE Trans. Veh. Technol.*, 1–14. doi:10.1109/tvt.2024.3350663

Chang, W. Y. (2013). The state of charge estimating methods for battery: a review. *Int. Sch. Res. Notices* 2013, 1–7. doi:10.1155/2013/953792

Chen, D., Hong, W., and Zhou, X. (2022). Transformer network for remaining useful life prediction of lithium-ion batteries. *Ieee Access* 10, 19621–19628. doi:10.1109/access.2022.3151975

Chen, J., Zhang, Y., Wu, J., Cheng, W., and Zhu, Q. (2023). SOC estimation for lithium-ion battery using the LSTM-RNN with extended input and constrained output. *Energy* 262, 125375. doi:10.1016/j.energy.2022.125375

Dey, R., and Salem, F. M. (2017). "Gate-variants of gated recurrent unit (GRU) neural networks," in 2017 IEEE 60th international midwest symposium on circuits and systems (MWSCAS), Boston, Massachusetts, USA, 6-9 August 2017, 1597–1600. doi:10.1109/mwscas.2017.8053243

Han, K., Xiao, A., Wu, E., Guo, J., Xu, C., and Wang, Y. (2021). Transformer in transformer. *Adv. neural Inf. Process. Syst.* 34, 15908–15919. doi:10.48550/arXiv.2103.00112

How, D. N., Hannan, M. A., Lipu, M. H., and Ker, P. J. (2019). State of charge estimation for lithium-ion batteries using model-based and data-driven methods: a review. *IEEE Access* 7, 136116–136136. doi:10.1109/access.2019.2942213

Hussein, H. M., Esoofally, M., Donekal, A., Rafin, S. S. H., and Mohammed, O. (2024). Comparative study-based data-driven models for lithium-ion battery state-of-charge estimation. *Batteries* 10 (3), 89. doi:10.3390/batteries10030089

Li, C., Chen, Z., Cui, J., Wang, Y., and Zou, F. (2014). "The lithium-ion battery state-of-charge estimation using random forest regression," in 2014 Prognostics and System Health Management Conference (PHM-2014 Hunan), Zhangiiajie City, Hunan, China, 24-27 August 2014, 336–339. doi:10.1109/phm.2014.6988190

Peng, D. (2009). Pseudo-linear Kalman Filter in passive target tracking. *Softw. Guide* 11, 32–34.

Philip, K., Carlos, V., Mina, N., and Michael, S. (2020). Data from: LG 18650HG2 Li-ion battery data and example deep neural network xEV SOC estimator script. *Mendeley Data* V3. doi:10.17632/cp3473x7xv.3

Rivera-Barrera, J. P., Muñoz-Galeano, N., and Sarmiento-Maldonado, H. O. (2017). SoC estimation for lithium-ion batteries: review and future challenges. *Electronics* 6 (4), 102. doi:10.3390/electronics6040102

Schmietendorf, K., Peinke, J., and Kamps, O. (2017). The impact of turbulent renewable energy production on power grid stability and quality. *Eur. Phys. J. B* 90, 222–226. doi:10.1140/epjb/e2017-80352-8

Shen, H., Zhou, X., Wang, Z., and Wang, J. (2022). State of charge estimation for lithium-ion battery using Transformer with immersion and invariance adaptive observer. *J. Energy Storage* 45, 103768. doi:10.1016/j.est.2021.103768

Shi, K., Zhang, D., Han, X., and Xie, Z. (2022). Digital twin model of photovoltaic power generation prediction based on LSTM and transfer learning. *Power Syst. Technol.* 46 (4), 1363–1371. (in Chinese). doi:10.13335/j.1000-3673.pst.2021.0738

Song, Y., Liu, D., Liao, H., and Peng, Y. (2020). A hybrid statistical data-driven method for on-line joint state estimation of lithium-ion batteries. *Appl. Energy* 261, 114408. doi:10.1016/j.apenergy.2019.114408

Wang, K., Qi, X., and Liu, H. (2019). A comparison of day-ahead photovoltaic power forecasting models based on deep learning neural network. *Appl. Energy* 251, 113315. doi:10.1016/j.apenergy.2019.113315

Yu, G., Liu, C., Tang, B., Chen, R., Lu, L., Cui, C., et al. (2022a). Short term wind power prediction for regional wind farms based on spatial-temporal characteristic distribution. *Renew. Energy* 199, 599–612. doi:10.1016/j.renene.2022.08.142

Yu, G. Z., Lu, L., Tang, B., Wang, S. Y., and Chung, C. Y. (2022b). Ultra-short-term wind power subsection forecasting method based on extreme weather. *IEEE Trans. Power Syst.* 38 (6), 5045–5056. doi:10.1109/tpwrs.2022.3224557

Zhang, L., Xu, G., Zhao, X., Du, X., and Zhou, X. (2020). Study on SOC estimation method of aging lithium battery based on neural network. *J. power supply* 18 (01), 54–60. doi:10.13234/j.issn.2095-2805.2020.1.54

Zhou, W., Zheng, Y., Pan, Z., and Lu, Q. (2021). Review on the battery model and SOC estimation method. *Processes* 9 (9), 1685. doi:10.3390/pr9091685

frontiers | Frontiers in Energy Research

TYPE Original Research
PUBLISHED 08 July 2024
DOI 10.3389/fenrg.2024.1421277

OPEN ACCESS

EDITED BY
Yingjun Wu,
Hohai University, China

REVIEWED BY
Yulin Chen,
Zhejiang University, China
Haibo Li,
Tsinghua University, China

*CORRESPONDENCE
Wenjia Zhang,
1721892518@qq.com

RECEIVED 22 April 2024
ACCEPTED 12 June 2024
PUBLISHED 08 July 2024

CITATION
Zhang W, Peng Z, Wang Q, Qi W and Ge Y (2024), Optimal power flow method with consideration of uncertainty sources of renewable energy and demand response. *Front. Energy Res.* 12:1421277. doi: 10.3389/fenrg.2024.1421277

Optimal power flow method with consideration of uncertainty sources of renewable energy and demand response

Wenjia Zhang*, Zhuyi Peng, Quanquan Wang, Wanchun Qi and Yi Ge

State Grid Jiangsu Electric Power Co. Ltd. Economic Research Institute, Nanjing, Jiangsu, China

Optimal power flow (OPF) calculation methods are important for the power system operation and mainly focus on the deterministic power flow calculation, neglecting the impact of demand response on online security calculation of power systems with renewable energy sources. Therefore, this paper proposes an OPF calculation method that considers the uncertainties of wind power, photovoltaic (PV) power generation and demand-side response. Firstly, the research focuses on the renewable energy grid, considering the uncertainties of wind power and PV power generation, and establishes uncertainty models for wind power and PV output. Secondly, based on cloud model theory, an uncertainty model for demand response is established. According to the established models, an efficient OPF model is constructed with a linearized submodels considering multiple uncertainties. By testing on the IEEE 30-bus system as a typical example, we found the effectiveness and superiority of the proposed OPF calculation method can benefit the power system economic operation and demand side resource utilization.

KEYWORDS

optimal power flow, demand response, renewable energy grid, cloud model theory, multiple uncertainties

1 Introduction

In recent years, the global energy crisis has become increasingly prominent, and the environmental pollution caused by the combustion of fossil fuels such as coal and oil has also attracted widespread attention (Xin et al., 2022). To address this issue, countries around the world have actively invested a large amount of funds and research personnel in renewable energy technologies to replace fossil fuels. New renewable and clean energy sectors, including wind and solar power generation, have experienced vigorous growth (Chen et al., 2020). As the proportion of wind power, PV and other renewable energy generation in power grid generation continues to increase, the inherent randomness and fluctuation of these energy sources gradually exert a growing impact on the operational state of the electric power system. Therefore, to precisely evaluate how the integration of renewable energy sources with high capacity affects the operational state of the electric power system, and to enhance the reliability and cost-effectiveness of power systems incorporating wind and PV generation, extensive research has been conducted on OPF calculation methods for electric power systems (Yang et al., 2018). Traditional deterministic power flow calculation methods are mainly used in typical scenarios where the grid

structure information of the power system is fixed and the input power at each node of the power system remains basically unchanged. They are unable to accurately reflect the actual operational state of the current power grid where renewable energy sources constitute a significant portion (Pourbehzadi et al., 2019).

Currently, scholars have conducted extensive research on the OPF calculation problem for power grids containing wind power and PVs. In Refs. (Li et al., 2015; Guo et al., 2018), the uncertainty of wind power output is taken into account, and a probabilistic OPF model for wind power integration is proposed. Ref. (Li et al., 2020). introduces a prediction method for PV output that considers correlation and analyzes the OPF of PV output at different time points. Additionally, Ref. (Morshed et al., 2018). addresses the issue of correlation between the outputs of wind farms and proposes a correlation modeling method based on fuzzy C-means clustering for calculating the power flow in a distribution network that includes wind power generation. In Ref. (Yan et al., 2018), Latin Hypercube Sampling (LHS) and its improved algorithm were employed for sampling the probability distributions pertaining to wind power, photovoltaics, and other renewable energy forms, enhancing the speed and accuracy of power flow calculations. In Refs. (Liao et al., 2019; Liu et al., 2019), the linearization semi-variance approach was developed for probabilistic power flow calculations, effectively reducing the impact of uncertainty in clean energy sources like wind power and PVs on power flow calculation results.

However, existing research has not taken into account the impact of demand-side response on OPF calculation. On the load side, demand-side response has a significant influence on the optimal allocation of the power grid. By guiding users' electricity consumption behavior through demand-side response and matching load characteristics with power generation characteristics such as wind power and PVs, it is possible to reduce the configured capacity and optimizes the overall cost-effectiveness of the power grid (Yang et al., 2022). Based on considering the uncertainty of renewable energy generation, Ref. (Zhao et al., 2018). introduced demand-side response, effectively reducing the economic cost of the system. Additionally, due to differences in user demographics, price incentives, and other factors, demand response also exhibits significant uncertainty. Ref. (Lin and Zhang, 2020). considered the impact of demand-side response on system scheduling under different incentive levels, finding that system scheduling costs decrease as incentive levels increase.

In summary, although numerous studies have been conducted on OPF calculation methods for power systems with renewable energy sources, none of them have taken into account the impact of demand-side response on the renewable energy accommodation capacity. As a result, demand-side response has not been incorporated into the OPF calculation methods. Therefore, this paper aims to develop an OPF calculation method that considers the uncertainties of wind power, PV power generation and demand-side response. The decision variables such as the output and terminal voltage of wind turbines, transformer ratio, and reactive power compensation capacity have been reasonably adjusted. This not only reduces the system operating costs while satisfying safety constraints, but also enhancing the speed and accuracy of online security calculation and analysis in power systems.

The remainder of this paper is organized as follows. Section II establishes uncertainty models for wind power and PV output. Section III constructs an uncertainty model for demand-side response. Based on the previously established uncertainty models, and Section IV establishes an OPF model and proposes a linearized method for OPF calculation considering multiple uncertainties. Section V validates the effectiveness and superiority of the proposed method using the IEEE 30-bus system as an example. Finally, Section VI presents the conclusions of this paper.

2 Uncertainty models for wind power and PV output

The fluctuations and intermittency of wind speed and solar irradiance pose new problems and complexities to the stable and economic dispatch of the power grid. This necessitates the use of appropriate mathematical models for accurate calculations of wind power and PV output, facilitating subsequent scenario simulations and uncertainty handling.

2.1 Wind power output model

A wind turbine generator converts wind energy into mechanical energy by driving the rotation of its blades, and then converts this mechanical energy into electrical power. This paper employs the Weibull distribution to fit the measured wind speed data, and the resulting probability density function (PDF) of wind speed is presented as follows in Eq. 1:

$$f(v) = \frac{k}{A}\left(\frac{v}{A}\right)^{k-1} e^{-\left(\frac{v}{A}\right)^{k}} \tag{1}$$

Where, v represents the actual wind speed (m/s). k and A are the two parameters of the Weibull distribution, which are obtained through fitting the actual data.

The specific mathematical model expression is as follows (Xie et al., 2019) in Eq. 2:

$$P_{wt} = \begin{cases} 0 & v_{out} < v < v_{in} \\ \dfrac{v^3 - v_{in}^3}{v_N^3 - v_{in}^3} P_N & v_{in} \le v \le v_N \\ P_N & v_N < v \le v_{out} \end{cases} \tag{2}$$

Where, P_{wt} is the power of the wind turbine generator. v_{out}, v_{in} and v_N represent the cut-out wind speed, cut-in wind speed and rated wind speed of the wind turbine generator, respectively. P_N is the rated power of the wind turbine generator.

During the operation of a wind turbine generator, only the costs associated with its operation and maintenance are taken into account, and these costs are specifically related to the output power of the turbine. The detailed expression is as follows in Eq. 3:

$$C_{wt}(t) = c_{wt} P_{wt}(t) \tag{3}$$

Where, c_{wt} refers to the cost associated with the routine maintenance and operational expenses of a wind turbine for generating a unit of power. $C_{wt}(t)$ refers to the total cost related

to the routine maintenance and operational expenses of wind turbines during the time period t.

2.2 PV output model

The working principle of PV modules is based on the photoelectric effect, and their power generation is positively correlated with the intensity of light. This paper employs the Beta distribution to fit the measured light intensity data, and the resulting PDF of light intensity is presented as follows in Eq. 4:

$$f(r) = \frac{\Gamma(\alpha+\beta)}{\Gamma(\alpha)\Gamma(\beta)}\left(\frac{r}{r_{\max}}\right)^{\alpha-1}\left(1-\frac{r}{r_{\max}}\right)^{\beta-1} \tag{4}$$

Where, r represents the light intensity (W/m^2), $r_{\max}$ is the maximum possible light intensity that the photovoltaic power plant can receive, Γ is the Gamma function, which along with parameters α and β, controls the shape of the Beta distribution curve. The values of α and β are obtained through fitting the actual data.

The expression for its output power is as follows (Zhao et al., 2022) in Eq. 5:

$$P_{pv} = rS_{pv}\eta_{pv} \tag{5}$$

Where, P_{pv} signifies the electrical power produced by the PV array. S_{pv} signifies the equivalent area of vertical sunlight received by the photovoltaic cell. η_{pv} represents the photoelectric conversion coefficient.

Similar to wind turbines, only the costs associated with the operation and maintenance of PV cells are considered during their operation. The specific expression is as follows in Eq. 6:

$$C_{pv}(t) = c_{pv}P_{pv}(t) \tag{6}$$

Where, c_{pv} refers to the cost associated with the routine maintenance and operational expenses required for the PV cell to produce a unit of power output. C_{pv} is the total cost related to the routine maintenance and operational expenses incurred by the PV cell during the time period t.

2.3 Simulation of scenarios in wind and solar generation based on monte carlo sampling

When utilizing scenario analysis to tackle the uncertainty inherent in wind and solar generation, it is necessary to first perform scenario simulation to obtain a large-scale scenario sample set. Meanwhile, the method of time series analysis should be employed to consider the coupling characteristics between wind and solar power output at different times. Then, scenario reduction techniques are applied to extract a few typical scenarios from the sample set to describe and characterize the power fluctuations of the entire sample set.

Utilizing Monte Carlo sampling techniques, this paper performs extensive sampling of wind and solar energy production to generate a comprehensive collection of predictive scenarios. Monte Carlo method is based on probabilistic mathematical models and uses numerical simulation experiments to describe physical geometric characteristics and geometric quantities in order to approximate solutions (Zhao et al., 2023).

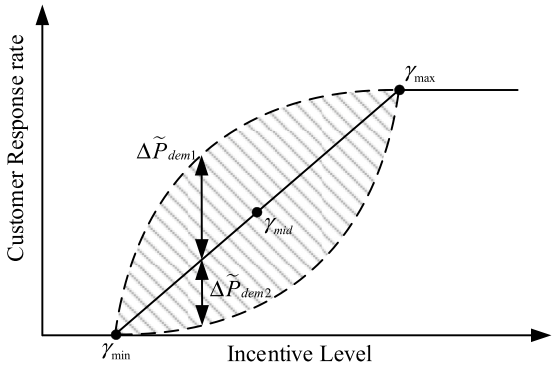

FIGURE 1
Demand response uncertainty curve.

For the prediction of wind and solar power output over a scheduling period $T = 24h$, a scenario set of size $N = 1{,}000$ is obtained through Monte Carlo sampling. The specific description is as follows in Eq. 7:

$$\Omega_S = \left\{S_{wt}^1, S_{wt}^2, S_{wt}^3, ..., S_{wt}^T, S_{pv}^1, S_{pv}^2, S_{pv}^3, ..., S_{pv}^T,\right\} \tag{7}$$

Where, S_{wt}^t represents the set of predicted wind generation scenarios for time t. S_{pv}^t represents the set of predicted PV generation scenarios for the same time t.

Based on the mathematical models established for wind turbines and PV modules in this section, a sample size of $N = 1{,}000$ and a scheduling period of $T = 24h$ were chosen. The cut-in wind speed is designated as $v_{in} = 2.5m/s$, the cut-out wind speed as $v_{out} = 27m/s$, the rated wind speed as $v_N = 15m/s$. $r = 0.9kW/m^2$. Monte Carlo method was used to obtain 1,000 simulated wind power and photovoltaic output scenarios.

3 Uncertainty model of demand side response

3.1 Controllable load model

The response level of the demand side largely depends on the price compensation strategy issued by the system operator, resulting in significant uncertainty. As shown in Figure 1, when the incentive level is below $\gamma_{\min}$, users generally do not participate in the response. When the incentive level falls between $[\gamma_{\min}, \gamma_{\max}]$, users engage in the response, and the amount of response increases as the incentive level rises. Once the incentive level reaches $\gamma_{\max}$, user response saturates, reaching the maximum response level. It is worth noting that the relationship between user response fluctuations and incentive levels is not linear. As the incentive level increases, the response fluctuations first increase and then decrease. γ_{mid} represents the critical point in the trend of response fluctuation changes.

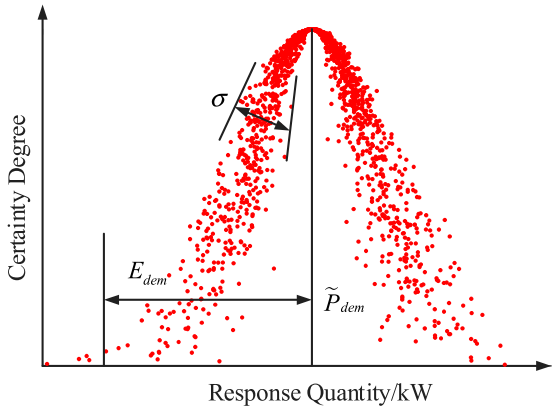

FIGURE 2
Demand response load distribution.

3.2 Establishment of the uncertainty model for demand-side response

In this paper, the theory of cloud model is adopted to describe the uncertainty of demand-side response. Assuming that the single response quantity P^s_{dem} of a user fluctuates around the expected single response value E_{dem}, the joint effect of n response results from the user forms a user response quantity P_{dem} with an expected response of $\tilde{P}_{dem}$ (Sun et al., 2018). Both P^s_{dem} and P_{dem} follow a normal distribution, and under the condition of $P^s_{dem} = \sigma_s$, the probability density function of P_{dem} is as follows in Eq. 8:

$$f(P_{dem}) = \int_{-\infty}^{+\infty} \frac{1}{\sqrt{2\pi\sigma_s^2}} \exp\left\{-\frac{\left(P_{dem} - \tilde{P}_{dem}\right)^2}{2\sigma_s^2}\right\} \cdot \frac{1}{\sqrt{2\pi\sigma^2}} \exp\left\{-\frac{(\sigma - E_{dem})^2}{2\sigma^2}\right\} d\sigma_s \tag{8}$$

It can be seen that the demand response quantity is a random variable with expected value p_{dem} and variance $E^2_{dem} + \sigma^2$. When the demand-side compensation price is set at c_{dem}, the cloud distribution of the demand-side load response is illustrated in Figure 2. p_{dem} represents the expected response quantity of users when the compensation price is fixed. E_{dem} characterizes the distribution range of the response quantity, reflecting the degree of uncertainty in the response. σ indicates the concentration of the user response distribution.

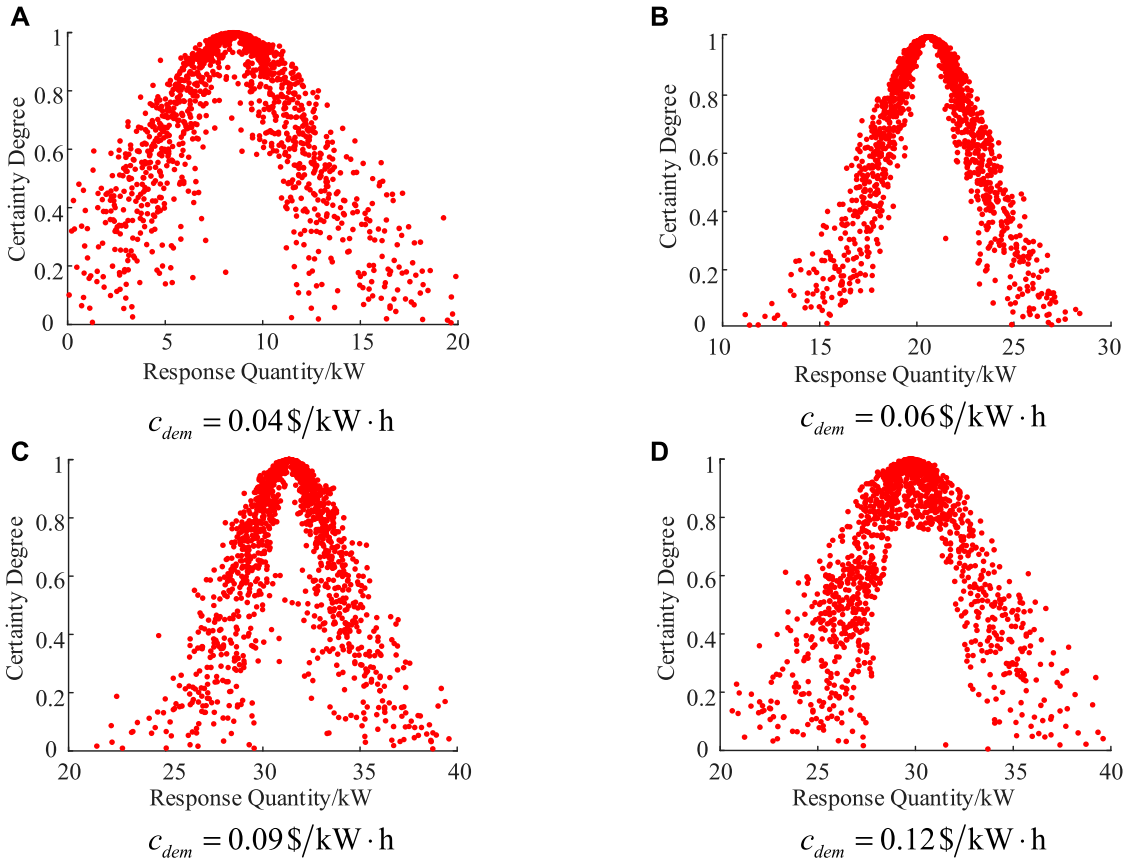

FIGURE 3
Demand response distribution cloud map with different compensation price.

3.3 Simulation of demand-side response load scenarios based on the response cloud model

Figure 3 shows the distribution diagram of user responses for 1,000 times under four cases where the compensation price c is 0.04 $/kW·h, 0.06 $/kW·h, 0.09 $/kW·h and 0.12 $/kW·h respectively.

4 OPF model and solution

4.1 Establishment of the OPF model

To perform OPF calculations, the initial step involves establishing an OPF model. This paper proposes an OPF model that comprehensively incorporates multiple uncertainties, primarily the fluctuations in wind turbine output and PV generation, along with the uncertainty associated with demand-side response. The specific composition of the OPF model includes: the objective function, the equality constraints for power balance, and a set of inequality constraints (Sun et al., 2018).

4.1.1 Objective function

$$f = \min\left[\sum_{i=1}^{m}\left(a_i + b_i P_{Gi} + c_i P_{Gi}^2\right) + C_{comp}\right] \tag{9}$$

$$C_{comp} = c_{dem} P_{dem} \tag{10}$$

Where, the objective function f is composed of two parts in Eqs 9 and 10: the system's generation expenses and the compensation expenses for user load shedding, excluding expenses such as unit outages. a_i, b_i and c_i represent the generation cost factors within the power grid. P_{Gi} represents the active power outputted by the generator situated at node i. m denotes the quantity of generator nodes present within the power grid. C_{comp} represent the compensation expenses for user load shedding.

4.1.2 Equality constraints

The equality constraints primarily consist of the nodal power flow balance constraints in Eq. 11:

$$\begin{cases} P_{Gi} + P_{wt}^i + P_{pv}^i - P_{load}^i - P_{node}^i = 0 \\ Q_{Gi} + Q_{wt}^i + Q_{pv}^i - Q_{load}^i - Q_{node}^i = 0 \end{cases} \tag{11}$$

Where, Q_{Gi} represents the reactive power generated by the generator at node i. P_{node}^i and Q_{node}^i are the active and reactive power injection at node i, respectively. P_{lode}^i and Q_{lode}^i are the active power and reactive power flowing into node i, respectively.

4.1.3 Inequality constraints

$$\begin{cases} P_{Gi}^{\min} \le P_{Gi} \le P_{Gi}^{\max} \\ Q_{Gi}^{\min} \le Q_{Gi} \le Q_{Gi}^{\max} \\ U_i^{\min} \le U_i \le U_i^{\max} \\ P_{\text{nodei}}^{\min} \le P_{node}^i \le P_{nodei}^{\max} \\ Q_{\text{nodei}}^{\min} \le Q_{node}^i \le Q_{nodei}^{\max} \end{cases} \tag{12}$$

In Eq. 12, where, U_i denotes the voltage magnitude at node i. $P_{Gi}^{\max}$, $P_{Gi}^{\min}$, $Q_{Gi}^{\max}$ and $Q_{Gi}^{\min}$ represent the upper and lower limits of the active power output and the upper and lower limits of the reactive power output of the generator at node i, respectively. $U_i^{\max}$ and $U_i^{\min}$ represent the upper and lower limits of the voltage at node i, respectively. $P_{\text{nodei}}^{\max}$, $P_{\text{nodei}}^{\min}$, $Q_{\text{nodei}}^{\max}$ and $Q_{\text{nodei}}^{\min}$ represent the upper and lower limits of active power and the lower and upper limits of reactive power carried by node i, respectively (Li et al., 2023).

4.2 Solution of OPF model

The nonlinearity of the OPF model considering multiple uncertainties is primarily concentrated in the equality constraints of the nodal power balance equations and the line active power flow equations. This paper introduces a linearization approach for OPF calculations, incorporating uncertainties in wind and solar energy generation, along with demand-side response considerations, through simplified approximations of the node power balance equations.

The power inflow at node i is expressed as follows:

$$\begin{cases} P_{node}^i = \sum_{j=1}^{n} G_{ij} U_i U_j \cos\theta_{ij} + \sum_{j=1}^{n} B_{ij} U_i U_j \sin\theta_{ij} \\ Q_{node}^i = \sum_{j=1}^{n} G_{ij} U_i U_j \sin\theta_{ij} - \sum_{j=1}^{n} B_{ij} U_i U_j \cos\theta_{ij} \end{cases} \tag{13}$$

Where, G_{ij} and B_{ij} are respectively the real part and the imaginary part of the element in the ith row and jth column of the node admittance matrix. θ_{ij} is the voltage phase angle difference between node i and node j.

The node admittance matrix of a power system exhibits a unique structure, where the diagonal elements are the sums of the admittances of the non-diagonal elements as well as the shunt components connected to each node.

$$Y_{ij} = \begin{cases} -y_{ij} & i \ne j \\ y_{ii} + \sum_{k=1, k\ne i}^{n} y_{ik} & i = j \end{cases} \tag{14}$$

Where, Y_{ij} is the node admittance matrix element of line i-j. y_{ij} is the admittance of line i-j. y_{ii} is the self-admittance of node i. Based on this, Eq. 13 is reformulated.

$$\begin{aligned} P_{node}^i &= \sum_{j=1}^{n} G_{ij} U_i U_j \cos\theta_{ij} + \sum_{j=1}^{n} B_{ij} U_i U_j \sin\theta_{ij} \\ &= g_{ii} U_i^2 + \sum_{j=1, j\ne i}^{n} \left[g_{ij} U_i \left(U_i - U_j \cos\theta_{ij}\right) - b_{ij} U_i U_j \sin\theta_{ij} \right] \end{aligned} \tag{15}$$

Where, g_{ij} and b_{ij} are the conductance and susceptance of line i-j, respectively. An expression can be derived from mathematical approximation formulas as follows in Eq. 16:

$$\begin{aligned} U_i\left(U_i - U_j\cos\theta_{ij}\right) &\approx U_i\left(U_i - U_j\right) \\ &= (1 + \Delta U_i)\left(\Delta U_i - \Delta U_j\right) \approx \left(\Delta U_i - \Delta U_j\right) \\ &= \left[1 + \Delta U_i - \left(1 + \Delta U_j\right)\right] = U_i - U_j \end{aligned} \tag{16}$$

TABLE 1 Basic parameter table.

	Scenario 1	Scenario 2	Scenario 3	Scenario 4
c_{dem}($/kW·h)	0.04	0.06	0.09	0.12
Probability	0.216	0.175	0.308	0.301

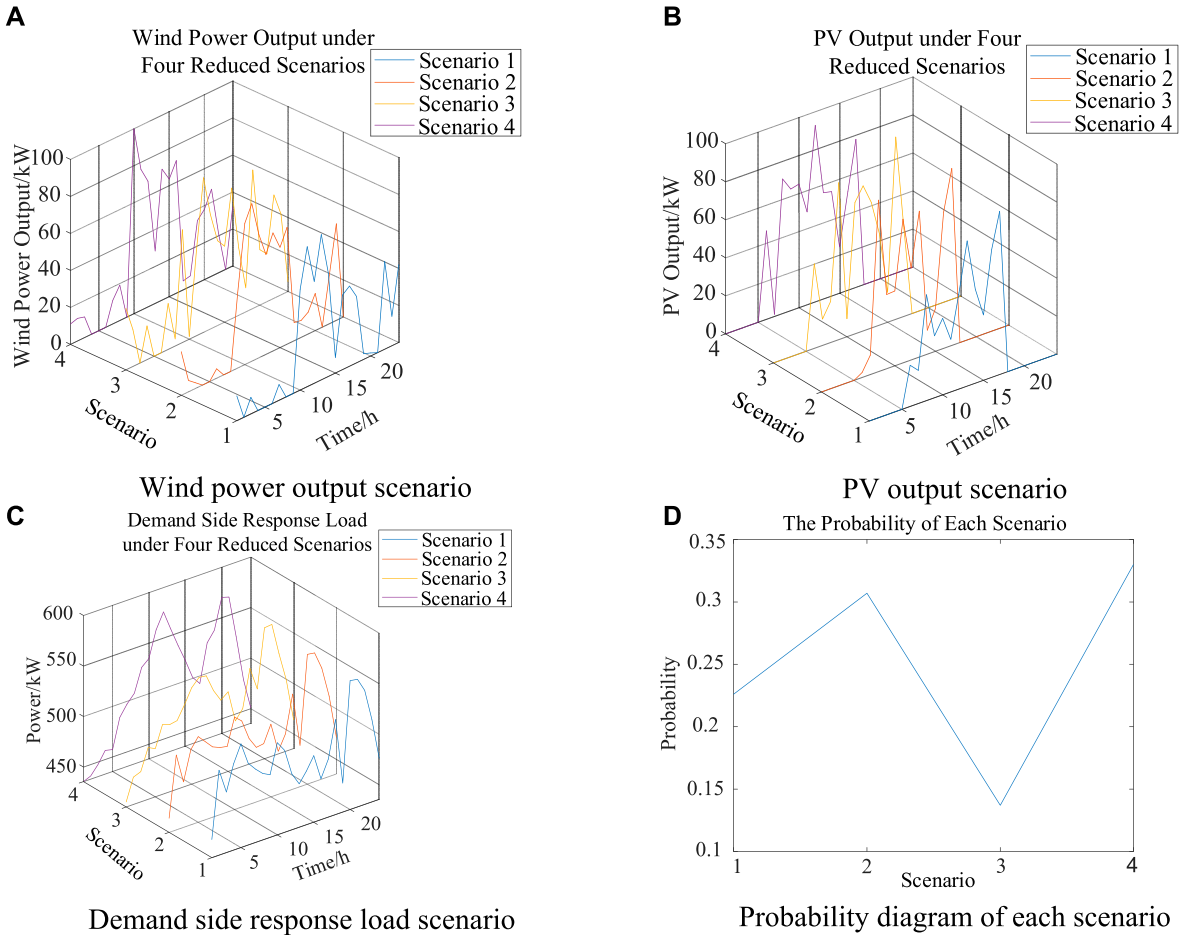

FIGURE 4
The four scenes reduced through K-means clustering.

Where, ΔU_i represents a small increment in the voltage magnitude at node i, with a value approximately equal to 0. In most power systems, the magnitude of node voltages is approximately 1.0 per unit (pu), while the absolute value of the phase angle difference between nodes at both ends of a line rarely exceeds 30°, with most of them falling within 10° or less. Based on this scenario, the expression can be approximated as follows:

$$\begin{cases} U_i, U_j \approx 1, \quad U_i^2 \approx U_i \\ \sin\theta_{ij} \approx \theta_{ij}, \quad \cos\theta_{ij} \approx 1 \end{cases} \tag{17}$$

Thus, Eq. 15 can be further deformed, and finally the injected active power of linearized node i, as follows in Eq. 18:

$$\begin{aligned} P_{node}^{i} &= g_{ii}U_i + \sum_{j=1,j\neq i}^{n} g_{ij}\left(U_i - U_j\right) - \sum_{j=1,j\neq i}^{n} b_{ij}\left(\theta_i - \theta_j\right) \\ &= \left[U_i\sum_{j=1}^{n} g_{ij} + \sum_{j=1,j\neq i}^{n}\left(-g_{ij}U_j\right)\right] - \left[\theta_i\sum_{j=1}^{n} b_{ij} + \sum_{j=1,j\neq i}^{n}\left(-b_{ij}\theta_j\right)\right] \\ &= \sum_{j=1}^{n} G_{ij}U_j - \sum_{j=1}^{n} B_{ij}^{'}\theta_j \end{aligned} \tag{18}$$

Where, $B_{ij}^{'}$ excluding the self-admittance of the node. Similarly, Eq. 13 can be simplified and transformed to obtain Eq. 19. The detailed transformation process is omitted here.

$$Q_{node}^{i} = -\sum_{j=1}^{n} B_{ij}U_j - \sum_{j=1}^{n} G_{ij}^{'}\theta_j \tag{19}$$

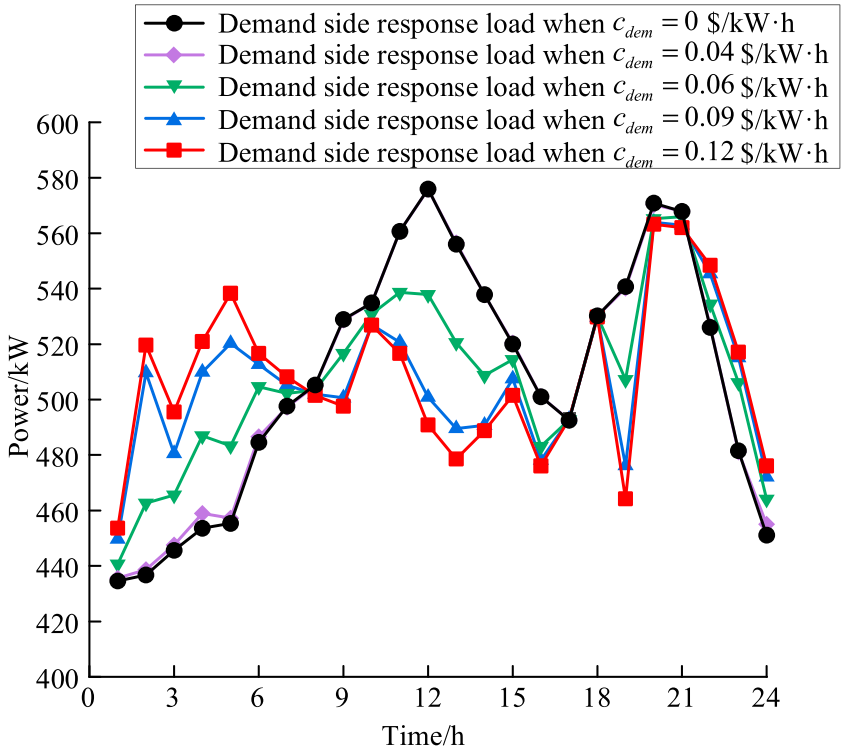

FIGURE 5
Schematic diagram of demand side response effect.

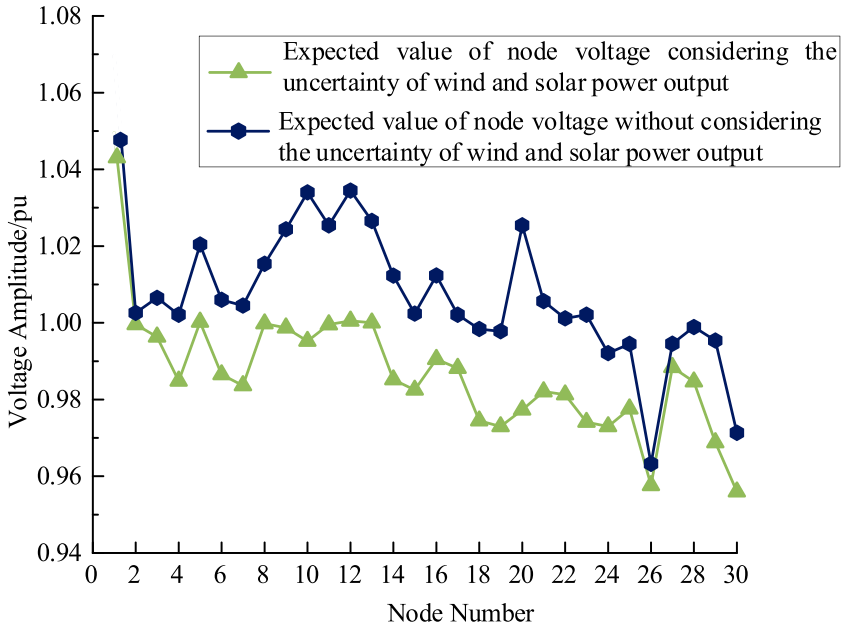

FIGURE 6
Schematic diagram of expected node voltage values.

TABLE 2 The results of each model in four cases.

Model	Optimal cost/$			
	Scenario 1	Scenario 2	Scenario 3	Scenario 4
Model A	62340.987	60867.414	61175.57	63266.206
Model B	60652.546	59160.675	60048.546	61796.699
Model C	67145.944	65956.654	66115.554	67984.578
Model D	59946.549	59076.592	59491.264	60683.198
Model E	61578.254	60076.592	61019.984	62683.199

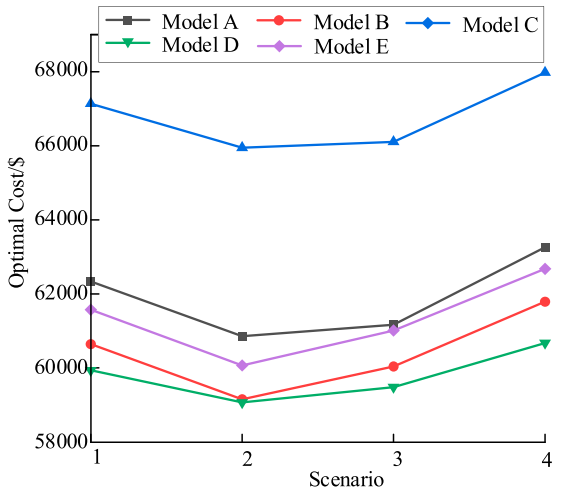

FIGURE 7
The optimal cost of each model in four scenarios.

Finally, based on the calculation formula and approximate simplification of line power flow, the active power flow of line *i-j* can be derived.

After linearizing the nodal power balance equations, the OPF described in Section 4.1 was established on the MATLAB platform using the YALMIP toolbox, and solved by the commercial solver GUROBI.

5 Case study

5.1 Basis data

To validate the efficacy of the model introduced in this paper, a test was conducted on the IEEE 30-bus system. Detailed parameters for each generating unit, node, and transmission line can be found in the software package provided by MATPOWER 4.1. Two wind farms and two PV plants were integrated into the test system. The wind farms adopted constant power factor control, with an assumed power factor of 1 for all wind farms. For ease of description, the AC OPF model that accounts for the uncertainties in wind and PV power output, coupled with demand-side response, is defined as Model A. The DC OPF model considering the same uncertainties is Model B. Model C is a linear OPF model that only considers the uncertainty of wind and PV power, while Model D focuses on the uncertainty of demand-side response. The proposed linear OPF model in this paper, which considers both wind and PV uncertainties as well as demand-side response uncertainties, is designated as Model E.

The K-means clustering method is used to reduce the generated wind power, PV and demand-side response load scenarios (Wen et al., 2023), and finally the compensated electricity price c_{dem} is 0.04 $/kW·h, 0.06 $/kW·h, 0.09 $/kW·h and 0.12 $/kW·h, respectively, as shown in Table 1 and Figure 4.

To facilitate observation and analysis, the results obtained from solving Model A are used as the benchmark and denoted as ρ_0. The specific expressions for the relative errors of the computational results from each model are detailed as follows in Eq. 20:

$$\Delta\rho = \frac{|\rho - \rho_0|}{\rho_0} \times 100\% \tag{20}$$

5.2 Case analysis

Demand-side response enables load shifting based on real-time electricity prices, avoiding usage during peak hours when electricity prices are high. This helps reduce electricity costs for users, improves economy, and serves to flatten the peak and fill the trough, thereby enhancing system stability.

By means of incorporating demand-side response and refining load curves, the resilience of the grid against uncertainties associated with renewable energy generation can be enhanced. The shifting effect of demand-side response on the load under different incentive levels is shown in Figure 5. It can be observed that as the compensation electricity price increases, the expected response quantity of users also increases, enabling a better optimization of the load curve.

As can be seen from Figure 6, the expected voltage value of the system considering the uncertainty of wind and solar power output decreases significantly. This is because the integration of wind and PV power generation can meet the active power demand of nearby nodes, thereby altering the direction and magnitude of power flow in various branches. In addition, as the output of wind and PV power generation increases, their reactive power demand also increases correspondingly, resulting in a general reduction in the voltage levels at various nodes in the system.

TABLE 3 Calculation results of five models.

Model	Optimal cost/$			Relative error/%		
	Maximum value	Minimum value	Expected value	Maximum value	Minimum value	Expected value
Model A	63266.206	60867.414	61,021.492	-	-	-
Model B	61796.699	59160.675	59604.612	2.804	2.323	2.322
Model C	67984.587	65956.654	66036.104	-	-	-
Model D	60683.198	59076.592	59,283.928	-	-	-
Model E	62683.199	60076.592	60,548.288	1.299	0.922	0.775

Table 2 and Figure 7 present the computational results of the five models under various scenarios in the test system.

As can be seen from Figure 7, a higher compensation electricity price is not necessarily better. When the compensation electricity price is between 0.09 $/kW·h and 0.12 $/kW·h, the system's scheduling cost gradually increases. Considering both the economy and uncertainty of the system scheduling cost, there exists an optimal compensation electricity price range of 0.06 $/kW·h to 0.09 $/kW·h that can result in relatively low system scheduling costs. Therefore, the average of the system dispatch costs when the compensation prices are set at 0.06 $/kW·h and 0.09 $/kW·h is taken as the expected system scheduling cost for the operator.

From Table 3, it can be observed that all five models are able to obtain optimal solutions under different scenarios, indicating that each model is feasible and effective. In various scenarios, the relative errors of Model B are all greater than 2%, with the maximum relative error approaching 3%. In contrast, the relative errors of Model E are all around 1%, representing an improvement in computational accuracy of approximately 57% compared to Model B. Therefore, the linear OPF calculation method proposed in this paper exhibits stronger applicability and can be effectively applied to online safety calculation and analysis of power systems with renewable energy sources.

Since Model C only considers the uncertainty of wind and PV outputs, its optimal cost is significantly higher than the other models. Although Model D has the lowest optimal cost, it only takes into account the uncertainty of demand-side response, which may lead to voltage and power violations, causing greater losses to the system and lacking economic feasibility. Model E has a significantly lower optimal cost than Model C, effectively reducing system operating costs. Although it is slightly higher than Model D, Model E can fully guarantee the stability and security of the system's functioning. Hence, the linear OPF model put forth in this paper, which considers the uncertainties of wind, PV and demand-side response, exhibits good economic performance while balancing system operational safety.

6 Conclusion

The OPF computation method put forth in this paper takes into account the uncertainties of wind and PV output, analyzes the uncertainty and volatility of the power system's operating state, and avoids situations where some lines of the power system are overloaded or the voltage at some nodes exceeds the limit, thereby enhancing the safety of system operation. Meanwhile, through the introduction of demand-side response, the load curve has been optimized. This significantly boosts the system's capacity to handle intermittency and unpredictability in power generation from renewable sources, further elevating the system's safety level. Additionally, it decreases the required system configuration capacity, ultimately leading to increased cost-effectiveness in the power system. The proposed method also linearizes the power flow calculations that consider multiple uncertainties, significantly reducing the computational burden and improving the calculation accuracy. This approach is more aligned with the demands of real-time safety calculation and analysis in power systems, exhibiting strong applicability and holding significant importance for online calculation and analysis of actual power systems containing uncertainty factors.

Data availability statement

The raw data supporting the conclusions of this article will be made available by the authors, without undue reservation.

Author contributions

WZ: Conceptualization, Investigation, Methodology, Software, Writing–original draft, Writing–review and editing. ZP: Conceptualization, Data curation, Formal Analysis, Methodology, Writing–review and editing. QW: Data curation, Formal Analysis, Methodology, Project administration, Validation, Writing–review and editing. WQ: Data curation, Methodology, Supervision, Writing–review and editing. YG: Formal Analysis, Funding acquisition, Project administration, Resources, Supervision, Writing–review and editing.

Funding

The author(s) declare that financial support was received for the research, authorship, and/or publication of this article. This work is supported by State Grid Jiangsu Electric Power Co. Ltd Economic Research Institute (SGJSJY00GHJS2310012).

Conflict of interest

Authors WZ, ZP, QW, WQ, and YG were employed by State Grid Jiangsu Electric Power Co. Ltd. Economic Research Institute.

The authors declare that this study received funding from State Grid Jiangsu Electric Power Co. Ltd Economic Research Institute. The funder had the following involvement in the study: inspiring the study design, providing basic data collection and practical engineering scenario description.

Publisher's note

References

Chen, G., Dong, Y., and Liang, Z. (2020). Analysis and reflection on high-quality development of new energy with Chinese characteristics in energy transition. *Proc. CSEE* 40 (17), 5493–5506.

Guo, X., Gong, R., and Bao, H. (2018). Mixed probabilistic and interval optimal power flow considering uncertain wind power and dispatchable load. *IEEJ Trans. Electr. Electron. Eng.* 13 (2), 246–252. doi:10.1002/tee.22520

Li, B., Wan, C., Li, Y., Jiang, Y., and Yu, P. (2023). Generalized linear-constrained optimal power flow for distribution networks. *IET Generation, Transm. Distribution* 17 (6), 1298–1309. doi:10.1049/gtd2.12735

Li, H., Li, H., Lu, W., Wang, Z., and Bian, J. (2020). Optimal power flow calculation considering large-scale photovoltaic generation correlation. *Front. Energy Res.* 8, 590418. doi:10.3389/fenrg.2020.590418

Li, X., Cao, J., and Du, D. (2015). Probabilistic optimal power flow for power systems considering wind uncertainty and load correlation. *Neurocomputing* 148, 240–247. doi:10.1016/j.neucom.2013.09.066

Liao, X., Xu, Y., and Wei, Z. Probabilistic power flow analysis of integrated electricity-heat energy system based on GMM and multi-point linear cumulant method Electric Power Automation Equipment, 2019, 39(08): 55–62.

Lin, Li, and Zhang, Yu (2020). *Uncertainty analysis of incentive demand response participating in optimal scheduling of active distribution network*. Jilin: Journal of North China Electric Power University 47 (5), 10–20.

Liu, Z., Wei, Z., and Gao, S. (2019). Adaptive-linearized probabilistic power flow calculation for power grid integrated with high proportion wind power in source-load interactive environment. *Power Syst. Technol.* 43 (11), 3926–3937.

Morshed, M. J., Hmida, J. B., and Fekih, A. (2018). A probabilistic multi-objective approach for power flow optimization in hybrid wind-PV-PEV systems. *Appl. Energy* 211, 1136–1149. doi:10.1016/j.apenergy.2017.11.101

Pourbehzadi, M., Niknam, T., Aghaei, J., Mokryani, G., Shafie-khah, M., and Catalão, J. P. (2019). Optimal operation of hybrid AC/DC microgrids under uncertainty of renewable energy resources: a comprehensive review. *Int. J. Electr. Power and Energy Syst.* 109, 139–159. doi:10.1016/j.ijepes.2019.01.025

Sun, Y., Wang, Y., and Wang, B. (2018). Multi-time scale decision method for source-load interaction considering demand response uncertainty. *Automation Electr. Power Syst.* 42 (02), 106–113+159.

Wen, Y., Luo, Y., Dong, X., and Xie, X. (2023). Thermal and electrical demand response based on robust optimization. *Electr. Power Syst. Res.* 225, 109883. doi:10.1016/j.epsr.2023.109883

Xie, P., Cai, Z., and Liu, P. (2019). Cooperative optimization of energy storage capacity for renewable and storage involved microgrids considering multi time scale uncertainty coupling influence. *Proc. CSEE* 39 (24), 7126–7136.

Xin, B., Shan, B., and Li, Q. (2022). Rethinking of the "three elements of energy" toward carbon peak and carbon neutrality. *Proc. CSEE* 42 (09), 3117–3126.

Yan, Y., Su, H., and Che, Y. (2018). Probabilistic power flow calculation of power system considering wind power based on improved LHS. *Acta Energiae Solaris Sin.* 39 (04), 1111–1118.

Yang, Y., Wang, Y., Gao, Y., and Gao, C. (2022). Peak shaving analysis of power demand response with dual uncertainty of unit and demand-side resources under carbon neutral target. *Energies* 15 (13), 4588. doi:10.3390/en15134588

Yang, Z., Zhong, H., Xia, Q., and Kang, C. (2018). Fundamental review of the OPF problem: challenges, solutions, and state-of-the-art algorithms. *J. Energy Eng.* 144 (1), 04017075. doi:10.1061/(asce)ey.1943-7897.0000510

Zhao, B., Wang, X., and Zhang, X. (2018). Two-layer method of microgrid optimal sizing considering demand-side response and uncertainties. *Trans. CHINA Electrotech. Soc.* 33 (14), 3284–3295.

Zhao, L., Zeng, Y., Li, Y., Peng, D., and Wang, Y. (2023). Coordinated planning of power systems under uncertain characteristics based on the multilinear Monte Carlo method. *Energies* 16 (23), 7761. doi:10.3390/en16237761

Zhao, S., Wu, Y., and Li, Z. (2022). Analysis of power system peaking capacity and economy considering the uncertainty of wind and solar output. *Power Syst. Technol.* 46 (5), 1752–1761.

frontiers | Frontiers in Energy Research

TYPE Original Research
PUBLISHED 18 July 2024
DOI 10.3389/fenrg.2024.1429664

OPEN ACCESS

EDITED BY
Yitong Shang,
Hong Kong University of Science and Technology, Hong Kong SAR, China

REVIEWED BY
Qianhao Sun,
Beijing Jiaotong University, China
Yongning Zhao,
China Agricultural University, China
Srinvasa Rao Gampa,
Seshadri Rao Gudlavalleru Engineering College, India

*CORRESPONDENCE
Jing Li,
jing20180806@163.com

RECEIVED 08 May 2024
ACCEPTED 24 June 2024
PUBLISHED 18 July 2024

CITATION
Li J, Gao X, Guo D, Xia J, Jia Z and Wang Y (2024), Low-carbon optimization operation of integrated energy system considering comprehensive demand response under improved carbon trading mechanism. *Front. Energy Res.* 12:1429664. doi: 10.3389/fenrg.2024.1429664

Low-carbon optimization operation of integrated energy system considering comprehensive demand response under improved carbon trading mechanism

Jing Li*, Xiying Gao, Dan Guo, Jingyi Xia, Zhuting Jia and Yue Wang

Elect Intens Control Department State Grid Liaoning Mkt, Shenyang, Liaoning, China

The integrated energy system considering comprehensive demand response can realize cascade utilization of energy and reduce carbon emissions. However, few studies explore the operation of Integrated energy system considering the coupling markets of electricity and carbon trading. Based on the characteristics and specific needs of the integrated energy system, this paper establishes the mathematical model of each energy supply equipment, and studies the optimal energy supply method of the system. First, demand response is categorized into price and substitution types based on load response characteristics. Second, the price demand response models are established utilizing the price elasticity matrix, and substitution demand response models are developed considering the mutual conversion of electric and heat energy on the user-side. Subsequently, a baseline method is employed to allocate carbon emission quotas to the system without charge with considering the actual carbon emissions from gas turbines and gas boilers. This results in the formulation of an improved carbon trading mechanism tailored for integrated energy system. Finally, a low-carbon optimization operational model for integrated energy system is constructed with the multi-objective functions. The results of numerical case studies are presented to validate the performance of the proposed control method.

KEYWORDS

improved carbon trading mechanism, demand response, integrated energy system, baseline method, carbon emission quotas

1 Introduction

Integrated energy system (IES) has garnered increased attention as a highly efficient method for the comprehensive utilization of various energy systems, encompassing electricity, heat, and natural gas (Zhou et al., 2019). Various IES communities worldwide have exemplified the practical implementation of combined heat and power (CHP) as well as power-heat-gas systems to optimize the utilization of energy resources more effectively (Fang et al., 2018).

The carbon trading mechanism optimizes the allocation of system resources and promotes energy conservation and emissions reduction (Li et al., 2018). In Saboori and Hemmati (2016), initial carbon emission rights are distributed free of charge based on the actual output of nuclear power units, heat power units, and wind power (WP) units. The calculation of carbon trading costs takes into account the actual carbon emissions of heat power units, and economic and low-carbon benefits are balanced. In Yang et al. (2019), a carbon trading mechanism is integrated into a virtual power plant. By employing the baseline methodology and considering the output of renewable energy units, initial carbon quotas are allocated freely as carbon sources. This approach enhances the overall absorption capacity for renewable energy. Demand Response (DR) is a method enabling flexible modulation of the demand side load of IES, thereby enhancing the effectiveness of communication between the supply and demand sides. Stemming from the actual demands on the user-side, DR can facilitate the flexible adjustments on the user-side, thus coordinating the economic operation of IES. In Ceseña and Mancarella (2019), a price elasticity matrix is introduced to describe DR behavior, and the effectiveness of DR in alleviating peak load pressure on the system is analyzed. In Clegg and Mancarella (2016), a DR model for electricity and gas loads is developed using the price elasticity matrix method. Additionally, a heat load DR model is formulated and validated, taking into account the fuzzy perception and time-delay characteristics of heat loads. This model aims to enhance energy utilization efficiency. In Li et al. (2017), the modeling approach for traditional DR to electric loads was applied to heat and cooling loads, achieving integrated scheduling and operation of multiple loads, including electric, heat, and cooling.

The existing literature either exclusively analyzes carbon trading mechanisms or solely considers demand response, which is detrimental to the coordination of system low-carbon characteristics and economic efficiency (Shang and Li, 2024). In the context of IES, the introduction of carbon trading mechanisms can transform carbon emission rights into economically valuable and dispatchable resources. The consideration of DR has the potential to exploit demand-side flexibility (Khani and Farag, 2018), thereby achieving a system-wide low-carbon economic operation. In Chen et al. (2018), a comparative analysis is conducted on the overall operational costs and curtailed wind and solar power generation for systems under different electric and heat load comfort levels. The study ensures user comfort while realizing the synergistic integration of multiple energy sources, reducing operational costs, and enhancing the integration of new energy sources. However, the DR for electric loads is only modeled for interruptible and shiftable loads, simplifying the modeling process. In Fang et al. (2018), the price transmission mechanisms of both the electricity market and the carbon trading market are incorporated to convert renewable energy generation, such as wind and solar, into emission reductions. The study proposes a comprehensive demand-side response solution for multi-energy systems, which includes the operation of combined cooling, heating, and power units, as well as energy storage control strategies. This approach achieves economically efficient operation of multi-energy systems, although a detailed model for the load side is not constructed (Li et al., 2018). It is worth noting that the aforementioned studies, while providing valuable insights, overlook the consideration of improved carbon trading mechanism associated with DR. Therefore, a comprehensive analysis incorporating environmental implications is warranted.

This paper proposes an optimized operation model for an improved carbon trading mechanism considering comprehensive DR in an IES. First, consider the combined influence of a ladder carbon trading mechanism, CHP units, and the operational scenarios of DR on IES. Second, an optimization scheduling scheme is formulated with the objective of minimizing the sum of energy procurement cost, carbon trading cost, and operation and maintenance cost. Finally, the scheme is subsequently solved using CPLEX, and multiple optimized scheduling scenarios are compared and analyzed to validate the economic and low-carbon characteristics of the model. This provides a reference for the low-carbon economic operation of IES. The contributions of this paper can be summarized as follows:

- The load is transferred from high electricity price periods to low electricity price periods, realizing mutual substitution of user-side electric energy and heat energy, and smoothing the load curve.
- A low-carbon optimization model of the IES that takes into account DR under the improved carbon trading mechanism is proposed based on the impact of the carbon trading mechanism to the IES.
- Based on the low-carbon optimization model of the comprehensive energy system considering DR under the improved carbon trading mechanism, the operating cost of the system is reduced.

2 IES framework

2.1 IES architecture

The IES achieves complementary synergy between electric and heat energy, enhancing energy utilization efficiency while ensuring a sustained and reliable power supply for diverse user demands in a cascaded energy utilization manner (Saboori and Hemmati, 2018). This paper establishes an IES architecture incorporating DR, as illustrated in Figure 1. Electric energy and gas energy are supplied by the upper-level electric grid, photovoltaic energy (PV), and the gas network. The acquired gas from the upper-level gas network is utilized for the supply of CHP and gas boiler (GB), with surplus electric energy available for sale to the higher-level electric grid. Energy coupling devices include CHP, heat pump (HP), and GB, enabling bidirectional flow of electric and heat energy (Li et al., 2020). The CHP comprises a gas turbine (GT), waste heat boiler (WHB), and a low-temperature waste heat power (WHP) generation unit based on the Organic Rankine Cycle (ORC) (Cheng et al., 2019). The operational mode is characterized by heat-electric decoupling, providing adaptability to various system operating conditions. The HP (mainly ground source heat pumps) and GB assimilate renewable energy and bear a portion of the heat load. The introduction of DR serves to mitigate load curve fluctuations, facilitating interactive coupling of electric and heat energy, peak shaving, and cost reduction in operation.

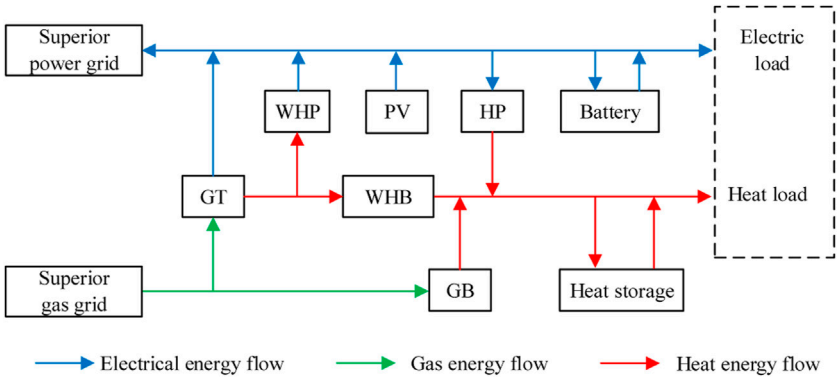

FIGURE 1
IES structure.

2.2 *B. DR Model*

User-side participation in grid interaction involves changing their energy usage patterns based on current electricity prices and relevant incentive mechanisms, thereby achieving peak shaving and valley filling in the load curve and improving the operational efficiency of the IES (Shang et al., 2022). Based on the response characteristics of the load, it can be divided into basic load, curtailable load (CL), shiftable load (SL), and replaceable load (RL) (Wang et al., 2020). The basic load belongs to uncontrollable load and does not participate in DR.

2.2.1 Analysis and modeling of CL characteristics

The primary function of CL operates during periods of high energy demand, aiming to influence user energy consumption patterns through price factors. That is, users voluntarily decide whether to reduce their energy consumption at that specific moment by comparing electricity prices before and after DR. The DR characteristics of CL are represented by Eq. 1.

$$A_{CL} = \begin{bmatrix} a_{1,1} & a_{1,2} & \cdots & a_{1,k} \\ a_{2,1} & e_{2,2} & \cdots & a_{2,k} \\ \vdots & \vdots & \vdots & \vdots \\ a_{k,1} & a_{k,2} & \cdots & a_{n,k} \end{bmatrix} \tag{1}$$

CL determines its load curtailment based on the comparison of electricity price variations before and after DR. In this paper, k is set to 24. The elements of the elasticity matrix $A_{\mathrm{CL}}(i, j)$, where the element in the ith row and jth column represents the elasticity coefficient of the load at time i to the electricity price at time j, is represented by Eq. 2.

$$a_{i,j} = \frac{\Delta Q_i / Q_i^0}{\Delta p_j / p_j^0} \tag{2}$$

where ΔQ_i represents the variation in load at time i subsequent to DR, Q_i^0 represents the initial load at time i, Δp_j represents the change in electricity price at time j following DR, and p_j^0 represents the initial electricity price at time j. The CL variation at time i following DR, represented as $\Delta Q_{\mathrm{CL},i}$, is represented by Eq. 3.

$$\Delta Q_{\mathrm{CL},i} = Q_{\mathrm{CL},i}^0 \left[\sum_{j=1}^{k} A_{\mathrm{CL}}(i, j) \frac{p_j - p_j^0}{p_j^0} \right] \tag{3}$$

where $Q_{\mathrm{CL},i}^0$ represents the initial CL at time i, $A_{\mathrm{CL}}(i, j)$ represents the matrix of price demand elasticity for CL, characterized as a diagonal matrix, and p_j represents the electricity price at time j.

2.2.2 Analysis and modeling of SL characteristics

The concept of SL refers to users responding to electricity prices based on their individual demands, enabling flexible adjustments to workload during working hours (Liotta et al., 2016). Utilizing peak-valley time-of-use electricity prices as signals, users can be guided to shift their peak-load demand to off-peak periods. Employing a price demand elasticity matrix to describe DR characteristics, the change in transferable load at time i after DR, represented as $\Delta Q_{\mathrm{SL},i}$, is represented by Eq. 4.

$$\Delta Q_{\mathrm{SL},i} = Q_{\mathrm{SL},i}^0 \left[\sum_{j=1}^{k} A_{\mathrm{SL}}(i, j) \frac{p_j - p_j^0}{p_j^0} \right] \tag{4}$$

where $Q_{\mathrm{SL},i}^0$ represents the initial SL quantity at time i, and $A_{\mathrm{SL}}(i, j)$ represents the matrix of price demand elasticity for SL.

2.2.3 Analysis and modeling of RL characteristics

The concept of RL refers to heat loads directly supplied with heat or electric energy. During periods of low electricity prices, electric energy can be consumed, while during periods of high electricity prices, heat energy can be directly utilized to fulfill its own demands, thereby achieving mutual substitution of electric and heat energy (Correa-Posada and Sanchez-Martin, 2015). This paper focuses on replaceable heat loads. In the operational process of IES, the energy consumption characteristics of users are subject to uncertainties arising from user preferences and energy costs. To accurately assess the replaceability of heat loads, this paper comprehensively considers user demand preferences and energy consumption costs, and establishes a model for RL. The RL model characteristics are represented by Eq. 5.

$$\begin{cases} \Delta Q^{e}_{RL,i} = -\theta_{e,h}\Delta Q^{h}_{RL,i} \\ \theta_{e,h} = \dfrac{\alpha_e \beta_e}{\alpha_h \beta_h} \end{cases} \tag{5}$$

where $\Delta Q^{e}_{RL,i}$ and $\Delta Q^{h}_{RL,i}$ represent the substitutable electric load and the corresponding replaced heat load, $\theta_{e,h}$ represents the electric-heat substitution coefficient, α_e and α_h represent the unit calorific values of electric energy and heat energy, β_e and β_h represent the energy utilization efficiencies of electric energy and heat energy. In (4), the negative sign represents that the reduction in substitutable electric load corresponds to an increase in the replaced heat load. For this category of loads, it is imperative to consider constraints on the maximum RL, are represented by Eq. 6.

$$\begin{cases} \Delta Q^{RL,e}_{min} \leqslant \Delta Q^{RL,e}_{i} \leqslant \Delta Q^{RL,e}_{max} \\ \Delta Q^{RL,h}_{min} \leqslant \Delta Q^{RL,h}_{i} \leqslant \Delta Q^{RL,h}_{max} \end{cases} \tag{6}$$

where $\Delta Q^{RL,e}_{min}$ and $\Delta Q^{RL,e}_{max}$ represent the minimum and maximum replaceable electric load, $\Delta Q^{RL,h}_{min}$ and $\Delta Q^{RL,h}_{max}$ represent the minimum and maximum replaceable heat load.

2.3 Carbon trading model

The ladder carbon trading mechanism model is divided into three parts: the initial carbon emission quota model, the actual carbon emission model, and the ladder carbon trading cost calculation model.

2.3.1 Carbon emission quota model

In this IES, carbon emission sources include GT, GB, upper-level power purchases, and DR on the demand side. The initial carbon emission quota model is represented by Eq. 7.

$$\begin{cases} Q_{IES} = Q_{GT} + Q_{GB} + Q_{buy} + Q_{gas} \\ Q_{GT} = \varepsilon_g \sum_{t=1}^{T} \left(P_{GT,e}(t) + P_{GT,h}(t)\right) \\ Q_{GB} = \varepsilon_g \sum_{t=1}^{T} P_{GB,h}(t) \\ Q_{buy} = \varepsilon_e \sum_{t=1}^{T} P_{buy}(t) \\ Q_{gas} = \varepsilon_g \sum_{t=1}^{T} P_{gas}(t) \end{cases} \tag{7}$$

where Q_{IES}, Q_{GT}, Q_{GB}, Q_{buy} and Q_{gas} represent the gratuitous carbon emission quotas for the comprehensive energy system, gas turbine, gas boiler, electricity purchased from the upper level, and gas load on the demand side, σ_e and σ_h represent the gratuitous carbon emission quotas obtained per unit of electricity and heat generated, ε_g and ε_e represent the carbon emission quotas per unit of heat for GT or GB and per unit of electricity purchased from the upper grid, $P_{GT,e}$ and $P_{GT,h}$ represent the supply of electric power and heat power from the GT during time period t, $P_{GB,h}$ represents the supply of heat power from the GB during time period t, P_{buy} represents the power purchased from the upper level by the system during time period t, P_{gas} represents the consumption of gas load on the demand side during time period t, T represents the scheduling period.

2.3.2 Actual carbon emission model

The estimation of actual carbon emissions Q^{*}_{IES} in the system requires a comprehensive consideration of externally purchased electricity, CHP, the operation status of GB equipment, and the gas load on the demand side. The actual carbon emission model is represented by Eq. 8 (Zhou et al., 2018).

$$\begin{cases} Q^{*}_{IES} = Q^{*}_{GT} + Q^{*}_{GB} + Q^{*}_{buy} + Q^{*}_{gas} \\ Q^{*}_{GT} = \alpha_g \sum_{t=1}^{T} \left(P_{GT,e}(t) + P_{GT,h}(t)\right) \\ Q^{*}_{GB} = \alpha_g \sum_{t=1}^{T} P_{GB,h}(t) \\ Q^{*}_{buy} = \alpha_e \sum_{t=1}^{T} P_{buy}(t) \\ Q^{*}_{gas} = \alpha_g \sum_{t=1}^{T} P_{gas}(t) \end{cases} \tag{8}$$

where Q^{*}_{IES} represents the actual total carbon emissions of IES, Q^{*}_{GT}, Q^{*}_{GB}, Q^{*}_{buy} and Q^{*}_{gas} represent the actual carbon emissions of gas turbines, gas boilers, electricity purchased from upper grid systems, and demand side gas load, α_e represents the carbon emission coefficient for electricity purchased from higher-level systems, α_g represents the carbon emission coefficient during the operation of CHP and GB.

2.3.3 Ladder carbon trading cost calculation model

The carbon emission trading volume that IES can participate in is the carbon emission trading amount Q, the difference between the actual carbon emissions and the carbon emission quota is represented by Eq. 9.

$$Q = Q^{*}_{IES} - Q_{IES} \tag{9}$$

The ladder carbon trading mechanism initially establishes the length of carbon emission intervals, wherein the greater the carbon emissions generated by IES, the higher the corresponding carbon emission quota price within the respective interval. Therefore, the cost of ladder carbon trading, denoted as C_{CO_2}, is represented by Eq. 10.

$$C_{CO_2} = \begin{cases} \mu Q & Q \leq m \\ \mu(1+\delta)(Q-m) + \mu m & m \leq Q \leq 2m \\ \mu(1+2\delta)(Q-2m) + \mu(2+\delta)m & 2m \leq Q \leq 3m \\ \mu(1+3\delta)(Q-3m) + \mu(3+3\delta)m & 3m \leq Q \leq 4m \\ \mu(1+4\delta)(Q-4m) + \mu(4+6\delta)m & 4m \leq Q \end{cases} \tag{10}$$

where μ represents the carbon trading base price, δ represents the price escalation rate, and m represents the length of the carbon emission interval.

3 IES optimization operation model

3.1 Objective function

This paper adopts the total operating cost C of IES as the objective function, which comprises energy purchase cost C_{buy}, carbon trading cost C_{CO_2}, and equipment maintenance cost C_{eq}, is represented by Eq. 11.

$$C_{min} = \left(C_{buy} + C_{CO_2} + C_{eq}\right) \tag{11}$$

1) Energy purchase cost is represented by Eq. 12.

The system can conduct electricity transactions with the upper-level power grid (Shao et al., 2017). When the power generation cannot meet its own needs, it purchases power from the upper-level power grid. Correspondingly, when the power generation is surplus, the excess power is sold to the upper-level power grid. In addition, the system needs to purchase natural gas to maintain the operation of CHP and GB. The energy purchase cost is obtained by (12).

$$C_{buy} = \sum_{t=1}^{T}\left(\alpha_t P_{buy}^{e}(t) - \beta_t P_{sell}^{e}(t) + \gamma_t Q_{buy}^{g}(t)\right) \tag{12}$$

where T $P_{buy}^{e}(t)$, $P_{sell}^{e}(t)$ and $Q_{buy}^{g}(t)$ represent the purchased electricity quantity, sold electricity quantity, and purchased gas quantity during time period t, α_t, β_t and γ_t represent the purchase electricity price, selling electricity price, and gas price during time period t.

2) Carbon trading cost is represented by Eq. 10.

3) Equipment maintenance cost is represented by Eq. 13.

$$C_{eq} = \sum_{t=1}^{T}\sum_{i=1}^{N}\omega_i P_{i,t} \tag{13}$$

where N represents the total number of maintenance equipment, ω_i represents the operation and maintenance coefficient of equipment i, $P_{i,t}$ represents the output of equipment i.

3.2 Constraints

The IES optimization operation constraints that consider DR under the carbon trading mechanism include: energy balance constraints, CHP constraints, and user electricity usage satisfaction constraints.

1) PV output constraint is represented by Eq. 14.

Considering the influence of ambient temperature, solar radiation intensity, and the limitation of energy conversion efficiency, the system is often unable to absorb all the PV, and the actual PV output is less than the predicted output.

$$0 \leqslant P_{\mathrm{PV},t} \leqslant P_{\mathrm{PV},t}^{\max} \tag{14}$$

where $P_{\mathrm{PV},t}$ and $P_{\mathrm{PV},t}^{\max}$ represent the actual PV output and predicted output at time t.

2) GB constraints are represented by Eq. 15.

$$\begin{cases} P_{GB,t}^{h} = \rho_{GB} P_{GB,t}^{\mathrm{g}} \\ P_{GB,\min}^{g} \leq P_{GB,t}^{\mathrm{g}} \leq P_{GB,\max}^{g} \end{cases} \tag{15}$$

where ρ_{GB} represents the power conversion rate of GB to heat energy, $P_{GB,t}^{\mathrm{g}}$ represents the power of natural gas input to GB at time t, $P_{GB,\max}^{g}$ and $P_{GB,\min}^{g}$ represent the upper and lower limits of the input power to GB.

3) CHP constraints are represented by Eq. 16.

The electricity generation in CHP comprises two components: GT electricity generation and ORC electricity generation. The heat generation in CHP corresponds to the heat generation in the WHB.

$$\begin{cases} P_{\mathrm{CHP},t}^{\mathrm{e}} = P_{\mathrm{GT},t}^{\mathrm{e}} + P_{\mathrm{ORC},t}^{\mathrm{e}} \\ P_{\mathrm{GT},t}^{\mathrm{e}} = Q_{\mathrm{CHP},t}^{\mathrm{g}}\, \tau_{\mathrm{GT}}^{\mathrm{e}}\, V_{\mathrm{g}} \\ P_{\mathrm{ORC,t}}^{\mathrm{e}} = P_{\mathrm{GT,t}}^{\mathrm{h}} \alpha_t \delta_{\mathrm{ORC}} \\ P_{\mathrm{CHP},t}^{\mathrm{h}} = P_{\mathrm{GT},t}^{\mathrm{h}} \beta_t \tau_{\mathrm{WHB}} \\ \alpha_t + \beta_t = 1\ ;\ 0 \leqslant \alpha_t, \beta_t \leqslant 1 \end{cases} \tag{16}$$

where $P_{\mathrm{ORC},t}^{\mathrm{e}}$ represents the electric power generated by the low-temperature waste heat recovery device, β_t represents the proportion of waste heat generated by the GT at time t allocated to the WHB for heat production, τ_{WHB} represents the heat conversion efficiency of the WHB, $\tau_{\mathrm{GT}}^{\mathrm{e}}$ and $\tau_{\mathrm{GT}}^{\mathrm{h}}$ represent the gas-to-electricity and gas-to-heat efficiency of the GT, V_{g} represents the calorific value of natural gas, α_t represents the proportion of waste heat generated by the GT at time t allocated to the waste heat power generation device, δ_{ORC} represents the electric generation efficiency of the waste heat power generation device.

4) Electric power balance constraint is represented by Eq. 17.

$$P_{\mathrm{buy},t}^{\mathrm{e}} + P_{\mathrm{PV},t}^{\mathrm{e}} + P_{\mathrm{CHP},t}^{\mathrm{e}} + P_{\mathrm{ES},t}^{\mathrm{e,out}} = P_{\mathrm{L},t}^{\mathrm{e0}} + P_{sell}^{e} + P_{\mathrm{HP},t}^{\mathrm{e}} + P_{\mathrm{ES},t}^{\mathrm{e,in}} + \Delta Q_i^{\mathrm{RL,e}} \tag{17}$$

where $P_{\mathrm{ES},t}^{\mathrm{e,out}}$ and $P_{\mathrm{ES},t}^{\mathrm{e,in}}$ represent the discharging and charging power of the battery at time t, $P_{\mathrm{L},t}^{\mathrm{e0}}$ represents the electric load up to time t before DR, $P_{\mathrm{HP},t}^{\mathrm{e}}$ represents the power consumption of the HP at time t.

5) Heat power balance constraint is represented by Eq. 18.

$$P_{\mathrm{GB},t}^{\mathrm{h}} + P_{\mathrm{CHP},t}^{\mathrm{h}} + P_{\mathrm{HP},t}^{\mathrm{h}} + P_{\mathrm{HS},t}^{\mathrm{h,out}} = P_{\mathrm{HS},t}^{\mathrm{h,in}} + P_{\mathrm{L},t}^{\mathrm{h0}} + \Delta Q_i^{\mathrm{RL,h}} \tag{18}$$

where $P_{\mathrm{CHP},t}^{\mathrm{h}}$ represents the heat power generation of the CHP system at time t, $P_{\mathrm{HP},t}^{\mathrm{h}}$ represents the heat power generation of the HP system at time t, $P_{\mathrm{HS},t}^{\mathrm{h,dis}}$ and $P_{\mathrm{HS},t}^{\mathrm{h,ch}}$ represent the heat release and heat power stored in the heat storage tank at time t, $P_{\mathrm{L},t}^{\mathrm{h0}}$ represents the heat load at time t prior to DR.

6) Gas power balance constraint is represented by Eq. 19.

$$Q_{buy}^{g} = Q_{\mathrm{CHP},t}^{\mathrm{g}} + Q_{\mathrm{GB},t}^{\mathrm{g}} \tag{19}$$

where $Q_{\mathrm{GB},t}^{\mathrm{g}}$ represents the gas consumption of GB at time t.

7) User electricity usage satisfaction constraints are represented by Eq. 20.

Consider the constraints on user satisfaction with electricity usage (Good and Mancarella, 2019):

$$\begin{cases} I_{\min} \leqslant I \leqslant 1 \\ I = 1 - \dfrac{\sum_{t=1}^{T}\left|P_{\mathrm{L},t}^{\mathrm{e0}} + \Delta Q_{\mathrm{CL},i} + \Delta Q_{\mathrm{SL},i} + \Delta Q_i^{\mathrm{RL,e}}\right|}{\sum_{t=1}^{T} P_{\mathrm{L},t}^{\mathrm{e0}}} \end{cases} \tag{20}$$

where I and $I_{\min}$ represent the user's satisfaction with electricity usage and the minimum value of satisfaction.

3.3 Solution method

This paper addresses a mixed-integer linear programming problem. Firstly, an analysis is conducted on the demand response of both price and substitution components, resulting in the derivation of the load curve post-demand response. Subsequently, a carbon trading mechanism is introduced, with the carbon trading cost under this mechanism incorporated as a constituent of the objective function. Finally, considering constraints such as energy balance, CHP, and user satisfaction with electricity consumption, the problem is formulated and

TABLE 1 Parameters of devices.

Devices	Parameter	Values
GT	Installation capacity (kW)	4000
	Electric efficiency	0.3
	Heat efficiency	0.4
GB	Installation capacity (kW)	1000
	Efficiency	0.9
WHB	Efficiency	0.8
HP	Installation capacity (kW)	400
	Efficiency	4.4
WHP	Installation capacity (kW)	400
	Efficiency	0.8
	Resection coefficient	0.15
Heat storage	Maximum capacity (kW·h)	400
	Initial capacity (kW·h)	50
	Charging heat efficiency	0.95
	Heat release efficiency	0.9
	Maximum power (kW)	250
Battery	Maximum capacity (kW·h)	400
	Initial capacity (kW·h)	80
	Charging electricity efficiency	0.95
	Electricity release efficiency	0.9
	Maximum power (kW·h)	250

TABLE 2 Time-of-use price.

Periods type	Periods	Electricity price [$ (kW·h)]
Peak	09:00-12:00	0.15
	19:00-22:00	
Normal	08:00-09:00	0.095
	12:00-19:00	
	22:00-24:00	
Valley	00:00-08:00	0.049

solved utilizing the CPLEX solver invoked on the MATLAB platform.

4 Case analysis

Taking an industrial park in winter in Liaoning Province, China as the research object, 24 h is taken as an operation cycle, and the unit operation time is 1 h. The installed equipment in the system includes CHP, HP, and GB composed of GT, WHB and ORC-based low-temperature waste heat power generation (Fang et al., 2018). The parameters are shown in Table 1, the time-of-use electricity price are shown in Table 2.

To verify the rationality of the proposed model, this article conducts a comparative analysis of the following four cases.

Case 1: Only consider the carbon trading mechanism.

Case 2: Consider DR under the carbon trading mechanism.

Case 3: Only consider DR.

Case 4: Carbon trading mechanism is not considered and DR is not considered.

The optimization results of electric power output for each unit in case 1 are depicted in Figure 2, while the optimization results for heat power output are illustrated in Figure 3. Figure 2 indicates that during the periods (0:00-9:00) and (19:00-24:00), CHP contributes a substantial amount of electricity. In the interval (9:00-16:00), PV contributes significantly, and during (12:00-15:00), the electricity sales volume of the IES increases due to a higher output from CHP and PV. Consequently, the electric energy supplied by WHP is relatively low during the aforementioned time periods, with an increase in WHP output during (19:00-23:00) when CHP and PV outputs are reduced. Figure 3 demonstrates that during the periods (0:00-11:00) and (19:00-24:00), CHP provides a substantial amount of heat power. In the interval (9:00-17:00), owing to the higher output of CHP and PV, GB dominates in providing heat power, serving as a means to absorb excess CHP and PV.

Taking into account CHP, PV output, economic costs, and carbon emissions, the output and costs of each unit are comprehensively considered in Case 2. The optimization results of electric and heat power outputs for each unit during the scheduling period are depicted in Figure 4 and Figure 5. During low-price periods (00:00–08:00), the system relies on CHP, WHP output, and purchased electricity from the higher-level grid to meet the demands of HP, HS charging, and electric loads, maintaining power balance during this period. The heat load is supplied by HP, GB, and HS, achieving heat power balance. ES charges during low-price periods and discharges during high-price periods, while HS operates inversely, enhancing system flexibility. Prioritizing CHP output helps reduce overall operational costs. In Cases where CHP output alone cannot meet the system's electric load demands and electricity prices are low, the cost of purchasing electricity from the higher-level grid is lower than the cost of purchasing gas from the higher-level gas grid. In cases where HP cannot fully meet the heat load demands, and WHP is inactive during this period, GB is employed for heating during flat electricity price periods (08:00-09:00, 12:00-19:00, 22:00-24:00). During these periods, the system relies on CHP, PV, and WHP output to meet HP and electric load demands, with the heat load supplied by HP and WHP. The electricity prices are relatively higher during these periods, with the cost of purchasing electricity from the higher-level grid exceeding the cost of purchasing gas from the higher-level gas grid. In high-price periods (09:00-12:00, 19:00-22:00), the system relies on CHP, WHP output, and HS discharge to meet HP and electric load demands, with HP and GB supplying the heat load and HS providing heat storage. During these periods, the electricity prices are relatively higher, and purchasing gas from the higher-level gas grid is cheaper than purchasing electricity from the higher-level grid.

Figure 6 indicates that during the periods of (0:00-8:00) and (19:00-24:00), the IES electric load is primarily supplied by GT, with a

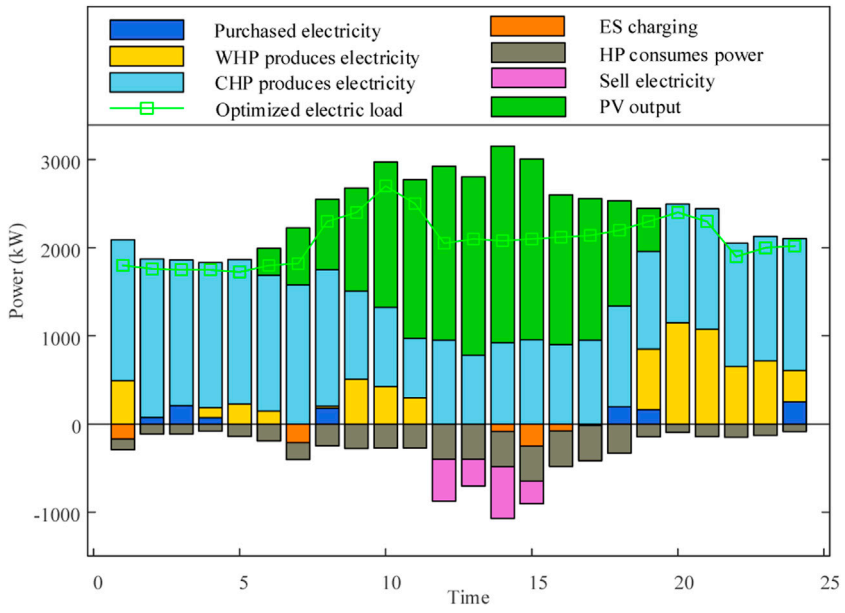

FIGURE 2
Electric power output in Case 1.

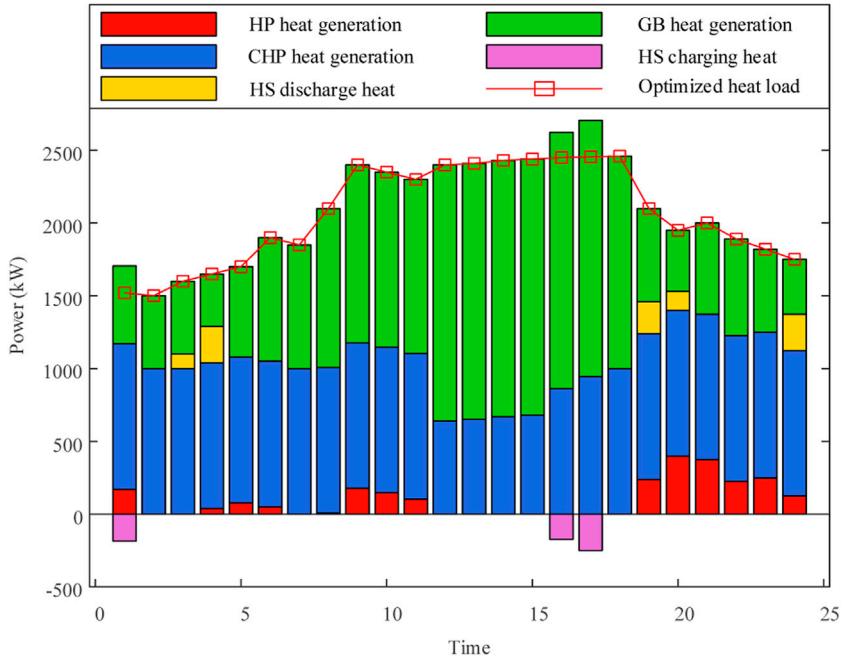

FIGURE 3
Heat power output in Case 1.

lower output from WHP. During the period of (9:00-17:00), the system's electric load is mainly supported by PV and WP, with no contribution from CHP. During the period of (12:00-15:00), due to the higher output of PV generation, there is surplus system electricity generation, leading to an increase in electricity sales. During the period of (19:00-23:00), when PV generation is inactive, CHP electricity output increases to meet the system's power demand. Figure 7 illustrates that during the periods of (0:00-10:00) and (18:00-24:00), the GB and HP provide a higher heat power, with lower heat power output from CHP. During the period of (11:00-17:00), due to the higher PV output, there is an abundance of system electricity generation during this period, resulting in a predominant role of HP in producing heat power to absorb excessive PV power.

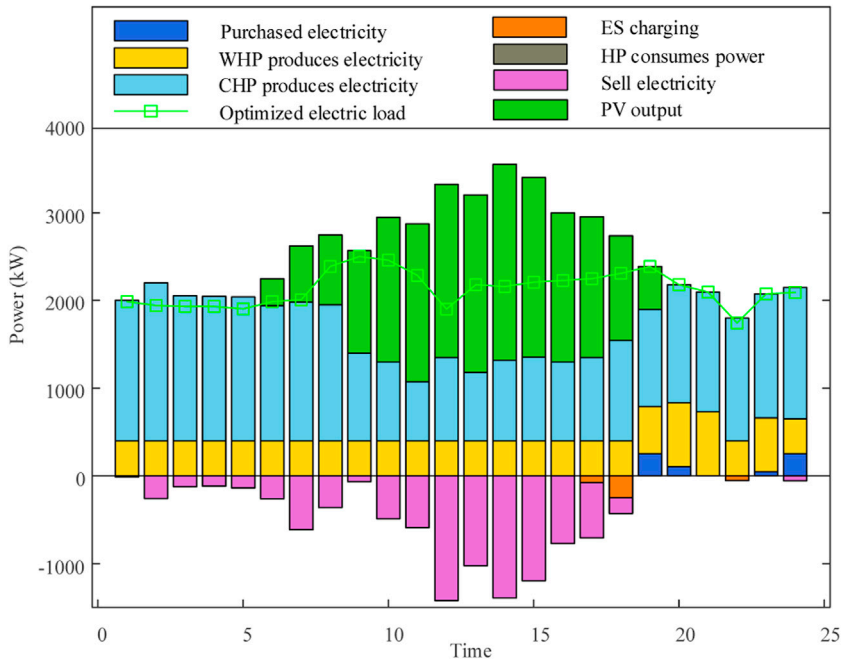

FIGURE 4
Electric power output in Case 2.

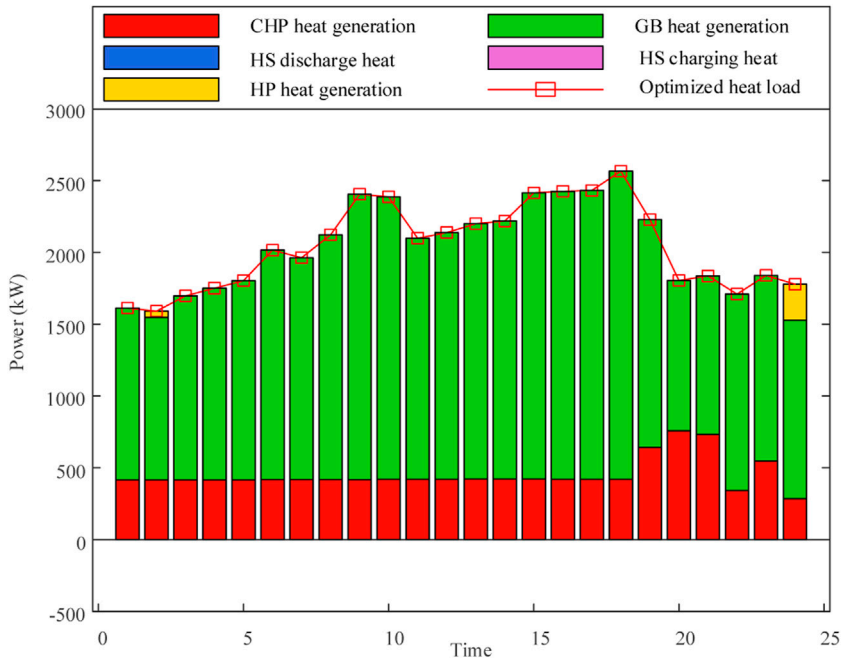

FIGURE 5
Heat power output in Case 2.

In Case 4, without considering the carbon trading mechanism and DR, depicts the electric and heat outputs of various devices as illustrated in Figure 8 and Figure 9. Figure 8 indicates that, during the period (0:00-5:00), the electric load of the IES is predominantly supplied by CHP, with limited output from ES, necessitating the procurement of electricity from the higher-level grid. In the period (8:00-18:00), the system's electric load is primarily supported by PV and CHP, with minimal output from CHP. During the period (19:00-24:00), when PV generation is inactive, CHP electric output increases

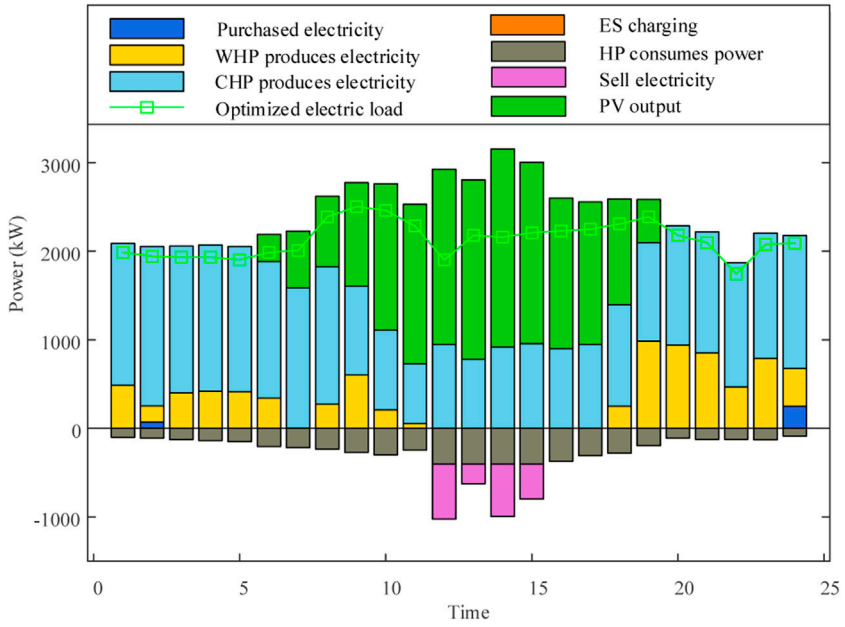

FIGURE 6
Electric power output in Case 3.

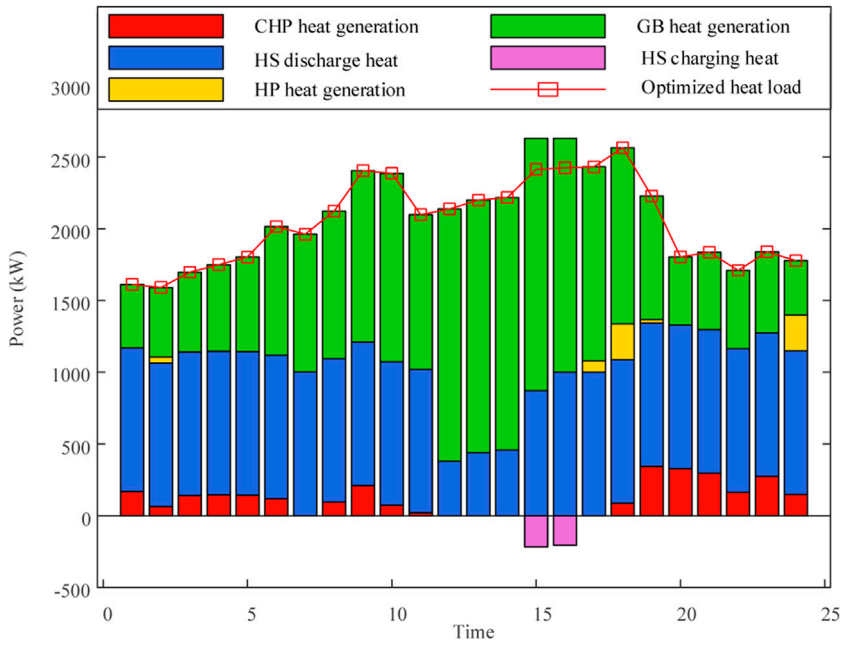

FIGURE 7
Heat power output in Case 3.

significantly to meet the system's power demand, leading to a notable increase in purchased electricity. Figure 9 illustrates that, during the period (2:00-11:00), GB and HS contribute a substantial amount of heat power, while CHP heat power output is relatively low. In the period (12:00-17:00), the system's heat power is mainly borne by GB and HS, with HS contributing the majority of the heat production.

The costs and actual carbon emissions of each scenario are shown in Table 3. Compared with Case 4, the carbon emission cost of Case 1 has decreased by 77.89%, with an actual reduction in carbon emissions of 4877.08 kg. This outcome is attributed to the consideration of a carbon emission mechanism in Case 1, which endows the system with initial carbon emission quotas, thereby offsetting a portion of the carbon emission costs. In contrast, Case

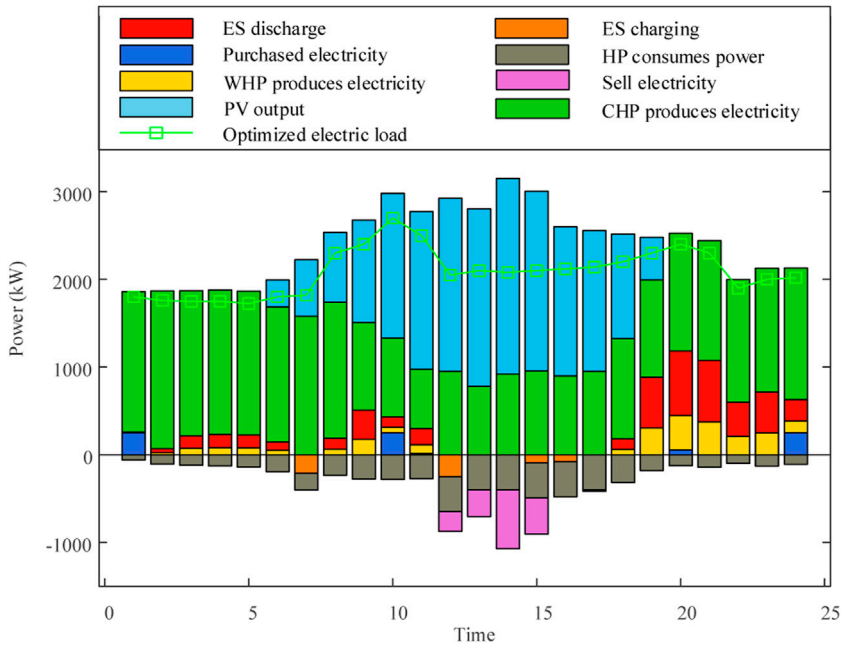

FIGURE 8
Electric power output in Case 4.

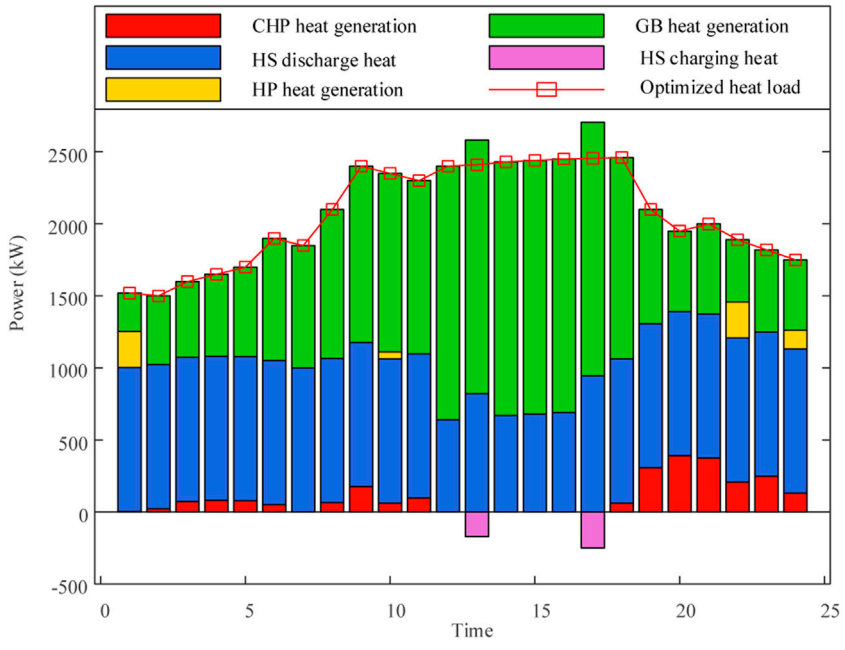

FIGURE 9
Heat power output in Case 4.

4 necessitates the consideration of the total cost associated with the actual carbon emissions. In comparison to Case 4, the energy procurement cost in Case 3 has decreased by 10.25%. This reduction is attributed to the incorporation of DR, which reduces peak electricity demand while increasing off-peak electricity demand. Consequently, the system can opt for a more economical energy procurement method. Compared with Cases 1 and 2, Case three exhibits higher total operational costs, lower energy procurement costs, and higher carbon trading costs and actual carbon emissions. This observation underscores the promotive role of carbon trading mechanisms in energy conservation and emission reduction. Case 2 demonstrates lower total operational costs, energy procurement costs, carbon trading costs, operational maintenance costs, and actual carbon emissions than Case 1. This outcome is attributed to

TABLE 3 Daily operation cost in 4 cases.

Cases	Total operating Costs ($)	Energy purchase Costs ($)	Carbon trading Costs ($)	Maintenance Costs ($)	Actual carbon emissions (kg)
1	2,304.60	1,833.08	62.12	419.39	25,301.89
2	2,266.06	1,800.75	59.97	415.35	24,225.94
3	2,542.22	1,731.22	390.74	420.26	28,037.56
4	2,596.59	1,929.11	281.02	386.46	30,178.97

the consideration of DR under the carbon trading mechanism, which not only shifts a portion of the load from high electricity price periods to low electricity price periods but also reduces energy consumption during certain load conditions. Furthermore, the mechanism facilitates the mutual substitution of electric and heat energy on the consumer side, smoothing the load curve. Consequently, the system, by comparing the costs of purchasing electricity and gas at different time periods and the outputs of GT and GB, selects an economically and environmentally favorable operational mode. This approach effectively coordinates the economic efficiency and low-carbon nature of the system's operation.

5 Conclusion

This study establishes an optimized operational model considering DR under the carbon trading mechanism for integrated energy systems. The impact of carbon trading prices on system operation is investigated with set four cases. The conclusions are as follows.

1) Under the carbon trading mechanism, considering DR not only shifts a portion of the load from high electricity price periods to low electricity price periods and reduces load energy consumption but also achieves the mutual substitution of electric and heat energy on the user side, smoothing the load curve.
2) Considering that the ladder carbon trading mechanism system with an initial carbon emission allowance, the operating cost of the system is reduced.

Data availability statement

The data analyzed in this study is subject to the following licenses/restrictions: To confidentiality requirements, the dataset will not be made public. Requests to access these datasets should be directed to JL, jing20180806@163.com.

Author contributions

JL: Writing–original draft, Conceptualization. XG: Writing–review and editing, Data curation. DG: Writing–review and editing, Investigation. JX: Writing–review and editing, Project administration. ZJ: Writing–review and editing, Resources. YW: Writing–review and editing, Supervision.

Funding

The author(s) declare that financial support was received for the research, authorship, and/or publication of this article. This work was supported by Science and Technology Project of State Grid Liaoning Electric Power Supply Co., Ltd. (SGLNYX00DFJS2310107). The funder was not involved in the study design, collection, analysis, interpretation of data, the writing of this article, or the decision to submit it for publication.

Conflict of interest

The authors declare that this study received funding from State Grid Liaoning Electric Power Supply Co., Ltd.. The funder was not involved in the study design, collection, analysis, interpretation of data, the writing of this article, or the decision to submit it for publication.

Publisher's note

References

Ceseña, E., and Mancarella, P. (2019). Energy systems integration in smart districts: robust optimisation of multi-energy flows in integrated electricity, heat and gas networks. *IEEE Trans. Smart Grid* 10 (1), 1122–1131. doi:10.1109/tsg.2018.2828146

Chen, X., Lv, J., McElroy, M. B., Han, X., Nielsen, C. P., and Wen, J. (2018). Power system capacity expansion under higher penetration of renewables considering flexibility constraints and low carbon policies. *IEEE Trans. Power Syst.* 33 (6), 6240–6253. doi:10.1109/tpwrs.2018.2827003

Cheng, Y., Zhang, N., Wang, Y., Yang, J., Kang, C., and Xia, Q. (2019). Modeling carbon emission flow in multiple energy systems. *IEEE Trans. Smart Grid* 10 (4), 3562–3574. doi:10.1109/tsg.2018.2830775

Clegg, S., and Mancarella, P. (2016). Integrated electrical and gas network flexibility assessment in low-carbon multi-energy systems. *IEEE Trans. Sustain. Energy* 7 (2), 718–731. doi:10.1109/tste.2015.2497329

Correa-Posada, C. M., and Sanchez-Martin, P. (2015). Integrated power and natural gas model for energy adequacy in short-term operation. *IEEE Trans. Power Syst.* 30 (6), 3347–3355. doi:10.1109/tpwrs.2014.2372013

Fang, J., Zeng, Q., Ai, X., Chen, Z., and Wen, J. (2018). Dynamic optimal energy flow in the integrated natural gas and electrical power systems. *IEEE Trans. Sustain. Energy* 9 (1), 188–198. doi:10.1109/tste.2017.2717600

Good, N., and Mancarella, P. (2019). Flexibility in multi-energy communities with electrical and thermal storage: a stochastic, robust approach for multi-service demand response. *IEEE Trans. Smart Grid* 10 (1), 503–513. doi:10.1109/tsg.2017.2745559

Khani, H., and Farag, H. E. Z. (2018). Optimal day-ahead scheduling of power to-gas energy storage and gas load management in wholesale electricity and gas markets. *IEEE Trans. Sustain. Energy* 9 (2), 940–951. doi:10.1109/tste.2017.2767064

Li, F., Qin, J., and Kang, Y. (2020). Closed-loop hierarchical operation for optimal unit commitment and dispatch in microgrids: a hybrid system approach. *IEEE Trans. Power Syst.* 35 (1), 516–526. doi:10.1109/tpwrs.2019.2931293

Li, G., Zhang, R., Jiang, T., Chen, H., Bai, L., and Li, X. (2017). Security-constrained bi-level economic dispatch model for integrated natural gas and electricity systems considering wind power and power-to-gas process. *Appl. Energy* 194, 696–704. doi:10.1016/j.apenergy.2016.07.077

Li, Y., Liu, M., Wen, W., Wen, F., Wang, K., and Huang, Y. (2018). Optimal operation strategy for integrated natural gas generating unit and power-to-gas conversion facilities. *IEEE Trans. Sustain. Energy* 9 (4), 1870–1879. doi:10.1109/tste.2018.2818133

Liotta, G., Kaihara, T., and Stecca, G. (2016). Optimization and simulation of collaborative networks for sustainable production and transportation. *IEEE Trans. Ind. Inf.* 12 (1), 417–424. doi:10.1109/tii.2014.2369351

Saboori, H., and Hemmati, R. (2016). Considering carbon capture and storage in electricity generation expansion planning. *IEEE Trans. Sustain. Energy* 7 (4), 1371–1378. doi:10.1109/tste.2016.2547911

Saboori, H., and Hemmati, R. (2018). Considering carbon capture and storage in electricity generation expansion planning. *IEEE Trans. Sustain. Energy* 7 (4), 1371–1378. doi:10.1109/tste.2016.2547911

Shang, Y., and Li, S. (2024). FedPT-V2G: security enhanced federated transformer learning for real-time V2G dispatch with non-IID data. *Appl. Energy* 358, 122626. doi:10.1016/j.apenergy.2024.122626

Shang, Y., Yu, H., Shao, Z., and Jian, L. (2022). Achieving efficient and adaptable dispatching for vehicle-to-grid using distributed edge computing and attention-based LSTM. *IEEE Trans. Ind. Inf.* 18 (10), 6915–6926. doi:10.1109/tii.2021.3139361

Shao, C., Wang, X., Shahidehpour, M., Wang, X., and Wang, B. (2017). An MILP-based optimal power flow in multicarrier energy systems. *IEEE Trans. Sustain. Energy* 8 (1), 239–248. doi:10.1109/tste.2016.2595486

Wang, Y., Qiu, J., Tao, Y., and Zhao, J. (2020). Carbon-oriented operational planning in coupled electricity and emission trading markets. *IEEE Trans. Power Syst.* 35 (4), 3145–3157. doi:10.1109/tpwrs.2020.2966663

Yang, J., Zhang, N., Yao, H., Kang, C., and Xia, Q. (2019). Modeling the operation mechanism of combined P2G and gas-fired plant with CO_2 recycling. *IEEE Trans. Smart Grid* 10 (1), 1111–1121. doi:10.1109/tsg.2018.2849619

Zhou, B., Xu, D., Cao, Y., Chan, K. W., Xu, Y., et al. (2018). Multiobjective generation portfolio of hybrid energy generating station for mobile emergency power supplies. *IEEE Trans. Smart Grid* 9 (6), 5786–5797. doi:10.1109/tsg.2017.2696982

Zhou, Y., Wei, H., Yong, M., and Dai, Y. (2019). Integrated power and heat dispatch considering available reserve of combined heat and power units. *IEEE Trans. Sustain. Energy* 10 (3), 1300–1310. doi:10.1109/tste.2018.2865562

Nomenclature

IES	Integrated Energy System
WP	Wind Power
DR	Demand Response
GT	Gas Turbine
GB	Gas Boiler
CL	Curtailable Load
RL	Replaceable Load
CHP	Combined Heat and Power
HP	Heat Pump
PV	Photovoltaics
ORC	Organic Rankine Cycle
WHP	Waste Heat Power
HS	Heat Storage
SL	Shiftable Load

frontiers | Frontiers in Energy Research

TYPE Original Research
PUBLISHED 18 July 2024
DOI 10.3389/fenrg.2024.1384760

OPEN ACCESS

EDITED BY
Yitong Shang,
Hong Kong University of Science and Technology, Hong Kong SAR, China

REVIEWED BY
Shuai Yao,
Cardiff University, United Kingdom
Zixuan Wang,
North China Electric Power University, China
Xu Xu,
Xi'an Jiaotong-Liverpool University, China
Chunyu Chen,
China University of Mining and Technology, China
Zhengmao Li,
Aalto University, Finland

*CORRESPONDENCE
Peiyun Feng,
pyfeng@ycit.edu.cn

RECEIVED 10 February 2024
ACCEPTED 20 June 2024
PUBLISHED 18 July 2024

CITATION
Feng P, Chen C and Wang L (2024), Coordinated energy storage and network expansion planning considering the trustworthiness of demand-side response. *Front. Energy Res.* 12:1384760. doi: 10.3389/fenrg.2024.1384760

Coordinated energy storage and network expansion planning considering the trustworthiness of demand-side response

Peiyun Feng[1,2]*, Chong Chen[1] and Lin Wang[1]

[1]Department of Electrical Engineering, Yancheng Institute of Technology, Yancheng, China, [2]Department of Automation, Hangzhou Dianzi University, Hangzhou, China

The enhancement of economic sustainability and the reduction of greenhouse gas (GHG) emissions are becoming more relevant in power system planning. Thus, renewable energy sources (RESs) have been widely used as clean energy for their lower generation costs and environmentally friendly characteristics. However, the strong random uncertainties from both the demand and generation sides make planning an economic, reliable, and ecological power system more complicated. Thus, this paper considers a variety of resources and technologies and presents a coordinated planning model including energy storage systems (ESSs) and grid network expansion, considering the trustworthiness of demand-side response (DR). First, the size of a single ESS was considered as its size has a close effect on maintenance costs and ultimately affects the total operating cost of the system. Second, it evaluates the influence of the trustworthiness of DR. Third, multiple resources and technologies were included in this high-penetration renewable energy integrated power system, such as ESSs, networks, DR technology, and GHG reduction technology. Finally, this model optimizes the decision variables such as the single size and location of ESSs and the operation parameters such as thermal generation costs, loss load costs, renewable energy curtailment costs, and GHG emission costs. Since the problem scale is very large not only due to the presence of various devices but also both binary and continuous variables considered simultaneously, we reformulate this model by decomposition. Then, we transform it into a master problem (MP) and a dual sub-problem (SP). Finally, the proposed method is applied to a modified IEEE 24-bus test system. The results show computational effectiveness and provide a helpful method in planning low-carbon electricity power systems.

KEYWORDS

generation and network expansion planning, energy storage systems, demand-side response, greenhouse gas emissions, trustworthiness

1 Introduction

The fuels used to power conventional power plants cause unsustainable and environmentally unfriendly impacts, especially during peak load-carrying hours and critical weather conditions. Therefore, the global common goal is to mitigate dependence on fossil fuels and reduce greenhouse gas (GHG) emissions. Renewable energy sources (RESs) (wind and photovoltaic power are the leading alternatives) have become the main focus of many recent energy policies (Paris agreement, 2015; Summary for

policymakers, 2021). According to the Energy Roadmap 2050 (European Commission and Energy Roadmap, 2050, 2011), the European Commission is moving toward a low GHG emission economic entity. Under this blueprint, the de-carbonization target will be possible with an even higher RES penetration level (Zappa et al., 2019). However, higher RES penetration faces greater volatility, resulting in the power grids having more fragile, less flexible, and low reliable characteristics. Then, under the circumstance of multiple resources and technologies, how to get a more flexible, reliable, environmentally friendly, and cost-efficient power system has gained increasing attention (Al-Shetwi, 2022). This paper presents a coordinated planning model for a high-penetration renewable energy integrated power system including energy storage systems (ESSs) and network expansion, considering the trustworthiness of DR).

To cope with fundamental challenges, a vast range of literature focuses on DR and its effects on the optimal performance of power grids. Qi et al. (2021) proposed a smart energy hub in which an analytical framework containing several DR programs is adopted. Results show that DR has a positive impact on long-term resource planning. Mansouri et al. (2022) showed a two-stage stochastic model based on DR and integrated DR programs. Many uncertainties are included in this model, such as electrical, heating, cooling loads, and the wind turbine's output power. According to Aghajani et al. (2017), with the consideration of suitable DR, the uncertainties caused by wind and photovoltaic power can be handled appropriately. Thus, optimal operation optimization to decrease costs and minimize GHG emissions has been presented. In a word, appropriate DR in a smart grid helps resist volatility. However, the trustworthiness of DR has a deep internal influence on power system planning, which is seldom included and needs to be further studied in the future.

Previous studies (Liu et al., 2018; Zhang et al., 2020; Jafari et al., 2022; Liu et al., 2022) focused on optimally utilizing novel resources or technologies to respond to any uncertain variation (it usually comes from RESs, demand, and equipment failures). It is well known that installing ESSs may enhance power system flexibility by providing higher ramp rates or ramp ranges for power grids. Therefore, fast-response ESSs are considered promising resources. Li Z. et al. (2021) applied a bilayer model with heterogeneous ESSs to alleviate the adverse effects of diverse uncertainties and obtain the economic multi-energy building microgrid operation. Ramos-Real et al. (2018) followed another approach to obtain a promising alternative from an economic and environmental perspective through a high deployment of RESs and ESSs in the Canary Islands. Shi et al. (2022) proposed a hierarchical optimization planning model, with its objective function including the cost of ESSs and renewable energy. To minimize the system's total expected cost, voltage deviation, and power loss mitigation, ALAhmad (2023) proposed a novel probabilistic optimization model by optimally placing and sizing ESSs to alleviate the negative impact of the high penetration of RESs and enhance grid stability.

Based on the above literature, the flexibility and reliability that ESSs brought to the system were expounded. However, how to effectively incorporate these ESSs into the power grids still needs to be investigated. Li et al. (2023) proposed a bi-level optimization model to minimize net load fluctuation, voltage deviation, and total costs by determining the optimal location, power rating, capacity, and hourly charging/discharging profile in a multiple-ESS-containing system. Jiang et al. (2020) simultaneously considered the location, capacity, and power rating of ESSs. The optimal deployment of ESSs provided benefits such as power curtailment reduction, power loss mitigation, and arbitrage profit maximization. Li J. et al. (2021) proposed a bi-level optimization problem that was decomposed by the decomposition–coordination algorithm into two sub-systems. The model determines the optimal location, power rating, and capacity of ESSs to maximize the system's net profit and minimize the system's total operation cost. Li Z. et al. (2020) presented a risk-averse method for heterogeneous ESS deployment in a residential multi-energy microgrid where a multistage adaptive stochastic optimization approach is utilized to deal with various uncertainties. However, these existing research studies have not fully addressed the single size, location, and degradation of ESSs simultaneously, all of which have a true existence in practical applications. Moreover, because of the geographical and labor management issues, the size of a single ESS will closely affect its maintenance costs and ultimately affect the total operating cost of the system. Thus, the optimal single size, location, and operation of ESSs to enhance system flexibility and reduce GHG emissions in power grids is an important ongoing research area that is worthy of further study.

Although there have been many researchers working on investigating the influence of multiple resources and technologies in photovoltaic or wind-integrated power systems, the need for comprehensive research considering not only ESSs and DR but also further CO_2 reduction still remains. Many carbon financing policies (e.g., carbon emission tax and building committed carbon emission operation regions) have been proven to be exceedingly effective methods to encourage participators toward emission reduction. For instance, carbon emission tax is utilized in Olsen et al. (2018) for achieving emission targets in the electricity market. Jiang et al. (2024) proposed the committed carbon emission operation region to characterize the low-carbon feasible space. Results show that it can achieve integrated energy system decarbonization. Hu et al. (2024) presented a bi-level carbon-oriented planning method containing shared ESSs for integrated energy systems. Simulation results show that it is more environmentally friendly and economical compared to the model without shared ESSs. Cheng et al. (2019) proposed a bi-level multi-energy system planning model, in which carbon emission flow was included. These decentralized approaches are employed to calculate the emission amount but fail to involve active DR simultaneously.

According to all the above, countries all around the world are pursuing a low-carbon power system to achieve sustainable development. Achieving this requires the coordination of a variety of electricity technologies. First, the vast emergence of RESs provides alternative generations, while traditional coal-fired generations are being phased out. However, high RES penetration causes huge challenges in the stability of voltage, frequency, and the balance between supply and demand. Second, various forms of ESSs, including electrochemical ESSs, are regarded as important sources that cut the peaks and fill the valleys to provide flexibility effectively. However, their size, location, and inherent degradation should be considered in the planning stage. Third, DR, as an active response on the demand side, helps resist system volatility. However, few researchers consider the trustworthiness of DR and reveal their deep internal impact on the system. Moreover, these latest

TABLE 1 Comparison between the proposed model of this work and previous studies.

Reference	ESS capacity	ESS degradation	Carbon emissions	Considering DR	Optimization target
Qi et al. (2021)	√	√	×	√	Energy hub
Mansouri et al. (2022)	√	×	×	√	Energy hub
Aghajani et al. (2017)	×	×	√	√	Microgrid
Li et al. (2021a)	√	√	×	√	Multi-energy building microgrid
Ramos-Real et al. (2018)	√	×	√	×	Canary Islands
Shi et al., 2022; ALAhmad (2023)	√	×	×	×	Power system
Li et al. (2023)	√	×	×	√	Electric and hydrogen systems
Jiang et al. (2020), Li et al. (2021b)	√	×	×	×	Transmission/distribution system
Li et al. (2020a)	√	×	×	√	Residential multi-energy microgrid
Jiang et al. (2024)	√	×	√	×	Integrated energy system
Hu et al. (2024)	√	×	√	×	Integrated energy system
Cheng et al. (2019)	×	×	√	×	Multiple energy system
This paper	√	√	√	√	Transmission system

technologies are usually expensive and eco-friendly in the early stages, which is contrary to the goal of minimizing total costs. However, the control of carbon emissions is the basis of sustainable development. Thus, this contradictory factor needs to be considered in the planning stage. In a word, this paper aims to provide a more practical method for power system planning under the background of a high proportion of renewable energy by comprehensively utilizing various types of latest technologies and taking carbon reduction into account. The comparison with related studies is presented in Table 1.

In response, we aim to bridge the gaps mentioned above and propose a novel model that optimizes local network reinforcement along with investment decisions on ESSs. The size, location, and degradation of ESSs and the trustworthiness of DR technology are included because they represent some promising options to provide flexibility in power grids. In addition, the presented expansion approach takes conventional generation costs, investment costs (including ESSs and transmission lines), loss load costs, energy curtailment costs, and GHG emission costs into account. However, the problem scale is very large not only due to various devices but also both binary and continuous variables considered simultaneously. To deal with this, we reformulate this model by decomposition and transform it into an MP and a dual SP. Then, it can be solved efficiently without falling into a poor, sub-optimal solution. Using this new framework, power systems can take a comprehensive methodology to better handle the inherent resources to get a more flexible, reliable, environmentally friendly, and cost-efficient power system. The proposed solution technique is tested in a modified 24-bus system. The results show the superiority of this method in terms of solution optimality and computational efficiency. To sum up, this model can help all agents who participate in power grids make their cost-effective plans in a carbon-constrained environment.

The main contributions of this paper are as follows:

1. To evaluate what the influences of multiple resources and technologies that act on power system planning are, we proposed a coordinated planning model that considers not only the effects of ESSs but also the trustworthiness of DR and CO_2 emissions.
2. Moreover, the size, location, and degradation of ESSs are included in this model and reveal how the deep internal influence of different trustworthiness of DR acts on power grids.
3. Our model can comprehensively investigate the goals between environmental benefits and cost-effectiveness. Thus, it can provide guidance for policymakers on how to formulate policy interventions for participants to achieve emission targets.
4. This framework was decomposed by the dual theory to reduce the computational burden without falling into a poor, sub-optimal solution.

The remainder of this paper is organized as follows: the detailed mathematical model is formulated in Section 2. Its compact vector form and its dual decomposition are presented in Section 3. Section 4 introduces the overall solution structure. The performance of the presented method is evaluated on a modified IEEE 24-bus test system, which is shown in Section 5. Finally, the main conclusions are summarized in Section 6.

2 Problem formulation

This section introduces the research framework and modeling process of this article. As shown in Figure 1, to consider the

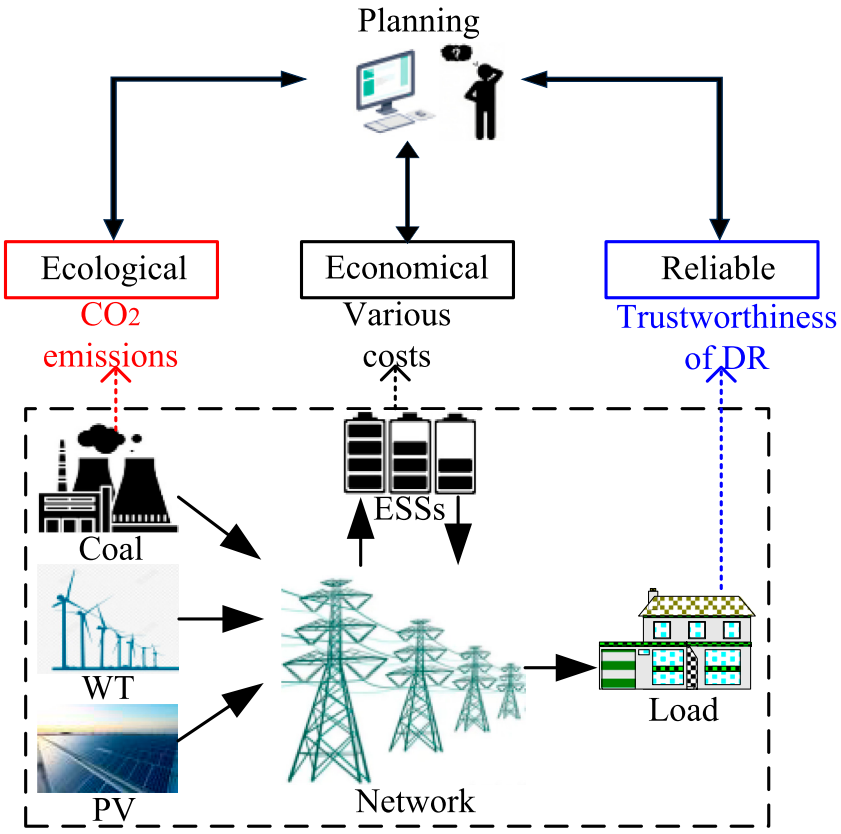

FIGURE 1
Framework of this article

environmental, economic, and reliability factors simultaneously during the planning phase, we conducted a planning study on a power system with a high penetration rate of renewable energy. First, coal-fired power plants emit GHGs, which may be advantageous for maximizing economic benefits but detrimental to the current sustainable development purport. This contradictory factor needs to be considered in the planning stage. Second, ESSs can perform peak shaving and valley filling and provide flexibility to the system. However, their size, location, and inherent degradation should be considered in the planning stage. Finally, DR, as an active response on the demand side, helps resist system volatility. However, the trustworthiness of DR is influenced by various factors and can ultimately affect the planning results of this system. Thus, this article presents a more practical method for power system planning from ecological, economic, and reliability perspectives with a high penetration rate of renewable energy.

2.1 Objective function

The objective function shown in Equation 1 (which contains four parts) seeks to make a tradeoff between minimizing the costs and CO_2 emissions. The first part refers to the total investment costs of new transmission lines and ESSs, which is indicated in Equation 2; the second part refers to the total operation costs, including conventional generation costs (PG^{ope}), ESSs maintenance costs (PS^{ope}), DR costs (DR^{ope}), and renewable energy curtailment costs (QWV^{ope}). The details of these compact forms are shown in Equations 4–7. It should be noted that the maintenance costs of per-unit ESSs decrease as their node-installed capacity increases. The third part (C^{reli}), as indicated in Equation 8, refers to the total costs of loss of demands. The last part (C^{em}) that is shown in Equation 9 is GHG emission costs for every time point in every representative day. If environmental considerations are not taken into account, the objective function only contains the first three costs. Note that GHG emission cost is closely related to traditional generations, which is shown in Equation 10 in detail.

$$\min C^{inv} + C^{ope} + C^{reli} + C^{em}, \tag{1}$$

$$C^{inv} = \frac{r(1+r)^{y}}{(1+r)^{y}-1}\left[\sum_{i} CL_i \cdot xl_i + \sum_{s} CS_s \cdot xs_s\right], \tag{2}$$

$$C^{ope} = \sum_{k} \rho_k \cdot \sum_{y,h} \cdot [PG^{ope} + PS^{ope} + DR^{ope} + QWV^{ope}], \tag{3}$$

$$PG^{ope} = \sum_{g} \alpha_{g,y,h} \cdot PG_{g,y,h,k}, \tag{4}$$

$$PS^{ope} = \sum_{s}\left(\beta_{y,h} - \frac{E_{y,h} - E_{0,y,h}}{E_{y,h}} * \hbar\right) \cdot E_{y,h}, \tag{5}$$

$$DR^{ope} = -\sum_{l} \gamma_{y,h} \cdot DR_{l,y,h,k}, \tag{6}$$

$$QWV^{ope} = \sum_{w} CW_{w,h} \cdot QW_{w,y,h,k} + \sum_{v} CV_{v,h} \cdot QV_{v,y,h,k}, \tag{7}$$

10.3389/fenrg.2024.1384760

$$C^{reli} = VOLL \cdot \sum_{i,y,h,k} \rho_k \cdot LP_{i,y,h,k}, \tag{8}$$

$$C^{em} = \sum_{k} \rho_k \cdot \sum_{g,y,h} EM_{g,y,h} \cdot CG^{em}_{g,y,h} \cdot e_{g,y,h,k}, \tag{9}$$

$$e_{g,y,h,k} = PG_{g,y,h,k} \cdot h, \forall g, y, h, k. \tag{10}$$

2.2 Constraints

Various expansion and operation constraints are presented as follows:

The constraints of Equations 11–15 are introduced for conventional generators' operation limits. Considering the upward and downward reserve, constraints of Equations 11, 12 limit the active power production of each conventional generator between its minimum and maximum capacities. The ramp-up and ramp-down limits of traditional generator units are shown in Equations 13, 14. In Equation 15, the reactive power production was limited.

$$PG_{g,y,h,k} + RU_{g,y,h,k} \le PG^{\max}_{g}, \forall g, y, h, k, \tag{11}$$

$$RD_{g,y,h,k} \le PG^{\min}_{g}, \forall g, y, h, k, \tag{12}$$

$$PG_{g,y,h,k} - PG_{g,y,h-1,k} + RU_{g,y,h,k} \le RUW_{g}, \forall g, y, h, k, \tag{13}$$

$$PG_{g,y,h-1,k} - PG_{g,y,h,k} + RD_{g,y,h,k} \le RDW_{g}, \forall g, y, h, k, \tag{14}$$

$$QG^{\min}_{g} \le QG_{g,y,h,k} \le QG^{\max}_{g}, \forall g, y, h, k. \tag{15}$$

The upward and downward spinning reserves are modeled to resist the inevitable uncertainties due to renewable energy and demand, which are bounded from Equations 16–19. Wf_h and Vf_h are the hourly representative factors of the wind and photovoltaic farms' output. It affects the final output of these generations. Load forecasting is almost patterned, and its prediction is relatively easy. However, the trustworthiness of DR is complicated because it is affected by several factors. Moreover, as RESs are highly penetrated, their outputs are affected by the weather, causing larger forecast errors. Thus, we assume the lower bound for the upward and downward spinning reserves at every time resolution as 3% for the load and 5% for renewable energy (see in Equations 16, 17). The hourly total upper bounds of the upward and downward reserves are presented in Equations 18, 19.

$$3\% \cdot (1 + LG_k)^k \cdot \sum_h Lf_h \cdot PD^{PK}_{i,k} + 5\% \cdot \left(\sum_h Wf_h \cdot \sum_{w,k} PW_{w,k} + \sum_h Vf_h \cdot \sum_{v,k} PV_{v,k} \right) \le \sum_{g,h} RU_{g,y,h,k}, \forall y, k, \tag{16}$$

$$3\% \cdot (1 + LG_k)^k \cdot \sum_h Lf_h \cdot PD^{PK}_{i,k} + 5\% \cdot \left(\sum_h Wf_h \cdot \sum_{w,k} PW_{w,k} + \sum_h Vf_h \cdot \sum_{v,k} PV_{v,k} \right) \le \sum_{g,h} RD_{g,y,h,k}, \forall y, k, \tag{17}$$

$$\sum_{g,h} RU_{g,y,h,k} \le RUW_{g}, \forall g, y, h, k, \tag{18}$$

$$\sum_{g,h} RD_{g,y,h,k} \le RDW_{g}, \forall g, y, h, k. \tag{19}$$

Constraints related to renewable energy are presented in Equations 20–22. Constraints of Equations 20, 21 limit the power production of RESs (including wind farms and photovoltaic generations) from zero to their maximum capacity. The constraint of Equation 22 ensures the penetration of renewable energy; in other words, it guarantees the percentage of the total load supplied by renewable energy. The parameter χ represents the expected contributions of RESs in supplying the total demand.

$$0 \le PW_{w,y,h,k} \le PW^{\max}_{w,y,h}, \forall w, y, h, k, \tag{20}$$

$$0 \le PV_{v,y,h,k} \le PV^{\max}_{v,y,h}, \forall v, y, h, k, \tag{21}$$

$$xw_{w,y-1,h,k} \le xw_{w,y,h,k}, \forall w, y, h, k, \tag{22}$$

$$xv_{v,y-1,h,k} \le xv_{v,y,h,k}, \forall v, y, h, k, \tag{23}$$

$$\chi \cdot (1 + LG_k)^k \cdot \sum_h Lf_h \cdot PD^{PK}_{i,y,h,k} \le \sum_h Wf_h \cdot \sum_{w,k} (PW_{w,k} - QW_{w,k}) + \sum_h Vf_h \cdot \sum_{v,k} (PV_{v,k} - QV_{v,k}), \forall k. \tag{24}$$

Due to wind and photovoltaic power intermittency and transmission line congestion, renewable energy spillage occurs. Wind and photovoltaic power curtailment constraints were bounded by Equations 25, 26. Based on Equation 27, the load shedding in each bus is specified. κ is the maximum allowable load shedding at each stage.

$$0 \le QW_{w,h,k} \le Wf_h \cdot PW_{w,k}, \forall w, h, k, \tag{25}$$

$$0 \le QV_{v,h,k} \le Vf_h \cdot PV_{v,k}, \forall v, h, k, \tag{26}$$

$$0 \le LP_{i,h,k} \le \kappa \cdot (1 + LG_k)^k \cdot Lf_h \cdot PD^{PK}_{i,k}, \forall i, h, k. \tag{27}$$

Constraints related to DR are proposed from Equations 28–30. The first equation denotes the actual proportion of the available load participating in DR. The latter shows the relationship between the actual participating DR and its trustworthiness. Equation 30 guarantees that total energy consumption remains constant. In other words, the effect of DR is cutting the peak and filling the valley.

$$-CF(H) \cdot PD_{i,y,h,k} \le DR_{i,y,h,k} \le CF(H) \cdot PD_{i,y,h,k}, \forall i, y, h, k, \tag{28}$$

$$CF(H) = CF(H, E)^* \max\{0, CF(E)\}, \tag{29}$$

$$\sum_h DR_{i,y,h,k} = 0, \forall i, y, h, k. \tag{30}$$

Constraints related to ESSs are presented in Equations 31–40. Constraints of Equation 31 and Equation 32 guarantee the charging and discharging rates, respectively. The constraint of Eq. 33 limits the storage energy of each ESS. The stored energy value at the beginning is set to be the same as that at the end, which is shown in the former part of Equation 34. Moreover, the second half of this equation is to prevent the model from choosing the maximum state of charge (SOC) at the initial time and fully discharging at the end to increase revenue. The constraint of Equation 35 is used to avoid simultaneous charging and discharging of constructed ESSs. The minimum and maximum allowable changes are limited by Equation 36. The constraint of Equation 37 states that the maximum allowable change in SOC is a fraction of $E_{s,y,h,k}$. Taking batteries for example, the theoretical degradation function of ESSs is proposed in Equations 38, 39. Constraints of Equation 40 guarantee that the installed ESSs at each stage will remain at the next stages.

$$0 \le PS^{ch}_{s,y,h,k} \le BS^{ch}_{s,y,h,k} \cdot PS^{\max}_{s}, \forall s, y, h, k, \tag{31}$$

$$0 \le PS^{dch}_{s,y,h,k} \le BS^{dch}_{s,y,h,k} \cdot PS^{\max}_{s}, \forall s, y, h, k, \tag{32}$$

$$xs_s \cdot E^{\min}_{s,y,h,k} \le SOC_{s,y,h-1,k} + \sum_{h=1}^{t}\left(\eta_{ch} \cdot PS^{ch}_{s,y,h,k} - \frac{1}{\eta_{dch}} \cdot PS^{dch}_{s,y,h,k}\right) \le xs_s \cdot E^{\max}_{s,y,h,k}, \forall s, y, h, k, \tag{33}$$

$$SOC_{s,y,1,k} = SOC_{s,y,48,k} = 0.14 \cdot E_{s,y,h,k}, \forall s, y, h, k, \tag{34}$$

$$BS^{ch}_{s,y,h,k} + BS^{dch}_{s,y,h,k} \le xs_s, \forall s, y, h, k, \tag{35}$$

$$-\overline{\Delta SOC}_{s,y,h,k} \le SOC_{s,y,h,k} - SOC_{s,y,h-1,k} \le \overline{\Delta SOC}_{s,y,h,k}, \forall s, y, h, k, \tag{36}$$

$$\overline{\Delta SOC}_{s,y,h,k} = \pi \cdot E_{s,y,h,k}, \forall s, y, h, k, \tag{37}$$

$$E_{s,y,h,k} = SoH_{s,y,h,k} \cdot E^{Rate}_{s,y,h,k}, \forall s, y, h, k, \tag{38}$$

$$SoH_{s,y,h,k} = 1 - \alpha_{sei} e^{-f_{sei}} - (1 - \alpha_{sei}) e^{-f_d}, \tag{39}$$

$$xs_{s,y-1,h,k} \le xs_{s,y,h,k}, \forall s, y, h, k. \tag{40}$$

The hourly power flow limits of the transmission lines are modeled in Equations 41–44. In Equations 41, 42, the active and reactive power flow from node i to node j is guaranteed. Constraints of Equation 43 enforce line nominal capacity at an hour h for every scenario s in one representative year y. The constraint of Equation 44 confirms that the constructed line at a certain stage will remain until the end of the planning horizon.

$$PL_{i,j,y,h,k} = V^2_{i,y,h,k} \cdot G_i - V_{i,y,h,k} \cdot V_{j,y,h,k} \cdot \left[\overbrace{G_i \cos\left(\theta_{i,y,h,k} - \theta_{j,y,h,k}\right) + B_i \sin\left(\theta_{i,y,h,k} - \theta_{j,y,h,k}\right)}^{A_{i,y,h,k}}\right] \cdot xl_i, \forall i, y, h, k, \tag{41}$$

$$QL_{i,j,y,h,k} = -V^2_{i,y,h,k} \cdot \left(B_i + \frac{B^c_i}{2}\right) - V_{i,y,h,k} \cdot V_{j,y,h,k} \cdot \left[\overbrace{B_i \cos\left(\theta_{i,y,h,k} - \theta_{j,y,h,k}\right) - G_i \sin\left(\theta_{i,y,h,k} - \theta_{j,y,h,k}\right)}^{B_{i,y,h,k}}\right] \cdot xl_i, \forall i, y, h, k, \tag{42}$$

$$\left(PL_{i,j,y,h,k}\right)^2 + \left(QL_{i,j,y,h,k}\right)^2 \le \left(SL_{i,j}{}^{\max}\right)^2, \forall i, j, y, h, k. \tag{43}$$

$$xl_{i,y-1,h,k} \le xl_{i,y,h,k}, \forall i, y, h, k. \tag{44}$$

The voltage magnitude deviation must be kept between the operation limits shown in the constraint of Equation 45. The constraint of Equation 46 bounds the variation ranges of the phase angle.

$$V^{\min}_i \le V_{i,y,h,k} \le V^{\max}_i, \forall i, y, h, k, \tag{45}$$

$$-\theta^{\min}_i \le \theta_{i,y,h,k} \le \theta^{\max}_i, \forall i, y, h, k. \tag{46}$$

In Equations 47, 48, the hourly nodal active and reactive power production–consumption balance including conventional generation units, renewable energy sources, ESS devices, DR, renewable energy curtailment, and load shedding is formulated.

$$\sum_g AG_{i,g} \cdot PG_{g,y,h,k} + \sum_w AW_{i,w} \cdot PW_{w,y,h,k} + \sum_v AV_{i,v} \cdot PV_{v,y,h,k} - \sum_s AS_{i,s} \cdot \left(PS^{ch}_{s,y,h,k} - PS^{dch}_{s,y,h,k}\right) + \sum_{i \in \Omega^e_l} PL_{i,y,h,k} - \sum_{j \in \Omega^s_l} PL_{j,y,h,k} = \sum_l AD_{i,l} \cdot PD_{i,y,h,k} - \sum_l AD_{i,l} \cdot DR_{i,y,h,k} - \sum_i LP_{i,y,h,k}, \forall i, y, h, k, . \tag{47}$$

$$\sum_g AG_{i,g} \cdot QG_{g,y,h,k} + \sum_{i \in \Omega^e_l} QL_{i,y,h,k} - \sum_{j \in \Omega^s_l} QL_{j,y,h,k} = \sum_l AD_{i,l} \cdot QD_{i,y,h,k} - \sum_i LQ_{i,y,h,k}, \forall i, y, h, k. \tag{48}$$

2.3 Uncertainties

The load and renewable energy (including wind and photovoltaic power) are subject to uncertainties shown in Equation 49 (i.e., $PD_{i,y,h,k}$; $PW_{w,y,h,k}$; $PV_{v,y,h,k}$). Polyhedral uncertainty sets shown in Equations 50–52 are used in this paper to deal with this inherent uncertainty (Dehghan et al., 2017; Li et al., 2018; Dehghan et al., 2020; Velloso et al., 2020; Hamzehkolaei et al., 2021; Zheng et al., 2021).

$$\Omega^{\Gamma} = \{\Omega_D, \Omega_W, \Omega_V\}. \tag{49}$$

Here,

$$\Omega_D = \left\{\tilde{PD}_{i,y,h,k} - \Gamma_D \hat{PD}_{i,y,h,k} \le PD_{i,y,h,k} \le \tilde{PD}_{i,y,h,k} + \Gamma_D \hat{PD}_{i,y,h,k}\right\}, \tag{50}$$

$$\Omega_W = \left\{\tilde{PW}_{w,y,h,k} - \Gamma_W \hat{PW}_{w,y,h,k} \le PW_{w,y,h,k} \le \tilde{PW}_{w,y,h,k} + \Gamma_W \hat{PW}_{w,y,h,k}\right\}, \tag{51}$$

$$\Omega_V = \left\{\tilde{PV}_{v,y,h,k} - \Gamma_V \hat{PV}_{v,y,h,k} \le PV_{v,y,h,k} \le \tilde{PV}_{v,y,h,k} + \Gamma_V \hat{PV}_{v,y,h,k}\right\}. \tag{52}$$

Here, Γ_D controls the conservativeness of DR, $\tilde{PD}_{i,y,h,k}$ is the nominal value of DR, $\hat{PD}_{i,y,h,k}$ is the variability of DR, and $PD_{i,y,h,k}$ is the probable value for DR. Accordingly, symbols $PW_{w,y,h,k}$, $\hat{PW}_{w,y,h,k}$, and $\tilde{PW}_{w,y,h,k}$ stand for wind generation and $PV_{v,y,h,k}$, $\hat{PV}_{v,y,h,k}$, and $\tilde{PV}_{v,y,h,k}$ relate to photovoltaic power.

2.4 Linearization

The model presented above is a MINLP optimization problem because of non-linear constraints of Equations 39, 41–43. It takes more time to solve this model without guaranteeing its global optimality. According to Xu et al. (2018), ESS' aging consists of calendar aging and cycle aging. Assuming that the average temperature T_c and the average SOC ∂ of all cycles are the same, then, these are linear degradation processes concerning the number of cycles. Equation 39 can be rewritten as accumulated cycling life, as shown in Equation 53. According to the literature (Pirouzi et al., 2018; Pirouzi and Aghaei, 2019), constraints of Equations 41, 42 can be recast into Equations 54, 55 through the big-M linearization technique without reducing the solution accuracy. Constraints of Equation 43 can be transformed into Equation 56 through piecewise linearization. According to Pirouzi et al. (2017), the constraints of Equation 56 can be seen as expressions for the circles centered at (0,0). The circle is divided into n equal parts, and when n is large enough, that is, $\Delta\alpha$ is small enough, the inner regular polygon of a circle approximates the circle infinitely. In other words, Equation 56 is transformed into Equation 57

approximately. Thus, the MILP optimization model was obtained (see Eqs 1–38, 40, 44–48, 53–55, 57).

$$SoH_{s,y,h,k} = N \cdot f_d(t, \varsigma, \partial, T_c, 1), \tag{53}$$

$$\begin{aligned} &-M(1-xl_i) \le PL_{i,j,m,y,h,k} \\ &-\left[\left(2V_{i,y,h,k}-1\right)\cdot G_i - \frac{\partial A_{i,m,y,h,k}}{\partial \delta}\left(\delta_{i,y,h,k}-\bar{\delta}_{i,m,y,h,k}\right)\right. \\ &\left.-\frac{A_{i,m,y,h,k}}{\delta}\left(V_{i,y,h,k}+V_{j,y,h,k}-1\right)\right] \le M(1-xl_i), \forall i,m,y,h,k, \end{aligned} \tag{54}$$

$$\begin{aligned} -M(1-xl_i) \le QL_{i,j,m,y,h,k} - \Bigg[&-\left(2V_{i,y,h,k}-1\right)\cdot\left(B_i+\frac{B_i^c}{2}\right) \\ &-\frac{\partial B_{i,m,y,h,k}}{\partial \delta}\left(\delta_{i,y,h,k}-\bar{\delta}_{i,m,y,h,k}\right) \\ &-\frac{B_{i,m,y,h,k}}{\delta}\left(V_{i,y,h,k}+V_{j,y,h,k}-1\right)\Bigg] \\ \le M(1-xl_i), &\forall i,m,y,h,k, \end{aligned} \tag{55}$$

$$\left(\sum_m PL_{i,j,m,y,h,k}\right)^2 + \left(\sum_m QL_{i,j,m,y,h,k}\right)^2 \le xl_i \cdot \left(SL_{i,j}{}^{\max}\right)^2, \forall i,j,m,y,h,k. \tag{56}$$

$$\begin{aligned} &\cos(n\Delta\alpha)\cdot\sum_m PL_{i,j,m,y,h,k} + \sin(n\Delta\alpha)\cdot\sum_m QL_{i,j,m,y,h,k} \\ &\le xl_i \cdot SL_{i,j}{}^{\max}, \forall i,j,n,m,y,h,k. \end{aligned} \tag{57}$$

3 Compact form and dual decomposition

3.1 Compact form

For brevity's sake, the above MILP model can be compactly rewritten in an epigraph form. Specifically, the objective functions of Equations 1–10 are compacted by Equation 58. Constraints only related to binary variables (i.e., Eqs 22, 23, 40, 44) are recast by Equation 59. Equality constraints related to not only binary variables but also continuous variables (i.e., Eqs 29, 30, 34, 37, 38, 53) are presented in Equation 60. The inequality constraint of Equation 61 corresponds to Equations 11–21, 24–28, 31–33, 35, 36, 45, 46, 54, 55, 57. The constraint of Equation 62 represents the equality that was independent of continuous variables (i.e., Eqs 47, 48).

$$\min I^T Y + H^T P + J^T \xi, \tag{58}$$

s.t.

$$AY \ge B, \tag{59}$$

$$C_1 Y + E_1 P + F_1 \cdot Z + D_1 \cdot \xi = G_1 : \lambda, \tag{60}$$

$$C_2 Y + E_2 P + F_2 \cdot Z + D_2 \cdot \xi \ge G_2 : \mu, \tag{61}$$

$$KP + LZ + N\xi = M : \sigma, \tag{62}$$

$$P \ge 0, Y \in \{0,1\}. \tag{63}$$

Here, vector Y stands for binary variables such as xs_s, xl_i, $BS^{ch}_{s,y,h,k}$, and $BS^{dch}_{s,y,h,k}$. Vector P stands for positive continuous operational variables (i.e., $PG_{g,y,h,k}$; $RU_{g,y,h,k}$; $RD_{g,y,h,k}$; $PS^{ch}_{s,y,h,k}$; $PS^{dch}_{s,y,h,k}$; $QW_{w,y,h,k}$; $QV_{v,y,h,k}$; and $LP_{i,y,h,k}$). Z represents free continuous variables (i.e., $PL_{i,j,y,h,k}$; $QL_{i,j,y,h,k}$; $V_{i,y,h,k}$; and $\theta_{i,y,h,k}$). The letter ξ represents uncertain vectors (i.e., $PD_{i,y,h,k}$; $PW_{w,y,h,k}$; and $PV_{v,y,h,k}$). The compact dual variables $\lambda, \mu,$ and σ are introduced for Equations 60–62, respectively. Letters $A, C_1, C_2, E_1, E_2, F_1, F_2, D_1, D_2, K, L,$ and N are the coefficient matrices of the power network. $B, G_1, G_2,$ and M are the constant matrices.

3.2 Dual decomposition in compact form

Since the binary variables (i.e., new lines and ESSs) and the continuous variables (i.e., conventional generation units, renewable energy spillage, and loss of load) are optimized simultaneously, the above robust MILP optimization model has higher computation complexity. To improve the computation efficiency, we reformulate this model by decomposition. Then, it can be transformed into a master problem (MP) and a dual sub-problem (SP). In the MP, the binary investment variables are optimized, and then, they are fixed in the SP. On the contrary, the continuous variables are optimized in the SP, and the feasibility of its MP solution is also examined. Then, the feasibility cuts are generated and returns to MP. By introducing an auxiliary constraint $I_{SP}Y_{SP} = \bar{Y}: \eta$ (η is the compact dual variable), the formulation of the MP is presented in Equations 59, 64–67. The lower bound (LB) value of the MP is presented in Equation 65. Constraints of Equations 66, 67 define the optimality and feasibility cuts. The superscript $\hat{\bullet}$ shows that the variables are obtained and fixed in the SP. The letter p is the number of iterations.

$$\min LB, \tag{64}$$

s.t.

$$LB \ge I^T \cdot Y, \tag{65}$$

$$LB \ge I^T Y + \left[G_1^T \hat{\lambda} + G_2^T \hat{\mu} + M^T \hat{\sigma}\right]^{(P)} + \hat{\eta}^{(p)}\left(Y - \hat{Y}^{(P-1)}\right), \tag{66}$$

$$\left[G_1^T \hat{\lambda} + G_2^T \hat{\mu} + M^T \hat{\sigma}\right]^{(P)} + \hat{\eta}^{(p)}\left(Y - \hat{Y}^{(P-1)}\right) \le 0. \tag{67}$$

After the optimization of the MP, the binary variables are obtained and assumed as constant parameters in the SP. Then, the SP is introduced from Equations 68–72.

$$\max G_1^T \lambda + G_2^T \mu + M^T \sigma + \hat{Y}^T \eta. \tag{68}$$

s.t.

$$C_1^T \lambda + C_2^T \mu + I_{SP}{}^T \eta \le 0, \tag{69}$$

$$E_1^T \lambda + E_2^T \mu + K^T \sigma \le H, \tag{70}$$

$$F_1^T \lambda + F_2^T \mu + L^T \sigma = 0, \tag{71}$$

$$D_1^T \lambda + D_2^T \mu + N^T \sigma \le J. \tag{72}$$

If the solution is bounded, after solving the SP, the upper bound (UB) value can be obtained through the function $UB = G_1^T \lambda + G_2^T \mu + M^T \sigma + \hat{Y}^T \eta + I^T \hat{Y}$, which then generates the optimality cut. Otherwise, if the solution is unbounded, then we generate the feasibility cut and go to the MP. Finally, if the formulation (see in Eq. 73) is satisfied, the iteration ends; otherwise, the next iteration starts.

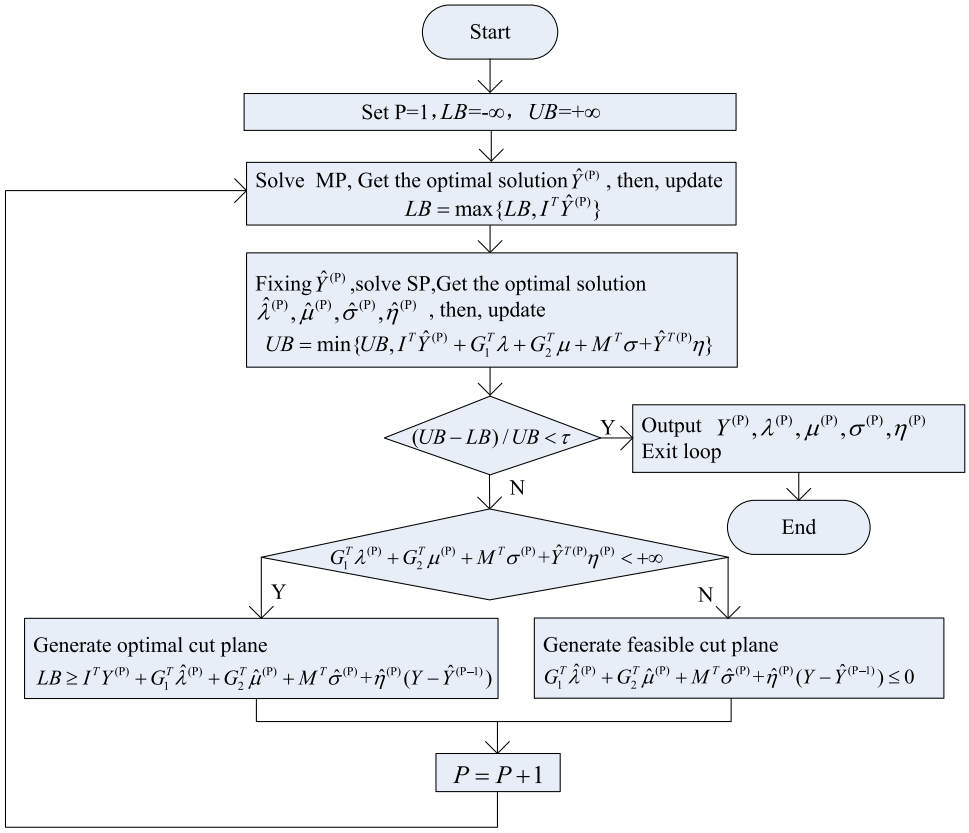

FIGURE 2
Solution flowchart.

$$\frac{(UB - LB)}{UB} \leq \tau. \tag{73}$$

4 Overall solution structure

According to the above, the decomposed optimization model can be solved effectively. This section proposes the holistic solution structure (Tan et al., 2021; Velloso and Van Hentenryck, 2021) See Figure 2.

Step 1: Set the loop parameter $p = 1$ and the initial value of the parameters.

Step 2: Solve the MP and get the optimal solution of binary variables $\hat{Y}^{(P)}$. Update the lower bound through $LB = \max\left\{LB, I^T\hat{Y}^{(P)}\right\}$.

Step 3: Solve the robust dual SP by fixing the condition $Y = \hat{Y}^{(P)}$ and obtaining the optimal solution $\hat{\lambda}^{(P)}, \hat{\mu}^{(P)}, \hat{\sigma}^{(P)}, \hat{\eta}^{(P)}$. Then, update $UB = \min\left\{UB, I^T\hat{Y}^{(P)} + G_1^T\lambda + G_2^T\mu + M^T\sigma + \hat{Y}^{T(P)}\eta\right\}$, and UB is the upper bound of the solution.

Step 4: Check $(UB - LB)/UB \leq \tau$. If satisfied, output $Y^{(P)}$, $\lambda^{(P)}, \mu^{(P)}, \sigma^{(P)}, \eta^{(P)}$ and exit the loop. Otherwise, go to Step 5.

Step 5: Check the optimal solution of the dual SP; in other words, $G_1^T\lambda^{(P)} + G_2^T\mu^{(P)} + M^T\sigma^{(P)} + \hat{Y}^{T(P)}\eta^{(P)} < +\infty$. If satisfied, go to Step 6. Otherwise, go to Step 7.

Step 6: Generate the optimal cut plane $LB \geq I^TY^{(P)} + G_1^T\hat{\lambda}^{(P)} + G_2^T\hat{\mu}^{(P)} + M^T\hat{\sigma}^{(P)} + \hat{\eta}^{(P)}(Y - \hat{Y}^{(P-1)})$ and P = P + 1, and then, go to Step 2.

Step 7: Generate the feasible cut plane $G_1^T\hat{\lambda}^{(P)} + G_2^T\hat{\mu}^{(P)} + M^T\hat{\sigma}^{(P)} + \hat{\eta}^{(P)}(Y - \hat{Y}^{(P-1)}) \leq 0$ and P = P + 1, and then, go to Step 2.

5 Case study

5.1 Description of the test system

The modified IEEE 24-node system (Probability Methods Subcommittee, 1979) includes 38 existing lines, 9 traditional generator units, 6 wind farms, and 3 photovoltaic power stations, as seen in Figure 3. Compared to the standard IEEE 24-bus system, its grid structure is the same. The difference is that we added photovoltaic and wind farms, with their specific location shown in Figure 3. To reveal how the deep internal influence acts on power grids with different trustworthiness of DR, we set it to vary from 0.0 to 1.0. The value 0.0 means no trust, and 1.0 represents full trust. In other words, as the

10.3389/fenrg.2024.1384760

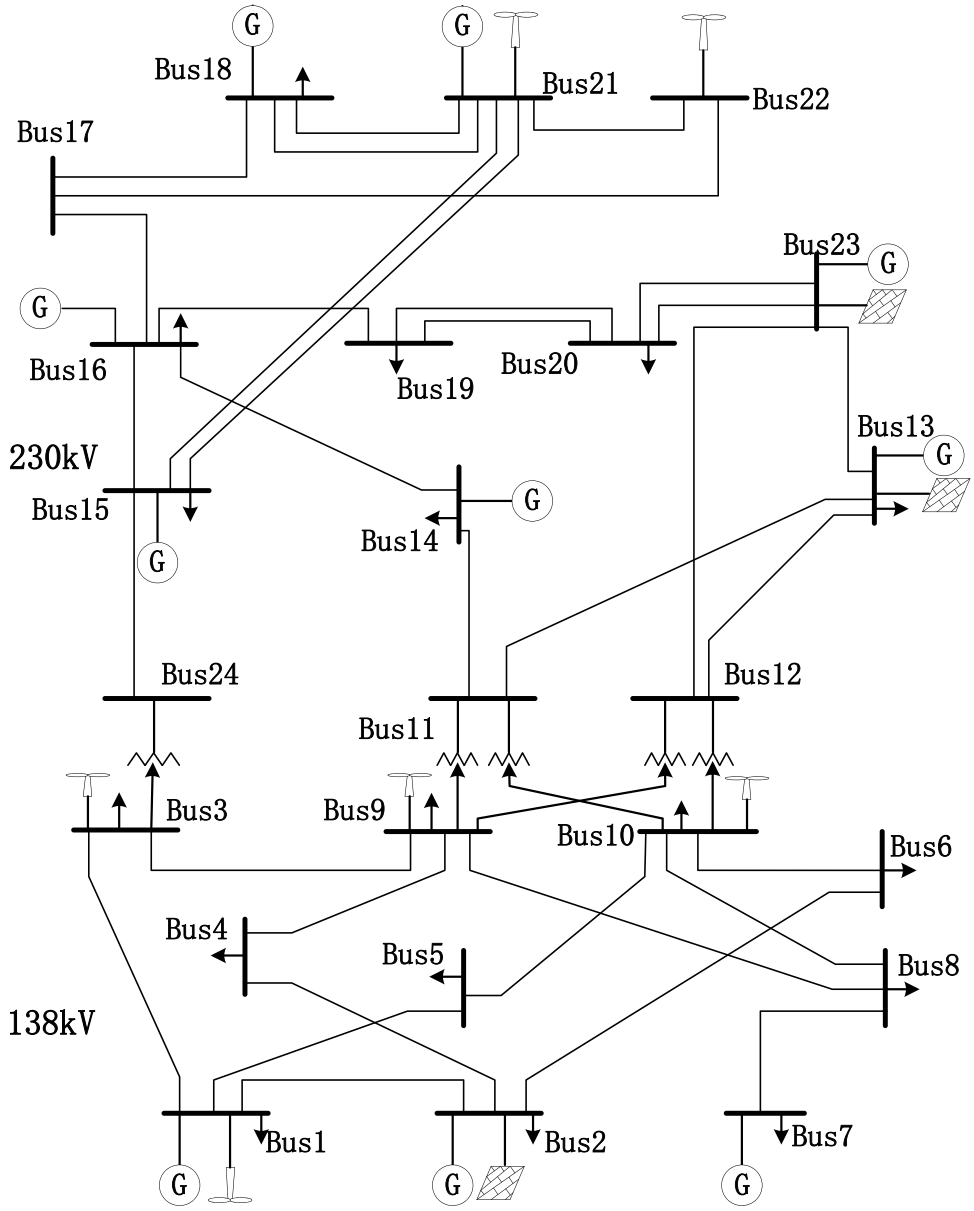

FIGURE 3
Modified IEEE 24-node system.

value increases, the level of trust increases. The time series (e.g., wind, photovoltaic power output, and electricity loads) were extracted from the practical cases obtained in Li H. et al. (2020). In addition, the penetration level of RESs is assumed to be 60% of their installed capacity. The decreased rate of ESS maintenance costs $\hbar$ is set to 5%. To make a trade-off between computational efficiency and accuracy, the k-medoids clustering technique (Park and Jun, 2009) is used instead of solving 8,760 h for the whole year. Each representative period is considered as one scenario, and the scenario probability is obtained from the clustering process. It should be noted that besides several special days, natural days during 1 year can be mainly clustered into working days splicing weekends. Therefore, it is more conducive to the system solution based on the week consisting of two consecutive days. Moreover, ensuring the consideration of the data's sequential nature and making the benefits of ESSs more obvious, we showed the state for 48 consecutive periods. During these 48 consecutive periods, there is a difference in renewable energy and load.

On the other hand, the economic data, namely, investment cost, operation cost (i.e., fuel costs, O&M costs, renewable energy spillage costs, and loss load costs,), and environmental parameters (i.e., CO_2 emission costs), are presented in Table 2. Note that linear generation-cost functions were used for traditional generation units due to their acceptable accuracy and the already complex nature of the optimization problem.

The simulations have been solved by using Gurobi9.1.1 as the solver. We considered a convergence tolerance of 0.01%. All studies were operated on an Intel-Core i7 (64-bit) 3.4-GHz individual laptop with 16GB RAM.

TABLE 2 Values of several parameters used in the optimization problem.

Parameter		Value	Unit
Variable	Description		
cx1	Cost per kilometer of building transmission lines (138 kV)	50*10^4	$/km
cx2	Cost per kilometer of building transmission lines (230 kV)	80*10^4	$/km
cxs	Cost of installing a new storage	20.08*10^4	$/MWh
cg	Fuel and O&M cost of traditional generations	83	$/MWh
cw	Wind curtailment cost	28.6	$/MWh
cv	Photovoltaic curtailment cost	20	$/MWh
cr	Cost of lost loads	1,350	$/MWh
cdr	Demand response cost	30	$/MWh
CG	CO_2 emission license costs	80	$/ton
EM	CO_2 emitted per kWh	650	g/kWh
$\hbar$	Decreased rate of ESS maintenance costs	5%	-
η	ESS charge and discharge efficiencies	0.9	-
Base MVA	Base power of the system	100	MVA

TABLE 3 Simulation results of the power system with different ESS sizes.

Single ESS size	Position	New lines	Investment cost (10^9)	Operation cost (10^9)	Total cost (10^9)	Renewable energy curtailment	Loss load cost (10^5)	CO_2 emission cost (10^9)
50	All	1–5 7–8 14–16 16–17 17–18	1.5512	3.1897	4.7409	55.6680	7.1629	1.1257
100	1 2 3 5–12 14–24	1–5 7–8 14–16 16–17 17–18	1.7393	2.9164	4.6557	50.0168	1.9189	1.1414
300	2 3 9 11 14 18 23	1–5 7–8 14–16 16–17 17–18	1.7461	2.9145	4.6606	58.8060	2.2554	1.1484
600	1 9 16 19	1–5 7–8 14–16 16–17 17–18	1.8458	2.9155	4.7613	144.7932	1.9369	1.1488

5.2 Simulation results and discussions

To understand what the impact of varied resources and technologies on power system planning is, three different experiments were conducted: 1) case 1 ignores the trustworthiness of DR, that is, all available DR responses, only considering the difference of one single ESS capacity, in which whether to install and where to construct are both considered. In this case, we find a suitable size for one single ESS capacity because it affects the maintenance costs in this system. 2) It is fixed according to the suitable size of each single ESS. Case 2 only considers the impact of different trustworthiness of DR. It should be noted that in

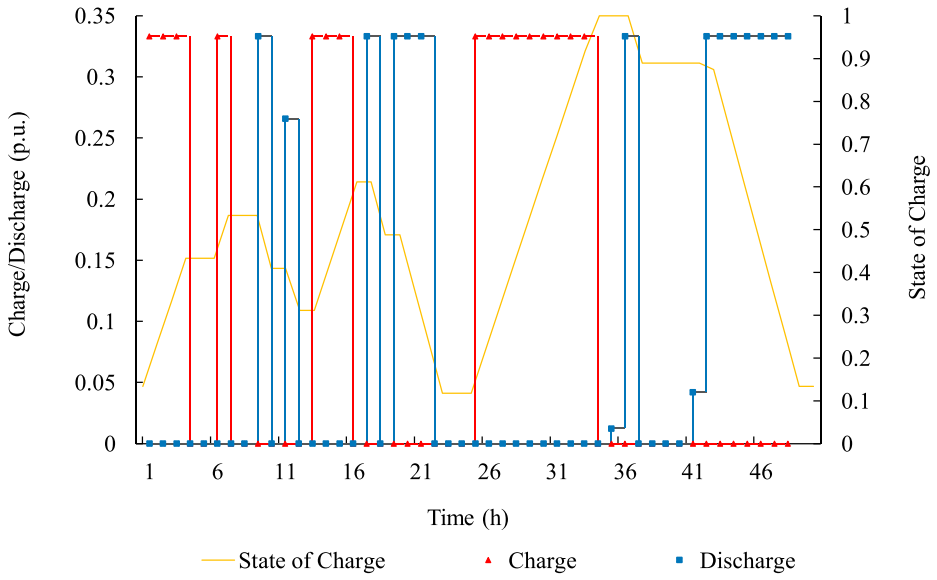

FIGURE 4
Details of a newly installed ESS in one representative period.

this case, the objective function does not contain Equations 9, 10. 3) Based on case 2, besides minimizing total costs, CO_2 emissions are considered simultaneously, and a trade-off is made between them. Here, cost-savings and reducing CO_2 emissions are of equal importance.

5.2.1 Ignoring the trustworthiness of DR

In this experiment, to select an appropriate size of ESSs, we only consider single-size changes, which includes all available DR responses. Table 3 demonstrates the expansion planning results of this optimization model. The location, degradation of ESSs, and whole-system CO_2 emission costs were included. In addition, the decreased amount of ESS maintenance costs has been contained in operation costs. It is clear that with different sizes of each ESS, their optimal location changes. The new energy storage stations need to be installed more when their single size is small because the investment cost is proportional to its capacity, and the system needs more storage to improve its flexibility.

Specifically, first of all, we compared the first two rows. Although the single capacity of the first row is small and its investment cost is low, however, its operation cost is higher. This is partly due to the surge of renewable energy curtailment, loss of load, and ESS maintenance costs. Moreover, the high flexibility requirements of some nodes are not fully met. Afterward, the last three lines are compared. As the individual ESS capacity increases, the investment cost increases, but the operation cost changes slightly. This is because renewable energy curtailment and loss of load increases, while ESS maintenance costs decrease. In other words, the number of ESSs is lessened so that the labor cost is reduced, which is related to the maintenance cost. Overall, the total cost increases as the individual ESS capacity increases. In other words, the capacity of ESSs has a close impact on power system expansion planning.

What needs to be illustrated is that when the single ESS capacity is larger, CO_2 emission costs change very slightly. This is because the penetration of renewable energy is not very high. So when the individual size is larger, the number that should be newly installed will be reduced. It is worth mentioning that the degradation of ESSs was taken into account, so the storage investment cost was more grounded in reality. In addition, renewable energy curtailment and loss load were the lowest when the single storage capacity was 100 MWh. Finally, taking renewable energy curtailment, loss of load, and total costs into account, individual ESS capacity will be appropriate at 100 MWh in this system.

Figure 4 shows the details of charge–discharge energy and the SOC of a newly installed ESS connected to bus 9 in a representative period. The initial value of ESSs is 0.14 p.u., and it needs to stay the same at the beginning and at the end of one period. As can be seen, the charging time always appears at low load hours and vice versa on the contrary. Because the RES output changed significantly in two consecutive periods, the charging and discharging behavior changed as well. Note that the experiments we performed in this section with available DR are fixed at 0.02, and their trustworthiness is 1.0.

Figure 5 shows the operating points of the source and demand status under the condition that the ESS capacity is 100 MWh and its actual DR is set at 0.02 in one representative period. As can be seen, at the beginning of 1–6 h, its load is relatively small, and charging occurs (see the yellow bar below the x-axis). When time goes to 8–11, due to load increases, the system preferentially discharges from ESSs to meet the demand (see the blue bars in this figure). In 13–16 h, the whole output of renewable energy surges. On one hand, the output of traditional generations is reduced because of their high operating costs and emissions costs. On the other hand, the power system charges ESSs in preparation for evening peak load hours (also see the yellow bar below the x-axis). Then, the system enters the night charging

10.3389/fenrg.2024.1384760

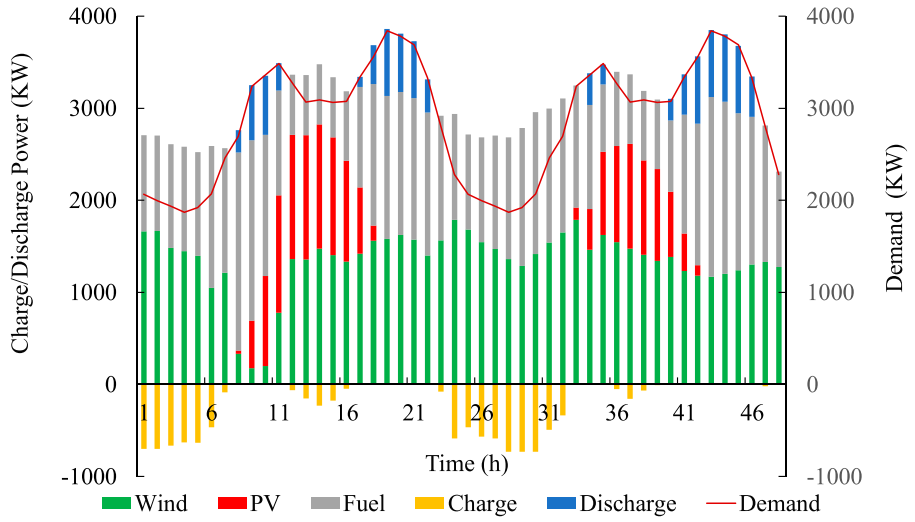

FIGURE 5
Sources and demand status in one representative period.

TABLE 4 Simulation results of the system with different DR without considering the impact of CO_2 emissions.

Trustworthiness of DR	New lines	New storage	Investment cost (10^9)	Operation cost (10^9)	Total cost (10^9)	Loss energy	Loss load (10^5)	CO_2 emission cost (*10^9)
0.0	1–5 7–8 14–16 16–17 17–18	All	1.8381	2.9033	4.7414	129.5827	2.0898	1.1503
0.1	1–5 7–8 14–16 16–17 17–18	1–3 5–12 14–24	1.7393	2.9164	4.6557	50.0168	1.9189	1.1414
0.5	1–5 7–8 14–16 16–17 17–18	1–6 9–14 17–19 21 23	1.5925	2.9527	4.5452	0	1.4571	1.1516
1.0	1–2 7–8 14–16 16–17 17–18	1	1.1610	3.0283	4.1893	16.9379	1.2909	1.1545

period. The next day is much the same, except for the decrease in photovoltaic power output, and there is a slight loss of load in 41–45. This is in line with the discussion presented above.

5.2.2 Different trustworthiness of DR

To compare what impacts act on the expansion planning optimization problem with different trustworthiness of DR, we performed the following experiments. In this section, the individual ESS capacity is set at 100 MWh, as discussed before. Simulation results are shown in Table 4. It should be noted that the second row in Table 4 should be the same as in Table 3. This is because the available DR is fixed at 0.2 with its trustworthiness setting at 0.1, which equals the actual DR being set at 0.02. As shown in each column, the expanded transmission line changes slightly with different trustworthiness of DR. However, the number of newly installed ESSs decreases when the trustworthiness of DR increases. It also causes little change in CO_2 emission costs when the actual DR increases. This is because DR plays the role of peak cutting and valley filling, and the total load remains constant.

The investment cost narrows down due to new ESSs that need to be installed being reduced when the trustworthiness of DR increases. So, even though the unavoidable DR subsidy cost grows, the value of both loss energy and loss load decreases, which leads to the operation cost increasing slightly. Thus, in a word, the total cost

10.3389/fenrg.2024.1384760

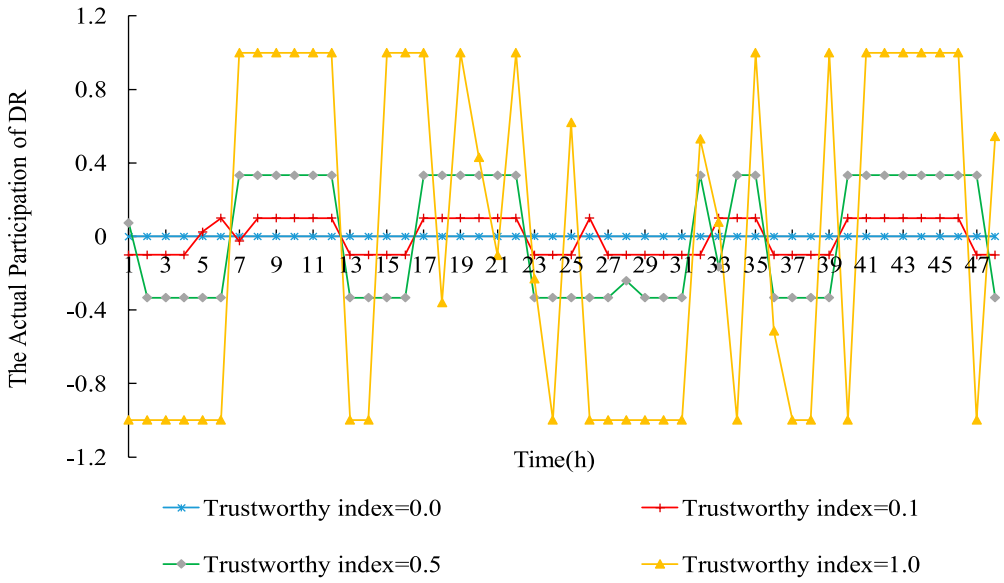

FIGURE 6
Different trustworthiness of DR at bus18.

TABLE 5 Simulation results with different trustworthiness of DR considering the impact of CO_2 emissions.

Trustworthiness of DR	New lines	New storage	Investment cost (10^9)	Operation cost (10^9)	Total cost (10^9)	Loss energy	Loss load (10^5)	CO_2 emission cost (*10^9)
0.0	1–5 7–8 14–16 16–17	All	1.9791	2.8861	4.8652	468.7139	2.0846	1.1414
0.1	1–5 7–8 14–16 16–17 17–18	1–6 8–24	1.9670	2.8789	4.8459	309.5893	1.4518	1.1341
0.5	1–5 7–8 14–16 15–16	1–6 8–15 17–20 23 24	1.89396	2.8805	4.7745	78.0662	0.7631	1.1449
1.0	1–5 7–8 14–16	3 11 14 16	1.5631	2.9490	4.5121	83.4359	0.6330	1.1312

of this expansion-planning problem is reduced because of the higher trustworthiness of DR. In other words, the appropriate application of DR can help reduce expansion costs and lessen loss load and RES curtailment. Note that the experiments we performed in this section with available DR are fixed at 0.2.

Figure 6 shows the participation situation of different trustworthiness of the available DR at bus18. In general, the higher the trustworthiness of DR, the more actual DR participates in the system. As can be seen, the positive value of participating DR equals the negative one in 48 h. Moreover, when the electricity demand is high, DR is mostly positive. While the electricity demand is low, and vice on the contrary. However, the symbol of DR is not always positive in peak load hours due to its abundant flexibility resources and renewable energy volatility. See hours 13, 14, 15, and 16. Therefore, DR can improve the flexibility of the system. In hours 18 and 21, the actual participating DR is not at its maximum. This illustrates the need for precise control of DR rather than crude subsidies.

5.2.3 A trade-off between minimizing total costs and reducing CO_2 emissions

Since GHG emissions have a heavy influence on our environment, obtaining a sustainable and environmentally

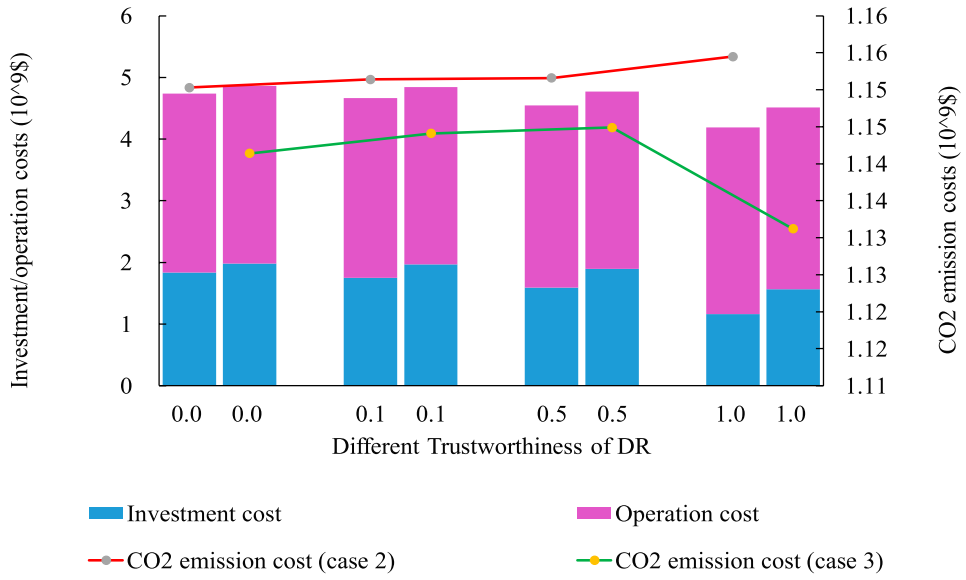

FIGURE 7
Comparison of considering only cost minimization and considering both minimizing costs and reducing CO_2 emissions.

TABLE 6 Simulation results using different solving methods when the trustworthiness of DR is 1.0

Method	New lines	New storage	Investment cost (10^9)	Operation cost (10^9)	Total cost (10^9)	Loss energy	Loss load (10^5)	CO_2 emission cost (*10^9)
Centralized	1–5 7–8 14–16	3 11 14 16	1.5631	2.9484	4.5115	83.0662	0.6301	1.1312
Dual decomposition	1–5 7–8 14–16	3 11 14 16	1.5631	2.9490	4.5121	83.4359	0.6330	1.1312

friendly power system became the global common goal. It is not appropriate to aim only at cost minimization because new technology is generally expensive at the beginning stage but are environmentally friendly. Therefore, this study makes a trade-off between minimizing total costs and reducing CO_2 emissions. We assume these two goals are of equal importance in this paper. In other words, Equations 9, 10 are included in the objective function. As shown in each column of Table 5, the number of newly installed ESSs also decreases as the trustworthiness of DR increases. However, the newly installed number should be more compared with that of the previous experiment (case 2), which only focuses on cost minimization (shown in Table 4). The most important factor is that CO_2 emission costs decreased with each different trustworthiness of DR, as compared to the cost minimization experiment. Specifically, the data on CO_2 emission cost reduced from 1.1545$ to 1.1312$, which reduced by 2.1%, when the trustworthiness of DR was 1.0.

Figure 7 presents an intuitive comparison of case 2 (only considering cost minimization) and case 3 (a trade-off between minimizing total costs and reducing CO_2 emissions). On equal terms compared to the previous case, although fewer new lines need to be constructed to strengthen the transmission network, however, more ESSs need to be installed. Thus, the investment cost increased considerably as it went up from 1.7393*10^9$ (the second row and fourth column in Table 4) to 1.9670*10^9$ (the second row and fourth column in Table 5). Moreover, the operation cost decreased slightly in case 3, with its value decreasing from 2.9164*10^9$ to 2.8789*10^9$. Thus, in a word, the total cost is larger than the condition without considering CO_2 emissions. Specifically, statistics of total cost rose from 4.6557*10^9$ to 4.8459*10^9$, an increase of 3.9%, when the trustworthiness of DR was 0.1. To maximize renewable energy consumption, the system takes priority utilization of all newly installed ESSs rather than conventional generations. In case 3, the loss load costs were reduced for each different trustworthiness of the DR condition. It indicated that the power supply reliability was improved.

To sum up, case 3 is a more appropriate strategy for the following reasons: 1) it can help reduce GHG emissions, which is consistent with the current environmental protection concept; 2) it improves power system reliability because it uses flexible resources preferentially and lessens the value of loss load; 3) it defers

transmission expansion due to abundant flexible resources. Thus, it alleviated the bottleneck of unbalanced development of the short-term renewable energy expansion period and the long-term transmission expansion period.

5.2.4 Analysis of the effectiveness of the dual-decomposition method

To verify the effectiveness of the dual-decomposition algorithm, we compared the simulation results of case 3, where the trustworthiness of DR is set to 1.0, using both the centralized algorithm and the dual-decomposition algorithm. As shown in Table 6, it can be observed that regardless of the solving algorithm, the newly constructed lines and ESSs are identical, resulting in the same investment cost for both algorithms. Moreover, the two algorithms yield the same cost for GHG emissions. Additionally, the centralized algorithm produces slightly different RES curtailment and loss-load costs compared to the decomposition algorithm. This leads to a small difference in total costs. This discrepancy is due to the convergence tolerance being set at 0.01% during program design, but it does not affect the final results.

6 Conclusion

This paper proposed a robust coordinated planning model for power systems, in which large shares of variable renewable energy are integrated. For the sake of accuracy and efficiency, piecewise linearization, big-M method, and dual decomposition were introduced due to the already complex nature of the optimization problem. The inevitable uncertainty (variable RESs and demand) is described by polyhedral sets. To understand the impact of varied resources and technologies (such as wind power, photovoltaic resources, ESSs, and the trustworthiness of DR) on the development of power system planning, several computational experiments are presented. First, the capacity, location, and degradation of ESSs have a close impact on power system expansion planning. It is necessary to select an appropriate capacity and location for every single energy storage station in the planning stage. Second, higher trustworthiness of DR can help reduce the total expansion costs. However, it has little impact on GHG emissions if we consider cost minimization only. The last study makes a trade-off between minimizing total costs and reducing CO_2 emissions. According to this, a more sustainable and environmentally friendly power system was obtained. Moreover, it improves power system reliability and alleviates the unbalanced development of the short-term renewable energy expansion period and the long-term transmission expansion period.

Data availability statement

The raw data supporting the conclusions of this article will be made available by the authors, without undue reservation.

Author contributions

PF: data curation, software, validation, writing–original draft, and writing–review and editing. CC: methodology, supervision, and writing–review and editing. LW: supervision, visualization, and writing–review and editing.

Funding

The author(s) declare that financial support was received for the research, authorship, and/or publication of this article. This work was supported by the Yancheng Fundamental Research Program. Paper no. YCBK2023010.

Conflict of interest

The authors declare that the research was conducted in the absence of any commercial or financial relationships that could be construed as a potential conflict of interest.

Publisher's note

Supplementary material

The Supplementary Material for this article can be found online at: https://www.frontiersin.org/articles/10.3389/fenrg.2024.1384760/full#supplementary-material

References

Aghajani, G. R., Shayanfar, H. A., and Shayeghi, H. (2017). Demand side management in a smart micro-grid in the presence of renewable generation and demand response. *Energy* 126, 622–637. doi:10.1016/j.energy.2017.03.051

Alahmad, A. K. (2023). Voltage regulation and power loss mitigation by optimal allocation of energy storage systems in distribution systems considering wind power uncertainty. *J. Energy Storage* 59, 106467. doi:10.1016/j.est.2022.106467

Al-Shetwi, A. Q. (2022). Sustainable development of renewable energy integrated power sector: trends, environmental impacts, and recent challenges. *Sci. Total Environ.* 822, 153645. doi:10.1016/j.scitotenv.2022.153645

Cheng, Y., Zhang, N., Lu, Z., and Kang, C. (2019). Planning multiple energy systems toward low-carbon society: a decentralized approach. *IEEE Trans. Smart Grid* 10 (5), 4859–4869. doi:10.1109/TSG.2018.2870323

Dehghan, S., Amjady, N., and Aristidou, P. (2020). A robust coordinated expansion planning model for wind farm-integrated power systems with

flexibility sources using affine policies. *IEEE Syst. J.* 14 (3), 4110–4118. doi:10.1109/JSYST.2019.2957045

Dehghan, S., Amjady, N., and Conejo, A. J. (2017). Adaptive robust transmission expansion planning using linear decision rules. *IEEE Trans. Power Syst.* 32 (5), 4024–4034. doi:10.1109/TPWRS.2017.2652618

European Commission, Energy Roadmap 2050 (2011). Brussels, Belgium, EU COM (2011) 885 final, 2011. Available at: http://ec.europa.eu/energy/energy2020/roadmap/index_en.htm.

Hamzehkolaei, F. T., Amjady, N., and Bagheri, B. (2021). A two-stage adaptive robust model for residential micro-CHP expansion planning. *J. Mod. Power Syst. Clean Energy* 9 (4), 826–836. doi:10.35833/MPCE.2021.000001

Hu, J., Wang, Y., and Dong, L. (2024). Low carbon-oriented planning of shared energy storage station for multiple integrated energy systems considering energy-carbon flow and carbon emission reduction. *Energy* 290, 130139. doi:10.1016/j.energy.2023.130139

Jafari, M., Botterud, A., and Sakti, A. (2022). Decarbonizing power systems: a critical review of the role of energy storage. *Energy Rev.* 158, 112077. doi:10.1016/j.rser.2022.112077

Jiang, X., Jin, Y., Zheng, X., Hu, G., and Zeng, Q. (2020). Optimal configuration of grid-side battery energy storage system under power marketization. *Appl. Energy* 272, 115242. doi:10.1016/j.apenergy.2020.115242

Jiang, Y., Ren, Z., and Li, W. (2024). Committed carbon emission operation region for integrated energy systems: concepts and analyses. *IEEE Trans. Sustain. Energy* 15 (2), 1194–1209. doi:10.1109/TSTE.2023.3330857

Li, H., Lu, Z., Qiao, Y., and Zhang, B. (2020b). Flexibility test system. Available at: https://github.com/HaoLi9401/DatasetofflexibilitytestsystemFTS-213.

Li, J., Li, Z., Liu, F., Ye, H., Zhang, X., Mei, S., et al. (2018). Robust coordinated transmission and generation expansion planning considering ramping requirements and construction periods. *IEEE Trans. Power Syst.* 3 (1), 268–280. doi:10.1109/TPWRS.2017.2687318

Li, J., Lu, B., Wang, Z., and Zhu, M. (2021b). Bi-level optimal planning model for energy storage systems in a virtual power plant. *Renew. Energy* 165, 77–95. doi:10.1016/j.renene.2020.11.082

Li, J., Yang, B., Huang, J., Guo, Z., Wang, J., Zhang, R., et al. (2023). Optimal planning of electricity–hydrogen hybrid energy storage system considering demand response in active distribution network. *Energy* 273, 127142. doi:10.1016/j.energy.2023.127142

Li, Z., Wu, L., Xu, Y., and Zheng, X. (2021a). Stochastic-weighted robust optimization based bilayer operation of a multi-energy building microgrid considering practical thermal loads and battery degradation. *IEEE Trans. Sustain. Energy* 13 (2), 668–682. doi:10.1109/TSTE.2021.3126776

Li, Z., Xu, Y., Feng, X., and Wu, Q. (2020a). Optimal stochastic deployment of heterogeneous energy storage in a residential multienergy microgrid with demand-side management. *IEEE Trans. Industrial Inf.* 17 (2), 991–1004. doi:10.1109/TII.2020.2971227

Liu, J., Cheng, H., Zeng, P., and Yao, L. (2018). Rapid assessment of maximum distributed generation output based on security distance for interconnected distribution networks. *Int. J. Electr. Power Energy Syst.* 101, 13–24. doi:10.1016/j.ijepes.2018.03.018

Liu, J., Tang, Z., Zeng, P. P., Li, Y., and Wu, Q. (2022). Distributed adaptive expansion approach for transmission and distribution networks incorporating source-contingency-load uncertainties. *Int. J. Electr. Power Energy Syst.* 136, 107711. doi:10.1016/j.ijepes.2021.107711

Mansouri, S. A., Ahmarinejad, A., Sheidaei, F., Javadi, M. S., Jordehi, A. R., Nezhad, A. E., et al. (2022). A multi-stage joint planning and operation model for energy hubs considering integrated demand response programs. *Int. J. Electr. Power Energy Syst.* 140, 108103. doi:10.1016/j.ijepes.2022.108103

Olsen, D. J., Dvorkin, Y., Fernandez-Blanco, R., and Ortega-Vazquez, M. A. (2018). Optimal carbon taxes for emissions targets in the electricity sector. *IEEE Trans. Power Syst.* 33 (6), 5892–5901. doi:10.1109/TPWRS.2018.2827333

Paris agreement (2015). United nations framework convention on climate change, UN. Available at: https://unfccc.int/sites/default/files/english_paris_agreement.pdf.

Park, H.-S., and Jun, C.-H. (2009). A simple and fast algorithm for K-Medoids clustering. *Expert Syst. Appl.* 36 (2), 3336–3341. doi:10.1016/j.eswa.2008.01.039

Pirouzi, S., and Aghaei, J. (2019). Mathematical modeling of electric vehicles contributions in voltage security of smart distribution networks. *Simul. Trans. Soc. Model. Simul. Int.* 95 (5), 429–439. doi:10.1177/0037549718778766

Pirouzi, S., Aghaei, J., Latify, M. A., Yousefi, G. R., and Mokryani, G. (2018). A robust optimization approach for active and reactive power management in smart distribution networks using electric vehicles. *IEEE Syst. J.* 12 (3), 2699–2710. doi:10.1109/JSYST.2017.2716980

Pirouzi, S., Aghaei, J., Niknam, T., Shafie-Khah, M., Vahidinasab, V., and Catalao, J. P. S. (2017). Two alternative robust optimization models for flexible power management of electric vehicles in distribution networks. *Energy* 141, 635–651. doi:10.1016/j.energy.2017.09.109

Probability Methods Subcommittee (1979). IEEE reliability test system. *IEEE Trans. Power App. Syst.* 98 (6), 2047–2054. doi:10.1109/TPAS.1979.319398

Qi, H. J., Yue, H., Zhang, J. F., and Lo, K. L. (2021). Optimisation of a smart energy hub with integration of combined heat and power, demand side response and energy storage. *Energy* 234, 121268. doi:10.1016/j.energy.2021.121268

Ramos-Real, F. J., Barrera-Santana, J., Ramírez-Díaz, A., and Perez, Y. (2018). Interconnecting isolated electrical systems. The case of Canary Islands. *Energy Strategy Rev.* 22, 37–46. doi:10.1016/j.esr.2018.08.004

Shi, Z., Wang, W., Huang, Y., Li, P., and Dong, L. (2022). Simultaneous optimization of renewable energy and energy storage capacity with the hierarchical control. *CSEE J. Power Energy Syst.* 8 (1), 95–104. doi:10.17775/CSEEJPES.2019.01470

Summary for policymakers (2021). In: climate Change 2021: the physical science basis. contribution of working group I to the sixth assessment report of the inter-governmental panel on climate change. *IPCC*, 3–32. doi:10.1017/9781009157896.001

Tan, H., Ren, Z., Yan, W., Wang, Q., and Mohamed, M. A. (2021). A wind power accommodation capability assessment method for multi-energy microgrids. *IEEE Trans. Sustain. Energy* 12 (4), 2482–2492. doi:10.1109/TSTE.2021.3103910

Velloso, A., Street, A., Pozo, D., Arroyo, J. M., and Cobos, N. G. (2020). Two-stage robust unit commitment for co-optimized electricity markets: an adaptive data-driven approach for scenario-based uncertainty sets. *IEEE Trans. Sustain. Energy* 11 (2), 958–969. doi:10.1109/TSTE.2019.2915049

Velloso, A., and Van Hentenryck, P. (2021). Combining deep learning and optimization for preventive security-constrained DC optimal power flow. *IEEE Trans. Power App. Syst.* 36 (4), 3618–3628. doi:10.1109/TPWRS.2021.3054341

Xu, B., Oudalov, A., Ulbig, A., Andersson, G., and Kirschen, D. S. (2018). Modeling of lithium-ion battery degradation for cell life assessment. *IEEE Trans. Smart Grid* 9 (2), 1131–1140. doi:10.1109/TSG.2016.2578950

Zappa, W., Junginger, M., and van den Broek, M. (2019). Is a 100% renewable European power system feasible by 2050? *Appl. Energy* 233–234, 1027–1050. doi:10.1016/j.apenergy.2018.08.109

Zhang, M., Fang, J., Ai, X., Shuai, H., Yao, W., He, H., et al. (2020). Feasibility identification and computational efficiency improvement for two-stage RUC with multiple wind farms. *IEEE Trans. Sustain. Energy* 11 (3), 1669–1678. doi:10.1109/TSTE.2019.2936581

Zheng, X., Qu, K., Lv, J., Li, Z., and Zeng, B. (2021). Addressing the conditional and correlated wind power forecast errors in unit commitment by distributionally robust optimization. *IEEE Trans. Sustain. Energy* 12 (2), 944–954. doi:10.1109/TSTE.2020.3026370

Nomenclature

A. Variables

xr_r	Binary variable represents the installation status of new RESs
xl_i	Binary variable represents the installation status of transmission lines
xs_s	Binary variable represents the installation status of ESSs
$PG_{g,y,h,k}$ and $QG_{g,y,h,k}$	Active and reactive power output of traditional generations
PG^{ope}, PS^{ope}, and DR^{ope}	Operation cost of conventional generations, ESSs maintenance costs, and DR costs
QWV^{ope}	Renewable energy curtailment costs
$e_{g,y,h,k}$	Energy of traditional generations
$LP_{i,y,h,k}$ and $LQ_{i,y,h,k}$	Active and reactive power loss of the system
$QW_{w,y,h,k}$ and $QV_{v,y,h,k}$	Wind and photovoltaic farm curtailment power
$PS^{ch}_{s,y,h,k}$, $PS^{dch}_{s,y,h,k}$	Charge and discharge power of ESSs
$DR_{i,y,h,k}$	Power participated in DR
$PW_{w,k}$ and $PV_{v,k}$	Active power of wind and photovoltaic farms
$PD_{i,y,h,k}$, $QD_{i,y,h,k}$	Active and reactive power of loads
$PL_{i,j,y,h,k}$, $QL_{i,j,y,h,k}$	Active and reactive power flow in transmission lines
$BS^{ch}_{s,y,h,k}$, $BS^{dch}_{s,y,h,k}$	Binary value representing the charging and discharging status of ESSs
$SOC_{s,y,h,k}$ and $\overline{SOC}_{s,y,h,k}$	State of charge (SOC) of ESSs; the maximum allowable change in SOC
$V_{i,y,h,k}$ and $\theta_{i,y,h,k}$	Voltage and angle in the power system
$E_{s,y,h,k}$	Actual energy capacity of ESSs

B. Parameters

CL_i	Investment costs for candidate transmission lines
CS_s	Investment costs for new ESSs
CR_r	Investment costs for variable RESs. Note that CR_r includes investment costs for wind power generations and photovoltaic generations with different coefficients
$\alpha_{g,y,h}$	Operation-related conventional generator fuel costs
$\beta_{y,h}$	Maintenance costs of a single ESS
$\gamma_{y,h}$	Operation-related DR costs
ħ	Decreased rate of ESS maintenance costs
$E_{0,y,h}$, $E_{y,h}$	Single energy capacity and the node-installed capacity of ESSs
$CW_{w,h}$, $CV_{v,h}$	Cost of wind and photovoltaic power curtailments
C^{reli} and C^{em}	Costs of loss of demands and GHG emissions
χ	Expected contributions of renewable energy sources in supplying the total demand
Lf_h, Wf_h, Vf_h	Hourly representative factors of load demand, wind, and photovoltaic farm outputs
LG_k	Load growth factor at scenario k
$PD^{PK}_{i,k}$	Peak load at bus i
RDW_g, RUW_g	Total hourly upper bound of upward and downward reserves
$RD_{g,y,h,k}$, $RU_{g,y,h,k}$	Ramp-down and ramp-up limits of traditional generation units
κ	Maximum allowable load shedding at each stage
π	Maximum allowable change in SOC
$CW_{w,h}$ and $CV_{v,h}$	Wind farms and photovoltaic generation curtailment costs
$EM_{g,y,h}$	GHG emissions per kWh
$CG^{em}_{g,y,h}$	Costs of GHG emission licenses per ton
VOLL	Value of the lost load
ρ_k	Probability of scenarios
$AG_{i,g}$	Bus-generation incidence matrices
$AW_{i,w}$ and $AV_{i,v}$	Bus-wind and bus-photovoltaic farm incidence matrices
$AS_{i,s}$	Bus-ESS incidence matrices
$AD_{i,l}$	Bus-load incidence matrices
$SL_{i,j}{}^{\max}$	Capacity of transmission lines
V	Voltage magnitude (p.u.)
θ	Phase angle (rad)
G, B	Conductance and susceptance of transmission lines
η_{ch}, η_{dch}	Charging and discharging efficiencies of ESSs
δ	Phase angle difference in transmission lines
α_{sei}, f_{sei}	Coefficients for the solid electrolyte interphase model
$SoH_{s,y,h,k}$	State of health of ESSs
$E^{Rate}_{s,y,h,k}$	Installed capacity of ESSs
N	Number of cycles
f_d	General form of the linearized degradation model
ς	Cycle depth of charge
∂	Average SOC of all cycles
T_c	Average operation temperature of ESSs
M	Large enough constant
Y	Binary variable vectors
P	Positive continuous operational variable vectors
Z	Free continuous variable vectors
λ, μ, σ	Compact dual variable vectors
ξ	Uncertain vectors
I	Constant vector
Γ_D, Γ_W, Γ_V	Conservative parameters of DR, wind, and photovoltaic power
$CF(H, E)$	Intensity with which condition E supports conclusion H
$CF(E)$, $CF(H)$	Trustworthiness of condition E and conclusion H

C. Sets

r	Index for counting renewable sources
i, j	Index for buses

g	Index for counting conventional generations
w, v	Index for wind and photovoltaic farms
s	Index for counting energy storage systems
n, m	Indexes for linearization segments
l	Index for load
k	Index for scenarios
h	Index for the planning hour
y	Index for the representative year

frontiers | Frontiers in Energy Research

TYPE Original Research
PUBLISHED 30 July 2024
DOI 10.3389/fenrg.2024.1425197

OPEN ACCESS

EDITED BY
Yitong Shang,
Hong Kong University of Science and Technology, Hong Kong SAR, China

REVIEWED BY
Xiaolong Jin,
Technical University of Denmark, Denmark
Tao Jiang,
Northeast Electric Power University, China

*CORRESPONDENCE
Jinzhou Sun,
1094790979@qq.com

RECEIVED 29 April 2024
ACCEPTED 18 June 2024
PUBLISHED 30 July 2024

CITATION
Wang X, Zhang B, Li D, Sun J, Wang Y, Wang X, Liang Q and Tang F (2024), Research on data-driven, multi-component distribution network attack planning methods.
Front. Energy Res. 12:1425197.
doi: 10.3389/fenrg.2024.1425197

Research on data-driven, multi-component distribution network attack planning methods

Xueyan Wang[1], Bingye Zhang[1], Dengdiao Li[1], Jinzhou Sun[2,3]*, Yu Wang[1], Xinyu Wang[1], Qu Liang[1] and Fei Tang[2,3]

[1]Taizhou Power Supply Company State Grid Zhejiang Electric Power Co., Ltd., Hangzhou, Jiangsu, China, [2]School of Electrical and Automation, Wuhan University, Wuhan, China, [3]Hubei Engineering and Technology Research Center for AC/DC Intelligent Distribution Network, Wuhan, China

As the physical power information system undergoes continual advancement, mobile energy storage has become a pivotal component in the planning and orchestration of multi-component distribution networks. Furthermore, the evolution and enhancement of big data technologies have significantly contributed to enhancing the rationality and efficacy of various distribution network planning and layout approaches. At the same time, multi-distribution networks have also confronted numerous network attacks with increasing probability and severity. In this study, a Petri net is initially employed as a modeling technique to delineate the network attack flow within the distribution network. Subsequently, the data from prior network attacks are consolidated and scrutinized to evaluate the vulnerability of the cyber-physical system (CPS), thereby identifying the most critical network attack pattern for a multi-component distribution network. Following this, the defender–attacker–defender planning methodology is applied for scale modeling, incorporating rapidly evolving mobile energy storage into the pre-layout, aiming to mitigate the detrimental impact of network attacks on the power grid. Ultimately, the column and constraint generation (C&CG) algorithm is utilized to simulate and validate the proposed planning strategy in a 33-node system with multiple control groups established to demonstrate the viability and merits of the proposed strategy.

KEYWORDS

multi-component distribution network, cyber attack, DAD planning model, mobile energy storage, C&CG algorithm, data-driven

1 Introduction

With the rapid development of the global energy Internet, the distribution network has become an important part of the power system, and its operation safety is directly related to the stability and reliability of the power supply. However, with the rapid development of computers and communication technology, the traditional power system and information communication system are more and more closely combined, forming a fused power and information physical system known as a cyber-physical system (CPS). With the continuous upgrading of network attacks, the security problem of power networks is becoming increasingly prominent (Shelar and Amin, 2017). In order to cope with this challenge, this study aims to explore a multi-component distribution network planning method under power network attacks to improve the anti-attack capability and operational stability of the distribution network.

In recent years, many CPS studies have emerged. Based on the establishment of the CPS dependency model and the characterization of the coupling mechanism between them, Nguyen et al. (2013) studied and analyzed the factors affecting the vulnerability of distribution networks under network attacks. Gao et al. (2013) analyzed the interdependence and connection between power and information nodes. Through the communication process between the power system and the information system, Long et al. (2019) conducted network modeling to verify the relationship between the degree of system loss and the proportion of fault nodes in the network. Zhang et al. (2021) analyzed CPS modeling through a dependency network. However, most of the modeling processes above are mainly from a topological perspective, resulting in some differences between the final model and actual system characteristics. Currently, research on network attacks mostly focuses on large power grid information physical systems, with most information attacks concentrated in transmission grids. For example, Yu et al. (2016) verified that communication delay between AC and DC changes the optimization strategy of control centers in UHV systems. Cai et al. (2016) studied potential major failures (catastrophic failures) in different structural information networks under random or deliberate attacks. Based on the semi-Markov process, Lau et al. (2020) modeled SCADA systems and developed optimal mixed strategies for defense strategy allocation through competitive games. Yu et al. (2019) proposed a transfer model of the CPS system that integrates physical equipment and information decision making and realizes dynamic control of the transfer process by establishing an information control flow. Yi et al. (2016) analyzed, defined, and classified the network attacks suffered by CPS based on examples. At present, the network attack planning methods for distribution networks are relatively few. The influence of pre-layout defense measure configuration on network attacks is ignored, and defender–attacker–defender (DAD) planning is rarely taken into account in distribution network configuration planning.

Based on the above research background and research status, this article proposes a multi-component distribution network planning method that considers network attacks. First, vulnerability attacks under Petri net and power network attacks are used to analyze and obtain the vulnerability of distribution networks under network attacks, and with the help of data-driven (Stephane et al., 2022), the corresponding extreme scenarios are simplified and generated. Second, based on the DAD planning model, mobile energy storage is introduced for pre-layout in advance to reduce the cost of fault recovery. Third, the C&CG algorithm is used to analyze the three-layer, two-stage optimization problem of the DAD planning model. Finally, a 33-node IEEE system is tested and evaluated to verify the economy and effectiveness of the proposed method.

2 Power network attack modeling

2.1 Typical power network attack model

As the key infrastructure supporting the normal operation of society, the security and stability of the power network are very important (Yang et al., 2022). With the rapid development of computer and communication technology, traditional power systems and information and communication systems are more and more closely combined, forming a typical CPS. However, with the continuous evolution of the means of network attack, the threat to the power network is becoming more and more serious.

In the diversified and chain-oriented environment of network attacks, it is difficult for traditional methods to deal with random and highly interlocked attacks, mainly because it is difficult to describe dynamic attack and defense behaviors. The state of the whole system cannot be directly observed, which affects the selection of defense behaviors. Therefore, this article chooses a Petri net as the modeling method to describe the attack state and provides the basis for the subsequent defense strategy selection.

The elements of a Petri net include a library (Place) circular node, a Transition square node, a directed arc (Connection) that is the directed arc between a library and a transition, and a token (Token) that is a dynamic object in a library that can be moved from one library to another (Deka et al., 2014). Figure 1 shows a common network attack flow model.

When the actual transition probability and delay are determined, a Petri net can be equated with a Markov chain (MC) (Lin et al., 2005). At the same time, the trigger matrix data are easily obtained in the reachable graph. The analysis of system performance can have a very good effect. The specific method of obtaining trigger matrix parameters is as follows: a random Petri net is represented by a quadruple $SPN = (P, T, M_o, M_f)$, where M_o represents the initial mark, and M_f represents the final mark. The calculation formula of the trigger matrix is as follows in Eq. (1) (Amini et al., 2018):

$$\boldsymbol{M_f} = \boldsymbol{M_o} + \boldsymbol{C^T U_k}. \tag{1}$$

In this formula, C is the integration matrix, U_k is the trigger matrix, and the tag and integration matrix can be derived from the library and transition states.

2.2 Vulnerability analysis under power network attack

2.2.1 Analysis of vulnerability indicators

2.2.1.1 Critical damage degree index

With the development of information technology, the power system's dependence on the information network also increases. Therefore, security will be seriously threatened when network attacks occur. It is necessary to assess the vulnerability of the distribution network under network attacks (Dahmen et al., 2019). Widely used mainstream evaluation methods are based on complex network and transient energy functions and service transmission (Shahsanee and Zareei, 2018).

At present, vulnerability assessment of network nodes is mainly focused on the static condition, but when the network is running, the vulnerability index will change constantly. Zhou et al. (2024) put forward the concept of destructiveness to indicate the degree to which the network is on the verge of destruction when attacked in Eq. (2):

$$\boldsymbol{P_{ij}} = \begin{cases} \dfrac{\boldsymbol{t_{ij}}}{\boldsymbol{T_i}}, \ \boldsymbol{t_{ij}} < \boldsymbol{T_i} \\ \\ \boldsymbol{1}, \boldsymbol{t_{ij}} \geq \boldsymbol{T_i} \end{cases} \tag{2}$$

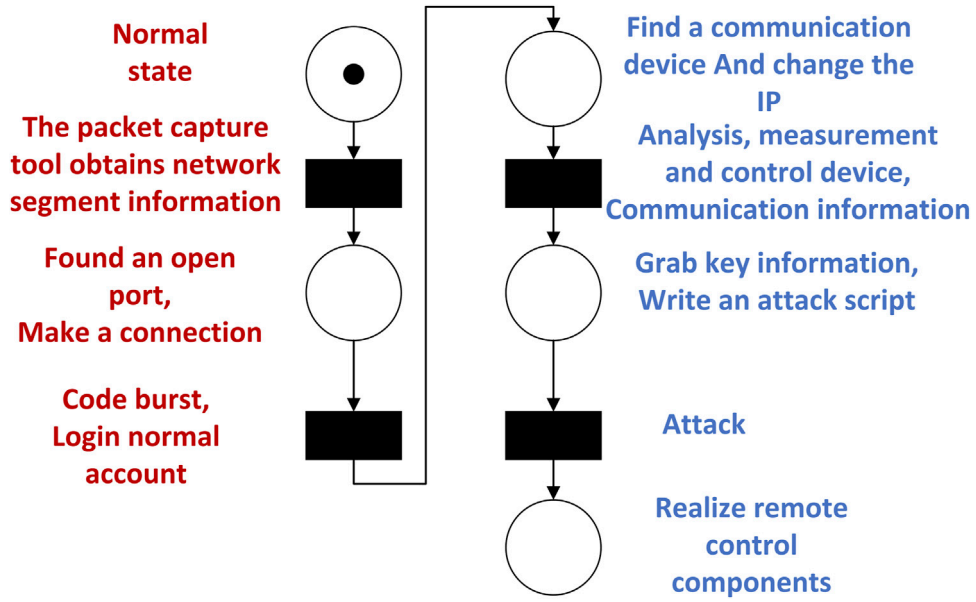

FIGURE 1
Common network attack flow model.

In this expression, P_i is the destructivity index and t_{ij} is the delay range of the *ith* service beside *j*. T_i is the ruin value of the Class i business.

For the case of multiple lines, according to the change of P_{ij}, the accuracy of vulnerability assessment is ensured by the following Eq. (3):

$$\mathbf{C_p}\left[\mathbf{E_p}\left(\mathbf{i},\mathbf{j}\right)\right] = \delta_t \sum_{j=1}^{i}\left(\frac{\mathbf{V_i}}{\sum_{j=1}^{i}\mathbf{V_j}}\mathbf{P_{ij}}\right). \tag{3}$$

In this formula, $C_p[E_p(i,j)]$is the vulnerability of the communication branch, $E_p(i,j)$ is the vulnerability value of the communication branch from Article i to Article j, δ_t is the actual delay of communication transmission, V_i is the traffic contained in the communication branch, and V_j is the transmission rate of Class *j* services on the communication branch.

2.2.1.2 Fault impact degree

When the distribution network is attacked and a fault occurs, the node will lose load. Therefore, the analysis must also consider the results caused by the failure of the distribution network and the shutdown of nodes (Nazemi et al., 2019).

In view of the fact that the distribution network is generally a radial network and operates in an open loop, the impact caused by node outage can be quantitatively analyzed Eqs 4,5:

$$\mathbf{S_{Ni}} = \omega_i \mathbf{P}\frac{\mathbf{S_i}}{\mathbf{S_B}}. \tag{4}$$

$$\boldsymbol{P} = \frac{\boldsymbol{\lambda}}{\boldsymbol{\lambda}+\boldsymbol{\mu}}. \tag{5}$$

In this formula, ω_i represents the load class weighting coefficient, P represents the node failure rate, and S_B represents the power reference value of the system. λ represents the failure rate, and μ represents the repair rate.

2.2.2 Assessment model of distribution network vulnerability

Considering the existence of static and dynamic indicators of the vulnerability of the distribution network, several nodes are selected from different levels of the distribution network for assessment. Different vulnerability assessment indicators are assigned according to the levels and importance of different nodes (Yan et al., 2015).

Because the existing distribution network is coupled by the power network and the communication network, the components are diverse, and the coupling relationship is complicated. The complex network theory can be used to model and analyze the distribution network. Among them, the bus and line in the power network are abstracted as nodes and edges. The relationships between intelligent terminal devices and communication nodes in a communication network are abstracted as nodes and edges. Based on this, the power–communication coupling network model of the distribution network shown in Figure 2 can be constructed.

The two types of nodes in the model, power node and communication node, have two operating states, namely, normal and fault. The model's running state can be expressed by setting the state variable in Eqs 6,7 (Guo et al., 2019).

$$\mathbf{f}/\mathbf{k_{x,n}} = \mathbf{f}/\mathbf{k_{x,ne}} + \mathbf{if}/\mathbf{k_{x,nc}} = \begin{cases} \mathbf{1} & \mathbf{x} \in \Omega_\mathbf{e} \\ \mathbf{i} & \mathbf{x} \in \Omega_\mathbf{c} \\ \mathbf{0} & \mathbf{x} \notin \Omega_\mathbf{e} \cup \Omega_\mathbf{c} \end{cases}. \tag{6}$$

$$\mathbf{f_{xy,1}} = \mathbf{f_{yx,1}} = \mathbf{f_{xy,le}} + \mathbf{if_{xy,lc}} = \begin{cases} \mathbf{1+i} & \mathbf{xy} \in \Omega_{\mathrm{Le}}, \mathbf{xy} \in \Omega_{\mathrm{Le}} \\ \mathbf{1} & \mathbf{xy} \in \Omega_{\mathrm{Le}}, \mathbf{xy} \notin \Omega_{\mathrm{Le}} \\ \mathbf{i} & \mathbf{xy} \notin \Omega_{\mathrm{Le}}, \mathbf{xy} \in \Omega_{\mathrm{Le}}. \\ \mathbf{0} & \mathbf{xy} \notin \Omega_{\mathrm{Le}}, \mathbf{xy} \notin \Omega_{\mathrm{Le}} \end{cases} \tag{7}$$

In this formula, $f_{x,i}$ represents the initial, power, and communication operating states of nodes, respectively; $k_{x,i}$ represents the actual, power, and communication operating states of nodes; $f_{xy,i}$ is the overall status of line xy, the power line and the communication line, respectively; Ω_e、Ω_c、*and* Ω_v is the set of

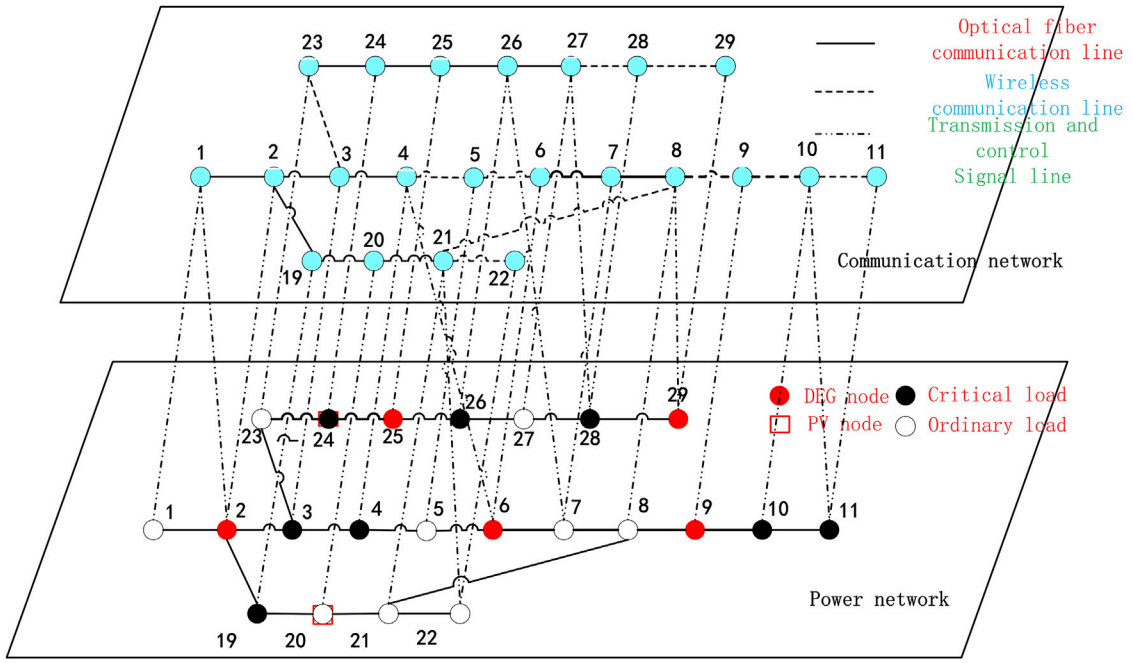

FIGURE 2
Power-communication coupling network model of distribution network.

power, communication, and effective operation nodes, respectively; and Ω_{Le}、Ω_{Lc}、*and* Ω_{Lv} is the set of power, communication, and effective operation lines, respectively.

In the power–communication network, M nodes are extracted, where $M = \{m_1, m_2, m_3, ..., m_n\}$. If there is a path between the nodes, the coefficient k is 1, and otherwise 0. Static vulnerability assessment indicators are defined as Eq. 8

$$\boldsymbol{N}(\boldsymbol{M_i}) = \boldsymbol{\varepsilon_1 P_{ij}}(\boldsymbol{m_i}) + \boldsymbol{\varepsilon_2 N}(\boldsymbol{m_i}). \tag{8}$$

In this formula, $N(M_i)$ is the static vulnerability assessment index, a is the weight of each static factor, and $P_{ij}(m_i)$ is the destructivity index of the m_i node. $N(m_i)$ indicates the pressure indicator of the service layer. As can be seen from the above formula, the static vulnerability assessment index is a constant.

The dynamic vulnerability assessment index is defined as Eq. 9

$$\boldsymbol{N_{vi}}(\boldsymbol{M_i}) = \frac{\boldsymbol{1}}{\boldsymbol{N}(\boldsymbol{M_i}).} \tag{9}$$

Based on the above formula, the vulnerability assessment model is constructed, and the expression is as follows Eq. 10:

$$\begin{aligned} \boldsymbol{M'} &= \sqrt{\frac{\boldsymbol{1}}{\boldsymbol{N}} \sum_{\boldsymbol{m_i \in M}} \left(\boldsymbol{N}(\boldsymbol{M_i}) - \overline{\boldsymbol{N}(\boldsymbol{M_i})}\right)^2}. \\ &+ \sqrt{\frac{\boldsymbol{1}}{\boldsymbol{P}} \sum_{\boldsymbol{m_i \in M}} \left(\boldsymbol{N}(\boldsymbol{M_i}) - \overline{\boldsymbol{N}(\boldsymbol{M_i})}\right)^2} \end{aligned} \tag{10}$$

In this formula, M' is the expression of the vulnerability assessment model, N is static loss, and P is dynamic loss. The loss of power service when the network is attacked is judged according to the change of the M' value to realize the effective assessment of the vulnerability of the power–communication network.

2.3 Power network attack scenario generation

Before vulnerability assessment, different network attack modes need to be analyzed; that is, attack scenarios need to be generated. In this article, the K-means clustering algorithm (Hagh et al., 2018) is used to reduce the typical M_{s0} attack scenarios obtained from previous network attack data to a typical scenario set containing M_d attack scenarios, in which the ith sample is represented as $\lambda_i = [\nu_i, T_{st,i}, T_{dr,i}]$. The specific steps to reduce the attack scenario are as follows:

Step 1: In M_{s0} samples, randomly select $K(K = M_d)$ initial cluster centers $(\lambda_1, \lambda_2, \ldots, \lambda_K)$;

Step 2: Calculate the Euclidean distance between each sample λ_i and the cluster center, and aggregate each sample with the nearest cluster center to form K cluster samples;

Step 3: Calculate D_{km}, the sum of the distance between the sample and the respective clustering center, according to the following formula and iteratively update the contents of the K cluster sample in Eq. 11.

$$\mathbf{D}_{\boldsymbol{km}} = \sum_{i=1}^{K} \sum_{z \in Y_i} \| \mathbf{z} - \lambda_i \|_2^2. \tag{11}$$

In this formula, z and λ_i are the noncentral samples and the central samples of cluster Y_i, respectively.

Step 4: Calculate the iteratively updated K clustering centers according to the following formula (12):

$$\lambda_i = \frac{1}{Y_i}\sum_{z\in Y_i} z. \tag{12}$$

Step 5: Repeat steps 2 to 4 until the maximum number of iterations is reached or convergence conditions are met;

Step 6: Calculate the probability distribution of the final K samples according to the Eq. 13.

$$P_d = \frac{|Y_i|}{M_{s0}}. \tag{13}$$

In this formula, $|Yi|$ is the number of samples contained in cluster Yi.

The probability density of the ith scenario after clustering is P_{di}, and its cumulative probability distribution F_{di} is shown in the following Eq. 14.

$$F_{dt} = \sum_{k=1}^{i} P_{dk}\,(i = 1, ..., M_d). \tag{14}$$

Similar to the determination of line fault state p_l, the non-sequential Monte Carlo simulation method can also be used to generate uniformly distributed random numbers x_d in the interval [0, 1] and randomly select attack scenarios for the subsequent resilience assessment process. When $F_{d(i-1)}<x_d < F_{di}$, it indicates that scenario i is selected. A set of samples$[v_i, T_{st,i}, T_{dr,i}]$ can be obtained, and the fault scenario can be further generated according to the parameters of extreme events.

3 Multi-grid distribution network model and toughness analysis

3.1 Distribution network model construction

3.1.1 Construction of the renewable energy output model

With the development of global renewable energy, growing renewable energy in multiple distribution networks is increasingly important, followed by the network attack probability. The attackers may be aimed at the control system of renewable energy itself and may also use the renewable energy system as a springboard through the data exchange system to attack multiple distribution networks. Therefore, renewable energy must also be included in the construction of the network attack model. Considering the proportion and representativeness of renewable energy in the grid, wind power and photovoltaic are selected to construct renewable energy output models in this article.

3.1.1.1 Wind power

In general, the probability density of the wind speed conforms to the Weibull distribution (Eq. 15):

$$f_F(v) = \frac{k}{c}\left(\frac{v}{c}\right)^{k-1} e^{-\left(\frac{v}{c}\right)^k}. \tag{15}$$

Among them, k and c are, respectively (Eq. 16):

$$\begin{cases} k = \left(\dfrac{\sigma}{\mu}\right)^{1.086} \\ c = \dfrac{\mu}{\Gamma\left(1+1/k\right)}. \end{cases} \tag{16}$$

In this formula, σ is the standard deviation of wind speed in statistical time, and μ is the expected wind speed in statistical time. Γ is a gamma function.

The output power of the fan is related to the size of the wind speed and the power characteristics of the fan itself. The output power is (Eq. 17) (Nan et al. (2022):

$$P_{wind}(v) = \begin{cases} 0, v \le v_{ci}, v > v_{co} \\ k_1 v + k_2, v_{ci} < v < v_r. \\ P_r, v_{ci} \le v \le v_r \end{cases} \tag{17}$$

In this formula, v_{ci} and v_{co} are the cut-in wind speed and cut-out wind speed of the fan, v_r is the rated wind speed of the fan, P_r is the rated output power of the fan, and k_1 and k_2 are constants.

3.1.1.2 Photovoltaic

The output of distributed photovoltaics is directly related to the magnitude of the light intensity. However, due to the intermittent type and uncertainty of the light intensity, the photovoltaic output will also change with the light intensity. Overall, the photovoltaic output power is P_{PV}. The probability density curve can be approximated by a beta distribution (Eq. 18):

$$f(P_{PV}) = \frac{\Gamma(\alpha+\beta)}{\Gamma(\alpha)\Gamma(\beta)}\left(\frac{P_{PV}}{P_{M\pi}}\right)^{\alpha-1}\left(1-\frac{P_{PV}}{P_{M\pi}}\right)^{\beta-1}. \tag{18}$$

In this formula, $P_{\max}$ indicates the maximum output power of the photovoltaic power supply. α and β are the two parameters of the beta distribution probability density function, respectively, which can be calculated by calculating the average light intensity μ and the variance σ of the light intensity within a day.

3.1.2 Typical load model construction

Saccentie et al. (2019) proposed a way of fitting a normal distribution curve based on the analysis of extensive data, taking the expectation of a normal distribution curve as a typical load curve.

Using a large amount of power grid load data, the load data at the same time on different days are fitted to a normal distribution, and, finally, the expectation of normal distribution at each time is taken as the load value at that time of the typical day. The load data at the same time on different days were fitted by maximum likelihood estimation by calculating the load value of 24 periods to the final fitted typical day, and the fitted data were calculated (Eqs 19,20):

$$L(\theta_i) = L(x_{i1}, x_{i2}, \cdots, x_{ia}\,; \theta_i) = \prod_{a=1}^{n-b_i} f(x_{ia}\,; \theta_i). \tag{19}$$

$$E(x_i) = \int x_i f(x_i) dx_i. \tag{20}$$

In this formula, x_{ia} indicates the load remaining after duplicate data are removed from the same period on different days. θ_i is the unknown quantity to be estimated, a represents the ath load value in the sample at time i, and b_i indicates the number of repeated load

values in period *i*. Represents the formula E(xi) expectation for period *i*, and x_i represents the argument of the normal distribution function for the *ith* period.

3.1.3 Energy storage equipment, model construction

The output of new energy units, such as wind power and photovoltaic, in the distribution network is often intermittent and uncertain. Access to energy storage equipment can suppress the output power of new energy, improve the power absorption capacity of the distribution network, and bring certain economic benefits (Nan et al., 2022).

The energy storage system is equivalent to connecting the distributed power supply to some nodes during some operating periods and connecting with different power loads during other periods. That is, the energy storage absorbs active power when charging and emits active power when discharging (Eq. 21):

$$\begin{cases} SOC(t+\Delta t) = SOC(t) + \dfrac{P_c(t+\Delta t)\eta_c \Delta t}{E}. \\ SOC(t+\Delta t) = SOC(t) + \dfrac{P_d(t+\Delta t)\Delta t}{E\eta_d} \end{cases} \tag{21}$$

In this formula, *SOC(t)* represents the SOC value of the energy storage system at time t, *Pc* and *Pd* represent the absorption and emitted power of the energy storage, *ηc* and *ηd* represent the efficiency of the absorption and emitted power of the energy storage system, and *Δt* represents the capacity of the energy storage system and the duration of charge and discharge.

3.2 DAD planning model construction

The DAD model is suitable for the development of defense plans for important infrastructure, including power systems. Generally, the interactive concept of attack and defense in traditional DAD planning models can be divided into the following three layers:

(1) System planning layer: Defenders of this layer need to consider all possible attack scenarios in advance and analyze and classify these scenarios to facilitate the development of defensive measures against these possible attacks to reduce the losses caused by attacks. Common countermeasures can include strengthening the hardened target and adding backup equipment and smart equipment, *etc.*, to minimize the system loss caused by the attack.

(2) System damage layer: Attackers in this layer usually develop unique attack methods and approaches for these advanced layout defense measures after knowing the measures formulated by the system planning layer and try to identify the worst and most serious attack scenarios so as to cause the greatest loss to the system.

(3) System operation layer: after completing the pre-layout defense, the defender of this layer takes some recovery measures to deal with the attack after the attacker carries out the worst attack in order to minimize the system loss. Common recovery measures include load cutting, putting energy storage devices or standby devices in use, and isolating faulty or infected devices to minimize subsequent losses and impact on system operation.

In short, the purpose of the defender is to minimize the system loss, while the purpose of the attacker is to maximize the system loss.

4 Building and solving a DAD model of distribution network considering a network attack

4.1 Model construction under a network attack

Compared with the traditional distribution network, much energy storage equipment is connected to the current multiple distribution network. When the network attack receives faults or fluctuations, energy storage can be an important resource in the planning of the distribution network DAD. The DAD planning model of a multi-distribution network considering the participation of energy storage under network attack is shown in Figure 3.

The first layer in the figure is the system planning layer. This article proposes the coordination measures of "line reinforcement and energy storage configuration" that can operate with energy storage in distant and important load disasters to reduce the investment cost of grid prevention and minimize the load loss in the distribution network emergency response. The second layer is the disaster attack layer, from the perspective of the attacker, and the third layer of system operation minimizes the load loss in the emergency response determined in the second layer.

4.2 Model solution algorithm and steps

The DAD planning model for energy storage configuration established in this article is a three-layer and two-stage optimization problem, which has the same mathematical form as the two-stage adaptive robust optimization model, namely, the three-layer and two-stage structure of min–max–min. Generally, most existing studies use the Bender decomposition and the C&CG algorithms to solve such problems. Compared with the Bender decomposition algorithm, the C&CG algorithm has stronger convergence and solution power (Nan et al., 2022). Therefore, the C&CG algorithm is used.

4.2.1 C and CG, the algorithm for solving

According to the DAD planning model constructed in Section 3.1, the following matrix is listed (Eq. 22):

$$\begin{cases} \min_X \max_{u\in U_x} \min_{V\in\Theta(X,u)} b^T Y \\ \Theta(X,u) = \begin{cases} s.t. AX \le a \\ Y \mid MY \ge NX, KY = u, \\ \| J_m Y \|_2 \le f_m^T Y, m = 1,2,\ldots,n \end{cases} \end{cases}. \tag{22}$$

In this formula, *X* is the optimization variable in the first stage, *u* is the optimization variable in the second stage, which belongs to an uncertain set *Us*, and *Y* is the optimization variable of the running

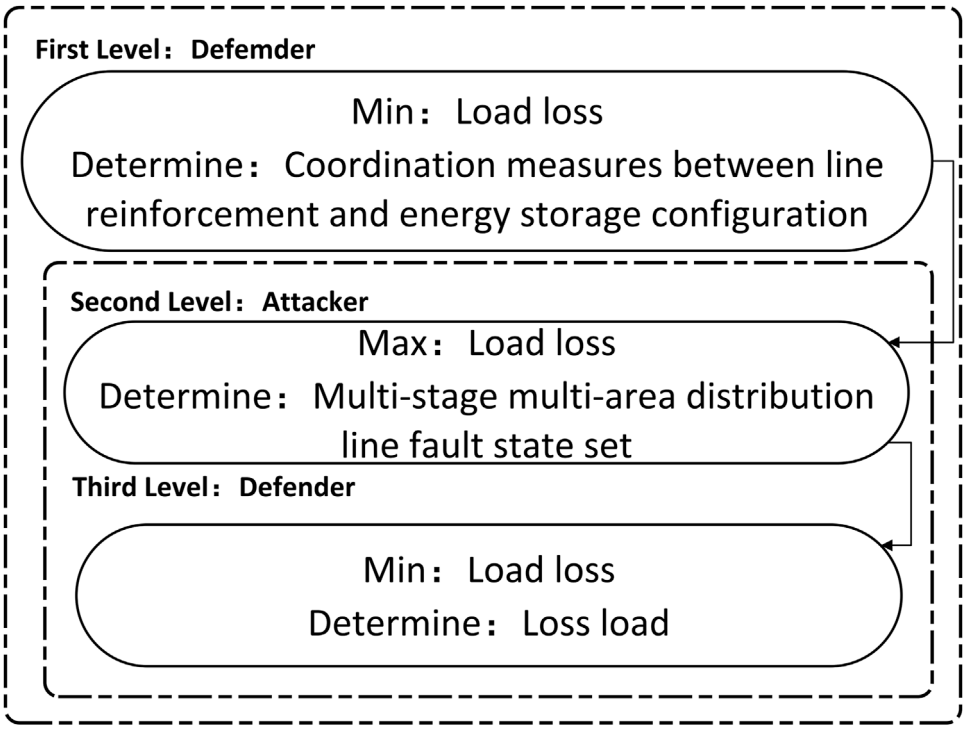

FIGURE 3
DAD planning model considering energy storage.

layer in the second stage. *A*, *M*, *N*, *K*, and J_m are the constant coefficient matrix. *a*, *b*, and f_m are the constant coefficient vector.

According to the application scope of the DAD planning model 1 and the C&CG algorithm constructed above, when using the C&CG algorithm, the solution is necessary to assemble the established model into the main problem (MP) and the subproblem (SP) in advance.

In the DAD planning model of resilient distribution network established in this article (Yang et al., 2024), pre-disaster planning measures need to be formulated for the main problem, that is, to solve the coordinated measures x_1 *and* x_2 of line reinforcement and energy storage configuration under the given distribution line fault state scenario u_l (Eq. 23):

$$\begin{cases} \boldsymbol{min}_{x,\varphi} \boldsymbol{F} \\ \boldsymbol{s.t.AX} \le \boldsymbol{a} \\ \boldsymbol{F} \ge \boldsymbol{b}^T \boldsymbol{Y}_i \\ \boldsymbol{MT}_i \ge \boldsymbol{NX} \\ \boldsymbol{KY} = \boldsymbol{u}^? \\ \| \boldsymbol{J}_m \boldsymbol{Y}_i \|_2 \le \boldsymbol{f}_m^T \boldsymbol{Y}_i, \boldsymbol{m} = \boldsymbol{1}, \boldsymbol{2}, ..., \boldsymbol{n} \end{cases} . \tag{23}$$

In this formula, *F* is the main goal of the problem, *i* is the number of iterations, and all the variables with subscripts *i* in the formula are the variables obtained by the *ith* iteration.

The purpose of the subproblem (SP) is to find the distribution network fault state scenario with the greatest loss. That is, in the case that the optimal solution x_1^*、 x_2^* of MP is given, the worst fault scenario *u* is obtained (Eq. 24):

$$\max_{u \in U_s} \min_{Te\Theta(X',n)} \boldsymbol{b}^T \boldsymbol{Y}. \tag{24}$$

Following Zhang et al. (2020), this article adopts the strong duality theory to transform the inner min form of the subproblem into the max form and combine the outer problem into a single-layer optimization problem (Eq. 25).

$$\begin{cases} \min_{u,\eta,\xi,\mu_n,\sigma_n} (\boldsymbol{MX}^*)^T \boldsymbol{\eta} + \boldsymbol{u}^T \boldsymbol{\xi} \\ \boldsymbol{s.t.} \boldsymbol{M}^T \boldsymbol{\eta} + \boldsymbol{K}^T \boldsymbol{\xi} + \sum_{m=1}^{n} (\boldsymbol{J}_m^T \boldsymbol{\mu}_m + \boldsymbol{f}_m \boldsymbol{\sigma}_m) = \boldsymbol{b}. \\ \| \boldsymbol{\mu}_m \|_2 \le \boldsymbol{\sigma}_m \\ \boldsymbol{\eta} \ge \boldsymbol{0} \end{cases} \tag{25}$$

In this formula, η、ξ、μ_m、σ_m is the variable after dual processing. The above formula contains a non-convex bilinear term, $u^T\xi$, so ρ_i, a 0–1 integer variable, is introduced to represent the strongest attack and the weakest attack on the distribution network. When ρ_i is set to 1, the distribution network suffers the strongest attack, and when ρ_i is set to 0, the distribution network suffers the weakest attack. The linearization process is as follows (Eq. 26):

$$\boldsymbol{u}^T \boldsymbol{\xi} = \sum \boldsymbol{u}_i \boldsymbol{\xi}_i = \sum [\boldsymbol{u}_{i,min} \boldsymbol{\xi}_i + (\boldsymbol{u}_{i,max} - \boldsymbol{u}_{i,min}) \boldsymbol{\rho}_i \boldsymbol{\xi}_i]. \tag{26}$$

In this formula, u_i and ξ_i are the elements in sets u and ξ, respectively, and $u_{i,\max}$ and $u_{i,\min}$ represent the attacks that cause the most and least damage to the distribution network, respectively. $\rho_i\xi_i$ is relaxed by the big-M method. The relaxation process is as follows (Eq. 27):

$$\begin{cases} -\boldsymbol{M}\boldsymbol{\rho}_i \le \boldsymbol{w}_i \le \boldsymbol{M}\boldsymbol{\rho}_i \\ -\boldsymbol{M} \backslash (\boldsymbol{1} - \boldsymbol{\rho}_i) + \boldsymbol{\xi}_i \le \boldsymbol{w}_i \le \boldsymbol{M}(\boldsymbol{1} - \boldsymbol{\rho}_i) + \boldsymbol{\xi}_i. \end{cases} \tag{27}$$

In this formula, w_i is an intermediate variable, and *M* is a positive integer with a relatively large value. After the above conversion, the

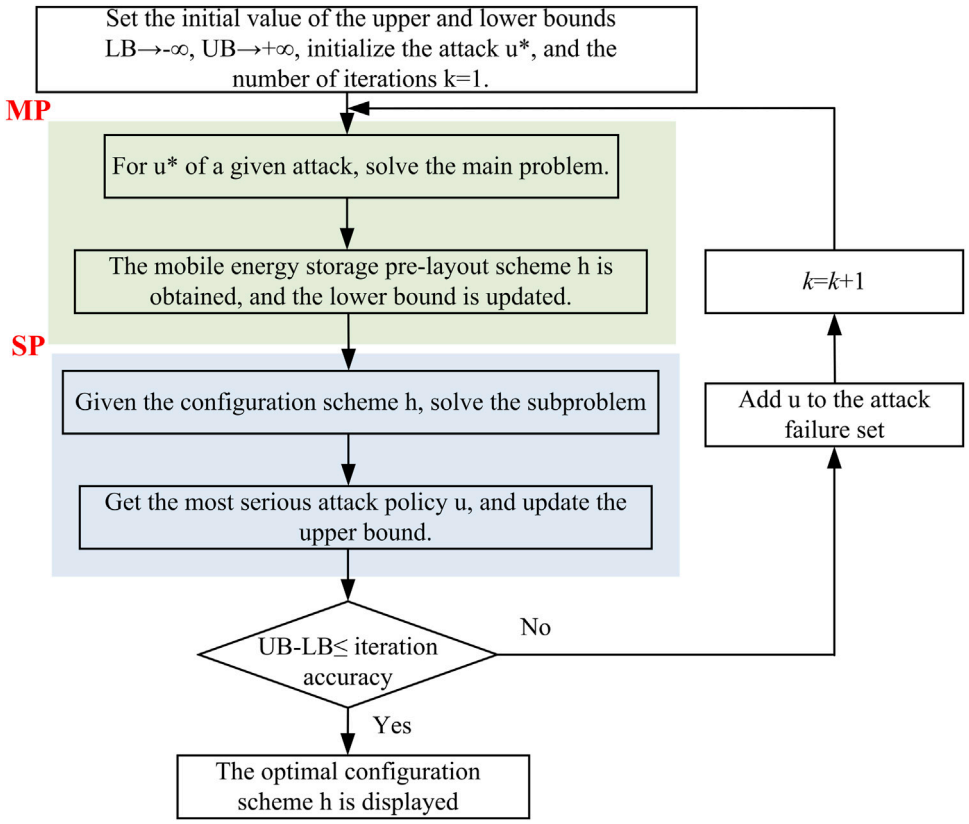

FIGURE 4
C&CG algorithm solution process.

problem is converted into a convex and linear problem, which is easy to solve.

The specific solution process is shown in Figure 4.

5 Example analysis

5.1 Simulation process and environment configuration

Based on the above analysis, the specific process of DAD planning of the multi-distribution network for network attacks is shown in Figure 5.

As shown in the figure, the corresponding Petri net attack model is first constructed according to common network attacks and converted into the corresponding MC matrix to facilitate the subsequent calculation of power grid vulnerability and vulnerable nodes. The vulnerable nodes when network attacks occur are determined by calculating the ruin degree of each node and the MC matrix determined above, and on this basis, the fault scenario for the weak nodes under network attacks in the multi-component power grid is generated.

Considering the generation process of network attack scenarios in the distribution network established in Section 1, after analysis and in combination with the literature [19], the network attack mode in this article will attack nodes in the system and deliberately attack nodes with the most vulnerable analysis results to enhance the effectiveness of attacks and the severity of consequences. At the same time, considering that both power nodes and communication nodes exist in the physical fusion system of power information and considering the inter-network failure probability when the two types of nodes fail, this article chooses to directly attack the power nodes because, in the case of the same inter-network failure probability, continuous attacks on power nodes are more likely to cause chain failures (Wang et al., 2018).

DAD is a three-layer planning model, so it is necessary to plan the first defense layer before carrying out network attacks. Coordination measures for line reinforcement, including energy storage, are taken in this article. After network attacks, corresponding measures are taken for damage and attacks so as to minimize load loss to the greatest extent.

5.2 Simulation results

The simulation in this article is carried out under IEEE33 nodes. The specific node configuration and wiring are shown in Figure 6. Among these nodes, 2, 6, 9, 25, and 29 are DEG nodes, and 3, 4, 6, 10, 11, 15, 17, 19, 24, 26, 28, and 33 are important loads; 13, 18, 20, 24, and 33 are PV nodes. The remaining parts are ordinary load nodes.

The main objective is to reduce the cost of the overall pre-layout and ensure as few island nodes as possible after the fault branch is disconnected. Each unit cost is shown in Table 1.

Based on the model established above, this article sets the following scenarios for verification and comparison:

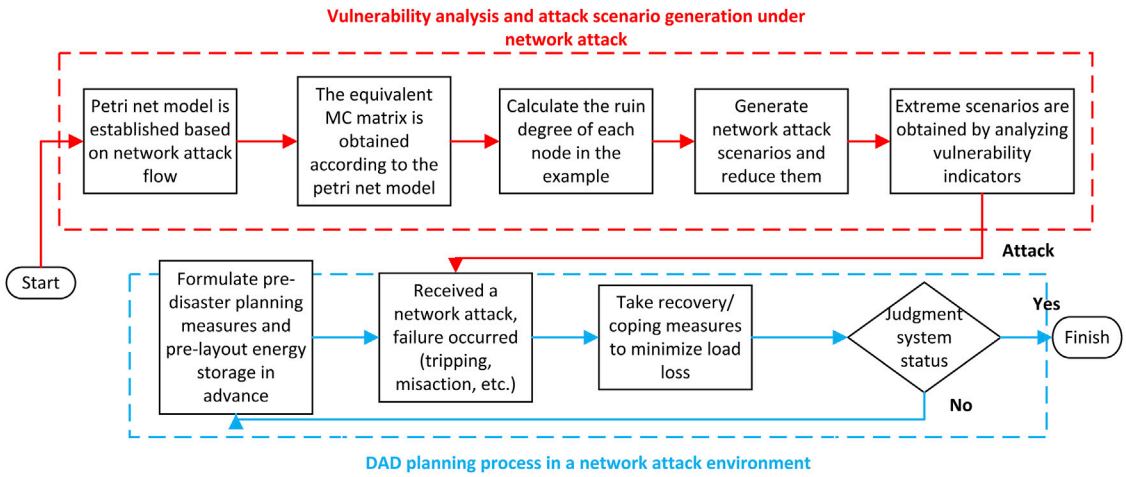

FIGURE 5
DAD planning process under network attacks.

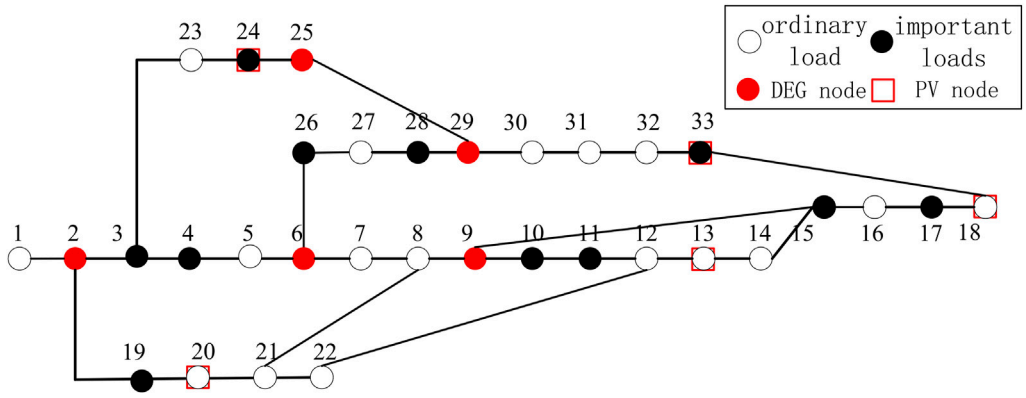

FIGURE 6
33 Node distribution.

1) A pre-layout robust optimization planning model considering energy storage coordination participation;
2) A robust optimization planning model considering energy storage coordination participation;
3) A pre-layout deterministic optimal planning model considering energy storage coordination participation;
4) A deterministic optimal planning model considering energy storage coordination participation.

Under the above scenario, the pre-layout cost of various optimization planning models and the node wiring situation after failure are shown in Figure 7.

The figure shows the sum of the various costs in each of the four cases, that is, whether pre-layout is performed and whether robust or deterministic optimization is used. In the figure, the two columns on the left show the impact of pre-layout on cost when robust optimization is adopted. It can be seen that the cost of the scheme with pre-layout is lower than that without pre-layout. On the right is the cost situation under the condition of deterministic optimization. The pre-layout has obvious advantages, and the cost will be reduced by approximately 15%–20%. For the same pre-layout scheme, robust optimization and deterministic optimization also have a certain impact on the cost, as shown in the blue columns in the figure. A comparison indicates that under the premise of the same pre-layout, the robust optimization method has a lower cost than the deterministic optimization method, and the cost can be reduced by approximately 10%. Based on the above simulation results, we can find that the pre-layout and robust optimization methods have better effects and more advantages for cost control.

Figures 8–11 show the cable connections between nodes after faults in the four scenarios.

In view of the introduction of energy storage coordination and participation in the previous DAD planning model, the impact of the addition of energy storage equipment on the overall layout cost and

TABLE 1 Unit costs.

Unit	Preconfigured energy storage	Load reduction	Important load cuts
Cost/10^3 yuan	500	1	10

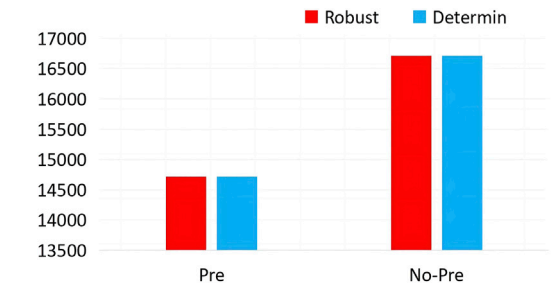

FIGURE 7
Cost/thousand yuan under each simulation scenario.

line operation status is verified in the simulation. The main scenarios are as follows:

1) The pre-layout robustness optimization planning model considering the participation of energy storage coordination;

2) The pre-layout robustness optimization planning model without considering the participation of energy storage coordination.

In the above scenario, the cost and failure of the node distribution of each scheme are shown in Figures 12, 13 and Table 2.

From the above simulation results, it can be observed that before energy storage is taken into account, the overall layout cost and fault recovery cost are approximately 8085.7 thousand yuan. When mobile energy storage is introduced, the overall cost is reduced to 5,085.8 thousand yuan, a reduction of approximately 40%. In addition, on the premise of fault recovery and line connection operation, comparing Figures 12, 13 indicates that when energy storage is involved, the number of islands composed of three or fewer nodes is three, including one of the important users, and one island is equipped with mobile energy storage, which can be temporarily used as power supply. When energy storage is not considered, the corresponding number of islands is four, including one important user, and there is a DEG node disconnected from the network.

It can be seen that the participation of energy storage has a better effect on the operation of the distribution network after the failure. The main reason for the 60% overall layout cost reduction caused by energy storage participation is that when energy storage is not considered and the network is attacked, the layout mode without energy storage will cause more important load nodes to disconnect, thus increasing the cost. At the same time, the number of island nodes is large, which affects the normal operation of the network. This fully proves the effectiveness and superiority of energy storage coordination participation.

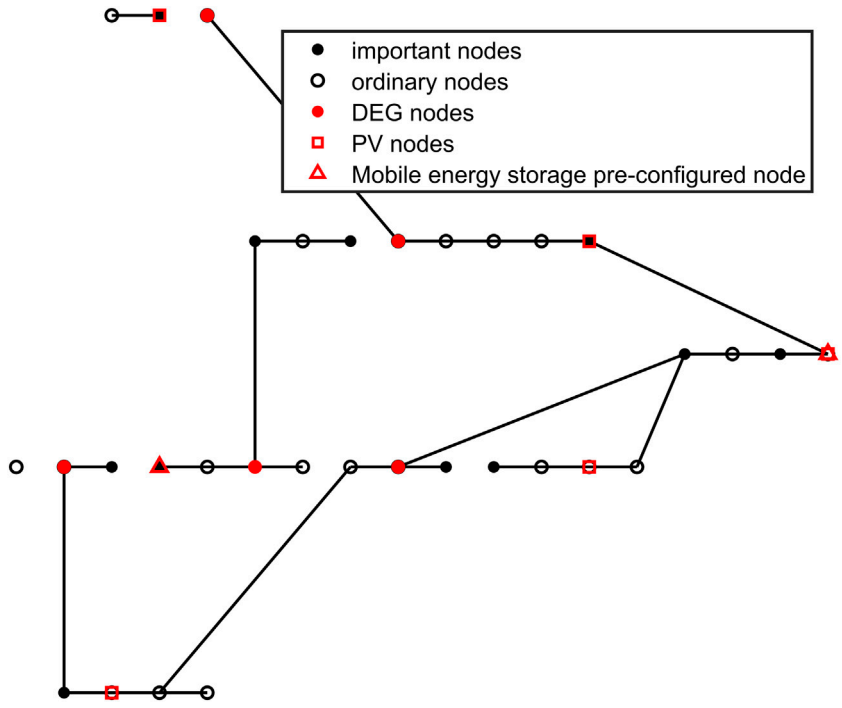

FIGURE 8
Pre-layout robustness optimization.

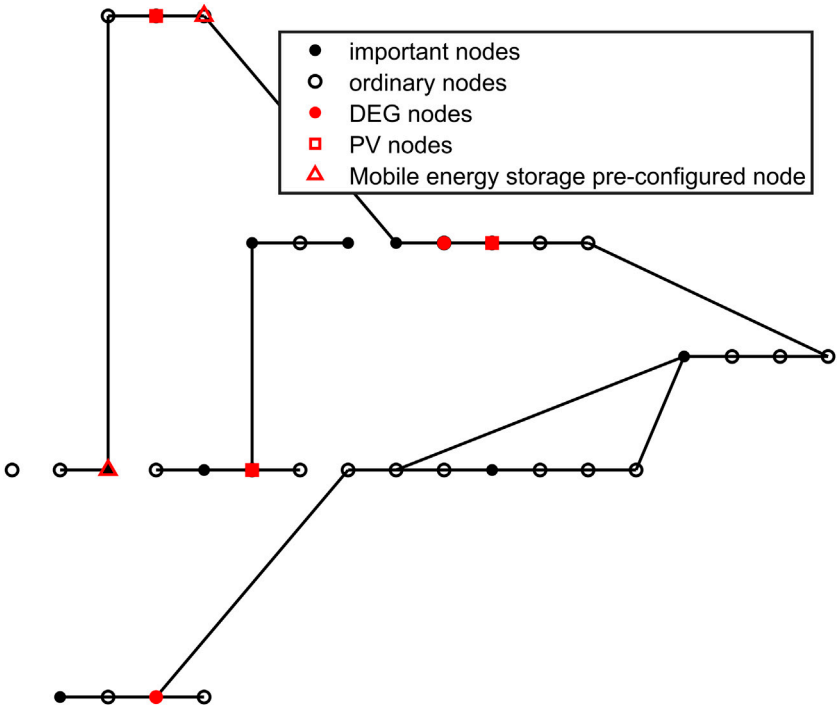

FIGURE 9
Pre-layout deterministic optimization.

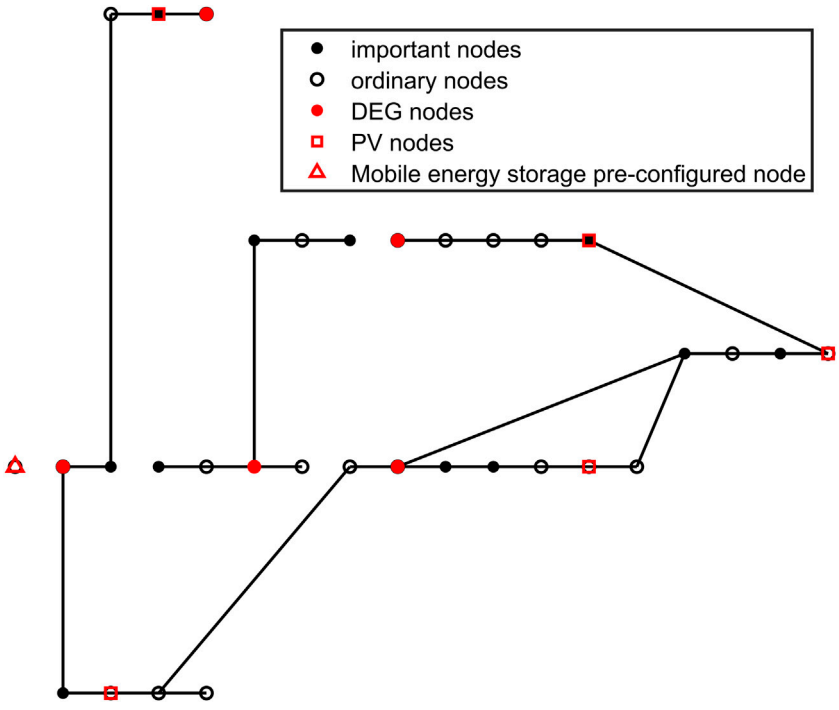

FIGURE 10
Robust optimization without prelayout.

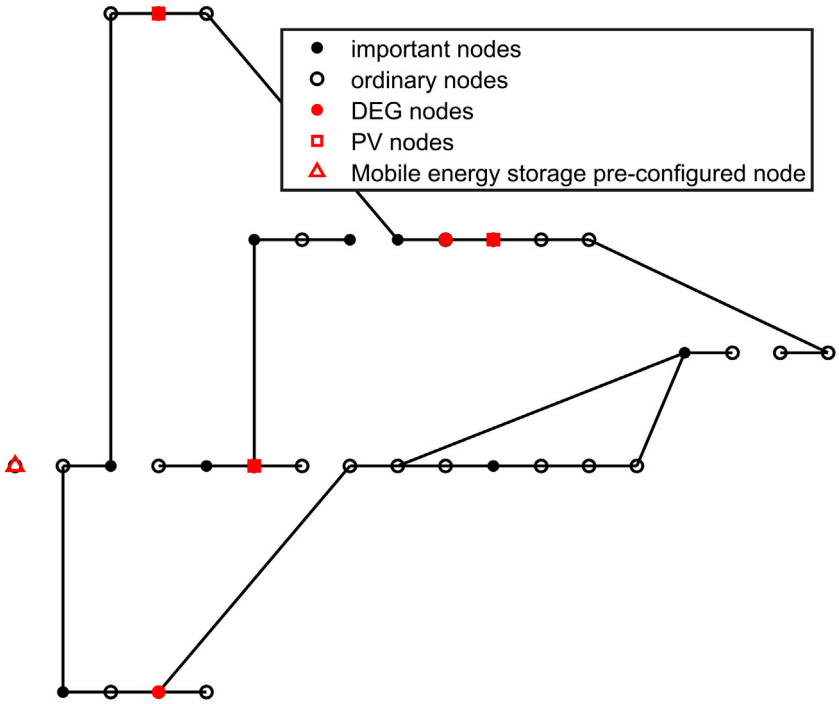

FIGURE 11
Deterministic optimization without prelayout.

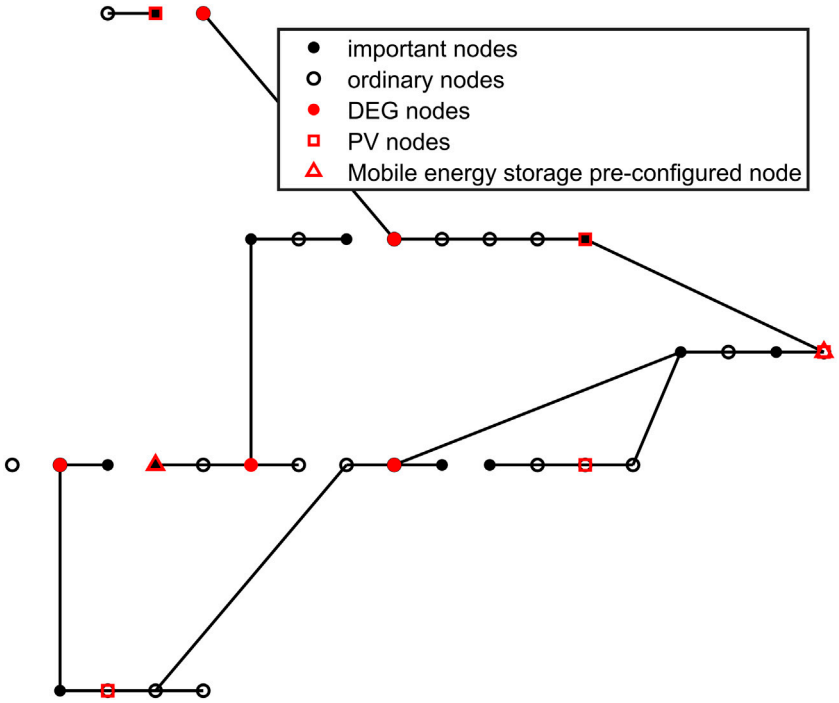

FIGURE 12
Robust optimization of prelayout considering the participation of energy storage.

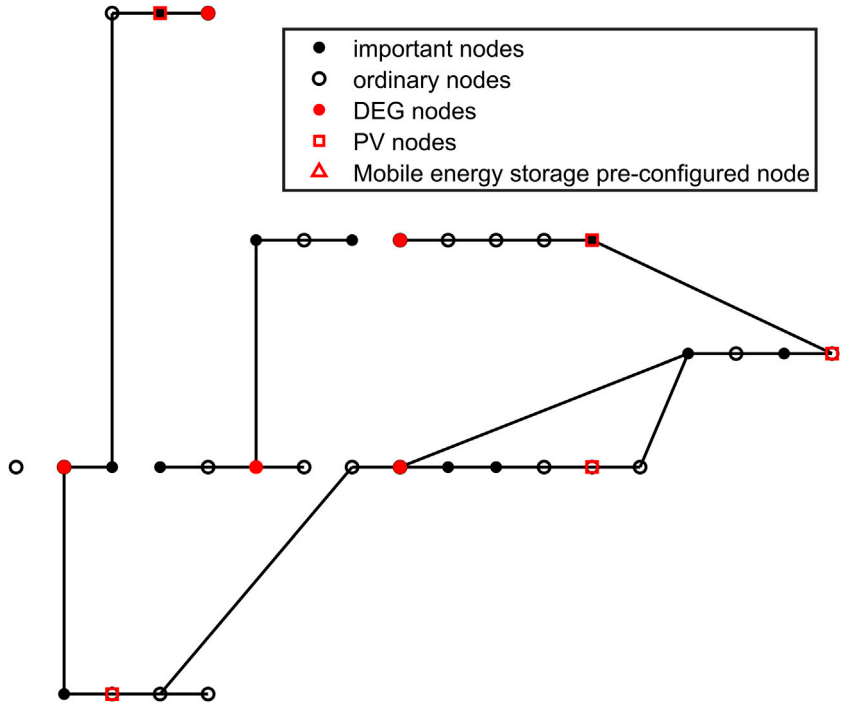

FIGURE 13
Prelayout robust optimization without energy storage participation.

TABLE 2 Overall layout cost of each scenario.

Scene	Consider energy storage	Energy storage is not considered
Cost/10^3 yuan	5085.8	8085.7

6 Conclusion

In the context of the integration of traditional power systems with information and communication systems, resulting in a distinctive power information physical fusion system, this article delves into and validates the influence of a DAD planning model that incorporates mobile energy storage coordination on the layout cost and line operation of a multi-distribution network in the event of network attacks. The key contributions of this work are as follows:

1. First, a common network attack flow model is built using a Petri net model, which is transformed and simplified with a matrix. On this basis, considering the vulnerability of the multi-distribution network under network attacks, two parameters, namely, the degree of failure and the degree of failure impact, are introduced to analyze the vulnerability strength of each node in the power-communication network under network attacks. The network attack scenario of the multi-distribution network is simulated and simplified with the help of big data from previous network attack scenarios.
2. Characteristic analysis and model construction are carried out for wind power, photovoltaic, and mobile energy storage that frequently appear in current multi-component distribution networks. At the same time, on the basis of the traditional DAD planning model, mobile energy storage is introduced into the planning to complete the DAD planning model construction under network attacks. In this article, the C&CG algorithm is used to solve the three-layer, two-stage problem of the DAD planning model, and the specific solving steps and flow chart are given.
3. Based on the DAD planning model proposed above, a robust pre-layout optimization planning scheme considering the participation of mobile energy storage is proposed in order to reduce the cost required for adjustment after failure and improve the operation condition. To verify the effectiveness and superiority of the scheme, a control group is also set up according to whether pre-layout is carried out and whether robustness optimization or deterministic top optimization is adopted. A control group was set to determine whether mobile energy storage participated in the pre-layout robustness. The simulation results are verified in a 33-node system.

Finally, according to the simulation results, it is concluded that a DAD planning pre-layout in advance and robust optimization methods have certain effects on cost reduction, and their effects can be superimposed. On the basis of the robustness optimization method of pre-layout, the introduction of coordinated control of mobile energy storage has a significant effect on cost reduction, which proves its effectiveness and superiority.

Data availability statement

The original contributions presented in the study are included in the article/Supplementary Material; further inquiries can be directed to the corresponding author.

Author contributions

XuW: conceptualization, visualization, and writing–review and editing. BZ: data curation, validation, and writing–review and editing. DL: formal analysis, supervision, and writing–review and editing. JS: conceptualization, funding acquisition, and writing–original draft. YW: investigation, project administration, and writing–review and editing. XiW: data curation, investigation, and writing–review and editing. QL: investigation, methodology, and writing–review and editing. FT: conceptualization, funding acquisition, and writing–review and editing.

Funding

The author(s) declare that financial support was received for the research, authorship, and/or publication of this article. This research was funded by Taizhou Hongchuang Power Group Co., LTD., Science and Technology branch. (SGTYHT/20-JS-224).

Conflict of interest

Authors XuW, BZ, DL, YW, XiW, and QL were employed by Taizhou Power Supply Company of State Grid Zhejiang Electric Power Co., Ltd.

The remaining authors declare that the research was conducted in the absence of any commercial or financial relationships that could be construed as a potential conflict of interest.

The authors declare that this study received funding from Taizhou Hongchuang Power Group Co, LTD. Science and technology branch. The funder had the following involvement in the study: Study design, data collection and analysis, decision to publish and preparation of the manuscript.

Publisher's note

All claims expressed in this article are solely those of the authors and do not necessarily represent those of their affiliated organizations, or those of the publisher, the editors, and the reviewers. Any product that may be evaluated in this article, or claim that may be made by its manufacturer, is not guaranteed or endorsed by the publisher.

References

Amini, S., Pasqualetti, F., and Mohsenian-Rad, H. (2018). Dynamic load altering attacks against power system stability: attack models and protection schemes. *IEEE Trans. Smart Grid* 9 (4), 2862–2872. doi:10.1109/tsg.2016.2622686

Cai, Y., Cao, Y., Li, Y., Huang, T., and Zhou, B. (2016). Cascading failure analysis considering interaction between power grids and communication networks. *IEEE Trans. Smart Grid* 7(1):530–538. doi:10.1109/tsg.2015.2478888

Dahmen, T., Trampert, P., Boughorbel, F., Sprenger, J., Klusch, M., Fischer, K., et al. (2019). Digital reality: a model-based approach to supervised learning from synthetic data. *AI Perspect.* 1 (1), 2–12. doi:10.1186/s42467-019-0002-0

Deka, D., Baldick, R., and Vishwanath, S. (2014) "Data attack on strategic buses in the power grid:design and protection," in 2014 IEEE PES general meeting | conference and Exposition. July 27-31, 2014. MD,USA: IEEE National Harbor, 1–5.

Gao, J., Buldyrev, S. V., Stanley, H. E., Xu, X., and Havlin, S. (2013). Percolation of a general network of networks. *Phys. Rev. E.* 88 (6), 062816. doi:10.1103/physreve.88.062816

Guo, D. R., He, X. T., Lin, G. Q., Luo, C., and Zhong, B. (2019) "Service recovery algorithm for power communication network based on SDN multi-mode channel," in Proceedings of the 9th International Conference on Computer Engineering and Networks, Changsha, China, October 18–20, 2019.

Hagh, M. T., Amiyan, P., Galvani, S., and Valizadeh, N. (2018). Probabilistic load flow using the particle swarm optimisation clustering method. *IET Generation Transm. Distribution* 12 (3), 780–789. doi:10.1049/iet-gtd.2017.0678

Lau, P., Wei, W., Wang, L., Liu, Z., and Ten, C.-W. (2020). A cyber security insurance model for power system reliability considering optimal defense resource allocation. *IEEE Trans. Smart Grid* 5 (11), 4403–4414. doi:10.1109/tsg.2020.2992782

Lin, C. (2005). *Stochastic Petri net and performance evaluation of system[M]*. 2nd ed. Beijing: Tsinghua University Press, 1–42.

Long, Q., Wang, T., Gu, X., and Wang, T. (2019). Modeling of power communication dependent network and its damage resistance analysis based on community overlap. *Power autom. Equip.* 39 (11), 165–173 + 204.

Nan, Y., Qin, T., Wu, L., Huang, Yu, Huang, Y., Xing, C., et al. (2022). A multi-agent game based joint planning approach for electricity-gas integrated energy systems considering wind power uncertainty. *Electr. Power Syst. Res.* doi:10.1016/j.PSR.2021.107673

Nazemi, M., Moeini-Aghtaie, M., Fotuhi-Firuzabad, M., and Dehghanian, P. (2019). Energy storage planning for enhanced resilience of power distribution networks against earthquakes. *IEEE Trans. Sustain. Energy* ([43]GB/Z29328-2012), 1.

Nguyen, D. T., Shen, Y., and Thai, M. T. (2013). Detecting critical nodes in interdependent power networks for vulnerability assessment. *IEEE Trans. Smart Grid* 4 (1), 151–159. doi:10.1109/tsg.2012.2229398

Saccentie, E., Hendriks, M., and Smildeak, A. (2019). Corruption of the Pearson correlation coefficient by measurement error and its estimation, bias, and correction under different error models. *Sci. Rep.* 10 (1), 438. doi:10.1038/s41598-019-57247-4

Shahsanee, S., and Zareei, S. A. (2018). Seismic vulnerability evaluation of power substations' equipment: a review. *Infrastruct. Asset Manag.* 5 (4), 145–150. doi:10.1680/jinam.17.00008

Shelar, D., and Amin, S. (2017). Security assessment of electricity distribution networks under DER node compromises. *IEEE Trans. Control Netw. Syst.* 4 (1), 23–36. doi:10.1109/tcns.2016.2598427

Stephane, D., Raja, C., Sirko, S., and Kirchner, F. (2022). Human-centered AI and robotics. *AI Perspect.* 4 (1), 1. doi:10.1186/s42467-021-00014-x

Wang, T., Sun, C., Gu, X., and Qin, X. (2018). Modeling and vulnerability analysis of power communication coupling network. *Proc. CSEE* 38 (12), 3556–3567. doi:10.13334/J.0258-8013.PCSEE.170233

Yan, J., Tang, Y., He, H., and Sun, Y. (2015). Cascading failure analysis with DC power flow model and transient stability analysis. *IEEE Trans. Power Syst.* 30 (1), 285–297. doi:10.1109/tpwrs.2014.2322082

Yang, N., Dong, Z., Wu, L., Zhang, L., Shen, X., Chen, D., et al. (2022). A comprehensive review of security-constrained unit commitment. *J. Mod. Power Syst. Clean Energy* 10 (3), 562–576. doi:10.35833/mpce.2021.000255

Yang, N., Xun, S., Liang, P., Ding, L., Yan, J., Xing, C., et al. (2024). Spatial-temporal optimal pricing for charging stations: a model-driven approach based on group price response behavior of EVs. *IEEE Trans. Transp. Electrification*, 1. doi:10.1109/TTE.2024.3385814

Yi, T., Qian, C., Mengya, L., Qi, W., Ming, N., and Yun, L. (2016). Network attack in power information physical fusion system Analysis on. *Automatization electromechanical Syst.* 40 (6), 1–4. doi:10.7500/AEPS20160315001

Yu, An, Dong, L., Chen, F., and Wei, W. (2019). Risk analysis of cyber physical distribution network operation considering cyber attack. *Power Syst. Technol.* 43 (7), 2345–2352. doi:10.13335/j.1000-3673.pst.2018.1483

Yu, W., Xue, Y., Luo, J., Ni, M., Tong, H., and Huang, T. (2016). An UHV grid security and stability defense system:considering the risk of power system communication. *IEEE Trans. Smart Grid* 7 (1), 491–500. doi:10.1109/tsg.2015.2392100

Zhang, P. (2020). Research on Collaborative optimal allocation of distributed power and energy storage in distribution network based on two-layer programming model [D]. *Xian Univ. Sci. Technol.* doi:10.27398/dcnki.gxalu.2020.000621

Zhang, P. (2021). *Research on risk assessment and network attack of power distribution network information physical system [D]*. Beijing: North China Electric Power University.

Zhou, Z. (2024). Vulnerability assessment of electric power communication network based on failure degree. *Electr. Technol. Econ.* (01), 346–348.

frontiers | Frontiers in Energy Research

TYPE Original Research
PUBLISHED 31 July 2024
DOI 10.3389/fenrg.2024.1402566

OPEN ACCESS

EDITED BY
Yingjun Wu,
Hohai University, China

REVIEWED BY
Yuanshi Zhang,
Southeast University, China
Jianfeng Dai,
Nanjing University of Posts and Telecommunications, China
Jintao Han,
Opal-Rt Technologies, Canada
Neeraj Kumar Singh,
HCL Technologies, India

*CORRESPONDENCE
Xiaoke Wang,
xiaokewang2024@163.com

RECEIVED 17 March 2024
ACCEPTED 12 June 2024
PUBLISHED 31 July 2024

CITATION
Wang X, Ji Y, Sun Z, Liu C and Jing Z (2024), Improving cyber-physical-power system stability through hardware-in-loop co-simulation platform for real-time cyber attack analysis.
Front. Energy Res. 12:1402566.
doi: 10.3389/fenrg.2024.1402566

Improving cyber-physical-power system stability through hardware-in-loop co-simulation platform for real-time cyber attack analysis

Xiaoke Wang*, Yan Ji, Zhongwang Sun, Chong Liu and Zhichun Jing

Jiangsu Donggang Energy Investment Co., Ltd., Lianyun Gang, Jiangsu, China

With advancements in communication systems and measurement technologies, smart grids have become more observable and controllable, evolving into cyber-physical-power systems (CPPS). The impact of network security and secondary equipment on power system stability has become more evident. To support the existing grid toward a smart grid scenario, smart metering plays a vital role at the customer end side. Cyber-Physical systems are vulnerable to cyber-attacks and various techniques have been evolved to detect a cyber attack in the smart grid. Weighted trust-based models are suggested as one of the most effective security mechanisms. A hardware-in-loop CPPS co-simulation platform is established to facilitate the theoretical study of CPPS and the formulation of grid operation strategies. This paper examines current co-simulation platform schemes and highlights the necessity for a real-time hard-ware-in-the-loop platform to accurately simulate cyber-attack processes. This consideration takes into account the fundamental differences in modeling between power and communication systems. The architecture of the co-simulation platform based on RT-LAB and OPNET is described, including detailed modeling of the power system, communication system, and security and stability control devices. Additionally, an analysis of the latency of the co-simulation is provided. The paper focuses on modeling and implementing methods for addressing DDOS attacks and man-in-the-middle at-tacks in the communication network. The results from simulating a 7-bus system show the effectiveness and rationality of the co-simulation platform that has been designed.

KEYWORDS

active distribution networks, CPPs, smart grid, hardware-in-loop, cyber-attack, co-simulation

1 Introduction

With the development of the economy and society, the demand for energy is increasing. Traditional thermal power generation is unable to meet the electricity demand, and environmental issues such as greenhouse gas emissions are becoming more prominent. Guided by the national goal of reaching peak carbon emissions and achieving carbon neutrality, the integration and adoption of new energy sources have become an inevitable

trend in energy development. The development and utilization of distributed energy provide an important approach for adjusting and upgrading China's energy structure.

Distributed energy is a user-side energy supply method that can operate independently or be connected to the grid. It maximizes resource and environmental benefits and determines the method and capacity based on them. It represents an important direction for the future development of global energy technology. Compared to traditional power sources, distributed power sources have unique advantages including cost-effectiveness, environmental friendliness, and flexibility. They are usually located on the user side, which reduces the construction cost of transmission and distribution networks, minimizes energy loss, and has a short construction cycle and quick return on investment. Additionally, they are technologically advanced, flexible, and easy to maintain, allowing for rapid start-up and shutdown. They can also smooth out peak loads, providing great flexibility. With the integration of a large number of distributed power sources, the safe, reliable, and stable operation of the distribution network is influenced by multiple uncertain factors, primarily manifested in terms of voltage at network nodes, flow direction, fault current in lines, and system protection. The randomness and intermittency of distributed power sources exacerbate issues such as node voltage deviation, severe load fluctuations, and increased network losses in the distribution system, thereby potentially leading to a series of problems including deteriorated power quality, equipment overload, reverse power flow, and excessive terminal voltage (Zhang et al., 2020a; Zhang et al., 2021; Nguyen et al., 2022).

Cyber-Physical systems are vulnerable to cyber-attacks. Various techniques have been evolved to detect a cyber attack in the smart grid (Singh N K et al., 2020). With massive data transmission on the CEEO network, the trustworthiness of the service node exerts an enormous influence on data privacy. To realize securely share data and decrease the local storage, end-user prefer to encrypt data and upload it to the cloud (Fan et al., 2021). Integration of renewable resources and increased growth in energy consumption has created new challenges for the traditional electrical network. To adhere to these challenges, Internet of Everything (IoE) has transformed the existing power grid into a modernized electrical network called Smart Grid (Desai et al., 2019).

Active distribution networks (ADNs) serve as networks for energy exchange and distribution, facilitating the bidirectional flow of both power and fault currents. Traditional power distribution networks are no longer adequate for flow and fault analysis, reactive power control, relay protection methods, and operational management. They require corresponding adjustments and improvements. Referred to as active distribution networks (ADNs), the focus is on distributed energy resources actively regulating their reactive and active outputs and utilizing modern communication means for coordinated control over the distribution network. This enables the full optimization of network operations by harnessing the potential of distributed energy resources (Zhang et al., 2020b; Cao et al., 2023; Cao et al., 2024).

The key technologies of ADNs include ADN planning, flow and fault analysis computations, relay protection, reactive power control techniques, and operational scheduling of distributed energy resources (Jabr, 2013). For example, efficient demand-side management tools allow operators to have better control over the operation and management of distributed energy resources. Additionally, integrating energy storage facilities helps absorb excess output or mitigate load fluctuations from distributed energy resources.

The ongoing advancements in power electronics technology are enabling various control and regulatory equipment to better serve active distribution networks. This enhancement facilitates the utilization of new energy generation within distribution networks while ensuring safety and stability. Zhao and You (2021) introduces a multi-level adaptive robust optimization framework based on deep learning to tackle uncertainties arising from the high penetration of distributed energy sources into distribution networks. Moreover, adaptive optimization control methods, relying on real-time measurement data, effectively model the input-output relationship of the distribution network using live measurements.

Through iterative interactions with the distribution network, these methods effectively overcome the reliance on extensive training associated with neural network methods, thereby enabling real-time control of the distribution network (Hou and Xu, 2009; Zhang et al., 2022). Zhao et al. (2016) utilizes a controller comprising three modules—voltage regulation, reactive power control, and active-frequency regulation—that adapt locally without the need for frequency measurements. Guo et al. (2019) proposes an optimization control frame-work for interconnected AC-DC microgrids based on model-free adaptive control, effectively addressing issues of AC-DC coordinated power control. Addressing the time-series characteristics of controlled systems, Zhang et al. (2021) integrates predictive control principles into model-free adaptive control, achieving superior control performance through adaptive predictive control. Bi et al. (20223) introduces a data-physical fusion-driven adaptive voltage control method for active distribution networks, effectively curbing frequent voltage excursions and enhancing the adaptive optimization control level of the distribution network. In the smart grid substation each wireless sensor node can be modeled using graph theory. Then each node is assigned with predefined weight, which gets effected during cyber intrusion. Each sensor node monitors the trust value of neighboring nodes (Singh et al., 2020). Cyber-Physical systems are vulnerable to cyber-attacks. Various techniques have been evolved to detect a cyber attack in the smart grid. Weighted trust-based models are suggested as one of the most effective security mechanisms. A two-level hierarchical network is examined, with the smart wireless sensors at the bottom and server at the top of the network. The direct and indirect trust of the node is calculated using "One Time Code" to determine the overall trust of nodes. Trust depends on the performance of the sensors, communication between sensors, and the server of the nodes. It also depends on the previous communication between the nodes (Singh and Mahajan 2020). As a cyber-embedded infrastructure, it must be capable of detecting cyberattacks and responding appropriately in a timely and effective manner. Previous work tries to introduce an advanced and unique intrusion detection model capable of classifying binary-class, trinary-class, and multiple-class CDs and electrical network incidents for smart grids. It makes use of the gray wolf algorithm (GWA) for evolving training of artificial neural networks (ANNs) as a successful machine learning model for intrusion detection (Yu et al., 2022). The intrusion detection model is based on a whale optimization algorithm (WOA)-trained artificial neural network

(ANN). The WOA is applied to initialize and adjust the weight vector of the ANN to achieve the minimum mean square error (Haghnegahdar and Wang, 2020).

The impact of network security and secondary equipment on power system stability has become increasingly evident, emphasizing the urgent need for advanced simulation tools that can effectively model and mitigate these threats. To bridge this critical gap, a hardware-in-loop CPPS co-simulation platform is established to facilitate the theoretical study of CPPS and the formulation of grid operation strategies. A sophisticated HIL simulation environment is proposed in Riquelme-Dominguez et al. (2023), that addresses system frequency responses in power systems with low inertia. This aligns closely with our focus, demonstrating the importance of accurate real-time simulations under both normal and emergency conditions. The cybersecurity challenges in modern power systems are further emphasizes in Fu et al. (2023), which highlights the need for HIL simulations that not only handle physical system dynamics but also integrate cybersecurity threat scenarios. The method of virtualized environments complement HIL simulations is analyzed in Zhang et al. (2021), particularly in applying machine learning techniques for anomaly detection. This study supports our method of incorporating machine learning to enhance the predictive capabilities of our co-simulation platform. Specialized applications of HIL simulations for maritime control systems are described in Vu et al. (2023), highlighting the versatility and critical need for robust HIL environments across different sectors, including the specific challenges posed by cyber-physical threats. This paper examines current co-simulation platform schemes and highlights the necessity for a real-time hardware-in-the-loop platform to accurately simulate cyber-attack processes, considering the fundamental differences in modeling between power and communication systems. An independent, distributed, and lightweight trust evaluation model is proposed and evaluated. The trust model is implemented at two levels: first at the smart meter level, where nodes collect information on its neighbor nodes and forward it to the collecting node (Alnasser and Rikli, 2014). In previous work a Hierarchical Trust based Intrusion detection System (HTBID) has been proposed to effectively deal with various attacks in wireless sensor network. HTBID deals with different types of attack with the help of Hierarchical Trust evaluation protocol (HTEP). This work identifies different parameters and factors that affect trust of wireless sensor network. HTEP considers attributes derived from communication as well as social trust to calculate the overall trust of sensor node (Dhakne and Chatur, 2017).

The co-simulation platform based on RT-LAB and OPNET is proposed, including detailed modeling of the power system, communication system, and security and stability control devices. Our approach significantly advances the state of the art by enabling more precise and dynamic responses to cybersecurity threats within CPPS environments. Our solution leverages cutting-edge advancements in real-time simulation technology and cyber-attack modeling to provide a comprehensive tool for power system operators. This enables the proactive identification of vulnerabilities and the testing of countermeasures under controlled yet realistic conditions, which was not feasible with previous methodologies. This paper focuses on modeling and implementing methods for addressing DDOS attacks and man-in-the-middle attacks in the communication network. The results from simulating a 7-bus system show the superiority and practicality of the co-simulation platform that has been designed.

2 Co-simulation platform framework and design

2.1 Platform framework

Advanced sensors and high-speed networks have enabled real-time monitoring of power grids, providing data on various electrical measurements such as voltage, current, and frequency, as well as environmental information like temperature, humidity, and light (Luo, 2016; Zhang et al., 2021; Mittal et al., 2023). This data is utilized to support grid monitoring, protection, regulation, and other functions.

The smart grid control system in CPPS consists of three main components: the power system as dipicted in Figure 1 (including generators, loads, power electronic equipment, energy storage systems, measuring units, and control units), the communication system (comprising routers, optical fibers, servers, and other devices), and the security and stability control device (a decision-making system with a master station and substation).

Measuring units collect data on the grid's status and transmit it to the master station via a wide-area communication network (Osanaiye et al., 2016; Zhang et al., 2020c). The master station calculates control commands based on a strategy and sends them to each substation. Substations then execute specific operations using control units based on local control strategies (Othman et al., 2018; Menezes et al., 2023).

This paper utilizes a modular design to integrate discrete event simulation and continuous-time simulation. The co-simulation platform comprises four modules: power system, communication system, master station, and substation. These modules are connected via Ethernet to streamline data interface design and enhance modeling efficiency. Real-time performance is ensured through the use of appropriate simulation tools for the power system and communication system. Figure 2 illustrates the architecture of the co-simulation platform.

2.2 Power system

The real-time requirements of the co-simulation platform present a challenge, as most power simulation systems are PC-based and cannot handle large-scale simulations in real-time with small time steps (Zhang et al., 2024). To tackle this problem, the OPAL-RT modeling software RT-LAB was chosen as the power system simulator (Amaizu et al., 2021). Simulink models can be compiled into multiple subroutines that can be executed in parallel using RT-LAB.

Modeling in RT-LAB involves four main components: the power grid, a measuring unit, a control unit, and a network interface (Cil et al., 2021), as shown in Figure 1. The original power grid is simplified into an equivalent network for real-time simulation, and the grid model is designed accordingly and verified through offline simulations (Mittal et al., 2023). Regarding the

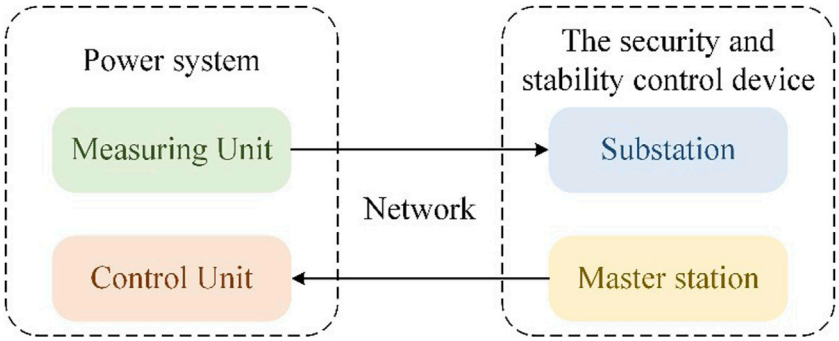

FIGURE 1
The structure of smart grid control system.

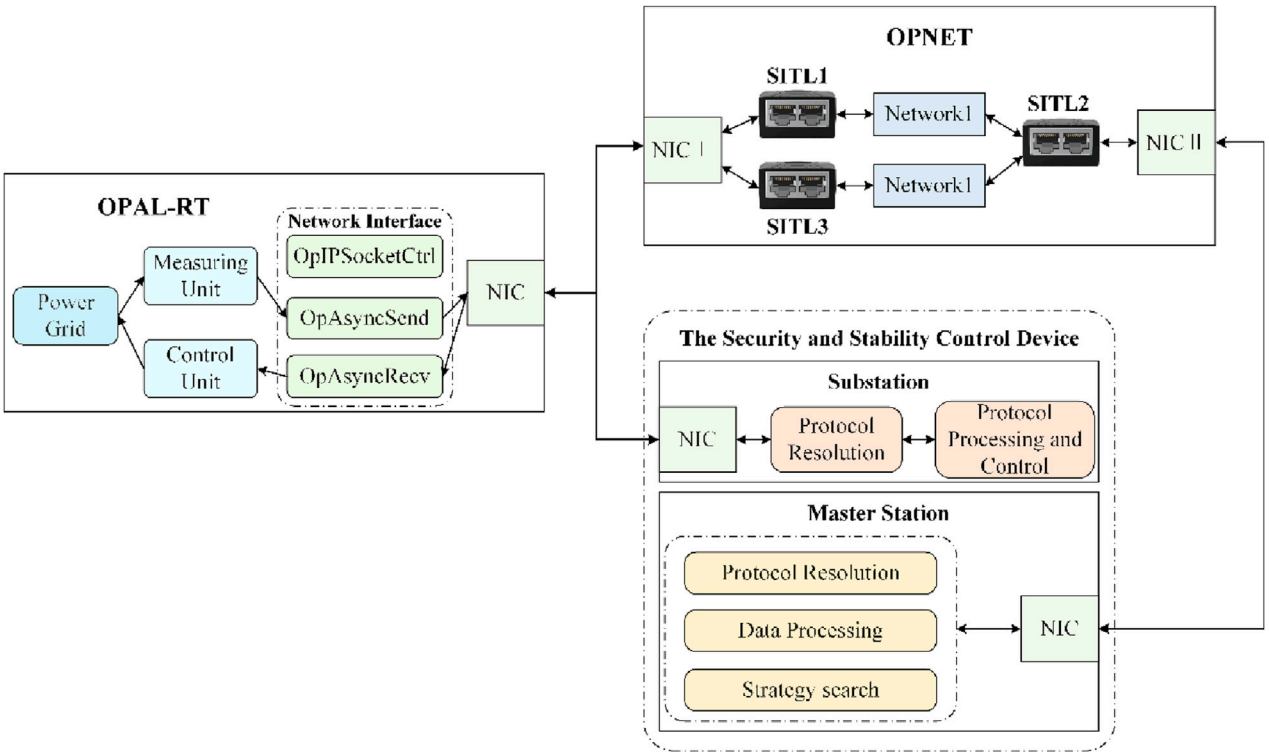

FIGURE 2
The architecture of co-simulation platform.

measuring unit, it is essential to define the sampling frequency and data type of the packets, which include parameters such as voltage, current, frequency, and power-angle (Alnasser and Sun, 2017; Singh and Mahajan, 2020; Singh and Mahajan, 2021; Yu et al., 2022; Zhang et al., 2021a; Zhang et al., 2021b; Zhang et al., 2021c). Additionally, timestamps are included to analyze latency. In the control unit, it is crucial to determine the target and structure of commands sent from the substation. The control unit is responsible for converting these commands into control quantities and outputting them to the control target. OPAL-RT uses TCP and UDP protocols for external communication. The network interface consists of three modules: OpIPSocketCtrl, which controls the communication protocol, port, and IP address; OpAsyncRecv, for receiving packets; and OpAsyncSend, for sending packets. Multiple sets of network interfaces can be included in the power system model, distinguished by port numbers.

2.3 Communication system

To ensure real-time performance, this paper utilizes OPNET to simulate the communication system. The modeling in OPNET is categorized into three layers: net-work, node, and process, depending on the level of the communication network. This

three-level modeling allows for the construction of communication networks, protocols, algorithms, and equipment. OPNET also offers a range of standard applications, such as Database, E-mail, HTTP, Print, Remote Login, Video Conferencing, and Voice, which can be combined to cover most power services (Kaur et al., 2021; Zhang et al., 2023). For unique power businesses, the standard application model can be modified at the process layer to create a customized application model.

To establish end-to-end business connections between real and virtual networks, a semi-physical simulation interface can be employed (Priyadarshini and Barik, 2022). OPNET offers three types of such interfaces: HLA-API, ESA-API, and System in the loop (SITL). While HLA-API and ESA-API require defining process and node models and designing corresponding interface programs, SITL is an existing model provided by OPNET. Although it supports limited protocols and requires mapping real packets to virtual ones, it enables easy access to external devices in the simulation system. As communication between modules uses the UDP protocol, we have chosen SITL as the data interface to simplify model design.

Data is exchanged between measuring units and substations with the master station through a communication system. Control units exchange data with substations directly through a switch. To facilitate this, two network interface cards (NICs) are inserted into the OPNET host. NIC1 communicates with the OPAL-RT and substation via the switch, while NIC2 communicates directly with the master station. The network model includes multiple SITL modules that correspond to the master station, substation, and measuring units by setting filters. Network 1 connects measuring units to the master station, while network 2 connects the substation to the master station.

2.4 The security and stability control device

The security and stability control device plays a crucial role as the second and third lines of defense for the power grid. It is responsible for responding to emergencies such as load shedding, generator trips, or valve fast shutdowns in order to prevent further spread of faults in the grid. This device consists of both a master station and substations. The master station monitors the power grid's status through measuring units and compares any faults found with the security control strategy based on the fault type and location. Once the optimal control strategy is determined, the master station sends control commands to the substations. The substations report the controllable load amount to the master station and receive control commands from it. Finally, the substations send commands to the control units and execute the actual operation according to the local control strategy.

The master station is constructed on the Linux platform and is programmed using the C language, allowing it to perform complex operations. It retrieves real-time power grid status information from OPAL_RT and receives control commands from the security and stability control device to efficiently monitor and manage the power system. The master station consists of four modules, which are as follows:

2.4.1 Protocol analysis module

The protocol analysis module is responsible for examining packets sent by the measuring unit and the substation. Each packet consists of a padding section and a data section. The data section includes a header, a command code, and a checksum. Upon receiving a packet, the master station extracts the data section using a preset offset and verifies its accuracy. Then, the header is read to identify the message type and source, and subsequently, the corresponding operation is executed based on the command code. I have improved the grammar, added transitional phrases, and simplified certain words and phrases for better clarity without altering their original meaning.

2.4.2 Grid status database

The purpose of this module is to store up-to-date information on the power grid's status, including the status of breakers, positions of transformer taps, as well as voltage and frequency levels.

2.4.3 Fault detection module

This module is triggered whenever there is an update to the grid status in the database, and it sends an alarm in case of system failure.

2.4.4 Control module

Upon receiving an alarm from the fault detection module, the control module formulates multiple coordinated control strategies according to the pre-established plan. It assesses their effectiveness and determines the optimal scheme to create a control queue for the substation.

The master station operates in parallel and dynamically assigns individual processes to each client. The client's type can be automatically identified by the master station based on the self-descriptive packet. There are four types of commands: retrieving grid status from the database, updating grid status in the database, accessing control commands in the control queue, and adding control commands to the control queue. The master station can synchronize, analyze, and manage the power system, communication system, and substation.

This paper presents a substation that utilizes embedded Linux and comprises five components, as depicted in Figure 3: a control module, an input/output (I/O) module, a measuring module, a man-machine interface, and a communication module. The substation communicates with the master station every 0.833 ms. During a control cycle, the substation performs four steps:

Initially, the substation dispatches a packet that includes the controllable load quantity to the master station and then awaits the response packet.

After receiving the packet from the master station, the substation identifies its type by analyzing the packet header.

The substation performs different actions depending on the type of packet received. For synchronization packets, it revises the system clock. For command packets, it generates a control queue based on the local control strategy. If an abnormal packet is received, it is returned to the master station. If the control queue is not empty, all commands will be sent to the control unit.

2.5 System latency

Figure 4 illustrates the real-time simulation timeline of a co-simulation platform that includes a power system, communication

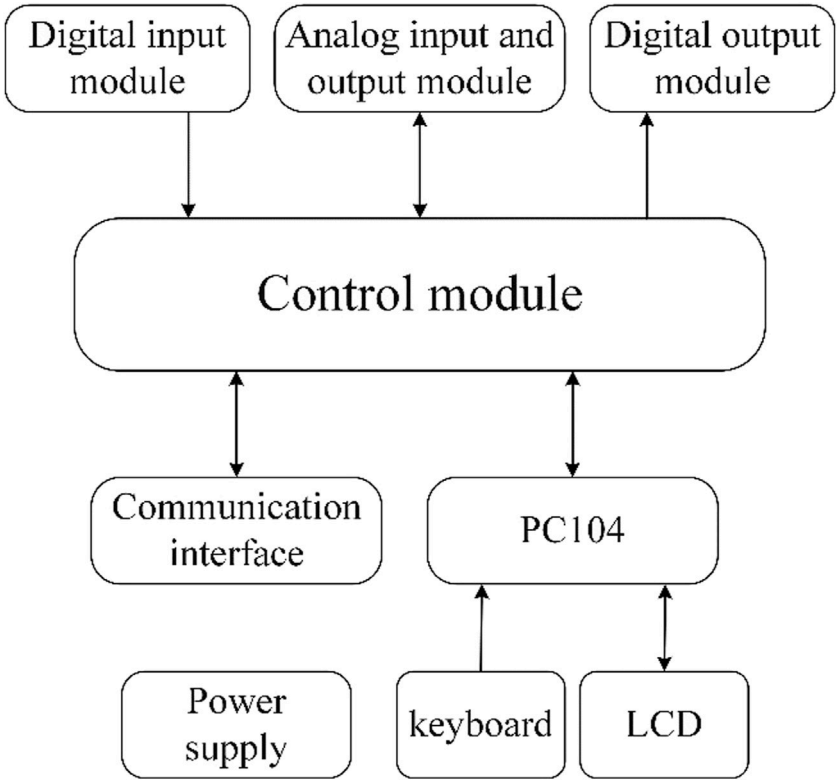

FIGURE 3
Structure of substation.

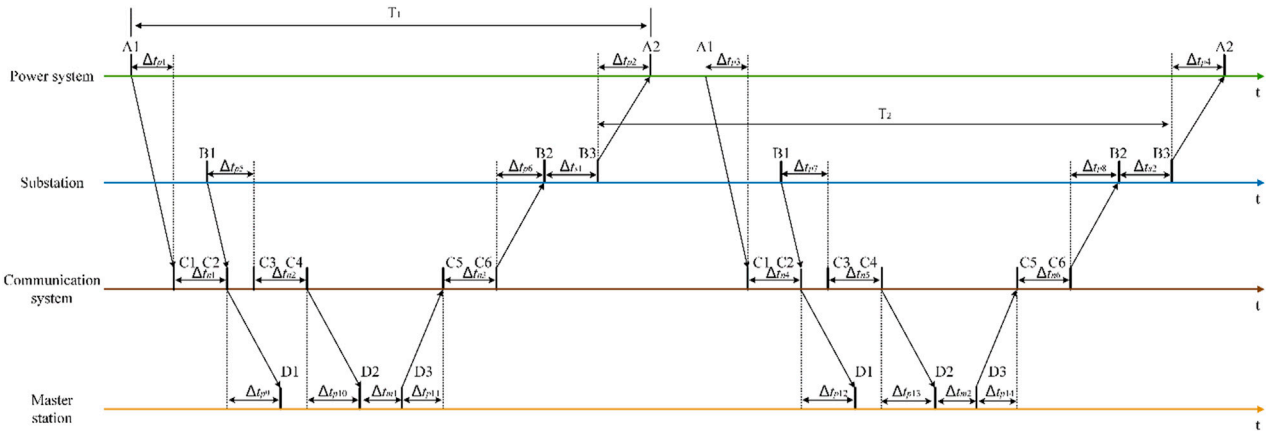

FIGURE 4
Timeline of real-time simulation.

system, master station, and substation. This timeline considers the simplified structure of the control system in the power grid.

To simplify the modeling process and clarify the function of each module, the measuring unit is limited to sending data only, while the control unit can only receive data. The communication cycle between the measuring unit and the master station is T_1, and the cycle between the control unit and the substation is T_2. At moment A1 in the simulation, the measuring unit sends sampled data to the master station, which receives the data at D1. At moment B1, the substation system sends the data of controllable load to the master station. After processing the data upon receiving them at D2, the master station issues a synchronization message or control order message to the substation. The substation analyzes the message and issues a control order to the control unit at B3. Finally, the control unit updates the relevant parameters in the power system node at A2.

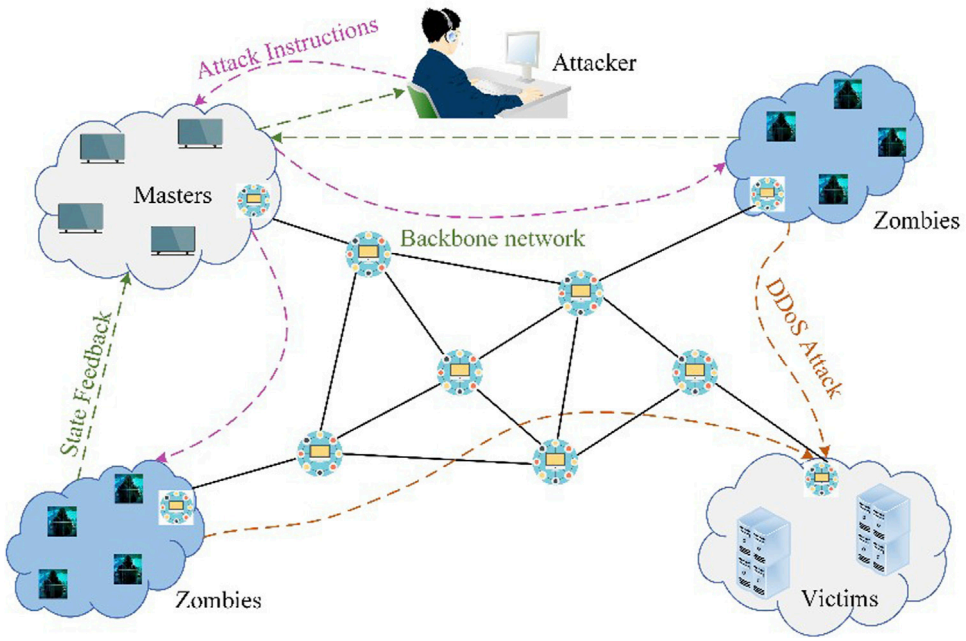

FIGURE 5
Attack steps of DDOS.

The system latency consists of four main components: network latency, master station latency, substation latency, and inherent simulation platform latency. Network latency is the delay caused by communication systems, including issues such as packet loss, bit errors, routing problems, bandwidth limitations, and server performance. Master station latency is a result of hardware and software limitations, encompassing hardware latency and software latency. Hardware latency involves delays within the master station system, including network card performance and data transfer. Software latency refers to the time required for power service computations, such as state estimation, measurement information management, and power quality monitoring. Substation latency is similar to master station latency, involving hardware and software limitations that lead to delays. Inherent simulation platform latency arises from communication between modules in the platform. This includes factors like OPAL-RT operating system latency, OPAL-RT network card latency, OPNET operating system latency, OPNET host network card latency, switch latency, and more.

In actual CPPS, the platform's inherent latency cannot be eliminated and varies randomly depending on the amount of data flow between modules. When data packets are less than 64 bytes, the inherent latency is approximately 1–2 ms. However, as the total latency of network, master station, and substation is already in the range of tens to hundreds of milliseconds, the impact of inherent latency is negligible and will not significantly affect the simulation accuracy. To further minimize the influence of inherent latency, one common approach is to use the Ping command to measure the communication latency between modules, record it as inherent latency, and subtract it from the controllable latency in the master station system.

3 Cyber-attack modeling

3.1 DDOS attack

A Distributed Denial of Service (DDOS) attack is a form of resource-exhaustion attack. Attackers employ Client/Server techniques to manipulate multiple computers as sources of attack, thereby enhancing the attack's effectiveness. There are various types of DDOS attacks, including Sy flood, Smurf, and Land-based attacks. When a host is targeted by a DDOS attack, it experiences a high volume of pending connections, causing the network to be flooded with useless packets, leading to network congestion. Consequently, the target of the attack becomes incapable of communicating with the outside world.

Figure 5 illustrates the DDOS attack scheme, consisting of four components: the attacker, control puppet, attack puppet, and target. Attackers gain either partial or complete control of both the control puppet and attack puppet. The control puppet transmits the attack program to the attack puppet. Through the control puppet, the attacker instructs the attack puppet to send actual attack packets to the target.

This paper deploys an attacker node in an OPNET simulation. The attacker randomly scans and attacks all terminals in phase one, and infected computers send confirmations back to the attacker. In phase two, the infected computers flood the network connecting to the target with tons of meaningless packets.

3.2 MITM attack

The Man in the Middle (MITM) attack is an indirect method of gaining control over a target. By spoofing IP addresses and ports, the

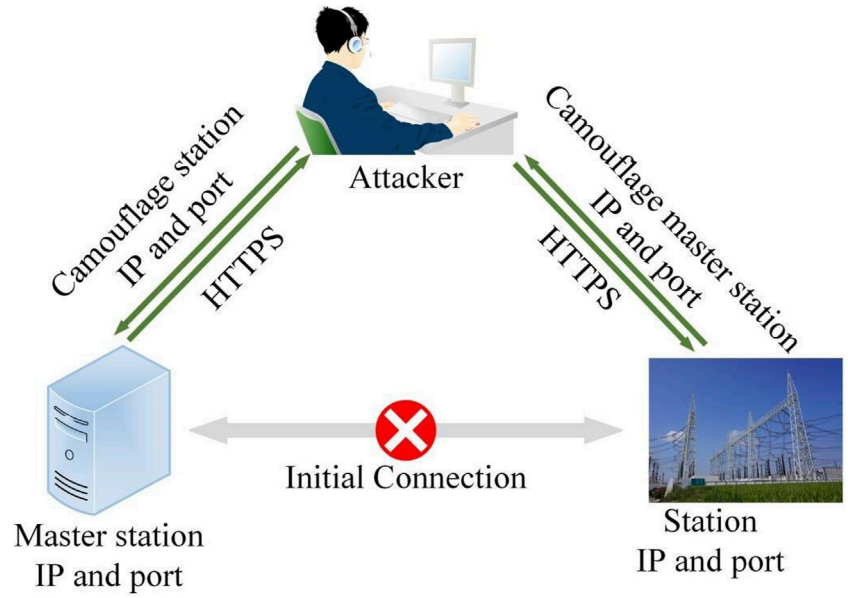

FIGURE 6
Man-in-the-middle attack.

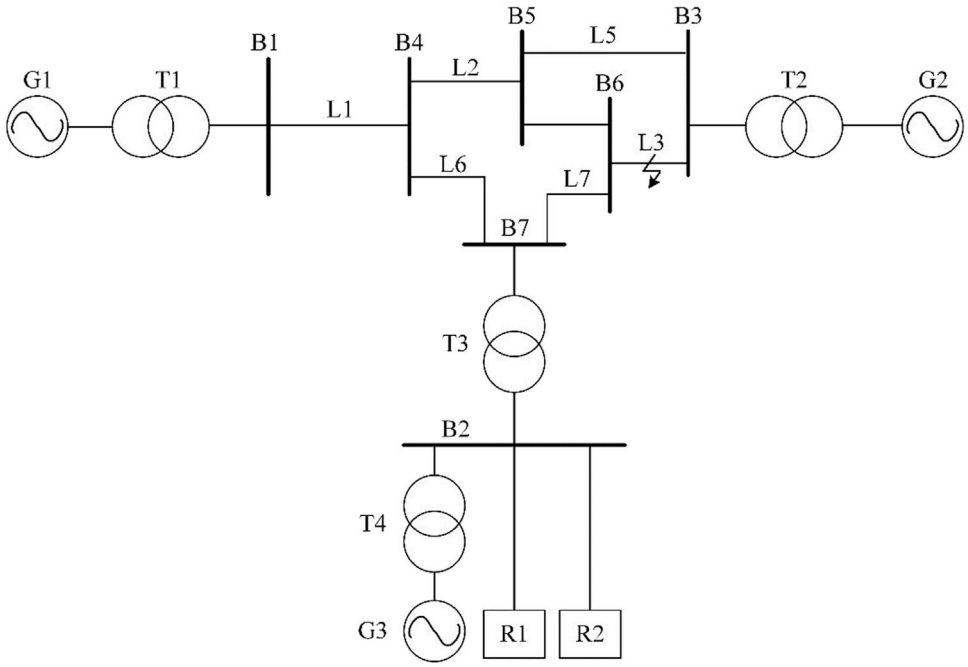

FIGURE 7
Structure of 7-bus system.

attacker can invade and take control of a virtual computer, creating a new communication channel between the original nodes. This new channel allows packets to be easily modified, leading the target to make incorrect decisions. Common examples of MITM attacks include Careto, Crypto locker, Dexter, and Fin Fisher.

In the research depicted in Figure 6, a computer is utilized as the attacker and equipped with two network interface cards (NICs). One NIC connects to OPNET while the other connects to the substation. The IP address of the NIC connected to the substation serves as the gateway IP address for the substation, while a virtual NIC is established within the computer and assigned the IP of the

TABLE 1 Parameters of the device.

Bus number	Device number	Device type	Voltage (kV)	Capacity
B1	G1	Generator	13.8	100MVA
	T1	Transformer	13.8/218.5	100MVA
B2	G3	Generator	13.8	100MVA
	T4	Transformer	13.8/110	100MVA
	R1	Controllable load	110	80MVA
	R2	Controllable load	110	40MVA
B3	G2	Ideal voltage source	13.8	∞
	T2	data	13.8/218.5	100MVA
B7	T3	data	110/230	100MVA

master station. The IP address of the NIC connected to the substation is configured as the substation's IP address.

Two methods of Man-in-the-Middle (MITM) attack are proposed as follows:

3.2.1 Data interception

In this method, the attacker intercepts packets from both the substation and master station, analyzes the packet header to determine its function, and copies any time packets to a buffer which is then sent to the substation. If a command packet is detected, it will be replaced by the time packet in the buffer. This attack prevents the substation from receiving commands from the master station.

3.2.2 Data modification

Similarly, in this method, once a command packet is detected, all subsequent packets will be replaced by a modified command packet that forces the substation to execute unreasonable load shedding and casting actions.

4 Case study

4.1 Model description

To verify the impact of communication systems and devices on power system simulations, as well as the necessity of co-simulation platforms in power system analysis, a 7-bus system was constructed in RT-Lab, as shown in Figure 7. The system includes seven buses, two controllable loads, two generators, one ideal voltage source, four transformers, and seventeen circuit breakers. Measuring units monitor buses B1, B2, and B3. The protection unit and control unit jointly manage the controllable load and generator, with the protection unit preventing the control unit from operating the protected device once it has been broken out. The simulation is based on a reference AC voltage of 230 kV, frequency of 60 Hz, and a simulation step of h = 2.5 × 10^(−5) s. Table 1 provides the parameters for each device.

The strategy for system protection and security control during a three-phase short-circuit fault on transmission line L3 is as follows: The short-circuit protection unit will disconnect L3 within 0.1 s of the fault occurring. The over-current protection unit will disconnect L1 after a 2-second delay and disconnect L5 after a 3.5-second delay from the occurrence of the fault. Additionally, the security and stability control device will disconnect R2 after a 2-second delay following the short-circuit fault.

Figure 8 illustrates the communication network constructed in OPNET, which comprises eight router nodes, multiple servers, and terminals designed to simulate data transmission across various services. Notably, the measuring unit, master station, and substation do not directly correspond to individual nodes within this network. Instead, these physical components are interconnected to the OPNET communication network at specific boundary nodes using the SITL (System-in-the-Loop) module. This setup reflects the hierarchical nature of our system, where multiple physical devices may connect to a single communication node that serves as a gateway or aggregation point, rather than having a direct one-to-one mapping with the communication nodes.

Furthermore, the control unit is integrated into the network via a connection to the substation through a switch, emphasizing the layered interaction between control operations and network communication. The routers in this network are linked by a 2 Mbps optical fiber, ensuring a consistent communication delay of 1 ms across the system.

After the occurrence of a three-phase short-circuit fault on L3, a DDOS attack and MITM attack are conducted to assess the effects of cyber-attacks on the power system.

4.2 DDOS attack

In this scenario, there is an attacker node connected to router A, as shown in Figure 9. The attacker sends malware to all terminals in the network and infects approximately 70% of them randomly. The infected terminals are then controlled by the attacker to send meaningless requests to the server, causing a congestion in network traffic.

All the loads in the system are connected to B2. However, the output of G3 is insufficient to meet the load requirements. As a result, the current of B2 directly indicates the behavior and stability of the system. The comparison of B2 current in three scenarios is illustrated in Figure 10.

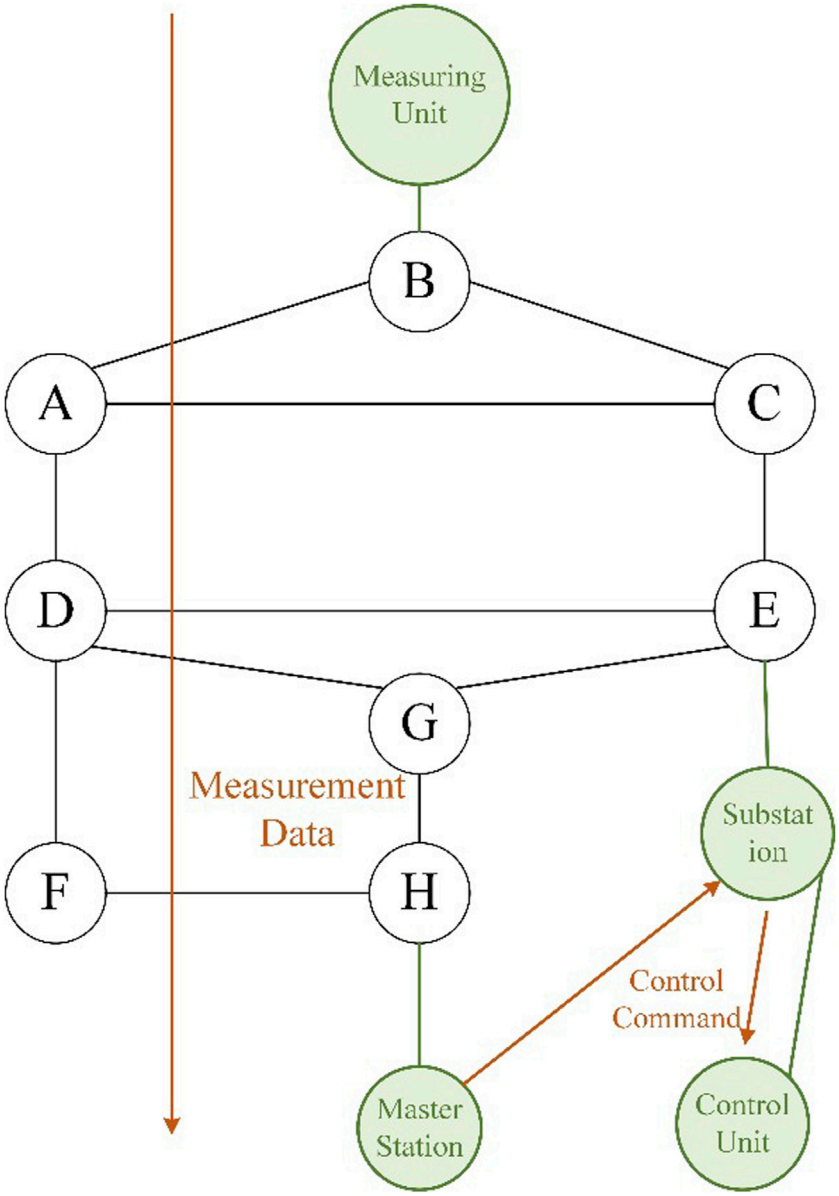

FIGURE 8
Structure of communication network.

Under ideal conditions, without taking into account the communication system and actual devices, the security and stability control device had a response delay of 0 ms. As a result, the control unit disconnected R2 within 2 s of the occurrence of a short-circuit fault, ensuring the stability of the system.

Taking into account the communication system and the actual devices, the channel remained unobstructed and free from congestion in typical situations. The average latency between the substation and the master station was 233.9 ms. The substation promptly disconnected R2, resulting in a reduction of current in L5. This action effectively curbed the further spread of the fault.

During the DDOS attack, the average latency between the substation and the master station significantly increased to 2,136.7 ms due to a high volume of meaning-less packets congesting the channel. Despite the substation responding to the commands from the master station, the prolonged latency resulted in system instability and further propagation of the fault by the protection device.

Figure 11 illustrates the average latency between the substation and the master station for various levels of attack intensity, including infection rates of 30%, 50%, 70%, and 90%. In the case of a mild DDOS attack, the communication system exhibited the capacity to handle the packets sent by the compromised machines, resulting in minimal changes in latency. However, as the number of infected terminals grew, the communication system's resources were depleted, leading to a significant increase in latency.

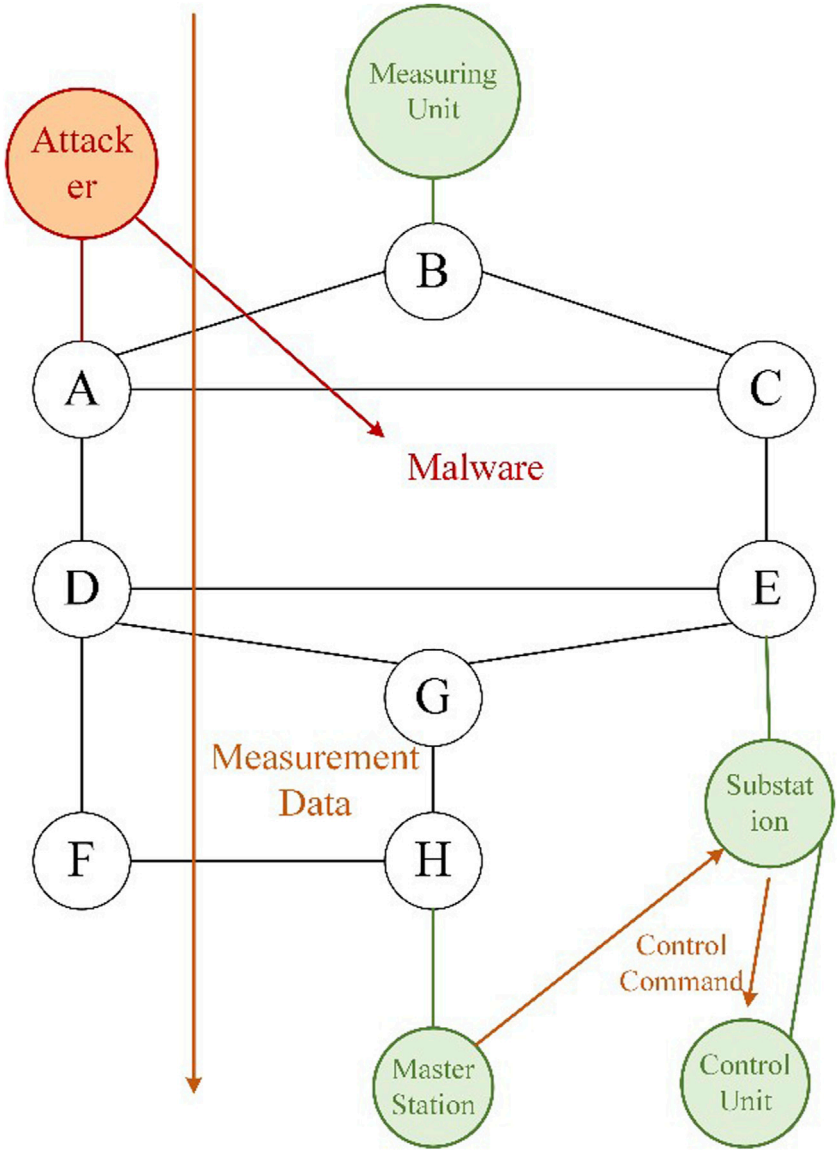

FIGURE 9
DDOS attack.

4.3 MITM attack in mode 1

In this situation, the attacker intercepted the packet sent from the master station to the substation. This prevented the substation from receiving the command, resulting in a missed trip. Table 2 displays the breaker's operating time under both normal conditions and attack conditions following the occurrence of a three-phase short-circuit fault.

As depicted in Figures 12, 13 the attacker intercepted and filtered the control commands sent by the master to the substation, resulting in a missed trip and preventing the breaker from disconnecting R2. As a consequence, the overcurrent protection disconnected L5 at 12.74s and L1 at 15.25s. Unfortunately, the failure continued to spread, eventually causing G3 to go out of step.

4.4 MITM attack in mode 2

In this scenario, the attacker eavesdropped on the packets sent by the master station. Upon detecting a command packet, the attacker intercepted all subsequent packets and randomly sent switching load commands to the substation. As depicted in Figures 14, 15, the current of B2 and the speed of G3 exhibited differences under the MITM attack compared to normal conditions. In the absence of an attack, the substation would disconnect R2, resulting in a gradual decline and stabilization of the current in B2, with only occasional fluctuations in the speed of G3 during load shedding. However, during the attack, the substation indiscriminately switched the load, causing sharp fluctuations in both the current of B2 and the speed of G3. Although the system did not become destabilized in this particular example, the continuous

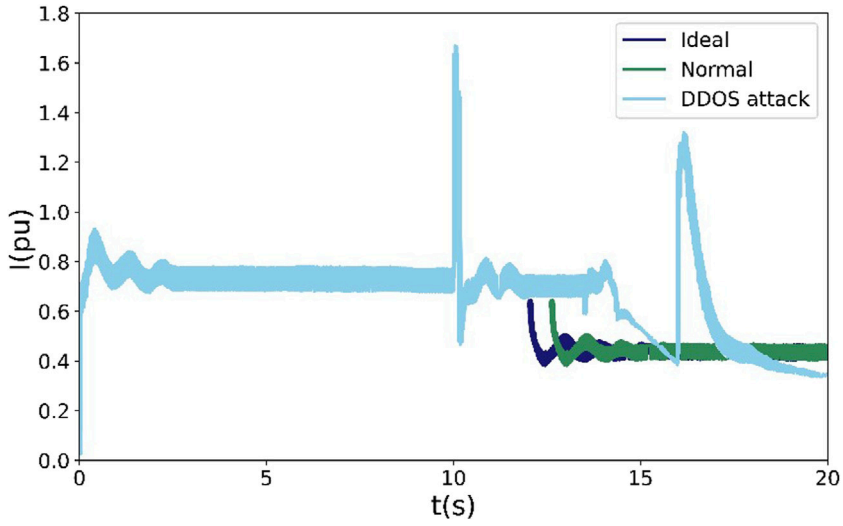

FIGURE 10
Current comparison of B2.

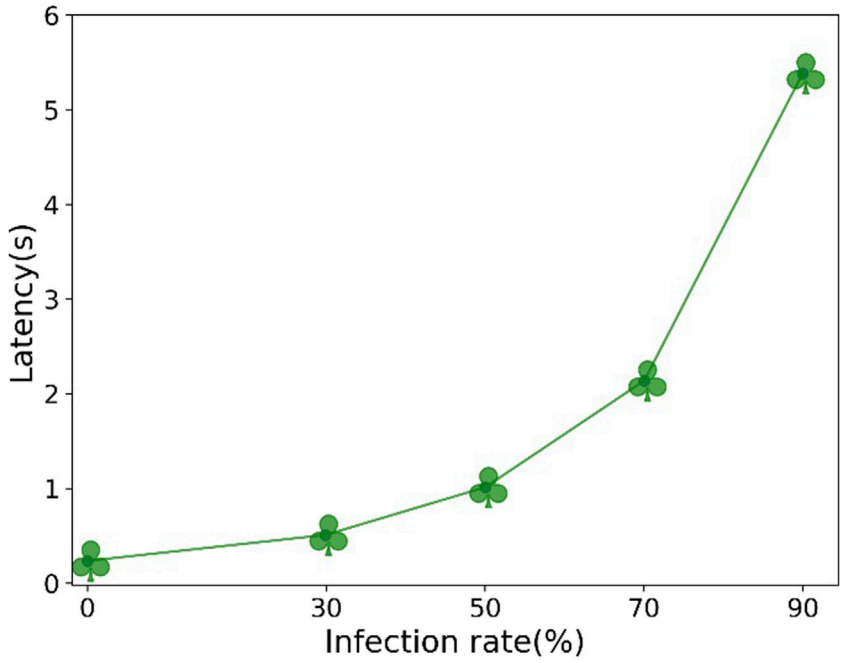

FIGURE 11
Communication latency under different DDOS attack intensity.

injection of disturbances by the malfunctioning substation compromised the stability of the overall system.

In conclusion, the integration of communication networks and cyber-attack considerations greatly enhances the security and stability control of smart grid operations. Without simulating the communication network and utilizing actual devices, it becomes challenging to accurately predict system responses. The co-simulation platform proposed in this study successfully integrates the power system, communication system, and actual devices, providing an effective method for studying Cyber-Physical Systems (CPS) in smart grids.

5 Conclusion

The co-simulation platform proposed in this paper, based on hardware-in-loop, offers several advantages compared to traditional power system simulation:

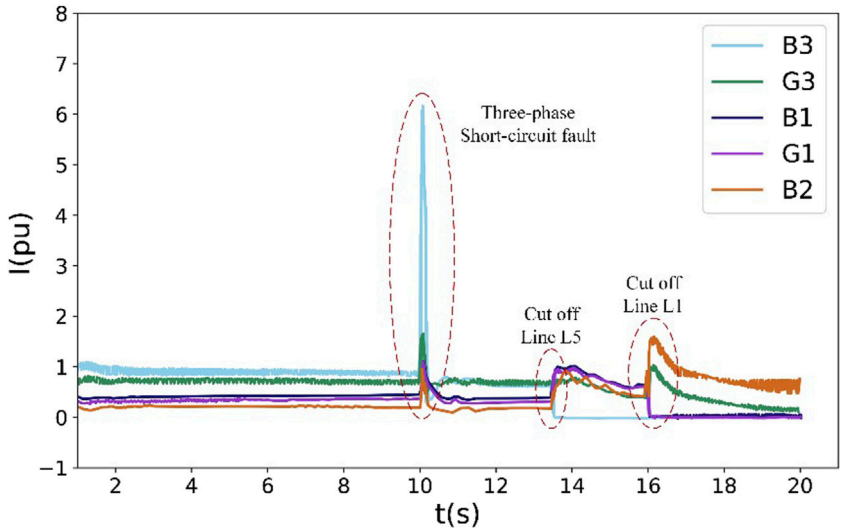

FIGURE 12
Bus current under MITM attack in mode1.

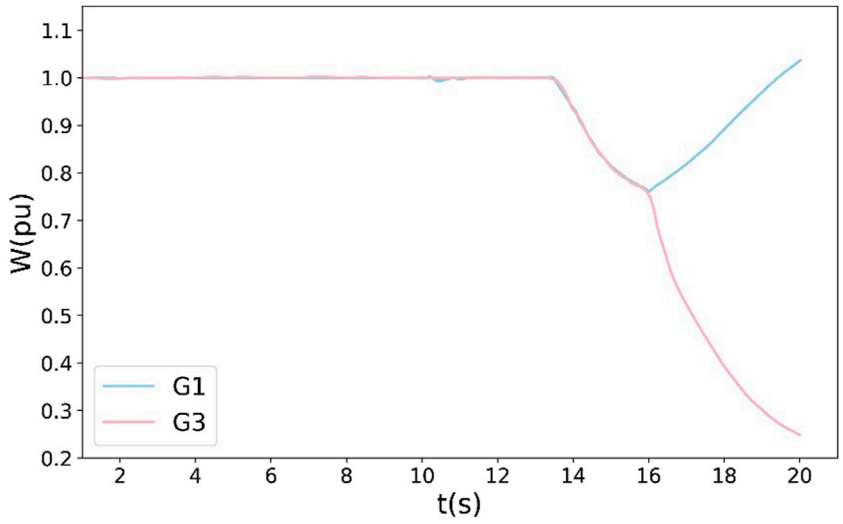

FIGURE 13
Generator speed under MITM attack in mode1.

TABLE 2 The comparison of breaker action moment.

Position	Action	Normal	MITM attack
L3	Off	10.10s	10.10s
R2	Off	12.49s	~
L5	Off	~	13.47s
L1	Off	~	15.98s

1) The co-simulation platform considers the communication system and actual devices present in a typical Cyber-Physical Power System (CPPS). This enables the analysis of various factors such as communication latency, data loss, bit errors, device response delays, and their impact on the power system. The simulation environment closely resembles reality, allowing for comprehensive vulnerability assessments of the entire system,as depicted in Figures 12, 13.
2) Unlike traditional power system simulation that relies on simplified control system models with limited functionality, the co-simulation platform with hardware-in-loop allows for flexible deployment and the accomplishment of complex power system services by incorporating actual devices into the control loop.
3) By integrating security and stability control systems into the co-simulation platform, it becomes possible to simulate cyber-

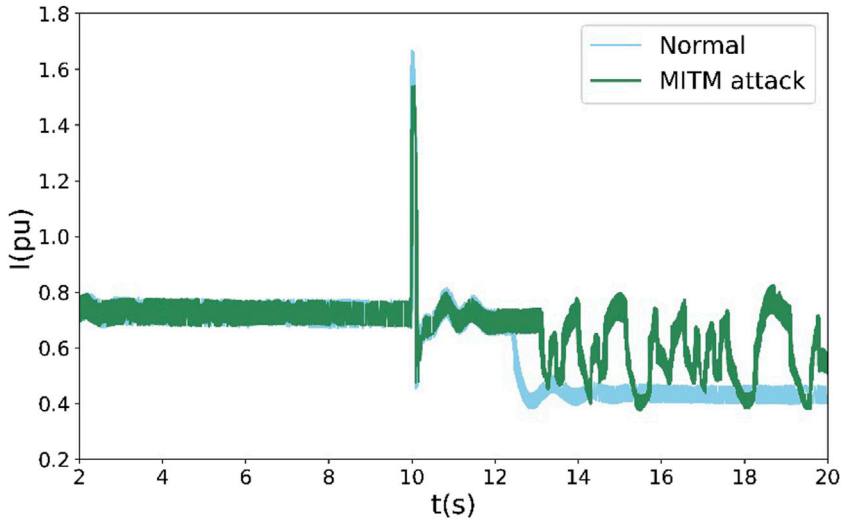

FIGURE 14
Current comparison of B2.

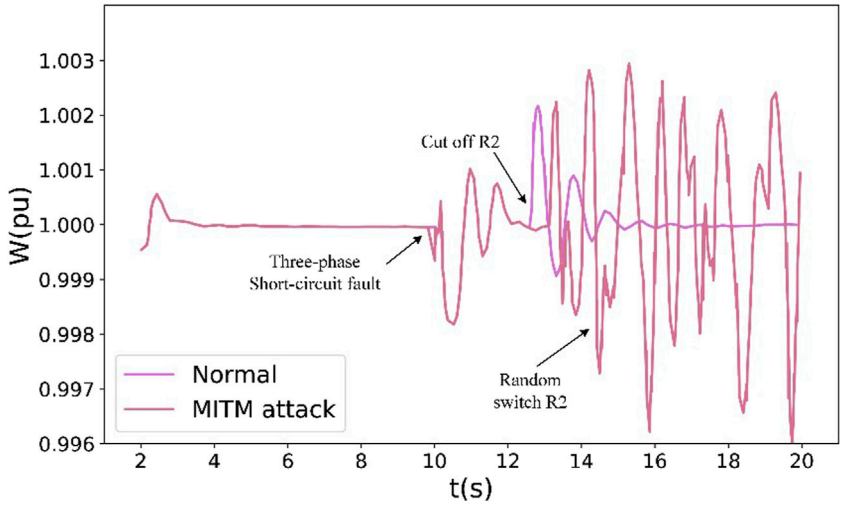

FIGURE 15
Speed comparison of G3.

attacks and assess the propagation of failures for studying security defenses.

However, it is important to note that due to inherent latency in the simulation platform, errors may occur in the results if the network, master station, and device latencies significantly exceed the inherent latency. To address this, further research and development of the co-simulation platform are underway, focusing on the following areas:

1) Studying interface technology and synchronization techniques to reduce or eliminate the inherent latency of the simulation platform, thereby improving the accuracy of simulation results.
2) Quantitatively analyzing communication latency and establishing simulation models to characterize its effects.
3) Expanding the application of the platform to analyze the generation of cyber-attacks and the propagation of failures within CPPS.

Data availability statement

The original contributions presented in the study are included in the article/Supplementary Material, further inquiries can be directed to the corresponding author.

Author contributions

XW: Investigation, Methodology, Writing–original draft. YJ: Formal Analysis, Project administration, Writing–review and editing. ZS: Validation, Writing–review and editing. CL: Resources, Validation, Writing–review and editing. ZJ: Data curation, Writing–review and editing.

Funding

The authors declare that no financial support was received for the research, authorship, and/or publication of this article.

Conflict of interest

Authors XW, YJ, ZS, CL, and ZJ were employed by Jiangsu Donggang Energy Investment Co., Ltd.

Publisher's note

All claims expressed in this article are solely those of the authors and do not necessarily represent those of their affiliated organizations, or those of the publisher, the editors and the reviewers. Any product that may be evaluated in this article, or claim that may be made by its manufacturer, is not guaranteed or endorsed by the publisher.

References

Alnasser, A., and Rikli, N. E. (2014). "Design of a trust security model for smart meters in an urban power grid network," in *Proceedings of the 10th ACM symposium on QoS and security for wireless and mobile networks*, 105–108.

Alnasser, A., and Sun, H. (2017). A fuzzy logic trust model for secure routing in smart grid networks. *IEEE access* 5, 17896–17903. doi:10.1109/access.2017.2740219

Amaizu, G. C., Nwakanma, C. I., Bhardwaj, S., Lee, J. M., and Kim, D. S. (2021). Composite and efficient DDoS attack detection framework for B5G networks. *Comput. Netw.* 188, 107871. doi:10.1016/j.comnet.2021.107871

Bi, J., Li, J., Wu, K., Gao, Y., Chen, Z., Feng, D., et al. (2023). A data-driven flow surrogate model based on a data-driven and physics-driven method. *Petr. Geol. Rec. Effi* 30 (3), 104–114. doi:10.13673/j.pgre.202205049

Cao, Y., Zhou, B., Chung, C. Y., Shuai, Z., Hua, Z., and Sun, Y. (2023). Dynamic modelling and mutual coordination of electricity and watershed networks for spatio-temporal operational flexibility enhancement under rainy climates. *IEEE Trans. Smart Grid* 14 (5), 3450–3464. doi:10.1109/tsg.2022.3223877

Cao, Y., Zhou, B., Chung, C. Y., Wu, T., Ling, Z., and Shuai, Z. (2024). A coordinated emergency response scheme for electricity and watershed networks considering spatio-temporal heterogeneity and volatility of rainstorm disasters. *IEEE Trans. Smart Grid*, 1. doi:10.1109/TSG.2024.3362344

Cil, A. E., Yildiz, K., and Buldu, A. (2021). Detection of DDoS attacks with feed forward based deep neural network model. *Expert Syst. Appl.* 169, 114520. doi:10.1016/j.eswa.2020.114520

Desai, S., Alhadad, R., Chilamkurti, N., and Mahmood, A. (2019). A survey of privacy preserving schemes in IoE enabled smart grid advanced metering infrastructure. *Clust. Comput.* 22, 43–69. doi:10.1007/s10586-018-2820-9

Dhakne, A. R., and Chatur, P. N. (2017). Design of hierarchical trust based intrusion detection system for wireless sensor network. *Int. J. Appl. Eng. Res.* 12 (8), 1772–1778.

Fan, K., Chen, Q., Su, R., Zhang, K., Wang, H., Li, H., et al. (2021). Msiap: a dynamic searchable encryption for privacy-protection on smart grid with cloud-edge-end. *IEEE Trans. Cloud Comput.* 11 (2), 1170–1181. doi:10.1109/tcc.2021.3134015

Fu, R., Lichtenwalner, M. E., and Johnson, T. J. (2023). A review of cybersecurity in grid-connected power electronics converters: vulnerabilities, countermeasures, and testbeds. *IEEE Access* 11, 113543–113559. doi:10.1109/access.2023.3324177

Guo, Y., Hou, Z., Liu, S., and Jin, S. (2019). Data-driven model-free adaptive predictive control for a class of MIMO nonlinear discrete-time systems with stability analysis. *IEEE Access* 7, 102852–102866. doi:10.1109/access.2019.2931198

Haghnegahdar, L., and Wang, Y. (2020). A whale optimization algorithm-trained artificial neural network for smart grid cyber intrusion detection. *Neural Comput. Appl.* 32 (13), 9427–9441. doi:10.1007/s00521-019-04453-w

Hou, Z. S., and Xu, J. X. (2009). On data-driven control theory: the state of the art and perspective. *Acta. Autom. Sin.* 35, 650–667. doi:10.3724/sp.j.1004.2009.00650

Jabr, R. A. (2013). Adjustable robust OPF with renewable energy sources. *IEEE Trans. Power Syst.* 28, 4742–4751. doi:10.1109/tpwrs.2013.2275013

Kaur, S., Kumar, K., Aggarwal, N., and Singh, G. (2021). A comprehensive survey of DDoS defense solutions in SDN: taxonomy, research challenges, and future directions. *Comput. Secur* 110, 102423. doi:10.1016/j.cose.2021.102423

Luo, G. (2016). A review of automatic selection methods for machine learning algorithms and hyper-parameter values. *Netw. Model. Anal. Health Inf. Bioinforma.* 5, 18. doi:10.1007/s13721-016-0125-6

Menezes, G. K., Astolfi, G., Martins, J. A. C., Tetila, E. C., Junior, A. D. S. O., Gonçalves, D. N., et al. (2023). Pseudo-label semi-supervised learning for soybean monitoring. *Smart Agri. Tech.* 4, 100216. doi:10.1016/j.atech.2023.100216

Mittal, M., Kumar, K., and Behal, S. (2023). DDoS-AT-2022: a distributed denial of service attack dataset for evaluating DDoS defense system. *Proc. Indian Natl. Sci. Acad.* 89 (2), 306–324. doi:10.1007/s43538-023-00159-9

Mittal, M., Kumar, K., and Behal, S. (2023). DL-2P-DDoSADF: deep learning-based two-phase DDoS attack detection framework. *J. Inf. Secur. Appl.* 78, 103609. doi:10.1016/j.jisa.2023.103609

Nguyen, T. T., Nguyen, T. T., and Le, B. (2022). Artificial ecosystem optimization for optimizing of position and operational power of battery energy storage system on the distribution network considering distributed generations. *Expert Syst. Appl.* 208, 118127. doi:10.1016/j.eswa.2022.118127

Osanaiye, O., Choo, K. K. R., and Dlodlo, M. (2016). Distributed denial of service (DDoS) resilience in cloud: review and conceptual cloud DDoS mitigation framework. *J. Netw. Comput. Appl.* 67, 147–165. doi:10.1016/j.jnca.2016.01.001

Othman, S. M., Ba-Alwi, F. M., Alsohybe, N. T., and Al-Hashida, A. Y. (2018). Intrusion detection model using machine learning algorithm on Big Data environment. *J. Big Data* 5 (1), 34–12. doi:10.1186/s40537-018-0145-4

Priyadarshini, R., and Barik, R. K. (2022). A deep learning based intelligent framework to mitigate DDoS attack in fog environment. *J. King Saud University-Computer Inf. Sci.* 34 (3), 825–831. doi:10.1016/j.jksuci.2019.04.010

Riquelme-Dominguez, J. M., Gonzalez-Longatt, F., Melo, A. F. S., Rueda, J. L., and Palensky, P. (2023). Cyber-physical testbed Co-simulation real-time: normal and abnormal system frequency response. *IEEE Trans. Ind. Appl.* 60 (2), 2643–2652. doi:10.1109/tia.2023.3342764

Singh, N. K., Gupta, P. K., and Mahajan, V. (2020). Intrusion detection in wireless network of smart grid using intelligent trust-weight method. *Smart Sci.* 8 (3), 152–162. doi:10.1080/23080477.2020.1805679

Singh, N. K., and Mahajan, V. (2020). Detection of cyber cascade failure in smart grid substation using advance grey wolf optimization. *J. Interdiscip. Math.* 23 (1), 69–79. doi:10.1080/09720502.2020.1721664

Singh, N. K., and Mahajan, V. (2021). End-user privacy protection scheme from cyber intrusion in smart grid advanced metering infrastructure. *Int. J. Crit. Infrastructure Prot.* 34, 100410. doi:10.1016/j.ijcip.2021.100410

Vu, L., Nguyen, T. L., Abdelrahman, M. S., Vu, T., and Mohammed, O. A. (2023). A cyber-HIL for investigating control systems in ship cyber physical systems under communication issues and cyber attacks. *IEEE Trans. Ind. Appl.* 60 (2), 2142–2152. doi:10.1109/tia.2023.3311429

Yu, T., Da, K., Wang, Z., Ling, Y., Li, X., Bin, D., et al. (2022). An advanced accurate intrusion detection system for smart grid cybersecurity based on evolving machine learning. *Front. Energy Res.* 10, 903370. doi:10.3389/fenrg.2022.903370

Zhang, D., Kang, C., Lu, X., Liu, X., Zhang, N., and Xu, Y. (2021). Demonstration on the scale of energy storage deployment in high-proportion new energy power system. *South. Power Syst. Technol.* 16, 3–11.

Zhang, Y., Meng, X., Malik, A., and Wang, L. (2022). The use of analytical converter loss formula to eliminate DC slack/droop bus iteration in sequential AC-DC power flow algorithm. *Int. J. Electr. Power and Energy Syst.* 137, 107596. doi:10.1016/j.ijepes.2021.107596

Zhang, Y., Meng, X., Shotorbani, A. M., and Wang, L. (2020a). Minimization of AC-DC grid transmission loss and DC voltage deviation using adaptive droop control and improved AC-DC power flow algorithm. *IEEE Trans. Power Syst.* 36 (1), 744–756. doi:10.1109/tpwrs.2020.3020039

Zhang, Y., Mohammadpour Shotorbani, A., Wang, L., and Mohammadi-Ivatloo, B. (2021a). Enhanced PI control and adaptive gain tuning schemes for distributed

secondary control of an islanded microgrid. *IET Renew. Power Gener.* 15 (4), 854–864. doi:10.1049/rpg2.12074

Zhang, Y., Qian, W., Shao, J., Zhang, F., Wang, L., Hu, Q., et al. (2024). Adaptive voltage reference based controls of converter power sharing and pilot voltage in HVDC system for large-scale offshore wind integration. *IEEE Open Access J. Power Energy* 11, 55–67. doi:10.1109/oajpe.2024.3354079

Zhang, Y., Qian, W., Ye, Y., Li, Y., Tang, Y., Long, Y., et al. (2023). A no*vel non*-intrusive load monitoring method based on ResNet-seq2seq networks for energy disaggregation of distributed energy resources integrated with residential houses. *Appl. Energy* 349, 121703. doi:10.1016/j.apenergy.2023.121703

Zhang, Y., Shotorbani, A. M., Wang, L., and Li, W. (2020b). Distributed voltage regulation and automatic power sharing in multi-terminal HVDC grids. *IEEE Trans. Power Syst.* 35 (5), 3739–3752. doi:10.1109/tpwrs.2020.2986168

Zhang, Y., Shotorbani, A. M., Wang, L., and Li, W. (2021b). A combined hierarchical and autonomous DC grid control for proportional power sharing with minimized voltage variation and transmission loss. *IEEE Trans. Power Deliv.* 37 (4), 3213–3224. doi:10.1109/tpwrd.2021.3125254

Zhang, Y., Shotorbani, A. M., Wang, L., and Mohammadi-Ivatloo, B. (2021c). Distributed secondary control of a microgrid with a generalized PI finite-time controller. *IEEE Open Access J. Power Energy* 8, 57–67. doi:10.1109/oajpe.2021.3056507

Zhang, Y., Wang, L., and Li, W. (2020c). Autonomous DC line power flow regulation using adaptive droop control in HVDC grid. *IEEE Trans. Power Deliv.* 36 (6), 3550–3560. doi:10.1109/tpwrd.2020.3044978

Zhao, N., and You, F. (2021). New York State's 100% renewable electricity transition planning under uncertainty using a data-driven multistage adaptive robust optimization approach with machine-learning. *Adv. Appl. Ene* 2, 100019. doi:10.1016/j.adapen.2021.100019

Zhao, Y., Yuan, Z., Lu, C., Zhang, G., Li, X., and Chen, Y. (2016). Improved model-free adaptive wide-area coordination damping controller for multipleinput-multiple-output power systems. *IET Gener. Transm. Distrib.* 10, 3264–3275. doi:10.1049/iet-gtd.2016.0069

frontiers | Frontiers in Energy Research

TYPE Original Research
PUBLISHED 09 August 2024
DOI 10.3389/fenrg.2024.1459667

OPEN ACCESS

EDITED BY
Yitong Shang,
Hong Kong University of Science and Technology, Hong Kong SAR, China

REVIEWED BY
Jian Chen,
Shandong University, China
Jiehui Zheng,
South China University of Technology, China

*CORRESPONDENCE
Shiwei Xie,
shiwei_xie@126.com

RECEIVED 04 July 2024
ACCEPTED 19 July 2024
PUBLISHED 09 August 2024

CITATION
Yan Y, Xie S, Tang J, Qian B, Lin X and Zhang F (2024), Transaction strategy of virtual power plants and multi-energy systems with multi-agent Stackelberg game based on integrated energy-carbon pricing.
Front. Energy Res. 12:1459667.
doi: 10.3389/fenrg.2024.1459667

Transaction strategy of virtual power plants and multi-energy systems with multi-agent Stackelberg game based on integrated energy-carbon pricing

Yanyu Yan[1], Shiwei Xie[1]*, Jianlin Tang[2,3], Bin Qian[2,3], Xiaoming Lin[2,3] and Fan Zhang[2,3]

[1]School of Electrical Engineering and Automation, Fuzhou University, Fuzhou, China, [2]Electric Power Research Institute of CSG, Guangzhou, China, [3]Guangdong Provincial Key Laboratory of Intelligent Measurement and Advanced Metering for Power Grid, Guangzhou, China

A virtual power plant (VPP) has the ability to aggregate numerous decentralized distributed energy resources using advanced control technology, offering a promising approach for low-carbon development. In order to enhance the VPP's contribution to reducing carbon emissions, a bi-level framework is proposed that incorporates an integrated energy-carbon price response mechanism. This model allows VPPs to participate in a multi-energy system through a multi-agent Stackelberg game framework. Initially, a transaction model is established where the power distribution system operator and the gas distribution system operator act as leaders, while the virtual power plant operator acts as a follower in the multi-energy system. Subsequently, an integrated energy-carbon pricing method, rooted in carbon emission flow theory, is introduced to encourage VPPs to proactively adjust their energy-use and trading strategies within multi-energy systems, thereby promoting multi-principal interactive trading. To achieve a distributed solution among multiple entities while maintaining the privacy of each entity's information, the adaptive step-size alternating direction multiplier method is employed. The feasibility and effectiveness of the proposed model and method are then demonstrated through case studies.

KEYWORDS

virtual power plant, multiple energy systems, carbon emission flow, energy-carbon integrated price, multi-agent Stackelberg game

1 Introduction

The construction of a new type of power system primarily based on new energy resources is being accelerated, emphasizing both centralized and distributed energy resources. However, distributed energy resources (DERs), characterized by strong uncertainty, decentralization, and heterogeneity (Chen et al., 2021), pose significant threats to the security of grid-connected power systems due to their large numbers. Virtual power plants (VPPs) are widely employed to effectively aggregate large, dispersed, and diverse DERs through advanced control, metering, communication, and other technologies (Vasirani et al., 2013; Zhao et al., 2018; Bhuiyan et al., 2021). This facilitates accurate control of internal resources, providing a viable pathway for low-carbon

development. In the context of the interactive integration of multiple energy systems (Wang et al., 2018), VPPs participating in both the power distribution and gas distribution systems can leverage the complementary characteristics of electricity and gas. This enables the realization of synergistic operations within a multi-energy network, enhancing the economic efficiency and promoting low-carbon objectives for all stakeholders involved.

To advance the role of VPPs in the low carbon economy, several research studies have been conducted. Previous works in (Zhang et al., 2023) examine the interactions between VPPs and the higher-level grid based on peak and off-peak time-sharing tariffs. It also developed an operational model for VPPs under carbon trading and green certificate trading mechanisms, considering both economic and low-carbon aspects. Reference (Yi et al., 2020a) addresses power flow constraints in the distribution network by formulating a two-layer planning problem involving VPPs and the distribution network, optimizing dynamic pricing for VPPs. Reference (Yi et al., 2020b) proposes a two-layer model for VPPs and the distribution system, achieving co-optimization of multiple VPPs with the distribution network through an integrated active and reactive power pricing approach. These studies primarily focus on transaction pricing strategies for VPPs in the distribution market, with an increasing involvement of VPPs in multi-energy system transactions due to the close integration of various energy systems. Reference (Yang et al., 2021) introduces a model for energy trading in micro-energy networks that considers electricity-heat multi-energy sharing, ultimately reducing energy costs for multi-energy micro-grids. Additionally, works in (Zhang and Hu, 2022) suggest an optimal scheduling model for VPPs to engage in simultaneous trading within the electricity-gas multi-energy market, considering security constraints of the natural gas network and bidirectional flow of electricity and natural gas. However, the majority of these studies view VPPs predominantly as passive recipients of energy prices, ignoring their potential for active participation in multi-energy system trading and interactions with other entities.

With the advancement of VPP technology, conflicts of interest stemming from the involvement of various entities in competitive multi-energy markets have become inevitable. Game theory is increasingly being utilized to address optimization problems related to VPPs. In (Xu et al., 2022), a VPP pricing strategy is proposed within a two-tier market structure involving multiple VPPs and distribution markets. A non-cooperative pricing game model is established to enhance the economic efficiency of multiple entities. Meanwhile, Reference (Liu, 2022) introduces a cooperative game model for VPP scheduling in the context of multiple regional integrated energy systems. This model aims to optimize multiple energy sources to meet the electricity-heat-gas demand of each integrated energy system within the VPP coordinated scheduling strategy, fostering cooperative benefit sharing among members. In analyzing the intricate interactions among providers and responders of energy prices across multiple entities in multi-energy system transactions, a master-slave game model is deemed more appropriate for understanding the sequential order of the game. The research in (Zangeneh et al., 2018) adopts a multi-leader-follower master-slave game model to describe the competition between multiple VPPs and the superior market, determining the optimal pricing strategy for multiple parties to realize optimal transactions for each entity. The study in (Wei et al., 2017) investigates multi-energy interaction transaction strategies between multiple distributed energy stations and users by constructing an energy transaction model based on a multi-leader-multiple-follower game. A model in (Chen et al., 2023) constructs a Stackelberg game trading model involving energy retailers and VPPs, where the energy operator guides the power purchase and sale behavior of VPP through tariff optimization. Research in (Lu Q. et al., 2023) proposes a one-master-many-slave game optimization model for community integrated energy systems, considering carbon trading mechanisms and integrated demand response, which realizes interactive equilibrium between energy suppliers and load aggregators, significantly improving the economic and low-carbon benefits of each entity.

However, there are still research gaps in the above studies, which are mainly manifested in the following two aspects: 1) Existing studies on low-carbon operation of VPPs primarily focus on carbon emission measurement from the power supply side, with less emphasis on the demand side. This limitation hinders the ability to guide load-side low-carbon electricity consumption behavior. Carbon emission flow (CEF) theory, as an effective analytical method for the low-carbon development of power systems (Cheng et al., 2019a; Cheng et al., 2019b; Sun et al., 2023), offers new perspectives on load-side carbon emission responsibility sharing and facilitates low-carbon demand response. Studies (Lu Z. et al., 2023; Yan et al., 2023) have proposed low-carbon optimal dispatch models for multi-energy systems based on CEF theory. These models implement carbon-aware distribution locational marginal pricing (CDLMP) and stepped carbon pricing to actively guide loads in reducing system carbon emissions. 2) The measurement methods of VPP carbon emissions in existing studies are not sufficiently accurate. Most studies only consider the internal carbon emissions of VPPs, neglecting the indirect carbon emissions resulting from purchasing electricity from the higher grid and gas from the gas grid. Furthermore, the purchase and sale of energy are usually based on fixed or time-based pricing, which does not account for the significant potential of integrated energy-carbon pricing to reduce VPP carbon emissions.

This paper proposes a bi-level model that optimizes a multi-agent Stackelberg game with VPP participation in multi-energy systems under an integrated energy-carbon price response mechanism. In this model, the distribution system operator (DSO) and gas system operator (GSO) act as leaders, while the VPP operator (VPPO) acts as a follower. The model focuses on VPP participation in a multi-energy system under the energy-carbon integrated price response mechanism. The paper also introduces an integrated energy-carbon pricing method based on CEF theory to help VPPs adjust their energy consumption and trading strategies to reduce carbon emissions. The study includes carbon flow tracking for distributed VPP energy transactions, taking into account the carbon emission responsibilities of VPPs when purchasing electricity and natural gas. To ensure privacy, the adaptive step-size alternating direction method of multipliers (ADMM) is used for a distributed solution. The effectiveness of the proposed model and method is demonstrated through case analysis.

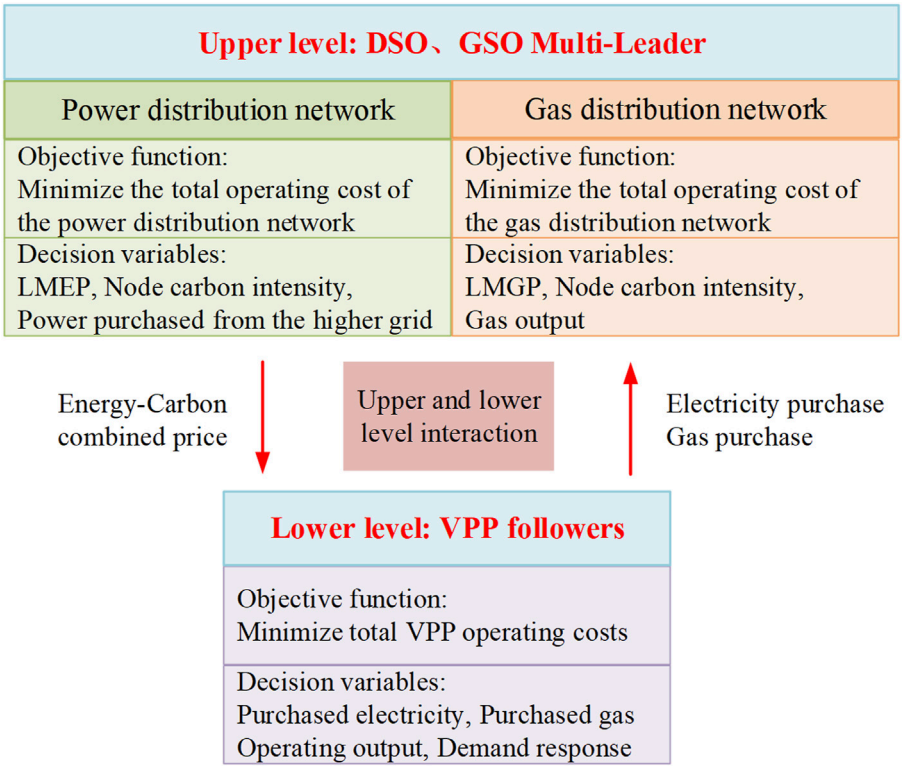

FIGURE 1
A bi-level framework for electric-gas multi-energy systems and VPP transactions.

2 Electric-gas multi-energy system and VPP low-carbon operation bi-level framework

The study aims to develop a low-carbon economic operational model suitable for power distribution networks, gas distribution networks, and VPPs. Due to conflicting objective functions among the three stakeholders, i.e., DSO, GSO, and VPPO, and the presence of multiple variables, a bi-level model for the interactions between multi-energy systems and the VPP considering integrated energy-carbon pricing is proposed. The transaction dynamics between DSO, GSO, and VPPO are modeled as a multi-agent Stackelberg game, where DSO and GSO are considered as the leaders and VPPO as the follower. The bi-level transaction framework is illustrated in Figure 1.

The upper level features the optimal scheduling model for the electricity-gas multi-energy system. The DSO and GSO calculate the optimal power flow (OPF) for the power distribution network and the gas distribution network based on the energy purchasing demand transmitted from the lower level. Their objective is to minimize the total operating cost for each of them. They also integrate the distribution network trends to solve the distribution of the CEF and formulate the integrated energy-carbon price. For energy pricing, this paper adopts the locational marginal electricity price (LMEP) and locational marginal gas price (LMGP). The decision information derived from this process is then provided back to the lower-level model.

The follower VPP at the lower level responds to the integrated energy-carbon price information by optimizing the energy use of internal gas turbine CHP units, gas boilers, power storage equipment, and distributed wind power, with the goal of minimizing the total operating cost. The VPP develops the internal optimal scheduling strategy and uploads the power purchasing demand and gas purchasing demand information to the upper-level DSO and GSO, respectively.

In summary, the power distribution network and the gas distribution network optimize OPF and CEF based on the energy purchase demand of the VPP and its internal optimization results. They then pass the integrated energy-carbon price and node carbon intensity obtained from the solution back to the VPP. The VPP uses this information to formulate the latest internal optimization scheduling strategy and update its energy purchase demand. This iterative process continues until the transactions of each subject in the bi-level model reach a consensus and meet the convergence conditions, thus achieving the overall optimal operation of the power distribution network, gas distribution network, and VPP.

3 A bi-level formulation for energy transaction

Since DSOs, GSOs, and VPPOs represent different stakeholders, it is essential to establish transaction models for each party that consider the interaction of electricity and natural gas between the distribution and the VPP. This includes the energy pricing model of

the upper-tier electricity-gas multi-energy system, the carbon pricing model, and the lower-level VPP energy optimization model.

3.1 Energy pricing modeling for electric-gas multi-energy systems

3.1.1 Pricing model for power distribution networks

In this section, the LMEP pricing model for power distribution networks based on second order cone programming (SOCP) is constructed with the objective of minimizing the operating cost of power distribution networks (Xie et al., 2023; Xie et al., 2024).

3.1.1.1 Objective function

The objective of the DSO is to minimize the total operating cost f_{DSO} of the power distribution network, including the cost C_t^{b} of coal-fired unit generation and the cost C_t^{grid} of purchased power from the higher grid, as presented in Eqs 1–3 as follows:

$$\min f_{\mathrm{DSO}} = \sum_{t=1}^{T}\left(C_t^{\mathrm{b}} + C_t^{\mathrm{grid}}\right) \tag{1}$$

$$C_t^{\mathrm{b}} = \sum_{g\in G}\left(a_g\left(P_{g,t}\right)^2 + b_g P_{g,t} + c_g\right) \tag{2}$$

$$C_t^{\mathrm{grid}} = \lambda_t^{\mathrm{grid}} P_t^{\mathrm{grid}} \tag{3}$$

where T is the total number of scheduling hours; G is the set of coal-fired units in the distribution network; a_g, b_g and c_g are the generation cost coefficients of the coal-fired units g; $P_{g,t}$ is the active power output of the units at the moment t; $\lambda_t^{\mathrm{grid}}$ is the selling price of the higher-level grid at the moment t; and P_t^{grid} is the active power purchased by the DSO from the higher-level grid at the moment t.

3.1.1.2 Power system constraints

$$\sum_{g\in n} P_{g,t} + \sum_{w\in n} P_{w,t}^{\mathrm{wind}} + P_t^{\mathrm{grid}} - P_t^{\mathrm{buy}} = P_{n,t}^{\mathrm{L}} + \sum_{b(n,\cdot)\in n} P_{b,t}^{\mathrm{DN}} - \sum_{l(\cdot,n)\in n}\left(P_{l,t}^{\mathrm{DN}} - a_{l,t}r_l\right): \lambda_{n,t}^{\mathrm{LMEP}}$$
$$n \in N_{\mathrm{DN}} \tag{4}$$

$$\sum_{g\in n} Q_{g,t} + Q_t^{\mathrm{grid}} - \eta P_t^{\mathrm{buy}} = Q_{n,t}^{\mathrm{L}} + \sum_{b(n,\cdot)\in n} Q_{b,t}^{\mathrm{DN}} - \sum_{l(\cdot,n)\in n}\left(Q_{l,t}^{\mathrm{DN}} - a_{l,t}x_l\right) \tag{5}$$

$$\left(P_{b,t}^{\mathrm{DN}}\right)^2 + \left(Q_{b,t}^{\mathrm{DN}}\right)^2 \le S_l^2 \tag{6}$$

$$\left(P_{l,t}^{\mathrm{DN}} - a_{l,t}r_l\right)^2 + \left(Q_{l,t}^{\mathrm{DN}} - a_{l,t}x_l\right)^2 \le S_l^2 \tag{7}$$

$$\left(P_{l,t}^{\mathrm{DN}}\right)^2 + \left(Q_{l,t}^{\mathrm{DN}}\right)^2 \le a_{l,t}U_{n',t} \tag{8}$$

$$U_{n',t} - 2\left(r_l P_{l,t}^{\mathrm{DN}} + x_l Q_{l,t}^{\mathrm{DN}}\right) + a_{l,t}\left(r_l^2 + x_l^2\right) = U_{n,t} \tag{9}$$

$$U_{\min}^2 \le U_{n,t} \le U_{\max}^2 \tag{10}$$

$$\begin{cases} P_{g,\min} \le P_{g,t} \le P_{g,\max} \\ Q_{g,\min} \le Q_{g,t} \le Q_{g,\max} \end{cases} \tag{11}$$

where $g \in n$, $w \in n$ denotes the coal-fired unit g and fan w connected to node n, respectively; $b(n,\cdot) \in n$ denotes the line injected from node n to other nodes, denoted as b; $l(\cdot,n) \in n$ denotes the branch l injected from other nodes to node n, respectively; N_{DN} is the set of nodes in the distribution network; $P_{w,t}^{\mathrm{wind}}$ is the active power output of fan w at the moment t; P_t^{buy} is the purchased power of VPP to the distribution network at the moment t; $P_{n,t}^{\mathrm{L}}, Q_{n,t}^{\mathrm{L}}$ are the active and reactive power loads connected to node n at the moment t, respectively; $P_{b,t}^{\mathrm{DN}}$, $P_{l,t}^{\mathrm{DN}}$, $Q_{b,t}^{\mathrm{DN}}$, $Q_{l,t}^{\mathrm{DN}}$ are the active and reactive power flowing through lines b and l at time t, respectively; $a_{l,t}$ denotes the square of the current of branch l at time t; r_l, x_l are the resistance and reactance of branch l, respectively; $\lambda_{n,t}^{\mathrm{LMEP}}$ is the dyadic variable corresponding to the active power balance constraint; $Q_{g,t}$ is the reactive power output of coal-fired unit g at time t; Q_t^{grid} is the reactive power purchased by the distribution network from the higher-level grid at time t; η denotes the power factor of the loads; $U_{n,t}$ is the square of the magnitude of the node n at time t; S_l is the upper limit of the apparent power of line l; $U_{\min}, U_{\max}$ are the lower and upper limit of the magnitude of the node voltage, respectively; $P_{g,\min}$, $P_{g,\max}$, $Q_{g,\min}$, $Q_{g,\max}$ are the lower and upper limit of the active and reactive power output of unit g, respectively. Eqs 4, 5 represent the nodal active and reactive power balance constraints. Eqs 6, 7 represent the power flow limits in each line. Eq. 8 represents convex SOC relaxation to the original equality of the apparent power. Eq. 9 is the forward voltage drop equation. Eq. 10 is the limits of the nodal voltage. Eq 11 represents the generator active and reactive output constraints.

3.2 Pricing model for gas distribution networks

This section constructs a SOCP-based LMEP pricing model for gas distribution networks with the objective of minimizing the gas distribution network operating costs.

3.2.1 Objective function

The gas distribution network consists of the gas source, gas pipeline, air compressor, and gas load, and in this paper it is assumed that the flow of natural gas in the gas pipeline has been determined. The objective of the GSO is to minimize the operating cost f_{GSO} of the gas distribution network, i.e., to minimize the cost of natural gas purchased by the GSO from the natural gas company, which is expressed in the Eq. 12 as follows:

$$\min f_{\mathrm{GSO}} = \sum_{t=1}^{T}\left(\sum_{s\in N_s} y_{s,t}^{\mathrm{well}} w_{s,t}^{\mathrm{well}}\right) \tag{12}$$

where $y_{s,t}^{\mathrm{well}}$, $w_{s,t}^{\mathrm{well}}$ are the price and volume of gas purchased by the GSO from gas source s at time t, respectively; N_s is the set of gas sources.

3.2.2 Gas system constraints

$$\sum_{s\in j} w_{s,t}^{\mathrm{well}} + \sum_{ij\in z(j)} w_{ij,t} - \sum_{jk\in v(j)} w_{jk,t} - w_{j,t}^{\mathrm{load}} - w_t^{\mathrm{buy}} = 0: \lambda_{j,t}^{\mathrm{LMGP}}$$
$$j \in N_{GN} \tag{13}$$

$$w_{ij,t} = sign\left(\pi_{i,t} - \pi_{j,t}\right)C_{ij}\sqrt{\left|\left(\pi_{i,t}\right)^2 - \left(\pi_{j,t}\right)^2\right|} \tag{14}$$

$$w_{ij}^{\min} \le w_{ij,t} \le w_{ij}^{\max} \tag{15}$$

$$\pi_j^{\min} \le \pi_{j,t} \le \pi_j^{\max} \tag{16}$$

$$\pi_{j,t} \le k\pi_{i,t} \tag{17}$$

$$w_s^{\min} \le w_{s,t}^{\text{well}} \le w_s^{\max} \tag{18}$$

where $s \in j$ denotes the natural gas source s at node j; $z(j)$ is the set of pipelines at the end node j; $v(j)$ is the set of pipelines at the first node j; N_{GN} is the set of nodes in the distribution network; $w_{ij,t}$, $w_{jk,t}$ are the amount of natural gas flowing through the pipelines ij and jk, respectively, at time t; $w_{j,t}^{\text{load}}$ is the gas load at node j of the gas distribution network; w_t^{buy} is the amount of natural gas purchased from the gas distribution network by the VPP, respectively, at time t; $\lambda_{j,t}^{\text{LMGP}}$ is the dyadic variable corresponding to the natural gas node flow equilibrium constraints; $\pi_{i,t}$ and $\pi_{j,t}$ are the pressures at nodes i and j at time t, respectively; C_{ij} is the pipeline transmission characteristic parameters; $w_{ij}^{\max}$, $w_{ij}^{\min}$ are the upper and lower bounds on the amount of natural gas to be transmitted by the pipeline; $\pi_j^{\max}$, $\pi_j^{\min}$ are the upper and lower bounds on the gas pressure at node j, respectively; k is the compressor coefficients; $w_s^{\max}$, $w_s^{\min}$ are the upper and lower bounds on the output of the natural gas source s, respectively. Eq 13 is the natural gas node flow balance constraint. Eq 14 is the Weymouth equation (Chen et al., 2019) for the pipeline gas flow, where $sign(\cdot)$ is a sign function that one when $\pi_{i,t} \ge \pi_{j,t}$ and −1 otherwise. Eq 15 is the gas network pipeline flow limit. Eqs 16, 17 denote the natural gas nodal pressure constraints. Eq. 18 denotes the gas supply constraints of gas wells.

3.3 Carbon pricing model for multi-energy systems based on CEF theory

3.3.1 CEF modeling for multi-energy systems

While most of the CO2 in the energy industry is generated on the source side, the ultimate driver of carbon emissions is on the load side. The focus of this paper is on how to price carbon emissions from generation to end-users so that the right incentives can be provided between electricity-gas multi-energy systems. The theory of CEF, which is based on the energy flow of the system, can intuitively characterize the flow direction of carbon emission during the system operation, and improve the new analysis perspective for the low-carbon economic dispatch (Cheng et al., 2020). In the CEF model, the carbon flow index is usually used to describe the carbon emission apportionment, this paper mainly needs to obtain the carbon intensity of each node of the electric-gas multi-energy system as a carbon signal, and through the carbon tax to establish the link between the carbon price and the node carbon intensity accessed by the VPP, and the CEF model is established as follows.

3.3.1.1 CEF modeling of power distribution networks

The node carbon intensity represents the value of carbon emissions equivalent to the generation side caused by a unit of electricity consumed at that node, calculated in Eq. 19 as follows:

$$e_{n,t}^{\text{ele}} = \frac{\sum_{g\in n} P_{g,t}e_g + \sum_{l(\cdot,n)\in n}\left(P_{l,t}^{\text{DN}} - a_{l,t}r_l\right)\rho_{l,t}}{\sum_{g\in n} P_{g,t} + \sum_{w\in n} P_{w,t}^{\text{wind}} + \sum_{l(\cdot,n)\in n}\left(P_{l,t}^{\text{DN}} - a_{l,t}r_l\right)} \tag{19}$$

where $e_{n,t}^{\text{ele}}$, $\rho_{l,t}$ denote the nodal carbon intensity of node n and the carbon flow intensity of branch l at time t, respectively; e_g is the carbon emission intensity of coal-fired unit g.

The branch carbon intensity denotes the equivalent value of carbon emission on the generation side caused by a unit of electricity transmitted by a tributary. According to the proportional sharing principle (Kang et al., 2015), the carbon flow intensity of all transmission lines flowing from node n is equal to the carbon intensity of that node, which is expressed in Eq. 21 as follows:

$$\rho_{l,t} = e_{n,t}^{\text{ele}}, \forall l(n,\cdot) \in n \tag{20}$$

3.3.1.2 CEF modeling of gas distribution networks

The gas distribution network CEF model is similar to that of the power distribution network, and the carbon intensity of each node and the branch carbon intensity are calculated as follows:

$$e_{j,t}^{\text{gas}} = \frac{\sum_{s\in j} w_{s,t}^{\text{well}} e_s^{\text{well}} + \sum_{ij\in z(j)} w_{ij,t}\rho_{ij,t}}{\sum_{s\in j} w_{s,t}^{\text{well}} + \sum_{ij\in z(j)} w_{ij,t}} \tag{21}$$

$$\rho_{ij,t} = e_{i,t}^{\text{gas}}, \forall ij \in z(j) \tag{22}$$

where $e_{j,t}^{\text{gas}}$ is the carbon intensity of node j of the gas network at time t; $\rho_{ij,t}$ is the carbon flow intensity of the gas flow into pipeline ij of the pipeline connected to node j at time t; e_s^{well} is the carbon emission intensity of the gas source s connected to node j.

3.3.1.3 An integrated energy-carbon pricing approach based on the CEF theory

As consumers, the VPP must acknowledge their carbon emission responsibility when procuring electricity and gas from the power distribution and gas distribution networks. By utilizing the CEF model to calculate the nodal carbon intensity of these networks, a connection is established between the carbon price and nodal carbon intensity through carbon tax. Subsequently, the integrated electricity/gas energy-carbon pricing method is developed by combining the LMEP/LMGP with the carbon price in Eqs 23, 24 as follows:

$$\varsigma_{n,t}^{\text{ele}} = \lambda_{n,t}^{\text{LMEP}} + \tau e_{n,t}^{\text{ele}}, \forall n,t \tag{23}$$

$$\varsigma_{j,t}^{\text{gas}} = \lambda_{j,t}^{\text{LMGP}} + \tau e_{j,t}^{\text{gas}}, \forall j,t \tag{24}$$

where $\varsigma_{n,t}^{\text{ele}}$ is the integrated electricity-carbon price at node n of the power distribution network at time t; $\varsigma_{j,t}^{\text{gas}}$ is the integrated gas-carbon price at node j of the gas distribution network at time t; τ is the carbon tax. The integrated energy-carbon pricing system encourages VPPs to proactively adjust their energy purchases and internal scheduling strategies, leading to reduced carbon emissions and operating costs.

3.4 VPP energy optimization model

The operational framework of the VPP established in this study is illustrated in Figure 2. It comprises gas turbine combined heat and power (CHP) units, gas boilers, distributed wind power,

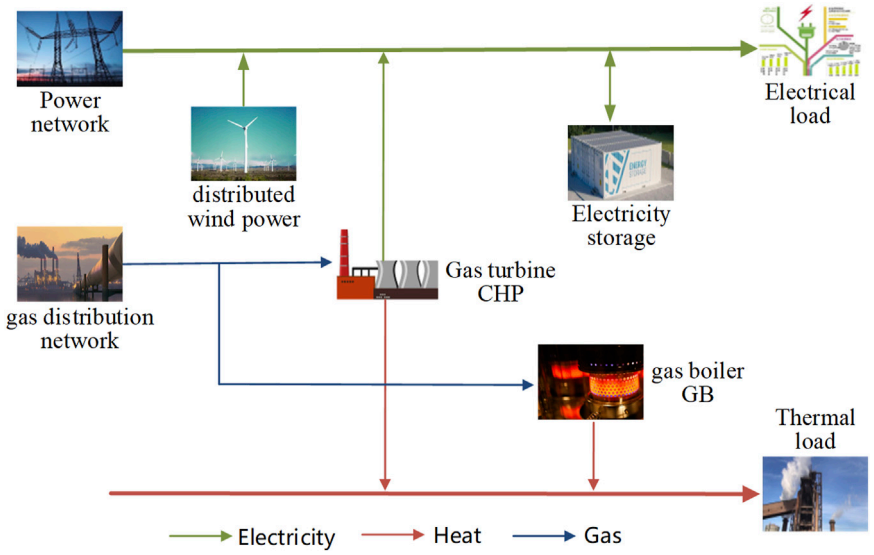

FIGURE 2
VPP operational framework.

and energy storage units. The flexible loads encompass electric and thermal loads, with consideration given to demand response for both to assist users in making informed energy demand adjustments. The VPP interfaces with the power distribution network via an electric power contact line and transports natural gas through a pipeline connecting it to the gas distribution network. Notably, this paper does not address the scenario of natural gas sales to the GSOs at this time.

3.4.1 VPP Objective Function

The objective of the VPP energy optimization model is to minimize the total operating cost f_{VPPO} in Eqs 25–28 as follows:

$$\min f_{\mathrm{VPPO}} = \sum_{t=1}^{T}\left(C_t^{\mathrm{ele,buy}} + C_t^{\mathrm{gas,buy}} + C_t^{\mathrm{DR}}\right) \tag{25}$$

$$C_t^{\mathrm{ele,buy}} = \varsigma_t^{\mathrm{ele}} P_t^{\mathrm{buy}} \tag{26}$$

$$C_t^{\mathrm{gas,buy}} = \varsigma_t^{\mathrm{gas}} w_t^{\mathrm{buy}} \tag{27}$$

$$C_t^{\mathrm{DR}} = \lambda_e^{\mathrm{cut}} P_t^{\mathrm{cut}} + \lambda_e^{\mathrm{tran}} P_t^{\mathrm{tran}} + \lambda_h^{\mathrm{cut}} H_t^{\mathrm{cut}} \tag{28}$$

where $C_t^{\mathrm{ele,buy}}$ is the cost of electricity purchased by VPP interacting with the power distribution network; $C_t^{\mathrm{gas,buy}}$ is the cost of natural gas purchased by VPP from the gas distribution network; C_t^{DR} is the cost of integrated demand response of electricity and heat in VPP; P_t^{tran}, P_t^{cut} denotes the amount of electric load transfer and load reduction in VPP at time t, respectively; H_t^{cut} denotes the amount of heat load reduction in VPP at time t; λ_e^{cut}, $\lambda_e^{\mathrm{tran}}$ are the unit price of compensation for electric load reduction and transfer; λ_h^{cut} denotes the unit price of compensation for heat load reduction.

3.4.2 VPP operational constraints

3.4.2.1 Power balance constraints

The power balance constraints for multiple energy flows within the VPP are given in Eq. 29 as follows:

$$\begin{cases} P_t^{\mathrm{CHP}} + P_t^{\mathrm{Wind}} + P_t^{\mathrm{ES,dis}} + P_t^{\mathrm{buy}} = P_t^{\mathrm{ES,cha}} + P_t^{\mathrm{load}} \\ H_t^{\mathrm{CHP}} + H_t^{\mathrm{GB}} = H_t^{\mathrm{load}} \\ w_t^{\mathrm{buy}} = w_t^{\mathrm{GT}} + w_t^{\mathrm{GB}} \end{cases} \tag{29}$$

where P_t^{CHP}, H_t^{CHP} are the power supplied by the gas turbine and the heat production power at time t, respectively; P_t^{Wind} is the actual output of renewable energy at time t; $P_t^{\mathrm{ES,cha}}$, $P_t^{\mathrm{ES,dis}}$ are the charging and discharging power of the electrical energy storage at time t; P_t^{load}, H_t^{load} are the amount of load after the demand response of electric and thermal loads at moment t; H_t^{GB} is the gas boiler heat power at time t; w_t^{GT}, w_t^{GB} are the amount of natural gas input to the gas turbine and gas boiler at moment t, respectively.

3.4.2.2 Gas turbine CHP unit constraints

The mathematical model and constraints for power and heat supply of CHP units are in Eq. 30 as follows:

$$\begin{cases} P_t^{\mathrm{CHP}} = \eta_{\mathrm{P}}^{\mathrm{CHP}} \dfrac{L_{\mathrm{CH_4}}}{Q_{\mathrm{EH}}} w_t^{\mathrm{GT}} \\ P_{\min}^{\mathrm{CHP}} \le P_t^{\mathrm{CHP}} \le P_{\max}^{\mathrm{CHP}} \\ H_t^{\mathrm{CHP}} = \eta_{\mathrm{H}}^{\mathrm{CHP}} \dfrac{L_{\mathrm{CH_4}}}{Q_{\mathrm{EH}}} w_t^{\mathrm{GT}} \end{cases} \tag{30}$$

where $\eta_{\mathrm{P}}^{\mathrm{CHP}}$, $\eta_{\mathrm{H}}^{\mathrm{CHP}}$ are the gas turbine power supply efficiency and heat production efficiency; $L_{\mathrm{CH_4}}$ is the calorific value of natural gas per unit volume; Q_{EH} is the thermal energy converted per unit of electrical energy; $P_{\max}^{\mathrm{CHP}}$, $P_{\min}^{\mathrm{CHP}}$ are the upper and lower limits of the power supply of the gas turbine.

3.4.2.3 Gas boiler output constraints

$$\begin{cases} H_t^{\mathrm{GB}} = \eta_{GB} \dfrac{L_{\mathrm{CH_4}}}{Q_{\mathrm{EH}}} w_t^{\mathrm{GB}} \\ H_{\min}^{\mathrm{GB}} \le H_t^{\mathrm{GB}} \le H_{\max}^{\mathrm{GB}} \end{cases} \tag{31}$$

where η_{GB} is the electric heat conversion efficiency of the gas boiler; $H_{\max}^{GB}$, $H_{\min}^{GB}$ are the upper and lower limits of the heat output of the gas boiler in the VPP, respectively. Eq. 31 represents the operating constraints of GB.

3.4.2.4 Energy storage unit constraints

The introduction of energy storage devices can further improve the operational flexibility of the VPP, the energy storage device is modeled in Eq. 32 as follows:

$$\begin{cases} S_t = \left(1-\eta^{\text{loss}}\right)S_{t-1} + \eta^{\text{cha}}P_t^{\text{ES,cha}} - \dfrac{P_t^{\text{ES,dis}}}{\eta^{\text{dis}}} \\ S_1 = S_{24} \\ 0 \le P_t^{\text{ES,cha}} \le \mu_t^{\text{ES,cha}} P_{\max}^{\text{ES,cha}} \\ 0 \le P_t^{\text{ES,dis}} \le \mu_t^{\text{ES,dis}} P_{\max}^{\text{ES,dis}} \\ \mu_t^{\text{ES,cha}} + \mu_t^{\text{ES,dis}} \le 1 \\ S^{\min} \le S_t \le S^{\max} \end{cases} \tag{32}$$

where S_t is the capacity of the energy storage device in the VPP at time t; η^{loss}, $\eta^{\text{ES,cha}}$, $\eta^{\text{ES,dis}}$ are the energy storage device energy loss coefficient, energy charging and discharging efficiency; where $\eta^{\text{loss}} \ll 1$; $P_{\max}^{\text{ES,cha}}$, $P_{\max}^{\text{ES,dis}}$ are the maximum charging and discharging power of the energy storage device; $S^{\min}$, $S^{\max}$ are the minimum and maximum storage capacity of the energy storage device; $\mu_t^{\text{ES,cha}}$, $\mu_t^{\text{ES,dis}}$ are the binary variable, respectively, represents the charging and discharging state of the energy storage device at t time.

3.4.2.5 Electric heat integrated demand response constraints

$$\begin{cases} P_t^{\text{load}} = P_t^0 + P_t^{\text{tran}} - P_t^{\text{cut}} \\ \left|P_t^{\text{tran}}\right| \le P_{\max}^{\text{tran}} \\ \sum_{t=1}^{T} P_t^{\text{tran}} = 0 \\ 0 \le P_t^{\text{cut}} \le P_{\max}^{\text{cut}} \\ H_t^{\text{load}} = H_t^0 - H_t^{\text{cut}} \\ 0 \le H_t^{\text{cut}} \le H_{\max}^{\text{cut}} \end{cases} \tag{33}$$

Eq. 33 represents the Electric heat integrated demand response constraints, where P_t^0 denotes the initial load of electric load in VPP at time t; $P_{\max}^{\text{tran}}$ denotes the upper limit of transferable electric load; $P_{\max}^{\text{cut}}$ denotes the upper limit of curtailable electric load; H_t^0 denotes the initial load of thermal load at time t; $H_{\max}^{\text{cut}}$ denotes the maximum curtailable thermal load.

4 Solution method for the muti-agent stackelberg game trading model

In the context of a multi-agent Stackelberg game transaction model involving the leader DSO, GSO, and follower VPP in an electricity-gas multi-energy system, each participant optimizes its operation state according to individual interest objectives and devises energy transaction strategies accordingly. Given the intricate internal information and substantial transaction volume, traditional centralized optimization algorithms are inadequate in meeting the information privacy needs of each participant within this model. Therefore, the proposed solution involves solving the multi-participant Stackelberg game model through a distributed approach using the adaptive ADMM algorithm.

4.1 Stackelberg game trading model

The game model contains three elements: the set of participants, the set of strategies and the set of benefits (Li et al., 2022), and the Stackelberg game is modeled in Eq. 34 as follows:

$$G = \left\{ \begin{array}{c} \{\text{DSO, GSO, VPPO}\}; \\ \left\{P_{g,t}, P_t^{\text{grid}}, w_{s,t}^{\text{well}}, \varsigma_{n,t}^{\text{ele}}, \varsigma_{j,t}^{\text{gas}}\right\}; \\ \left\{P_t^{\text{buy}}, w_t^{\text{buy}}\right\}; \\ f_{\text{DSO}}, f_{\text{GSO}}, f_{\text{VPPO}} \end{array} \right\} \tag{34}$$

(1) Participant set: {DSO, GSO, VPPO} represents the set of all participants. Where DSO and GSO are leaders and VPPO are followers.
(2) Strategy set: the strategy of the leader DSO is the amount of electricity purchased from each distributed generator and the higher grid at each moment and the integrated electricity-carbon price set, denoted as $\left\{P_{g,t}, P_t^{\text{grid}}, \varsigma_{n,t}^{\text{ele}}\right\}$; the strategy of the leader GSO is the amount of natural gas purchased from each distribution station and the integrated gas-carbon price set, denoted as $\left\{w_{s,t}^{\text{well}}, \varsigma_{j,t}^{\text{gas}}\right\}$; the strategy of the follower VPPO is the amount of electricity purchased with the DSO and the amount of gas purchased from the GSO, denoted as $\left\{P_t^{\text{buy}}, w_t^{\text{buy}}\right\}$.
(3) Benefits: The benefits to each participant are their objective functions, which can be expressed as f_{DSO}, f_{GSO} and f_{VPPO}, respectively.

4.2 Distributed solution of stackelberg game transaction model based on adaptive ADMM algorithm

The adaptive ADMM algorithm is utilized in this study for distributed solving of the proposed multi-agent Stackelberg game model. This approach ensures that the interaction between participating subjects does not compromise their internal privacy. Only the boundary information of each subject at the time of the transaction is required, enabling distributed and efficient solving while safeguarding the privacy of transactional information.

Based on the principle of ADMM algorithm, the auxiliary condition is introduced as shown in Eq. 35 as follows:

$$P_t^{\text{buy}} - P_t^{\text{ex}} = 0, w_t^{\text{buy}} - w_t^{\text{ex}} = 0 \tag{35}$$

where P_t^{buy}, P_t^{ex} are the amount of electricity that the VPPO expects to trade with the DSO and the amount of electricity that the DSO expects to trade with the VPPO at time t, respectively; w_t^{buy}, w_t^{ex} are the amount of natural gas that the VPPO expects to buy from the GSO and the amount of natural gas that the GSO expects to sell to the VPPO at time t, respectively.

Distributed models for optimal pricing of power distribution network, optimal pricing of gas distribution network and VPP

energy optimization are obtained based on ADMM principle, respectively.

4.2.1 Optimal pricing of power distribution network

$$L_{\mathrm{DSO}}=\begin{cases}\min\left(f_{\mathrm{DSO}}+\sum_{t=1}^{T}\left[\lambda_t^{\mathrm{DSO}}\left(P_t^{\mathrm{ex}}-P_t^{\mathrm{buy}}\right)+\frac{\rho}{2}\left\|P_t^{\mathrm{ex}}-P_t^{\mathrm{buy}}\right\|_2^2\right]\right)\\ \text{s.t.}\quad (1)—(11)、(19)—(20)、(23)\end{cases} \tag{36}$$

The optimal pricing of power distribution network is presented in Eq. 36, where λ_t^{DSO} and ρ are the corresponding Lagrange multipliers and penalty factors of the DSO, respectively.

4.2.2 Optimal pricing of gas distribution network

$$L_{\mathrm{GSO}}=\begin{cases}\min\left(f_{\mathrm{GSO}}+\sum_{t=1}^{T}\left[\lambda_t^{\mathrm{GSO}}\left(w_t^{\mathrm{ex}}-w_t^{\mathrm{buy}}\right)+\frac{\rho}{2}\left\|w_t^{\mathrm{ex}}-w_t^{\mathrm{buy}}\right\|_2^2\right]\right)\\ \text{s.t.}\quad (12)—(18)、(21)—(22)、(24)\end{cases} \tag{37}$$

The optimal pricing of gas distribution network is presented in Eq. 37, where λ_t^{GSO} is the Lagrangian multiplier for the GSO distribution solution.

4.2.3 Distributed model for VPP energy optimization

$$L_{\mathrm{VPPO}}=\begin{cases}\min\left(\begin{array}{l}f_{\mathrm{VPPO}}+\sum_{t=1}^{T}\left[\lambda_t^{1}\left(P_t^{\mathrm{buy}}-P_t^{\mathrm{ex}}\right)+\frac{\rho}{2}\left\|P_t^{\mathrm{buy}}-P_t^{\mathrm{ex}}\right\|_2^2\right]+\\ \sum_{t=1}^{T}\left[\lambda_t^{2}\left(w_t^{\mathrm{buy}}-w_t^{\mathrm{ex}}\right)+\frac{\rho}{2}\left\|w_t^{\mathrm{buy}}-w_t^{\mathrm{ex}}\right\|_2^2\right]\end{array}\right)\\ \text{s.t.}\quad (25)—(33)\end{cases} \tag{38}$$

Distributed model for VPP energy optimization is presented in Eq. 38, where λ_t^1, λ_t^2 are the corresponding Lagrange multipliers when the VPPO expects to trade with the DSO and GSO, respectively.

The coupled variables and Lagrange multipliers are updated as follows:

$$\begin{cases}z_t^{\mathrm{ex},k+1}=\mathrm{argmin}L_z\left[z_t^{\mathrm{ex},k},z_t^{\mathrm{buy},k},\lambda_t^{z,k}\right]\\ z_t^{\mathrm{buy},k+1}=\mathrm{argmin}L_{\mathrm{VPPO}}\left[z_t^{\mathrm{ex},k+1},z_t^{\mathrm{buy},k},\lambda_t^{z,k}\right]\\ \lambda_t^{z,k+1}=\lambda_t^{z,k}+\rho\left(z_t^{\mathrm{ex},k+1}-z_t^{\mathrm{buy},k+1}\right)\end{cases} \tag{39}$$

where z represents the energy type; k is the number of iterations for distributed solving.

The original residuals, pairwise residuals are calculated and the convergence conditions are provided in Eqs 40, 41 as follows:

$$\begin{cases}r_t^{k+1}=z_t^{\mathrm{ex},k+1}-z_t^{\mathrm{buy},k+1}\\ s_t^{k+1}=z_t^{\mathrm{ex},k+1}-z_t^{\mathrm{ex},k}\end{cases} \tag{40}$$

$$\begin{cases}\sum_{t=1}^{T}\left\|r_t^{k+1}\right\|_2\le\varepsilon^{\mathrm{pri}}\\ \sum_{t=1}^{T}\left\|s_t^{k+1}\right\|_2\le\varepsilon^{\mathrm{dual}}\end{cases} \tag{41}$$

where r_t^{k+1}, s_t^{k+1} are the original residuals and pairwise residuals in the $k+1$ iteration, respectively; $\varepsilon^{\mathrm{pri}}$, $\varepsilon^{\mathrm{dual}}$ are the convergence thresholds of the original and pairwise residuals, respectively.

The choice of step size significantly affects the speed of the ADMM solution. An inappropriate value can hinder convergence. This paper proposes an adaptive ADMM algorithm that dynamically updates the step size based on the relationship between original residuals and pairwise residuals. This approach aims to enhance algorithm convergence and reduce iteration time, as formulated in Eq. 42:

$$\rho^{k+1}=\begin{cases}\tau^{\mathrm{incr}}\rho^k & \left\|r^k\right\|_2>\mu\left\|s^k\right\|_2\\ \frac{\rho^k}{\tau^{\mathrm{decr}}} & \left\|s^k\right\|_2>\mu\left\|r^k\right\|_2\\ \rho^k & \text{other}\end{cases} \tag{42}$$

where μ is the scaling factor between the original residuals and the pairwise residuals; τ^{incr} and τ^{decr} are the acceleration and deceleration factors of the step change, respectively.

The coupling variables are updated by the iterative form shown in Eq. 39 until the convergence condition in Eq. 41 is satisfied, and the specific algorithmic solution flowchart is shown in Figure 3.

5 Case study

5.1 Case description

In order to validate the models and algorithms proposed in this paper, the IEEE 33-bus power distribution network, 7-node gas distribution network, and 1 VPP coupling composition are utilized. The network topology is illustrated in Figure 4, where W represents the wind turbine located at node 31 in the power distribution network. Additionally, G1 to G5 represent five coal-fired units situated at nodes 3, 9, 29, 14, and 21, with their operating parameters detailed in Supplementary Appendix Table SA1; Supplementary Appendix Figure SA1. W1 and W2 denote the gas distribution stations connected to nodes six and seven of the gas distribution network. Prediction curves for renewable energy output and load within the VPP can be found in Supplementary Appendix Figure SA2, along with unit parameters in Supplementary Appendix Table SA2.

It is assumed that the power factor η of the node loads in the distribution network is 0.85, and the price of power purchased from the higher-level grid is set to 160$/MWh. The price of gas purchased by GSO from the gas source is set at 0.52$/m3, and the carbon tax τ is set to 45$/tCO2. In the ADMM algorithm of adaptive step-size, the initial step-size ρ is set to 1, and the μ is set to 10, τ^{incr}, τ^{decr} are set to 2, $\varepsilon^{\mathrm{pri}}$ and $\varepsilon^{\mathrm{dual}}$ the thresholds of convergence, and are set to 10-3. In this paper, we build the simulation model based on the platform of Matlab 2018b and

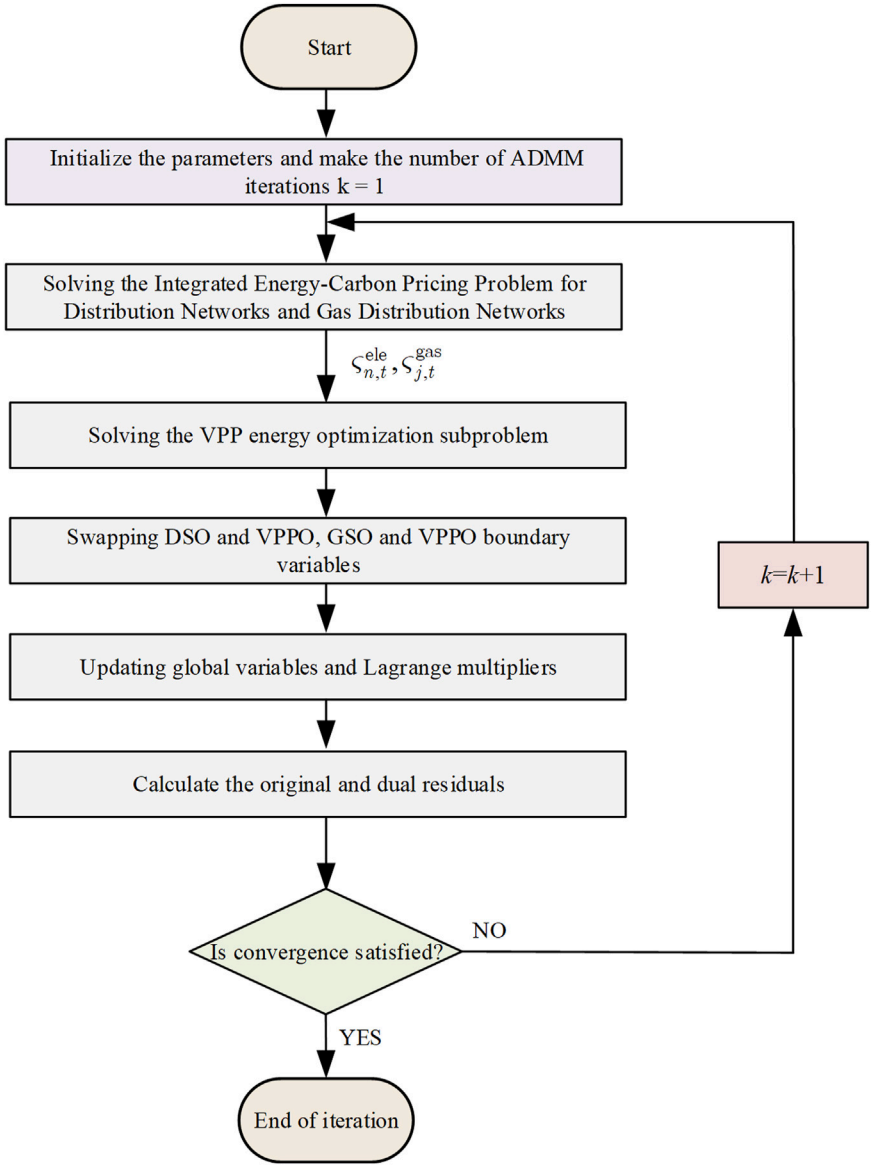

FIGURE 3
Flowchart for solving the multiagent Stackelberg game model based on integrated energy-carbon price.

the Gurobi solver is adopted to solve the simulation model. Solved using Gurobi solver.

In order to verify the impact of the multi-agent Stackelberg game on electricity-gas trading and the cost of energy purchase by each subject under the energy-carbon integrated price response mechanism, the following four energy settlement scenarios are set up.

Case 1 : The settlement electricity price adopts fixed time-sharing electricity price, the settlement gas price adopts fixed natural gas price, the specific data are shown in Supplementary Appendix Table SA3, carbon emission flow is not considered, VPPOs completely act as the recipient of the price for the electricity-natural gas transaction, and the flexible loads in VPPs are not considered for the optimal scheduling.

Case 2: Based on Case 1, and the flexible loads within the VPP are considered for integrated demand response for electricity and heat.

Case 3: The LMEP and LMGP obtained after the game equilibrium of each subject are used for the power distribution network settlement price and the gas distribution network settlement price, respectively, without considering the carbon emission flow, and the flexible loads within the VPP are considered for optimal dispatch; Case 4: the electricity-carbon integrated price and gas-carbon integrated price obtained after the game equilibrium of each subject are adopted for the power distribution network settlement price and gas distribution network settlement price respectively, carbon emission flow is considered, and optimal dispatch is considered for the flexible loads within the VPP, i.e., the model proposed in this paper.

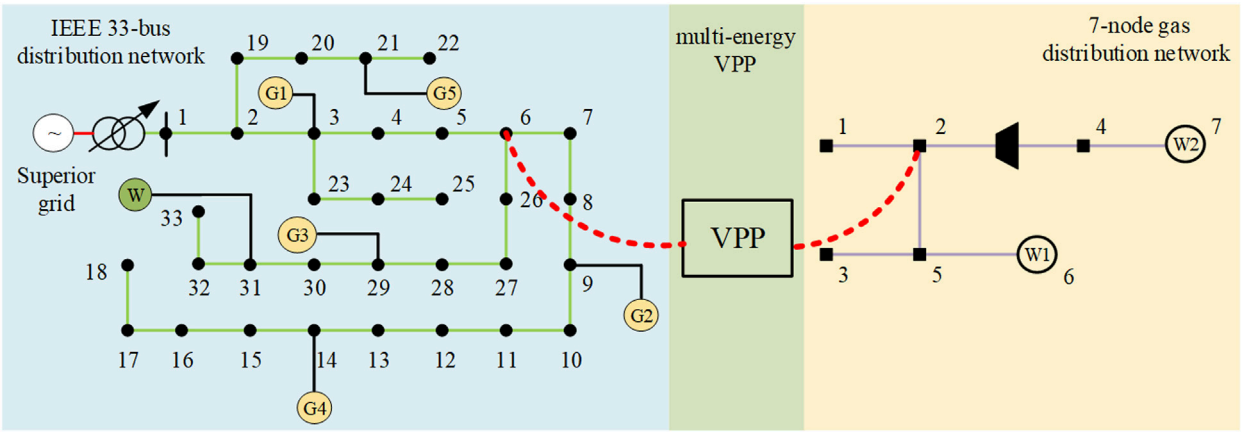

FIGURE 4
Containing multi-energy VPP E33-G7 test system topology diagram.

TABLE 1 Comparison results of operating costs and carbon emissions of each subject under different scenarios.

Case	VPPO operating costs ($)	DSO operating costs ($)	GSO operating costs ($)	Total cost of energy purchases ($)	VPP carbon emissions (t)
Case 1	16118.5	8672.1	17926.5	42717.1	47.73
Case 2	12153.6	5338.9	16097.6	33590.1	32.84
Case 3	11539.2	4832.8	16817.2	33189.2	29.59
Case 4	13009.4	4776.7	18079.3	35865.4	27.43

5.2 Analysis of VPP simulation results

5.2.1 Comparative analysis of operation under different scenarios

The simulation results of the above four scenarios are shown in Table 1.

Table 1 illustrates that operating costs decrease and carbon emissions are effectively reduced when considering integrated demand response in Cases 2, 3, and 4 compared to Case 1. The dependency of VPP on power and gas distribution networks is also reduced through demand response of flexible loads, leading to decreased electricity and gas purchases. Case 3, which incorporates the interaction of VPPO with DSO and GSO master-slave game, shows a reduction in total energy purchase cost and carbon emissions by $400.9 and 3.25 t CO2, respectively, compared to Case 2 with fixed energy settlement price. This demonstrates that settling energy prices using LMEP and LMGP can guide VPP energy optimization in a more cost-effective manner, enhancing both economic and environmental aspects of VPP.

By comparing Case 3 and Case 4, it is evident that in Case 4, the integrated energy-carbon price led to a 7.29% decrease in carbon emissions from the VPP compared to Case 3. However, the energy purchase costs and total costs of the VPP increased in Case 4 due to the higher carbon price. Moreover, the inclusion of a carbon price incentivized VPPs to use more natural gas over purchased electricity, resulting in increased operating costs for GSOs and decreased costs for DSOs in Case 4. Overall, the proposed multi-agent Stackelberg game trading strategy proves beneficial in enhancing the economic and low-carbon advantages for each agent.

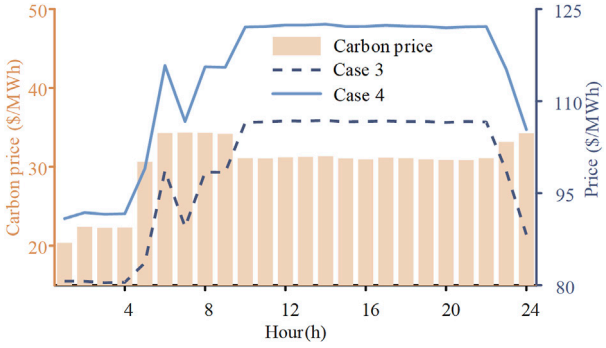

FIGURE 5
Electricity prices in different scenarios.

5.2.1.2 Analysis of price response mechanism.

The impact of different pricing methods on the power purchased by VPPs is analyzed by examining the power distribution network settlement tariffs and carbon price change curves for the nodes where the VPPs are located in Cases 3 and 4, as shown in Figure 5. Additionally, Figure 6 illustrates the carbon intensity for all nodes of the power distribution network under Case 4.

As shown in Figure 5, considering the carbon tax on VPP's electricity demand from the power distribution network

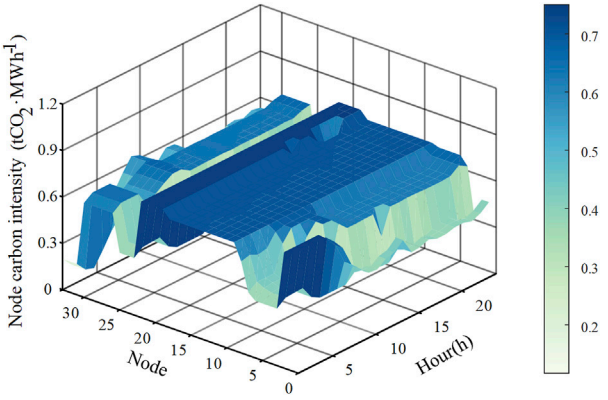

FIGURE 6
Variation of carbon intensity at power distribution network nodes under Case 4.

increases the purchase price. The integrated energy-carbon price is consistently higher than the LMEP, with its incremental increase varying over time. The difference between the integrated energy-carbon price and the LMEP is more pronounced at certain times (e.g., from 05:00 to 09:00) when the nodes have higher carbon emission densities. In contrast, while the combined gas-carbon price also rises, its change is minimal because the carbon intensity of each node in the gas distribution network is relatively uniform. The carbon emissions for VPPs purchasing gas from the gas distribution network depend solely on the amount of gas used. Consequently, the combined gas-carbon price remains essentially unchanged over time. In this paper, the LMGP of VPP coupled with the gas distribution network is calculated to be 0.5120 $/m^3, and the integrated gas-carbon price, considering the carbon tax, is 0.6174 $/m^3.

An examination of the carbon intensity of individual nodes in both Figure 6 and the IEEE 33-node system topology diagram indicates that nodes with wind turbines and their adjacent nodes have lower carbon intensity, attributed to the low carbon emissions of wind turbines. On the other hand, nodes connected to VPPs' power distribution network are situated near coal-fired units with high carbon emissions, impacting their carbon intensity. Nevertheless, the carbon intensity of these nodes aligns closely with that of thermal units. As a result, the carbon pricing of nodes linked to the power distribution network, as depicted in Figure 5, demonstrates minimal fluctuations over time.

To further investigate the impact of carbon pricing on the amount of electricity and gas purchased by VPPs, Figure 7 illustrates a comparison between the two scenarios. The results show that during the 05:00-10:00, Case 4, with carbon pricing, acquires less electricity but more natural gas compared to Case 3, without carbon pricing. This is due to the higher carbon intensity at the node connected to the power distribution network, as depicted in Figure 5. The node's carbon intensity is higher during 05:00-10:00, leading to a greater use of natural gas over electricity. Therefore, incorporating a carbon price incentivizes VPPs to utilize more natural gas and decrease electricity consumption.

In order to better understand the demand for purchased energy and carbon emissions of a VPP utilizing an integrated energy-carbon price response mechanism, a comparison and analysis between Case 3 and Case 4 is conducted. The results of this comparison are illustrated in Figure 8. The visualization in Figure 8 demonstrates that, in Case 4 where carbon price is considered, natural gas becomes a more competitive option compared to Case 3 where carbon price is not a factor. Consequently, the VPP tends to procure natural gas with lower carbon intensity, leading to an increase in total gas volume purchased and a decrease in the purchase of electricity from the power distribution network with higher carbon intensity. This results in a reduction of 1.91 MWh in the total purchased electricity of the VPP. Furthermore, with the inclusion of carbon price, the total carbon emissions of the VPP decrease from 29585.8 kg to 27436.6kg, showcasing a significant reduction in carbon emissions due to the integrated energy-carbon price response mechanism. These findings suggest that the proposed multi-agent Stackelberg game energy settlement price effectively facilitates carbon emission reduction and enhances the low-carbon benefits of the VPP.

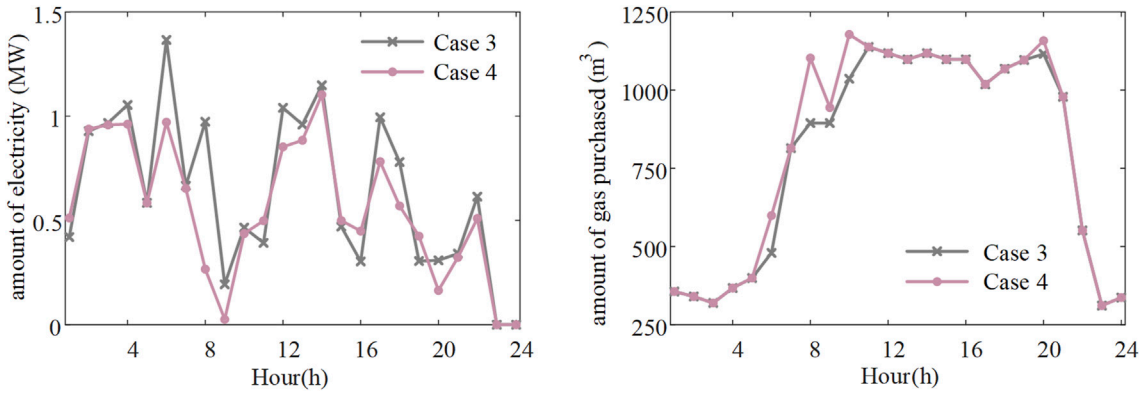

FIGURE 7
Power and gas purchases of VPP in different scenarios.

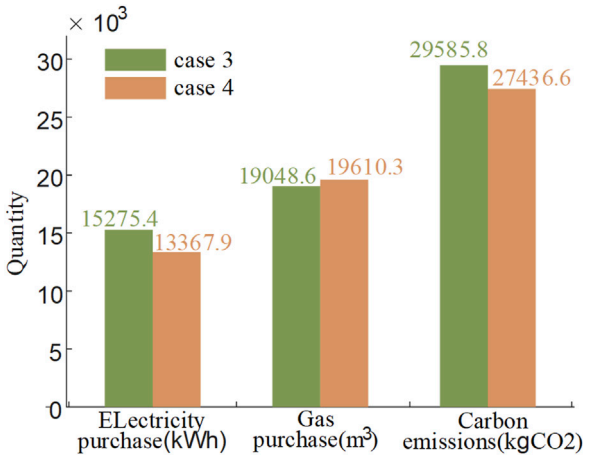

FIGURE 8
Comparison of VPP energy purchase demand and Carbon emissions under different scenarios.

5.2.2 Analysis of VPP optimal schedule

The results of the optimization of electric power and thermal power inside the VPP are shown in Figure 9. For the VPP internal units, new energy consumption has the highest priority to minimize wind abandonment, and the VPP completes the internal optimal scheduling according to the combined energy-carbon price. The gas turbine CHP unit generates electricity and heat within the output range, and the electric energy storage is mainly charged when the energy-carbon integrated price is lower, such as 01:00-04:00 and 07:00 moments, and discharged at 06:00 and 12:00-14:00 when the electricity-carbon integrated price is higher, so as to reduce the purchase of electricity from the power distribution network and reduce the total operating cost and carbon emissions, while the electric and heat loads are considered Comprehensive demand response can realize peak shaving and valley filling to alleviate the pressure of grid peaking; only when the internal unit output cannot meet its load demand, it purchases electricity from the power distribution network and

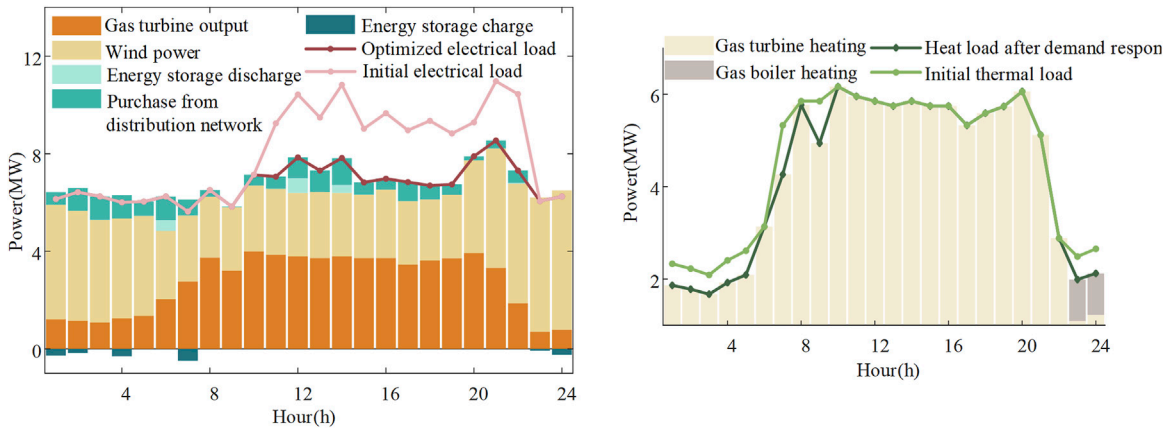

FIGURE 9
VPP internal optimization results.

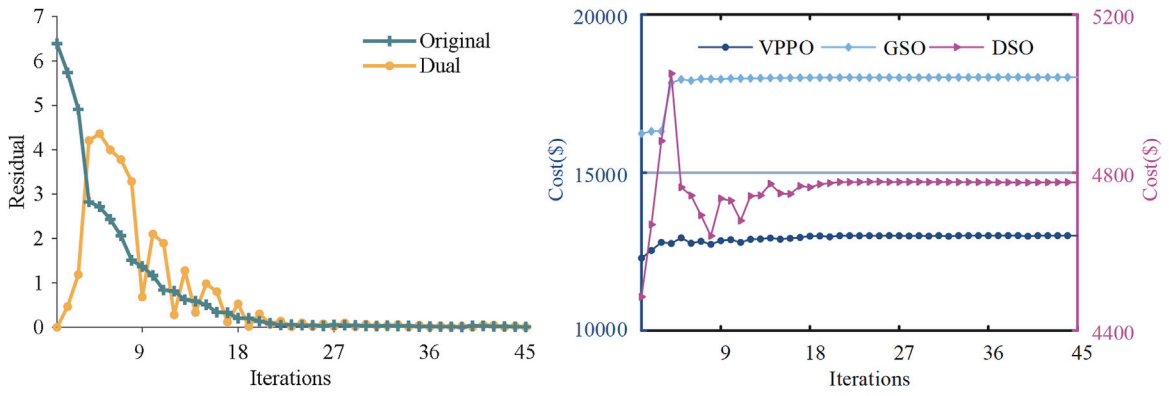

FIGURE 10
Convergence result for interactive iterative of multi-agent Stackelberg game.

TABLE 2 Comparison between traditional ADMM and ADMM with adaptive step size.

Algorithm	Step	Iterations/time	Solution time/s
Traditional ADMM	0.1	109	674
	1	63	402
	50	92	580
adaptive step size ADMM	0.1	68	451
	1	45	329
	50	75	483

gas from the gas distribution network. Considering that the heat load demand within the VPP is prioritized to be met by the gas turbine CHP unit, after considering the heat load demand response, the vast majority of the moments are heat production by the gas turbine only, and only when the gas turbine is not enough to supply heat at the 23:00-24:00 moments, the gas boiler GB unit will be powered up.

5.3 Algorithm convergence analysis

This section examines the iterative convergence of the proposed multi-agent Stackelberg game trading strategy. Figure 10A illustrates the converged iterations of the original and pairwise residuals in Case 4, while Figure 10B demonstrates the iterative convergence of the game interactions among DSO, GSO, and VPPO.

Based on the residual convergence analysis presented in Figure 10A, it is evident that the proposed algorithm achieves the desired level of accuracy after 45 iterations, converging within 10–3, with a computation time of 329 s. Figure 10B visually demonstrates that the cost of purchased energy for the leading DSO and GSO converges to $4776.7 and $18,079.3, respectively, while the cost for the follower VPPO converges to $13009.4. This convergence indicates that the Stackelberg game between the DSO, GSO, and VPPO has reached equilibrium, where each agent cannot further reduce its operational cost by adjusting its trading strategy in isolation. These results highlight the strong convergence performance and computational efficiency of the distributed optimization algorithm proposed in this study.

In order to further validate the effectiveness of the adaptive ADMM algorithm proposed in this study, a comparative analysis with the fixed-step ADMM is conducted. The solution performance is documented in Table 2 for both fixed step size and adaptive step size ADMM. It is evident from Table 2 that the adaptive step-size ADMM, as opposed to the traditional ADMM, diminishes the reliance on the initial value selection through step size correction. This results in fewer iterations, reduced solving time, and enhanced solving efficiency.

6 Conclusion

This paper introduces a bi-level model and its solution method for a multi-agent Stackelberg game focused on synergistic low-carbon trading within Virtual Power Plants (VPPs) participating in multi-energy systems under an energy-carbon integrated price response mechanism. The proposed trading strategy is analyzed and validated through an arithmetic example, leading to the following conclusions.

(1) The integrated energy-carbon pricing approach, based on the CEF theory, is more effective in incentivizing VPPs to adjust their energy-use and trading strategies with multi-energy systems compared to LMEP and LMGP pricing approaches. This encourages VPPs to procure energy from both power distribution and gas distribution networks during periods of low carbon intensity, thereby reducing carbon emissions.
(2) The proposed trading framework and multi-participant Stackelberg game model enhance energy interactions among participants, improving the economics and low-carbon benefits for each participant. Compared to traditional energy settlement methods, the integrated energy-carbon pricing method is shown to be more effective in this regard.

This study focuses on the trading of electricity and natural gas within a VPP with a multi-energy system. Future research will explore trading multiple energy sources and carbon emissions to achieve synergistic low-carbon trading. Furthermore, the impacts of renewable energy integration and load demand uncertainty in VPPs are also important areas for further investigation.

Data availability statement

The original contributions presented in the study are included in the article/Supplementary Material, further inquiries can be directed to the corresponding author.

Author contributions

YY: Writing–original draft, Writing–review and editing. SX: Conceptualization, Investigation, Methodology, Software, Supervision, Writing–review and editing. JT: Data curation, Funding acquisition, Methodology, Resources, Writing–review and editing. BQ: Investigation, Supervision, Visualization, Writing–original draft. XL: Software, Supervision, Validation, Writing–review and editing. FZ: Data curation, Formal Analysis, Software, Supervision, Validation, Writing–review and editing.

Funding

The author(s) declare that financial support was received for the research, authorship, and/or publication of this article. Project supported by Guangdong Provincial Key Laboratory of Intelligent Measurement and Advanced Metering of Power Grid Open-end Fund.

Conflict of interest

The authors declare that the research was conducted in the absence of any commercial or financial relationships that could be construed as a potential conflict of interest.

Publisher's note

All claims expressed in this article are solely those of the authors and do not necessarily represent those of their affiliated organizations, or those of the publisher, the editors and the reviewers. Any product that may be evaluated in this article, or claim that may be made by its manufacturer, is not guaranteed or endorsed by the publisher.

Supplementary material

The Supplementary Material for this article can be found online at: https://www.frontiersin.org/articles/10.3389/fenrg.2024.1459667/full#supplementary-material

References

Bhuiyan, E. A., Hossain, M. Z., Muyeen, S. M., Fahim, S. R., Sarker, S. K., and Das, S. K. (2021). Towards next generation virtual power plant: technology review and frameworks. *Renew. Sustain. Energy Rev.* 150, 111358. doi:10.1016/j.rser.2021.111358

Chen, S., Conejo, A. J., Sioshansi, R., and Wei, Z. (2019). Unit commitment with an enhanced natural gas-flow model. *IEEE Trans. Power Syst.* 34 (5), 3729–3738. doi:10.1109/tpwrs.2019.2908895

Chen, W., Qiu, J., Zhao, J., Chai, Q., and Dong, Z. Y. (2023). Customized rebate pricing mechanism for virtual power plants using a hierarchical game and reinforcement learning approach. *IEEE Trans. Smart Grid* 14 (1), 424–439. doi:10.1109/tsg.2022.3185138

Chen, W., Qiu, J., Zhao, J., Chai, Q., and Dong, Z. Y. (2021). Bargaining game-based profit allocation of virtual power plant in frequency regulation market considering battery cycle life. *IEEE Trans. Smart Grid* 12 (4), 2913–2928. doi:10.1109/tsg.2021.3053000

Cheng, Y., Zhang, N., Lu, Z., and Kang, C. (2019b). Planning multiple energy systems toward low-carbon society: a decentralized approach. *IEEE Trans. Smart Grid* 10 (5), 4859–4869. doi:10.1109/tsg.2018.2870323

Cheng, Y., Zhang, N., Wang, Y., Yang, J., Kang, C., and Xia, Q. (2019a). Modeling carbon emission flow in multiple energy systems. *IEEE Trans. Smart Grid* 10 (4), 3562–3574. doi:10.1109/tsg.2018.2830775

Cheng, Y., Zhang, N., Zhang, B., Kang, C., Xi, W., and Feng, M. (2020). Low-carbon operation of multiple energy systems based on energy-carbon integrated prices. *IEEE Trans. Smart Grid* 11 (2), 1307–1318. doi:10.1109/tsg.2019.2935736

Kang, C., Zhou, T., Chen, Q., Wang, J., Sun, Y., Xia, Q., et al. (2015). Carbon emission flow from generation to demand: a network-based model. *IEEE Trans. Smart Grid* 6 (5), 2386–2394. doi:10.1109/tsg.2015.2388695

Li, Y., Wang, B., Yang, Z., Li, J., and Chen, C. (2022). Hierarchical stochastic scheduling of multi-community integrated energy systems in uncertain environments via Stackelberg game. *Appl. Energy* 308, 118392. doi:10.1016/j.apenergy.2021.118392

Liu, X. (2022). Research on optimal dispatch method of virtual power plant considering various energy complementary and energy low carbonization. *Int. J. Electr. Power and Energy Syst.* 136, 107670. doi:10.1016/j.ijepes.2021.107670

Lu, Q., Guo, Q., and Zeng, W. (2023a). Optimal dispatch of community integrated energy system based on Stackelberg game and integrated demand response under carbon trading mechanism. *Appl. Therm. Eng.* 219, 119508. doi:10.1016/j.applthermaleng.2022.119508

Lu, Z., Bai, L., Wang, J., Wei, J., Xiao, Y., and Chen, Y. (2023b). Peer-to-Peer joint electricity and carbon trading based on carbon-aware distribution locational marginal pricing. *IEEE Trans. Power Syst.* 38 (1), 835–852. doi:10.1109/tpwrs.2022.3167780

Sun, G., Zhang, Z., Zhou, Y., Han, H., Zang, H., and Wei, Z. (2023). Bi-level model for integrated energy service providers in joint electricity and carbon P2P market. *J. Clean. Prod.* 393, 136303. doi:10.1016/j.jclepro.2023.136303

Vasirani, MATTEO, Kota, RAMACHANDRA, Cavalcante, RENATO L. G., Ossowski, S., and Jennings, N. R. (2013). An agent-based approach to virtual power plants of wind power generators and electric vehicles. *IEEE Trans. Smart Grid* 4 (3), 1314–1322. doi:10.1109/tsg.2013.2259270

Wang, C., Wei, W., Wang, J., Liu, F., and Mei, S. (2018). Strategic offering and equilibrium in coupled gas and electricity markets. *IEEE Trans. Power Syst.* 33 (1), 290–306. doi:10.1109/tpwrs.2017.2698454

Wei, F., Jing, Z. X., Wu, P. Z., and Wu, Q. (2017). A Stackelberg game approach for multiple energies trading in integrated energy systems. *Appl. energy* 200, 315–329. doi:10.1016/j.apenergy.2017.05.001

Xie, S., Wu, Q., Hatziargyriou, N. D., Zhang, M., Zhang, Y., and Xu, Y. (2023). Collaborative pricing in a power-transportation coupled network: a variational inequality approach. *IEEE Trans. Power Syst.* 38 (1), 783–795. doi:10.1109/tpwrs.2022.3162861

Xie, S., Wu, Q., Zhang, M., and Guo, Y. (2024). Coordinated energy pricing for multi-energy networks considering hybrid hydrogen-electric vehicle mobility. *IEEE Trans. Power Syst.*, 1–13. doi:10.1109/TPWRS.2024.3369633

Xu, Z., Guo, Y., and Sun, H. (2022). Competitive pricing game of virtual power plants: models, strategies, and equilibria. *IEEE Trans. Smart Grid* 13 (6), 4583–4595. doi:10.1109/tsg.2022.3184171

Yan, Z., Li, C., Yao, Y., Lai, W., Tang, J., Shao, C., et al. (2023). Bi-level carbon trading model on demand side for integrated electricity-gas system. *IEEE Trans. Smart Grid* 14 (4), 2681–2696. doi:10.1109/tsg.2022.3229278

Yang, Z., Hu, J., Ai, X., Wu, J., and Yang, G. (2021). Transactive energy supported economic operation for multi-energy complementary microgrids. *IEEE Trans. Smart Grid* 12 (1), 4–17. doi:10.1109/tsg.2020.3009670

Yi, Z., Xu, Y., Gu, W., and Wu, W. (2020a). A multi-time-scale economic scheduling strategy for virtual power plant based on deferrable loads aggregation and disaggregation. *IEEE Trans. Sustain. Energy* 11 (3), 1332–1346. doi:10.1109/tste.2019.2924936

Yi, Z., Xu, Y., Zhou, J., Wu, W., and Sun, H. (2020b). Bi-level programming for optimal operation of an active distribution network with multiple virtual power plants. *IEEE Trans. Sustain. Energy* 11 (4), 2855–2869. doi:10.1109/tste.2020.2980317

Zangeneh, A., Shayegan-Rad, A., and Nazari, F. (2018). Multi-leader–follower game theory for modelling interaction between virtual power plants and distribution company. *IET Gener. . Transm. Dis.* 12 (21), 5747–5752. doi:10.1049/iet-gtd.2018.5798

Zhang, L., Liu, D., Cai, G., Lyu, L., Koh, L. H., and Wang, T. (2023). An optimal dispatch model for virtual power plant that incorporates carbon trading and green certificate trading. *Int. J. Electr. Power and Energy Syst.* 144, 108558. doi:10.1016/j.ijepes.2022.108558

Zhang, T., and Hu, Z. (2022). Optimal scheduling strategy of virtual power plant with power-to-gas in dual energy markets. *IEEE Trans. Industry Appl.* 58 (2), 2921–2929. doi:10.1109/tia.2021.3112641

Zhao, B., Conejo, A. J., and Sioshansi, R. (2018). Coordinated expansion planning of natural gas and electric power systems. *IEEE Trans. Power Syst.* 33 (3), 3064–3075. doi:10.1109/tpwrs.2017.2759198

frontiers | Frontiers in Energy Research

TYPE Original Research
PUBLISHED 20 August 2024
DOI 10.3389/fenrg.2024.1415796

OPEN ACCESS

EDITED BY
Yitong Shang,
Hong Kong University of Science and Technology, Hong Kong SAR, China

REVIEWED BY
Praveen Kumar Balachandran,
Vardhaman College of Engineering, India
Somporn Sirisumrannukul,
King Mongkut's University of Technology North Bangkok, Thailand

*CORRESPONDENCE
Chao Xing,
xingchao_yn@163.com

RECEIVED 11 April 2024
ACCEPTED 19 July 2024
PUBLISHED 20 August 2024

CITATION
Xing C, Xi X, He X and Deng C (2024), Parameter identification method of load modeling based on improved dung beetle optimizer algorithm. *Front. Energy Res.* 12:1415796.
doi: 10.3389/fenrg.2024.1415796

Parameter identification method of load modeling based on improved dung beetle optimizer algorithm

Chao Xing*, Xinze Xi, Xin He and Can Deng

Electric Power Research Institute of Yunnan Power Grid Co., Ltd., Kunming, China

The role of load modeling in power systems is crucial for both operational and regulatory considerations. It is essential to develop an effective and reliable method for optimizing load modeling parameter identification. In this paper, the dung beetle algorithm is improved by using the good point set, and a load model parameter identification strategy based on the good point set dung beetle optimization algorithm (GDBO) within the framework of the measurement-based load modeling method. The proposed parameter identification strategy involves utilizing PMU voltage data as input, selecting a comprehensive load model, and refining the initialization process based on the good point set to mitigate the influence of local maxima. Through iterative optimization of the objective function using the Dung Beetle Optimizer (DBO) algorithm, the optimal parameters for the comprehensive load model are determined, enhancing the model's ability to accurately capture the power curve. Analysis of examples pertaining to PMU-measured modeling parameter identification reveals that the proposed GDBO algorithm, which incorporates a good point set, outperforms alternative methods such as the improved differential evolution algorithm (IDE), particle swarm optimization algorithm (PSO), grey wolf optimization algorithm (GWO), and conventional DBO algorithm. This demonstrates the superior performance of the introduced approach in the context of load model parameter identification.

KEYWORDS

DBO algorithm, good point set, parameter identification, load modeling, electric power system

1 Introduction

At present, digital simulation plays an irreplaceable role in power systems across various domains such as power network planning, operation, control, and personnel training (Zhang et al., 2020; Yang et al., 2022a; Diao et al., 2023; Wu et al., 2023; Zhang et al., 2023a; Zhu et al., 2023). The accuracy of the simulation results depends on the conformity of the adopted component models and parameters. Selecting an inappropriate load model in power system simulation can lead to deviations in the simulation results from the actual situation, potentially resulting in misallocation of planning funds and operational decision-making errors (Ju, 2015; Xu et al., 2023). Therefore, in the process of dynamic simulation, it is very important to select a suitable load model to describe the load of a specific area (Swarupa et al., 2024).

Load modeling has two main approaches (Wang et al., 2014; Chen et al., 2020; Yang et al., 2022b) in power systems: component-based and measurement-based. The component-based load modeling first needs to count the characteristics of various typical loads, the proportion of load equipment, and the composition of loads (Wu et al., 2022; Fu et al., 2023; Yang et al., 2024), then derive the mathematical models and parameters of various typical loads, and finally integrate the statistical data to establish the model of load nodes. However, the load composition will change with time, the statistical workload is large, and the voltage characteristics of reactive power cannot be accurately obtained, so there are few practical applications. In contrast, measurement-based load modeling considers the power system as a stochastic system, first determines the model structure, then identifies the model parameters based on the measured data, and verifies its generalization ability (Wang et al., 2019; Zhang et al., 2023b; Zhou et al., 2023). This method requires the installation of a load characteristic recording device at the load node, which usually obtains data for identification under large disturbances. Although there are some drawbacks to measurement-based load modeling, it can be widely used in practice by using input-output models to solve the problem of complex load components without much statistical work (Zhang, 2007; Yang et al., 2018).

With the continuous development and popularization of artificial intelligence, intelligent algorithms have been widely used in the research of load modeling technology (Wang et al., 2011; Wang et al., 2020; Kang et al., 2021; Guo et al., 2022). Reference (Wang et al., 2020; Guo et al., 2022) has applied the grey wolf optimization (GWO) algorithm to load modeling based on its advantages of better global convergence, fewer adjustment parameters, and easy identification. It has been proven that the GWO algorithm can improve the accuracy of load modeling. Reference (Kang et al., 2021) adds the weight of flight inertia, global optimum, and flight interference factor to the butterfly algorithm to avoid the butterfly algorithm falling into the local optimum prematurely and improve the accuracy of the comprehensive load model. In order to prevent local convergence of the algorithm and increase the accuracy of identification findings, the chaos algorithm is incorporated into the ant colony method in Reference (Wang et al., 2011). However, due to the mixing of algorithms, the selection of parameters becomes complicated.

The dung beetle optimization (DBO) algorithm is an intelligent optimization algorithm that achieves global exploration and local development through the ball rolling, oviposition, foraging and stealing behavior of dung beetles (Yang et al., 2022c; Xue and Shen, 2022). The algorithm has the ability for global exploration and local development, which can speed up convergence and prevent premature phenomena. Presently, it has found extensive application in diverse research domains, including but not limited to range-free localization (Pan and Bu, 2023) and neural network training (Li et al., 2023). However, few scholars have applied the DBO algorithm to the research of load modeling.

In summary, this study employs the Dung Beetle Optimizer (DBO) algorithm, alternatively recognized as the Good Point Set Dung Beetle Optimizer (GDBO), to ascertain and refine the essential parameters inherent in the comprehensive load model. The PMU measured data is used as the input samples for load modeling. The optimal parameters of the load model are achieved through repeated optimization of the objective function, improving the model's fit to the power curve. Finally, a comparison between the optimized sample curves and model responses produced by the proposed algorithm and the algorithms for improved differential evolution (IDE) (Xu et al., 2009a; Pattanaik et al., 2017), particle swarm optimization (PSO) (Fang et al., 2022), GWO (Wang et al., 2020; Guo et al., 2022), and DBO is made. This confirms that the proposed method is more accurate and solves load modeling parameters more quickly.

The paper is organized as follows: The establishment of the comprehensive load model is shown in the second chapter. The third chapter introduces the parameter identification of the integrated load model, including the principle of parameter identification, parameter identification method, the improvement of the identification method and the specific process of the identification algorithm. In the fourth chapter, the example simulation of parameter identification is carried out. The fifth chapter gives the conclusion.

2 Comprehensive load model

The comprehensive load model comprises a static ZIP load model and a three-order induction motor model in parallel (Liu, 2007; Sheng et al., 2021; Yang et al., 2022d; Wang et al., 2023). The model is shown in the following Figure 1.

The static ZIP part adopts a polynomial model, which can be described as follows Equation 1:

$$\begin{cases} P_s = P_Z\left(\dfrac{U}{U_0}\right)^2 + P_I\left(\dfrac{U}{U_0}\right) + P_P \\ Q_s = Q_Z\left(\dfrac{U}{U_0}\right)^2 + Q_I\left(\dfrac{U}{U_0}\right) + Q_P \end{cases} \tag{1}$$

in the above formula, we use P_Z to represent the static active power under the load constant impedance model, P_I to represent the static active power under the load constant current model, and P_P to represent the static active power under the load constant power model and constant power, satisfying the following formulaic conditions: $P_Z + P_I + P_P = 1 - K_{pm}$.The static ZIP part's active and reactive powers are denoted by P_s and Q_s.Under static reactive load, components Q_Z, Q_I, and Q_P satisfy the following requirements: $Q_Z + Q_I + Q_P = 1 - \frac{Q_{motor}}{Q_0}$.

The induction motor part can be described as Equations 2, 3:

$$\begin{cases} \dfrac{dE_d'}{dt} = -\dfrac{1}{T'}\left[E_d' + (X_m - X_m \| X_r) I_q\right] - w' E_q' \\ \dfrac{dE_q'}{dt} = -\dfrac{1}{T'}\left[E_q' - (X_m - X_m \| X_r) I_d\right] + w' E_d' \\ \dfrac{dw}{dt} = -\dfrac{1}{2H}\left[(A\omega^2 + B\omega + C)T_0 - \left(E_d' I_d + E_q' I_q\right)\right] \end{cases} \tag{2}$$

$$\begin{cases} I_d = \dfrac{1}{Z'^2}\left[R_s\left(U_d - E_d'\right) + (X_s + X_m \| X_r)\left(U_q - E_q'\right)\right] \\ I_q = \dfrac{1}{Z'^2}\left[R_s\left(U_q - E_q'\right) - (X_s + X_m \| X_r)\left(U_d - E_d'\right)\right] \end{cases} \tag{3}$$

In the formula: $T' = \frac{X_r + X_m}{R_r}$; $Z'^2 = R^2 + (X_s + X_m \| X_r)^2$; $w' = w - 1$; The stator winding resistance and leakage reactance are

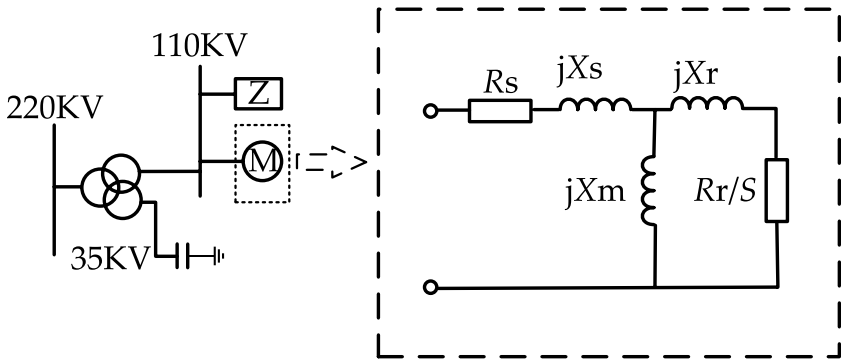

FIGURE 1
Equivalent structure of integrated load model.

represented by R_s and X_s, respectively; X_m represents mutual inductance of stator and rotor; The rotor winding's resistance and leakage reactance are represented by numbers R_r and X_r (Kang et al., 2021); The above parameters are all per-unit values under the base value of their own capacity; $E_q^{'}$ represents the potential of the equivalent motor under the q-axis sub-transient state; $E_d^{'}$ denotes the potential of the equivalent motor under the d-axis sub-transient state; Where $A + B + C = 1$ is satisfied; w represents the rotational speed of the equivalent motor; H is the corresponding motor's inertia time constant (Xu et al., 2009b). $X_m \| X_r$ means that X_m and X_r are connected in parallel to form $\frac{X_m X_r}{X_m + X_r}$. In addition to the above 12 parameters, in order to transform the model parameters into per-unit values, two parameters K_{pm} and M_{1f} are defined as follows Equations 4, 5:

$$K_{pm} = \frac{P_0^{'}}{P_0} \tag{4}$$

$$M_{1f} = \left(\frac{P_0^{'}}{S_{MB}}\right) \Big/ \left(\frac{U_0}{U_B}\right) \tag{5}$$

where: $P_0^{'}$ is the corresponding motor's starting active power; P_0 stands for the load's initial active power; K_{pm} represents the distribution parameter of initial active power; S_{MB} represents the rated capacity of induction motor (Guo et al., 2022). The rated starting load rate coefficient is denoted by M_{1f}.

To sum up, the parameters to be identified are R_s, X_s, X_m, X_r, R_r, P_Z, P_P, Q_Z, Q_P, K_{pm}, M_{1f}, H, A, and B. The use of this integrated load model makes the load modeling more comprehensive and accurate, and can better meet the needs of practical applications. The identification and improvement of model parameters can enhance the dependability and relevance of load modeling, hence offering a crucial point of reference for power system management and planning.

3 Parameter identification of load model

3.1 Principle of parameter identification

After determining the model structure, it is necessary to select an efficient and reliable optimization algorithm for parameter identification. At the core of parameter identification lies the estimation of model parameters by fitting a mathematical model of the system using input and output data. The principles of this process are illustrated in Figure 2.

The system input in the above figure is voltage. In the actual system, this curve specifically showcases the accurately measured values of active and reactive power for the load. Similarly, the simulation system's output curve mirrors this scenario, providing a simulated perspective on the active and reactive power of the load in response to voltage disturbance.

Initially, it is imperative to establish both the model structure and the objective function. Subsequently, the parameter identification process unfolds through the utilization of input and output data, employing an optimization method with the core principle of minimizing the objective function value. The central focus of this paper lies in defining the objective function, as articulated below Equation 6:

$$J = \sqrt{\frac{1}{n}\left(\sum_{i=1}^{n}\left(\hat{P}_i - P_{m,i}\right)^2 + \sum_{i=1}^{n}\left(\hat{Q}_i - Q_{m,i}\right)^2\right)} \tag{6}$$

in the formula: $P_{m,i}$, $Q_{m,i}$ represent the active and reactive power measured at time i, and n represents the number of samples. $\hat{P}_i$ and $\hat{Q}_i$ represent the active and reactive power computed at time i.

3.2 Dung beetle optimization algorithm (DBO)

The DBO algorithm specifically comes from the four living habits of DB, which are rolling, spawning, foraging and stealing. The Dung Beetle Optimizer (DBO) algorithm is a nature-inspired optimization technique based on the behavior of dung beetles. These insects exhibit unique foraging strategies that have been effectively translated into optimization algorithms to solve complex problems. The algorithm adapts the movement strategies of the dung beetles based on their success in finding good solutions. This adaptive mechanism enhances the efficiency of the search process. The principle

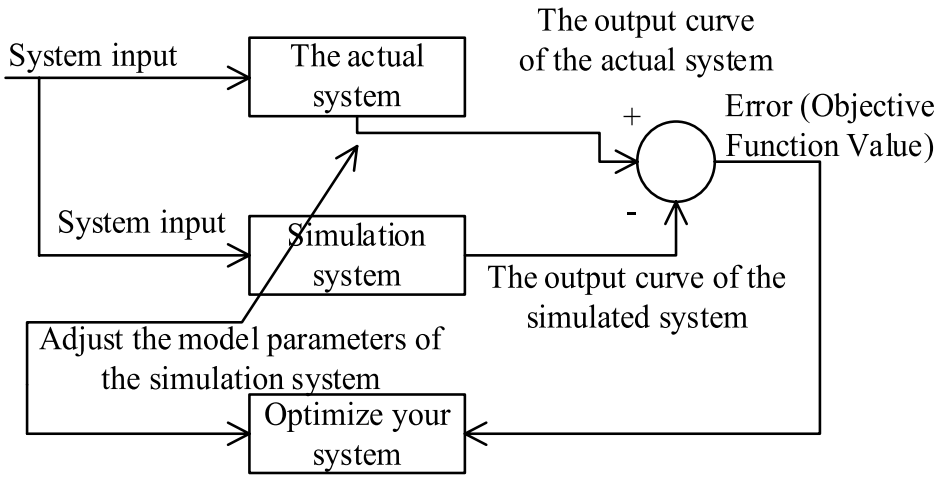

FIGURE 2
Schematic diagram of parameter identification system.

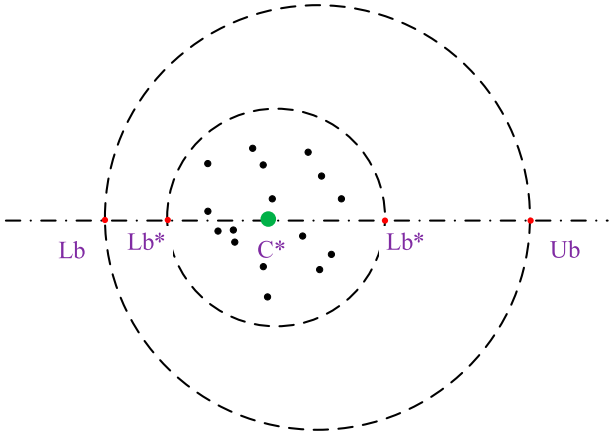

FIGURE 3
DBO algorithm schematic diagram.

diagram of the dung beetle optimization algorithm is shown in Figure 3, and the global optimal solution can be found after multiple iterations.

3.2.1 Rolling DB

Rolling dung balls is a common behavior among dung beetles. These insects have a tendency to roll dung balls that are larger than their own size to their preferred location. During this rolling process, they utilize celestial cues, such as the Sun and Moon, to maintain a straight trajectory for the dung ball. The passage delineates the navigational conduct of a dung beetle within a designated search space. In order to replicate this behavioral phenomenon, adherence to a predetermined trajectory is imperative. This emulation is encapsulated within a formalized rolling mathematical model, wherein the dynamic repositioning of both the dung beetle and the concomitantly propelled ball undergo continuous updates throughout the rolling process. The rolling mathematical model is as follows Equation 7:

$$\begin{aligned} y_i(t+1) &= y_i(t) + \beta m y_i(t-1) + c\Delta y, \\ \Delta y &= \left| y_i(t) - C^w \right| \end{aligned} \tag{7}$$

the current iteration times are denoted by t in the formula, where $y_i(t)$ is the location information of the i-th DB at the t-th iteration; According to the references (Pan and Bu, 2023), $0 < m \leq 1/5$ is a constant value that represents the defect coefficient. c is a constant value between Zero and One, and β is a coefficient with a value of −1 or 1. The worst place in the world is represented by C^w, the change of Δy means the change of light intensity, and the higher the value of Δy, the weaker the light source. The values of m and c are critical; m and c are set to 0.1 and 0.3, respectively. Natural causes that can lead DB to diverge from its original path are denoted by β. Specifically, when $\beta = -1$, it means that the update position deviates from the original dung beetle position, and when $\beta = 1$, it means that the update position has no deviation. To imitate the complicated environment in the actual world, β is set to 1 or -1 using a probability strategy in this study. Δy can promote rolling ball DB by providing the following two benefits:

1) In the optimization process, explore the entire problem space as fully as feasible.
2) Improved search performance, with less reliance on the local optimal.

When DB encounters obstacles that hinder its progress, it adopts a unique strategy akin to a dance to overcome the impediment and discover an alternative route. The essence of this method involves utilizing the tangent function to calculate a fresh roll direction, mirroring the intricate movements observed in a dance routine. Once the appropriate direction is determined, DB seamlessly continues its journey by rolling the associated ball backward. This dynamic approach constitutes the core of DB's ability to adapt and navigate challenging environments. In essence, the process encompasses the update of DB's position and establishes a comprehensive definition of its distinctive dance-like behavior Equation 8:

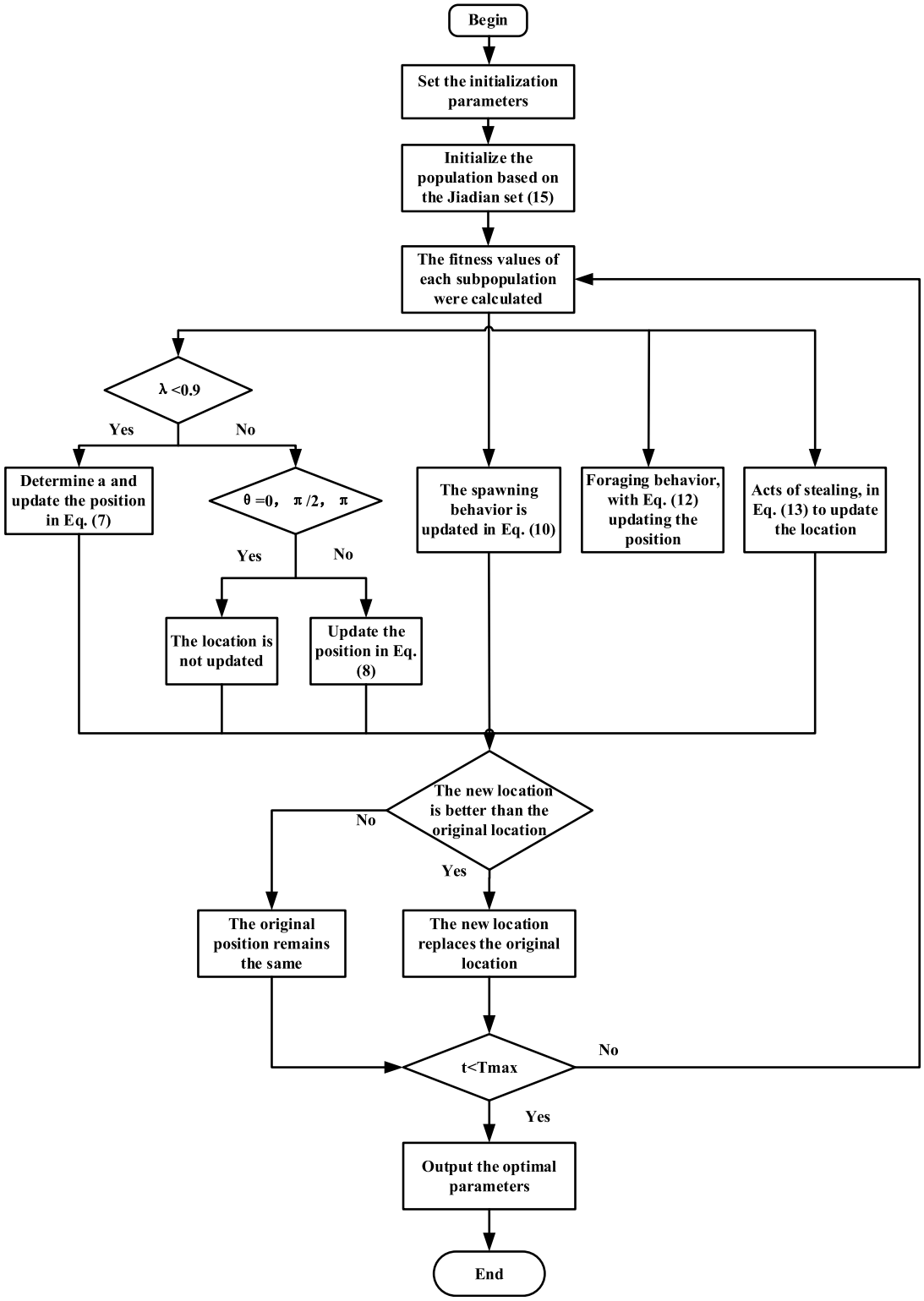

FIGURE 4
GDBO Flowchart.

$$y_i(t+1) = y_i(t) + \tan(\theta)\left|y_i(t) - y_i(t-1)\right| \quad (8)$$

in the formula: $y_i(t)$ represents the position of the i-th DB in the t-th iteration update, $y_i(t-1)$ represents the position of the i-th DB in the t-1-th iteration update, similarly, $y_i(t+1)$ represents the position of the i-th DB in the t+1-th iteration update. θ refers to the offset angle during the position update process, and its value range is

0–180°, if θ equals 0, $\pi/2$, or π, the location of the DB is not updated.

3.2.2 Spawning DB

Dung beetles show a fascinating behavior in nature. They carefully roll the dung balls, roll the cow dung into a dung ball with a diameter of about 2.5 cm, and quickly push it underground and bury it as the next-generation of food. This process is crucial for dung beetles (DB), as they carefully select a suitable spawning site to establish a safe habitat for the upcoming generation. The previous discussion underscored the importance of this behavior and motivated the introduction of boundary selection methods. This method is designed to simulate the specific area of female oviposition. The focus is on mimicking the natural conditions that ensure the safety and wellbeing of beetle offspring. The upper and lower limits of the selected region can be expressed by Formula 9:

$$\begin{aligned} Lb^c &= \max\left\{\left[\left(1-\left(1-\frac{t}{T_{\max}}\right)\right]C^{\star}, Lb\right\}\right. \\ Ub^c &= \min\left\{\left[\left(1+\left(1-\frac{t}{T_{\max}}\right)\right]C^{\star}, Ub\right\}\right. \end{aligned} \tag{9}$$

where: Ub^c and Lb^c are used to characterize the upper and lower boundaries of the dung beetle's renewal spawning area respectively, while Ub and Lb represent the upper and lower limits of the optimization problem. $T_{\max}$ represents the upper bound constraint on the number of iterations; $C^{\star}$ means the current local position optimal solution.

In the DBO algorithm, each female DB only lays a single egg per iteration to maintain ecological balance. This process prompts dynamic alterations in the boundary range of the spawning area, predominantly governed by adjustments to the R value. The determination of this R value may change at different stages of the iteration, thus affecting the size and shape of the spawning area. Therefore, in the whole iteration process, not only the number of eggs is regulated, but also the position of the hatching ball remains dynamic, evolving with the continuous adjustment of the boundary range. The specific position iteration formula can be articulated as follows Equation 10:

$$Y_i(t+1) = C^{\star} + \sum_{m=1}^{2} d_m\left(Y_i(t) - Lb^c\right) \tag{10}$$

in the formula, $B_i(t)$ denotes the update position of the i-th DB breeding ball during the t-th iteration. d_m $(m = 1, 2)$ are independent random vectors, Only the spawning area—that is, a specific area—is permitted to have the breeding ball.

3.2.3 Foraging DB

The little DB that emerges from the breeding ball wants to feed, so we build the best foraging area and direct it there. The small DB's position is updated in this way:

$$\begin{aligned} Lb^d &= \max\left((1-R)C^b, Lb\right) \\ Ub^d &= \min\left((1+R)C^b, Ub\right) \end{aligned} \tag{11}$$

the ideal foraging area's boundary division is shown above. C^b denotes the best position in the foraging area of all range classes;

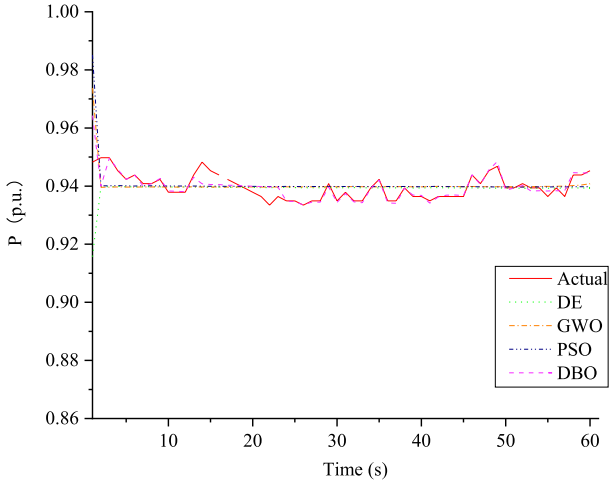

FIGURE 5
Fitting diagram of active power identification.

as the definition of the above formula, Lb^d and Ub^d are defined as the upper and lower limits of the optimal foraging area, respectively, along with other parameters stated in Formula 9. As a result, the little database's location is changed as Formula 12:

$$y_i(t+1) = y_i(t) + \sum_{m=1}^{2} k_m \times \left(y_i(t) - Lb^d\right) \tag{12}$$

in the formula, the variables $y_i(t)$ represent the location information of the i-th tiny DB at the t-th iteration, k_m $(m = 1, 2)$ represent the random number that follows the normal distribution.

3.2.4 Stealing DB

There are also some DBs who steal turds from other DBs. Furthermore, Eq. 11 shows that C^d is the best position for the dung ball (food), and it stands to reason that the best area for competition for food is in the vicinity of C^d. The following iterative formula is used to describe the position update of the thief dung beetle Equation 13:

$$y_i(t+1) = C^b + a \cdot l \cdot \left(\left|y_i(t) - C^{\star}\right| + \left|y_i(t) - C^b\right|\right) \tag{13}$$

in the formula, $y_i(t)$ is the position of the i-th thief at the t-th iteration; The value of a is constant. l is a stochastic vector generated from a normal distribution, with its dimensionality denoted by $1 \times D$.

3.3 The good point set

Nowadays, the initialization method of most swarm intelligence optimization algorithms is a random initialization form. The randomly generated population is unevenly distributed in the whole solution space. It is very gathered in some areas and scattered in others, resulting in the algorithm's utilization of the entire search space not being high and the population diversity not being strong. Aiming at the problem of random initialization, many scholars have proposed and used good point-set initialization. The theory of the good point set originated from Hua Luogeng, a famous

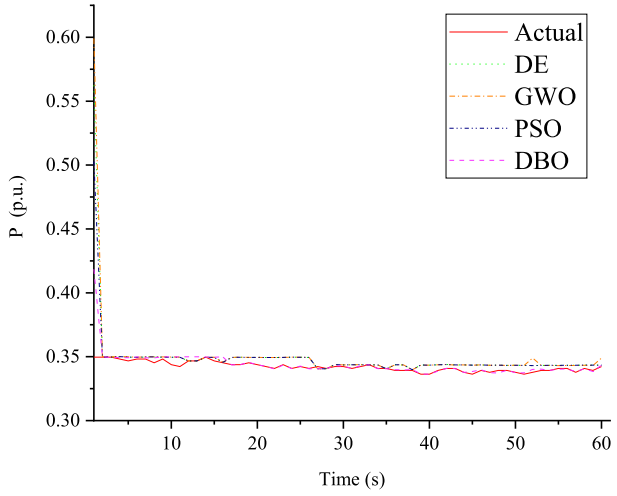

FIGURE 6
Reactive power identification fitting diagram.

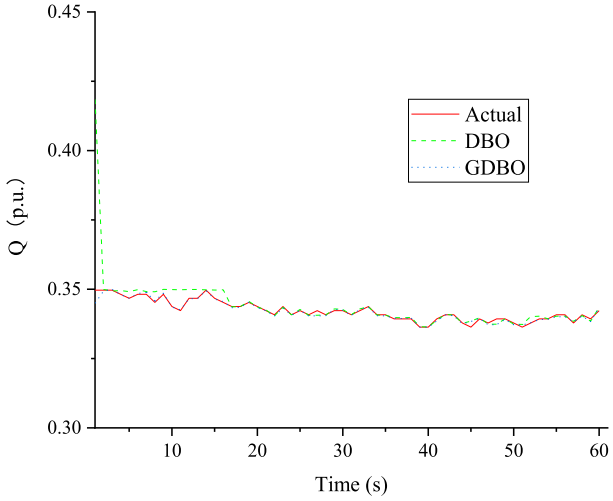

FIGURE 8
Comparison between reactive power DBO and GDBO.

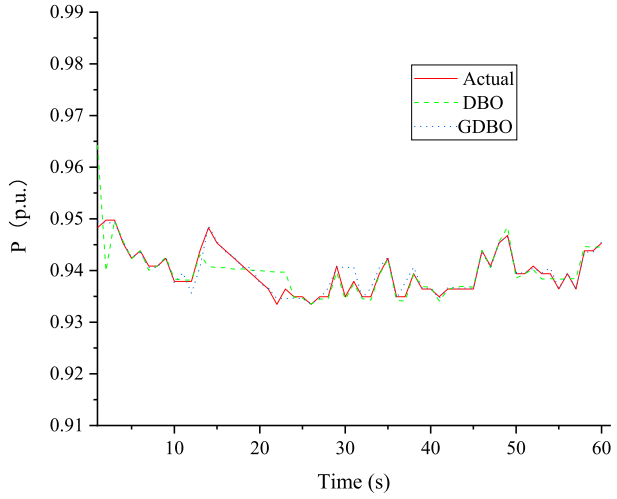

FIGURE 7
Comparison between active power DBO and GDBO.

Chinese mathematician. The randomness of random initialization is too high, and there may be a phenomenon where the first-generation solution is very far from the optimal value. If the value of the first-generation solution is very close to the optimal value, it can not only improve the convergence speed but also the optimization accuracy under the premise of a certain number of iterations.

Using the good point set for initializing the population in optimization algorithms ensures uniform coverage of the search space, which improves the balance between exploration and exploitation, accelerates convergence, reduces bias, and enhances performance, particularly in high-dimensional spaces. This leads to more effective and efficient optimization, making it a preferred choice for initializing candidate solutions. To ensure population diversity and ergodicity, which can ultimately enhance the algorithm's search performance, it is crucial to maintain a uniform distribution within the initial population. Achieving population diversity in DBO can be challenging due to the random selection of individuals during initialization.

A uniform and effective method for point selection is employed to initialize the population, aiming to address the aforementioned challenges, enhance population diversity, and optimize the utilization of the current solution. Leveraging the uniform distribution attribute of an excellent point set bolsters the flexibility and comprehensiveness of the population initialization process, enabling more thorough exploration of the solution space.

Currently, numerous clever algorithms (Cheng and Ding, 2020; Yan et al., 2023) have implemented the excellent point set initialization method with successful outcomes. The population's initialization can be dispersed over the solution space by employing the good point set, which increases population variety and helps the algorithm find the globally optimal solution more effectively. The following is the principle: Let us assume that the person in the DBO algorithm is a point in n-dimensional Euclidean space, or, alternatively, that it is a position in the unit cube. When the number of individuals in a population exceeds the volume of the unit cube, it will cause individual repetition. The following actions can be performed to lower the repetition rate Equation 14:

$$P_m(n) = \left\{\left(\left\{g_1^{(m)} \cdot n\right\}, \cdots, \left\{g_R^{(m)} \cdot n\right\}\right), 1 \le n \le m\right\} \tag{14}$$

in the formula: $P_m(n)$ is a set of good points, and the deviation $\phi(m) = C(g,\varepsilon)m^{-1+\varepsilon}$, where $\varphi(m) = C(g,\varepsilon)m^{-1+\varepsilon}$ is a constant only related to g and ε; g is a good point; Taking the fractional part is represented by $\left\{g_R^{(n)} \cdot n\right\}$, n represents the number of points, $g_k = \left\{2\cos\left(\frac{2n\pi}{p}\right), 1 \le n \le R\right\}$; The smallest prime number satisfying $(p - D/2) \ge D$ is p. In the search space, map the set of good spots (Equation 15).

$$y_i(j) = \left(Ub_j - Lb_j\right) \cdot \left\{g_j^{(i)} \cdot n\right\} + Lb_j \tag{15}$$

in the formula: The top and lower boundaries of the j-th dimension are denoted by Ub_j and Lb_j.

10.3389/fenrg.2024.1415796

TABLE 1 Parameter identification results of measured data.

Strategy	Optimal fitness	Iteration time/s	R_s	X_s	X_m	R_r	X_r	H	A	B	k_{pz}	k_{pp}	k_{qz}	k_{qp}	k_{pm}	M_{1f}
IDE	0.358	440.243	0.124	0.123	2.677	0.08	0.113	1.197	0.533	0.147	0.298	0.706	0.494	3.993	0.194	0.439
PSO	0.352	403.098	0.35	0.102	2.604	0.01	0.07	0.60	1	0	0.1	1	0	0.071	0.1	0.752
GWO	0.353	435.56	0.35	0.195	2.461	0.079	0.18	1.101	0.235	0.266	0.150	0.932	0.322	3.95	0.541	0.101
DBO	0.36	419.02	0.268	0.178	2.221	0.08	0.143	1.192	0.935	0.761	0.294	0.716	0.498	3.997	0.571	0.711
GDBO	0.363	404.75	0.276	0.196	2.187	0.075	0.129	1.451	1	0.952	0.298	0.721	0.872	3.472	0.517	0.732

3.4 Algorithm flow

In this paper, the DBO algorithm enhanced by initializing the population with a good point set before updating the iterative position. The specific process is shown in Figure 4, which can be divided into seven steps:

Step 1: During the initial phase of the algorithm, a set of initial parameters is defined, serving as the starting point for subsequent optimization processes.

Step 2: Utilizing Formula 15, the algorithm initializes the population based on a pre-defined optimal point set, providing a well-founded starting configuration for the optimization process.

Step 3: By executing the objective function, the algorithm calculates fitness values for each dung beetle in the population, reflecting their performance at their current positions.

Step 4: Positions of all dung beetles are adjusted using a specified strategy to seek more optimal solutions. This step propels the population towards favorable directions.

Step 5: Examine the positions of each dung beetle to ensure they adhere to the defined problem boundaries, maintaining the problem's feasibility and validity.

Step 6: In each iteration, it is essential to review and update the current optimal solution along with its corresponding fitness value to prevent the algorithm from disregarding potential global optima.

Step 7: Iterate through Steps 3 to 6 iteratively until the pre-defined termination criterion is satisfied. Upon termination, report the attained global optimal solution and its corresponding fitness value, concluding the entire optimization process.

4 Case analysis

4.1 Algorithm initialization and parameter setting

The optimization algorithm's parameter selection significantly impacts the optimization outcomes; hence, it is essential to meticulously choose optimal parameter values for simulation. Within each dung beetle colony, four distinct agents are present namely, the rolling ball DB, the spawning DB, the foraging DB, and the stealing DB. In the GDBO algorithm, the position vector of the i-th DB is represented by $x_i(t)=(y_{i1}(t), \ldots, y_{iD}(t))$ at the t-th iteration. In this paper, the size of DB group is N = 70 (the population size of other algorithms is 70). The numbers of rolling, spawning, foraging and thief DB were 14, 14, 16, and 26, respectively. The prescribed maximum iteration count is established at 500, where the primary scaling factor, secondary scaling factor, and crossover probability of IDE are set to 0.5, 0.3, and 0.8. Both learning factors of PSO are set to 0.5.

4.2 Measured data of a power plant and example simulation

To assess the efficacy of the DBO algorithm in the context of parameter identification for load modeling, this paper uses IDE,

TABLE 2 Evaluation of model fitting effect.

Algorithm	Active power				Reactive power			
	MAE	I_{MAE}%	RMSD	I_{RMSE}%	MAE	I_{MAE}%	RMSD	I_{RMSE}%
IDE	0.003870	82.14%	0.084758	73.64%	0.007184	93.05%	0.027833604	96.92%
PSO	0.004020	82.81%	0.078759	71.64%	0.006203	91.96%	0.020259353	95.77%
GWO	0.003846	82.03%	0.089420	75.02%	0.007996	93.76%	0.03254387	97.37%
DBO	0.001432	51.75%	0.046723	52.19%	0.002183	77.14%	0.009065738	90.56%
GDBO	0.000691	—	0.022338	—	0.000499	—	0.000856037	—

PSO, and GWO to identify the PMU measured data recorded by a power plant in Ruilijiang, Yunnan Province, at 10:14 on 20 November 2019, sampling once every 10 ms, for a total of 6,000 times. Figures 5, 6 illustrate the correlation between active and reactive power for both empirical and simulated datasets, respectively. The unit of each parameter is p.u.

According to the above Figures 5, 6, it is not difficult to see that the DBO algorithm used in this paper is more accurate for the fitting value of parameter identification results and basically achieves coincidence. However, the traditional Dung Beetle Optimizer algorithm has a wide range for the first iteration of the initial population, resulting in a higher fitting value in the front, and then tends to be stable. Hence, the algorithm denominated as the Dung Beetle Optimizer, founded upon the well-defined point set articulated in this study, aptly addresses the aforementioned issue. The comparative outcomes pertaining to active and reactive power are visually presented in Figures 7, 8. The parameter values for identification derived through the application of the Dung Beetle Optimizer algorithm are delineated in Table 1.

Figures 7, 8 show that the DBO algorithm based on the good point set has a faster initial iteration speed and can fit to the real value faster than the traditional DBO. The identification instances given above demonstrate that the DBO based on good point set has superior accuracy and speed than the other four algorithms in parameter identification of load modeling through a large number of practices.

4.3 Fitting effect evaluation

In this research, the assessment of fitting performance between observed data and simulated data relies on the utilization of specific metrics, namely the Mean Absolute Error (MAE) and the Root Mean Square Error (RMSE). These metrics serve as quantitative measures to evaluate the accuracy of the simulated data in comparison to the actual observations. The corresponding formulations for MAE and RMSE are precisely defined by Eqs 16, 17, respectively. By employing these metrics and their associated mathematical expressions, this study establishes a rigorous framework for quantifying the level of agreement or discrepancy between the simulated data and the observed data, thereby enhancing the precision and reliability of the evaluation process.

$$\mathbf{MAE} = \frac{\sum_{i=1}^{m}|y_i - x_i|}{m} \tag{16}$$

$$\mathbf{RMSD} = \sqrt{\frac{\sum_{i=1}^{m}(y_i - x_i)^2}{m}} \tag{17}$$

within the mathematical expression, x_i denotes the i-th actual value of either active or reactive power, y_i represents the i-th simulated value of active or reactive power, and m corresponds to the total number of data sets.

Compared with the traditional method, the improvement rates of the Mean Absolute Error (MAE) and the Root Mean Square Error (RMSE) of the method used in this paper are represented by $\mathbf{I}_{MAE}$% and $\mathbf{I}_{RMSD}$% respectively.

$$\mathbf{I}_{MAE}\% = \frac{MAE_{RA} - MAE_{GDBO}}{MAE_{RA}} * 100\% \tag{18}$$

$$\mathbf{I}_{RMSE}\% = \frac{RMSE_{RA} - RMSE_{GDBO}}{RMSE_{RA}} * 100\% \tag{19}$$

MAE_{RA} represents the absolute average error of the traditional algorithm, and MAE_{GDBO} represents the absolute average error of the GDBO algorithm proposed in this paper. $RMSE_{RA}$ represents the root mean square error of the traditional algorithm, and $RMSE_{GDBO}$ represents the root mean square error of the GDBO algorithm proposed in this paper.

The assessment outcomes for the fitting efficacy of measured data using the GDBO algorithm, which relies on the proposed favorable point set in this study, along with comparisons to alternative algorithms, are presented in Table 2.

Through a comparative analysis with alternative algorithms, upon careful examination, in the active power fitting, the GDBO algorithm used in this paper is compared with the IDE, PSO, GWO and traditional DBO algorithm in reducing the absolute average error, which is increased by 82.14%, 82.81%, 82.03%, and 51.75% respectively. In terms of reducing the root mean square error, the improvement rate of the GDBO algorithm also reached 73.64%, 71.64%, 75.02%, and 52.19%, respectively. At the same time, as shown in Table 2, the GDBO algorithm demonstrates remarkable performance when fitting reactive power applied to measured data of the model. Specifically, it exhibits the most minimal mean absolute error and root mean square error among the tested algorithms. This compelling observation underscores the superior efficacy of the proposed algorithm in the realm of parameter identification. The algorithm's ability to minimize errors in fitting the measured data points to the model highlights its robustness and accuracy, signifying its potential as an effective tool in practical applications requiring precise parameter estimation. Moreover, the

algorithm demonstrates increased robustness in the face of fluctuations in both active and reactive power.

5 Conclusion

DBO is utilized in this paper for load modeling and parameter identification. The results of the identification of load modeling reveal that DBO has a considerable improvement in accuracy and speed when compared to the other three methods. Consequently, DBO can be effectively utilized for parameter identification in load modeling, which can improve load modeling accuracy. Furthermore, the DBO method based on the good point set outperforms the classic DBO algorithm in terms of accuracy and speed, and gives a higher level of solution for parameter identification of load modeling.

Data availability statement

The original contributions presented in the study are included in the article/supplementary material, further inquiries can be directed to the corresponding author.

Author contributions

CX: Conceptualization, Validation, Writing–original draft, Writing–review and editing. XX: Conceptualization, Methodology, Writing–review and editing. XH: Methodology, Writing–review and editing. CD: Validation, Writing–review and editing.

Funding

The author(s) declare that financial support was received for the research, authorship, and/or publication of this article.

Conflict of interest

Authors CX, XX, XH and CD were employed by Electric Power Research Institute of Yunnan Power Grid Co., Ltd.

Publisher's note

All claims expressed in this article are solely those of the authors and do not necessarily represent those of their affiliated organizations, or those of the publisher, the editors and the reviewers. Any product that may be evaluated in this article, or claim that may be made by its manufacturer, is not guaranteed or endorsed by the publisher.

References

Chen, H., Hao, R., Liu, Y., Wang, H., Wang, T., and Li, D. (2020). Parameter identification of time-varying power function load model based on improved RLS algorithm. *High. Volt. Eng.* 46 (07), 2380–2388. doi:10.13336/j.1003-6520.hve.20200310013

Cheng, M., and Ding, R. (2020). Multi-path coverage test case generation based on good-point set genetic algorithm. *Comput. Digital Eng.* 50 (09), 1940–1944. doi:10.3969/j.issn.1672-9722.2022.09.013

Diao, H., Li, P., Guo, S., Lin, S., Su, H., and Shen, Y. (2023). Parameter identification method for composite load model of PMU under small disturbance signal. *Prot. Control Electr. Power Syst.* 51 (13), 37–49. doi:10.19783/j.cnki.pspc.221680

Fang, C., Tang, X., Li, W., Zhang, N., Wei, X., and Chen, J. (2022). Optimal design of fast mechanical switches for 500 kV DC circuit breakers based on multi-strategy particle swarm optimization algorithm. *High. Volt. Appar.* 58 (01), 79–88. doi:10.13296/J.1001-1609.Hva.2022.01.011

Fu, W., Jiang, X., Li, B., Tan, C., Chen, B., and Chen, X. (2023). Rolling bearing fault diagnosis based on 2D time-frequency images and data augmentation technique. *Meas. Sci. Technol.* 34 (4), 045005. doi:10.1088/1361-6501/acabdb

Guo, C., Xie, H., Meng, X., He, P., Yang, L., and Wang, D. (2022). Parameter identification of load model based on grey wolf optimization algorithm. *J. Electr. Power Sci. Technol.* 37 (02), 30–37. doi:10.19781/j.issn.1673-9140.2022.02.004

Ju, P. (2015). *Modern power system control and identification*. Tsinghua University Press.

Kang, P., Zhu, S., Wang, H., Fan, G., and Yang, G. (2021). Parameter identification of PV integrated load model based on improved butterfly algorithm. *Renew. Energy* 39 (11), 1541–1547. doi:10.13941/j.cnki.21-1469/tk.2021.11.018

Li, B., Gao, P., and Guo, Z. (2023). Improved dung beetle algorithm to optimize LSTM for photovoltaic array fault diagnosis. *J. Electr. Power Syst. Automation*, 1–10. doi:10.19635/j.cnki.csu-epsa.001317

Liu, Zi. (2007). *Application of modern optimization algorithm in load model identification*. Beijing: North China Electric Power University. doi:10.7666/d.y1058213

Pan, Z., and Bu, F. (2023). DV-Hop localization algorithm optimized by dung beetle algorithm [J/OL]. *J. Electron. Meas. Instrum.*, 1–10. doi:10.13382/j.jemi.B2306338

Pattanaik, J. K., Basu, M., and Dash, D. P. (2017). Opposition-based differential evolution for hydrothermal power system. *Prot. Control Mod. Power Syst.* 2, 2. doi:10.1186/s41601-017-0033-5

Sheng, X., Ouyang, T., Yang, N., and Zhuang, J. (2021). Sample-based neural approximation approach for probabilistic constrained programs. *IEEE Trans. neural Netw. Learn. Syst.* 34, 1058–1065. doi:10.1109/TNNLS.2021.3102323

Swarupa, M. L., Kumar, V. G., Latha, K. S., Ravindra, M., and Kumar, B. P. (2024). Distribution state estimation and its impact of load modeling. *Contemp. Math.*, 527–545. doi:10.37256/cm.5120242696

Wang, B., Huang, Y., Song, T., and Dong, J. (2011). Parameter identification of load model based on chaotic ant colony algorithm. *Power Syst. Prot. Control* 39 (14), 47–51. doi:10.3969/j.issn.1674-3415.2011.14.008

Wang, X., Sheng, X. K., Mu, K., and Wang, X. (2020). Research on electrical performance detection method of transformer oil based on multi-frequency ultrasonic technology and GWO-BP algorithm. *High. Volt. Appar.* 56 (08), 114–120. doi:10.13296/J.1001-1609.Hva.2020.08.018

Wang, Y., Gu, J., and Yuan, L. (2023). Distribution network state estimation based on attention-enhanced recurrent neural network pseudo-measurement modeling. *Prot. Control Mod. Power Syst.* 8, 31. doi:10.1186/s41601-023-00306-w

Wang, Y., Lu, C., and Zhang, X. (2019). Applicability comparison of different algorithms for ambient signal based load model parameter identification. *Int. J. Electr. Power and Energy Syst.* 111, 382–389. doi:10.1016/j.ijepes.2019.03.061

Wang, Z., Bian, S., Liu, X., Yu, K., and Shi, Y. (2014). Study on parameter identification of load model based on combination of chaos and quantum-behaved particle swarm optimization. *Trans. China Electrotech. Soc.* 29 (12), 211–217. doi:10.19595/j.cnki.1000-6753.tces.2014.12.027

Wu, P., Zhang, X., Lu, C., Wang, Y., Ye, H., and Ling, X. (2023). A composite load model aggregation method and its equivalent error analysis. *Inter-national J. Electr. Power Energy Syst.* 150, 109098. doi:10.1016/j.ijepes.2023.109098

Wu, Z., Fan, D., and Fan, Z. (2022). Traction load modeling and parameter identification based on improved sparrow search algorithm. *Energies* 15 (14), 5034. doi:10.3390/en15145034

Xu, J., Ma, J., Tang, Y., and He, R. (2009a). Parameter identification of load modeling based on improved differential evolution algorithm. *Power Syst. Prot. Control* 37 (24), 36–40 + 45. doi:10.3969/j.issn.1674-3415.2009.24.008

Xu, J., Ma, J., Tang, Y., and He, R. (2009b). Parameter identification of load modeling based on improved hybrid genetic algorithm. *Mod. Electr. Power* 26 (003), 23–27. doi:10.19725/j.cnki.1007-2322.2009.03.005

Xu, P., Fu, W., Lu, Q., Zhang, S., Wang, R., and Meng, J. (2023). Stability analysis of hydro-turbine governing system with sloping ceiling tailrace tunnel and upstream surge tank considering nonlinear hydro-turbine characteristics. *Renew. Energy* 210, 556–574. doi:10.1016/j.renene.2023.04.028

Xue, J., and Shen, B. (2022). Dung beetle optimizer: a new meta-heuristic algorithm for global optimization. *J. Supercomput.* 2022, 7305–7336. doi:10.1007/s11227-022-04959-6

Yan, S., Yang, P., Zhu, D., Wu, F., and Yan, Z. (2023). Improved sparrow search algorithm based on good point set. *J. Beijing Univ. Aeronautics Astronautics*, 1–13. doi:10.13700/J.BH.1001-5965.2021.0730

Yang, N., Dong, Z., Wu, L., Zhang, L., Shen, X., Chen, D., et al. (2022d). A comprehensive review of security-constrained unit commitment. *J. Mod. Power Syst. Clean Energy* 10 (No.3), 562–576. doi:10.35833/MPCE.2021.000255

Yang, N., Qin, T., Wu, L., Huang, Y., Huang, Y., Xing, C., et al. (2022c). A multi-agent game based joint planning approach for electricity-gas integrated energy systems considering wind power uncertainty. *Electr. Power Syst. Res.* 204, 107673. ISBN: 0378-7796. doi:10.1016/j.epsr.2021.107673

Yang, N., Shen, X., Liang, P., Ding, L., Yan, J., Xing, C., et al. (2024). Spatial-temporal optimal pricing for charging stations: a model-driven approach based on group price response behavior of evs. *IEEE Trans. Transp. Electrification*, 1. doi:10.1109/TTE.2024.3385814

Yang, N., Yang, C., Wu, L., Shen, X., Jia, J., Li, Z., et al. (2022a). Intelligent da-ta-driven decision-making method for dynamic multisequence: an E-Seq2Seq-based SCUC expert system. *IEEE Trans. Industrial Inf.* 18 (No.5), 3126–3137. doi:10.1109/TII.2021.3107406

Yang, N., Yang, C., Xing, C., Ye, D., Jia, J., Chen, D., et al. (2022b). Deep learning-based SCUC decision-making: an intelligent data-driven approach with self-learning capabilities. *IET Generation, Transm. Distribution* 16 (No.4), 629–640. doi:10.1049/gtd2.12315

Yang, N., Ye, D., Zhou, Z., Cui, J., Chen, D., and Wang, X. (2018). Research on modelling and solution of stochastic SCUC under AC power flow constraints. *IET Generation Transm. Distribution* 12, 3618–3625. doi:10.1049/iet-gtd.2017.1845

Zhang, J. (2007). *Power system load model and identification*. China Electric Power Press.

Zhang, X., Lu, C., Lin, J., and Wang, Y. (2020). Experimental test of PMU measurement errors and the impact on load model parameter identification. *IET Generation, Transm. Distribution* 14 (20), 4593–4604. doi:10.1049/iet-gtd.2020.0297

Zhang, Y., Wei, L., Fu, W., Chen, X., and Hu, S. (2023a). Secondary frequency control strategy considering DoS attacks for MTDC system. *Electr. Power Syst. Res.* 214, 108888. doi:10.1016/j.epsr.2022.108888

Zhang, Y., Xie, X., Fu, W., Chen, X., Hu, S., Zhang, L., et al. (2023b). An optimal combining attack strategy against economic dispatch of integrated energy system. *IEEE Trans. Circuits Syst. II Express Briefs* 70 (1), 246–250. doi:10.1109/TCSII.2022.3196931

Zhou, D., Peng, X., Huang, X., Cheng, G., Tang, W., Zou, K., et al. (2023). Optimization method of power grid material warehousing and allocation based on multi-level storage system and reinforcement learning. *Comput. Electr. Eng.* 109, 108771. doi:10.1016/j.compeleceng.2023.108771

Zhu, B., Yang, Y., Wang, K., Liu, J., and Vilathgamuwa, D. M. (2023). High transformer utilization ratio and high voltage conversion gain flyback converter for photovoltaic application. *IEEE Trans. Industry Appl.* 60, 2840–2851. doi:10.1109/TIA.2023.3310488

Nomenclature

P_Z	The static active power under the load constant impedance model
P_I	The static active power under the load constant current mode
P_P	The static active power under the load constant power model
P_s	The static zip part's active powers
Q_s	The static zip part's reactive powers
Q_Z	The static reactive power under the load constant impedance model
Q_I	The static reactive power under the load constant current mode
Q_P	The static reactive power under the load constant power model
R_s	The stator winding resistance
X_s	The stator winding leakage reactance
R_r	The rotor winding resistance reactance
X_r	The rotor winding leakage reactance
X_m	Mutual inductance of stator and rotor
$E_q^{'}$	The potential of the equivalent motor under the q-axis sub-transient state
$E_d^{'}$	The potential of the equivalent motor under the d-axis sub-transient state
$P_0^{'}$	The corresponding motor's starting active power
P_0	The load's initial active power
K_{pm}	The distribution parameter of initial active power
S_{MB}	The rated capacity of induction motor
$P_{m,i}$	The active power measured at time i, and n represents the number of samples
$Q_{m,i}$	The reactive power measured at time i, and n represents the number of samples
$\hat{P}_i$	The active power computed at time i
$\hat{Q}_i$	The reactive power computed at time i
m	A constant value that represents the defect coefficient
c	A constant value between Zero and One
β	A coefficient with a value of −1 or 1
C^w	The worst place
Δy	The change of light intensity
$y_i(t)$	The position of the i-th DB in the t-th iteration update
$y_i(t-1)$	The position of the i-th DB in the t-1-th iteration update
$y_i(t+1)$	The position of the i-th DB in the t+1-th iteration update
θ	The offset angle during the position update process
Ub^c	The upper boundaries of the dung beetle's renewal spawning area
Lb^c	The lower boundaries of the dung beetle's renewal spawning area
$T_{\max}$	The upper bound constraint on the number of iterations
C^*	The current local position optimal solution
$B_i(t)$	The update position of the i-th DB breeding ball during the t-th iteration
C^b	The best position in the foraging area of all range classes
Ub^d	The upper limits of the optimal foraging area
Lb^d	The lower limits of the optimal foraging area
k_m	The random number that follows the normal distribution
C^d	The best position for the dung ball
$P_m(n)$	A set of good points

frontiers | Frontiers in Energy Research

TYPE Original Research
PUBLISHED 29 August 2024
DOI 10.3389/fenrg.2024.1450986

OPEN ACCESS

EDITED BY
Chenghong Gu,
University of Bath, United Kingdom

REVIEWED BY
Zhengyi Chen,
Princeton University, United States
Junjie Zhong,
Changsha University of Science and Technology, China

*CORRESPONDENCE
Wenhan Zhang,
powerzwh@ncepu.edu.cn

RECEIVED 18 June 2024
ACCEPTED 05 August 2024
PUBLISHED 29 August 2024

CITATION
Gong C, Wang W, Zhang W, Dong N, Liu X, Dong Y and Zhang D (2024) Active power optimisation scheduling method for large-scale urban distribution networks with distributed photovoltaics considering the regulating capacity of the main network.
Front. Energy Res. 12:1450986.
doi: 10.3389/fenrg.2024.1450986

Active power optimisation scheduling method for large-scale urban distribution networks with distributed photovoltaics considering the regulating capacity of the main network

Cheng Gong[1], Wei Wang[1], Wenhan Zhang[2]*, Nan Dong[1], Xuquan Liu[2], Yechun Dong[2] and Dongying Zhang[2]

[1]Electric Power Research Institute, State Grid Beijing Electric Power Company, Beijing, China, [2]School of Electrical and Electronic Engineering, North China Electric Power University, Beijing, China

Introduction: When a distributed photovoltaic (PV) system has access to a large urban distribution network, the active balance is primarily borne by the main network gas unit; when the scale of the distributed PV system is very large, the main network can only provide limited regulation capacity, and the distribution network must determine the active optimal scheduling strategy.

Methods: This work proposes an active optimization scheduling model for the distribution network by considering the regulation capacity of the main network. In terms of the optimisation objectives, the maximum consumption of the distributed PVs and minimum power fluctuation at the demarcation point of the main distribution network are proposed as the main objectives, while the minimum total exchanged power in a cycle at the main distribution demarcation point and minimum distribution network loss are considered as the secondary objectives. In terms of constraints, it is proposed that the main network's regulation capacity be characterized by the main network's gas-fired unit creep constraints. A fast solution method for active optimization of the distribution network is designed herein to formulate the priority control order of the adjustable units according to the dispatch economic performances of various types of adjustable resources in the distribution network; this reduces the number of variables involved in the optimization at each step and improves the optimized solution speed.

Results: Finally, Simulation verification by IEEE 33-node distribution network arithmetic example based on Matlab simulation platform.

Discussion: Simulation results show the effectiveness of the method in achieving maximum PV consumption and reflecting the limited regulation capacity of the main grid.

KEYWORDS

large urban distribution network, active power optimal scheduling, distributed photovoltaic, photovoltaic consumption, main distribution cooperation

1 Introduction

Large urban distribution networks often experience large loads, and the distribution network has a few conventional power sources with small capacities that are mostly supplied by the main grid (Lu et al., 2015). The power in the main urban grid is partly derived from the external grid and partly from the gas-fired units in the main grid. The power supplied by the external grid cannot fluctuate significantly according to the power supply agreement; therefore, the gas units in the main grid assume the function of active balance regulation.

With the rapid development of new energy generation methods, distributed photovoltaic (PV) systems have gained a high proportion of access to urban distribution networks. When the PV output is high and load is low, the gas-fired units in the main grid must reduce their outputs or even shut down; conversely, when the PV output is low and load is high, the gas-fired units in the main grid must increase their outputs or even startup the standby units. The main grid units are generally operated within the economic output range, and the maximum regulation capacity is ensured to not exceed the safe output range; this means that the units require a lot of time to startup, and frequent startups and shutdowns could affect the lifetimes of the units (Hu et al., 2008). Therefore, the startup mode of the main network units cannot be changed over a wide range, resulting in limited regulation capacity of the main network. When the PV supply fluctuates widely in the distribution network, the main network can only provide limited regulation capacity. Therefore, urban distribution networks must perform active balancing and carry out optimal dispatch within the main grid regulation capacity.

The optimal scheduling of large urban distribution networks containing distributed PV sources is studied by considering the main grid regulation capacity as follows:

(1) How to take into account the regulating capacity of the main network in terms of the distribution network.
(2) What are the dispatchable resources in a large urban distribution network, and what optimization objectives must be considered.
(3) What constraints should be imposed on the optimization model, and how to design a solution method applicable to real scheduling operations.

Problem (1) entails cooperative active scheduling of the main distribution. Owing to the randomness and volatility of distributed PV output, there is easy lack of coordination between the distribution and main grids in terms of the power generation and consumption plans, making it difficult to fully consume the distributed energy. Therefore, optimal scheduling of the main and distribution networks is necessary to achieve main power balance and other objectives while maximally consuming the distributed PV power. The existing cooperative optimal scheduling of the main and distribution networks is divided into subproblems concerning optimization of the main and distribution networks, which are then solved iteratively (Zhang et al., 2017; Deng, 2019; Wu et al., 2019; Zhang and Wang, 2019). The optimization objective is to optimize the overall economy of the main distribution network while ensuring that the active power transmitted at its boundary meets the consistency constraints. In distribution network optimization, the main network is considered to be an infinite power source, and only the active power exchanged by the main and distribution networks is required to be within the capacity of the transmission channel without considering the regulation capacity of the main network units and their ability to support a wide range of changes in the exchanged power.

Jiang et al. (2019) proposed a collaborative optimal operation method based on multiparameter planning for the main and distribution networks, where the distribution network needs to be optimized under the conditions of the power planning curve transmitted by the main network. This is to solidify the main network power supply capacity as the planning curve, which does not reflect the power supply margin of the main network, thereby producing conservative scheduling results. Therefore, to fully exploit the regulation capacity of the main network, it should be reflected as a limited range of power variations. Moreover, the amount of power exchange in the main network synergy should be minimized.

Problem (2) is the optimization objective of the distribution network. When a high proportion of the distributed PV supply is connected to the distribution network, it will impact the voltage security of the distribution network, which causes not only voltage overruns at the grid nodes but also branch current overloads, voltage shifts, and high harmonics (Ge, 2023). Among these, voltage overrun is one of the most important reasons affecting the ability to consume PV power (Zhang, 2021).

Most of the existing optimization objectives of distribution networks containing distributed PVs are strategies for ensuring their voltage stabilities. Li et al. (2018) investigated the impacts of various voltage regulation measures on the PV admittance capacities of the distribution network and used the trial method to solve for the maximum PV admittance capacity before and after adding the voltage regulation measures without voltage regulation; some authors analyzed the impact of the access power at each node on the voltages at the other nodes based on the voltage sensitivity matrix (Xu et al., 2016; Cai et al., 2017) along with the PV admittance capacity of the distribution network based on the analytical method. Huang et al. (2020) used the intelligent optimization method and proposed a distributed PV grid-connected limit capacity calculation method based on the adaptive weighted particle swarm optimization algorithm. Ding et al. (2017) proposed a method to avoid network overvoltage by controlling the PV inverters and formulated a two-stage robust centralized optimal scheduling model by considering the PV output uncertainties.

The optimal distribution network operation economics has also been considered based on the voltage stability of the distribution network. Lin et al. (2017) developed a multiregion dynamic economic dispatch model to minimize the total multiregion generation cost. Pan (2015) established an optimal scheduling model for the units by reflecting the demands for energy savings and emission reductions in the power grid. In terms of the demand-side responses, Chen et al. (2024) developed an operation scheduling optimization methodology for electric ready-mixed concrete vehicles (ERVs). These studies do not analyze the roles of adjustable devices, such as energy storage systems (ESSs), gas units, and controllable loads (CLs), in achieving the maximum consumption of distributed PV power; at the same time, they do not take into account the impact of the regulating capacity of the main grid on PV consumption in the distribution network.

Problem (3) is concerned with the distribution network constraints and solution methods. Lin et al. (2017) considered the generator set creep constraints as well as the contact line transmission power constraints; Pan (2015) considered the unit start–stop and creep rate constraints. These studies only focus on the units within the distribution network and do not consider the main network units or analyze the impacts of the creep rate constraints of the units on distributed PV consumption. Therefore, the creep rate constraints of the gas-fired units in the main grid should be considered, which are reflected in the fact that the exchanged power between the main and distribution networks cannot fluctuate significantly during adjacent time periods.

In terms of optimal solutions, there are various algorithms in literature to solve the scheduling model (Dvorkin et al., 2015; Pandžić et al., 2016; Li et al., 2021; Wang et al., 2023). Ruan et al. (2020) proposed a distributed voltage control model with a novel network partitioning approach. Li et al. (2016) proposed a coordinated transmission and distribution AC optimal flow model based on a heterogeneous decomposition algorithm; Li (2013) proposed an application-based coordinated optimal flow for transmission and distribution network decomposition. The above algorithms require large numbers of control quantities to participate in the iterative solution at the same time, and the solution space of the problem is too large, which may slow or fail to solve the computation. Therefore, to meet the real-time scheduling requirements, it is necessary to develop a fast and reliable optimization method that minimizes the amount of control involved in the solution each time.

The main contributions of this work are as follows:

1. In the optimization objective of the distribution network, the regulating capacity based on the gas units in the main network is taken into account to minimize the fluctuations in the interaction power of the main distribution network during a dispatch cycle while ensuring that the total exchanged power is minimal.
2. A distributed PV maximum consumption model is proposed for the distribution network by taking into account multiple adjustable resources such as reactive power compensation equipment, ESSs, and CLs, and the impact of the limited regulation capacity of the main network on maximum PV consumption is analyzed.
3. The limitations imposed by the creep rates of the gas units in the main network are considered in the constraints, and a fast solution method is designed for active optimization of the distribution network; here, the priority control order of the adjustable units is formulated on the basis of economy, and a stepwise solution process is designed to optimize the distribution network, which reduces the number of variables participating in the optimization at each step while improving the speed of the optimization solution.

2 Model assumptions

2.1 Basic assumptions

1. It is assumed that the transmission line parameters of the distribution network remain constant during operation.
2. At each moment in time, the load demand at each node is either known or predictable.

2.2 Assumptions for the regulatory capacity of the main network

1. We assume that the power supplied by the main grid to the distribution network is determined only by the outputs of the gas units in the main grid, and the influences of the power injected into the main grid from the external network and power delivered to other distribution networks are not taken into consideration.
2. The maximum and minimum outputs of the gas units are known and remain unchanged during a dispatch cycle.
3. The rate of change (creep rate) of the output of a gas unit is known and remains constant during a dispatch cycle while not exceeding the specified range.

2.3 Assumptions for the adjustable units of the distribution network

1. We assume that the distributed PV power generation can be predicted accurately and that the predicted value is certain during a dispatch cycle based on ignoring the effects of volatility due to changes in the solar radiation intensity and temperature factors as well as disregarding the effects of sudden weather changes (e.g., cloudy and rainy) on the PV outputs.
2. The PV inverter can be controlled to reduce the PV output and may also be withdrawn from operation if necessary so that the minimum PV output can be reduced to 0.
3. We assume that the customer loads respond positively and instantly to the load regulation commands while ignoring the influences of factors such as customer behaviors and satisfaction.
4. It is assumed that the energy storage devices can be charged and discharged many times in a single dispatch cycle while ignoring the limitations on the rates of change of charging and discharging.
5. The impacts of short-circuits, disconnections, equipment failure, and other unexpected accidents on the power grid are not considered.

3 Optimized scheduling model for the urban distribution network considering the regulation capacity of the main network

3.1 Objective function

In this work, the objective function was established with the optimization objectives of maximum consumption of the distributed PV power and minimum active fluctuations at the demarcation point of the main distribution network; furthermore, the objectives accounted for the minimum distribution network loss as well as

minimum total exchanged power of the main distribution network during a scheduling cycle, are shown in Equation 1–Equation 5:

$$F = min(\lambda_1 f_1 + \lambda_2 f_2 + \lambda_3 f_3 + \lambda_4 f_4), \tag{1}$$

where

$$f_1 = \sum_{i=1}^{n}\sum_{t=1}^{T} \frac{P^i_{PV,0}(t) - P^i_{PV}(t)}{P^i_{PV,0}(t)}, \tag{2}$$

$$f_2 = \sqrt{\frac{1}{T}\sum_{t=0}^{T}\left(P_l(t) - \overline{P_l}\right)^2}, \tag{3}$$

$$f_3 = \sum_{i=1}^{n}\sum_{j=1}^{n} I_{ij}^2 r_{ij}, \tag{4}$$

$$f_4 = \sum_{t=1}^{T} P_l(t). \tag{5}$$

In the above formulas, f_1 is the objective function of PV consumption capacity; $P^i_{PV}(t)$ and $P^i_{PV,0}(t)$ are the actual and planned active outputs of the i-th PV at moment t, respectively; f_2 is the objective function for the fluctuation of power exchanged with the main distribution network that is expressed by the standard deviation, in which $\overline{P_l}$ is the average exchange power in a scheduling cycle given by $\overline{P_l} = \frac{1}{T}\sum_{t=0}^{T} P_l(t)$; f_3 is the distribution network loss; I_{ij} is the current in branch ij; r_{ij} is the equivalent resistance of branch ij; f_4 is the total power exchanged during interaction with the main distribution network during a scheduling cycle, in which $P_l(t)$ is the active power exchanged at the division point of the main distribution network at moment t and its expression is shown in Equation 6

$$P_l(t) = \sum_{i=1}^{n}\begin{pmatrix} P^i_{load}(t) - P^i_{tl,out}(t) + P^i_{tl,in}(t) \\ -P^i_{ESS,d}(t) + P^i_{ESS,c}(t) - P^i_{PV}(t) \end{pmatrix} - P_{lost}(t). \tag{6}$$

Here, $P^i_{load}(t)$ is the load of node i in the distribution network at time t; $P^i_{tl,out}(t)$ and $P^i_{tl,in}(t)$ are the controllable load transfer out of and into node i in the distribution network at time t; $P^i_{ESS,c}(t)$ and $P^i_{ESS,d}(t)$ are the respective charging and discharging powers of the ESS i in the distribution network at time t; $P_{lost}(t)$ is the total loss of the distribution network at time t.

3.2 Main network regulation capacity constraints

3.2.1 Range of power changes at the main distribution cutoff point

Under the condition of transmitting a certain active power at the demarcation point of the main distribution network, there are corresponding active and reactive power regulation ranges that indicate the power supply capacity of the main network to the distribution network. The expressions are shown in Equation 7 and Equation 8, respectively.

$$P_{l,min} \le P_l(t) \le P_{l,max}. \tag{7}$$

$$Q_{l,min} \le Q_l(t) \le Q_{l,max}. \tag{8}$$

Here, $Q_{l,min}$ and $Q_{l,max}$ are the extreme values of the reactive power range transmitted by the main distribution network and are determined according to the active power and power factor values of the gas units in the main network. $P_{l,min}$ and $P_{l,max}$ are the extreme values of the active power range transmitted by the main distribution network, which are determined by the power supply capacities of the gas units in the main network and given as Equation 9, Equation 10:

$$P_{l,min} = \sum_{i=1}^{N} P^i_{GT,min}, \tag{9}$$

$$P_{l,max} = \sum_{i=1}^{N} P^i_{GT,max}, \tag{10}$$

where N is the number of nodes in the main network; $P^i_{GT,min}$ and $P^i_{GT,max}$ are the respective upper and lower limits of the output of the gas-fired unit i in the main network.

3.2.2 Creep power constraint at the main distribution cutoff point

Since the regulation capacity of the main network is determined by its gas units, the creep power constraints of the gas units in the main network limit the power exchanged at the demarcation point from varying over a wide range per unit of time. The creep power constraint of the transmission power at the demarcation point of the main distribution network is given as Equation 11

$$|P_l(t+1) - P_l(t)| \le P_{ramp,max}, \tag{11}$$

where $P_{ramp,max}$ are the maximum values of the creep powers of the gas units in the main network.

3.3 Adjustable unit operation constraints of the distribution network

The adjustable units in the distribution network include the distributed PVs, CLs, ESSs, on-load tap changers (OLTCs), static var compensators (SVCs), and capacitor banks (CBs) that have their own constraints

3.3.1 Power regulation range of the distributed PV

The active regulation of PV power is embodied by self-curtailment of the active outputs, which can be expressed with the range of curtailment as Equation 12.

$$0 \le P^i_{PV}(t) \le P^i_{PV,0}(t). \tag{12}$$

3.3.2 Active range of the CL

The load that can be shifted at time t cannot exceed 20% of the total load at that moment. As shown in Equation 13, Equation 14

$$0 \le P_{tl,in}(t) \le 0.2P_{load}(t). \tag{13}$$

$$0 \le P_{tl,out}(t) \le 0.2P_{load}(t). \tag{14}$$

The CLs dispatched in a cycle should therefore be managed such that the total load transfers in and out are equal as shown in Equation 15:

$$\sum_{t=1}^{T} P_{tl,out}(t) = \sum_{t=1}^{T} P_{tl,in}(t). \tag{15}$$

3.3.3 Operational constraints of the OLTC

The main voltage constraint is given by Equation 16

$$U_j(t) = \frac{U_i(t).}{k(t)} \tag{16}$$

where $U_i(t)$ and $U_j(t)$ are the primary and secondary voltages of the OLTC at time t, respectively; $k(t)$ indicates the ratio of these voltages at time t.

The variable ratio constraints are given by Equation 17–Equation 19

$$k(t) = k_{min} + \Delta k \cdot r(t). \tag{17}$$

$$|r(t+1) - r(t)| \le \Delta r_{max}. \tag{18}$$

$$\sum_{t=0}^{T} |r(t+1) - r(t)| \le r_{max}. \tag{19}$$

where k_{min} is the minimum ratio of primary to secondary voltages of the OLTC, Δk is the step size of the ratio, $r(t)$ is the stall of the OLTC at time t, Δr_{max} is the maximum range of each stall change, and r_{max} is the maximum number of stall adjustments in a scheduling cycle.

3.3.4 Capacity constraints of the ESS

The charge/discharge state constraint is given by Equation 20

$$\chi_d^i(t) + \chi_c^i(t) \le 1, \tag{20}$$

where $\chi_d^i(t)$ and $\chi_c^i(t)$ are the charge and discharge states of the ESS i at time t, respectively.

The upper and lower bound constraints of the charging and discharging power are given by Equation 21, Equation 22

$$0 \le P_{ESS,d}^i(t) \le \chi_d^i(t) P_{ESS,dmax}^i, \tag{21}$$

$$0 \le P_{ESS,c}^i(t) \le \chi_c^i(t) P_{ESS,cmax}^i, \tag{22}$$

where $P_{ESS,dmax}^i$ and $P_{ESS,cmax}^i$ are the maximum charging and discharging powers of the ESS i, respectively.

The energy storage capacity constraints are given by Equation 23, Equation 24

$$E_{ESS}^i(t+1) = E_{ESS}^i(t) + \eta_c P_{ESS,c}^i(t) - \eta_d P_{ESS,d}^i(t), \tag{23}$$

$$E_{ESS,min}^i(t) \le E_{ESS}^i(t) \le E_{ESS,max}^i(t), \tag{24}$$

where the energy storage capacity is dynamically balanced over a dispatch cycle as shown in Equation 25.

$$E_{ESS}^i(0) = E_{ESS}^i(T). \tag{25}$$

Here, η_c and η_d are the charging and discharging efficiency coefficients of the ESS, and $E_{ESS}^i(t)$ is the amount of electricity stored in the ESS i at time t; $E_{ESS,min}^i(t)$ and $E_{ESS,max}^i(t)$ are the minimum and maximum values of the power in the ESS i at time t, respectively.

3.3.5 Operational constraint of the SVC

The SVC reactive output constraint is shown in Equation 26

$$Q_{svc,min}^i \le Q_{svc}^i(t) \le Q_{svc,max}^i, \tag{26}$$

where $Q_{svc}^i(t)$ denotes the reactive power output of the static reactive power compensator i at time t, and $Q_{svc,min}^i$ and $Q_{svc,max}^i$ denote the respective upper and lower limits of the reactive power output of the static reactive power compensator i.

3.3.6 Operational constraints of the CB

The CB reactive output constraint is shown in Equation 27

$$Q_{cb}^i(t) = N_{cb}^i(t) Q_{cb,step}, \tag{27}$$

where $Q_{cb}^i(t)$ is the reactive power output of the casting capacitor i at time t, $N_{cb}^i(t)$ is the number of groups of casting capacitors i operating at time t, and $Q_{cb,step}$ is the reactive power capacity of a group of casting capacitors.

The constraint on the change in the number of cast–cut groups at adjacent time periods is given by Equation 28.

$$N_{cb}^i(t+1) - N_{cb}^i(t) \le \Delta N_{cb,max}. \tag{28}$$

The throw–cut CB constraint is given by Equation 29.

$$0 \le N_{cb}^i(t) \le N_{cb,max}. \tag{29}$$

where $\Delta N_{cb,max}$ is the maximum limit on the number of groups of capacitors to be switched each time, and $N_{cb,max}$ is the maximum number of capacitor groups that can be switched at each node.

3.4 Branch circuit tidal equation constraints

A second-order cone-relaxation-based branch current model can be used for the distribution network as follows Equation 30–Equation 32:

$$\begin{cases} \sum_{i \in u(j)} \left(P_{ij} - i_{ij} r_{ij}\right) - \sum_{k \in v(j)} P_{jk} = P_j \\ \sum_{i \in u(j)} \left(Q_{ij} - i_{ij} x_{ij}\right) - \sum_{k \in v(j)} Q_{jk} = Q_j \end{cases}. \tag{30}$$

$$v_i = v_j + 2\left(r_{ij} P_{ij} + x_{ij} Q_{ij}\right) - \left(r_{ij}^2 + x_{ij}^2\right) i_{ij}. \tag{31}$$

$$\left\| \begin{matrix} 2P_{ij} \\ 2Q_{ij} \\ i_{ij} - v_i \end{matrix} \right\| \le i_{ij} + v_i. \tag{32}$$

In these equations, v_i and i_{ij} denote the squares of the node voltage and branch current, respectively; P_{ij} denotes the active power flowing in branch ij; $u(j)$ denotes the set of branches with j as the tail node; $v(j)$ denotes the set of branches with j as the head node. P_j, Q_j denote the values of the active and reactive powers injected into node j, respectively, and are given by Equation 33, Equation 34

$$P_j = P_{PV} + P_{ESS,d} + P_l - P_{ESS,c} - P_{load} + P_{tl,out} - P_{tl,in}. \tag{33}$$

$$Q_j = Q_{SVC} + Q_{CB} + Q_l - Q_{load}. \tag{34}$$

3.5 System operational constraints

The system voltage constraints and branch current constraints are given in Equations 35–36.

$$\left|I_{ij}\right| \le I_{ij}^{max}, \tag{35}$$

$$0.95 U_N \le U_i \le 1.05 U_N, \tag{36}$$

where U_N is the rated voltage of the distribution network, and I_{ij}^{max} is the maximum value of the branch current.

4 Solution for the active optimal scheduling model

4.1 Design considerations

The active optimization dispatch method of the distribution network with distributed PVs must achieve maximum consumption of the distributed PV power under the limited regulation capacity of the main network by integrating all kinds of adjustable equipment in the distribution network; simultaneously, the auxiliary OLTCs and reactive power compensation equipment must maintain the voltage stability, minimize the network loss, and enhance the economy of system operation. Under the premise of main power balance, the limited regulating capacity of the main network mainly includes the following considerations:

(1) The main network ideally supplies the least total power to the distribution network during a dispatch cycle.
(2) There must be minimal fluctuations in the power supply from the main network to the distribution network during a dispatch cycle.
(3) The main network supplying power to the distribution network must have minimal variation between adjacent time periods.

The distribution grid system studied herein is powered only by large-scale distributed PVs and needs to be configured with large-capacity distributed ESSs combined with PVs; this can smooth the fluctuations in PV power generation while improving the self-usage rate of the distribution grid and economic benefits. Through the ESSs, users can store excess PV power during low electricity demand and use this stored power during peak electricity demand. This reduces the dependence on grid power, avoids the phenomenon of abandoned daylight, and improves the self-use rate of PV power. The ESSs can also respond to grid demand in milliseconds, and this rapid response capability allows them to quickly respond to fluctuations in grid loads to provide immediate power support while also providing the grid with certain degrees of frequency regulation and voltage support capabilities.

Although direct optimization of CL regulation helps maintain balance between power supply and demand in the grid, it must be achieved through price signal or incentive mechanisms to guide the user to adjust to electricity behaviors; hence, the user must be involved in the regulation of user needs to achieve high economic compensation, which increases the operating cost of the power system compared to that of the ESS as the scheduling cost is high. Concurrently, the response speed is significantly lower than that of the ESS, and it may be difficult to meet the needs of a power grid system that requires high real-time regulation capabilities. In terms of the regulation order of adjustable units, ESSs have higher priority than the CLs.

The present study is dedicated to maximizing the consumption of distributed PV power to achieve the goals of sustainable development while meeting the regulation capacity limitation of the main grid. Optimal scheduling of the power system through curtailing distributed PV not only wastes renewable energy but also negatively affects sustainable development goals. Maximizing the use of PV power could help reduce carbon emissions and environmental pollution, mitigate climate changes, reduce energy costs, reduce dependence on imported fossil fuels, and enhance energy independence and security while helping accelerate the construction of smart grids, establish a sound power market mechanism, and improve the new power system.

In summary, when the interacting power at the demarcation point of the main distribution network exceeds the range of its regulation capacity, the outputs of the adjustable units in the distribution network are regulated in the following order of priority:

1. Increasing the charging and discharging powers of the ESSs;
2. Shifting the CLs;
3. Reducing the distributed PV power.

The principle of regulation is based on minimizing the active fluctuations in the main distribution network with minimal transfer of CLs and minimal PV curtailment.

4.2 Solution strategy for the active optimal scheduling model

From the planned outputs of the distributed PVs and predicted outputs of the loads in a complete dispatch cycle (24 h) without consideration of other adjustable devices in the distribution network, the initial interactive power at the demarcation point of the main distribution network is calculated using the forward backgeneration trend to obtain the voltage overruns at each node, and the specifics of the forward power flow are shown in Figure 1.

The power of the root-node-connected branch circuit obtained from this trend calculation is the power exchanged at the demarcation point of the main distribution network, and the subsequent optimization is based on this power. The flowchart showing specific regulation of the active optimization scheduling method of the distribution network with distributed PVs considering the regulation capacity of the main network is shown in Figure 2.

5 Example analysis

In this section, we demonstrate improvement of the basic IEEE 33 node power network by adding some active and reactive power regulation devices as well as conducting arithmetic simulations on this test system to verify the effects of the active optimal scheduling method of the distribution network with distributed PVs limited by the main grid regulation capacity. The optimization algorithm implementation is achieved using MATLAB software and the YALMIP toolbox along with the Cplex12.10 solver.

5.1 Calculation setup

The system diagram of the 33-node distribution network modified based on the setup scheme in this work is presented in Figure 3. The base capacity of the system is 1 MVA, base voltage level

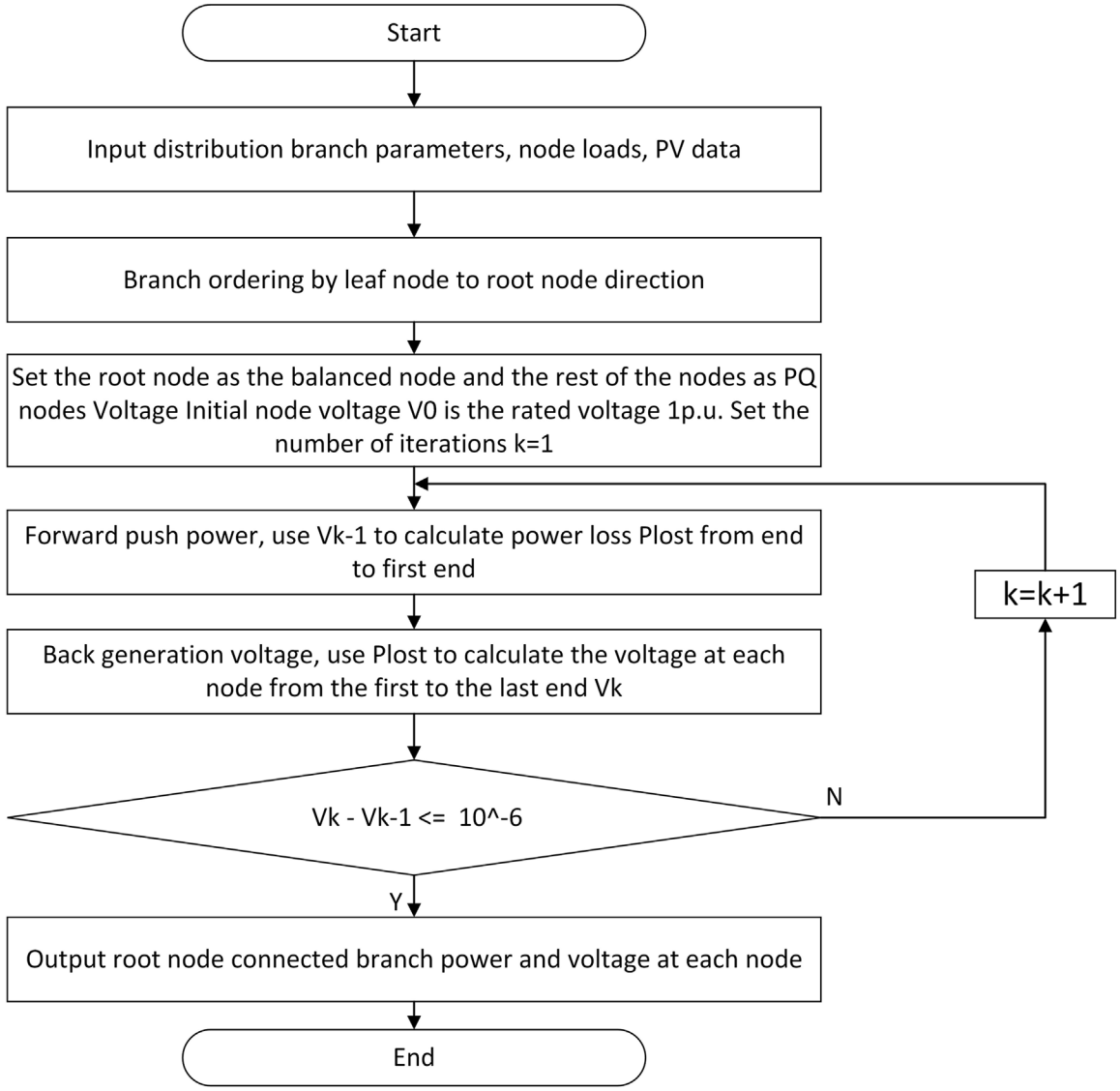

FIGURE 1
Flowchart of the power flow calculation.

is 12.66 kV, total active load capacity of the system is 3,715 kW, total reactive load capacity is 2,300 kVar, and voltage per-unit value at the balancing node (i.e., node 33) is 1 p.u. As shown in Figure 3, reactive power compensation devices such as the OLTCs, PV generator, ESSs, and CBs are added on the basis of the network structure of the basic IEEE 33 node distribution system, and the specific configurations are shown in Table 1.

Under actual conditions, the area encompassed by the distribution network system is often not very large; however, to facilitate analysis of the results, the system access between the PVs as well as between the power characteristics of the loads are set to be only slightly different so as to be considered the same output characteristics, based on the same predicted power curve that would be analyzed. The typical load demand and PV active power curves during summer are normalized to obtain the all-day predicted power curves for the total system load and total distributed PV output, as shown in Figure 4.

5.2 Analysis of simulation results

To reflect the influence of the main grid regulation capacity on the output of each equipment in the distribution network and maximum consumption of PV power, the weighting coefficients in Equation 1 are set to $\lambda_1 = 0.4$, $\lambda_2 = 0.4$, $\lambda_3 = 0.1$, and $\lambda_4 = 0.1$. In this work, the following three scenarios are considered during the simulations to validate the active optimization scheduling method of the distribution network with distributed PVs that takes into consideration the regulation capacity of the main grid.

Scenario 1: No controls are considered.

Scenario 2: The controls used include PV curtailment, ESSs, SVCs, and CBs.

Scenario 3: Based on Scenario 2, optimization calculations are carried out with the objective of minimizing the active fluctuations between the main distribution network by considering the creep power constraints of the gas units in the main network and CLs.

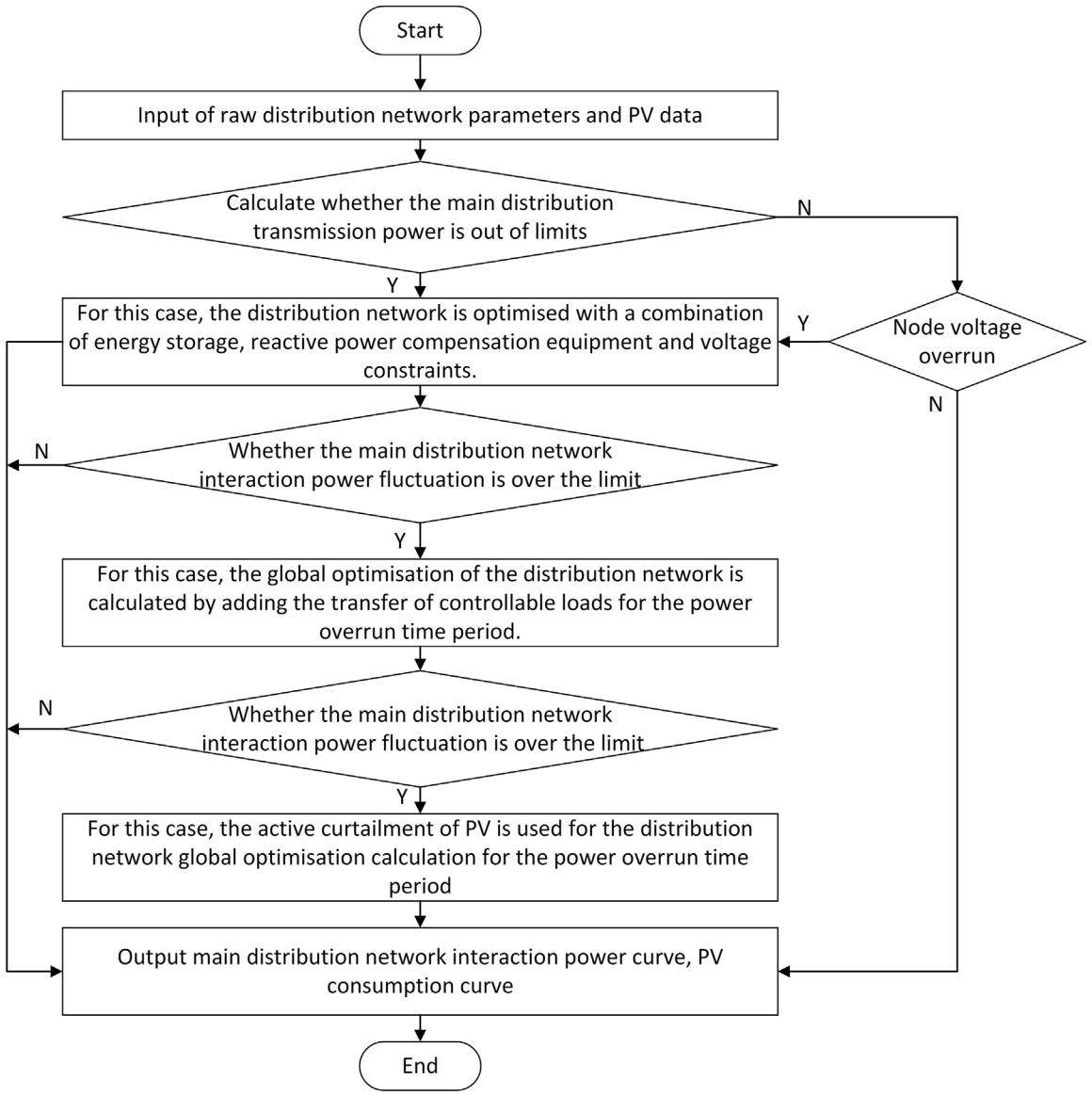

FIGURE 2
Flowchart for the optimisation strategy.

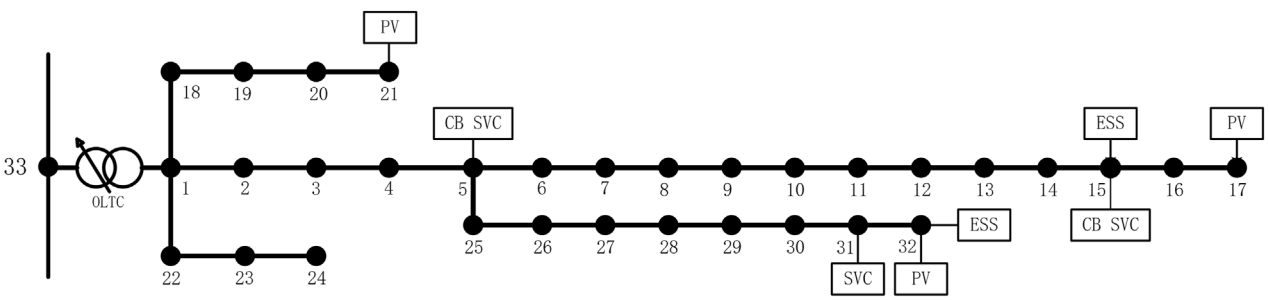

FIGURE 3
Arithmetic grid map of the modified IEEE 33 node distribution system.

TABLE 1 Parameters of the adjustable units.

Adjustable unit	Specific parameters		
On-load tap changers (OLTCs)	Voltage regulation range	0.95–1.05 p.u.	
	Number of adjustable gears	10	
	Adjustment step	0.01 p.u.	
	Limit on number of gears per adjustment	1	
	Limit on number of daily adjustments	5	
Photovoltaics (PVs)	Adjustment range of the output	Zero to planned contribution	
Capacitor banks (CB1/CB2/CB3)	Adjustable capacity	500 kVar	
	Adjustment step	100 kVar	
Static var compensators (SVC1/SVC2/SVC3)	Adjustable range	−100 to 300 kVar	
Energy storage systems		ESS1	ESS2
	Maximum rated power	1800 kWh	1000 kWh
	Minimum rated power	180 kWh	100 kWh
	Charge and discharge power limits	± 300 kW	± 200 kW
	Charging efficiency	90%	90%
	Discharge loss efficiency	111%	111%

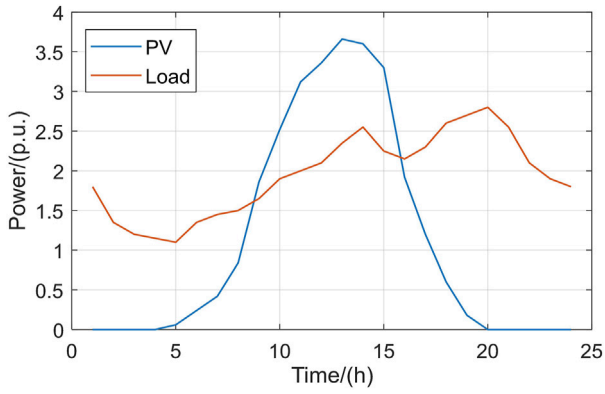

FIGURE 4
Photovoltaic (PV) and output load curves.

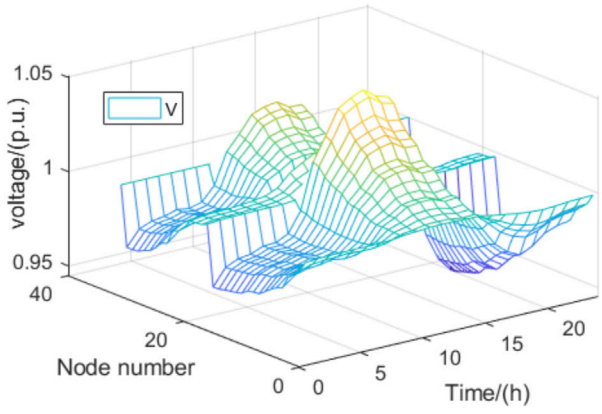

FIGURE 5
Node voltage diagrams over 24 h for scenario 1.

5.2.1 Analysis of simulation results for scenario 1

In the modified IEEE 33 node distribution system, nodes 17, 21, and 32 are selected to represent the single-point PV grid-connection points, and all distributed PVs are connected to the system with the planned output without controls to explore the impacts on system node voltage and power exchanged by the main distribution network; the simulation results are shown in Figures 5, 6. From Figure 5, it is seen that when the PVs are connected to the planned outputs, the voltages at some nodes during 11–15 h exceed 1.05 p.u., exhibiting voltage overruns.

From Figure 6, it is seen that the power delivered from the main grid to the distribution network decreases from 1,122 kW to 668 kW at 6–8 h due to continuous increases in the PV outputs; at 9–15 h, the distribution network is seen to deliver power to the main grid; at 13 h, the distribution network delivers a maximum power of 1,208 kW to the main grid; thus, the maximum power fluctuation at the demarcation point of the main distribution network is 2,330 kW. When the active demand in the distribution network decreases and results in backward power delivery to the main grid, there are decreases in the outputs of the main grid units or even shutdowns. In the time period of 16–20 h, the interaction power at the demarcation point of the main distribution network rises sharply from 254 kW at 16 h to 2,880 kW at 20 h due to continuous reduction of PV output and increase in user load, demonstrating a maximum fluctuation of 2,626 kW; when the active demand of the distribution network continues to increase, it will lead to increases in the outputs of the

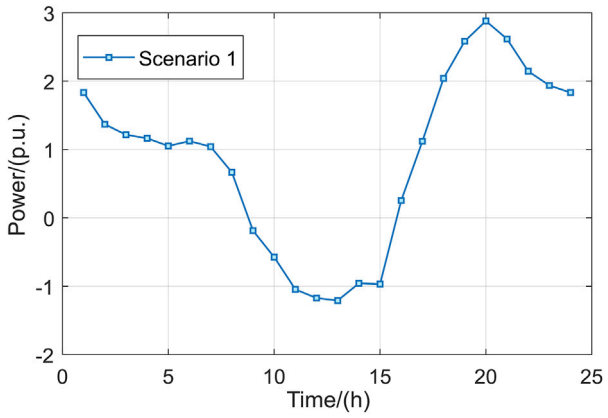

FIGURE 6
Interaction power at the cutoff point of the main distribution network under scenario 1.

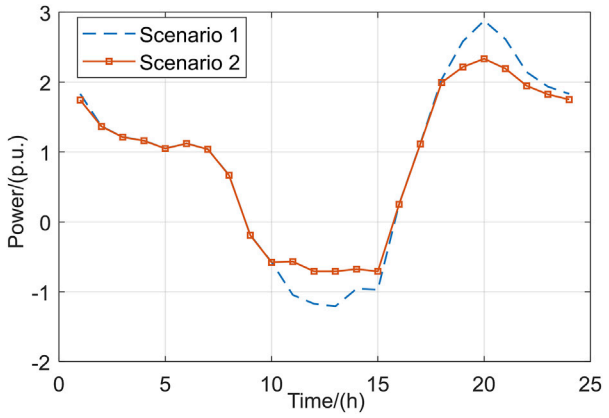

FIGURE 7
Interaction power at the cutoff point of the main distribution network under scenario 2.

main network units and perhaps even startup of the standby units.

During actual operation, the main network units cannot be started and stopped frequently; the transmission power change cycle in the main network is longer, so the sharp increase in active power demand from the distribution network cannot be met over a short duration. Thus, there may be an active power shortage between the main and distribution networks, which affects the frequency and voltage stabilities of the distribution network; this serious situation may result in short-term power outages for the user loads, so it is necessary to use the adjustable resources of the distribution network to reduce the power fluctuations between the main and distribution networks.

5.2.2 Analysis of simulation results for scenario 2

Based on scenario 1, given the minimum active fluctuation and maximum PV consumption at the demarcation point of the main distribution network as the main objectives as well as node voltages remaining within the limit as the constraint, the optimization of the interaction power at the demarcation point of the main distribution network is as shown in Figure 7, the active outputs of the ESSs are as shown in Figure 8, and the reactive outputs of the SVCs and CBs are as shown in Figure 9.

The distributed PV power in this scenario can still be consumed fully, and the reactive power compensation device appropriately consumes reactive power during 10–15 h to maintain voltage stability when the PV output is maximum, such that the ESS is charged with 1,080 kW of power; the backward transmission of power from the distribution network to the main network decreases by 2,230 kW during 9–15 g, and the stored energy decreases by 1,140 kW over 17–23 h when the load is higher and PV output is zero. This total of 1,140 kW is discharged, and the interactive power of the main distribution network decreases by 1,693 kW, such that the maximum power fluctuation over 16–20 h decreases from 2,626 kW in scenario 1 to 2,084 kW. Hence, the ESSs play positive roles in smoothing the power fluctuations between the main distribution network and reactive power compensation device to achieve maximum dissipation of the PV power and

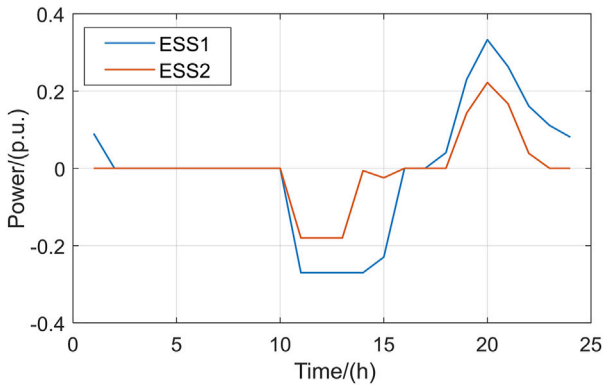

FIGURE 8
Energy storage charging and discharging powers under scenario 2.

maintain voltage stability. However, the interactive power of the main distribution network still fluctuates greatly and needs to be optimised further.

5.2.3 Analysis of simulation results for scenario 3

In scenario 2, the interactive power fluctuation in the main distribution network is large and the power change amplitude during the adjacent time period is drastic; therefore, the addition of CLs is considered to smooth the power fluctuation in the main distribution network, whose output changes are shown in Figure 10, active outputs of the ESSs are shown in Figure 11, and PV dissipations are shown in Figure 12.

To suppress the sharp increase in main grid supply power caused by reduction of the PV outputs, it is necessary to guide the user loads so as to reduce power consumption during the peak period of 17–23 h; at the same time, to achieve maximum consumption of PV power, it is necessary to guide the user loads to increase their power consumption as much as possible during 9–16 h. It is seen from Figure 10 that the user loads lower power

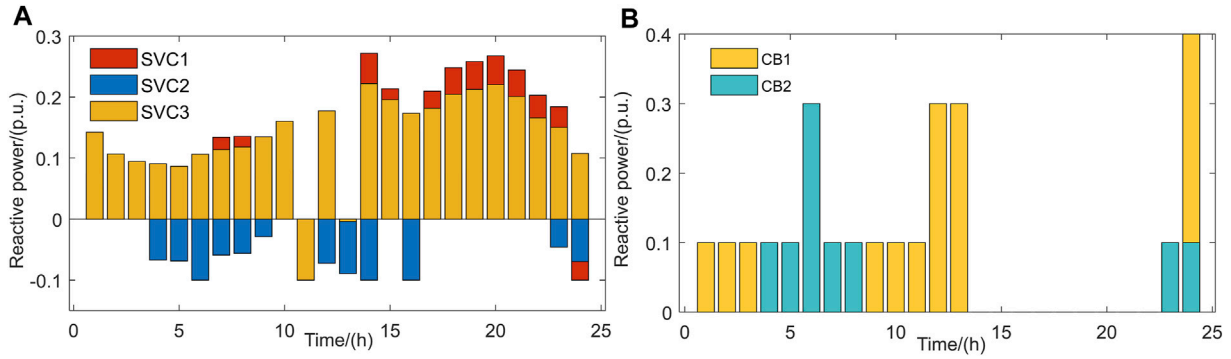

FIGURE 9
Reactive outputs of the **(A)** static var compensators (SVCs) and **(B)** capacitor banks (CBs) under scenario 2.

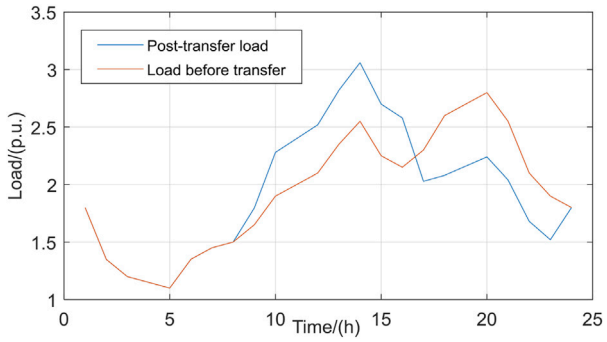

FIGURE 10
Shifting load power under scenario 3.

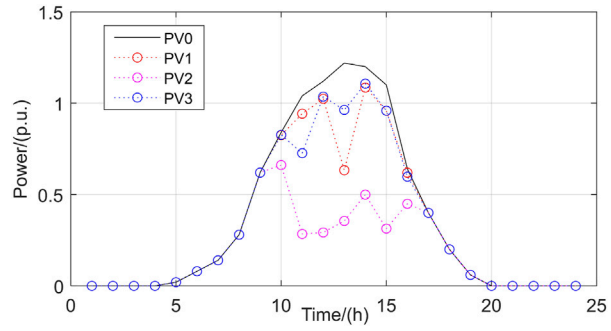

FIGURE 12
PV output for scenario 3.

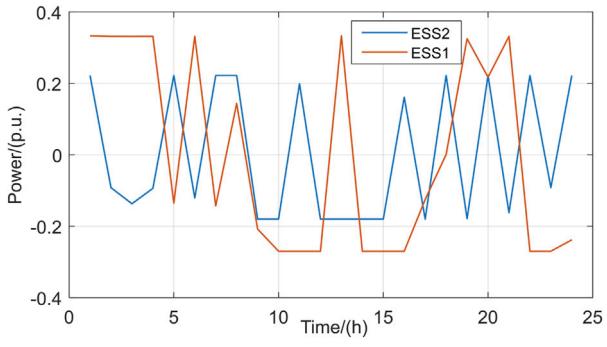

FIGURE 11
Energy storage charging and discharging powers under scenario 3.

consumption by 3,201 kW over 17–23 h and increase power consumption by 3,201 kW during 9–16 h. These kinds of transferable loads in the distribution network are mainly composed of production-type and service-type users who demonstrate great flexibility in electricity consumption, strong peak-shifting ability, and large calling potential to weaken the negative impacts of PV power fluctuations.

Owing to the relatively small capacities of ESSs in the distribution network, the numbers of charging and discharging times of the ESSs in a cycle increase significantly under scenario 3. In practical applications, ESSs generally have one-charging and one-discharging or two-charging and two-discharging strategies in accordance with the dispatch instructions as frequent charging and discharging can exacerbate their lifespans due to wear and tear, thereby reducing the economy of system operation. Therefore, failure to consider the constraints regarding the number of charge/discharge times of the ESSs is an area for improvement in this study.

In contrast to scenarios 1 and 2 where distributed PVs are able to operate at the planned outputs, the actual total PV output in scenario 3 is 20,559 kW, which is a reduction of 6,330 kW. Although the adjustable resources are used maximally, they still inevitably cut a part of the distributed PV output, which is mainly attributable to the limited regulation capacity constraint of the main grid resulting from actual grid operation; the gas units in the main grid can further reduce the output until shutdown to consume the distributed PV outputs in the present distribution network or to deliver a part of this residual energy to another distribution network

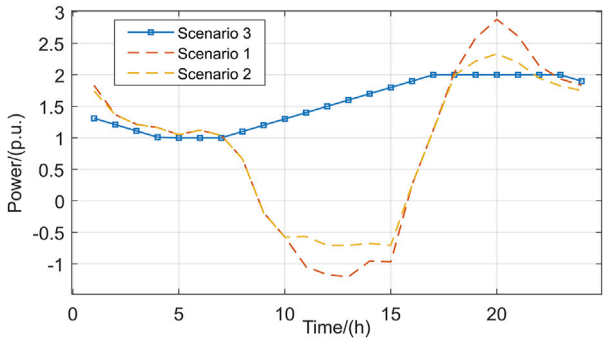

FIGURE 13
Interaction power at the main distribution cutoff point for scenario 3.

to achieve the required PV power consumption. Therefore, subsequent studies can examine methods to further reduce the distributed PV outputs in the distribution network through coordination of network clusters.

The simulation of the power change at the cutoff point of the main distribution network is shown in Figure 13. From Figure 13, it is seen that the maximum interaction power of the main distribution network in scenario 3 is 2,000 kW while the minimum is 1,010 kW, for a maximum fluctuation of 990 kW of the main grid supply power. Meanwhile, the power curve is relatively flat, and the maximum power change in the adjacent time period is 100 kW, which are in line with the creep power limitations of the gas-fired units of the main grid during actual operation.

The power statistics at the demarcation point of the main distribution network under the three scenarios are shown in Table 2. As seen from Table 2, the fluctuation range of the interaction power of the main distribution network in scenario 3 is lower by 3,062 kW and 2,051 kW compared to those in scenarios 1 and 2, respectively, and the power fluctuation decreases significantly. At the same time, the maximum power fluctuation in the adjacent time period decreases by 1,123 kW and 857 kW compared to those in scenarios 1 and 2, respectively. The simulation results of scenario 3 reflect the limited regulation capacity of the main network; however, during actual operation, these results meet the requirement that the change in power supplied by the main network to the distribution network cannot be too fast. The simulation results of scenario 3 reflect the effectiveness of the active optimal scheduling method proposed for the distribution network.

6 Conclusion and prospects

At present, most of the studies on optimal dispatch of distribution networks containing high proportions of distributed PVs are based on the optimization of voltage stability and optimal economy as the objectives given a single means of regulation; at the same time, the impact of the limited regulating capacity of the gas units of the main grid on the optimal dispatch of distribution networks is neglected, especially with regard to maximum consumption of PV power. Hence, the following methods are proposed herein to address this issue:

1. We establish a model for maximum consumption of the distributed PV power in the distribution network by taking into account the reactive power compensation equipment, energy storage systems, controllable loads, and other adjustable resources and design an optimal distribution solution for the distribution network; this reduces the number of variables participating in the optimization at each step and accelerates the speed of optimization.
2. The proposed distribution network optimization scheduling method fully takes into account the limited regulation capacity of the main network to ensure that the distribution network purchases the least amount of power from the main network; further, the fluctuation amplitude and creep rate of the interacting power between the main and distribution networks are minimized to meet the actual operation of the gas-fired units of the main network. This helps in the analysis of the impact of the limited regulation capacity of the main network on maximum PV power consumption.

Although more types of regulation are considered in the proposed model, their scheduling costs are not analyzed, especially with regard to the compensation cost of the controllable loads, installation cost, and charge/discharge losses of the energy storage devices. During actual operation, frequent scheduling of user loads lowers user satisfaction and high-frequency redischarging of the energy storage devices reduces their service lives; hence, future studies could focus on balancing the interests of both supply and demand as well as improving the comprehensive economy of distribution network operation.

Given the accelerated pace of construction of new power systems, the connections between the distribution networks are increasingly becoming close. Thus, future research efforts can consider balancing and dispatching the surplus local PV outputs through other distribution networks, thereby reducing the burden of

TABLE 2 Comparison of interaction power at the cutoff point of the main distribution network before and after optimization.

Power scenarios	Minimum value (kW)	Maximum value (kW)	Maximum swing (kW)	Maximum power change in the adjacent time period (kW)
Scenario 1	−1,172	2,880	4,052	1,223
Scenario 2	−707	2,334	3,041	957
Scenario 3	1,010	2,000	990	100

regulation of the main grid; moreover, new types of distribution networks can be constructed to handle higher proportions of distributed PV power.

Data availability statement

The original contributions presented in the study are included in the article/supplementary material, and any further inquiries may be directed to the corresponding author.

Author contributions

CG: conceptualization, resources, supervision, and writing–review and editing. WW: conceptualization, resources, and writing–review and editing. WZ: methodology, validation, and writing–original draft. ND: resources and writing–review and editing. XL: methodology and writing–review and editing. YD: methodology and writing–review and editing. DZ: conceptualization, methodology, resources, supervision, validation, and writing–review and editing.

Funding

The authors declare that no financial support was received for the research, authorship, and/or publication of this article.

Conflict of interest

Authors CG, WW, and ND were employed by State Grid Beijing Electric Power Company.

The remaining authors declare that the research was conducted in the absence of any commercial or financial relationships that could be construed as potential conflicts of interest.

Publisher's note

References

Cai, Y. X., Zhang, L., Tang, W., Xu, O. Y., Wang, J. L., and Song, Q. P. (2017). A voltage control strategy for LV distribution network with high proportion residential PVs considering reactive power adequacy of PV inverters. *Power Syst. Technol.* 41 (9), 2799–2808. doi:10.13335/j.1000-3673.pst.2017.0133

Chen, Z. Y., Wang, H., Wang, B. Y., Yang, L., Song, C., Zhang, X., et al. (2024). Scheduling optimization of electric ready mixed concrete vehicles using an improved model-based reinforcement learning. *Automation Constr.* 160, 105308. doi:10.1016/j.autcon.2024.105308

Deng, X. Y. (2019) Research on optimal dispatching of active distribution network considering "source-load-storage" collaborative interaction. Dissertation/Master's Thesis. Beijing: North China Electric Power University.

Ding, T., Li, C., Yang, Y. H., Jiang, F. J., Bie, Z. H., and Blaabjerg, F. (2017). A two-stage robust optimization for centralized-optimal dispatch of photovoltaic inverters in active distribution networks. *IEEE Trans. Sustain. Energy* 8 (2), 744–754. doi:10.1109/TSTE.2016.2605926

Dvorkin, Y., Pandžić, H., Ortega-Vazquez, M. A., and Kirschen, D. S. (2015). A hybrid stochastic/interval approach to transmission-constrained unit commitment. *IEEE Trans. Power Syst.* 30 (2), 621–631. doi:10.1109/PESGM.2015.7285684

Ge, H. (2023). Impact of high proportion distributed photovoltaic integration into the grid network. *Electron. Technol.* 52 (3), 290–291.

Hu, Z. D., Liu, Y., and Zhong, L. (2008). Analysis of generator synchronization systematic test and synchronization process. *Hunan Electr. Power* 28 (6), 13–15.

Huang, Y. F., Liu, S. Y., Pang, S. L., and Gao, C. L. (2020). Calculation of ultimate capacity of network on acceptance of distribution PV system based on adaptive weight PSO algorithm. *Guangdong Electr. Power* 33 (4), 34–40.

Jiang, T., Fang, B. W., Chen, Y. P., Zhang, Y., Yang, L., Wang, K., et al. (2019). Coordinative optimal operation method of transmission and distribution networks based on multi-parametric programming. *South. Power Syst. Technol.* 17 (9), 10–19. doi:10.13648/j.cnki.issn1674-0629.2023.09.002

Li, D. X., Wang, J. R., and Zhang, J. J. (2021). Analysis of energy storage output characteristics based on photovoltaic volatility. *Power Syst. Clean Energy* 37 (2), 99–107.

Li, W. B. (2013) Studies on theory of power flow and optimization in power transmission-distribution grid. Dissertation/Master's Thesis. Shandong: Shandong University.

Li, Z., Guo, Q., Sun, H., and Wang, J. (2016). Coordinated transmission and distribution AC optimal power flow. *IEEE Trans. Smart Grid* 9 (2), 1228–1240. doi:10.1109/TSG.2016.2582221

Li, Z. K., Bao, X. Y., Shao, Y. Y., Peng, P., and Wang, W. J. (2018). Studying accommodation ability of distributed photovoltaic considering various voltage regulation measures. *Power Syst. Prot. Control* 46 (8), 10–16.

Lin, Y. C., Li, J. P., Meng, A. B., Wang, L., and Ding, L. J. (2017). Multi-area dynamic economic dispatching based on improved differential evolution with crisscrossed optimization algorithm. *Guangdong Electr. Power* 30 (5), 69–76.

Lu, Z. G., Chen, W. K., Zhang, X. H., Zhang, D., and Ma, L. Y. (2015). Global maximum power supply capability analysis of city power grid. *Power Syst. Technol.* 39 (6), 1623–1630. doi:10.13335/j.1000-3673.pst.2015.06.025

Pan, Q. (2015) Study on units scheduling optimization problem for power system considering energy saving and emission reduction. Dissertation/Master's Thesis. Shanghai: Shanghai Jiao Tong University.

Pandžić, H., Dvorkin, Y., Wang, Y. S., Qiu, T., and Kirschen, D. S. (2016). Toward cost-efficient and reliable unit commitment under uncertainty. *IEEE Trans. Power Syst.* 31 (2), 970–982. doi:10.1109/TPWRS.2015.2434848

Ruan, H. B., Gao, H. J., Liu, Y. B., Wang, L. F., and Liu, J. Y. (2020). Distributed voltage control in active distribution network considering renewable energy: a novel network partitioning method. *IEEE Trans. Power Syst.* 35 (6), 4220–4231. doi:10.1109/TPWRS.2020.3000984

Wang, Y. F., Li, Y. Z., Ye, H. B., Ling, X. B., and Lu, C. (2023). Dynamic voltage control of distribution network considering coordinated optimization of active power. *Electr. Power Autom. Equip.* 43 (2), 60–66. doi:10.16081/j.epae.202208034

Wu, M., Xu, B., Ji, Y., Song, Z. H., Sun, L. J., Ma, J., et al. (2019). Transmission-distribution-network-coordinated calculation method of maximum integration capacity of distributed generations. *Power Syst. Technol.* 43 (11), 3883–3890. doi:10.13335/j.1000-3673.pst.2019.1197

Xu, Z. C., Zhao, B., Ding, M., Zhou, J. H., and Wei, L. K. (2016). Photovoltaic hosting capacity evaluation of distribution networks and inverter parameters optimization based on node voltage sensitivity. *Proc. CSEE* 36 (6), 1578–1587. doi:10.13334/j.0258-8013.pcsee.2016.06.013

Zhang, S. H. (2021) Research on the ability of high permeability photovoltaic grid connection. Dissertation/Master's Thesis. Beijing: North China Electric Power University.

Zhang, X., and Wang, H. T. (2019). Optimal dispatch method of transmission and distribution coordination for power systems with high proportion of renewable energy. *Automation Electr. Power Syst.* 43 (3), 67–75. 115.

Zhang, Z. W., Zhao, J. Q., Zhang, X. H., Han, J. B., Lin, C. N., and Wei, W. H. (2017). Collaborative optimization control of the transmission and distribution networks considering a large number of DGs connected. *Power Syst. Clean Energy* 33 (7), 110–115. 122.

frontiers | Frontiers in Energy Research

TYPE Original Research
PUBLISHED 29 August 2024
DOI 10.3389/fenrg.2024.1428303

OPEN ACCESS

EDITED BY
Yingjun Wu,
Hohai University, China

REVIEWED BY
Jiawei Wang,
Technical University of Denmark, Denmark
Zhengmao Li,
Aalto University, Finland
Dan Wang,
Tianjin University, China

*CORRESPONDENCE
Dongxu Zhou,
zdx2001@163.com

RECEIVED 06 May 2024
ACCEPTED 16 August 2024
PUBLISHED 29 August 2024

CITATION
Zhou D, Xu J, Zhang C, Wei P, Pan G and Gu Z (2024) A multi-agent optimal operation methodology of electric, thermal, and hydrogen integrated energy system based on ADMM algorithm.
Front. Energy Res. 12:1428303.
doi: 10.3389/fenrg.2024.1428303

A multi-agent optimal operation methodology of electric, thermal, and hydrogen integrated energy system based on ADMM algorithm

Dongxu Zhou[1]*, Jingzhou Xu[1], Can Zhang[1], Pengchao Wei[1], Guangsheng Pan[2] and Zhongfan Gu[2]

[1]State Grid Nanjing Power Supply Company, Information and Communication Branch, Nanjing, China, [2]School of Electrical Engineering, Southeast University, Nanjing, China

This article presents a study on the distributed optimization operation method for micro-energy grid clusters within an electric, thermal, and hydrogen integrated energy system. The research focuses on precisely modeling the Power-to-Hydrogen (P2H) conversion process in electrolytic cells by considering their startup characteristics. An optimization operation model is established, with each micro-energy grid as the principal entity, to cater to their individual interests and demands. The Alternating Direction Method of Multipliers (ADMM) algorithm is adopted for distributed solution. Case studies demonstrate that the connection topology between micro-energy grids significantly impacts the total operating cost, and the effectiveness of the ADMM algorithm is validated through a comparison with centralized optimization approaches.

KEYWORDS

power-to-hydrogen, integrated energy system, multi-agent optimal operation, alternating direction method of multipliers, electrolytic hydrogen

1 Introduction

By 2050, the projected increment in CO_2 emissions could span from 2.21 to 7.43 megatons, underscoring the urgency for decisive action. Amidst this backdrop, numerous nations worldwide have set forth ambitious carbon reduction targets, signaling a global commitment to mitigate climate change (Jiang et al., 2024). The Integrated Energy System (IES), a holistic approach that integrates power-to-heat conversion technologies and seamlessly intertwines heat and power generation, has emerged as a cornerstone in the pursuit of carbon emission reduction. This system, bolstered by its unique technological prowess, offers a pivotal pathway towards a greener future (Zhang et al., 2024).

The strategic deployment of complementary technologies within the IES framework further enhances renewable energy utilization, thereby mitigating adverse climate impacts (Pan et al., 2021). Among these, Power-to-Hydrogen (P2H) technology stands out as a highly efficient energy conversion mechanism, transforming electrical energy into hydrogen energy—a clean and versatile fuel source (Gu et al., 2024). As renewable energy capacity expands and electric vehicles, alongside other power-hungry devices, gain widespread adoption, the challenge of effectively managing surplus electricity has become paramount in the energy sector. P2H technology adeptly addresses this challenge by electrolyzing water, converting excess electrical energy into hydrogen, thereby not only alleviating the issue of surplus electricity but also

supplying a clean, green energy source for innovative applications like hydrogen-fueled vehicles. Moreover, P2H technology boasts several advantages that make it an attractive option for energy storage and conversion. Its high energy storage efficiency, prolonged storage capability, and zero-emission profile position it as a promising contender in the quest for sustainable energy solutions (Zhuang et al., 2023). By harnessing the full potential of both the IES and P2H technology, we can accelerate our transition towards a low-carbon, environmentally friendly future.

(He et al., 2021) proposes an integrated energy system optimization model that utilizes P2H technology to convert excess wind power into hydrogen, mitigating curtailment and filling load valleys. Case studies validate the effectiveness of this approach. Author in (Gu et al., 2023) propose a regional joint electrolytic hydrogen system framework to address differentiated electrolytic hydrogen capacity caused by resource characteristics in China. They established a decoupling model for cascade hydropower and compared its advantages over separate systems in terms of reducing hydrogen costs, carbon emissions, and renewable energy capacity. Differential models for electrolyzers were also established, providing insights into their evolution and development prospects (Gupta et al., 2023). studies the integration of P2H technology into utility-scale hybrid power plants (HPPs) consisting of wind, solar, and battery storage. As renewable energy resources and sector coupling increase, HPPs are evolving to include other energy vectors like heat and gas storage. Integrating P2H within HPPs reduces fluctuations from non-dispatchable production and curtailment, similar to storage devices. Case studies in Europe demonstrate the significant techno-economic benefits of HPPs with P2H. In (Zhao et al., 2022), the Integrated Energy Production Unit (IEPU) concept, combining P2H and Carbon Capture, Utilization, and Storage (CCUS) technologies, is proposed. This concept leverages existing synchronous turbines to provide synthetic active and reactive capabilities, validated using open-source software with European load data, optimizing capacity and simulating 8,760-h operations to minimize annual costs. In (Dong et al., 2023), the authors compare the technical characteristics of alkaline electrolyzers (AEC) and proton exchange membrane electrolyzers (PEMEC), and proposes an optimal planning model for P2H clusters. The model aims to minimize investment, operational, startup/shutdown, grid power purchase, network loss, and voltage deviation costs. A modified IEEE 33-node network case verifies the model's effectiveness and benefits (Lu et al., 2022). introduces an Approximate Dynamic Programming (ADP) method for optimizing real-time micro-energy grid operation with P2H devices. The ADP approach, leveraging a piecewise linear function, finds near-optimal strategies that adapt to uncertainties, outperforming Model Predictive Control (MPC) in case studies. Authors in (Cao et al., 2022) propose a dual-fuel cells hydrogen energy storage integrated energy system to enhance performance. Optimizing device capacities based on economic factors reveals an optimal configuration that outperforms single fuel cells. Sensitivity analysis highlights the influence of electricity, natural gas prices, and renewable energy capacity on the optimal hydrogen storage and fuel cell configuration.

However, a significant oversight in existing research lies in the neglect of electrolytic cells' start-up characteristics, notably the start-up delay and power requirements. While these cells are indispensable in converting renewable energy sources into hydrogen via the Power-to-Hydrogen (P2H) process, their initial operational phases, particularly the intricate start-up process, have remained largely unexamined. This oversight results in a lack of granularity in electrolytic cell models, which in turn fails to accurately mirror the system's true operational dynamics. This uncharted territory represents a crucial gap that necessitates urgent attention and further exploration. Such endeavors would not only refine our understanding of these systems but also propel us closer to a greener, more sustainable future by ensuring that P2H technologies operate at their optimal capacity.

The Alternating Direction Method of Multipliers (ADMM) algorithm, renowned for its prowess in tackling optimization challenges, stands out as a formidable tool for resolving large-scale, decentralized, and intricate constraint optimization problems within the energy sector. Its unparalleled advantages have fostered widespread adoption in energy optimization applications. By masterfully decomposing intricate energy systems into manageable subproblems and iteratively solving them in an alternating fashion, the ADMM algorithm drastically reduces problem complexity and computational overhead. Moreover, its inherent distributed nature harmoniously aligns with the decentralized characteristics of energy systems, enabling seamless distributed optimization management, thereby enhancing overall system efficiency and performance.

(Huang et al., 2023) proposes a blockchain-based distributed market framework for the bi-level carbon and energy trading between coal mine integrated energy systems and a virtual power plant (VPP). (Kong et al., 2020) introduces a distributed optimization approach for integrated energy systems (IES) using the ADMM. The method begins by analyzing uncertain factors from energy sources and loads, employing scenario analysis to capture their stochasticity. An optimal scheduling model for IES is then formulated. Leveraging ADMM, this model is reformulated to enable distributed optimization for multi-energy complementation. Case study results demonstrate the effectiveness and practicality of the proposed strategy. Authors in (Chen et al., 2018) propose an enhanced energy hub (EH) model for IES, incorporating electric and heat energy storage along with solar thermal collectors. The IES is structured as a multi-operator system, with each EH belonging to a distinct operator. A distributed energy management model accounts for storage operation costs and shows effectiveness in reducing energy bills, transmission losses, and prolonging energy storage life. (Pan et al., 2022) offers a distributed operation strategy using an enhanced ADMM. It establishes models for gas turbines and energy storage, incorporating dynamic characteristics of radial distribution and natural gas networks. An optimization model for day-ahead scheduling reduces operating costs while managing renewable energy uncertainty through chance constraints. An ADMM-based distributed operation method with adaptive step size addresses information opacity between electricity and gas systems. (Wu et al., 2021) addresses the challenges of centralized control in large-scale integrated energy parks by proposing a distributed computing method. The method decomposes joint scheduling into subproblems, considers the coupling of electricity, gas, and heat, and establishes a day-ahead scheduling model. A case study demonstrates the feasibility of the distributed optimization model. Authors in (Li et al., 2024) propose an optimal operation strategy with dynamic partitioning for centralized shared energy storage stations, considering day-ahead demands of renewable energy power plants. A multi-entity cooperative optimization model based on Nash bargaining theory is implemented and decomposed into subproblems solved by ADMM. Simulations show improved tracking of renewable energy output, higher energy storage utilization, and increased profits for each entity.

In this article, we delve into a comprehensive study exploring the distributed optimization operation methodology for clusters of micro-energy grids within a multifaceted energy system that integrates electricity, heat, and hydrogen resources. Our research meticulously models the intricate Power-to-Hydrogen (P2H) conversion process within electrolytic cells, meticulously accounting for their nuanced startup dynamics. This nuanced approach ensures a precise portrayal of the P2H process, pivotal for optimizing the holistic energy system's performance. To this end, we formulate an optimization framework that recognizes each micro-energy grid as an autonomous entity, respecting their distinct interests and operational imperatives. This model not only considers the efficiency of energy conversion but also the specific operational constraints and goals of each micro-energy grid. To tackle this intricate distributed optimization challenge, we harness the power of the Alternating Direction Method of Multipliers (ADMM) algorithm, renowned for its prowess in handling large-scale, decentralized optimization problems. By utilizing ADMM, we can decompose the overall optimization problem into smaller subproblems, which are then solved iteratively in a distributed manner. This approach not only reduces the computational complexity but also enables each micro-energy grid to operate independently while still contributing to the overall optimization of the entire energy system.

2 P2H module unified operation model

2.1 Introduction for P2H technologies

In the commercial landscape of hydrogen production equipment, the electrolytic cell stack stands as the cornerstone unit. Nevertheless, the inherent power limitations of a solitary stack, often constrained to below 10 kW, underscore the need for scalability. By harnessing the inherent scalability of electrolytic cell technology, we can orchestrate multiple stacks into formidable modules, capable of achieving capacities that soar from 100 kW to the megawatt realm. The extensive hydrogen production systems utilized in power systems often comprise numerous independently managed modules, where each module can be selectively activated, deactivated, and its output precisely controlled. Therefore, this paper focuses its modeling and selection planning efforts on the electric hydrogen production module as the fundamental research subject.

2.2 Startup model of P2H modules

When initiating the P2H process, the start-up delay associated with low-temperature electrolysis technologies, such as AEC and PEMEC, tends to be minimal. However, in the case of SOEC utilizing high-temperature electrolysis, hydrogen gas production does not commence until the stack has reached a specific temperature threshold. Notably, the heating duration required to attain this temperature can often be significant and should not be overlooked.

In the context of the given modeling, i, k, and t represent distinct indices: i signifies the i-th micro energy grid, k denotes the k-th electrolytic cell, and t represents the time instant. The variable α_{EC}^{k} captures the startup delay specific to the k-th electrolytic cell. The variable $x_{EC}^{i,k,t}$ represents the state of the k-th electrolytic cell within the i-th micro-energy grid at time t. Furthermore, $y_{EC}^{i,k,t}$ and $z_{EC}^{i,k,t}$ represent the start and stop actions, respectively, of the k-th electrolytic cell in the i-th micro-energy grid at time t. These actions indicate whether the electrolytic cell is being initiated or terminated at a given time.

The modeling of these variables allows for a comprehensive representation of the dynamic behavior and operational decisions within the integrated energy system.

The operating power of the EC is subject to upper and lower limits, which are mathematically constrained as expressed in Equation 1. This constraint ensures that the electrolytic cell operates within its safe and efficient range, preventing over- or under-utilization.

$$x_{EC}^{i,k,t} \cdot \delta_{EC,in,1,\min}^{i,k} \cdot Cap_{EC}^{i,k} \le P_{EC,in,1}^{i,k,t} \le x_{EC}^{i,k,t} \cdot \delta_{EC,in,1,\max}^{i,k} \cdot Cap_{EC}^{i,k} \quad (1)$$

where $P_{EC,in,1}^{i,k,t}$ represents the EC input power that is utilized for hydrogen production (output). This is the active power input that drives the electrolysis process and generates hydrogen gas. $Cap_{EC}^{i,k}$ represents the installed capacity of the EC. $\delta_{EC,in,1,\min}^{i,k}/\delta_{EC,in,1,\max}^{i,k}$ represents the ratio of the minimum/maximum value of $P_{EC,in,1}^{i,k,t}$ to the installed capacity.

The starting power constraint of EC is shown in Equation 2.

$$P_{EC,in,2}^{i,k,t} = \sum_{\tau=0}^{\alpha_{EC}^{k}-1} y_{EC}^{i,k,t-\tau} \cdot \delta_{EC,boot}^{i,k} \cdot Cap_{EC}^{i,k} \quad (2)$$

where $P_{EC,in,2}^{i,k,t}$ represents the EC input power used specifically for starting the electrolytic cell. This power is consumed only during the startup phase and does not contribute to hydrogen production. It is typically required to heat the stack and other components to the operating temperature. $\delta_{EC,boot}^{i,k}$ represents the ratio of the starting power $P_{EC,in,2}^{i,k,t}$ to the installed capacity.

The state constraints of EC are shown in Equation 3.

$$\begin{aligned} &y_{EC}^{i,k,t-\alpha_{EC}^{k}} - z_{EC}^{i,k,t} = x_{EC}^{i,k,t} - x_{EC}^{i,k,t-1} \\ &y_{EC}^{i,k,t} \le 1 - x_{EC}^{i,k,t-1} \\ &z_{EC}^{i,k,t} \le x_{EC}^{i,k,t-1} \end{aligned} \quad (3)$$

In Equation 3, the first equation represents the constraints imposed by the start-up and shutdown action variables on the state variables of the electrolytic cell. The second equation indicates that the electrolytic cell can only be started when it is in the off state, while the third equation indicates that the electrolytic cell can only be shut down when it is in the start-up state.

2.3 Comparison of main performance indicators of 3 P2H technologies

At present, there are three main types of electrolytic cells: alkaline electrolytic cells (AECs), proton exchange membrane electrolytic cells (PEMECs), and solid oxide electrolytic cells (SOECs).

Among the three P2H technologies, AECs boast the earliest research and development efforts, the most matured technology, and the lowest equipment cost. Nonetheless, they encounter challenges such as the difficulty in completely isolating hydrogen-

TABLE 1 The main technical indicators of the three electrolytic cells.

Parameters	AEC	PEMEC	SOEC
Current density (A/cm^2)	0.25–0.45	1.0–2.0	0.3–1.0
Voltage range (V)	1.87–2.10	1.65–1.85	1.78–1.85
Hydrogen production capacity (Nm^3/h)	1,400	400	<10
Electricity consumption (kWh/Nm^3)	4.2–4.8	4.4–5.0	3.0
Operating temperature (°C)	50–100	80–100	120
Efficiency (%)	62–82	74–87	90–100
Startup time	1–5min	<10s	15min
Investment cost (Thousand RMB/kW)	2.2–10.5	9.8–14.7	>14
Efficiency attenuation (%/year)	0.25–0.45	0.5–2.5	3–50
Minimum input power (Rated power %)	20–25	5–10	0

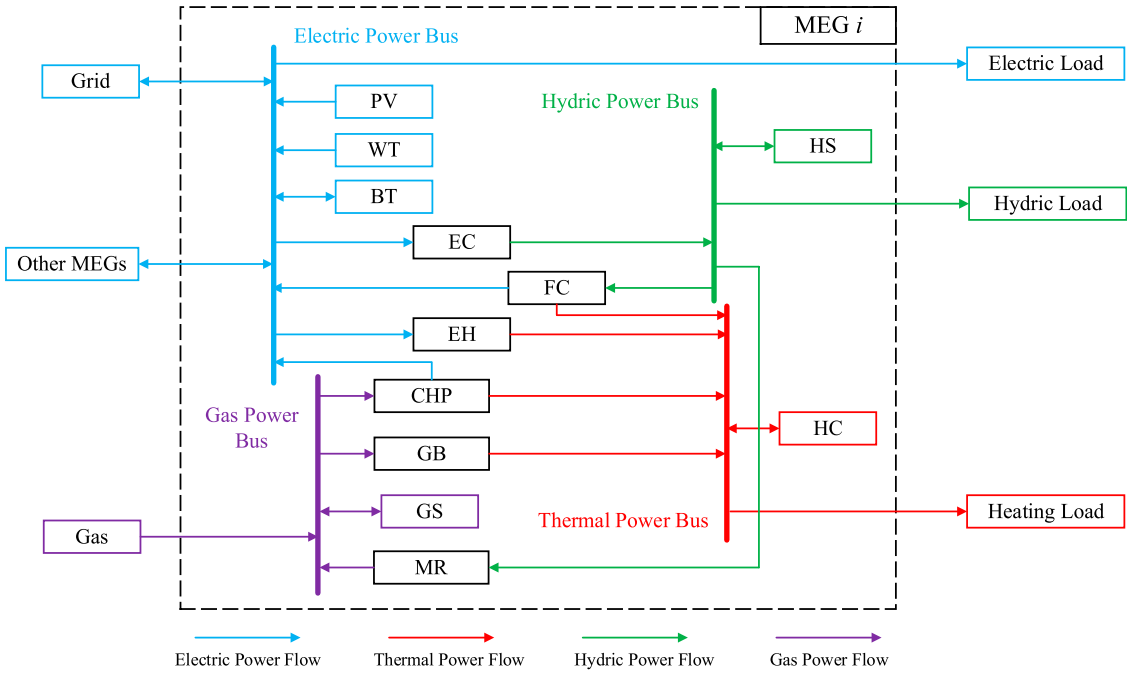

FIGURE 1
The structure of each micro-energy grid.

oxygen diffusion (especially under low loads), high electrolysis overvoltage, and the inertia of load ion conduction in electrolyte solutions. These factors limit their working load range and response speed.

In contrast, PEMECs have significantly improved load range and response speed compared to AECs, albeit with a slightly higher equipment cost. However, both AECs and PEMECs share a limitation: their rated hydrogen production efficiency does not exceed 70%.

SOECs, on the other hand, utilize solid oxide electrolytes to electrolyze gaseous water in high-temperature environments. By harnessing the thermodynamics and kinetics of the electrolysis reaction, SOECs are able to improve energy conversion efficiency by approximately 10%–15%. However, due to the constraints of operating in high-temperature environments, SOEC technology currently lags behind PEMECs in terms of cost and response speed.

Table 1 below provides a concise overview of the key technical indicators associated with each of the three electrolytic cells. It is evident that each of the three P2H technologies offers distinct advantages: AEC excels in cost-efficiency, PEMEC stands out in terms of flexibility, while SOEC boasts the highest energy conversion efficiency.

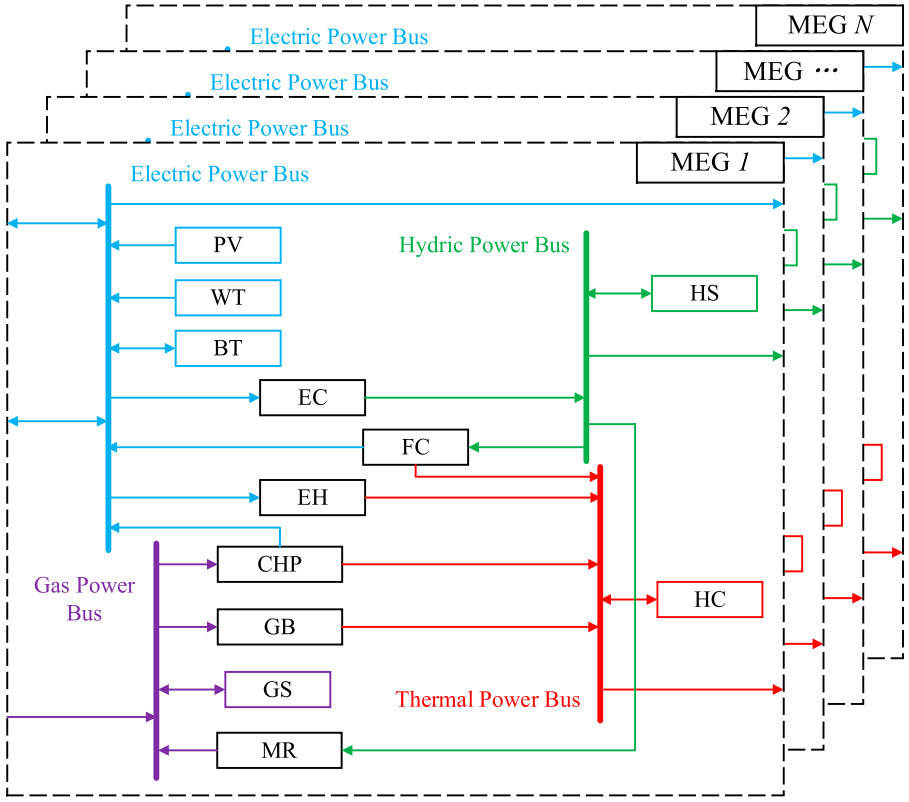

FIGURE 2
The structure of micro-energy grid cluster.

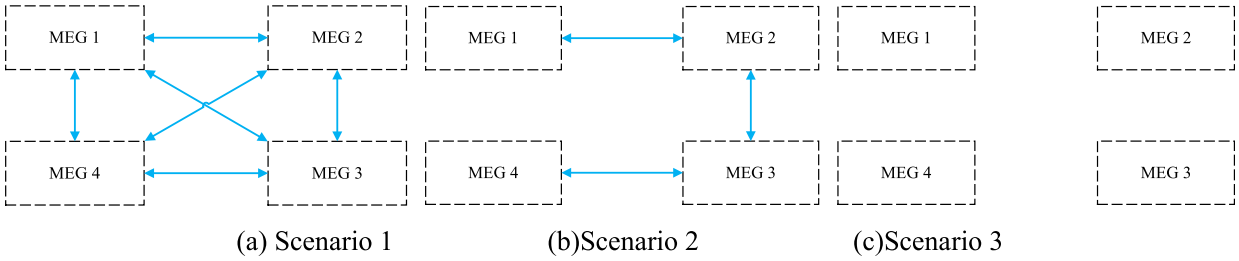

FIGURE 3
(A) Scenario 1 **(B)** Scenario 2 **(C)** Scenario 3. The connection topology between the micro-energy grids in each scenario.

3 Mathematical model for the optimal operation of micro-energy grids

3.1 System structure

The micro-energy grid incorporates a busbar design that comprises four essential power busbars: electricity, heat, hydrogen, and gas, as shown in Figure 1.

Within this micro-energy grid, the primary energy supply apparatus encompasses a harmonious blend of renewable energy generation systems and CHP units. Furthermore, the system is augmented by EH techniques and GB, enhancing the thermal energy supply capabilities. Within this intricate system, devices such as EC and FC play pivotal roles, facilitating seamless interconversion between electrical and hydrogen energy. Notably, the hydrogen energy generation process inherently yields thermal energy, thus further augmenting the grid's thermal output. Moreover, the refined hydrogen energy can undergo MR for conversion into natural gas, expanding the grid's energy portfolio.

This versatile micro-energy grid caters to three primary load demands: electrical energy, hydrogen energy, and thermal energy, ensuring a comprehensive range of energy services. Its input energy sources are diverse, incorporating electricity sourced directly from the main power grid or exchanged with other micro-energy grids, as well as

TABLE 2 TOU electricity price.

Period	Time	Price/[RMB/(kWh)]
Valley	23:00–07:00	0.47
Off-peak	07:00–08:00, 11:00–18:00	0.87
Peak	08:00–11:00, 18:00–23:00	1.09

TABLE 3 Capacity of the devices installed in each micro-energy grid.

Devices	MEG 1	MEG 2	MEG 3	MEG 4
PV (kW)	1,000	1,000	1,000	3,000
WT (kW)	1,000	1,000	1,000	3,000
CHP (kW)	5,000	5,000	5,000	5,000
FC (kW)	1,000	1,000	3,000	1,000
EC (kW)	1,000	1,000	3,000	1,000
EH (kW)	2000	2000	2000	2000
GB (kW)	3,000	3,000	3,000	3,000
MR (kW)	1,000	1,000	1,000	1,000
BT (kWh)	1,000	1,000	1,000	1,000
HC (kWh)	1,000	1,000	1,000	1,000
HS (kWh)	1,000	1,000	1,000	1,000
GS (kWh)	1,000	1,000	1,000	1,000

natural gas procured efficiently from gas utility companies. This integrated approach fosters a resilient and sustainable energy ecosystem, tailored to meet the evolving needs of modern communities.

The article delves into an integrated energy system encompassing electric, thermal, and hydrogen components, which comprises a cluster of interconnected micro-energy grids, as depicted in Figure 2. These micro-energy grids are capable of exchanging electrical power seamlessly through dedicated interconnection lines, fostering a dynamic and interactive network.

3.2 Objective function

For each micro-energy grid, the overarching objective is to minimize operating costs, as outlined in Equation 4. These costs comprise four distinct components: operational and maintenance costs, gas procurement costs, electricity acquisition costs, and power exchange costs.

$$\min\ C^i = C^i_{OM} + C^i_{gas} + C^i_{grid} + C^i_{EX} \tag{4}$$

where C^i_{OM} represents operational and maintenance costs, C^i_{gas} represents gas procurement costs, C^i_{grid} represents electricity acquisition costs, C^i_{EX} represents power exchange costs.

The operational and maintenance costs are shown in Equations 5, 6.

$$C^i_{OM} = \sum_{t=1}^{T}\left(\begin{array}{l} C^{i,t}_{PV,om} + C^{i,t}_{WT,om} + C^{i,t}_{CHP,om} + C^{i,t}_{FC,om} \\ +C^{i,t}_{EC,om} + C^{i,t}_{EH,om} + C^{i,t}_{GB,om} + C^{i,t}_{MR,om} \\ +C^{i,t}_{BT/HC/HS/GS,om} \end{array}\right)\cdot \Delta t \tag{5}$$

$$\begin{aligned}
&C^{i,t}_{PV,om} = c^{i,t}_{PV,om}\cdot P^{i,t}_{PV,out}\\
&C^{i,t}_{WT,om} = c^{i,t}_{WT,om}\cdot P^{i,t}_{WT,out}\\
&C^{i,t}_{CHP,om} = c^{i,t}_{CHP,om}\cdot P^{i,t}_{CHP,out,E}\\
&C^{i,t}_{FC,om} = \sum_{k=1}^{K}\left(c^{i,k,t}_{FC,om}\cdot P^{i,k,t}_{FC,out,E}\right)\\
&C^{i,t}_{EC,om} = \sum_{k=1}^{K}\left(c^{i,k,t}_{EC,om,1}\cdot P^{i,k,t}_{EC,out} + c^{i,k,t}_{EC,om,2}\cdot P^{i,k,t}_{EC,in,2}\right)\\
&C^{i,t}_{EH,om} = c^{i,t}_{EH,om}\cdot P^{i,t}_{EH,out}\\
&C^{i,t}_{GB,om} = c^{i,t}_{GB,om}\cdot P^{i,t}_{GB,out}\\
&C^{i,t}_{MR,om} = c^{i,t}_{MR,om}\cdot P^{i,t}_{MR,out}\\
&C^{i,t}_{BT/HC/HS/GS,om} = c^{i,t}_{BT/HC/HS/GS,om}\cdot\left(P^{i,t}_{BT/HC/HS/GS,c} + P^{i,t}_{BT/HC/HS/GS,d}\right)
\end{aligned} \tag{6}$$

The gas procurement costs are illustrated in Equation 7.

$$C^i_{gas} = \sum_{t=1}^{T}\frac{R^{i,t}_{FU}}{H^{i,t}_{FU}}\cdot P^{i,t}_{gas,b}\cdot\Delta t \tag{7}$$

The electricity acquisition costs from the power grid are shown in Equation 8.

$$C^i_{grid} = \sum_{t=1}^{T}\left(c^{i,t}_{GD,b}\cdot P^{i,t}_{GD,b} - c^{i,t}_{GD,s}\cdot P^{i,t}_{GD,s}\right)\cdot\Delta t \tag{8}$$

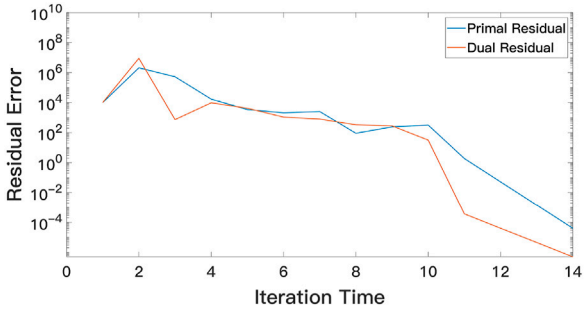

FIGURE 4
The variation of residual error with the iteration times in scenario 1

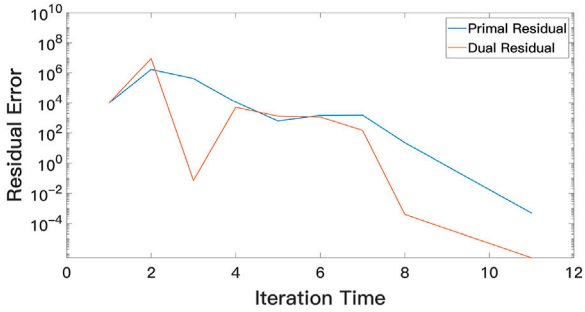

FIGURE 5
The variation of residual error with the iteration times in scenario 2.

The power exchange costs with other micro-energy grids are shown in Equation 9.

$$C_{EX}^{i} = \sum_{t=1}^{T} \sum_{j=1}^{IMG} c_{EX}^{i,j,t} \cdot \left(P_{EX,in}^{i,j,t} - P_{EX,out}^{i,j,t} \right) \cdot \Delta t \tag{9}$$

3.3 Constraints

3.3.1 Constraints on the power balance

The electric power balance is shown in Equation 10.

$$\begin{aligned} &P_{BT,d,EX}^{i,t} + P_{GD,b}^{i,t} + P_{PV,out}^{i,t} + P_{WT,out}^{i,t} + P_{CHP,out,E}^{i,t} + \sum_{k=1}^{K} P_{FC,out,E}^{i,k,t} + \sum_{j=1}^{IMG} P_{EX,in}^{i,j,t} \\ &= P_{BT,c,EX}^{i,t} + P_{GD,s}^{i,t} + P_{EL}^{i,t} + \sum_{k=1}^{K} \left(P_{EC,in,1}^{i,k,t} + P_{EC,in,2}^{i,k,t} \right) + P_{EH,in}^{i,t} + \sum_{j=1}^{IMG} P_{EX,out}^{i,j,t} \end{aligned} \tag{10}$$

The thermal power balance is shown in Equation 11.

$$\begin{aligned} &P_{HC,d,EX}^{i,t} + P_{CHP,out,H}^{i,t} + P_{GB,out}^{i,t} + P_{EH,out}^{i,t} + \sum_{k=1}^{K} P_{FC,out,H}^{i,k,t} \\ &= P_{HC,c,EX}^{i,t} + P_{HL}^{i,t} \end{aligned} \tag{11}$$

The hydric power balance is shown in Equation 12.

$$\begin{aligned} &P_{HS,d,EX}^{i,t} + \sum_{k=1}^{K} P_{EC,out}^{i,k,t} \\ &= P_{HS,c,EX}^{i,t} + P_{HGL}^{i,t} + \sum_{k=1}^{K} P_{FC,in}^{i,k,t} + P_{MR,in}^{i,t} \end{aligned} \tag{12}$$

The gas power balance is shown in Equation 13.

$$\begin{aligned} &P_{GS,d,EX}^{i,t} + P_{gas,b}^{i,t} + P_{MR,out}^{i,t} \\ &= P_{GS,c,EX}^{i,t} + P_{CHP,in}^{i,t} + P_{GB,in}^{i,t} \end{aligned} \tag{13}$$

3.3.2 Constraints on the purchased power of electricity and gas

The purchased/sold electric power constraints from/to the power grid are shown in Equation 14.

$$\begin{aligned} &x_{GD,b}^{i,t} \cdot P_{GD,b,\min}^{i,t} \le P_{GD,b}^{i,t} \le x_{GD,b}^{i,t} \cdot P_{GD,b,\max}^{i,t} \\ &x_{GD,s}^{i,t} \cdot P_{GD,s,\min}^{i,t} \le P_{GD,s}^{i,t} \le x_{GD,s}^{i,t} \cdot P_{GD,s,\max}^{i,t} \\ &0 \le x_{GD,b}^{i,t} + x_{GD,s}^{i,t} \le 1 \end{aligned} \tag{14}$$

The purchased gas power constraints from the gas company are shown in Equation 15.

$$P_{gas,b,\min}^{i,t} \le P_{gas,b}^{i,t} \le P_{gas,b,\max}^{i,t} \tag{15}$$

3.3.3 Constraints on the efficiency of the devices

The efficiency constraints of the devices are shown in Equation 16.

$$\begin{aligned} P_{CHP,out,E}^{i,t} &= \eta_{CHP,E}^{i,t} \cdot P_{CHP,in}^{i,t} \\ P_{CHP,out,H}^{i,t} &= V_{CHP}^{i,t} \cdot P_{CHP,out,E}^{i,t} \\ P_{FC,out,E}^{i,k,t} &= \eta_{FC,E}^{i,k,t} \cdot P_{FC,in}^{i,k,t} \\ P_{FC,out,H}^{i,k,t} &= V_{FC}^{i,k,t} \cdot P_{FC,out,E}^{i,k,t} \\ P_{EC,out}^{i,k,t} &= \eta_{EC}^{i,k,t} \cdot P_{EC,in,1}^{i,k,t} \\ P_{EH,out}^{i,t} &= \eta_{EH}^{i,t} \cdot P_{EH,in}^{i,t} \\ P_{GB,out}^{i,t} &= \eta_{GB}^{i,t} \cdot P_{GB,in}^{i,t} \\ P_{MR,out}^{i,t} &= \eta_{MR}^{i,t} \cdot P_{MR,in}^{i,t} \end{aligned} \tag{16}$$

3.3.4 Constraints on the upper and lower power limits of the devices

The upper and lower power limit constraints are shown in Equation 17.

$$\begin{aligned} &0 \le P_{PV,out}^{i,t} \le \delta_{PV,fore}^{i,t} \cdot Cap_{PV}^{i} \\ &0 \le P_{WT,out}^{i,t} \le \delta_{WT,fore}^{i,t} \cdot Cap_{WT}^{i} \\ &\delta_{CHP,out,E,\min}^{i,t} \cdot Cap_{CHP,E}^{i} \le P_{CHP,out,E}^{i,t} \le \delta_{CHP,out,E,\max}^{i,t} \cdot Cap_{CHP,E}^{i} \\ &\delta_{FC,out,E,\min}^{i,k,t} \cdot Cap_{FC,E}^{i,k} \le P_{FC,out,E}^{i,k,t} \le \delta_{FC,out,E,\max}^{i,k,t} \cdot Cap_{FC,E}^{i,k} \\ &x_{EC}^{i,k,t} \cdot \delta_{EC,out,\min}^{i,t} \cdot Cap_{EC}^{i} \le P_{EC,out}^{i,t} \le x_{EC}^{i,k,t} \cdot \delta_{EC,out,\max}^{i,t} \cdot Cap_{EC}^{i} \\ &\delta_{EH,out,\min}^{i,t} \cdot Cap_{EH}^{i} \le P_{EH,out}^{i,t} \le \delta_{EH,out,\max}^{i,t} \cdot Cap_{EH}^{i} \\ &\delta_{GB,out,\min}^{i,t} \cdot Cap_{GB}^{i} \le P_{GB,out}^{i,t} \le \delta_{GB,out,\max}^{i,t} \cdot Cap_{GB}^{i} \\ &\delta_{MR,out,\min}^{i,t} \cdot Cap_{MR}^{i} \le P_{MR,out}^{i,t} \le \delta_{MR,out,\max}^{i,t} \cdot Cap_{MR}^{i} \end{aligned} \tag{17}$$

3.3.5 Constraints on the ramping limit

The ramping limit constraints are shown in Equation 18.

$$\begin{aligned} &P_{CHP,out,E}^{i,t} - P_{CHP,out,E}^{i,t-1} \le \delta_{CHP,ramp,\max}^{i} \cdot Cap_{CHP,E}^{i} \\ &P_{FC,out,E}^{i,k,t} - P_{FC,out,E}^{i,k,t-1} \le \delta_{FC,ramp,\max}^{i,k} \cdot Cap_{FC,E}^{i,k} \\ &P_{EC,out}^{i,k,t} - P_{EC,out}^{i,k,t-1} \le \delta_{EC,ramp,\max}^{i,k} \cdot Cap_{EC}^{i,k} \end{aligned} \tag{18}$$

TABLE 4 Comparison of the optimization results between ADMM algorithm and centralized optimization method.

Total cost	Scenario 1	Scenario 2	Scenario 3
ADMM ($\times 10^4$ RMB)	1229.2547	1447.0512	1821.1192
Centralized Optimization ($\times 10^4$ RMB)	1225.0296	1434.3320	1820.5015
Percentage error	0.3449%	0.8868%	0.0339%

TABLE 5 The costs of each part of each micro-energy grid in scenario 1 ($\times 10^4$ RMB).

	Total	C_{OM}	C_{gas}	C_{grid}	C_{EX}
MEG 1	278.3116	46.3552	291.7262	−61.1824	1.4184
MEG 2	1,213.0038	83.1731	782.3969	−43.0653	390.5047
MEG 3	227.5857	45.2098	182.7660	−49.4083	49.0237
MEG 4	−489.6465	75.3573	78.9783	−203.0170	−440.9614
Total	1229.2547	250.0955	1335.8674	−356.6730	−0.0146

TABLE 6 The costs of each part of each micro-energy grid in scenario 2 ($\times 10^4$ RMB).

	Total	C_{OM}	C_{gas}	C_{grid}	C_{EX}
MEG 1	368.6905	48.2351	453.8950	−38.5750	−94.8646
MEG 2	1347.4063	84.1113	850.4238	116.3950	296.4769
MEG 3	246.0414	44.5781	200.0632	−116.3188	117.7186
MEG 4	−515.0870	72.5835	4.0948	−272.4343	−319.3309
Total	1447.0512	249.5080	1508.4768	−310.9332	0.0001

3.3.6 Constraints on the energy storage devices

The limitations pertaining to the energy storage device are delineated in Equations 19–21. Specifically, Equation 19 encapsulates the efficiency constraint during charging and discharging operations, Equation 20 outlines the upper and lower bounds for the charging and discharging power, and Equation 21 specifies the energy capacity constraint of the storage device.

$$\begin{aligned} P^{i,t}_{BT/HC/HS/GS,c} &= \eta^{i,t}_{BT/HC/HS/GS,c} P^{i,t}_{BT/HC/HS/GS,c,EX} \\ P^{i,t}_{BT/HC/HS/GS,d,EX} &= \eta^{i,t}_{BT/HC/HS/GS,d} P^{i,t}_{BT/HC/HS/GS,d} \end{aligned} \tag{19}$$

$$\begin{aligned} & x^{i,t}_{BT/HC/HS/GS,c} \cdot \delta^{i,t}_{BT/HC/HS/GS,c,\min} \cdot Cap^{i}_{BT/HC/HS/GS} \le P^{i,t}_{BT/HC/HS/GS,c} \\ & P^{i,t}_{BT/HC/HS/GS,c} \le x^{i,t}_{BT/HC/HS/GS,c} \cdot \delta^{i,t}_{BT/HC/HS/GS,c,\max} \cdot Cap^{i}_{BT/HC/HS/GS} \\ & x^{i,t}_{BT/HC/HS/GS,d} \cdot \delta^{i,t}_{BT/HC/HS/GS,d,\min} \cdot Cap^{i}_{BT/HC/HS/GS} \le P^{i,t}_{BT/HC/HS/GS,d} \\ & P^{i,t}_{BT/HC/HS/GS,d} \le x^{i,t}_{BT/HC/HS/GS,d} \cdot \delta^{i,t}_{BT/HC/HS/GS,d,\max} \cdot Cap^{i}_{BT/HC/HS/GS} \\ & 0 \le x^{i,t}_{BT/HC/HS/GS,c} + x^{i,t}_{BT/HC/HS/GS,d} \le 1 \end{aligned} \tag{20}$$

$$\begin{aligned} & v^{i,t}_{BT/HC/HS/GS,\min} \cdot Cap^{i}_{BT/HC/HS/GS} \le W^{i,t}_{BT/HC/HS/GS} \le v^{i,t}_{BT/HC/HS/GS,\max} \\ & \cdot Cap^{i}_{BT/HC/HS/GS} W^{i,t+1}_{BT/HC/HS/GS} \\ & = W^{i,t}_{BT/HC/HS/GS}\left(1 - \sigma^{i}_{BT/HC/HS/GS}\right) \\ & \quad + \left(P^{i,t}_{BT/HC/HS/GS,c} - P^{i,t}_{BT/HC/HS/GS,d}\right) \\ & \quad \cdot \Delta t, \ (t = 0, \cdots, T-1) W^{i,T}_{BT/HC/HS/GS} \\ & = W^{i,0}_{BT/HC/HS/GS} \end{aligned} \tag{21}$$

3.3.7 Constraints on the operation of the EC

As outlined in Section 3.2, the EC's upper and lower power constraints, initial power constraints, and start-stop state limitations are defined in Equations 22, 23. Furthermore, Equation 24 stipulates that the start-stop state must remain consistent at the beginning and end of each cycle, while Equation 25 imposes a maximum limit on the number of starts and stops that can occur within a single cycle.

$$\begin{aligned} & x^{i,k,t}_{EC} \cdot \delta^{i,k}_{EC,in,1,\min} \cdot Cap^{i,k}_{EC} \le P^{i,k,t}_{EC,in,1} \le x^{i,k,t}_{EC} \cdot \delta^{i,k}_{EC,in,1,\max} \cdot Cap^{i,k}_{EC} \\ & P^{i,k,t}_{EC,in,2} = \sum_{\tau=0}^{\alpha_{EC}-1} y^{i,k,t-\tau}_{EC} \cdot \delta^{i,k}_{EC,boot} \cdot Cap^{i,k}_{EC} \end{aligned} \tag{22}$$

$$\begin{aligned} & y^{i,k,t-\alpha_{EC}}_{EC} - z^{i,k,t}_{EC} = x^{i,k,t}_{EC} - x^{i,k,t-1}_{EC} \\ & y^{i,k,t}_{EC} \le 1 - x^{i,k,t-1}_{EC} \\ & z^{i,k,t}_{EC} \le x^{i,k,t-1}_{EC} \end{aligned} \tag{23}$$

$$x^{i,k,T}_{EC} = x^{i,k,0}_{EC} \tag{24}$$

$$\begin{aligned} & \sum_{t=1}^{T} y^{i,k,t}_{EC} \le y^{i,k}_{EC,\max} \\ & \sum_{t=1}^{T} z^{i,k,t}_{EC} \le z^{i,k}_{EC,\max} \end{aligned} \tag{25}$$

3.3.8 Constraints on the exchanged power with other micro-energy grids

Equation 26 establishes the upper and lower bounds for the interactive power exchange with other micro-energy grids. Meanwhile, Equation 27 stipulates that the diagonal elements of the

TABLE 7 The costs of each part of each micro-energy grid in scenario 3 (× 10^4 RMB).

	Total	C_{OM}	C_{gas}	C_{grid}	C_{EX}
MEG 1	295.2441	47.3659	321.8564	−73.9782	0
MEG 2	1730.3632	88.7430	974.1874	667.4329	0
MEG 3	267.9580	47.1172	267.4596	−46.6189	0
MEG 4	−472.4460	69.8329	0.9230	−543.2019	0
Total	1821.1192	253.0590	1564.4263	3.6339	0

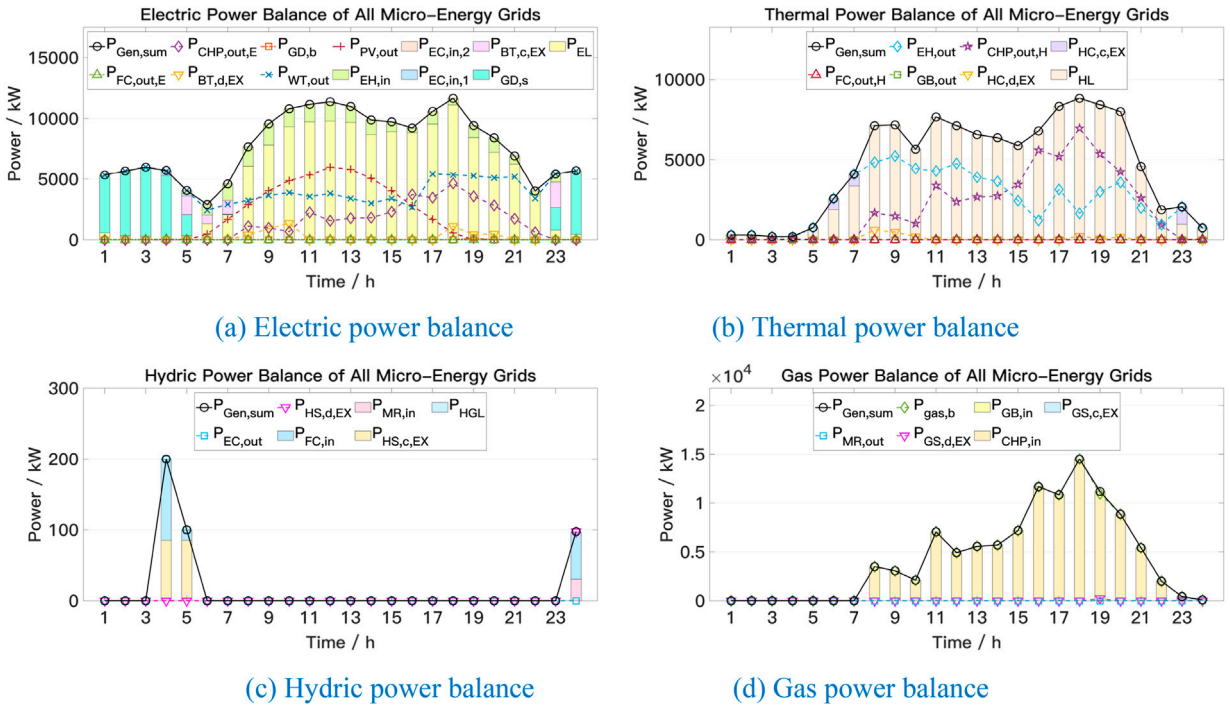

FIGURE 6
(A) Electric power balance **(B)** Thermal power balance **(C)** Hydric power balance **(D)** Gas power balance. The energy supply and consumption situation of the micro-energy grid cluster in scenario 1.

interaction state matrix must be zero, indicating that a grid cannot interact with itself, and furthermore, there can be no more than one input and one output state that is assigned a value of 1, signifying a single connection for power exchange in either direction.

$$\begin{aligned} A_{EX}^{i,j,t} \cdot x_{EX,out}^{i,j,t} \cdot P_{EX,\min}^{i,j,t} \le P_{EX,out}^{i,j,t} \le A_{EX}^{i,j,t} \cdot x_{EX,out}^{i,j,t} \cdot P_{EX,\max}^{i,j,t} \\ A_{EX}^{i,j,t} \cdot x_{EX,in}^{i,j,t} \cdot P_{EX,\min}^{i,j,t} \le P_{EX,in}^{i,j,t} \le A_{EX}^{i,j,t} \cdot x_{EX,in}^{i,j,t} \cdot P_{EX,\max}^{i,j,t} \end{aligned} \tag{26}$$

$$\begin{aligned} x_{EX,out}^{i,i,t}, x_{EX,in}^{i,i,t} = 0 \\ x_{EX,out}^{i,j,t} + x_{EX,in}^{i,j,t} \le 1 \end{aligned} \tag{27}$$

4 Algorithm for solving the multi-agent collaborative optimization model

4.1 ADMM algorithm

As a distributed algorithm, ADMM excels in addressing large-scale separable optimization problems by systematically breaking them down into smaller subproblems. This strategic decomposition not only simplifies the complexity but also paves the way for the precise identification of the elusive global optimal solution. The method seamlessly integrates the decomposition principles of the dual ascent method with the superior convergence properties of the Lagrange multiplier method, creating a potent synergy that ensures both robustness and unparalleled effectiveness.

The process of solving the problem shown in Equation 28 using the ADMM algorithm is as follows.

$$\begin{aligned} &\min_{x} \ f(\boldsymbol{x}) \\ &s.t. \ \boldsymbol{A}\boldsymbol{x} = \boldsymbol{b} \end{aligned} \tag{28}$$

where $\boldsymbol{x} \in \mathbb{R}^u$ is the decision variable, $f(\cdot)$ is the objective function, $\boldsymbol{A} \in \mathbb{R}^{p \times u}$ is the coefficient matrix, and $\boldsymbol{b} \in \mathbb{R}^p$ is the coefficient vector.

Split decision variable $\boldsymbol{x}$ in Equation 28 into two decision variables $\boldsymbol{y}$ and $\boldsymbol{z}$, as delineated in Equation 29:

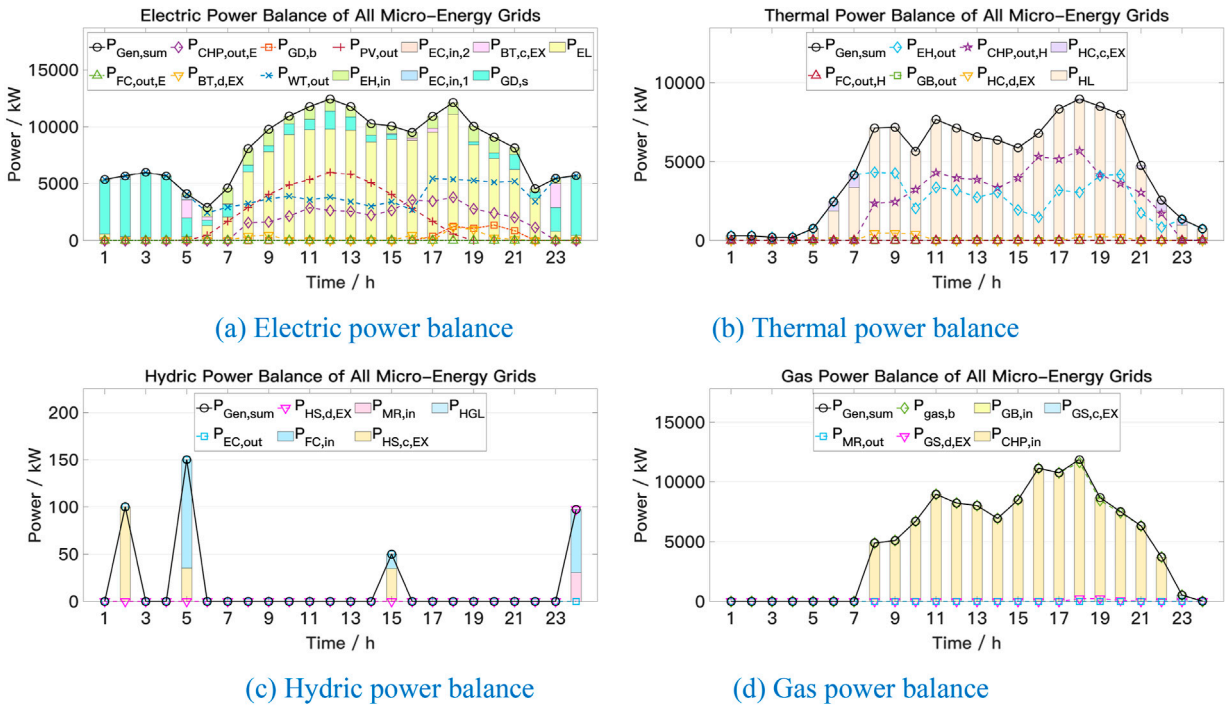

FIGURE 7
(A) Electric power balance **(B)** Thermal power balance. **(C)** Hydric power balance **(D)** Gas power balance. The energy supply and consumption situation of the micro-energy grid cluster in scenario 2.

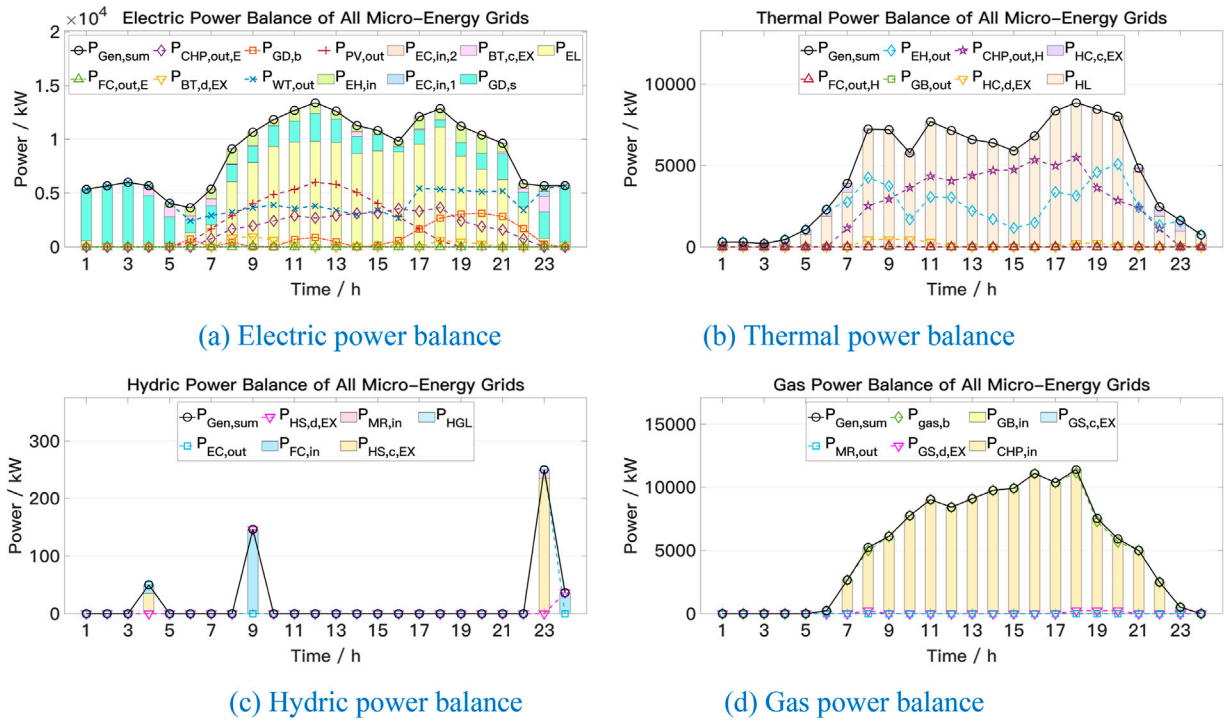

FIGURE 8
(A) Electric power balance **(B)** Thermal power balance. **(C)** Hydric power balance **(D)** Gas power balance. The energy supply and consumption situation of the micro-energy grid cluster in scenario 3.

$$\min_{y,z} g(y) + h(z) \quad s.t.\ Cy + Dz = e \tag{29}$$

where $y \in \mathbb{R}^n$ and $z \in \mathbb{R}^m$ are decision variables, $g(\cdot)$ and $h(\cdot)$ are sub optimization objectives, $C \in \mathbb{R}^{p\times n}$ and $D \in \mathbb{R}^{p\times m}$ are coefficient matrices, and $e \in \mathbb{R}^p$ is coefficient vector.

By incorporating a quadratic penalty term into the Lagrangian function, an augmented Lagrangian function is derived, providing an enhanced framework for addressing optimization problems, which is shown in Equation 30:

$$L_\rho(y,z,\lambda) = g(y) + h(z) + \lambda^T(Cy + Dz - e) + \frac{\rho}{2}\|Cy + Dz - e\|_2^2 \tag{30}$$

where $\lambda \in \mathbb{R}^p$ is the Lagrange multiplier, and $\rho > 0$ is the penalty factor.

Alternately solve variables y and z, and update the Lagrange multiplier, as shown in Equation 31, until the convergence condition is met.

$$\begin{cases} y^{m+1} = \underset{y}{\operatorname{argmin}} L_\rho(y, z^m, \lambda^m) \\ z^{m+1} = \underset{z}{\operatorname{argmin}} L_\rho(y^{m+1}, z, \lambda^m) \\ \lambda^{m+1} = \lambda^m + \rho(Cy^{m+1} + Dz^{m+1} - e) \end{cases} \tag{31}$$

where m stands for iterations.

4.2 Multi agent optimal operation model based on ADMM algorithm

Utilizing the mathematical model outlined in Chapter 3 for the optimal operation of micro-energy grids, and leveraging the power of the ADMM algorithm, the objective function is restructured in the following manner, as illustrated in Equation 32:

$$\min\ C^i = C^i_{OM} + C^i_{gas} + C^i_{grid} + C^i_{EX} + C^i_{Lag} + C^i_{Pen} \tag{32}$$

where C^i_{Lag} represents the Lagrange multiplier term, and C^i_{Pen} is the penalty term, which are illustrated in Equations 33, 34.

$$C^i_{Lag} = \sum_{j=1}^{IMG}\sum_{t=1}^{T}\lambda^{i,j,t,m}_{EX,out}\cdot\left(P^{i,j,t}_{EX,out} - P^{i,j,t,m}_{EX,out,ref}\right) + \sum_{j=1}^{IMG}\sum_{t=1}^{T}\lambda^{i,j,t,m}_{EX,in} \cdot\left(P^{i,j,t}_{EX,in} - P^{i,j,t,m}_{EX,in,ref}\right) \tag{33}$$

$$C^i_{Pen} = \frac{1}{2}\rho^{i,m}_{EX,out}\sum_{j=1}^{IMG}\sum_{t=1}^{T}\left(P^{i,j,t}_{EX,out} - P^{i,j,t,m}_{EX,out,ref}\right)^2 + \frac{1}{2}\rho^{i,m}_{EX,in} \times \sum_{j=1}^{IMG}\sum_{t=1}^{T}\left(P^{i,j,t}_{EX,in} - P^{i,j,t,m}_{EX,in,ref}\right)^2 \tag{34}$$

The constraints specified in Equation 10 through Equation 27 maintain their original form and remain unaltered.

4.3 The solving process

The process of employing the ADMM algorithm to address this problem is outlined below:

1. Start with $m = 1$. Set the convergence thresholds $\varepsilon_{EX,pri}$ and $\varepsilon_{EX,dual}$ for the primal and dual residuals. Initialize the dual multipliers $\lambda^{i,j,t,1}_{EX,out}$ and $\lambda^{i,j,t,1}_{EX,in}$, penalty factors $\rho^{i,1}_{EX,out}$ and $\rho^{i,1}_{EX,in}$, and coordinate variables $P^{i,j,t,1}_{EX,out,ref}$ and $P^{i,j,t,1}_{EX,in,ref}$.
2. Solve each subproblem individually.
3. Update the coordination variables $P^{i,j,t,m+1}_{EX,out,ref}$ and $P^{i,j,t,m+1}_{EX,in,ref}$ as shown in Equation 35 .

$$P^{i,j,t,m+1}_{EX,out,ref} = \frac{1}{2}\left(P^{i,j,t}_{EX,out} + P^{j,i,t}_{EX,in}\right)$$
$$P^{i,j,t,m+1}_{EX,in,ref} = \frac{1}{2}\left(P^{i,j,t}_{EX,in} + P^{j,i,t}_{EX,out}\right) \tag{35}$$

4. Compute the primal residual $r^{m+1}_{EX,pri}$ and the dual residual $r^{m+1}_{EX,dual}$, which are encapsulated in Equation 36, and assess their convergence based on conditions Equation 37.

$$\begin{aligned} r^{m+1}_{EX,pri} &= \sum_{i=1}^{IMG}\sum_{j=1}^{IMG}\sum_{t=1}^{T}\left(P^{i,j,t}_{EX,out} - P^{i,j,t,m}_{EX,out,ref}\right)^2 + \sum_{i=1}^{IMG} \times \sum_{j=1}^{IMG}\sum_{t=1}^{T}\left(P^{i,j,t}_{EX,in} - P^{i,j,t,m}_{EX,in,ref}\right)^2 r^{m+1}_{EX,dual} \\ &= \sum_{i=1}^{IMG}\sum_{j=1}^{IMG}\sum_{t=1}^{T}\left(P^{i,j,t,m+1}_{EX,out,ref} - P^{i,j,t,m}_{EX,out,ref}\right)^2 + \sum_{i=1}^{IMG} \times \sum_{j=1}^{IMG}\sum_{t=1}^{T}\left(P^{i,j,t,m+1}_{EX,in,ref} - P^{i,j,t,m}_{EX,in,ref}\right)^2 \end{aligned} \tag{36}$$

$$\begin{aligned} r^{m+1}_{EX,pri} &\le \varepsilon_{EX,pri} \\ r^{m+1}_{EX,dual} &\le \varepsilon_{EX,dual} \end{aligned} \tag{37}$$

5. Adjust the penalty factors $\rho^{i,m+1}_{EX,out}$ and $\rho^{i,m+1}_{EX,in}$ as expressed in Equation 38.

$$\rho^{i,m+1}_{EX,out/in} = \begin{cases} \varpi_{EX,i}\cdot\rho^{i,m}_{EX,out/in}, r^{m+1}_{EX,pri} \ge \chi_{EX} s^{m+1}_{EX,dual} \\ \varpi_{EX,d}\cdot\rho^{i,m}_{EX,out/in}, s^{m+1}_{EX,dual} \ge \chi_{EX} r^{m+1}_{EX,pri} \\ \rho^{i,m}_{EX,out/in}, \text{else} \end{cases} \tag{38}$$

6. Update the dual multipliers $\lambda^{i,j,t,m+1}_{EX,out}$ and $\lambda^{i,j,t,m+1}_{EX,in}$, and increment m by 1 ($m = m + 1$), which are defined in Equation 39.

$$\begin{aligned} \lambda^{i,j,t,m+1}_{EX,out} &= \lambda^{i,j,t,m}_{EX,out} + \rho^{i,m}_{EX,out}\cdot\left(P^{i,j,t}_{EX,out} - P^{i,j,t,m}_{EX,out,ref}\right) \\ \lambda^{i,j,t,m+1}_{EX,in} &= \lambda^{i,j,t,m}_{EX,in} + \rho^{i,m}_{EX,in}\cdot\left(P^{i,j,t}_{EX,in} - P^{i,j,t,m}_{EX,in,ref}\right) \end{aligned} \tag{39}$$

Repeat steps 2 through 6 until the desired convergence criteria are met.

5 Case studies

5.1 Description of the scenarios

In the case studies, three distinct operational scenarios were delineated: fully connected, partially connected, and independent operation, as depicted in Figure 3. The objective was to delve into the implications of varying connection topologies on the operational efficiency of micro-energy grid clusters. Specifically, in each of these scenarios, micro-energy grid 2 experienced a higher load level,

micro-energy grid 3 boasted a larger capacity for hydrogen production devices, and micro-energy grid 4 generated a more significant amount of renewable energy.

The cost of procuring electricity from the power grid is determined by the time-of-use pricing model, as outlined in Table 2. Meanwhile, Table 3 provides a comprehensive overview of the installed devices capacity within each micro-energy grid.

5.2 Convergence analysis

The convergence curves for the ADMM under Scenario 1 and Scenario 2 are presented in Figures 4, 5 respectively. As evident from the graphs, after exceeding ten iterations, the algorithm successfully converges to the designated threshold.

Furthermore, in Scenario 3, where the 4 micro-energy grids operate independently, the exchanged power between them inevitably amounts to 0. Consequently, the ADMM algorithm achieves convergence after the initial iteration.

5.3 Economic analysis

Table 4 presents a comparative analysis of the total costs incurred by the ADMM algorithm and the centralized optimization method across three distinct scenarios. Notably, it is evident that in each of these scenarios, the ADMM algorithm's error margin remains consistently below 1%, thus conclusively affirming the robustness and effectiveness of the proposed algorithm.

Tables 5–7 illustrate the breakdown of costs for each component of the micro-energy grids across three distinct scenarios. A noteworthy trend emerges, indicating that as the connection topology weakens, the total cost of micro-energy grid clusters rises incrementally. This underscores the pivotal role of power interchange between micro-energy grids in minimizing overall costs. Notably, micro-energy grid 2, which bears a heavier load, exhibits the most significant cost variation. The interaction of power between micro-energy grids substantially mitigates their electricity and gas procurement costs. Furthermore, despite micro-energy grid 1 and micro-energy grid 3 having comparable load levels, their costs differ due to the presence of electric hydrogen production equipment in the latter, which facilitates the storage of a portion of electrical energy.

5.4 Operation analysis

Figures 6–8 illustrate the operational dynamics of micro-energy grid clusters across three distinct scenarios. Notably, apart from renewable energy generation, CHP emerges as the primary source of electricity, while CHP and EH jointly constitute the main supply methods for thermal energy. As the interconnection topology between micro-energy grids weakens, a noteworthy surge in the output of CHP and grid-purchased power is observed. This increase arises from the inability to transmit excess electricity to other micro-energy grids via connecting lines, leading to its sale to the grid. Consequentially, this trend also prompts an augmentation in gas purchasing power. Additionally, energy storage devices play a pivotal role in effectively managing peak and valley load conditions, enabling effective load shaving and valley filling.

6 Conclusion

This article delves into the distributed optimization operation method for micro-energy grid clusters, focusing on the integrated energy system encompassing electricity, heat, and hydrogen. In developing the mathematical model for the electrolytic cell, we accounted for its startup characteristics to ensure an accurate portrayal of the P2H conversion process. With regard to optimizing the model algorithms, we established an optimization operation model centered on each micro-energy grid, taking into consideration their respective interests and demands. For distributed solution, we employed the ADMM algorithm. A case analysis revealed that the variance in total operating costs, attributed to different connection topologies between micro-energy grids, could be as significant as 48.15%. Furthermore, a comparison with the results obtained from centralized optimization algorithms underscores the efficacy of the ADMM algorithm.

Data availability statement

The original contributions presented in the study are included in the article/supplementary material, further inquiries can be directed to the corresponding author.

Author contributions

DZ: Conceptualization, Data curation, Formal Analysis, Funding acquisition, Investigation, Methodology, Project administration, Resources, Software, Supervision, Validation, Visualization, Writing–original draft. JX: Data curation, Formal Analysis, Funding acquisition, Investigation, Methodology, Resources, Software, Writing–original draft. CZ: Data curation, Investigation, Methodology, Writing–original draft. PW: Data curation, Formal Analysis, Methodology, Software, Writing–original draft. GP: Methodology, Supervision, Writing–original draft. ZG: Methodology, Supervision, Writing–original draft.

Funding

The author(s) declare that financial support was received for the research, authorship, and/or publication of this article. The study was supported by "Science and Technology Project of State Grid Jiangsu Electric Power Co., Ltd. (Grant No. J2023072)".

Conflict of interest

Authors DZ, JX, CZ, and PW were employed by State Grid Nanjing Power Supply Company.

The remaining authors declare that the research was conducted in the absence of any commercial or financial relationships that could be construed as a potential conflict of interest.

The authors declare that this study received funding from State Grid Jiangsu Electric Power Co., Ltd. The funder had the following involvement in the study: study design, data collection and analysis, writing of this article and decision to publish.

Publisher's note

References

Cao, W., Zhai, D., Zhang, J., Sha, H., Wang, Z., and Han, Q. (2022). "Study on optimal configuration of hydrogen energy storage IES with dual-fuel cells," in 2022 4th international conference on electrical engineering and control technologies (CEECT), Shanghai, China, 16-18 December 2022 (IEEE), 939–946. doi:10.1109/CEECT55960.2022.10030112

Chen, Q., Xia, M., Chen, M., and Hu, H. (2018). *Distributed energy management for integrated energy system considering multiple independent operators*. Portland, OR, USA: IEEE Power & Energy Society General Meeting PESGM, 1–5. doi:10.1109/PESGM.2018.8586052

Dong, Y., Ma, Z., Wang, Q., Ma, S., and Han, Z. (2023). "Optimal planning of multi-electrolyzer power-to-hydrogen(P2H) clusters in distribution network," in 2023 IEEE international conference on applied superconductivity and electromagnetic devices (ASEMD). Tianjin, China, October, 2023 (IEEE), 1–2. doi:10.1109/ASEMD59061.2023.10368814

Gu, Z., Pan, G., Gu, W., Qiu, H., and Lu, S. (2024). Robust optimization of scale and revenue for integrated power-to-hydrogen systems within energy, ancillary services, and hydrogen markets. *IEEE Trans. Power Syst.* 39 (3), 5008–5023. doi:10.1109/TPWRS.2023.3323660

Gu, Z., Pan, G., Gu, W., Zhou, S., Wu, Z., and Lu, S. (2023). Assessment and prospect of region joint electrolytic hydrogen systems considering multiple energy sources: wind, solar, hydro and thermal power. *IEEE Trans. Industry Appl.* 59 (5), 5269–5282. doi:10.1109/TIA.2023.3282923

Gupta, M., Das, K., Friis-Møller, M., and Leon, J. P. M. (2023). "Assessment of hybrid power plant operation including P2H in future energy markets," in *22nd wind and solar integration workshop (WIW 2023)*. Copenhagen, Denmark, 289–294. doi:10.1049/icp.2023.2750

He, X., Lu, T., Li, Y., Wang, S., and Li, J. (2021). Collaborative planning of integrated energy system considering P2H technology. *IEEE/IAS Industrial Commer. Power Syst. Asia (I&CPS Asia)*, 1219–1222. doi:10.1109/ICPSAsia52756.2021.9621567

Huang, H., Li, Z., Sampath, L. P. M. I., Yang, J., Nguyen, H. D., Gooi, H. B., et al. (2023). Blockchain-enabled carbon and energy trading for network-constrained coal mines with uncertainties. *IEEE Trans. Sustain. Energy* 14 (3), 1634–1647. doi:10.1109/TSTE.2023.3240203

Jiang, Y., Ren, Z., and Li, W. (2024). Committed carbon emission operation region for integrated energy systems: concepts and analyses. *IEEE Trans. Sustain. Energy* 15 (2), 1194–1209. doi:10.1109/TSTE.2023.3330857

Kong, A., Li, C., Chen, L., Zhu, X., and Xu, X. (2020). "ADMM-based distributed optimal dispatch of integrated energy system considering uncertainties of source and load," in 2020 IEEE sustainable power and energy conference (iSPEC), Chengdu, China, 23–25 November 2020 (IEEE), 1222–1227. doi:10.1109/iSPEC50848.2020.9351300

Li, J., Fang, Z., Wang, Q., Zhang, M., Li, Y., and Zhang, W. (2024). Optimal operation with dynamic partitioning strategy for centralized shared energy storage station with integration of large-scale renewable energy. *J. Mod. Power Syst. Clean Energy* 12 (2), 359–370. doi:10.35833/MPCE.2023.000345

Lu, X., Zhong, Z., Xue, X., Wu, Y., Ai, X., and Fang, J. (2022). "Optimal real-time operation strategy of microgrid with power-to-hydrogen device: an ADP approach," in 2022 5th international conference on energy, electrical and power engineering (CEEPE), Chongqing, China, 22-24 April 2022 (IEEE), 758–763. doi:10.1109/CEEPE55110.2022.9783327

Pan, B., Tian, Y., Chen, K., Li, W., and Tang, X. (2022). "Distributed operation strategy of electricity-gas integrated system based on improved ADMM," in 2022 12th international conference on power and energy systems (ICPES). Guangzhou, China, 23–25 December 2022 (IEEE), 310–314. doi:10.1109/ICPES56491.2022.10072950

Pan, G., Hu, Q., Gu, W., Ding, S., Qiu, H., and Lu, Y. (2021). Assessment of plum rain's impact on power system emissions in Yangtze-Huaihe River basin of China. *Nat. Commun.* 12 (6156), 6156. doi:10.1038/s41467-021-26358-w

Wu, Y., Yao, L., Liao, S., and Mao, B. (2021). "Distributed optimal scheduling of integrated energy system based on ADMM algorithm," in 2021 IEEE sustainable power and energy conference (iSPEC). Nanjing, China, 23–25 December 2021 (IEEE), 902–906. doi:10.1109/iSPEC53008.2021.9736049

Zhang, R., Chen, Y., Li, Z., Jiang, T., and Li, X. (2024). Two-stage robust operation of electricity-gas-heat integrated multi-energy microgrids considering heterogeneous uncertainties. *Appl. Energy* 371 (123690), 123690. doi:10.1016/j.apenergy.2024.123690

Zhao, F., Li, Y., Wei, Y., Wang, D., Li, F., and Yang, X. (2022). "Integrated energy production unit capacity optimization and year-round operation simulation," in 2022 7th international conference on power and renewable energy (ICPRE). Shanghai, China, 23–26 September 2022 (IEEE), 1206–1210. doi:10.1109/ICPRE55555.2022.9960424

Zhuang, W., Pan, G., Gu, W., Zhou, S., Hu, Q., Gu, Z., et al. (2023). Hydrogen economy driven by offshore wind in regional comprehensive economic partnership members. *Energy & Environ. Sci.* 16 (5), 2014–2029. doi:10.1039/D2EE02332F

Nomenclature

Abbreviations

PV	Photovoltaic generator
WT	Photovoltaic generator
CHP	Combines heat and power
GB	Gas boiler
EH	Electric heater
EC	Electrolytic cell
FC	Fuel cell
MR	Methanator
BT	Battery
HC	Heat storage tank
HS	Hydrogen storage tank
GS	Gas storage tank
EL	Electric load
HL	Heating load
HGL	Hydrogen load

Parameters

IMG	The number of micro-energy grids
T	Length of scheduling period
K	Types of EC and FC
Δt	Scheduling time resolution
$c^{i,t}_{PV,om}/c^{i,t}_{WT,om}$	Cost coefficient of PV and WT
$c^{i,t}_{CHP,om}/c^{i,k,t}_{FC,om}$	Cost coefficient of CHP and FC
$c^{i,k,t}_{EC,om,1}/c^{i,k,t}_{EC,om,2}$	Cost coefficient 1/2 of EC
$c^{i,t}_{EH,om}/c^{i,t}_{GB,om}/c^{i,t}_{MR,om}$	Cost coefficient of EH, GB and MR
$c^{i,t}_{BT/HC/HS/GS,om}$	Cost coefficient of BT/HC/HS/GS
$R^{i,t}_{FU}/H^{i,t}_{FU}$	The natural gas price and natural gas calorific value
$c^{i,j,t}_{EX}$	Electricity purchase price from other micro-energy grids
$c^{i,t}_{GD,b}/c^{i,t}_{GD,s}$	Electricity purchase/sell price from/to the power grid
$P^{i,t}_{GD,b,min}/P^{i,t}_{GD,b,max}$	The minimum/maximum power purchased from the power grid
$P^{i,t}_{GD,s,min}/P^{i,t}_{GD,s,max}$	The minimum/maximum power sold to the power grid
$P^{i,t}_{gas,b,min}/P^{i,t}_{gas,b,max}$	The minimum/maximum power purchased from the gas company
$\eta^{i,t}_{CHP,E}/\eta^{i,k,t}_{FC,E}$	The power generation efficiency of CHP/FC
$V^{i,t}_{CHP}/V^{i,k,t}_{FC}$	Thermoelectric ratio of CHP/FC
$\eta^{i,k,t}_{EC}/\eta^{i,t}_{EH}$	The efficiency of EC/EH
$\eta^{i,t}_{GB}/\eta^{i,t}_{MR}$	The efficiency of GB/MR
$Cap^{i}_{PV}/Cap^{i}_{WT}$	Installed capacity of PV/WT
$Cap^{i}_{CHP,E}/Cap^{i,k}_{FC,E}$	Installed capacity of CHP/FC
$Cap^{i}_{EC}/Cap^{i}_{EH}$	Installed capacity of EC/EH
$Cap^{i}_{GB}/Cap^{i}_{MR}$	Installed capacity of GB/MR
$\delta^{i,t}_{PV,fore}/\delta^{i,t}_{WT,fore}$	The ratio of the predicted output power to the installed capacity of PV and WT
$\delta^{i,t}_{CHP,out,E,min}/\delta^{i,t}_{CHP,out,E,max}$	The ratio of the minimum/maximum output power to the installed capacity of CHP
$\delta^{i,k,t}_{FC,out,E,min}/\delta^{i,k,t}_{FC,out,E,max}$	The ratio of the minimum/maximum output power to the installed capacity of FC
$\delta^{i,t}_{EC,out,min}/\delta^{i,t}_{EC,out,max}$	The ratio of the minimum/maximum output power to the installed capacity of EC
$\delta^{i,t}_{EH,out,min}/\delta^{i,t}_{EH,out,max}$	The ratio of the minimum/maximum output power to the installed capacity of EH
$\delta^{i,t}_{GB,out,min}/\delta^{i,t}_{GB,out,max}$	The ratio of the minimum/maximum output power to the installed capacity of GB
$\delta^{i,t}_{MR,out,min}/\delta^{i,t}_{MR,out,max}$	The ratio of the minimum/maximum output power to the installed capacity of MR
$\delta^{i}_{CHP,ramp,max}/\delta^{i,k}_{FC,ramp,max}/\delta^{i,k}_{EC,ramp,max}$	The ratio of the maximum ramping power to the installed capacity of CHP/FC/EC
$\eta^{i,t}_{BT/HC/HS/GS,c}/\eta^{i,t}_{BT/HC/HS/GS,d}$	The charging/discharging efficiency of BT/HC/HS/GS
$\delta^{i,t}_{BT/HC/HS/GS,c,min}/\delta^{i,t}_{BT/HC/HS/GS,c,max}$	The ratio of the minimum/maximum charging power to the installed capacity of BT/HC/HS/GS
$\delta^{i,t}_{BT/HC/HS/GS,d,min}/\delta^{i,t}_{BT/HC/HS/GS,d,max}$	The ratio of the minimum/maximum discharging power to the installed capacity of BT/HC/HS/GS
$\upsilon^{i,t}_{BT/HC/HS/GS,min}/\upsilon^{i,t}_{BT/HC/HS/GS,max}$	The ratio of the minimum/maximum energy stored to the installed capacity of BT/HC/HS/GS
$\sigma^{i}_{BT/HC/HS/GS}$	Self-discharge rate of BT/HC/HS/GS
$\delta^{i,k}_{EC,in,1,min}/\delta^{i,k}_{EC,in,1,max}$	The ratio of the minimum/maximum input power to the installed capacity of EC
$\delta^{i,k}_{EC,boot}$	The ratio of the startup power to the installed capacity of EC
$y^{i,k}_{EC,max}/z^{i,k}_{EC,max}$	The maximum startup/shut down times of EC within a typical day
$P^{i,j,t}_{EX,min}/P^{i,j,t}_{EX,max}$	The minimum/maximum exchanged power with other micro-energy grids
$A^{i,j,t}_{EX}$	The connection topology between micro-energy grids

Variables

$P^{i,t}_{PV,out}/P^{i,t}_{WT,out}$	The output power of PV and WT
$P^{i,t}_{CHP,in}/P^{i,t}_{CHP,out,E}/P^{i,t}_{CHP,out,H}$	The input/output electric/output thermal power of CHP
$P^{i,k,t}_{FC,in}/P^{i,k,t}_{FC,out,E}/P^{i,k,t}_{FC,out,H}$	The input/output electric/output thermal power of FC
$P^{i,k,t}_{EC,in,1}/P^{i,k,t}_{EC,in,2}/P^{i,k,t}_{EC,out}$	The input 1/input 2/output power of EC
$P^{i,t}_{EH,in}/P^{i,t}_{EH,out}$	The input/output power of EH

$P^{i,t}_{GB,in}/P^{i,t}_{GB,out}$	The input/output power of GB
$P^{i,t}_{MR,in}/P^{i,t}_{MR,out}$	The input/output power of MR
$P^{i,t}_{GD,b}/P^{i,t}_{GD,s}$	The purchased/sold power from/to the power grid
$x^{i,t}_{GD,b}/x^{i,t}_{GD,s}$	The purchased/sold status from/to the power grid, 0-1 variable
$P^{i,t}_{gas,b}$	The purchased gas power from the gas company
$P^{i,t}_{BT/HC/HS/GS,c}/P^{i,t}_{BT/HC/HS/GS,d}$	The charge/discharge power of BT/HC/HS/GS
$P^{i,t}_{BT/HC/HS/GS,c,EX}/P^{i,t}_{BT/HC/HS/GS,d,EX}$	The charge/discharge power of BT/HC/HS/GS exchanged with micro-energy grids
$W^{i,t}_{BT/HC/HS/GS}$	The stored energy of BT/HC/HS/GS
$x^{i,t}_{BT/HC/HS/GS,c}/x^{i,t}_{BT/HC/HS/GS,d}$	The charge/discharge status of BT/HC/HS/GS, 0-1 variable
$x^{i,k,t}_{EC}$	The input/output exchanged power with other micro-energy grids
$y^{i,k}_{EC}/z^{i,k}_{EC}$	The start and stop actions of EC, 0-1 variable
$P^{i,j,t}_{EX,in}/P^{i,j,t}_{EX,out}$	The input/output exchanged power with other micro-energy grids
$x^{i,j,t}_{EX,in}/x^{i,j,t}_{EX,out}$	The input/output exchanged power status with other micro-energy grids, 0-1 variable

frontiers | Frontiers in Energy Research

TYPE Original Research
PUBLISHED 10 September 2024
DOI 10.3389/fenrg.2024.1442194

OPEN ACCESS

EDITED BY
Yingjun Wu,
Hohai University, China

REVIEWED BY
Haoasn Yang,
Hong Kong Polytechnic University, Hong Kong SAR, China
Wenlong Liao,
Swiss Federal Institute of Technology Lausanne, Switzerland

*CORRESPONDENCE
Hongzhao Yang,
38762864@qq.com

RECEIVED 14 June 2024
ACCEPTED 26 August 2024
PUBLISHED 10 September 2024

CITATION
Yang H, Zhang Z, Liang R and Zhao W (2024) Research on time-of-use compensation pricing strategies for load aggregators based on user demand response.
Front. Energy Res. 12:1442194.
doi: 10.3389/fenrg.2024.1442194

Research on time-of-use compensation pricing strategies for load aggregators based on user demand response

Hongzhao Yang[1]*, Zhan Zhang[1], Rui Liang[2] and Weifeng Zhao[3]

[1]School of Software, Changsha Social Work College, Changsha, China, [2]School of Electrical and Information Engineering, Changsha University of Science and Technology, Changsha, China, [3]College of Electrical and Information Engineering, Hunan University, Changsha, China

As the electric power market reform deepens, the strategic role of load aggregators in demand-side response becomes increasingly important. The inherent variability of distributed renewable energy generation and user demand response often leads to a mismatch between the purchased electricity and the market bid volume, resulting in punitive costs for companies. To address this issue, this study treats demand-side controllable loads as dispatchable resources and proposes a tiered pricing strategy to adjust power distribution. By establishing a Stackelberg leader-follower game model, the study promotes a mutually beneficial relationship between load aggregators and controllable load users. Through case studies, this paper examines the operational profits of load aggregators and the power adjustment behaviors of controllable load users under tiered and fixed compensation pricing schemes. The results indicate that tiered compensation pricing significantly reduces punitive costs and enhances user participation in demand response.

KEYWORDS

load aggregators, controllable load management, tiered compensation strategies, stackelberg game theory, demand-side response

1 Introduction

In recent years, the deepening of electricity market reforms has increasingly highlighted the strategic role of load aggregators in demand-side response. Time-of-use pricing mechanisms, as a crucial tool for electricity demand-side management, more closely align electricity prices with supply costs through differentiated pricing. This effectively guides users to adjust their electricity consumption at different times, ensuring the safety and stability of the power system (Zhang et al., 2021; Liu et al., 2023). With the increasing complexity and interdependence of power systems, especially concerning False Data Injection Attacks (FDIA) and Voltage Stability Assessment (VSA), the vulnerability and resilience of power systems have become key research focuses (Yang and Wang, 2024). To address these challenges, various innovative methods have been proposed. For instance, Ding and Liu (2017) introduced an AC false data injection attack method based on robust tensor principal component analysis, which generates false data without requiring system parameters, overcoming the limitations of traditional bad data detection methods. Additionally, Yang et al. (2023) proposed a domain-adaptive voltage stability assessment method that quickly adapts to topological changes, reducing retraining needs and improving assessment accuracy. These research findings provide significant theoretical and practical support for further refining pricing mechanisms.

As key intermediaries in the electricity market, load aggregators are responsible for integrating and scheduling various demand-side resources. By providing aggregated load curves and related information, load aggregators can participate in competitive bidding for demand response and sign various trading contracts (Lv et al., 2023). Moreover, considering the potential threat of false data injection attacks to the power system, load aggregators need the capability to counter such attacks to ensure data authenticity and system stability (Yang et al., 2024).

Different countries exhibit significant differences in power adjustment and balancing mechanisms. For example, the UK and Nordic countries tend to adopt decentralized market models, adjusting and settling deviation power through intraday balancing markets (Khodadadi et al., 2020). In contrast, the US and Australia prefer centralized market models, where bids and quantities are submitted on trading platforms within a specified time and matched based on price and time priority (Çelebi and Flynn, 2020). Currently, China is transitioning from a long-term trading market to a combined long-term and spot trading market. Provinces are experimenting with decentralized or centralized market models in the spot market based on local conditions (Liangyuan et al., 2022). For instance, regions like Western Inner Mongolia and Fujian conduct decentralized spot markets based on long-term physical contracts (Zhu et al., 2023). In this model, generators and consumers independently determine power consumption curves in the day-ahead stage and adjust imbalances through day-ahead and balancing trades (Watanabe et al., 2018). The essence of this model lies in the scheduling arrangements based on bilateral contracts, with system dispatch departments ensuring contract fulfillment and power balance dispatch (Reddy et al., 2015). However, most regions in China still conduct spot market transactions through monthly settlement of long-term trades, leading to significant imbalance penalty costs for load aggregators (Jiang et al., 2019; Lu et al., 2022). Therefore, considering the uncertainties in load demand and distributed power output, it is crucial for load aggregators to maximize their benefits by setting reasonable compensation prices to incentivize controllable loads to participate in demand response transactions.

Designing reasonable, flexible, and effective demand-side pricing mechanisms is critical for motivating user participation in demand response and improving resource utilization efficiency (Xu et al., 2021; Jiang et al., 2023). In terms of organizing electricity market transactions, demand-side users can be classified into single market type transactions and multi-type market transactions. In single market type transaction scenarios, drawing from research experiences in the stock trading field, Chen et al. (2019) proposed a trading algorithm that combines auction and continuous bidding. Additionally, a fixed-ratio total deviation settlement method was designed for non-full transactions, and a phased user-side deviation evaluation mechanism was introduced (Wang L. et al., 2023). To address the economic rationality issues of traditional deviation balancing mechanisms, a pre-bid-based monthly deviation balancing mechanism was proposed to minimize deviation adjustment costs, encouraging low-cost units to replace high-cost units for power generation (Fu et al., 2022). In the context of coupled multi-type market transactions, the design methods of electricity price difference contracts were discussed, including setting contract prices, effective directions, benchmark prices, and design parameters for decomposing contract quantities (Nobis et al., 2020). Additionally, considering the practical situation of China's electricity trading and dispatch management system, a day-ahead market clearing model compatible with long-term physical contracts was proposed to bridge the gap between long-term physical contract delivery and grid operation constraints (Liu et al., 2020). The reinforcement learning methods for studying electricity spot market pricing mechanisms examined the impact of different pricing mechanisms on the organization of long-term trades (Wang Y. et al., 2023). Finally, Gong et al. (2021) proposed a government-authorized price difference contract settlement mechanism, considering fairness and hedging functions as a differentiated and predetermined approach.

Based on the above analysis, this paper aims to explore the optimization of interests between load aggregators and proxy power users. The innovations are in several aspects: First, considering the deviation penalties of long-term trading contracts, positive and negative balance penalty prices are introduced to evaluate the penalty costs arising from the discrepancy between bid volumes and actual electricity consumption. Second, utilizing demand-side storage, distributed photovoltaics, and controllable loads as dispatchable resources, a multi-option compensation contract for power regulation of controllable load/storage devices based on the cost functions of controllable load users or storage users is proposed. Furthermore, a Stackelberg game model is established to explore the application of tiered pricing strategies in demand response, aiming to reduce power trading deviation costs while enhancing user participation and economic benefits. Lastly, a reverse induction method based on genetic algorithms is employed to solve the proposed model, and the effectiveness of the model and method is verified through case simulations.

Main Contributions of This Paper:

1. Proposing a multi-option controllable load power regulation compensation contract based on hierarchical pricing, effectively reducing deviation costs in electricity transactions and providing flexible pricing options to meet different user needs.
2. Constructing a Stackelberg leader-follower game model to optimize compensation pricing strategies, achieving an economic benefit balance between load aggregators and users.
3. Using genetic algorithms to verify the effectiveness of the proposed model and strategies, providing theoretical support and empirical evidence for the formulation of demand response strategies in the electricity market.

2 Problem description

The operational model of load aggregators in the electricity market involves the integration of load resources, market bidding, and trading processes. By aggregating distributed renewable energy generation and user demand, load aggregators can more accurately predict and adjust loads, thereby reducing penalty costs associated with deviations. Additionally, by integrating different types of load resources, such as residential users, commercial users, and storage systems, load aggregators can enhance system flexibility and responsiveness, ensuring grid stability and efficiency. However, penalty costs related to power deviations increase operational pressure on load aggregators, necessitating effective demand response strategies and compensation mechanisms to mitigate these costs.

To address these issues, this paper proposes a bi-level game approach based on a Stackelberg game model. In the game, the load

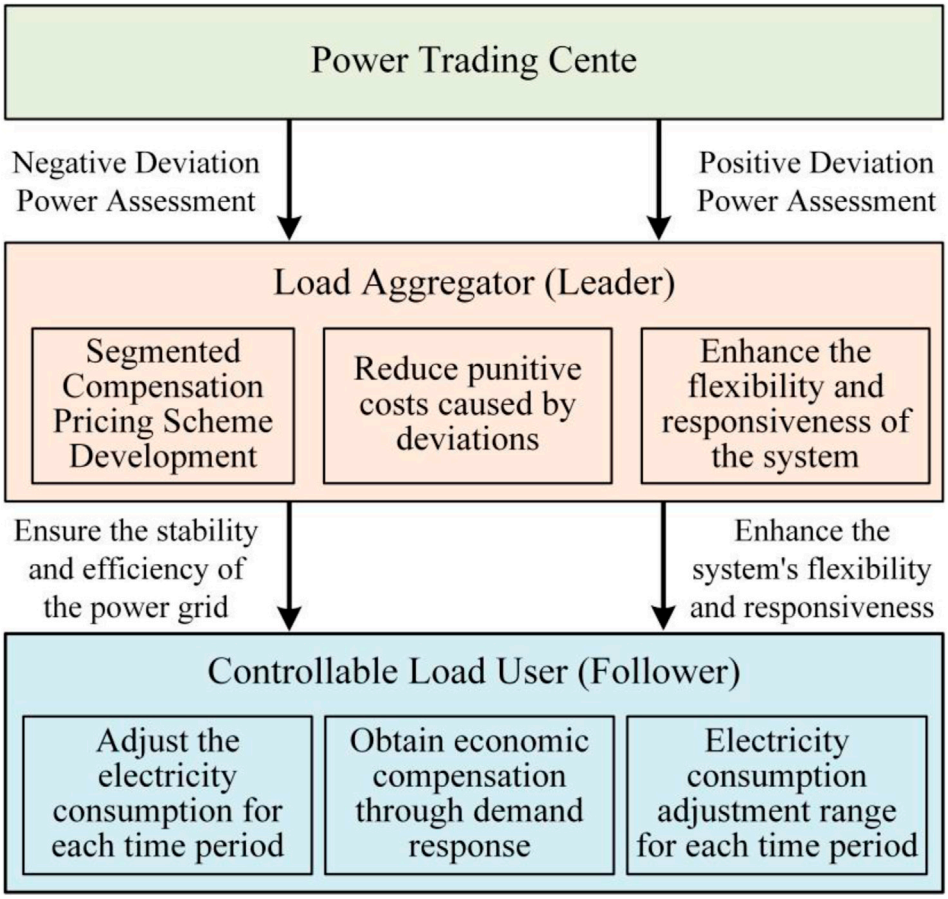

FIGURE 1
Schematic diagram of load aggregator operational model.

aggregator, acting as the leader, first formulates a reasonable power procurement strategy and tiered compensation pricing scheme to maximize operational revenue and incentivize user participation in demand response. The controllable load users, as followers, adjust their electricity consumption behavior according to the compensation strategy provided by the load aggregator, obtaining economic compensation by reducing electricity consumption during peak periods or increasing consumption during off-peak periods. Through this bi-level game model, load aggregators can significantly reduce deviation penalties and related costs while enhancing user participation in demand response, achieving mutually beneficial economic outcomes. The process flow of the problem description is illustrated in Figure 1.

2.1 Design of load aggregator operating mechanism

As renewable energy and energy storage systems continue to develop, traditional grid users are gradually transitioning from passive recipients to active participants in power balancing. Load aggregators play a crucial role by integrating the loads of numerous residential, commercial, and energy storage users. This not only enhances the overall flexibility and responsiveness of the system but also significantly reduces costs associated with power deviations. Load aggregators are essential in the electricity market, facilitating the effective utilization of distributed generation and demand response resources.

In medium-to long-term trading in the electricity market, load aggregators develop purchasing and flexible pricing strategies based on forecasts of end-user demand, expected production from distributed generation, and market fluctuation costs. The trading center assesses load aggregators to ensure the accuracy of their load responses and power assessments. In turn, load aggregators formulate their purchasing strategies and pricing schemes based on this information (Yang et al., 2022). This process requires load aggregators to possess precise forecasting capabilities and the flexibility to adjust strategies in a continuously evolving market environment.

Due to the volatility of distributed generation and the uncertainty of load demand, load aggregators may face discrepancies when assessing power deviations and actual consumption. The trading center imposes deviation assessment fees based on the positive and negative imbalance of deviation power, compelling load aggregators to make accurate forecasts and manage loads effectively. By utilizing a segmented compensation pricing mechanism, load aggregators incentivize users to modify their consumption behaviors, reducing usage during peak periods while increasing consumption during off-peak periods, thereby achieving overall system balance.

As illustrated in Figure 1, load aggregators serve a critical role in connecting the demand side with the power supply side. The demand side consists of a large number of dispersed and controllable load devices, such as air conditioners, electric vehicles, and water heaters. Load aggregators secure control over these controllable loads by signing contracts with end users of these devices (Bruninx et al., 2020). While ensuring that user comfort is not compromised, load aggregators optimize the operation and control of these devices to adjust power deviations during peak and off-peak periods, thereby minimizing the punitive costs associated with deviations. Load aggregators not only enhance system flexibility and responsiveness through the integration of load resources but also encourage users to adjust their consumption behaviors through effective pricing strategies. The specific power assessment formula established by load aggregators is as follows:

The trading center establishes the baseline electricity purchase quantity Q_d based on the monthly trading contracts signed with load aggregators. When a user's actual electricity consumption exceeds this baseline, excess usage within the threshold $x_1\%$ is exempt from deviation assessment, while any consumption beyond $x_1\%$ incurs a deviation assessment fee based on the positive imbalance price set by the trading center. Conversely, when a user's actual electricity consumption falls below the baseline, any shortfall within the threshold $x_2\%$ is also exempt from deviation assessment, whereas any shortfall beyond $x_2\%$ is subject to a deviation assessment fee based on the negative imbalance price set by the trading center. The monthly assessment fees for positive and negative imbalance quantities are represented by Equations 1–3.

$$p_t^{\text{pen}+} = \xi_+ \times \lambda_t \tag{1}$$

$$p_t^{\text{pen}-} = \xi_- \times \lambda_t \tag{2}$$

$$\Pi_2 = \begin{cases} \Delta Q_p p_t^{\text{pen}-} & ; \quad \Delta Q_p \le -x_2\% Q_d \\ 0 & ; \quad -x_2\% Q_d \le \Delta Q_p \le x_1\% Q_d \\ \Delta Q_p p_t^{\text{pen}+} & ; \quad x_1\% Q_d \le \Delta Q_p \end{cases} \tag{3}$$

In the formula $p_t^{\text{pen}+}$ and $p_t^{\text{pen}-}$ denote positive and negative deviation penalty prices, respectively; ξ_+ and ξ_- represent positive and negative penalty coefficients; λ_t stands for wholesale electricity prices, Π_2 indicates the end-of-month deviation penalty cost; ΔQ_p is the deviation quantity during the monthly settlement.

2.2 Design of segmented compensation mechanism for controllable load power adjustment

To implement effective power adjustments for controllable loads, load aggregators have designed a segmented compensation mechanism that includes both power reduction compensation contracts and power increase compensation contracts. These contracts provide varying levels of financial incentives based on the time sensitivity and cost differences of load adjustments, encouraging users to reduce consumption during peak electricity demand periods and increase usage during off-peak periods.

Through power reduction contracts, users are compensated for decreasing their electricity consumption during high-demand intervals, which helps alleviate the burden on the grid and reduce reliance on expensive emergency power sources. In contrast, power increase contracts incentivize users to take advantage of lower electricity prices during off-peak periods, thereby optimizing the energy distribution within the grid.

To ensure the effectiveness of this compensation mechanism, a multi-option segmented compensation design has been introduced, allowing different types of loads to select the most suitable compensation plan based on their specific circumstances (Bouakkaz et al., 2020). This flexible compensation strategy not only considers the economic costs associated with load adjustment for users but also reflects their contributions to grid stability, thus motivating various users to actively participate in demand response activities within the electricity market.

2.2.1 Compensation contract for controllable load power reduction

Demand aggregators create tiered power reduction compensation contracts for users participating in load shedding, offering m options. Each option consists of a specific load reduction power ΔP_i^-, and a corresponding compensation rate $p_i^{\text{com}-}$ denoted as $(\Delta P_i^-, p_i^{\text{com}-})$ where $i = 1, 2, \cdots, m$. When demand aggregators have a positive deviation in power, the economic compensation $U_{k,t}^-$ that a controllable load user k receives for reducing their power $\Delta P_{k,t}^-$ is calculated as follows:

$$U_{k,t}^- = \begin{cases} \Delta P_{k,t}^- p_1^{\text{com}-} & ; \quad \Delta P_0^- \le \Delta P_{k,t}^- \le \Delta P_1^- \\ \Delta P_{k,t}^- p_2^{\text{com}-} & ; \quad \Delta P_1^- \le \Delta P_{k,t}^- \le \Delta P_2^- \\ \vdots & \\ \Delta P_{k,t}^- p_m^{\text{com}-} & ; \quad \Delta P_{m-1}^- \le \Delta P_{k,t}^- \le \Delta P_m^- \end{cases} \tag{4}$$

Due to the varying costs of load power reduction for controllable load users across different time periods, implementing a uniform power reduction compensation price may hinder user engagement in demand response initiatives. Following the methodology proposed in the literature (Wang et al., 2021), the power reduction compensation price $p_i^{\text{com}-}$ for time period t is defined as the retail electricity price for that period multiplied by a compensation rate, as shown in Equation 5.

$$p_i^{\text{com}-} = \rho_t \delta_i \tag{5}$$

In the formula: ρ_t represents the retail electricity price during period t; δ_i denotes the compensation rate associated with the i option of the power reduction compensation contract.

2.2.2 Controllable load incremental power compensation contract

When demand aggregators experience a negative deviation in electricity volume, the economic compensation $U_{k,t}^+$ that controllable load user k receives for increasing load power $\Delta P_{k,t}^+$ can be expressed by Equations 6, 7.

$$U_{k,t}^+ = \begin{cases} \Delta P_{k,t}^+ p_1^{\text{com}+} & ; \quad \Delta P_0^+ \le \Delta P_{k,t}^+ \le \Delta P_1^+ \\ \Delta P_{k,t}^+ p_2^{\text{com}+} & ; \quad \Delta P_1^+ \le \Delta P_{k,t}^+ \le \Delta P_2^+ \\ \vdots & \\ \Delta P_{k,t}^+ p_m^{\text{com}+} & ; \quad \Delta P_{m-1}^+ \le \Delta P_{k,t}^+ \le \Delta P_m^+ \end{cases} \tag{6}$$

$$p_i^{\text{com}+} = \rho_t \pi_i \tag{7}$$

In the formula: $p_i^{\text{com}+}$ represents the compensation electricity price associated with the i option of the tiered incremental power compensation contract; π_i denotes the electricity price discount rate corresponding to the i option of the contract.

3 Dynamic compensation pricing model for controllable load power adjustment based on leader-follower game decision-making

Implementing controllable load management strategies within power systems presents a complex optimization challenge involving dynamic interactions between load aggregators and multiple controllable load users. These interactions are governed by supply interruption compensation contracts established between the load aggregator and users, where the operating costs of the load aggregator are directly influenced by the power adjustments of controllable load users. Users are required to adjust their electricity consumption behavior in accordance with the demand response directives issued by the load aggregator to achieve cost efficiency while ensuring the stability of the power supply system.

To address this issue, this paper constructs an interactive model among the load aggregator and multiple controllable load users, which can be framed as a $1-K$ type Stackelberg game model. In this model, the load aggregator acts as the leader, formulating preliminary strategies, while K users respond as followers.

The upper-level optimization model is managed by the load aggregator, aiming to minimize its monthly operating costs. These costs encompass wholesale electricity procurement expenses, penalties associated with monthly deviation in consumption, demand response costs for controllable loads, and operational maintenance costs for Battery Energy Storage Systems (BESS). To achieve this, the load aggregator must establish capacity increase or decrease compensation contracts and make charging and discharging decisions for the BESS. During the upper-level optimization process, constraints regarding power balance, storage operational limits, and charging/discharging regulations must be satisfied.

Conversely, the lower-level optimization model is handled by the controllable load users, who seek to maximize their demand response benefits. Users gain economic compensation by adjusting their loads to either reduce or increase electricity consumption. The lower-level optimization process must adhere to constraints related to participation in demand response, adjustments in controllable load power range, duration of power adjustments, frequency of power adjustments, and energy storage charging/discharging limitations.

To accurately simulate and predict system behavior under this game structure, the load aggregator can employ a Monte Carlo sampling method to generate typical daily scenarios based on monthly trading data, thereby estimating monthly deviation in consumption. This statistical simulation technique not only effectively captures the volatility of the electricity market but also provides decision support aimed at optimizing operational costs and maximizing user benefits.

By designing a segmented compensation pricing model, the load aggregator can incentivize users to participate in demand response programs, leading to effective control of monthly consumption deviations and significant reductions in penalty costs. This strategic pricing mechanism optimizes the operational costs of the load aggregator while fostering active user engagement through economic incentives, collectively promoting the stability and sustainable development of the electricity market.

Figure 2 illustrates the structure of the Stackelberg game model proposed in this paper, which simulates the interactive decision-making processes between load aggregators and controllable load users.

3.1 Upper-level optimization model

The upper-level optimization problem of the model aims to effectively reduce the monthly operating costs of the load aggregator by incorporating capacity increase or decrease power compensation contracts, along with the charging and discharging power of the Battery Energy Storage System (BESS), as key decision variables.

3.1.1 Upper-level optimization objective function

The monthly operational costs of demand aggregators consist of four components: the cost of purchasing electricity from the wholesale market, denoted as Π_1; the penalty cost for end-of-month electricity volume deviations, denoted as Π_2; the cost associated with controllable load demand response, denoted as Π_3; and the operational and maintenance costs of the Battery Energy Storage System (BESS), denoted as Π_4. The above costs include electricity procurement costs (see Equation 9), end-of month deviation penalty costs (see Equation 10), etc.

$$\min E_{\mathrm{M}} = \Pi_1 + \Pi_2 + \Pi_3 + \Pi_4 \tag{8}$$

$$Q_d = \sum_{w=1}^{W} \chi(w) \sum_{t=1}^{T} \left(\mu_{w,t}^{-} Q_{w,t}^{-} + \mu_{w,t}^{+} Q_{w,t}^{+} \right) \Delta t \tag{9}$$

$$\Pi_1 = Q_{\mathrm{d}} \lambda_t + \Delta Q_{\mathrm{p}} \lambda_t \tag{10}$$

$$\Pi_3 = \sum_{W=1}^{W} \chi(w) \sum_{t=1}^{T} \sum_{k=1}^{K} \left(U_{k,t}^{-} + \Delta P_{k,t}^{-} \rho_t + U_{k,t}^{+} - \Delta P_{k,t}^{+} \rho_t \right) \Delta t \tag{11}$$

$$\Pi_4 = \sum_{W=1}^{W} \chi(w) \sum_{t=1}^{T} \left(\left(P_t^{\mathrm{ch}} + P_t^{\mathrm{dh}} \right) C_{\mathrm{BESS}} \Delta t + C_{\mathrm{BESS}}^{\mathrm{ctd}} \alpha_t^{\mathrm{ctd}} + C_{\mathrm{BESS}}^{\mathrm{dtc}} \alpha_t^{\mathrm{dtc}} \right) \tag{12}$$

In the model, $\chi(w)$ represents the frequency of occurrence of typical days under monthly transactions (calculated daily); W is the total number of typical days; $Q_{w,t}^{+}$ and $Q_{w,t}^{-}$ respectively denote the positive and negative power deviations for the demand aggregator after implementing smoothing measures; $\mu_{w,t}^{+}$ and $\mu_{w,t}^{-}$ are binary variables, where $\mu_{w,t}^{+} = 1$ when $Q_{w,t}^{+} > 0$; Δt is the daily dispatch interval; T is the total number of daily dispatches; and K represents the total number of controllable load users. Q_{a} indicates the actual electricity consumption by the users. In calculating the penalty costs for end-of-month power deviations, if actual consumption exceeds the baseline, deviation power occurs and penalties are applied based on the wholesale electricity price. Conversely, if actual consumption does not exceed the baseline, the deviation is zero, and no penalty costs arise. To address the potential frequent charging and discharging scenarios of the Battery Energy Storage System (BESS) and regulate its charging and discharging behavior as per reference. Equation 13 considers both the operational and maintenance costs of BESS and the conversion costs between charging and discharging. Here, P_t^{ch} and P_t^{dh} represent the charging and discharging powers of BESS for the period t; C_{BESS} denotes the operational and maintenance costs of BESS; α_t^{ctd} and α_t^{dtc} are binary variables for the transitions from charging to discharging and discharging to charging, respectively; $C_{\mathrm{BESS}}^{\mathrm{ctd}}$ and $C_{\mathrm{BESS}}^{\mathrm{dtc}}$ correspond to the costs associated with these transitions.

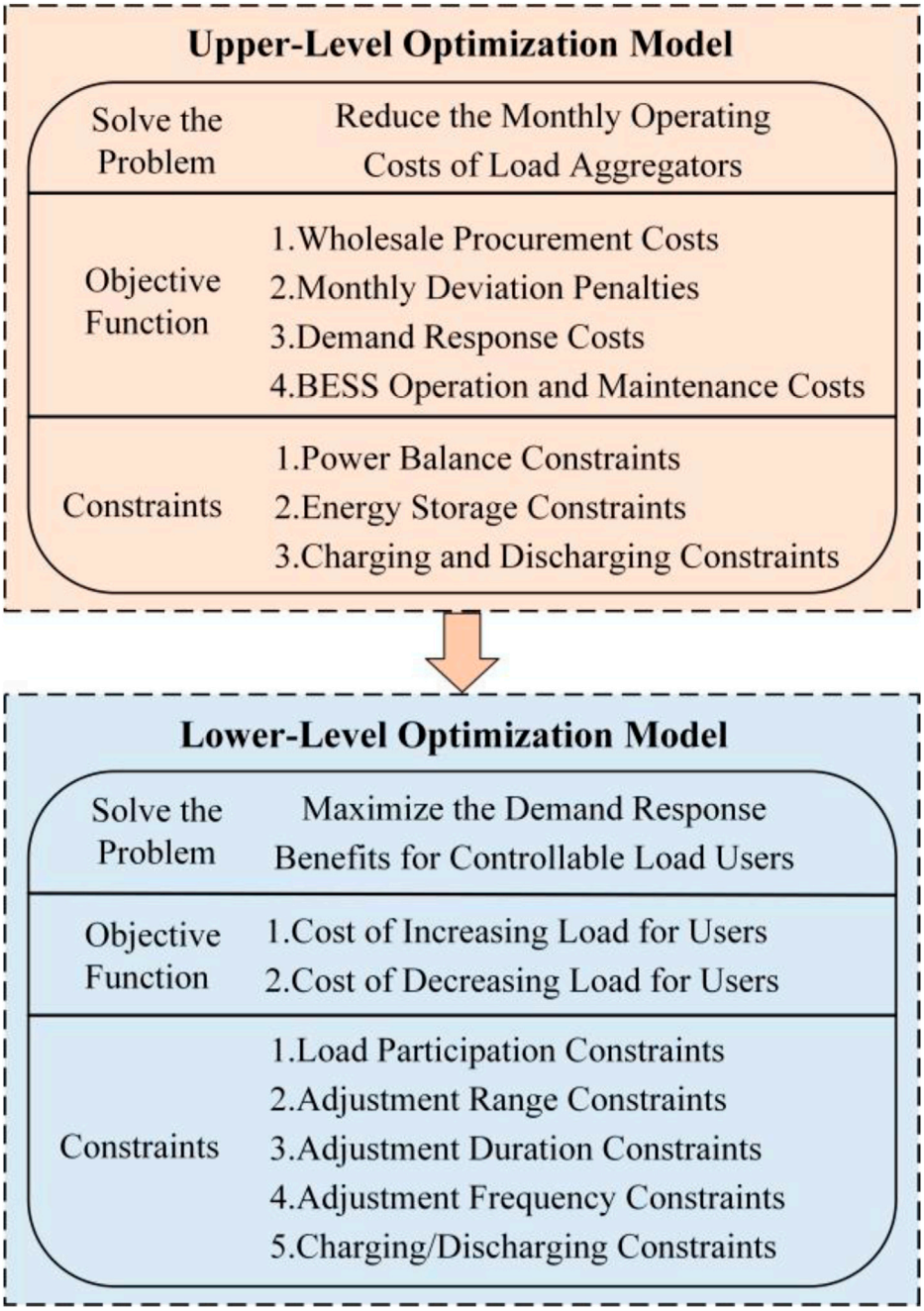

FIGURE 2
Structure of the stackelberg game model.

3.1.2 Upper-level optimization constraints

(1) Power Balance Constraints

$$Q_{w,t}^{-} = Q_{w,t}^{\mathrm{D}}\eta_{w,t} + P_t^{\mathrm{ch}} - P_t^{\mathrm{dh}} + \sum_{k=1}^{K}\left(\Delta P_{k,t}^{+} - \Delta P_{k,t}^{-}\right) \tag{13}$$

$$Q_{w,t}^{+} = P_t^{\mathrm{dh}} - P_t^{\mathrm{ch}} + \sum_{k=1}^{K}\left(\Delta P_{k,t}^{-} - \Delta P_{k,t}^{+}\right) - Q_{w,t}^{\mathrm{D}}\eta_{w,t} \tag{14}$$

In the formula: $Q_{w,t}^{\mathrm{D}}$ represents the load power during period t on a typical day w; $\eta_{w,t}$ is the power purchase deviation coefficient for the demand aggregator during period t on typical day w.

(2) Constraints on Energy Storage Operation

$$0 \le P_t^{\mathrm{ch}} \le \beta_t^{\mathrm{ch}} P_{\mathrm{ES}} \tag{15}$$

$$0 \le P_t^{\mathrm{dh}} \le \beta_t^{\mathrm{dh}} P_{\mathrm{ES}} \tag{16}$$

$$E_t = E_{t-1} + P_t^{\mathrm{ch}}\eta_{\mathrm{ch}}\Delta t - P_t^{\mathrm{dh}}\Delta t \big/ \eta_{\mathrm{dh}} \tag{17}$$

$$E_0 = E_T \tag{18}$$

$$\gamma_{\min} Q_{\mathrm{ES}} \le E_t \le \gamma_{\max} Q_{\mathrm{ES}} \tag{19}$$

In the equation: P_{ES} and Q_{ES} respectively represent the rated power and capacity of the Battery Energy Storage System (BESS); β_t^{ch} and β_t^{dh} are binary variables indicating the charging and discharging

states of BESS, with $\beta_t^{\mathrm{ch}} = 1$ denoting charging, and $\beta_t^{\mathrm{dh}} = 1$ denoting discharging; E_t is the nuclear capacity of BESS during period t; η_{ch} and η_{dh} respectively are the charging and discharging efficiencies of BESS; $\gamma_{\max}$ and $\gamma_{\min}$ respectively represent the maximum and minimum nuclear state coefficients of BESS.

(3) Energy Storage Charging and Discharging Constraints

$$\alpha_t^{\mathrm{ctd}} - \alpha_t^{\mathrm{dtc}} = \beta_{t+1}^{\mathrm{dh}} - \beta_t^{\mathrm{dh}} \tag{20}$$

$$\alpha_t^{\mathrm{ctd}} + \alpha_t^{\mathrm{dtc}} \le 1 \tag{21}$$

$$\beta_t^{\mathrm{ch}} + \beta_t^{\mathrm{dh}} \le 1 \tag{22}$$

$$u_{w,t}^{+} + u_{w,t}^{-} \le 1 \tag{23}$$

Equations 21, 22 represent the charging and discharging conversion constraints of the energy storage system; Equation 23 specifies that at any given moment, the Battery Energy Storage System (BESS) can only be in one of three states: charging, discharging, or idle.

3.2 Lower-level optimization model

3.2.1 Lower-level optimization objective function

The lower-level optimization problem in the model aims to maximize the demand response benefits for controllable load users (see Equations 24–31). By adjusting the power increases and decreases across different time periods, the model seeks to enhance system flexibility and efficiency under varying demand and market conditions, while also maintaining system stability and economic viability.

$$\max E_{\mathrm{SK}} = \sum_{t=1}^{T}\left\{\left(U_{k,t}^{+} - C_{k,t}^{+}\right) + \left(U_{k,t}^{-} - C_{k,t}^{-}\right)\right\} \tag{24}$$

As delineated in reference (Ma et al., 2023), the costs associated with increasing. $C_{k,t}^{+}$. and decreasing $C_{k,t}^{-}$ the load power for user k are represented as follows:

$$C_{k,t}^{+} = a_k^{+}\left(\Delta P_{k,t}^{+}\right)^2 + b_k^{+}\Delta P_{k,t}^{+} - b_k^{+}\Delta P_{k,t}^{+}\theta_k^{+} \tag{25}$$

$$C_{k,t}^{-} = a_k^{-}\left(\Delta P_{k,t}^{-}\right)^2 + b_k^{-}\Delta P_{k,t}^{-} - b_k^{-}\Delta P_{k,t}^{-}\theta_k^{-} \tag{26}$$

In the equation, b_k^{-} and a_k^{-} denote the linear and quadratic coefficients, respectively, for user k cost function related to load reduction. Similarly, b_k^{+} and a_k^{+} correspond to the linear and quadratic coefficients for the cost function associated with load increase. The type parameters, θ_k^{+} and θ_k^{-}, indicate user k propensity to engage in load adjustment, with higher values suggesting a stronger inclination to modify load levels.

3.2.2 Lower-level optimization constraints

(1) Controllable Load Participation Constraints

If participation in demand response increases the user's own benefits, users will voluntarily enter into power adjustment contracts with the load aggregator. Conversely, if participation does not yield additional benefits, users will choose not to participate. This means that the compensation received for power adjustments must not be less than the additional losses incurred by these adjustments. This condition can be expressed as:

$$U_{k,t}^{+} - C_{k,t}^{+} \ge 0 \tag{27}$$

$$U_{k,t}^{-} - C_{k,t}^{-} \ge 0 \tag{28}$$

(2) Controllable Load Power Adjustment Range Constraints

$$\nu_{k,t}^{+}\Delta P_{k,t,\min}^{+} \le \Delta P_{k,t}^{+} \le \nu_{k,t}^{+}\Delta P_{k,t,\max}^{+} \tag{29}$$

$$\nu_{k,t}^{-}\Delta P_{k,t,\min}^{-} \le \Delta P_{k,t}^{-} \le \nu_{k,t}^{-}\Delta P_{k,t,\max}^{-} \tag{30}$$

$$-\Delta P_{\max,k}^{-} \le \sum_{t=1}^{T}\left(\nu_{k,t}^{+}\Delta P_{k,t}^{+} - \nu_{k,t}^{-}\Delta P_{k,t}^{-}\right) \le \Delta P_{\max,k}^{+} \tag{31}$$

In the equation: $\nu_{k,t}^{+}$ and $\nu_{k,t}^{-}$ denote the binary state variables for user k, representing the power increase and decrease during period t. $\Delta P_{k,t,\min}^{+}$ and $\Delta P_{k,t,\max}^{+}$ specify the minimum and maximum permissible load increases for user. k. within period t, respectively. Similarly, $\Delta P_{k,t,\min}^{-}$ and $\Delta P_{k,t,\max}^{-}$ define the minimum and maximum permissible load reductions. $\Delta P_{\max,k}^{+}$ and $\Delta P_{\max,k}^{-}$ indicate the overall maximum allowable load reduction and increase for user k throughout the scheduling period.

(3) Controllable Load Power Adjustment Duration Constraints

$$\sum_{t=\tau}^{\tau+T_{\min,k}^{+}-1}\nu_{k,t}^{+} \ge T_{\min,k}^{+}\left(\nu_{k,\tau}^{+} - \nu_{k,\tau-1}^{+}\right), \tau = 1,\cdots,T - T_{\min,k}^{+} + 1 \tag{32}$$

$$\sum_{t=\tau}^{\tau+T_{\max,k}^{+}}\left(1 - \nu_{k,t}^{+}\right) \ge 1, \tau = 1,\cdots,T - T_{\max,k}^{+} \tag{33}$$

$$\sum_{t=\tau}^{\tau+T_{\min,k}^{-}-1}\nu_{k,t}^{-} \ge T_{\min,k}^{-}\left(\nu_{k,\tau}^{-} - \nu_{k,\tau-1}^{-}\right), \tau = 1,\cdots,T - T_{\min,k}^{-} + 1 \tag{34}$$

$$\sum_{t=\tau}^{\tau+T_{\max,k}^{-}}\left(1 - \nu_{k,t}^{-}\right) \ge 1, \tau = 1,\cdots,T - T_{\max,k}^{-} \tag{35}$$

In the equation, $T_{\max,k}^{-}$ and $T_{\min,k}^{-}$ denote the maximum and minimum time durations required for user k to decrease load power, respectively. Conversely, $T_{\max,k}^{+}$ and $T_{\min,k}^{+}$ specify the maximum and minimum time durations required for increasing load power. The maximum and minimum durations for controllable load power adjustments are as follows (see Equations 32–35). Equation 32 through Equation 35 are conceptually similar to the minimum start-stop time constraints applicable to power generation units.

(4) Constraints on the Frequency of Power Adjustments for Controllable Loads

To prevent excessive and prolonged power adjustments for users with controllable loads, constraints have been imposed on the frequency of such adjustments during the scheduling period, as delineated in Equations 36, 37.

$$\sum_{t=1}^{T-1}\left(\nu_{k,t+1}^{+} - \nu_{k,t}^{+}\right) \le N_{\max,k}^{+} \tag{36}$$

$$\sum_{t=1}^{T-1}\left(\nu_{k,t+1}^{-} - \nu_{k,t}^{-}\right) \le N_{\max,k}^{-} \tag{37}$$

In the equation, $N_{\max,k}^{+}$ and $N_{\max,k}^{-}$ denote the maximum permissible frequencies for increasing and decreasing power,

respectively, for controllable load user k over the entire scheduling period.

(5) Energy Storage Charging and Discharging Constraints

$$\nu_{k,t}^{+} + \nu_{k,t}^{-} \leq 1 \tag{38}$$

Equation 38 indicates that user k will select only one form of load power response, either to reduce or to increase their load.

4 Model solution method

In this study, we employ the Stackelberg game theory to model and address the interaction and decision-making processes between load aggregators and controllable load users. The Stackelberg game model is particularly suitable for such leader-follower scenarios, allowing for detailed analysis and prediction of the strategic interactions between the load aggregator (as the leader) and controllable load users (as the followers) in the electricity market. To account for the nonlinearity and complexity of the problem, we integrate nonlinear programming techniques with genetic algorithms for optimization.

The genetic algorithm generates new populations through operations such as selection, crossover, and mutation, increasing population diversity to prevent premature convergence while continually optimizing strategies throughout the iterative process.

In the model, the load aggregator acts as the leader and is represented by the variable M. Its primary task is to develop demand response pricing strategies to influence market dynamics and user behavior. The monthly operating costs of the load aggregator are calculated using appropriate algorithms and loss functions, and are determined according to Equation 8 for expected marginal E_M calculations. Conversely, controllable load users function as followers, responding to price signals and adjusting their strategies, represented by the variable S. Each controllable load user possesses a set of load adjustment strategies $S = \{S_1, S_2, \cdots, S_R\}$. Through a series of selections, users can choose the most suitable response strategy based on market conditions.

During the strategy selection process, the load aggregator selects the optimal strategy m from the strategy space M and analyzes each controllable load user's optimal decision S_i under the condition m_i. Based on the controllable load user's maximization problem $E_n(m, S)$, the optimal response strategy $V_i(m, S_{in})$ for each user is determined. The load aggregator forecasts and calculates the optimal strategy as S_i^* and solves the decision problem $\max E_M(\max V_i(m), \cdots, V_K(m))$ to obtain $m^* = \text{argmax} E_M(\max V_i(m), \cdots, V_K(m))$. Ultimately, by integrating the controllable load users' response strategies $S_i^* = V_i(m, S_{in})$, we obtain the Nash equilibrium solution S_i^* for the system.

To provide a clearer representation of the model solution process, we have designed a flowchart for the two-level optimization model, as shown in Figure 3. This diagram illustrates the steps from parameter initialization, initial population generation, fitness calculations, to strategy updates and optimization during the iterative process. Given the nonlinearity of the problem, the model utilizes genetic algorithms to solve the Stackelberg leader-follower game model.

The genetic algorithm generates new populations through operations such as selection, crossover, and mutation. First, the roulette wheel selection method is employed to choose high-fitness individuals (with a crossover probability denoted as p_c), followed by single-point crossover to create new individuals, and random mutations (with a mutation probability denoted as p_m) to enhance population diversity and prevent premature convergence. Next, the fitness S_i of the newly generated individuals is evaluated, and it is determined whether the iteration conditions are met.

In the initial population generation and adjustment phase, the load aggregator selects strategies from the strategy space M and analyzes the optimal decision combinations for each available load user $S = \{S_1, S_2, \cdots, S_R\}$. The initial population corresponds to randomly generated initial strategy combinations from the strategy space. Specifically, the initial strategy combinations encompass all potential strategies, with each strategy S_i representing the load response strategy selected by the load aggregator for a specific user.

If the new fitness results indicate an improvement in strategies, the selection, crossover, and mutation operations continue, calculating the fitness values $V_i(m, S_{in})$ for the new generation. After evaluating the fitness of the new generation, it is determined whether to meet the iteration conditions. If conditions are satisfied, the optimal strategy combination S_i^* is outputted; otherwise, the iteration continues until the termination criteria are met.

5 Analysis of case studies

5.1 Case study parameters

This study focuses on the participation of a load aggregator representing a mixed-use residential and commercial community in the electricity market. The community comprises six mixed-use buildings equipped with photovoltaic panels and houses a total of 200 households. The data used in this study is sourced from the actual load data of the Source-Load Aggregation Interaction Response Platform of Hunan Power Company in August 2023. This data is used to validate the model's effectiveness and practicality.

To comprehensively derive the power usage patterns of the entire community, we conducted a Monte Carlo simulation based on the electricity consumption data of these 200 households, generating scenarios for power deviation coefficients. These coefficients follow a Gaussian distribution with a mean of 0 and a standard deviation of 1.9651. The range for evaluating power deviations in all simulated scenarios is set to ±2%.

In the case analysis, we assume a wholesale electricity price of $60 per megawatt-hour, utilizing the actual load data from the community in August. The parameters involved in the model are listed in Table 1, "Price Range for Peak Shaving Services" and Table 2, "Key Parameters for Load Aggregator Pricing Strategies" These tables display the electricity demand of 100 households on a typical day in August. Figure 4 illustrates the load curve for the entire

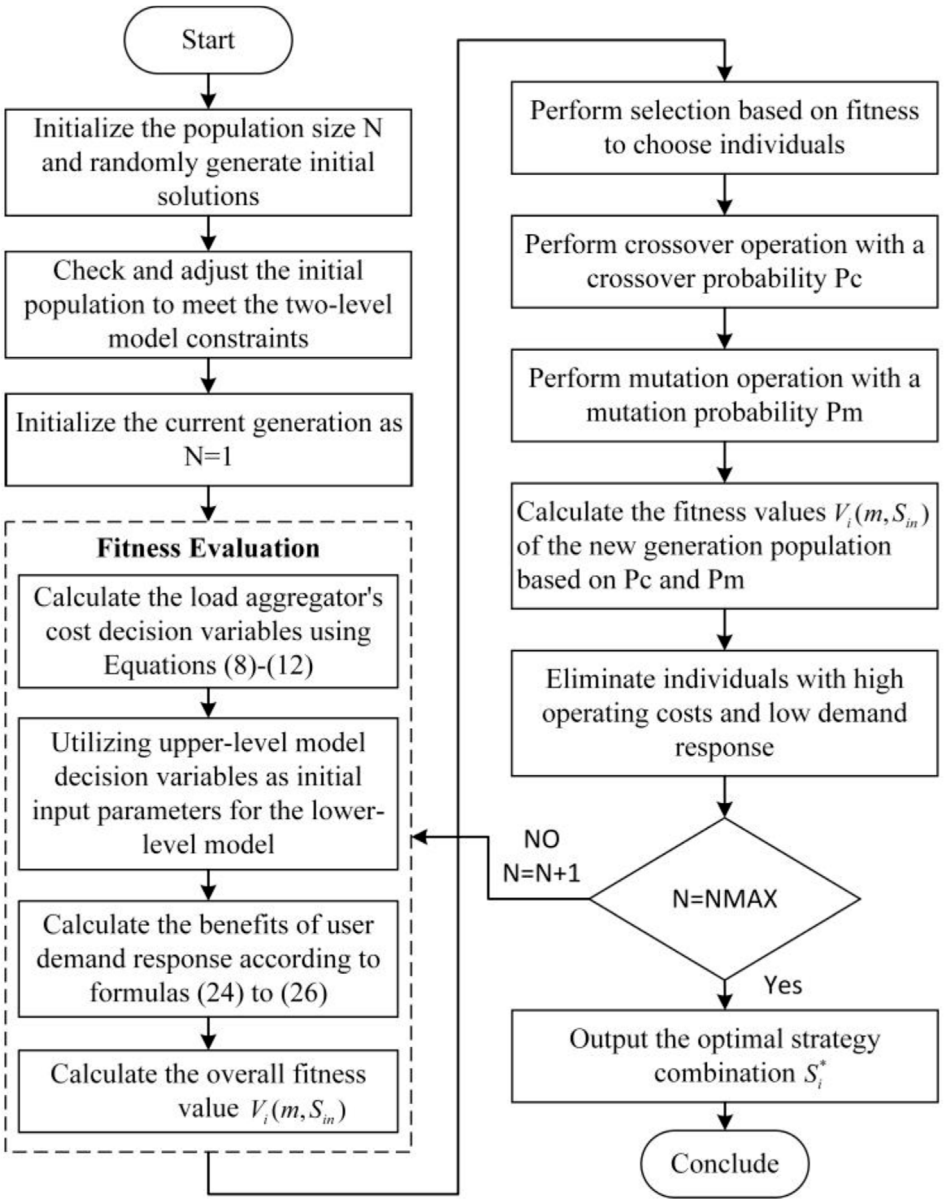

FIGURE 3
Two-level optimization model solution process.

community on a typical day in August, based on the simulation predictions.

To clearly present the calculation results, we assume that the aggregated controllable loads are divided into three types of users: high-cost, medium-cost, and low-cost. The maximum frequency of power adjustments for each type of controllable load is limited to four times within the entire scheduling period. The parameters for the battery energy storage system are set as follows: rated capacity of 200 kWh, rated power of 90 kW, maximum and minimum state of charge coefficients of 0.9 and 0.2, respectively, initial capacity of 100 kWh, charge and discharge efficiency of 95%, and both discharge-to-charge and charge-to-discharge conversion costs of $0.15. The parameters for different types of controllable loads are shown in Table 3.

5.2 Monthly market deviation assessment results under different scenarios

This section compares and analyzes the effectiveness of demand response programs by setting three different operational scenarios. The specific scenarios are described as follows:

1. Scenario 1: Traditional Mode: In this scenario, all loads are traditional, and no demand response programs are implemented. Consequently, deviations in electricity consumption are not effectively managed, leading to higher deviation assessment costs and the highest total cost.
2. Scenario 2: Fixed Compensation Price Mode: In this scenario, the load aggregator employs a fixed compensation price

TABLE 1 Price range for peak shaving services.

Number	Control duration	Price standard	Remarks
1	0 ≤ Control Duration ≤60 min	$0 - $0.7 per kW per event	Maximum $0.7 per kWh
2	60 min ≤ Control Duration ≤120 min	$0 - $1.7 per kW per event	Maximum $0.83 per kWh
3	120 min ≤ Control Duration ≤180 min	$0 - $2.9 per kW per event	Maximum $1 per kWh

TABLE 2 Key parameters for load aggregator pricing strategies.

Parameter Category	Parameter	Value
Deviation Assessment Range	Range	±2%
Wholesale Electricity Price	Price	$60/MWh
Battery Energy Storage System Parameters	Rated Capacity	200 kWh
	Rated Power	90 kW
	State of Charge Coefficient	0.9 (maximum), 0.2 (minimum)
	Initial Capacity	100 kWh
	Charge/Discharge Efficiency	95%
	Conversion Cost	$0.15
Positive Deviation Penalty Price	Price	$60/MWh
Negative Deviation Penalty Price	Price	$50/MWh
Positive Deviation Penalty Coefficient	Coefficient	1.2
Negative Deviation Penalty Coefficient	Coefficient	0.8
Distributed PV Feed-in Tariff	Electricity Price	$0.062/kWh
User Load Cost Parameters	Increased Load Power Cost Linear Coefficient	$a_k^+ = 0.5$
	Increased Load Power Cost Quadratic Coefficient	$b_k^+ = 0.1$
	Decreased Load Power Cost Linear Coefficient	$a_k^- = 0.4$
	Decreased Load Power Cost Quadratic Coefficient	$b_k^- = 0.05$

strategy to incentivize controllable loads to mitigate deviations in electricity consumption. This strategy induces a moderate level of user response, partially covering the deviation, resulting in lower overall costs compared to Scenario 1.

3. Scenario 3: Tiered Compensation Contract Mode: This scenario uses a tiered compensation contract to more actively incentivize controllable loads to balance electricity consumption deviations. Due to the highest level of user participation, deviation assessment costs are significantly reduced. Although the duration and frequency of power adjustments for controllable loads are constrained, this scenario achieves the lowest total cost and the most effective deviation mitigation among all scenarios.

Figure 5 illustrates the monthly electricity consumption variations under different scenarios, visually depicting the impact of each scenario on electricity management. Additionally, to gain deeper insights into the effectiveness of different scenarios, we analyzed the outlier data points and found that the tiered compensation strategy excels in managing fluctuating loads, significantly reducing overall deviation costs. This demonstrates that flexible compensation strategies not only motivate active user participation but also enhance system stability.

Table 4 compares the cost situations of load aggregators under different scenarios (see Table 4). From the table, it is evident that Scenario 3, employing a dynamic compensation strategy, performs best in reducing deviation energy and lowering overall costs.

5.3 Revenue analysis under different deviation penalty prices

To explore the impact of different deviation penalty prices on the economic behavior of electricity market participants, this section sets multiple deviation penalty coefficients to assess their effect on the monthly operating costs of load aggregators and the demand response benefits for controllable load users. Additionally, it analyzes how the compensation prices for power adjustments can be modified under these varying penalty prices to optimize market behavior and enhance overall system efficiency.

Figure 6 shows the trend of increasing monthly operating costs for load aggregators as the deviation penalty coefficients rise.

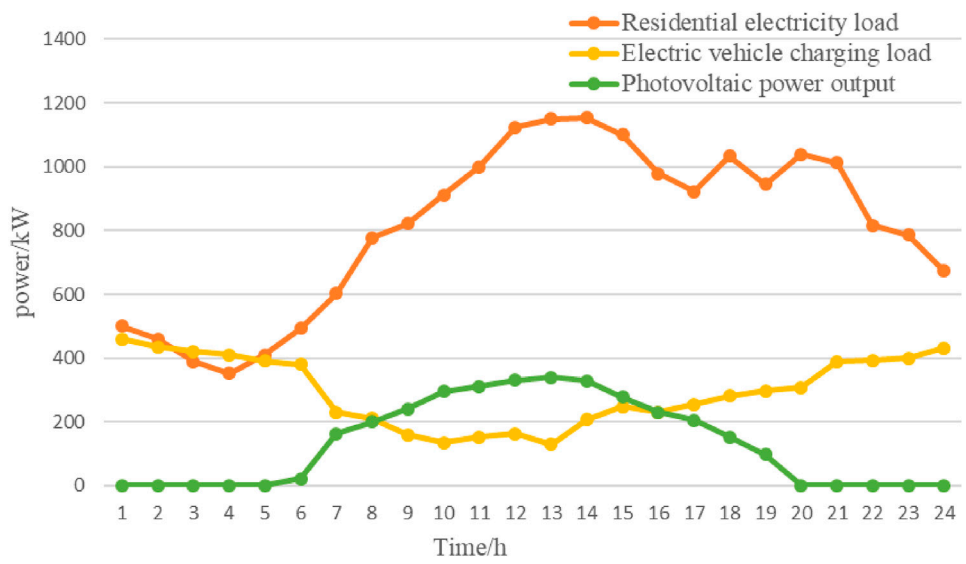

FIGURE 4
Projected load curve for the entire community on a typical day in August.

TABLE 3 Parameters of controllable loads.

Type	High cost	Medium cost	Low cost
Total number of controllable loads	50	70	80
Response range (%)	(0.95,1.0)	(0.9,0.95)	(0.95,0.9)
Adjustment power range (kW)	(90,95)	(80,85)	(75,80)
Compensation rate (%)	(0.4,0.45)	(0.4,0.45)	(0.35,0.38)
Load adjustment range (kW)	(140,165)	(140,165)	(185,205)

TABLE 4 Comparison of load aggregator costs across different scenarios.

Cost type	Scene 1 ($)	Scene 2 ($)	Scene 3 ($)
Market cost of electricity purchase	21,660	19,040	17,040
Tariff adjustment cost	0	2,520	3,020
Penalty for deviation	3,810	3,260	2,860
Total cost	29,040	25,020	21,760

Moreover, as illustrated in Figure 7, user compensation benefits also increase with higher penalty coefficients, reflecting the market's sensitivity to deviations and its response to strategic adjustments.

Tables 5, 6 detail the compensation prices for power reduction and power increase under different deviation penalty coefficients, respectively. The data indicate that as the penalty coefficients increase, both the compensation rate and the price discount rate for electricity show an upward trend. This strategy aims to incentivize users to adjust their electricity consumption behavior, thereby reducing the overall operating costs of the market and enhancing system stability.

As the deviation penalty coefficients increase, the monthly operating costs for load aggregators rise, compelling them to enhance the management of controllable loads and optimize their strategies. This economic pressure motivates load aggregators to actively seek efficient demand response solutions to minimize electricity procurement costs and deviation penalties.

By increasing the compensation prices for controllable loads, users are incentivized to flexibly adjust their electricity usage patterns. This not only helps aggregators control costs but also improves the load regulation capability and stability of the entire power system. Additionally, as compensation prices are adjusted, the participation and benefits of controllable load users increase accordingly.

This dynamic further promotes the application and development of demand-side response technologies, contributing

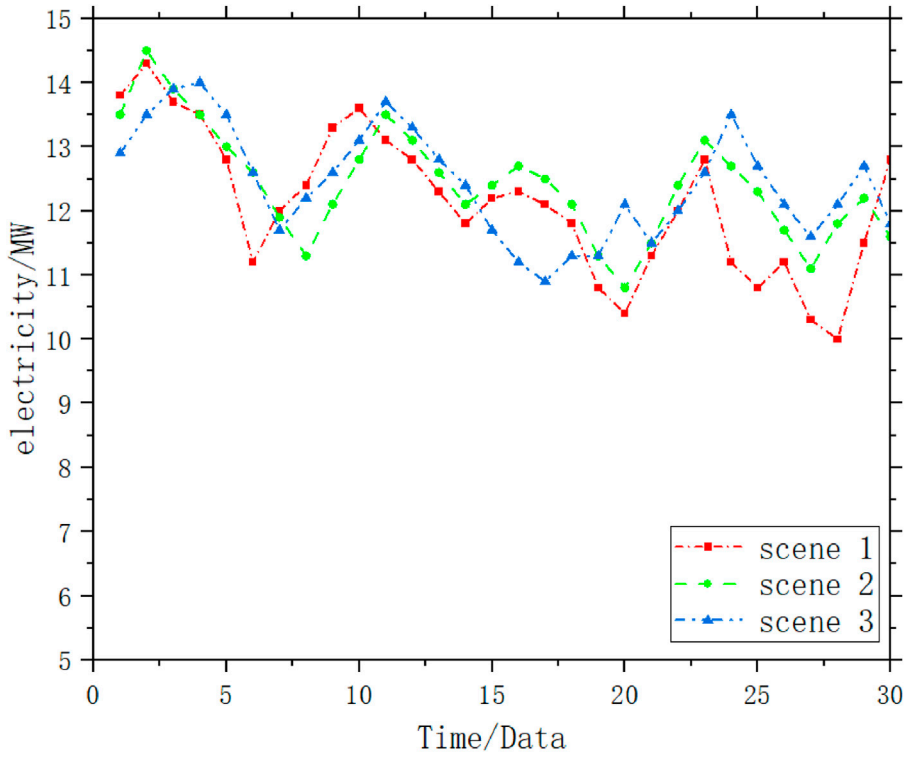

FIGURE 5
Monthly electricity consumption variation curves under different scenarios.

to the dual enhancement of economic and environmental benefits in the electricity market.

6 Conclusion

This paper proposes a segmented multi-option controllable load power adjustment compensation contract based on a game theory framework, aiming to optimize demand response strategies in the long-term market environment prior to the spot market. This approach treats demand-side controllable loads as dispatchable resources. By establishing segmented compensation contracts between load aggregators and users, the method gains control over the operation of controllable load equipment, optimizing their operation to reduce the discrepancy between bid volumes and actual power consumption.

1. Economic Win-Win Objective: To achieve an economic win-win situation for both load aggregators and controllable load users, this study constructs a 1-K type Stackelberg leader-follower game model. This model thoroughly considers the economic benefits of both load aggregators and controllable load users, reducing the operating costs of the load aggregators while enabling controllable load users to gain economic benefits through power adjustments.
2. Design of Segmented Compensation Price Contracts: The segmented compensation price contracts designed in this study are valuable for motivating users to participate in demand response. This not only helps load aggregators formulate more effective demand response pricing strategies but also enhances user participation in demand response by inducing controllable load users to demonstrate demand elasticity, thereby effectively reducing the penalty costs for load aggregators.
3. Monte Carlo Simulation and Optimization: Using the Monte Carlo method, the compensation prices for incentivizing controllable load user power adjustments were optimized based on deviation scenarios generated in typical daily scenarios of monthly transactions. Extending this model to shorter time scales, such as the intraday balancing market, could further smooth out deviations arising from day-ahead market transactions. However, due to the current maturity level of China's electricity market, along with market mechanisms and technological and economic constraints, this study has not delved deeper into the spot market analysis.

This research provides an innovative perspective to optimize demand response strategies in the electricity market and offers practical strategic recommendations for electricity market designers to enhance overall market efficiency and reliability. Future research can explore broader market conditions and additional model application scenarios to further validate and expand the findings of this study. Case studies indicate that segmented compensation pricing strategies significantly reduce the penalty costs for load aggregators by 25% and increase user participation by 30%. These results demonstrate the effectiveness and potential economic benefits of segmented compensation pricing strategies in demand response.

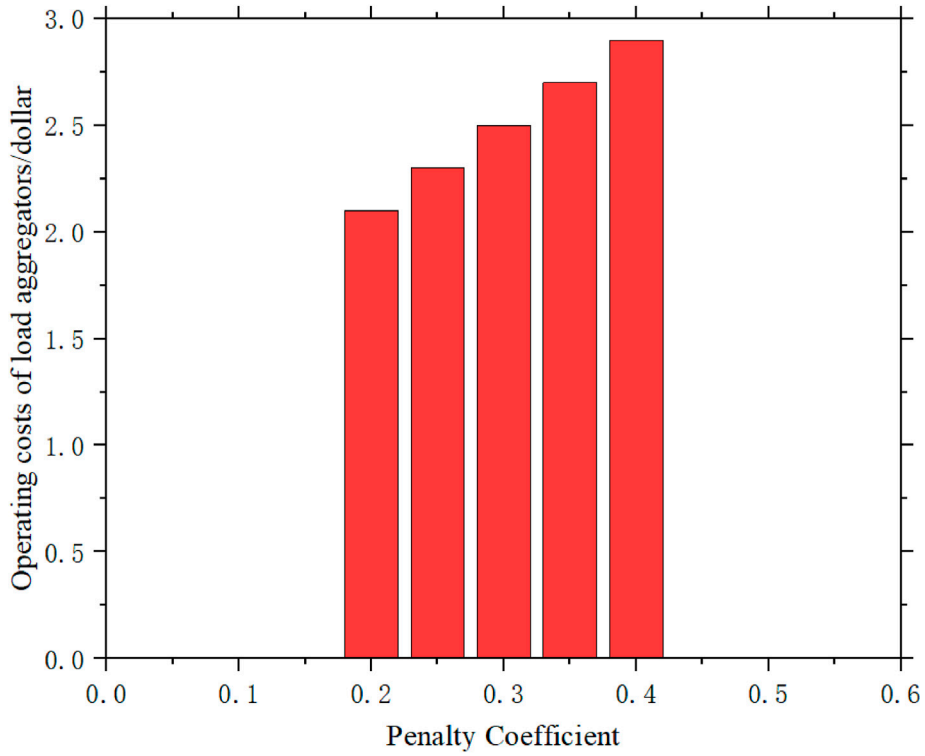

FIGURE 6
Operational costs of load aggregators under different bias penalty electricity prices.

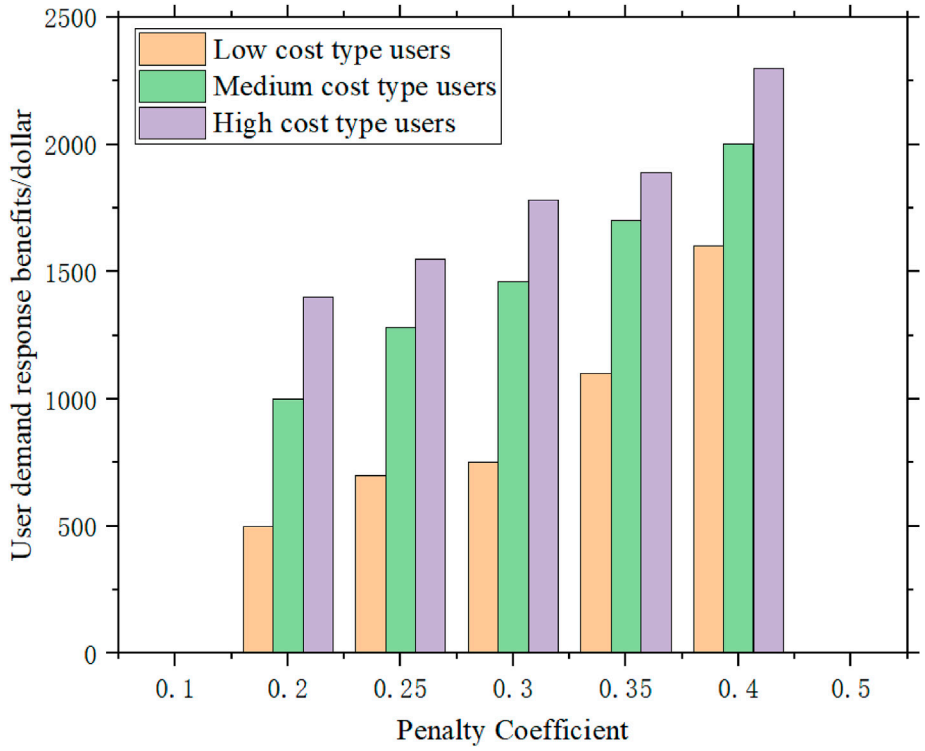

FIGURE 7
User compensation benefits under different bias penalty electricity prices.

TABLE 5 Compensation rates for reduced power under different bias penalty electricity prices.

Penalty Coefficient (ξ)	Electricity Price Compensation Rate(%)
0.20	{6.52, 8.57, 11.53, 14.54, 18.26}
0.25	{7.05, 9.22, 13.51, 17.48, 21.52}
0.30	{8.03, 10.54, 14.05, 18.57, 23.79}
0.35	{9.46, 12.31, 16.08, 21.49, 28.24}
0.40	{10.19, 14.12, 17.53, 24.17, 32.48}

TABLE 6 Compensation rates for increased power under different bias penalty electricity prices.

Penalty Coefficient (ξ)	Electricity price discount rate (%)
0.20	{5.81, 8.04, 10.48, 13.51, 16.52}
0.25	{6.48, 8.54, 11.04, 14.49, 19.05}
0.30	{7.53, 10.02, 13.22, 17.79, 22.65}
0.35	{8.75, 11.47, 15.20, 20.34, 27.51}
0.40	{9.52, 12.90, 16.12, 22.80, 30.75}

4. Future Work: In our future work, we will consider integrating artificial intelligence and machine learning technologies to optimize demand response strategies. Additionally, we will study the economic viability and implementation effects of segmented compensation strategies under different policy environments, providing decision support for policymakers.

Data availability statement

The datasets presented in this study can be found in online repositories. The names of the repository/repositories and accession number(s) can be found in the article/supplementary material.

Author contributions

HY: Conceptualization, Data curation, Formal Analysis, Funding acquisition, Investigation, Methodology, Project administration, Resources, Software, Supervision, Validation, Visualization, Writing–original draft, Writing–review and editing. ZZ: Data curation, Funding acquisition, Software, Writing–original draft. RL: Conceptualization, Funding acquisition, Investigation, Methodology, Validation, Writing–original draft, Writing–review and editing. WZ: Conceptualization, Methodology, Project administration, Writing–original draft.

Funding

The author(s) declare that financial support was received for the research, authorship, and/or publication of this article. This research was supported by the National Natural Science Foundation of China (7217010719 and 72171026); supported by Hunan Provincial Natural Science Foundation of China (2022JJ60103 and 2024JJ8025); funded by the Innovation Fund for Industry-University-Research Cooperation of Chinese Universities - Next-Generation Information Technology Innovation Project (2021ITA10023); and supported by the Hunan Province Science Popularization Special Project (2022ZK4045).

Conflict of interest

The authors declare that the research was conducted in the absence of any commercial or financial relationships that could be construed as a potential conflict of interest.

Publisher's note

References

Bouakkaz, A., Mena, A., Haddad, S., and Ferrari, M. (2020). Efficient energy scheduling considering cost reduction and energy saving in hybrid energy system with energy storage. *J. energy storage* 33, 101887. doi:10.1016/J.EST.2020.101887

Bruninx, K., Pandžić, H., Cadre, H., and Delarue, E. (2020). On the interaction between aggregators, electricity markets and residential demand response providers. *IEEE Trans. Power Syst.* 35, 840–853. doi:10.1109/TPWRS.2019.2943670

Çelebi, O., and Flynn, J. (2020). Priority design in centralized matching markets. *ERN Mark. Struct. Top.* doi:10.2139/ssrn.3382580

Chen, K., Lin, J., and Song, Y. (2019). Trading strategy optimization for a prosumer in continuous double auction-based peer-to-peer market: a prediction-integration model. *Appl. Energy* 242, 1121–1133. doi:10.1016/J.APENERGY.2019.03.094

Ding, Y., and Liu, J. (2017). "Real-time false data injection attack detection in energy internet using online robust principal component analysis," in *2017 IEEE conference on energy internet and energy system integration (EI2)*, 1–6. doi:10.1109/EI2.2017.8245663

Fu, T., Li, K., and Xie, T. (2022). Research on optimal model of generation dispatching for medium and long-term electricity contracts based on CPLEX algorithm. *IEEE 6th Inf. Technol. Mechatronics Eng. Conf. (ITOEC)* 6, 304–308. doi:10.1109/ITOEC53115.2022.9734662

Gong, J., Cheng, J., Qiao, S., Wang, K., Lai, X., Xu, C., et al. (2021). Decomposition method of government authorized contracts considering unbalanced funds. 2021. *IEEE 6th Int. Conf. Comput. Commun. Automation (ICCCA)*, 908–913. doi:10.1109/iccca52192.2021.9666362

Jiang, W., Lin, X., Yang, Z., Tang, J., Zhang, K., Zhou, M., et al. (2023). An efficient user demand response framework based on load sensing in smart grid, *Front. Energy Res.*, 11. doi:10.3389/fenrg.2023.1141374

Jiang, Y., Hou, J., Lin, Z., Wen, F., Li, J., He, C., et al. (2019). Optimal bidding strategy for a power producer under monthly pre-listing balancing mechanism in actual sequential energy dual-market in China. *IEEE Access* 7, 70986–70998. doi:10.1109/ACCESS.2019.2919347

Khodadadi, A., Herre, L., Shinde, P., Eriksson, R., Söder, L., and Amelin, M. (2020). Nordic balancing markets: overview of market rules. *17th Int. Conf. Eur. Energy Mark. (EEM)*, 1–6. doi:10.1109/EEM49802.2020.9221992

Liangyuan, W., Shuyuan, L., Xiaomin, L., and Linyan, W. (2022). "Research on coordination between medium-long-term electricity trade and spot market trade," in *2022 4th international conference on smart power and internet energy systems (SPIES)*, 2165–2170. doi:10.1109/SPIES55999.2022.10082397

Liu, S., Xu, J., Xing, C., Liu, Y., Tian, E., Cui, J., et al. (2023). Study on dynamic pricing strategy for industrial power users considering demand response differences in master–slave game. *Sustainability* 15, 12265. doi:10.3390/su151612265

Liu, S., Yang, Z., Xia, Q., Lin, W., Shi, L., and Zeng, D. (2020). Power trading region considering long-term contract for interconnected power networks. *Appl. Energy* 261, 114411. doi:10.1016/j.apenergy.2019.114411

Lu, T., Zhang, W., Wang, Y., Xie, H., and Ding, X. (2022). Medium- and long-term trading strategies for large electricity retailers in China's electricity market. *Energies* 15, 3342. doi:10.3390/en15093342

Lv, H., He, Y., Hu, L., Chen, S., Ma, R., and Ma, N. (2023). "A multi-market collaborative trading model for load aggregator," in *2023 IEEE/IAS industrial and commercial power system asia (I&CPS asia)*, 1235–1240. doi:10.1109/ICPSAsia58343.2023.10294764

Ma, L., Sun, C., Gao, S., Ma, Y., Ge, X., and Wang, F. (2023). A correction method for customer baseline load estimation considering demand response rebound effect based on equivalent electricity price model. 2023. *IEEE IAS Glob. Conf. Renew. Energy Hydrogen Technol. (GlobConHT)*, 1–6. doi:10.1109/GlobConHT56829.2023.10087836

Nobis, M., Wyrwoll, L., Moser, A., and Raths, S. (2020). "Impact of market-coupling on electricity price modeling in fundamental unit-commitment approaches," in *2020 6th IEEE international energy conference (ENERGYCon)*, 740–743. doi:10.1109/ENERGYCon48941.2020.9236434

Reddy, S., Bijwe, P., and Abhyankar, A. (2015). Real-time economic dispatch considering renewable power generation variability and uncertainty over scheduling period. *IEEE Syst. J.* 9, 1440–1451. doi:10.1109/JSYST.2014.2325967

Wang, L., Chen, J., Peng, K., Zhao, Y., and Zhang, X. (2021). Reward fairness-based optimal distributed real-time pricing to enable supply-demand matching. *Neurocomputing* 427, 1–12. doi:10.1016/j.neucom.2020.11.034

Wang, L., Xu, Q., Li, L., Bo, X., Wang, P., and Jiang, T. (2023a). "Pricing method for deviations in the electricity market taking into account load factor levels," in *2023 IEEE international conference on image processing and computer applications (ICIPCA)*, 1241–1245. doi:10.1109/ICIPCA59209.2023.10257957

Wang, Y., Swaminathan, V., Granger, N., Perez, C., and Michler, C. (2023b). Deep reinforcement learning for power trading. *ArXiv, abs/2301*, 08360. doi:10.48550/arXiv.2301.08360

Watanabe, F., Kawaguchi, T., Ishizaki, T., Takenaka, H., Nakajima, T., and Imura, J. (2018). *Machine learning approach to day-ahead scheduling for multiperiod energy markets under renewable energy generation uncertainty*. IEEE Conference on Decision and Control CDC, 4020–4025. doi:10.1109/CDC.2018.8619775

Xu, B., Wang, J., Guo, M., Lu, J., Li, G., and Han, L. (2021). A hybrid demand response mechanism based on real-time incentive and real-time pricing. *Energy* 231, 120940. doi:10.1016/J.ENERGY.2021.120940

Yang, G., Du, S., Duan, Q., and Su, J. (2022). Deep reinforcement learning-based trading strategy for load aggregators on price-responsive demand. *Comput. Intell. Neurosci.* 2022, 1–14. doi:10.1155/2022/6884956

Yang, H., and Wang, Z. (2024). A false data injection attack approach without knowledge of system parameters considering measurement noise. *IEEE Internet Things J.* 11 (1), 1452–1464. doi:10.1109/JIOT.2023.3288983

Yang, H., Wang, Z., and Qiu, R. C. (2023). Data domain adaptation for voltage stability evaluation considering topology changes. *IEEE Trans. Power Syst.* 38 (3), 2834–2844. doi:10.1109/TPWRS.2022.3185629

Yang, H., Zhang, W., Chung, C. Y., Wang, Z., Qiu, W., and Liang, Z. (2024). "AC false data injection attack based on robust tensor principle component analysis," in *IEEE transactions on industrial informatics*. doi:10.1109/TII.2024.3390389

Zhang, R., Jiang, T., Li, G., Li, X., and Chen, H. (2021). Stochastic optimal energy management and pricing for load serving entity with aggregated TCLs of smart buildings: a Stackelberg game approach. *IEEE Trans. Industrial Inf.* 17, 1821–1830. doi:10.1109/TII.2020.2993112

Zhu, J., Yin, H., Ma, Y., Sui, B., Wang, M., and Yang, K. (2023). Opinions on unbalanced funds in China's electricity market, *Front. Energy Res.*, 10. doi:10.3389/fenrg.2022.1040451

frontiers | Frontiers in Energy Research

TYPE Original Research
PUBLISHED 16 September 2024
DOI 10.3389/fenrg.2024.1422216

OPEN ACCESS

EDITED BY
Yingjun Wu,
School of Electrical and Power Engineering, Hohai University, China

REVIEWED BY
Yulin Chen,
Hainan Institute, Zhejiang University, China
Sheng Wang,
University College Dublin, Ireland
Rudrodip Majumdar,
National Institute of Advanced Studies, India
Heping Jia,
North China Electric Power University, China

*CORRESPONDENCE
Yongliang Yin,
scholarscholar@163.com

RECEIVED 23 April 2024
ACCEPTED 26 August 2024
PUBLISHED 16 September 2024

CITATION
Zhou Q, Wu J and Yin Y (2024) Regulation techniques and applications of distributed load resources in urban power grids based on internet of things.
Front. Energy Res. 12:1422216.
doi: 10.3389/fenrg.2024.1422216

Regulation techniques and applications of distributed load resources in urban power grids based on internet of things

Quan Zhou[1], Jiajia Wu[2] and Yongliang Yin[1]*

[1]Economy Research Institute of State Grid Zhejiang Electric Power Company, Hangzhou, China, [2]State Grid Zhejiang Yiwu Power Supply Co., Ltd., Jinhua, China

The power consumption of urban power systems is increasing rapidly with two typical trends: the first one is that the daily peak-valley difference of loads is more significant, and the power supply is tight during peak hours, which threatens the system's safe and stable operation; the second one is that the load energy efficiency in urban power systems is not high, which is the primary source of carbon emission in the power industry. Therefore, reducing the peak power and improving the system's energy efficiency are urgent tasks for enhancing the system's security and achieving the carbon emission goals. The rapid development of the Internet of Things (IoTs) ushers new opportunities for regulating demand-side loads. By analyzing the technical characteristics of load control based on IoTs, this paper investigates the modeling methods of load resources. On this basis, different control and optimization methods of load resources are analyzed and compared thoroughly. Besides, considering that load control is not only related to technical methods but also impacted by incentive strategies, the load control mechanisms under the mature and immature market environments are analyzed. Finally, the research gap and prospect of load regulation are proposed.

KEYWORDS

internet of things, urban power grids, load resources, demand response, regulation techniques

1 Introduction

The rapid increase in electricity consumption in urban power grids has presented two significant trends: firstly, the continuous widening gap between peak and off-peak periods, leading to a tight supply-demand balance during peak hours, which threatens the safe and stable operation of the power grid (Zhou Xiaoxin et al., 2018); secondly, the increasing proportion of new energy sources, which poses higher challenges for the real-time supply-demand balance due to their intermittent output (Sun et al., 2007). Therefore, reducing peak loads in urban power grids and enhancing system flexibility are essential pathways to achieve the power grid's safe, stable, and economically efficient operation (Song et al., 2016). The rapid development of the Internet of Things (IoTs) has enabled broader device connectivity, faster and more reliable data transmission, and enhanced privacy protection for the power system (Hui et al., 2020, Song Y. et al., 2017). It allows for regulating large-scale load resources in the power system to achieve peak shaving, valley filling, and new energy integration at lower costs and higher efficiency (Zhang et al., 2008). The essence of load regulation is to reduce or shift demand-side power consumption,

providing services such as standby, peak shaving, and frequency regulation to the power system (Xue et al., 2007). To ensure a satisfactory user experience and minimize impacts on production and life, load regulation mainly targets load types with energy storage characteristics or transferable characteristics, such as energy storage batteries, electric vehicles, and temperature control loads (Wang Ke et al., 2014). For example, implementing orderly charging based on dynamic time-of-use electricity prices for electric vehicles can assist in peak shaving and valley filling in the power system (Zhiwei et al., 2014). Optimized control strategies for temperature control load clusters can achieve smooth tracking of load aggregation power to set targets, utilizing load resources to achieve system supply-demand balance (Wang et al., 2012).

Based on extensive theoretical research, load regulation technology is also transitioning from pilot verification to large-scale application. For example, the ERCOT electricity market in Texas, USA, has incorporated load regulation resources into the ancillary services market, providing services such as spinning reserves, fast response, and emergency regulation to the system (Yi et al., 2017). Japan has established a megawatt market, allowing demand-side users to participate in load regulation, reducing peak demand for thermal power generation, and increasing the utilization of new energy (Yang, 2015). The European Union has launched the Smart Grid project, using real-time electricity prices to influence end-users' electricity consumption behaviors, assisting in integrating new energy into the power system (Ding et al., 2013). China has also conducted a series of demonstration projects in the field of load regulation, such as constructing a friendly interaction system between urban users and the power grid in Jiangsu Province, tapping into the coordinated regulation capabilities of load resources and generation resources (Hui et al., 2018a). Besides, the commercial buildings are constructed as virtual power plants in Shanghai to participate in peak shaving and valley filling in the power system (Shengchun et al., 2020). Flexible grids in Zhejiang Province are aggregated to promote the local integration of distributed photovoltaics (Zou et al., 2019).

Based on the above literature review, previous research gaps can be summarized as three points. i) Load modeling technology: traditional models only focus on power consumption while failing to comprehensively reflect real-time production processes, dynamic equipment parameters, and product quality, among other factors. ii) Load regulation technology: current load control mainly focuses on electricity, making it challenging to control multi-dimensional load resources such as heat, cold, and natural gas, leading to challenges in coordinating loads in integrated energy systems. iii) Load control for improving system resilience: current research mainly focuses on resilience assessment, unit planning, mobile energy storage resource scheduling, etc., with limited attention to load resources with significant control potential.

This paper discusses the technical characteristics of load resource regulation under the Internet of Things (View on 5G architecture, 2019; G network architecture, 2016; Embrace 5G new world, 2019; Telecom and GridHuawei, 2018; Yilmaz, 2016), including diversification of types (Yi Wang. et al., 2019; Knud, 2014; Hui et al., 2019; Siano, 2014; Shi et al., 2018), refinement of control (Hui et al., 2020), and data privacy protection (Zhou Z. et al., 2018; Leligou et al., 2018; Commercial feasibility analysis of smart, 2019). Besides, this paper investigates the modeling methods of load resources (JU and Ma, 2008; TANG et al., 2007; Yong, 2012; Ju et al., 2020; Yi Ding. et al., 2019; Yayuan et al., 2019; Ahmad et al., 2020; Das et al., 2020; Morello et al., 2018), especially including temperature-controlled loads (Sonderegger, 1978; Lu, 2012; Sun et al., 2016; Wang et al., 2016; Wang Dan et al., 2014; Mathieu and Callaway, 2012; Kirschen et al., 2000; Zhenfang, 2004; Liu et al., 2008; Technology information; Bachao, 2017; Song M. et al., 2017; Shao et al., 2004; Park et al., 2001; Zhang Q. et al., 2016; Hui et al., 2018b) and (Song et al., 2011; Xiang et al., 2015; Luo et al., 2011; Zhang Hongcai et al., 2014; Wang et al., 2019; Zhiwei et al., 2012; Junhua et al., 2010; Jinghong et al., 2012; Hongmei et al., 2015; Liu et al., 2016; Nosair and Bouffard, 2015; Wang et al., 2005; Yaping et al., 2017; Zhang Fang et al., 2014). On this basis, different control and optimization methods of load resources are analyzed and compared thoroughly (Hui et al., 2017; Dong et al., 2015; Bhattacharyya and Crow, 1996; Chu et al., 1993; Laurent et al., 1995; Meng, 2015; Qi et al., 2017; Zhang et al., 2015; Samarakoon et al., 2012; Vrettos et al., 2018; Babahajiani et al., 2018; Singh et al., 2017; Ledva et al., 2018; Li et al., 2020; Jia et al., 2013; Su et al., 2018; Shi et al., 2019; Cai et al., 2019; Zhang et al., 2017; Measurement of electrical and magnetic quantities. C37.118.1-2011, 2011; Douglass et al., 2013; Kaiqiao et al., 2016; Wenting et al., 2016; Bao et al., 2015; Weckx et al., 2014; Yao et al., 2018). Next, considering that load control is not only related to technical methods but also impacted by incentive strategies, the load control mechanisms under the mature (Albadi and El-Saadany, 2008; Xie et al., 2018; Hongtu et al., 2010; Ruan et al., 2013; Nyeng and Ostergaard, 2011; Siano and Sarno, 2016; Ding et al., 2013; Kai et al., 2020; Zhang Ning et al., 2016; Chen et al., 2018; Jian et al., 2017; Wang et al., 2020; Bin et al., 2018; Tai et al., 2016) and immature market environments are analyzed (Zeng et al., 2016; Zeng et al., 2013; Zeng et al., 2015; Zhong et al., 2013; Chen et al., 2017; Hui et al., 2022; Yi Ding et al., 2019). Finally, this paper summarizes the shortcomings of load regulation technology and provides prospects for future research (Rui, 2018; Antiy Institute, 2019; Ju et al., 2019; Qiu et al., 2020; Zhaohong et al., 2020; Bo et al., 2020; Zhang et al., 2019; Pierre, 1987; Chen et al., 2020; Yin et al., 2019).

2 Methodological approach

2.1 Characteristics of load regulation technologies based on IoTs

Information and communication technologies represented by 5G have facilitated the rapid development of the IoT (View on 5G architecture, 2019). First, massive machine communication technology enables large-scale access to load devices in the IoT, with up to 1 million devices per square kilometer (G network architecture, 2016). Secondly, enhanced mobile broadband technology enables fast data exchange between control centers and load devices in the IoT, with transmission speeds of up to 20 Gbps (Embrace 5G new world, 2019). Furthermore, ultra-reliable, low-latency communication technology allows for high-reliability data transmission and instantaneous load control in the IoT, with a data transmission failure rate as low as 10^{-9} fully meeting the 99.999% reliability requirements for load control in power grids (Telecom and GridHuawei, 2018). The data transmission latency

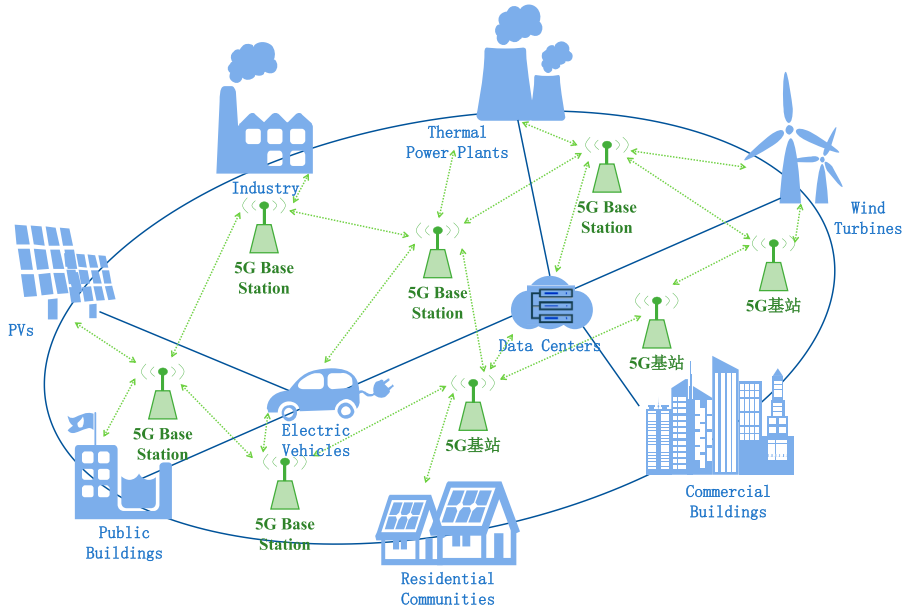

FIGURE 1
Internet of Things-based pluralistic load control.

can be reduced to as low as 1 ms, meeting the millisecond-level precise load control requirements (Yilmaz, 2016). Therefore, the IoT supported by next-generation communication technologies has promoted the rapid development of load control technology. This section discusses the technical characteristics of load control in the IoT from three aspects: diversification of control types, refinement of control, and data privacy protection.

2.1.1 Diversification of load regulation types

Diversification of regulation types has two layers of meaning. The first layer refers to diversifying user types participating in load control. Traditional load control, limited by communication methods and the number of control terminals, mainly targets large-capacity users, such as using fiber optic communication for load control in industrial enterprises and commercial buildings. However, the development of the IoT has led to the widespread deployment of smart meters and remote-control terminals for small and medium-sized users, such as smart sockets, which are rapidly increasing (Yi Wang. et al., 2019). Load control now covers many small and medium-sized users, leading to a more diverse range of user types, as shown in Figure 1 (Knud, 2014).

The second layer of meaning refers to the diversification of services provided to the power system. Traditional load control involves sending instructions from the dispatch department to end users, resulting in inevitable communication delays (Hui et al., 2019). Therefore, load control primarily provides auxiliary services with extended time scales to the power system, such as reserves and peak shaving (Siano, 2014). With the IoT based on next-generation communication technologies, data transmission speeds are fast, especially with 5G's ultra-reliable low-latency communication technology, which can reduce communication latency to the millisecond level. This enables load control to provide a more diverse range of services to the power system, such as frequency regulation and emergency backup (Shi et al., 2018).

2.1.2 Refinement of load regulation

The development of load control refinement can be divided into three stages (Hui et al., 2020). In the first stage, power reduction or transfer is achieved through the interconnection lines between control area grids and the primary grid, and direct disconnection occurs during power shortages. This regional control method cannot consider individual power demands and reduction losses. In the second stage, Home Energy Management Systems enables control over individual electricity users, allowing users to autonomously choose the method, capacity, and period for participating in load control. In the third stage, load control based on the IoT gives users more choices. Users can decide whether each load device participates in control and how it participates. For example, air conditioning loads can be set within a comfortable temperature range, allowing for independent and refined management of loads. This ensures a better electricity consumption experience for users under control.

2.1.3 Data privacy protection

The characteristics of diversification of control types and refinement of control can bring better economic benefits or electricity comfort to a broader range of users. However, a significant obstacle to the large-scale application of load control is the issue of user data security and privacy. The Internet of Things protects the transmission of load data, including software-defined networking technology (Zhou Z. et al., 2018), network function virtualization technology (Leligou et al., 2018), and network slicing technology (Commercial feasibility analysis of smart, 2019). For example, network slicing technology allows operators to construct multiple virtual networks based on a single network physical layer

for different application scenarios, achieving communication isolation between specific business data and enabling customized services and domain slicing management for "dedicated networks." Specifically, through massive machine communication slicing, fine-grained collection of energy usage information for many users can be achieved; through ultra-reliable low-latency communication slicing, real-time control of loads can be achieved (Telecom and GridHuawei, 2018).

2.2 Modeling methods of distributed load resources

The primary issue in load control is establishing accurate and applicable load models and quantifying different loads' adjustability. Traditional load models mainly include static models such as constant impedance-current-power, classical, and comprehensive load models, with model parameters determined through measurement, fault simulation, and statistics (Ju and Ma, 2008; Tang et al., 2007; Yong, 2012). However, these traditional load models primarily describe the electrical characteristics of loads, established for power scheduling and electrical characteristics to support simulation calculations and operational control of power systems without considering the comfort and experience of electricity users. Literature (Ju et al., 2020) defines loads whose electricity consumption can vary within specified ranges or be shifted in different periods as "demand response." Demand response requires considering the electrical characteristics of the load itself and its interactivity, controllability, and comfort of electricity use. Currently, the research objects of load control include water heaters, air conditioners, heat pumps, refrigerators, washing machines, energy storage batteries, electric vehicles, etc. Due to space limitations, this paper mainly introduces two typical load modeling methods: temperature-controlled loads represented by air conditioners and energy storage loads represented by electric vehicles. Air conditioners account for a high proportion of total loads, with significant adjustment potential, and have minimal impact on user electricity comfort during adjustments (Yi Ding. et al., 2019). Electric vehicles are increasing, and their charging and discharging can provide colossal energy storage resources to the power system.

On the one hand, the fast-charging technologies bring more fluctuations to the power systems (Yayuan et al., 2019). On the other hand, battery swapping technologies bring more opportunities to provide long-term charging battery storage for power systems (Ahmad et al., 2020). Besides, electric vehicles have different standards and charging voltage requirements (Das et al., 2020), which bring more regulation potentials on power systems to provide multi-type regulation services (Morello et al., 2018). Therefore, air conditioners represent the load type with the most development potential currently, while electric vehicles represent the load type with the most adjustment capacity in the future.

2.2.1 The first typical load: Temperature-controlled loads

Modeling temperature-controlled loads requires considering the electrical model of the interaction between the load and the power system and the thermodynamic model of the load and its spatial location. Equivalent thermodynamic parameters are the most representative modeling method (Sonderegger, 1978), equivalently representing temperature-controlled loads as equivalent circuits composed of capacitors and resistors, as shown in Figure 2 (Wang et al., 2012).

Where Q is the equivalent thermodynamic power of air conditioning load considers the cooling or heating states; the switch status represents the operating state of the air conditioner; T_iT_o and T_m represents indoor temperature, outdoor ambient temperature, and temperature of indoor objects, respectively, which are all equivalent to different node voltage values; R_1 and R_2 represent the equivalent thermal resistances between the building and outdoor environment, and between objects inside the building, respectively; C_1 and C_2 represent the specific heat capacities of the indoor air and objects, respectively, which are equivalent to capacitance values (Lu, 2012). Based on Kirchhoff's current law, the relationship between current, voltage, resistance, and capacitance in the equivalent thermodynamic parameter model can be expressed as Equations 1, 2:

$$\frac{dT_i}{dt} = \frac{Q}{C_1} - \frac{T_i - T_o}{C_1R_1} - \frac{T_i - T_m}{C_1R_2} \tag{1}$$

$$\frac{dT_m}{dt} = \frac{T_i - T_m}{C_2R_2} \tag{2}$$

where parameter Q is the cooling capacity from the air conditioning system. It is generally calculated by the operating power P and the Coefficient of Performance (COP), which can be expressed as $Q(t) = P(t) * COP$.

In addition to the equivalent thermodynamic parameter model for temperature-controlled loads, literature (Sun et al., 2016) proposes an exponential model describing the dynamic characteristics of a typical water heater, achieving peak shaving and valley filling in the power system through aggregated control of water heater demand response. Literature (Wang et al., 2016) presents an economically driven ice storage load model, participating in demand response in the medium to long-term electricity market environment. Literature (Wang Dan et al., 2014) establishes a temperature-controlled load model that considers user comfort constraints, aggregates temperature-controlled loads into energy-efficient power plants to participate in dynamic power system regulation and achieves the same objectives as conventional power plants. Literature (Mathieu and Callaway, 2012) uses a Markov chain model to describe the state change process of aggregated temperature-controlled loads and uses Kalman filtering technology for joint estimation of parameters and states, accurately tracking the operating power of the temperature-controlled load model. Literature (Kirschen et al., 2000; Zhenfang, 2004; Liu et al., 2008) establishes an elasticity matrix describing user electricity behavior based on the price elasticity coefficient in economics. The self-elasticity and cross-elasticity coefficients describe the amount of electricity adjustment for the user in the current and other periods, respectively, and the elasticity matrix can represent the mutual influence of electricity loads at different times.

Furthermore, with the advancement of power electronics technology, the market share of variable-frequency air conditioners equipped with rectifier-inverter devices is rapidly expanding, surpassing conventional fixed-frequency air conditioners in sales in China (Technology information). The

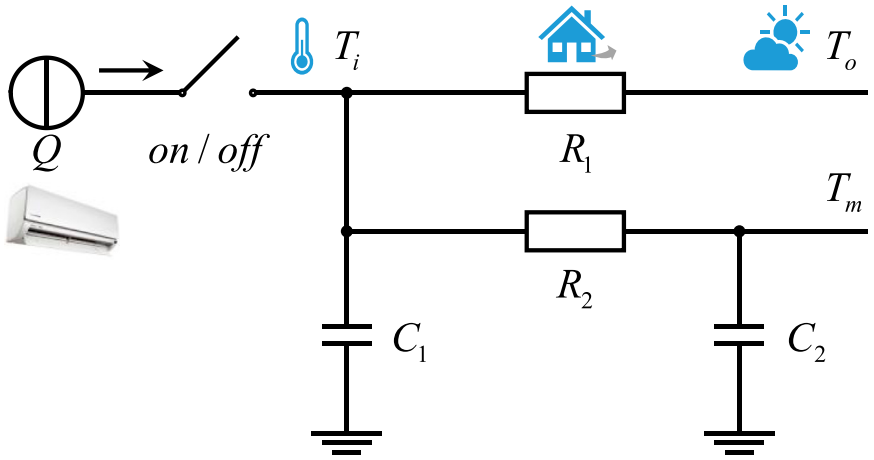

FIGURE 2
Model of thermostatically controlled loads.

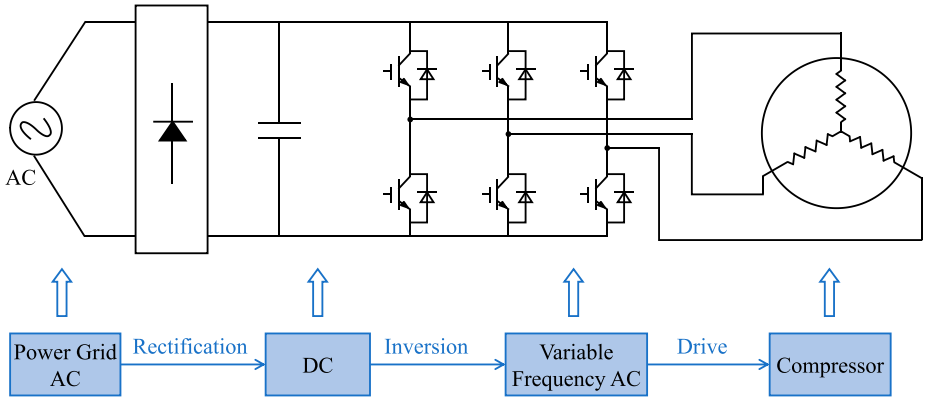

FIGURE 3
The operating principle of variable frequency air conditioners.

main difference between variable-frequency air conditioners and fixed-frequency air conditioners lies in the compressor's control mode, as shown in Figure 3 (Bachao, 2017).

The compressor of a fixed-frequency air conditioner has only two operating modes, on/off, with the operating power switching approximately between rated power and zero power, maintaining the indoor temperature within a specific range. In contrast, the compressor speed of a variable frequency air conditioner can be continuously adjusted through a frequency converter, making it more suitable for participating in dynamic responses of the power system. Literature (Song M. et al., 2017) and (Shao et al., 2004) establish variable frequency air conditioner models based on simulation methods and experimental data, proving their continuous adjustment characteristics. Literature (Park et al., 2001) analyzes the relationship between the operating performance of variable-frequency air conditioners and the compressor operating frequency, cooling capacity, and cooling efficiency ratio. Literature (Zhang Q. et al., 2016) constructs a dedicated, intelligent testing platform to compare the operating characteristics of variable-frequency air conditioners and conventional fixed-frequency air conditioners, analyzing their long-term operation, dynamic operation, startup, and shutdown processes. The results show that variable-frequency air conditioners can reach the set temperature indoors more quickly and have higher energy efficiency. Literature (Hui et al., 2018b) incorporates the variable frequency air conditioner model into the dynamic response process of the power system, considering the inertia element of compressor adjustment, making the variable frequency air conditioner cluster equivalent to traditional generator units participating in power system frequency regulation. Therefore, variable frequency air conditioners participating in load control are more flexible, have faster response speeds, and have minimal impact on user comfort.

2.2.2 The second typical load: Electric vehicles

The physical model parameters of electric vehicles mainly include battery capacity B_i, state of charge S_i, battery charging/discharging power $P_{c,i}P_{d,i}$, and battery charging/discharging

efficiency $\eta_{c,i}\eta_{d,i}$ (Song et al., 2011). Based on the above parameters, the charging/discharging model of electric vehicles can be obtained as the Equation 3:

$$S_i(t+1) = \begin{cases} S_i(t) + P_{c,i} \cdot \eta_{c,i} / B_i, P_{c,i} > 0 \\ S_i(t), P_{c,i} = P_{d,i} = 0 \\ S_i(t) - P_{d,i} \cdot \eta_{d,i} / B_i, P_{d,i} > 0 \end{cases} \quad (3)$$

Furthermore, the electric vehicle model also needs to consider constraints on charging/discharging power and battery capacity (Xiang et al., 2015), expressed as the Equation 4:

$$\begin{cases} 0 \le P_{c,i} \le P_{c,i}^{\max} \\ 0 \le P_{d,i} \le P_{c,i}^{\min} \\ S_i^{\min} \le S_i \le S_i^{\max} \end{cases} \quad (4)$$

Literature (Luo et al., 2011) proposes a charging load calculation model for different types of electric vehicles based on their different electricity usage behaviors. Literature (Zhang Hongcai et al., 2014) presents a spatiotemporal distribution-based electric vehicle charging load prediction model considering electric vehicles' driving and parking characteristics. Based on a single electric vehicle physical model, literature (Wang et al., 2019) constructs a large-scale aggregation state space model for electric vehicles, accurately describing the impact of heterogeneous charging characteristics and random driving behaviors on the capacity of electric vehicles to participate in power system frequency regulation. Literature (Zhiwei et al., 2012) establishes an electric vehicle charging station model and proposes an ordered charging model considering user travel demand and grid load levels to improve the economic benefits of charging stations. Literature (Junhua et al., 2010) constructs a probability model for the random charging and discharging of electric vehicles, jointly considering the random output of wind turbines, achieving the minimum total generation cost economic dispatch of the power system. Literature (Jinghong et al., 2012) establishes a two-stage constant current-constant voltage charging model for electric lithium batteries. It proposes an aggregation model for electric vehicle charging stations in residential areas based on the Poisson distribution. Literature (Hongmei et al., 2015) constructs an electric vehicle charging and discharging model. It proposes a microgrid energy storage capacity optimization operation method based on mixed-integer second-order cone programming, achieving ordered charging and discharging scheduling of electric vehicles and balanced support for microgrids. Literature (Liu et al., 2016; Nosair and Bouffard, 2015; Wang et al., 2005; Yaping et al., 2017; Zhang Fang et al., 2014) establishes a dynamic capacity degradation model for electric vehicle batteries and proposes an optimized scheduling model for electric vehicles considering charging and discharging losses, achieving multiple objectives optimization such as charging station profits, user benefits, and travel demand optimization.

3 Typical load control methods

Compared with the regulation capacity provided by traditional generating units, the regulation capacity provided by individual loads is minimal, requiring the control of large-scale loads. Load resources are geographically dispersed, with significant differences in operating characteristics, and they need to ensure diverse individual user electricity demands. Based on the existing control architecture, load control methods can be divided into three types: centralized, distributed, and hybrid.

3.1 Centralized control method

The centralized control method has a clear structure and can achieve real-time solid consistency control of load clusters, making it the current primary load control method. Literature (Hui et al., 2017) proposed a centralized control method for adjusting the set temperature of temperature-controlled loads, changing the operating power within the range users allow to provide operational reserves for the power system. Literature (Dong et al., 2015) adopted a centralized control architecture. It proposed an improved weighted coefficient queuing algorithm, considering the individual preferences of users participating in the system's dynamic response, achieving direct control of temperature-controlled loads such as air conditioners and heat pumps. Literature (Bhattacharyya and Crow, 1996) proposed a centralized control method based on fuzzy logic, which improves the dynamic response performance of loads and user satisfaction and reduces user electricity costs. Literature (Chu et al., 1993) used dynamic programming to control loads directly, targeting the minimum load reduction to solve the problem of insufficient generating capacity during peak summer loads in power systems. Literature (Laurent et al., 1995) integrated the advantages of linear programming and dynamic programming, proposing an optimization method based on column generation, which meets the requirements of electric water heaters while participating in peak shaving of power systems. Literature (Meng, 2015) proposed a centralized frequency control strategy for temperature-controlled loads and coordinated with electric vehicles to participate in power system frequency regulation. Literature (Qi et al., 2017) constructed a temperature-controlled load model for the cluster of electric water heaters. It proposed a new serialization control strategy to provide frequency control shedding auxiliary services to the power system.

However, centralized control methods also have drawbacks. For example, there are delays in sensing measurement, signal transmission, operation calculation, and terminal execution, leading to lag in load control (Zhang et al., 2015). Literature (Samarakoon et al., 2012) established a hardware and software platform to test communication delays during load direct control processes. The results showed that the load could eventually be disconnected, but the communication delay was between 3.3 and 4.6 s. Literature (Vrettos et al., 2018) conducted experiments on commercial buildings participating in power system frequency regulation, proving that communication delays cannot be ignored and require about 20 s to eliminate their effects. Currently, the primary methods to solve communication delays in centralized control are load state estimation and design feedback controllers. Literature (Babahajiani et al., 2018) proposed a fuzzy proportional-integral controller connecting generating units with adjustable loads. When delay-induced success rate fluctuations occur, the generating units can receive fluctuation signals and change their operating states, reducing the impact of delays. Literature (Singh et al., 2017)

linearized communication delays using the Padé approximation method and quantified the effects of communication delays on power fluctuations. Literature (Ledva et al., 2018) proposed a stochastic predictive controller and Kalman filtering state estimation method to reduce the impact of communication delays.

3.2 Distributed control method

Compared with centralized control, distributed control has better scalability, privacy, and reliability and is suitable for controlling numerous and geographically dispersed loads. However, distributed control has higher requirements for communication networks, data transmission, and terminal computing capabilities, and the development of IoT technology has promoted the application of distributed control in load control fields.

Literature (Li et al., 2020) proposed a distributed consistency control algorithm considering time-coupled characteristics, achieving robust control of large-scale load resources in scenarios with partial information loss and theoretically proving the convergence and optimality of this method in load control. Literature (Jia et al., 2013) took refrigerators as typical temperature-controlled loads. It proposed a distributed control strategy based on system frequency fluctuation amplitude and user participation level as decision metrics, dynamically adjusting the refrigerator's operating cycle to maintain the stable operation of microgrids in islanded states. Literature (Su et al., 2018) proposed a dispersed active power control strategy for large-scale temperature-controlled load groups by solving the coupled Fokker-Planck equation probability model, achieving load response in power system emergencies. Literature (Shi et al., 2019) separately proposed load-distributed control methods based on stable recovery technology, achieving primary and secondary frequency control for temperature-controlled loads. Literature (Cai et al., 2019) and (zhang et al., 2017), respectively, based on deep learning load prediction technology and load self-learning coordinated control technology, ensuring load distributed control while maintaining user comfort. Therefore, distributed control methods generally install terminal controllers on the load side to monitor parameters such as local system frequency deviation for load control, avoiding the communication delay issues generated in centralized control. However, compared with the measurement devices (phasor measurement unit, PMU) in centralized control (Measurement of electrical and magnetic quantities. C37.118.1-2011, 2011), the measurement accuracy of control terminals is lower, leading to control deviations (Douglass et al., 2013).

Note that the local control method is also a kind of method, which is a general concept by using the local or edge control devices. In this paper, the distributed control method is a kind of local control method by using the edge control devices and exchanging operating states with neighboring devices.

3.3 Hybrid control method

The hybrid control method combines the advantages of centralized and distributed control, ensuring efficient control and high consistency of load clusters while improving system scalability and responsiveness. However, the cost of the control system is relatively high. Literature (Kaiqiao et al., 2016) proposed an ordered charging layered control strategy for electric vehicles. The main control center obtains the charging load guidance curve through a two-stage optimization model of peak shaving and valley filling. Each secondary control center selects a centralized or distributed control strategy to follow the charging load. Literature (Hui et al., 2019) proposed a load hybrid control architecture based on dual-end measurement and retrospective correction. It uses PMUs to monitor power system frequency deviations as accurate values. Then, through terminal controllers monitoring local frequency deviations and combining with precise historical data sent by PMUs, real-time correction of local measurements is performed, improving load control accuracy. The control center sets the load response threshold in advance, avoiding real-time communication and eliminating control delays.

Additionally, literature (Wenting et al., 2016) proposed a hybrid control architecture for non-ideal communication states such as packet loss and error codes, aggregating loads such as electric heat pumps as a virtual power plant to participate in dynamic regulation of power systems, as shown in Figure 4. Literature (Bao et al., 2015) and (Weckx et al., 2014) designed a hybrid control method to involve temperature-controlled loads in system frequency regulation. By setting predetermined frequency response thresholds and minimum shutdown times for temperature-controlled loads, they achieved smooth regulation of temperature-controlled load aggregation groups, reducing power system frequency deviations and oscillations. Literature (Yao et al., 2018) proposed a hybrid dual-layer control architecture based on virtual automatic power generation control and distributed control, increasing the adjustable capacity of temperature-controlled loads to accommodate many renewable energy sources.

4 Market mechanism of load regulation

4.1 Load regulation mechanisms in mature markets

Load control involves technical issues such as modeling and control and economic considerations. Like power generation units having regulation costs, load control also involves market economic issues. Currently, load control mechanisms can be categorized into price-based and incentive-based, as shown in Figure 5 (Albadi and El-Saadany, 2008). Price-based mechanisms influence users' electricity consumption by varying electricity costs during different periods, mainly aiming to increase system revenue or reduce generation costs. Therefore, price-based mechanisms are market-oriented load control models (Xie et al., 2018), including time-of-use pricing, real-time pricing, and peak pricing. Incentive-based mechanisms require users to sign contracts in advance with fixed or time-varying subsidies, aiming to reduce electricity consumption during peak loads and ensure system stability (Hongtu et al., 2010). Thus, incentive-based mechanisms

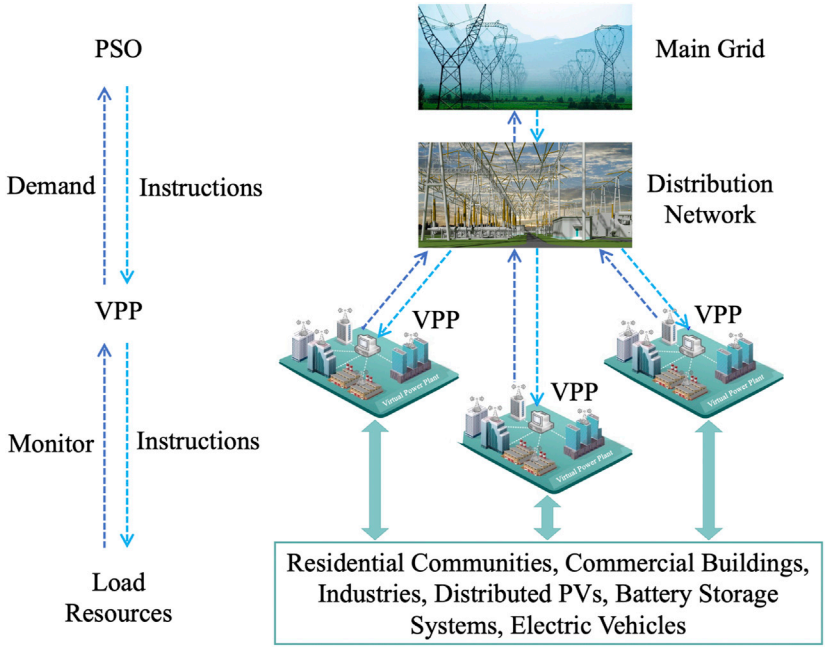

FIGURE 4
Structure of virtual power plants.

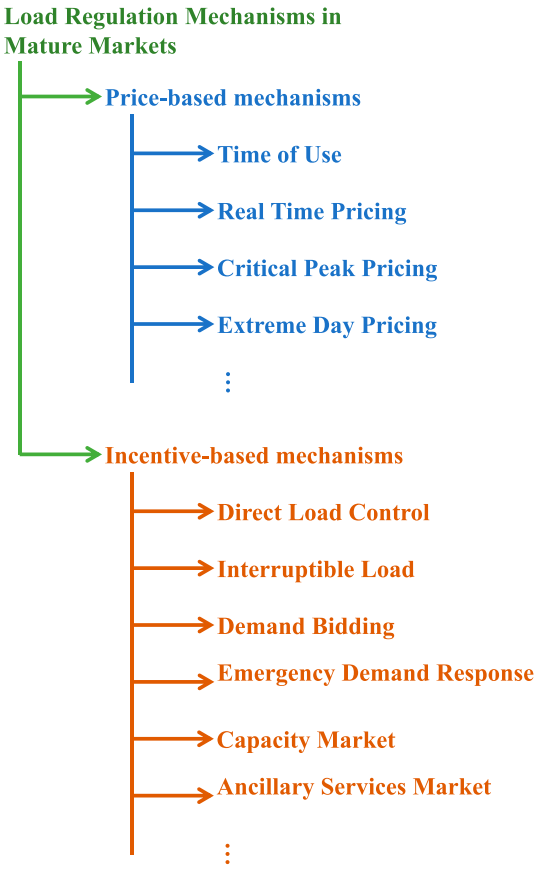

FIGURE 5
Load regulation mechanisms in mature markets.

ensure system stability, including interruptible loads, demand-side bidding, emergency demand response, and others (Ruan et al., 2013).

The IoT has facilitated broader device connectivity in the power system, enabling small and medium-sized users to participate in the load control market. Literature (Nyeng and Ostergaard, 2011) constructed terminal controllers, data interfaces, and communication systems to enable small users to respond to dynamic electricity prices, reducing user electricity costs by approximately 7%. Literature (Siano and Sarno, 2016) studied distribution network operators participating in real-time electricity markets and used marginal electricity prices to influence small users in adjusting temperature-controlled loads, reducing system operation costs. Literature (Ding et al., 2013) analyzed the Ecogrid EU project, a major innovative grid pilot project in the EU, where smart meters and electricity data monitoring devices were installed for small users. Real-time electricity prices influenced user electricity consumption, demonstrating that users can assist power systems in integrating more renewable energy.

Furthermore, the widespread deployment of IoT-enabled smart terminals has led to the application of blockchain technology in load control market mechanisms, ensuring faster and more reliable data transmission and enhanced privacy protection (Kai et al., 2020, Zhang Ning et al., 2016). Literature (Chen et al., 2018) designed a decentralized trading system based on blockchain for distributed adjustable load resources. Literature (Jian et al., 2017) proposed a multilateral trading mechanism for distribution grid markets based on smart contracts, enabling real-time local transactions of distributed generation and load resources, eliminating deviations between operating power and planned quantities.

Literature (Wang et al., 2020) proposed an electric vehicle charging rights trading mechanism based on blockchain, facilitating load distribution among different charging stations and ensuring the safe operation of transmission and distribution equipment. Literature (Bin et al., 2018) proposed a multilevel bidding mechanism in a non-trust environment, achieving effective trading of adjustable loads while protecting user privacy. Literature (Tai et al., 2016) focused on multi-energy systems and constructed a transaction system based on heterogeneous blockchain technology, enhancing market transaction security.

4.2 Load control mechanisms in non-mature markets

Many power systems worldwide need more mature market models, making it challenging to implement load control even by installing intelligent meters and terminals. Taking China as an example, the government determines the electricity prices for both power generation units and users through catalog prices, giving little decision-making power to the power generation side regarding grid prices. Users must accept the prices set for their category (Zeng et al., 2016). Therefore, users need more motivation in non-mature markets to participate in load control.

Currently, in these unified pricing markets, most load control projects are based on administrative measures with limited consideration for user demands, resulting in relatively unfair treatment for users (Zeng et al., 2013). In recent years, power companies have compensated users after load shedding, but these compensations are usually fixed prices that do not reflect real-time market costs (Zeng et al., 2015). Therefore, compared to mature markets with open competition, power companies in non-mature markets cannot directly implement price or incentive mechanisms (Yi et al., 2017). Inspired by the widespread use of coupons in the industrial sector, literature (Zhong et al., 2013, Chen et al., 2017) proposed a load control market strategy based on coupons. In this strategy, after electricity users voluntarily participate in response projects, they receive corresponding coupon rewards. The specific execution involves a real-time iterative bidding framework where an aggregator provides coupon face values to end users, who then submit load adjustment quantities based on these values. The aggregator optimizes the face values to maximize revenue and publishes new coupon face values to users in a cyclic process, eventually determining coupon face values and response capacity.

However, small and medium-sized end users (e.g., residential users) need more time or expertise to submit load adjustment quantities accurately. Most residential users need to be aware of their load power during different periods and are unlikely to accurately give feedback on load adjustment quantities to aggregators. To address this issue, the national critical R&D program "Friendly Interaction System Between Urban Users and Power Grid Supply and Demand" proposed a demand response points incentive model, fully considering the operability of users and power grid enterprises (Hui et al., 2022). In this model, users receive points notifications every 15 min, with positive points indicating an increase in points for electricity usage during that period and negative points marking a decrease (Yi Ding et al., 2019). Positive points typically occur during low load periods, encouraging users to increase electricity usage, while negative points occur during peak load periods, enabling users to decrease electricity usage. Points are settled monthly, and users with a positive point total can exchange them for corresponding reward money. In contrast, users with an opposing point total have their points reset to zero, avoiding increased electricity costs for users during the demonstration phase and alleviating user concerns about participating in load control. The positive and negative points market strategy reduces the difficulty of user participation in load control, respects users' autonomous choices in participating in adjustments, and is a beneficial supplement to electricity price policies in non-mature markets.

5 Limitations and prospects of load regulation

5.1 Limitations of load regulation technology

5.1.1 Load modeling technology

As the scale of load control increases, the accuracy of control capacity becomes increasingly crucial for the safe operation of power systems, necessitating the establishment of accurate load models. However, current load models based on classical models or historical statistical data need help to describe diverse loads' real-time states and operating conditions, resulting in delays or even failures in load response. Taking industrial loads as an example, traditional models only focus on power consumption. At the same time, it fails to comprehensively reflect real-time production processes, dynamic equipment parameters, and product quality, among other factors. Dispatching authorities may issue commands when equipment cannot respond, leading to response failures. Therefore, load models that can interact with load entities in real-time must be constructed, comprehensively describing the operational states throughout the entire lifecycle of loads to achieve an accurate assessment of load control capabilities.

5.1.2 Load regulation technology

Existing load control primarily involves direct switching or adjusting power output. However, under the Internet of Things (IoTs), load resources include small and medium-sized users' loads with small capacities and high uncertainties, compounded by operating time, space, and load types. Ensuring user comfort during control processes is challenging, making it difficult to apply traditional control methods uniformly.

Furthermore, with the deep coupling of electricity with heat, cold, natural gas, distributed energy, and other forms of energy, the connotation of load control is continuously expanding. Leveraging the conversion and complementarity of different energy forms can uncover more extensive and in-depth control potentials at the comprehensive energy system level. However, current load control mainly focuses on electricity,

making controlling multi-dimensional load resources such as heat, cold, and natural gas challenging. This leads to challenges in coordinating loads in integrated energy systems.

5.1.3 System resilience by regulating loads

Power systems are susceptible to natural disasters and human attacks, such as Typhoon Hato in 2017, causing widespread blackouts in Macau and other cities, and the 2019 blackout in Venezuela due to a cyberattack (Rui, 2018, Antiy Institute, 2019). In this context, resilient power systems emerged, referring to the ability to prevent, withstand, respond to, and quickly recover from extreme events (Ju et al., 2019). Resilient power systems primarily address small probability, high-loss extreme events beyond the traditional "three lines of defense" framework (Qiu et al., 2020).

Research on resilient power systems focuses on natural disasters like typhoons and floods, as well as human-made disasters like cyberattacks. The stages of accidents include primary systems like transmission and distribution lines, transformers, and secondary systems like communication networks and sensing devices (Zhaohong et al., 2020). However, current research mainly focuses on resilience assessment, unit planning, mobile energy storage resource scheduling, etc., with limited attention to load resources with significant control potential. Addressing extreme events that are low-probability in power systems through unit construction or energy storage configuration is costly. Utilizing existing loads as adjustment resources for extreme events is cost-effective with large capacities. For example, some insignificant loads can be shed at some extremely dangerous or urgent conditions. Additionally, due to the low probability of extreme events, it will not frequently impact user energy consumption. However, specific research in this aspect still needs to be completed.

Given the limitations of load control technology, the following prospects are outlined from three perspectives.

5.2 Prospects of load regulation technology

5.2.1 Digital twin-based load modeling technology

The development of the Internet of Things (IoTs) has expanded the application of digital twin technology to load modeling (Bo et al., 2020). Digital twins can leverage real-time monitored load data from the IoT to establish mechanical and data-driven models of loads. These models can then be used through simulation software to precisely describe, diagnose, and predict load entities (Zhang et al., 2019).

Digital twin technology inherently suits load modeling, enabling a bidirectional mapping between physical load objects and digital spaces. It accurately simulates multi-dimensional characteristics of loads, such as structure, state, and temporal aspects. Additionally, with the scalable nature of digital twins, dynamic replacement and integration of loads at multiple physical, hierarchical, and scale levels can be achieved. However, large-scale application research based on IoT and digital twin technology in load control still needs to be improved, necessitating further research on precise mapping of loads based on digital twins, virtual-real dynamic interactions, software-defined states, intelligent intervention operations, and other related technologies (Pierre, 1987).

5.2.2 Data-driven adaptive load regulation technology

Adaptive control technology is not new to power systems and has been applied in fields like generator excitation control and frequency control since the last century (Chen et al., 2020). With the development of IoT and the participation of various energy resources such as electricity, heat, cold, and natural gas in system control, further research is needed on applying adaptive control technology in integrated energy systems. This includes constructing control methods based on energy types and load endowments to tap into the potential of different energy forms of loads (Yin et al., 2019). Researching data-driven model-free adaptive control technology can achieve adaptive control of multi-input-output, nonlinear, and large time-delay energy types of load resources. Furthermore, considering the large scale of future load control resources, research on IoT-based distributed adaptive control of loads, edge computing, and other technologies is needed to reduce data communication requirements for large-scale load control, thereby enhancing network communication and load control reliability.

5.2.3 Enhancing system resilience with load regulation technology

In an IoT environment, the potential of load control can be explored in three stages: prevention, response, and recovery, to improve the system's adequacy to extreme events and the speed of recovery after events.

In the prevention stage, research on abnormal system monitoring, accident prediction, impact mechanisms, risk assessment, and load control strategies is needed to enhance the system's disaster warning capabilities. In the response stage, research on fine-grained identification of loads is necessary to identify critical loads and prioritize their power supply [126]. Additionally, research on optimizing the scheduling of loads such as electric vehicles can serve as temporary power sources to improve system adequacy. In the recovery stage, research on operating control strategies for black-start power sources on the load side is essential, along with load supply level recovery methods under limited monitoring data, to maximize system recovery speed, business production value, and user electricity experience.

6 Conclusion

Starting from the background of the high proportion of new energy power systems and the rapid development of the Internet of Things, this paper discusses the development opportunities and enormous potential of load control. This paper outlines the technical characteristics of load control under the IoT and studies the modeling methods of loads and methods for quantifying control capabilities. Based on this, this paper conducts an in-depth comparative analysis of control strategies for different load resources, exploring optimization methods for power system adjustment resources after load control. Considering the close

relationship between load control implementation and market policies, this paper further studies the load control mechanisms in mature electricity markets abroad and immature electricity markets domestically. Finally, this paper analyzes the shortcomings of current load control technologies. It provides prospects for future research, including digital twin-based load modeling, data-driven load adaptive control, and load control technologies to enhance system resilience. This paper will provide valuable literature on the development and application of load regulation technologies.

Data availability statement

The original contributions presented in the study are included in the article/supplementary material, further inquiries can be directed to the corresponding author.

Author contributions

QZ: Writing–original draft, Writing–review and editing. JW: Writing–original draft, Writing–review and editing. YY: Writing–original draft, Writing–review and editing.

Funding

The author(s) declare that financial support was received for the research, authorship, and/or publication of this article. The project with No. 5211JY220002 supports this work.

Conflict of interest

Authors QZ and YY were employed by Economy Research Institute of State Grid Zhejiang Electric Power Company, Hangzhou, China.

Author JW was employed by State Grid Zhejiang Yiwu Power Supply Co., Ltd., Jinhua, China.

Publisher's note

References

5G network architecture-A high-level perspective, China: huawei Technologies CO., Shenzhen, China: LTD., 2016.

Ahmad, F., Saad Alam, M., Saad Alsaidan, I., and Shariff, S. M. (2020). Battery swapping station for electric vehicles: opportunities and challenges. *IET Smart Grid* 3 (3), 280–286. doi:10.1049/iet-stg.2019.0059

Albadi, M. H., and EL-Saadany, E. F. (2008). A summary of demand response in electricity markets. *Electr. Power Syst. Res.* 78 (11), 1989–1996. doi:10.1016/j.epsr.2008.04.002

Antiy Institute (2019). CSGITSEC. Preliminary analysis and reflections on Venezuela's power outage. *Inf. Secur. And Commun. Priv.* 5, 28–39.

Babahajiani, P., Shafiee, Q., and Bevrani, H. (2018). Intelligent demand response contribution in frequency control of multi-area power systems. *IEEE Trans. Smart Grid* 9 (2), 1282–1291. doi:10.1109/tsg.2016.2582804

Bachao, B. (2017). What is inverter technology AC [EB/OL]. Available at: https://www.bijlibachao.com.

Bao, Y. Q., Li, Y., Hong, Y. Y., and Wang, B. (2015). Design of a hybrid hierarchical demand response control scheme for the frequency control. *IET Generation, Transm. and Distribution* 9 (15), 2303–2310. doi:10.1049/iet-gtd.2015.0628

Bhattacharyya, K., and Crow, M. L. (1996). A fuzzy logic based approach to direct load control. *IEEE Trans. Power Syst.* 11 (2), 708–714. doi:10.1109/59.496143

Bie, Z., Lin, C., Li, G., and Qiu, A. (2020). Development and prospect of resilient power system in the context of energy transition. *Proceeding CSEE* 40 (9), 2735–2744.

Bin, L. I., Wangzhang, C. A. O., Chao, L. U., et al. (2018). Security management and technique support for multi-level DR bidding under untrusted environment based on blockchain. *Proceeding CSEE* 38 (8), 2272–2283.

Bo, Z., Cheng, D., He, D., et al. (2020). "White paper on digital twin applications," in *China Institute of electronic technology standardization*. Beijing.

Cai, M., Pipattanasomporn, M., and Rahman, S. (2019). Day-ahead building-level load forecasts using deep learning vs. traditional time-series techniques. *Appl. Energy* 236, 1078–1088. doi:10.1016/j.apenergy.2018.12.042

Chen, B., Sun, H., Chen, Y., Guo, Q., Wu, W., and Qiao, Z. (2020). Energy circuit theory of integrated energy system analysis(I): gaseous circuit. *Proc. CSEE* 40 (2), 436–443.

Chen, Q., Wang, K., Chen, S., and Xia, Q. (2018). Transactive energy for distributed agents: architecture, mechanism and technology. *Automation Electr. Power Syst.* 42 (3), 1–7.

Chen, T., Pourbabak, H., Liang, Z., and Su, W. (2017). An integrated eVoucher mechanism for flexible loads in real-time retail electricity market. *IEEE Access* 5, 2101–2110. doi:10.1109/access.2017.2659704

Chu, W. C., Chen, B. K., and Fu, C. K. (1993). Scheduling of direct load control to minimize load reduction for a utility suffering from generation shortage. *IEEE Trans. Power Syst.* 8 (4), 1525–1530. doi:10.1109/59.260955

Commercial feasibility analysis of smart grid enabled by 5G network slicing by China Telecom, State Grid of China, Huawei, etc. Shanghai, China, 2019.

Das, H. S., Rahman, M. M., Li, S., and Tan, C. W. (2020). Electric vehicles standards, charging infrastructure, and impact on grid integration: a technological review. *Renew. Sustain. Energy Rev.* 120, 109618. doi:10.1016/j.rser.2019.109618

Ding, Y., Pineda, S., Nyeng, P., Ostergaard, J., Larsen, E. M., and Wu, Q. (2013). Real-time market concept architecture for EcoGrid EU—a prototype for European smart grids. *IEEE Trans. Smart Grid* 4 (4), 2006–2016. doi:10.1109/tsg.2013.2258048

Ding, Y., Hui, H., Lin, Z., Zheng, M., Qu, X., and Cui, W. (2017). Design of business model and market framework oriented to active demand response of power demand side. *Automation Electr. Power Syst.* 41 (14), 2–9.

Dong, WANG, Zeng, Y., Mu, Y., and Wang, Y. (2015). An optimization method for new energy utilization using thermostatically controlled appliances. *Power Syst. Technol.* 39 (12), 3457–3462.

Douglass, P. J., Garcia-Valle, R., Nyeng, P., Ostergaard, J., and Togeby, M. (2013). Smart demand for frequency regulation: experimental results. *IEEE Trans. Smart Grid* 4 (3), 1713–1720. doi:10.1109/tsg.2013.2259510

Embrace 5G new world. China: roland berger, 2019.

Hongmei, L. I., Hantao, C. U. I., and Qiulan, W. A. N. (2015). Distribution network reconfiguration based on second-order conic programming considering EV charging strategy. *Proc. CSEE* 35 (18), 4674–4681.

Hongtu, ZHAO, Zhu, Z., and Erkeng, Y. U. (2010). Study on demand response markets and programs in electricity markets. *Power Syst. Technol.* (5), 146–153.

Hui, H., Ding, Y., Liu, W., Lin, Y., and Song, Y. (2017). Operating reserve evaluation of aggregated air conditioners. *Appl. Energy* 196, 218–228. doi:10.1016/j.apenergy.2016.12.004

Hui, H., Ding, Y., Luan, K., Chen, T., Song, Y., and Rahman, S. (2022). Coupon-based demand response for consumers facing flat-rate retail pricing. *CSEE J. Power Energy Syst.* Early Access.

Hui, H., Ding, Y., Luan, K., and Xu, D. (2018a). *Analysis of 815 blackout in Taiwan and the improvement method of contingency reserve capacity through direct load control.* Portland, USA: IEEE Power and Energy Society General Meeting.

Hui, H., Ding, Y., Shi, Q., Li, F., Song, Y., and Yan, J. (2020). 5G network-based Internet of Things for demand response in smart grid: a survey on application potential. *Appl. Energy* 257, 113972. doi:10.1016/j.apenergy.2019.113972

Hui, H., Ding, Y., Song, Y., and Rahman, S. (2019). Modeling and control of flexible loads for frequency regulation services considering compensation of communication latency and detection error. *Appl. Energy* 250, 161–174. doi:10.1016/j.apenergy.2019.04.191

Hui, H., Ding, Y., and Zheng, M. (2018b). Equivalent modeling of inverter air conditioners for providing frequency regulation service. *IEEE Trans. Industrial Electron.* 66 (2), 1413–1423. doi:10.1109/tie.2018.2831192

Jia, H., Qi, Y., and Mu, Y. (2013). Frequency response of autonomous microgrid based on family-friendly controllable loads. *Sci. Sin. Technol.* (3), 247–256.

Jinghong, ZHENG, Mengting, D. A. I., Man, ZHANG, et al. (2012). Load clusters characteristic and modeling of EV charge station in residential district. *Proc. CSEE* 32 (22), 32–38.

Ju, P., Wang, C., Xin, H., Li, H., Jiang, D., and Shen, F. (2019). Flexibility, resilience and toughness of power system. *Electr. Power Autom. Equip.* 39 (11), 1–7.

Ju, P., Guo, D., Lu, C., Jin, Y., Wang, Z., Chen, Q., et al. (2020). Review and prospect of modeling on generalized synthesis electric load containing active loads. *J. Hohai Univ. Nat. Sci.* 48 (4), 367–376.

Ju, P., and Ma, D. (2008). *Power system load modeling*. Beijing: China Electric Power Press.

Kai, X. I. E., Zhang, X., and Zhang, S. (2020). Application and prospect of blockchain technology in electricity trading. *Automation Electr. Power Syst.* 44 (19), 19–28.

Kirschen, D. S., Strbac, G., Cumperayot, P., and de Paiva Mendes, D. (2000). Factoring the elasticity of demand in electricity prices. *IEEE Trans. Power Syst.* 15 (2), 612–617. doi:10.1109/59.867149

Knud, L. (2014). *IoT market-forecasts at a glance*. Germany, Hamburg: IoT Analytics.

Laurent, J. C., Desaulniers, G., Malhamé, R. P., and Soumis, F. (1995). A column generation method for optimal load management via control of electric water heaters. *IEEE Trans. Power Syst.* 10 (3), 1389–1400. doi:10.1109/59.466513

Ledva, G. S., Vrettos, E., Mastellone, S., Andersson, G., and Mathieu, J. L. (2018). Managing communication delays and model error in demand response for frequency regulation. *IEEE Trans. Power Syst.* 33 (2), 1299–1308. doi:10.1109/tpwrs.2017.2725834

Leligou, H., Zahariadis, T., Sarakis, L., Tsampasis, E., Voulkidis, A., and Velivassaki, T. (2018). "Smart Grid: a demanding use case for 5G technologies," in *2018 IEEE international conference on pervasive computing and communications workshops (PerCom workshops)*. Athens, Greece.

Li, J., Ye, Y., Papadaskalopoulos, D., and Strbac, G. (2020). Distributed consensus-based coordination of flexible demand and energy storage resources. *IEEE Trans. power Syst.* 36 (4), 3053–3069. doi:10.1109/tpwrs.2020.3041193

Li, Y., Yao, J., Yong, T, Ju, P, Yang, S, and Shi, X (2017). Estimation approach to aggregated power and response potential of residential thermostatically controlled loads. *Proc. CSEE* 37 (19), 3–12.

Liu, L., Liu, T., Zhang, T., and Liu, J. (2016). Orderly charging and discharging strategy optimization for electric vehicles considering dynamic battery-wear model. *Automation Electr. Power Syst.* 40 (5), 83–90.

Liu, Y., Junyong, L. I. U., and Tang, J. (2008). An optimal decision-making model for power supply company's power purchase in weekly market considering price elasticity matrix of demand side and risk. *Power Syst. Technol.* 32 (18), 18–24.

Lu, N. (2012). An evaluation of the HVAC load potential for providing load balancing service. *IEEE Trans. Smart Grid* 3 (3), 1263–1270. doi:10.1109/tsg.2012.2183649

Luo, Z., Hu, Z., Song, Y., Yang, X., and Wu, J. (2011). Study on plug-in electric vehicles charging load calculating. *Automation Electr. Power Syst.* 35 (14), 36–42.

Mathieu, J. L., and Callaway, D. S. (2012). "State estimation and control of heterogeneous thermostatically controlled loads for load following," in *45th IEEE Hawaii international conference on system sciences*. Hawaii, USA.

Measurement of electrical and magnetic quantities. C37.118.1-2011 (2011). *IEEE standard for synchrophasor measurements for power systems[S]*. USA: IEEE.

Meng, J. (2015). *Research on power system frequency modulation control strategy based on electric vehicles and temperature controlled load*. Tianjin: Tianjin University.

Morello, R., Di Rienzo, R., Roncella, R., Saletti, R., and Baronti, F. (2018). Hardware-in-the-loop platform for assessing battery state estimators in electric vehicles. *IEEE Access* 6, 68210–68220. doi:10.1109/access.2018.2879785

Nosair, H., and Bouffard, F. (2015). Reconstructing operating reserve: flexibility for sustainable power systems. *IEEE Trans. Sustain. Energy* 6 (4), 1624–1637. doi:10.1109/tste.2015.2462318

Nyeng, P., and Ostergaard, J. (2011). Information and communications systems for control-by-price of distributed energy resources and flexible demand. *IEEE Trans. Smart Grid* 2 (2), 334–341. doi:10.1109/tsg.2011.2116811

Park, Y. C., Kim, Y. C., and Min, M. K. (2001). Performance analysis on a multi-type inverter air conditioner. *Energy Convers. Manag.* 42 (13), 1607–1621. doi:10.1016/s0196-8904(00)00147-3

Pierre, D. A. (1987). A perspective on adaptive control of power systems. *IEEE Trans. power Syst.* 2 (2), 387–395. doi:10.1109/tpwrs.1987.4335139

Ping, J, Chen, S., Zhang, N, Yan, Z, and Yao, L (2017). Decentralized transactive mechanism in distribution network based on smart contract. *Proc. CSEE* 37 (13), 3682–3690.

Qiu, A., Guo, J., and Bi, C. (2020). *Research on the development strategy of elastic power system under energy transformation*. Xi'an: Xi'an Jiaotong University.

Qi, Y., Wang, D., Jia, H., Chen, N., Wei, W., and Fan, M. (2017). Research on under frequency load shedding strategy using aggregated thermostatically controlled loads based on demand response. *Proc. CSEE* 37 (3), 99–108.

Ruan, W., Sha, L. I. U., and Yang, L. I. (2013). Overview of demand response in the U.S.A. *Power Demand Side Manag.* 15 (2), 61–64.

Rui, T. (2018). "Research on Emergency Management of Large Area Power Outages in Zhongshan City Power Grid - Based on the Power Outage Case Caused by Typhoon," in *Tiange in 2017 [D]*. Guangzhou: Jinan University.

Samarakoon, K., Ekanayake, J., and Jenkins, N. (2012). Investigation of domestic load control to provide primary frequency response using smart meters. *IEEE Trans. Smart Grid* 3 (1), 282–292. doi:10.1109/tsg.2011.2173219

Shao, S., Shi, W., Li, X., and Chen, H. (2004). Performance representation of variable-speed compressor for inverter air conditioners based on experimental data. *Int. J. Refrig.* 27 (8), 805–815. doi:10.1016/j.ijrefrig.2004.02.008

Shengchun, T. U., Liu, X., and Zhang, H. (2020). Typical implementation of commercial building virtual power plant in Huangpu district of Shanghai. *Power Demand Side Manag.* 22 (1), 52–57.

Shi, Q., Li, F., Hu, Q., and Wang, Z. (2018). Dynamic demand control for system frequency regulation: Concept review, algorithm comparison, and future vision. *Electr. Power Syst. Res.* 154, 75–87. doi:10.1016/j.epsr.2017.07.021

Shi, Q., Li, F., Liu, G., Shi, D., Yi, Z., and Wang, Z. (2019). Thermostatic load control for system frequency regulation considering daily demand profile and progressive recovery. *IEEE Trans. Smart Grid* 10 (6), 6259–6270. doi:10.1109/tsg.2019.2900724

Siano, P. (2014). Demand response and smart grids—A survey. *Renew. Sustain. Energy Rev.* 30, 461–478. doi:10.1016/j.rser.2013.10.022

Siano, P., and Sarno, D. (2016). Assessing the benefits of residential demand response in a real time distribution energy market. *Appl. Energy* 161, 533–551. doi:10.1016/j.apenergy.2015.10.017

Singh, V. P., Samuel, P., and Kishor, N. (2017). Impact of demand response for frequency regulation in two-area thermal power system. *Int. Trans. Electr. Energy Syst.* 27 (2), e2246. doi:10.1002/etep.2246

Sonderegger, R. C. (1978). *Dynamic models of house heating based on equivalent thermal parameters*. USA, NJ, Princeton: Princeton University.

Song, M., Gao, C., Yan, H., and Yang, J. (2017b). Thermal battery modeling of inverter air conditioning for demand response. *IEEE Trans. Smart Grid* 9 (6), 5522–5534. doi:10.1109/tsg.2017.2689820

Song, Y., Lin, J., Hu, Z., and Dong, S. (2016). Energy distribution network: infrastructure, operation mode and market mechanism. *Proc. CSEE* 36 (21), 5776–5787, 6020.

Song, Y., Lin, J., Tang, M., and Dong, S. (2017a). An internet of energy things based on wireless LPWAN. *Engineering* 3 (4), 460–466. doi:10.1016/j.eng.2017.04.011

Song, Y., Yang, Y., and Zechun, H. U. (2011). Present Status and Development Trend of Batteries for Electric Vehicles. *Power Syst. Technol.* 35 (4), 1–7.

Su, J., Guo, Y., Liu, M., Zhang, G., and Wang, D. (2018). Strategy and probability model for thermostatically controlled loads in emergency load shedding system. *Power Syst. Technol.* 42 (3), 911–917.

Sun, J., Tang, S., Liu, F., Wang, D., and Wang, R. (2016). Modeling method and control strategy evaluation of electric water heater for demand response program. *Proc. CSU-EPSA* 28 (4), 51–55.

Sun, Y., Jun, W. U., and Guojie, L. I. (2007). Influence research of wind power generation on power systems. *Power Syst. Technol.* 31 (20), 55–62.

Tai, X., Sun, H., and Guo, Q. (2016). Electricity transactions and congestion management based on blockchain in energy internet. *Power Syst. Technol.* 40 (12), 3630–3638.

Tang, Y., Zhang, H., and Hou, J. (2007). A synthesis load model with distribution network. *Power Syst. Technol.* 31 (5), 34–38.

Technology information The market share of variable frequency air conditioning will exceed 50% [EB/OL]. Available at: http://www.techweb.com.cn/news/2011-03-21/1004599.shtml,2011-03-21.

Telecom, C., Grid, S., and Huawei. 5G Network Slicing Enabling Smart Grid. China, Beijing, 2018.

View on 5G architecture-version 3.0. 5G PPP architecture working group, Europe, 2019.

Vrettos, E., Kara, E. C., Macdonald, J., Andersson, G., and Callaway, D. S. (2018). Experimental demonstration of frequency regulation by commercial buildings—Part I: Modeling and hierarchical control design. *IEEE Trans. Smart Grid* 9 (4), 3213–3223. doi:10.1109/tsg.2016.2628897

Wang, C., Liu, M., and Lu, N. (2012). A tie-line power smoothing method for microgrid using residential thermostatically-controlled loads. *Proc. CSEE* 32 (25), 63–70.

Wang, D., Fan, M., and Jia, H. (2014b). User comfort constraint demand response for residential thermostatically-controlled loads and efficient power plant modeling. *Proc. CSEE* 34 (13), 2071–2077.

Wang, H., Chen, S., and Zheng, Y. A. N. (2020). Blockchain-enabled charging right trading among EV charging stations: mechanism, model and method. *Proceeding CSEE* 40 (2), 425–435.

Wang, J., Wang, X., and Zhang, X. (2005). The flexible operation reserve model in the power market. *Proc. CSEE* 25 (18), 20–27.

Wang, J., Zhong, H., Xia, Q., and Yang, S. (2016). Model and method of demand response for thermostatically-controlled loads based on cost-benefit analysis. *Automation Electr. Power Syst.* 40 (5), 45–53.

Wang, K., Yao, J., Yao, L., Yang, S., and Yong, T. (2014a). Survey of research on flexible loads scheduling technologies. *Automation Electr. Power Syst.* 38 (20), 127–135.

Wang, M., Mu, Y., Li, F., Jia, H., Li, X., Shi, Q., et al. (2019). State space model of aggregated electric vehicles for frequency regulation. *IEEE Trans. Smart Grid* 11 (2), 981–994. doi:10.1109/tsg.2019.2929052

Weckx, S., D'Hulst, R., and Driesen, J. (2014). Primary and secondary frequency support by a multi-agent demand control system. *IEEE Trans. Power Syst.* 30 (3), 1394–1404.

Wenting, W. E. I., Wang, D., and Jia, H. (2016). A hierarchical and distributed control strategy of thermostatically controlled appliances for city park based on load model prediction. *Proc. CSEE* 36 (8), 2049–2056.

Xiang, D., Hu, Z., Song, Y., and Ding, H. (2015). Business Model and Day-ahead Dispatch Strategy to Reduce Wind Power Curtailment Through Vehicle-to-Grid. *Proc. CSEE* 35 (24), 6293–6303.

Xie, D., Hui, H., Ding, Y., and Lin, Z. (2018). Operating reserve capacity evaluation of aggregated heterogeneous TCLs with price signals. *Appl. Energy* 216, 338–347. doi:10.1016/j.apenergy.2018.02.010

Xu, Z., Hu, Z., Song, Y., Luo, Z., Zhan, L., and Shi, H. (2012). Coordinated Charging of Plug-in Electric Vehicles in Charging Stations. *Automation Electr. Power Syst.* 36 (11), 38–43.

Xu, Z., Hu, Z., Song, Y., Zhang, H., and Chen, X. (2014). Coordinated charging strategy for pev charging stations based on dynamic time-of-use tariffs. *Proc. CSEE* 34 (22), 3638–3646.

Xue, Y., Luo, Y., Li, B., Luo, J., Dong, Z., and Ledwich, G. (2007). A review of interruptible load participating in system reserve. *Automation Electr. Power Syst.* 31 (10), 1–6.

Yang, J. (2015). Negative Watt: The Neglected Fifth Big Energy. *Energy* 8, 100–102.

Yao, Y. A. O., Zhang, P., and Wang, Y. (2018). A two-layer control method for thermostatically controlled loads to provide fast frequency regulation. *Proc. CSEE* 38 (17), 4987–4998.

Yayuan, L. I. U., Zhu, Y., and Yi, C. U. I. (2019). Challenges and opportunities towards fast-charging battery materials. *Nat. Energy* 4 (7), 540–550. doi:10.1038/s41560-019-0405-3

Yi, D., Luan, K., and Hongxun, H. (2019c). Energy conservation and emission reduction, starting from "fireflies" - demonstration of electricity demand response based on integral mechanism. *Sci. Technol. Overv.* 78, 76–78.

Yi, DING, Yonghua, SONG, Hongxun, H. U. I., and Shao, C. (2019b). *Integration of air conditioning and heating into modern power systems*. Singapore: Springer.

Wang, Y., Chen, Q., Zhang, N., Feng, C., Feng, F., and Sun, M. (2019a). Fusion of the 5G communication and the ubiquitous electric Internet of Things: application analysis and research prospects. *Power Syst. Technol.* 43 (5), 1575–1585.

Yilmaz, O. (2016). "Ultra-reliable and low-latency 5G communication," in *Proc. Of the europe conference on networks and communication*. Athens, Greece.

Yin, X., He, J., Wang, Y., Li, J., Li, C., et al. (2019). A review on distribution system restoration for resilience enhancement. *Trans. China Electrotech. Soc.* 34 (16), 3416–3429.

Yong, T. (2012). *Mathematical model and modeling technology of power load*. Beijing: Science Press.

Zeng, M., Li, S., and He, Y. (2015). Status, challenges and countermeasures of demand-side management development in China. *Renew. Sustain. Energy Rev.* 47, 284–294. doi:10.1016/j.rser.2015.03.028

Zeng, M., Xue, S., Ma, M., Lingyun, L., Min, C., and Yuejin, W. (2013). Historical review of demand side management in China: Management content, operation mode, results assessment and relative incentives. *Renew. Sustain. Energy Rev.* 25, 470–482. doi:10.1016/j.rser.2013.05.020

Zeng, M., Yang, Y., Wang, L., and Sun, J. (2016). The power industry reform in China 2015: Policies, evaluations and solutions. *Renew. Sustain. Energy Rev.* 57, 94–110. doi:10.1016/j.rser.2015.12.203

Zhang, H., Yao, L., and Yuan, X. (2019). Digital Twin White Paper. Beijing: China Institute of Electronic Information Industry Development.

Zhang, F., Lin, CHENG, Xiong, L. I., et al. (2014b). Prediction based on hierarchical compensation for delays of wide-area closed-loop control systems. *Proc. CSEE* 34 (19), 3194–3201.

Zhang, F., Sun, Y., Cheng, L., Li, X., Chow, J. H., and Zhao, W. (2015). Measurement and modeling of delays in wide-area closed-loop control systems. *IEEE Trans. Power Syst.* 30 (5), 2426–2433. doi:10.1109/tpwrs.2014.2359773

Zhang, H., Hu, Z., Song, Y., Xu, Z., and Jia, L. (2014a). A prediction method for electric vehicle charging load considering spatial and temporal distribution. *Automation Electr. Power Syst.* 38 (1), 13–20.

Zhang, N., Yi, WANG, Kang, C., Cheng, J., and He, D. (2016b). Blockchain technique in the energy internet: preliminary research framework and typical applications. *Proc. CSEE* 36 (15), 4011–4022.

Zhang, Q., Guo, Q., and Yu, Y. (2016a). "Research on the load characteristics of inverter and constant speed air conditioner and the influence on distribution network," in *2016 China international conference on electricity distribution (CICED)*. IEEE.

Zhang, Q., Wang, X., Wang, J., Feng, C., and Liu, L. (2008). Survey of demand response research in deregulated electricity markets. *Automation Electr. Power Syst.* 32 (3), 97–107.

Zhang, X., Pipattanasomporn, M., and Rahman, S. (2017). A self-learning algorithm for coordinated control of rooftop units in small-and medium-sized commercial buildings. *Appl. Energy* 205, 1034–1049. doi:10.1016/j.apenergy.2017.08.093

Zhao, J, Wen, F., Xue, Y., Dong, Z., and Xin, J. (2010). Power system stochastic economic dispatch considering uncertain outputs from plug-in electric vehicles and wind generators. *Automation Electr. Power Syst.* 34 (20), 22–29.

Zhenfang, Q. (2004). *Analysis of electricity price elasticity coefficient in the retail market*. Tianjin: Tianjin University.

Zhan, K, Hu, Z., Song, Y., Guo, X., Xu, A., and Lei, J. (2016). Electric vehicle coordinated charging hierarchical control strategy considering renewable energy generation integration. *Power Syst. Technol.* 40 (12), 3689–3695.

Zhong, H., Xie, L., and Xia, Q. (2013). Coupon incentive-based demand response: Theory and case study. *IEEE Trans. Power Syst.* 28 (2), 1266–1276. doi:10.1109/tpwrs.2012.2218665

Zhou, X., Chen, S., Lu, Z., Huang, Y., Ma, S., and Zhao, Q. (2018a). Technology features of the new generation power system in China. *Proc. CSEE* 38 (7), 1893–1904.

Zhou, Z., Tan, L., Gu, B., Zhang, Y., and Wu, J. (2018b). Bandwidth slicing in software-defined 5G: A stackelberg game approach. *IEEE Veh. Technol. Mag.* 13 (2), 102–109. doi:10.1109/mvt.2018.2814022

Zou, B., Dai, P., Wang, L., Ye, C., and Wang, G. (2019). Post-disaster restoration scheduling of resilient distribution networks based on mixed integer programming. *Zhejiang Electr. Power* 38 (8), 72–76.

frontiers | Frontiers in Energy Research

TYPE Original Research
PUBLISHED 19 September 2024
DOI 10.3389/fenrg.2024.1413769

OPEN ACCESS

EDITED BY
Lorenzo Ferrari,
University of Pisa, Italy

REVIEWED BY
Yunting Yao,
Nanjing Normal University, China
Duong Nguyen,
Arizona State University, United States

*CORRESPONDENCE
Feng Wang,
wf_scu@163.com

RECEIVED 07 April 2024
ACCEPTED 26 August 2024
PUBLISHED 19 September 2024

CITATION
Wang F, Wen X, Li J, Liu Y and Yu H (2024) Cooperative energy interaction for neighboring multiple distribution substation areas considering demand response.
Front. Energy Res. 12:1413769.
doi: 10.3389/fenrg.2024.1413769

Cooperative energy interaction for neighboring multiple distribution substation areas considering demand response

Feng Wang[1,2]*, Xiangyu Wen[1,2], Jianxiu Li[1,2], Yang Liu[1,2] and Haidong Yu[1,2]

[1]State Grid Shandong Electric Power Research Institute, Jinan, China, [2]Shandong Smart Grid Technology Innovation Center, Jinan, China

With the growing integration of renewable energy into medium- and low-voltage distribution networks, the distribution substation area (DSA) has emerged, encompassing energy storage and loads. This paper introduces an energy interaction framework for multiple DSAs aimed at enhancing local renewable energy consumption. The energy interaction issue among various DSAs is modeled as a Nash bargaining problem to encourage energy exchanges. However, the variability in pricing and internal demand response may influence scheduling decisions, necessitating further investigation. To address price forecast errors, scenarios are developed using a stochastic programming approach to represent price uncertainties while adjusting the DSA's load accordingly. Optimal power flow constraints are integrated into the model to bolster power system operation security. Additionally, the transmission capacity can impact scheduling outcomes and operational costs. The influence of transmission limitations on operational strategies is examined within the allowable capacity. To solve this issue, the bargaining model is divided into two subproblems, and an enhanced alternating direction multiplier method (ADMM) is used to maintain the privacy of DSAs. The simulation results obtained using the IEEE-33 bus system indicate that energy interaction among multiple DSAs significantly lowers operating costs and facilitates the integration of renewable energy.

KEYWORDS

multiple distribution substation areas, energy interaction, uncertain prices, demand response, generalized Nash bargaining

1 Introduction

The integration of distributed renewable energy is a key challenge within distribution networks. To facilitate energy interaction, a distribution substation area (DSA), comprising a renewable power station, energy storage, and loads, can support local consumption and reduce disturbances in the network (Hirsch et al., 2018). Using energy storage, the DSA can adjust the load demand and better accommodate renewable generation. However, the inherent unpredictability of renewable sources may lead to energy shortages or surpluses. To optimize renewable energy efficiency, DSAs can interconnect with neighbors to facilitate energy exchanges (Kumar and Saravanan, 2017). Guided by the time-of-use (TOU) pricing set by the distribution network operator, energy interaction among multiple DSAs is

encouraged, forming a small-scale interconnected DSA energy market (Vieira and Zhang, 2021). Given the shared interests, it is crucial to develop an interactive mechanism that incentivizes energy exchanges while maintaining economic viability and reliability within the region (Tushar et al., 2020).

A game theory-based mechanism is instrumental in studying and analyzing interactive strategies among multiple DSAs (Tushar et al., 2018). Generally, the game theory approach to interaction processes among participants can be categorized into non-cooperative and cooperative games (Tushar et al., 2019). In a non-cooperative game, buyers and sellers negotiate to establish interaction prices and quantities, achieving market clearing while maintaining the supply–demand balance (Paudel et al., 2019). A Stackelberg game-based negotiation process between buyers and sellers, which considers participant competition and achieves market clearing, is detailed by Jiang et al. (2022). Although Nash equilibrium solutions can be obtained in non-cooperative games, the decision-making processes are typically self-centered, and these solutions are not necessarily unique local optima (Chen et al., 2019).

To balance individual and collective interests, a cooperative game theory-based energy interaction model is proposed to achieve global optimization in energy sharing (Luo et al., 2022). The Nash bargaining game theory is well suited for energy interactions among multiple DSAs, ensuring equitable benefit allocation (Dehghanpour and Nehrir, 2017; Wang and Huang, 2016). Building on this cooperative model, optimal power flow constraints are incorporated into the system operation to enhance the model's practicality (Li et al., 2018). However, these studies often overlook the impact of the demand response on energy interaction, which could potentially increase operational costs.

The demand response is an effective and promising approach that shifts electricity demand to periods when renewable generation is more abundant or the demand is lower. By leveraging load baselines, the demand response aids in the integration of renewable generation and reduces operational costs, thereby facilitating energy interaction (Sarker et al., 2020). A bi-level optimization model has been introduced for energy storage planning and operation, considering the electricity–heat demand response while utilizing Nash bargaining methods for benefit allocation (Alizadeh et al., 2024). However, these studies often distribute cooperative benefits equally among participants, which may lead to fairness concerns (Luo et al., 2022). To address this, a generalized Nash bargaining theory is adopted to incentivize energy interaction among multiple DSAs and allocate cooperative benefits based on the quantities of energy interaction (Kim et al., 2019).

The aforementioned studies formulate energy interaction models based on deterministic optimization, often overlooking forecast errors in TOU prices. Price uncertainty significantly impacts the economic and security aspects of an energy system. Generally, stochastic programming (Li et al., 2022) and robust optimization (Wei et al., 2021) are two prevalent methods used for addressing uncertainties. Considering the conservative nature of robust optimization, a stochastic optimization model is developed for unpredictable prices, aiming to achieve optimal scheduling (Baharvandi et al., 2019) and effective energy management (Chang et al., 2020). However, the influence of uncertain prices on energy interaction, as well as Nash bargaining-based operation decisions, is often neglected in these studies. Given the uncertain prices, DSAs schedule their demand to respond dynamically, which may alter their final decisions and operational costs. Considering the interdependent relationship between prices and demand response, the decisions of DSAs should integrate these influencing factors to devise optimal strategies.

Another aspect investigated in energy interaction is the consideration of physical constraints. Voltage fluctuations at each node (Jin et al., 2020) and power losses resulting from energy interaction (Khorasany et al., 2020) are modeled as costs paid to the operator. Although these factors are considered costs, further analysis is needed to understand strategy changes when transferring power to neighbors within the specified capacity limits. In other words, the congestion of transmission lines is directly addressed during the energy interaction process. Therefore, an energy interaction model is established that incorporates uncertain prices, demand response, and transmission capacity during energy interaction.

To sum up, the main contribution of this paper is to derive optimal operation strategies by considering the interdependent relationship between uncertain prices and the demand response of DSAs. Specifically, this paper investigates the effect of price uncertainty on the Nash bargaining theoretical model, analyzing both operation costs and the internal decision-making strategies of DSAs. To mitigate these adverse effects, the demand response combined with energy storage is proposed to enhance the flexibility of DSAs by shifting the load demand to periods of lower prices. The final operation strategies should account for the interconnected nature of price uncertainty and demand response. Additionally, optimal power flow is integrated into the optimization model to improve its practicality. Transmission limitations are also included to examine the impact of capacity restrictions on operation costs. Finally, the cooperative benefits are allocated based on the interaction of DSAs, ensuring a fair distribution that reflects the contribution of each participant to the energy interaction process.

2 Problem description

As illustrated in Figure 1, an energy interaction problem with $\mathcal{M}$ DSAs is considered, formulated as an interaction set $\mathcal{M} = 1, \ldots, M$. Each DSA, which consists of PV/wind generation, energy storage, and loads, interacts with others to maintain the balance between supply and demand. Supported by the distribution network, these interconnected DSAs participate in energy interactions to share electricity with neighboring entities. In this process, electricity is transferred from one bus to another, which can be described as an AC power flow. To address the volatility of electricity prices, a stochastic programming approach is incorporated into the model, capturing price uncertainty through discrete scenarios.

Given the price scenarios, DSAs negotiate with each other and respond to the prices by shifting load demands. To this end,

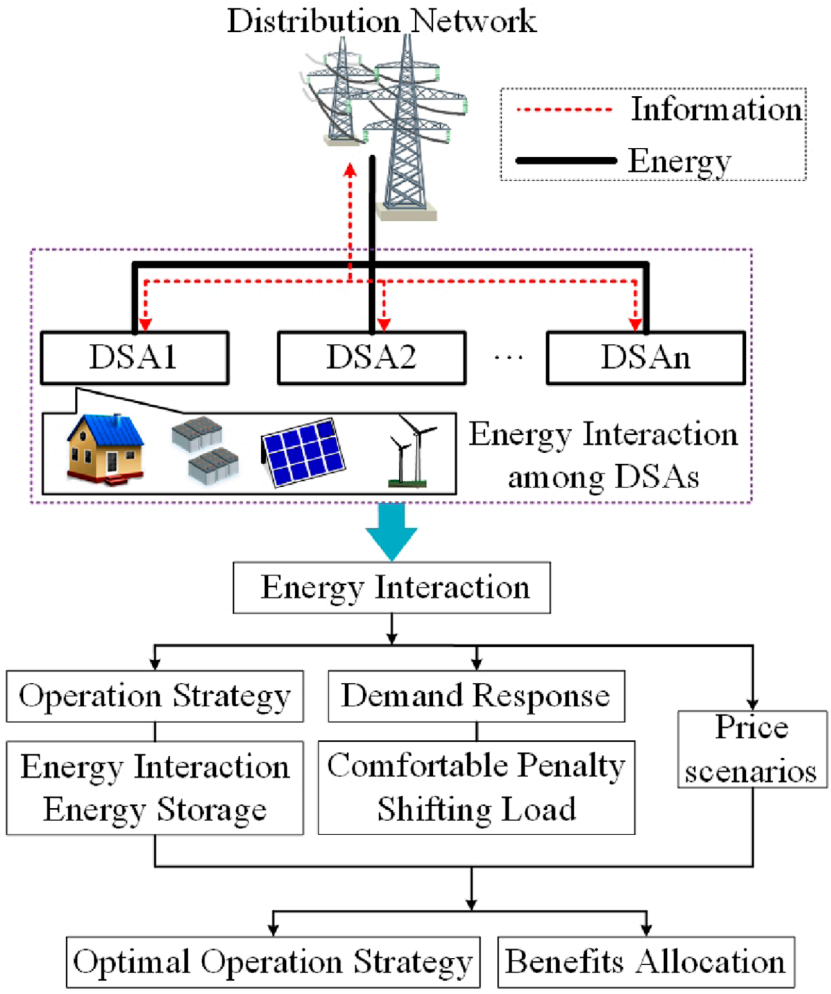

FIGURE 1
System with interconnected DSAs.

the energy interaction problem is formulated as a generalized Nash bargaining game model to incentivize energy interaction and achieve fair benefit allocation. Additionally, a penalty for DSAs caused by the demand response is incorporated into the model to account for comfort levels. DSAs develop optimal operation strategies to maximize cooperative benefits and allocate these benefits based on their respective contributions. Congestion may occur during the process of energy transmission, especially considering the energy interaction among DSAs. To address this issue, we adjust the operation strategies of DSAs and analyze the impact on operation costs.

3 Energy interaction model

An independent operation model of a DSA and an energy interaction model among multiple DSAs are established for the comparative analysis of the operation costs of DSAs. Compared to independent operations, DSAs achieve cost savings through energy interaction with neighbors, which includes energy sharing, renewable generation integration, energy storage scheduling, and load shifting. Then, based on the generalized Nash bargaining theory, cooperative benefits are allocated by leveraging the bargaining power parameters.

3.1 Basic operation optimization model of the individual DSA

The objective function of a DSA is to minimize operational costs in the face of uncertain pricing. To achieve this, the DSA uses demand response strategies and manages the charging and discharging of energy storage systems. The

model, accounting for various price scenarios, is structured as follows:

$$C^{i}_{Non}=\min_{\boldsymbol{x}^{i,t,w}_{\boldsymbol{Non}}} \sum_{w=1}^{\mathcal{W}} \sum_{t=1}^{\mathcal{T}} \frac{1}{\mathcal{W}} \Big[\mu^{t,w}_{Pb} P^{i,t,w}_{Pb} - \mu^{t,w}_{Ps} P^{i,t,w}_{Ps} + c_E \left(P^{i,t,w}_{Ec} + P^{i,t,w}_{Ed}\right) + c_{Load} \left(P^{i,t,w}_{Load} - P^{i,t}_{Load,Pre}\right)^2 \Big], \tag{1a}$$

$$s.t. P^{i,t,w}_{Pb} + P^{i,t,w}_{Gen} + P^{i,t,w}_{Ed} = P^{i,t,w}_{Ps} + P^{i,t,w}_{load} + P^{i,t,w}_{Ec}, \forall i \in \mathcal{M}, \forall t \in \mathcal{T}, \forall w \in \Omega, \tag{1b}$$

$$0 \le P^{i,t,w}_{Pb} \le P^{max}_{Pb,i}, \forall i \in \mathcal{M}, \forall t \in \mathcal{T}, \forall w \in \Omega, \tag{1c}$$

$$0 \le P^{i,t,w}_{Ps} \le P^{max}_{Ps,i}, \forall i \in \mathcal{M}, \forall t \in \mathcal{T}, \forall w \in \Omega, \tag{1d}$$

$$0 \le P^{i,t,w}_{Ec} \le P^{max}_{Ec,i}, \forall i \in \mathcal{M}, \forall t \in \mathcal{T}, \forall w \in \Omega, \tag{1e}$$

$$0 \le P^{i,t,w}_{Ed} \le P^{max}_{Ed,i}, \forall i \in \mathcal{M}, \forall t \in \mathcal{T}, \forall w \in \Omega, \tag{1f}$$

$$SOC^{min}_{i} \le SOC^{i,t,w} \le SOC^{max}_{i}, \forall i \in \mathcal{M}, \forall t \in \mathcal{T}, \forall w \in \Omega, \tag{1g}$$

$$SOC^{i,t,w} Cap^{i} = SOC^{i,t-1,w} Cap^{i} + \eta^{i,t,w}_{Ec} P^{i,t,w}_{Ec} - 1/\eta^{i,t,w}_{Ed} P^{i,t,w}_{Ed}, \forall i \in \mathcal{M}, \forall t \in \mathcal{T}, \forall w \in \Omega, \tag{1h}$$

$$SOC^{i,24,w} = SOC^{i}_{exp}, \forall i \in \mathcal{M}, \forall w \in \Omega, \tag{1i}$$

$$(1-\alpha_L) P^{i,t}_{Load,Pre} \le P^{i,t,w}_{Load} \le (1+\alpha_L) P^{i,t}_{Load,Pre}, \tag{1j}$$

$$\sum_{t=1}^{\mathcal{T}} P^{i,t,w}_{Load} = \sum_{t=1}^{\mathcal{T}} P^{i,t}_{Load,Pre}, \tag{1k}$$

where the objective function (1a) represents the individual operation cost C^{i}_{Non} of DSA $i \in \mathcal{M}$, which includes the interaction cost with the distribution network, degradation cost of the energy storage, and comfortable penalty cost. The purchasing and selling prices denoted as $\mu^{t,w}_{Pb}$ and $\mu^{t,w}_{Ps}$, respectively, and quantities $P^{i,t,w}_{Pb}$ and $P^{i,t,w}_{Ps}$ in scenarios $w \in \Omega$ are used to calculate the operation cost with the distribution network. The degradation cost of energy storage consists of the unit cost c_E and charging/discharging variables ($P^{i,t,w}_{Ec}$ and $P^{i,t,w}_{Ed}$, respectively). The comfort penalty cost is expressed as the product of the unit cost c_{Load} and load regulation quantities. The power balance constraint (Equation 1b) involves the forecast renewable generation $P^{i,t,w}_{Gen}$ and load demand $P^{i,t}_{load,pre}$ at time $t \in \mathcal{T}$, as well as the actual load demand $P^{i,t}_{load}$ during the decision process. Constraints in Equations 1c, d define the lower and upper bounds ($P^{max}_{Pb,i}$ and $P^{max}_{Ps,i}$, respectively) for purchasing/selling energy from/to a distribution network. The charging and discharging limitation of a battery is indicated by constraints in Equations 1e, f with upper bounds $P^{max}_{Ec,i}$ and $P^{max}_{Ed,i}$. The state of charge (SOC) is limited by constraints in Equations 1g, i, based on the storage capacity. The constraint in (1g) defines the minimum and maximum SOC values, while the constraint in (1h) specifies its balance expression. To ensure continuity in energy storage, the expected SOC must adhere to the constraint in (1i). For the demand response, the power reduction offered by each DSA i should satisfy the constraint in Equation 1j, where α_L represents the load shifting ratio. Given that load shifting is considered, the total daily demand should match the predicted value $P^{i,t}_{Load,Pre}$, as specified by the constraint in Equation 1k. The decision variables in the individual operation model are represented by the vector $\boldsymbol{x}^{i,t,w}_{\boldsymbol{Non}} = \left[P^{i,t,w}_{Pb}, P^{i,t,w}_{Ps}, P^{i,t,w}_{Ec}, P^{i,t,w}_{Ed}, SOC^{i,t,w}, P^{i,t,w}_{Load}\right]$.

3.2 Branch power-flow formulation

Following Farivar and Low (2013), the power flow model is established in a radial network using angle and conic relaxation. Additionally, quadratic terms in the power flow constraints are neglected since the branch powers $p_{j,t,w}$ and $q_{j,t,w}$ are significantly larger than the quadratic terms in the branch flow equation. Consequently, the expression is simplified as follows:

$$p_{j,t,w} = -\sum_{i:i\to j} P_{i,j,t,w} + \sum_{k:j\to k} P_{j,k,t,w}, \forall (i,j) \in \mathcal{E}, \tag{2a}$$

$$q_{j,t,w} = -\sum_{i:i\to j} Q_{i,j,t,w} + \sum_{k:j\to k} Q_{j,k,t,w}, \forall (i,j) \in \mathcal{E}, \tag{2b}$$

$$p_{i,t,w} = P^{i,t,w}_{g} - \left(P^{i,t,w}_{Pb} - P^{i,t,w}_{Ps}\right), \tag{2c}$$

$$q_{i,t,w} = Q^{i,t,w}_{g} - Q^{i,t}_{L,pre}, \tag{2d}$$

$$-P^{i,j}_{max} \le P_{i,j,t,w} \le P^{i,j}_{max}, \forall (i,j) \in \mathcal{E}, \tag{2e}$$

$$-Q^{i,j}_{max} \le Q_{i,j,t,w} \le Q^{i,j}_{max}, \forall (i,j) \in \mathcal{E}, \tag{2f}$$

$$-P^{i}_{g,max} \le P^{i,t,w}_{g} \le P^{i}_{g,max}, \tag{2g}$$

$$-Q^{i}_{g,max} \le Q^{i,t,w}_{g} \le Q^{i}_{g,max}, \tag{2h}$$

$$U_{j,t,w} = U_{i,t,w} - 2\left(P_{i,j,t,w} r_{i,j} + Q_{i,j,t,w} x_{i,j}\right), \forall (i,j) \in \mathcal{E}, \tag{2i}$$

$$U^{i}_{min} \le U_{i,t,w} \le U^{i}_{max}, \forall i,j \in \mathcal{N}, \forall t \in \mathcal{T}, \forall w \in \Omega, \tag{2j}$$

where the active and reactive powers in a branch are defined by constraints in Equations 2a, b, while the injection power of node $i \in \mathcal{N}$ can be obtained using constraints in Equations 2c, d. Constraints in Equations 2e, f set the limitation of branch flow for all branches $(i,j) \in \mathcal{E}$. The active and reactive bounds supported by the distribution network are specified by constraints in Equations 2g, h. The square of magnitudes of nodal voltage is provided by Equation 2i, and the constraint in Equation 2j ensures that $U_{i,t,w}$ always remains within the interval $\left[U^{i}_{min}, U^{i}_{max}\right]$.

3.3 Operation cost for cooperative DSAs

Supported by the distribution network, DSAs engage in energy interaction with neighbors to share idle energy while reducing disturbance to the main grid. Taking into account the impact of uncertain prices and the demand

response, their cooperative formulation is expressed as follows:

$$C^i_{Tra}=\min_{\boldsymbol{x}^{i,t,w}_{\boldsymbol{Tra}}} \sum_{w=1}^{\mathcal{W}}\sum_{t=1}^{\mathcal{T}} \frac{1}{\mathcal{W}}\Big(\mu^{t,w}_{Pb}P^{i,t,w}_{Pb}-\mu^{t,w}_{Ps}P^{i,t,w}_{Ps}+c^i_E\Big(P^{i,t,w}_{Ec}+P^{i,t,w}_{Ed}\Big) +c_{Load}\Big(P^{i,t,w}_{Load}-P^{i,t}_{Load,Pre}\Big)^2\Big), \tag{3a}$$

$$s.t.\,(1c)-(1k),(2a)-(2b),(2d)-(2j)$$

$$P^{i,t,w}_{Pb}+P^{i,t}_{Res}+P^{i,t,w}_{Ed}+P^{i,t,w}_{Tra}=P^{i,t,w}_{Ps}+P^{i,t}_{Load}+P^{i,t,w}_{Ec}, \tag{3b}$$

$$\sum_{i}^{\mathcal{M}} P^{i,t,w}_{Tra}=0, \tag{3c}$$

$$p_{i,t,w}=P^{i,t,w}_{g}-\Big(P^{i,t,w}_{Pb}+P^{i,t,w}_{Tra}-P^{i,t,w}_{Ps}\Big), \tag{3d}$$

$$\forall i\in\mathcal{M},\forall t\in\mathcal{T},\forall w\in\Omega.$$

Unlike the individual operation in model (1), the interaction variable $P^{i,t,w}_{Tra}$ is introduced by the constraint in Equation 3b. Considering energy interaction, DSAs maintain the supply–demand balance through energy exchange with the main grid and neighboring DSAs. The constraint in Equation 3c ensures that the total power output equals the power imported from neighbors'. Additionally, the net injection at node i incorporates energy interaction among DSAs, as detailed by the constraint in Equation 3d. The decision variables in cooperative mode are represented by the vector $\boldsymbol{x}^{i,t,w}_{\boldsymbol{Tra}}=\left[P^{i,t,w}_{Pb},P^{i,t,w}_{Ps},P^{i,t,w}_{Ec},P^{i,t,w}_{Ed},SOC^{i,t,w},P^{i,t,w}_{Tra},P^{i,t,w}_{Load}\right]$.

3.4 General Nash bargaining game-based energy interaction

The general Nash bargaining game-based scheduling strategy is proposed to incentivize energy interaction among DSAs and ensure that benefits are allocated according to the contribution of each participant.

$$\max\prod_{i=1}^{\mathcal{M}}\Big(C^i_{Non}-\Big(C^i_{Tra}+Ce^i_{Pay}\Big)\Big)^{\alpha_i}, \tag{4a}$$

$$\underbrace{C^i_{Tra}+Ce^i_{Pay}}_{C^i_{Total}}\le C^i_{Non},\forall\ i\in\ \mathcal{M}, \tag{4b}$$

$$\sum_{i}^{\mathcal{M}} Ce^i_{Pay}=0. \tag{4c}$$

DSAs engage in energy interaction with neighbors to maximize social welfare, as expressed in the objective function (Equation 4a). The constraint in Equation 4b ensures that the cooperation cost does not exceed the cost of individual operation, thereby encouraging DSAs to participate in energy interactions. The purchasing cost of a DSA in an energy interaction must equal be to the selling income of neighbors, as represented by the constraint in Equation 4c. Additionally, the contribution of each participant is calculated using the coefficient α_i, and the expression is

$$\alpha_i=\frac{\frac{1}{\mathcal{W}}\sum_{w=1}^{\mathcal{W}}\sum_{t}^{\mathcal{T}}|P^{i,t,w}_{Tra}|}{\frac{1}{\mathcal{W}}\sum_{w=1}^{\mathcal{W}}\sum_{i}^{\mathcal{M}}\sum_{t}^{\mathcal{T}}|P^{i,t,w}_{Tra}|}, \tag{5}$$

where the bargaining power α_i is determined by the ratio of net energy transmission of a DSA to the total energy transmission of all participants.

3.5 Decomposition and solution of the general Nash bargaining problem

According to the proposition put forward by Wang and Huang (2016), the optimal solution of the Nash bargaining problem is equivalent to the cost minimization of DSAs. By combining the individual rationality condition with the constraint in Equation 4b, a feasible payment allocation Ce^i_{Pay} always exists, which enhances cost reduction. Consequently, the general Nash bargaining-based energy interaction problem can be decomposed into two subproblems: the operation cost minimization problem (P1) and the bargaining problem (P2) (Kim et al., 2019). The optimal results are obtained by solving these two subproblems sequentially. Considering whether DSAs participate in energy interaction or not, the operation cost minimization problem (P1) encompasses both the individual operation model (1) and the cooperative operation model (3). Since the operation optimization problem (P1) consists of a quadratic objective and linear constraints, the optimal solution can be obtained by directly solving the convex problem. This optimal solution is then used to calculate the bargaining problem (P2), utilizing the value of α_i in (5):

$$\max\prod_{i}^{\mathcal{M}}\Big(\eta^{i*}-Ce^i_{Pay}\Big)^{\alpha_i} \quad s.t.\ (4b),(4c), \tag{6}$$

where $\eta^{i*}=C^{i*}_{Non}-C^{i*}_{Tra}$ represents the cost saving of cooperative DSA i through energy interaction. To allocate the benefits, the bargaining problem (P2) is transformed into a convex problem by taking the logarithm of (6):

$$\min\sum_{i}^{\mathcal{M}}-\alpha_i ln\Big(\eta^{i*}-Ce^i_{Pay}\Big) \quad s.t.\ (4b),(4c). \tag{7}$$

According to Zhong et al. (2020), since the objective function $ln(\bullet)$ increases monotonically, the optimal solution can be obtained by solving the model (7). An improved alternating direction multiplier method (ADMM) algorithm is proposed to solve the energy interaction problem in a distributed manner. To avoid updating the multiplier in a centralized way, each DSA interacts with its neighbors to share local information. For operation problem (P1), it is decomposed by introducing auxiliary variables $P^{j,t,w}_{Tra,i}$ and $P^{i,t,w}_{Tra,j}$. The details of the algorithm are shown in Algorithm 1. The couple constraint in Equation 3c is decomposed as:

$$P^{i,t,w}_{Tra}=P^{j,t,w}_{Tra,i}:\lambda^{i,t}$$
$$P^{j,t,w}_{Tra}=P^{i,t,w}_{Tra,j}:\lambda^{j,t}, \tag{8}$$

Input: Set iteration index $k \in [0,K]$, primal residue ϵ^{Pri}, dual residue ϵ^{Dual}, and step size $\rho_i(k)$.

1: **repeat**

2: Each DSA solves the local energy interaction problem (9).

3: Update the multipliers $\lambda^{i,t}(k)$ in (10).

4: Each DSA i computes the primal and dual residues. If the stopping criteria are satisfied, terminate; otherwise, repeat Step 4.

5: **until** Stopping criteria (11) are satisfied, terminate.

Algorithm 1. An improved ADMM algorithm for solving the energy interaction problem of the DSA.

where λ_i and λ_j represent the Lagrangian multipliers. The augmented Lagrangian function of the energy interaction model is then expressed as follows:

$$L_i^{DSA} = C_{Tra}^i + \sum_j^{\mathcal{M}} \sum_t^{\mathcal{T}} \lambda^{i,t} \left(P_{Tra}^{i,t,w} - P_{Tra,i}^{j,t,w} \right) + \sum_j^{\mathcal{M}} \rho_j / 2 \sum_t^{\mathcal{T}} \| P_{Tra}^{i,t,w} - P_{Tra,i}^{j,t,w} \|_2^2, \tag{9}$$

where ρ_j is the penalty parameter for DSA i. After each iteration, the updated expression of $\lambda^{i,t}$ at iteration k is

$$\lambda^{i,t}(k) = \lambda^{i,t}(k-1) + \rho_i(k) \left(P_{Tra}^{i,t,w} - P_{Tra,i}^{j,t,w} \right). \tag{10}$$

The iteration converges when the primal and dual residues satisfy the following conditions (ϵ^{Pri} and ϵ^{Dual}):

$$\begin{aligned} P_{Tra}^{i,t,w} - P_{Tra,i}^{j,t,w} &\le \epsilon^{Pri}, \\ P_{Tra}^{i,t,w}(k-1) - P_{Tra}^{i,t,w}(k) &\le \epsilon^{Dual}. \end{aligned} \tag{11}$$

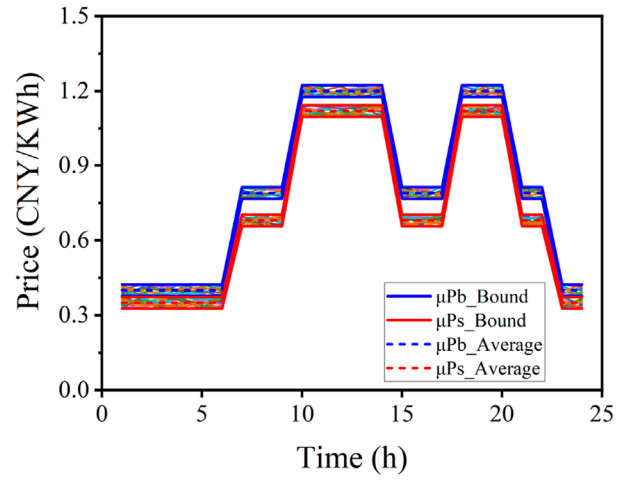

FIGURE 2
TOU price scenario with the distribution network.

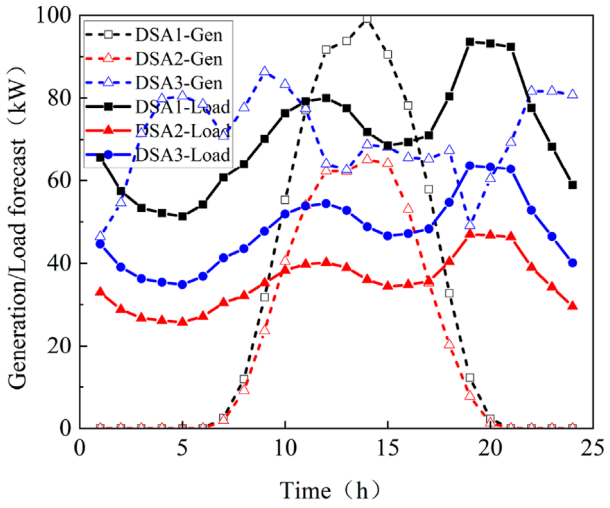

FIGURE 3
Forecast of renewable generations and loads.

4 Case study

Numerical simulations are conducted in a distribution network to evaluate the effect of the demand response and uncertain prices on energy interaction. The system aims to verify the performance of the operation strategy based on the general Nash bargaining game theory. In the case study, simulations are performed on an IEEE 33-bus system with three DSAs located at buses 11, 23, and 29. The operation data, including the forecast value of price, generation, and load demand, are obtained from the study by Chen et al. (2017) and Lu et al. (2020). All simulations are solved using the Gurobi solver (Gurobi Optimization, 2020) in the Python environment on an Intel Core i7 computer.

4.1 Operation cost considering the stochastic prices and demand response

The effect of stochastic prices on the operation strategy is analyzed by comparing the operation costs under multiple price scenarios with the forecast value. The fluctuation in the market prices is modeled using the given probability distribution function, which is assumed to obey the Gaussian distribution. As shown in Figure 2, the forecast values of TOU prices are selected as the mean value with a variance of 1×10^{-4}. Although large-scale scenarios are necessary to characterize random factors, they impose a heavy computational burden. To address this, a scenario reduction method is applied to decrease the number of scenarios. A total of 1,000 scenarios are generated by using Monte Carlo sampling, and K-means-based clustering reduction is utilized to generate 10 typical scenarios (Wang et al., 2021). The expected values of these multiple scenarios are selected as a result of the stochastic optimization, while the cost in the deterministic optimization is determined by the reaction of the DSAs to the predictable price. A general Nash bargaining-based interaction scheme is adopted to allocate the

TABLE 1 Operation costs without the demand response (CNY).

Congestion	Price	Cost	DSA 1	DSA 2	DSA 3	Total
No	Deterministic	C^i_{Non}	655.35	196.49	−322.42	529.42
		C^i_{Tra}	146.05	88.82	166.42	401.28
		Ce^i_{Pay}	456.37	91.31	−547.69	\
		C^i_{Total}	602.42	180.13	−381.27	401.28
Yes	Deterministic	C^i_{Tra}	73.49	80.76	93.65	247.90
		Ce^i_{Pay}	443.64	89.46	−533.09	\
		C^i_{Total}	517.12	170.22	−439.44	247.90
No	Stochastic	C^i_{Non}	647.84	195.57	−332.25	511.16
		C^i_{Tra}	319.15	461.45	−297.26	483.34
		Ce^i_{Pay}	314.76	−271.59	−43.17	\
		C^i_{Total}	633.91	189.86	−340.43	483.34
Yes	Stochastic	C^i_{Tra}	21.54	308.46	154.18	484.19
		Ce^i_{Pay}	612.48	−115.66	−496.82	\
		C^i_{Total}	634.03	192.80	−342.64	484.19

TABLE 2 Operation costs with the demand response (CNY).

Congestion	Price	Cost	DSA 1	DSA 2	DSA 3	Total
No	Deterministic	C^i_{Non}	622.26	177.55	−348.17	451.64
		C^i_{Tra}	53.00	61.59	51.46	166.04
		Ce^i_{Pay}	433.49	73.79	−507.28	\
		C^i_{Total}	486.49	135.37	−455.82	166.04
Yes	Deterministic	C^i_{Tra}	35.58	50.85	59.58	146.01
		Ce^i_{Pay}	432.35	83.45	−515.81	\
		C^i_{Total}	467.93	134.30	−456.22	146.01
No	Stochastic	C^i_{Non}	618.43	177.22	−356.44	439.21
		C^i_{Tra}	151.21	135.41	125.54	412.16
		Ce^i_{Pay}	455.30	40.18	−495.48	\
		C^i_{Total}	606.51	175.59	−369.94	412.16
Yes	Stochastic	C^i_{Tra}	140.86	133.07	137.88	411.81
		Ce^i_{Pay}	465.05	42.55	−507.60	\
		C^i_{Total}	605.92	175.62	−369.73	411.81

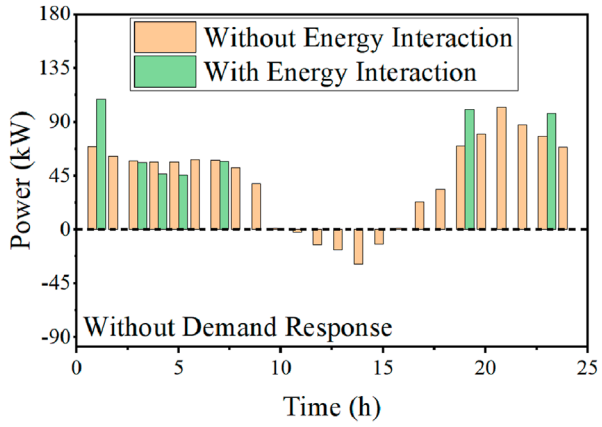

Figure 4a. DSA1.

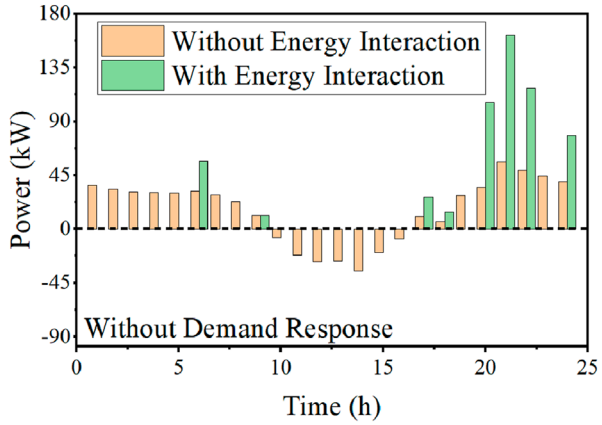

Figure 4b. DSA2.

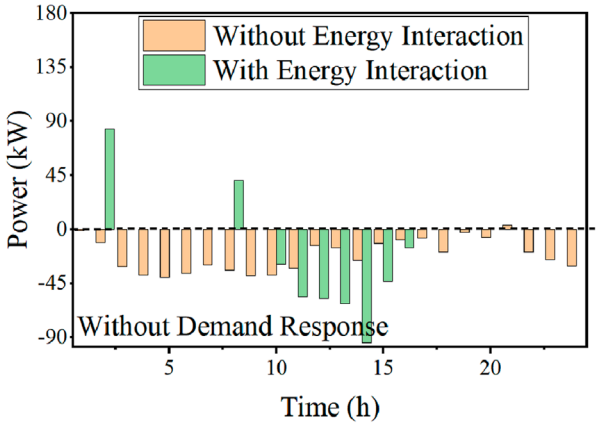

Figure 4c. DSA3.

FIGURE 4
Interaction between the distribution network and DSAs ignoring the demand response. **(A)** DSA 1, **(B)** DSA 2, and **(C)** DSA 3.

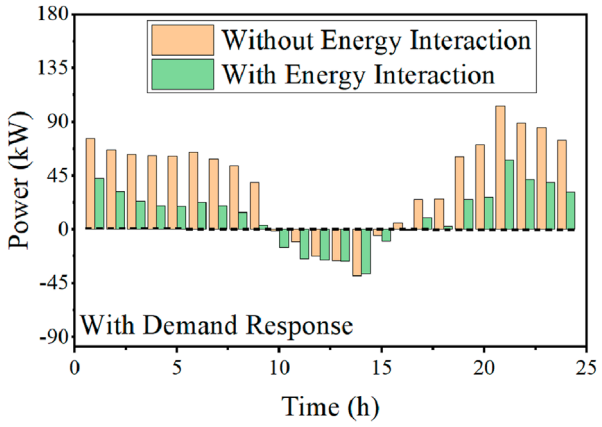

Figure 5a. DSA1.

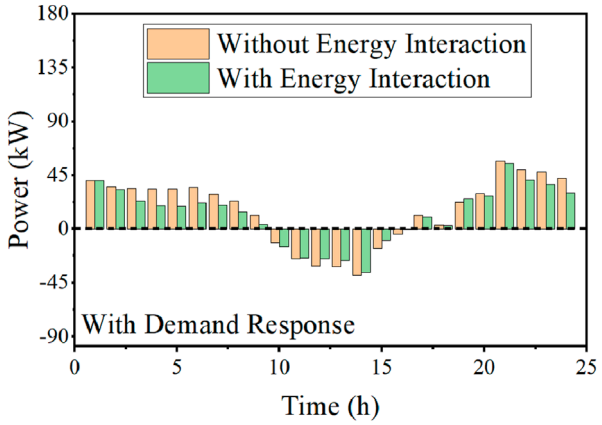

Figure 5b. DSA2.

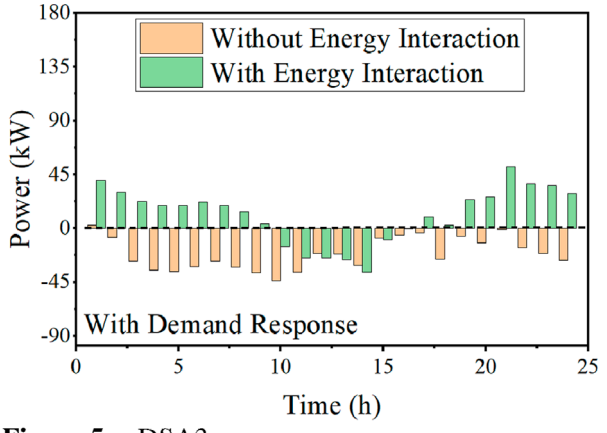

Figure 5c. DSA3.

FIGURE 5
Interaction between the distribution network and DSAs considering the demand response. **(A)** DSA 1, **(B)** DSA 2, and **(C)** DSA 3.

benefits when DSAs participate in energy interaction. To analyze the effect of the price on energy interaction, as shown in Figure 3, we assume that the predicted values of renewable generation and load demand are accurate. Since two important factors, energy interaction and demand response, affect the operation strategy, this paper analyzes the impact of these factors on the optimal operation strategy.

The deterministic and stochastic optimization results without/with the demand response are shown in Tables 1, 2, respectively. A negative value indicates the benefit that DSAs gain from selling energy to the distribution network or neighbors. It can be observed that DSAs reduce their operation cost when they participate in energy interaction. Considering the stochastic prices given in Table 1, the total operation cost of three DSAs is

TABLE 3 Total interaction quantity between DSAs and the distribution network (kWh).

Cooperation		Demand response	
		No	Yes
No	Buy	1,584.09	1,626.33
	Sell	732.95	775.18
Yes	Buy	1,208.73	1,262.64
	Sell	357.58	411.49

reduced by 24.20% under deterministic pricing, while the cost is reduced by 5.44% under uncertain pricing. In other words, compared with deterministic pricing, cooperative profit in energy interaction decreases by 16.98% in stochastic scenarios. The reason may be that, compared to deterministic prices, cooperative costs vary with the price scenarios, ultimately increasing the expected costs.

Considering the demand response, DSAs shift loads to periods of plentiful generation or lower demand through price adjustments or monetary incentives. They also enhance the efficiency of renewable energy utilization by coordinating the charging and discharging decisions of energy storage systems. As shown in Table 2, DSAs respond to prices through peak shaving and valley filling, which decreases the load demand during peak price periods. Consequently, operation costs—whether for individual or cooperative operations—significantly decrease compared to those given in Table 1. In other words, energy interaction among multiple DSAs enhances adaptable performance when considering the demand response.

The operation costs in energy interaction among DSAs will vary if the transmission lines have limitations within the distribution network. For simplicity, a maximum capacity of 100 kWh is considered for the line between nodes 2 and 3. This constraint causes decision changes for DSAs during the process of energy transactions with the distribution network and their neighbors. It can be observed that cooperative costs are always less than those of individual operations, and the demand response further reduces these operation costs.

Congestion impacts the operation decisions and, subsequently, the cooperative costs of DSAs. It restricts energy transmission for DSAs regardless of whether the demand response is considered. For deterministic prices, DSAs schedule battery usage to alleviate congestion, resulting in lower operation costs. However, stochastic prices compel DSAs to respond dynamically, leading to similar final operation costs with normal energy interaction since the total demand remains consistent.

4.2 Energy interaction with the distribution network

Figures 4, 5 illustrate the energy interaction results between the distribution network and DSAs over the course of a day.

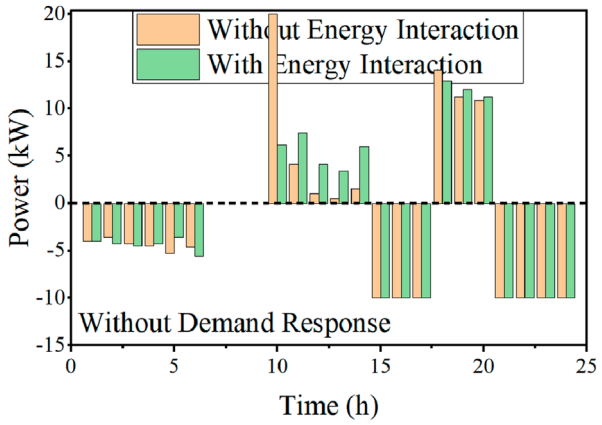

Figure 6a. DSA1.

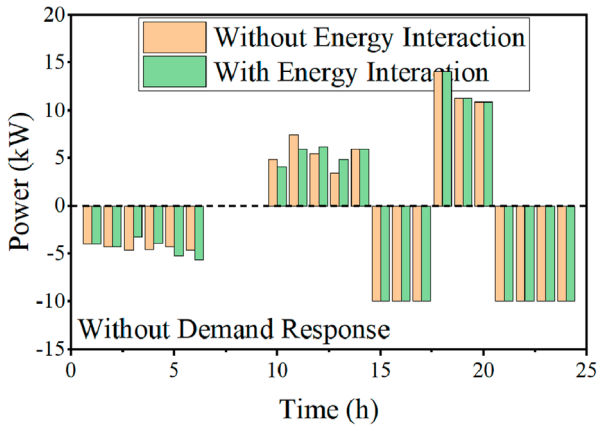

Figure 6b. DSA2.

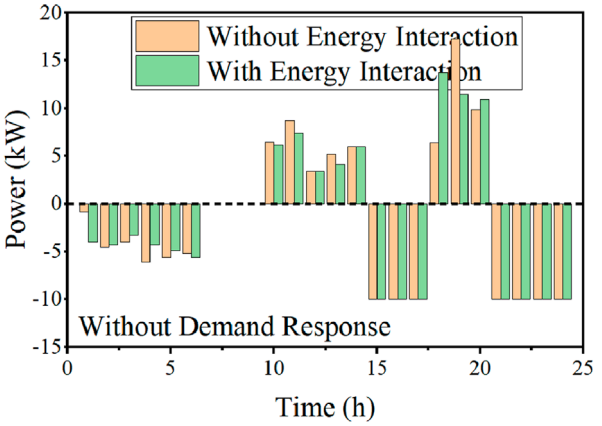

Figure 6c. DSA3.

FIGURE 6
Scheduling result of the energy storage without the demand response. **(A)** DSA 1, **(B)** DSA 2, and **(C)** DSA 3.

The positive/negative values represent the energy purchased/sold from/to the distribution network, respectively. We comparatively analyze the interaction quantities between the distribution network and multiple DSAs, regardless of their participation in energy interaction. Given the price scenarios, DSAs adjust their demand for purchasing/selling electricity to achieve cost minimization.

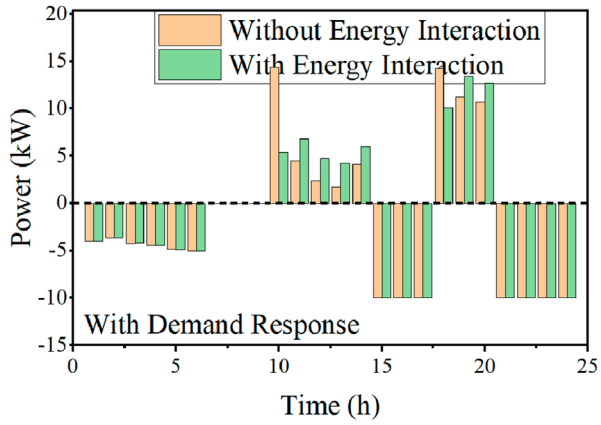

Figure 7a. DSA1.

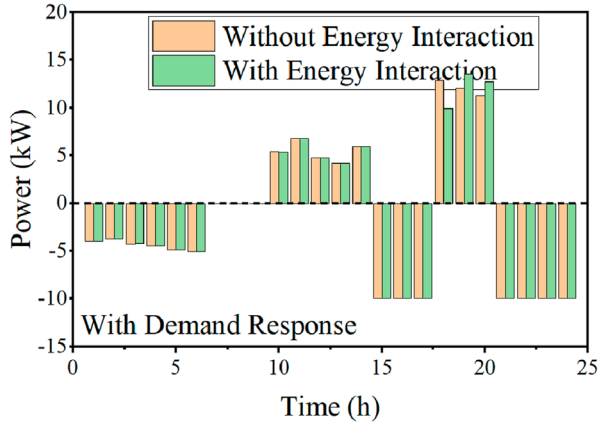

Figure 7b. DSA2.

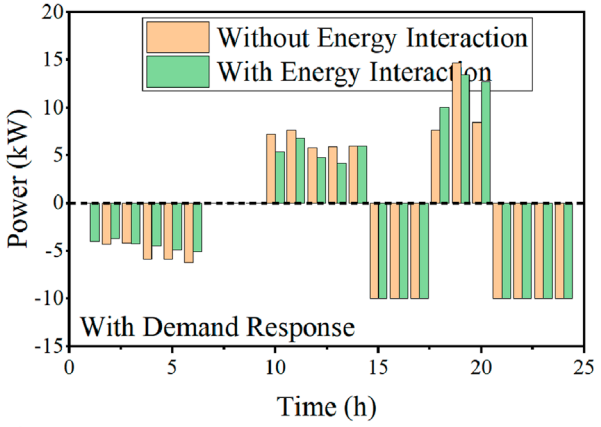

Figure 7c. DSA3.

FIGURE 7
Scheduling result of the energy storage with the demand response. **(A)** DSA 1, **(B)** DSA 2, and **(C)** DSA 3.

Figure 4 shows the comparison of the effects of individual versus cooperative operation among DSAs on energy interactions with the distribution network. An individual DSA satisfies power balance by leveraging the distribution network and energy storage. Due to the scheduling limitation of the battery, the individual DSA may need to purchase electricity at a high price, increasing the operation costs. In contrast, cooperative DSAs form a group and share idle energy to balance their energy needs. DSAs purchase energy at 0:00–5:00 and 20:00–24:00 while selling energy at 10:00–15:00 to maximize their cooperative benefits during energy interactions. The load regulation capability of DSAs is enhanced when considering the demand response. As shown in Figure 5, DSAs achieve peak shaving and valley filling by leveraging the demand response and energy interactions.

To further analyze the energy interaction, the total interaction quantity between DSAs and the distribution network is summarized in Table 3. The data show that the interaction between DSAs and the distribution network is influenced by both the interactive behavior of DSAs and demand response. We observed that the energy interaction among DSAs can reduce their dependence on the distribution network, enhancing their ability to cope with price uncertainty. To maintain energy balance, they purchase less energy from the distribution network and reduce the quantity of energy sold. Since the demand response is closely tied to electricity prices, DSAs increase their demand when the prices are lower, effectively responding to price uncertainties.

4.3 Analysis of optimal results of the energy storage

The scheduling results of energy storage without/with the demand response are given in Figures 6, 7, respectively. The positive values represent storage discharging, while the negative values indicate storage charging. These figures demonstrate that energy storage can be utilized to satisfy the supply–demand balance through an internal scheduling strategy. As shown in Figure 6, the depth of charge/discharge is higher for the DSA operating individually without a demand response as energy storage is the primary means of shifting energy demand to other periods. This is particularly evident for DSA 1 at 10:00 and DSA 3 at 19:00. Although cooperative DSAs reduce the depth of charging/discharging, energy storage still works in conjunction with energy interaction to maintain energy balance.

The scheduling results of the energy storage considering the demand response are shown in Figure 7. We can observe that the reliance on energy storage decreases as supply–demand balance can be achieved through load shifting. Consequently, the charging and discharging depth of the energy storage for DSA 1 and DSA 3 is reduced, which, in turn, lowers the degradation costs in the objective function.

4.4 Analysis of energy interaction among DSAs

The energy interaction quantities among DSAs are given in Figure 8 when they cooperate with neighbors to share idle energy. The positive values indicate DSA i purchasing energy from neighbors, while the negative values represent selling energy to others. Compared to individual operation, DSAs achieve energy balance by combining energy interaction, load shifting, and energy storage scheduling. This approach enhances energy self-sufficiency through energy interaction, potentially reducing the reliance on the distribution network.

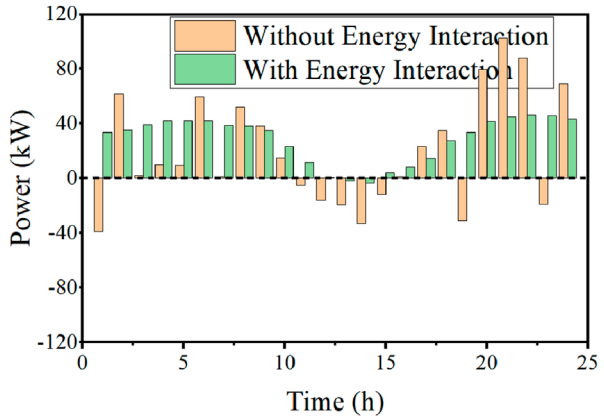

Figure 8a. DSA1.

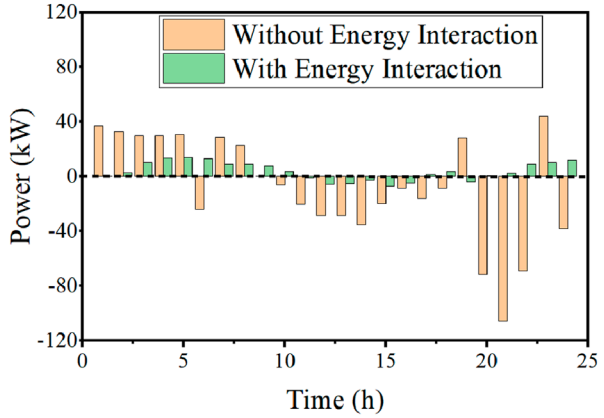

Figure 8b. DSA2.

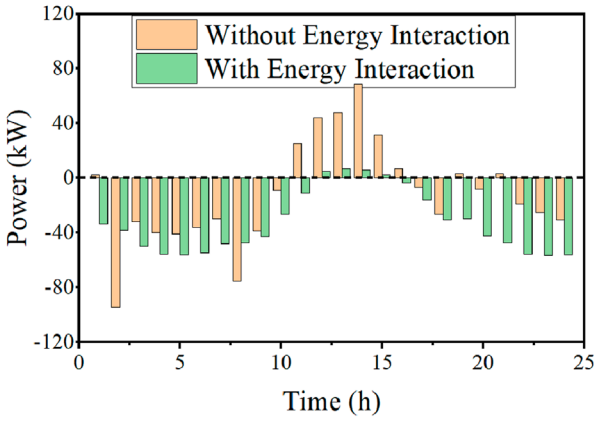

Figure 8c. DSA3.

FIGURE 8
Interaction among DSAs. **(A)** DSA 1, **(B)** DSA 2, and **(C)** DSA 3.

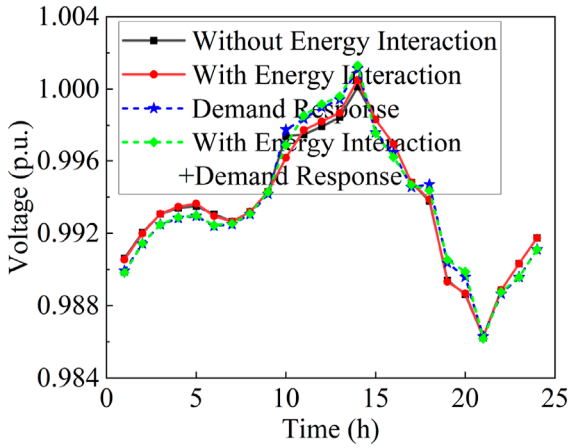

Figure 9a. DSA1.

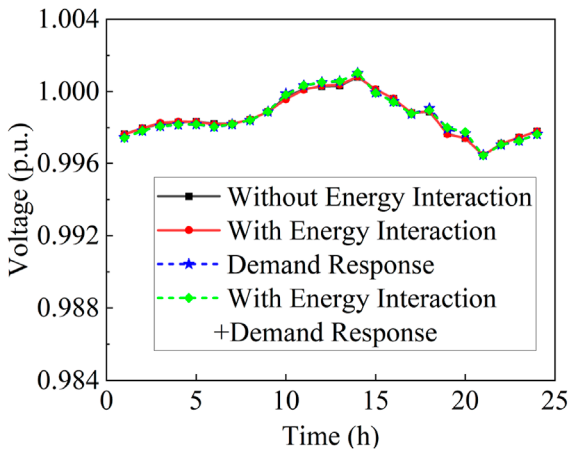

Figure 9b. DSA2.

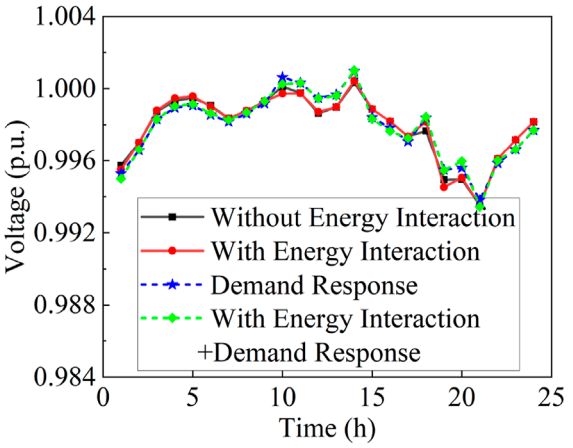

Figure 9c. DSA3.

FIGURE 9
Voltage of the node connected to multiple DSAs. **(A)** DSA 1, **(B)** DSA 2, and **(C)** DSA 3.

4.5 Distribution of the node voltage

The node voltage varies with the energy interaction and demand response. Nodes 11, 23, and 29, connected to DSAs, serve as examples, and their voltages are shown in Figure 9. Although the voltage fluctuates across various simulation scenarios and periods, it always remains within the boundary limits. DSA 1, which has the highest load demand, experiences the largest voltage fluctuation, ranging from 0.986 p.u. to 1.001 p.u. Conversely, DSA 2, with the smallest load demand, exhibits relatively smooth voltage fluctuations. The demand response also leads to significant voltage fluctuations at different times. As shown in Figures 9A, C, DSAs shift

loads to maintain the supply–demand balance, thereby altering the voltage distribution within the network.

5 Conclusion

This paper presents an energy interaction framework for DSAs to enhance the local consumption of renewable generation. A general Nash bargaining theoretic model is established, taking into account the effect of uncertain prices and demand response. The typical price scenarios are depicted via Monte Carlo sampling and clustering. Given the price scenarios, DSAs make the optimal decisions by shifting loads to the plentiful generation or lower demand time through prices or monetary incentives. To solve the energy interaction model, it is decomposed and transformed into a traceable problem by leveraging the logarithmic transformation. In addition, the optimal power flow constraints are incorporated to improve the model's practicality. The limitation of transmission capacity alters the operation strategies, which affects the operation costs. It decreases the energy exchange with the distribution network and increases the energy interaction among DSAs. An improved ADMM is proposed to solve the energy interaction problem using local information. Numerical simulations are conducted on an IEEE-33 bus system, demonstrating that uncertain prices may increase the total operation costs, while the demand response improves scheduling flexibility. Future work will focus on addressing energy transmission insufficiency due to capacity limitations during energy interactions.

Data availability statement

The original contributions presented in the study are included in the article/Supplementary Material; further inquiries can be directed to the corresponding author.

Author contributions

FW: investigation and writing–original draft. XW: conceptualization and writing–original draft. JL: software and writing–original draft. YL: methodology and writing–original draft. HY: conceptualization and writing–original draft.

Funding

The author(s) declare that financial support was received for the research, authorship, and/or publication of this article. This work was supported by the Research on key technologies to improve application capability of distribution automation in new power system (2023A-016).

Conflict of interest

The authors declare that the research was conducted in the absence of any commercial or financial relationships that could be construed as a potential conflict of interest.

Publisher's note

All claims expressed in this article are solely those of the authors and do not necessarily represent those of their affiliated organizations, or those of the publisher, the editors, and the reviewers. Any product that may be evaluated in this article, or claim that may be made by its manufacturer, is not guaranteed or endorsed by the publisher.

References

Alizadeh, A., Esfahani, M., Dinar, F., Kamwa, I., Moeini, A., Mohseni-Bonab, S. M., et al. (2024). A cooperative transactive multi-carrier energy control mechanism with p2p energy+ reserve trading using nash bargaining game theory under renewables uncertainty. *Appl. Energy* 353, 122162. doi:10.1016/j.apenergy.2023.122162

Baharvandi, A., Aghaei, J., Nikoobakht, A., Niknam, T., Vahidinasab, V., Giaouris, D., et al. (2019). Linearized hybrid stochastic/robust scheduling of active distribution networks encompassing pvs. *IEEE Trans. Smart Grid* 11, 357–367. doi:10.1109/tsg.2019.2922355

Chang, X., Xu, Y., Gu, W., Sun, H., Chow, M.-Y., and Yi, Z. (2020). Accelerated distributed hybrid stochastic/robust energy management of smart grids. *IEEE Trans. Industrial Inf.* 17, 5335–5347. doi:10.1109/tii.2020.3022412

Chen, S., Wei, Z., Sun, G., Cheung, K. W., Wang, D., and Zang, H. (2017). Adaptive robust day-ahead dispatch for urban energy systems. *IEEE Trans. Industrial Electron.* 66, 1379–1390. doi:10.1109/tie.2017.2787605

Chen, Y., Mei, S., Zhou, F., Low, S. H., Wei, W., and Liu, F. (2019). An energy sharing game with generalized demand bidding: model and properties. *IEEE Trans. Smart Grid* 11, 2055–2066. doi:10.1109/tsg.2019.2946602

Dehghanpour, K., and Nehrir, H. (2017). Real-time multiobjective microgrid power management using distributed optimization in an agent-based bargaining framework. *IEEE Trans. Smart Grid* 9, 6318–6327. doi:10.1109/tsg.2017.2708686

Farivar, M., and Low, S. H. (2013). Branch flow model: relaxations and convexification-part i. *IEEE Trans. Power Syst.* 28, 2554–2564. doi:10.1109/tpwrs.2013.2255317

Gurobi Optimization (2020). *Gurobi optimizer reference manual.*

Hirsch, A., Parag, Y., and Guerrero, J. (2018). Microgrids: a review of technologies, key drivers, and outstanding issues. *Renew. Sustain. Energy Rev.* 90, 402–411. doi:10.1016/j.rser.2018.03.040

Jiang, Q., Mu, Y., Jia, H., Cao, Y., Wang, Z., Wei, W., et al. (2022). A stackelberg game-based planning approach for integrated community energy system considering multiple participants. *Energy* 258, 124802. doi:10.1016/j.energy.2022.124802

Jin, Y., Choi, J., and Won, D. (2020). Pricing and operation strategy for peer-to-peer energy trading using distribution system usage charge and game theoretic model. *Ieee Access* 8, 137720–137730. doi:10.1109/access.2020.3011400

Khorasany, M., Paudel, A., Razzaghi, R., and Siano, P. (2020). A new method for peer matching and negotiation of prosumers in peer-to-peer energy markets. *IEEE Trans. Smart Grid* 12, 2472–2483. doi:10.1109/tsg.2020.3048397

Kim, H., Lee, J., Bahrami, S., and Wong, V. W. (2019). Direct energy trading of microgrids in distribution energy market. *IEEE Trans. Power Syst.* 35, 639–651. doi:10.1109/tpwrs.2019.2926305

Kumar, K. P., and Saravanan, B. (2017). Recent techniques to model uncertainties in power generation from renewable energy sources and loads in microgrids–a review. *Renew. Sustain. Energy Rev.* 71, 348–358. doi:10.1016/j.rser.2016.12.063

Li, G., Li, Q., Liu, Y., Liu, H., Song, W., and Ding, R. (2022). A cooperative stackelberg game based energy management considering price discrimination and risk assessment. *Int. J. Electr. Power and Energy Syst.* 135, 107461. doi:10.1016/j.ijepes.2021.107461

Li, J., Zhang, C., Xu, Z., Wang, J., Zhao, J., and Zhang, Y.-J. A. (2018). Distributed transactive energy trading framework in distribution networks. *IEEE Trans. Power Syst.* 33, 7215–7227. doi:10.1109/tpwrs.2018.2854649

Lu, S., Gu, W., Zhang, C., Meng, K., and Dong, Z. (2020). Hydraulic-thermal cooperative optimization of integrated energy systems: a convex optimization approach. *IEEE Trans. Smart Grid* 11, 4818–4832. doi:10.1109/tsg.2020.3003399

Luo, C., Zhou, X., and Lev, B. (2022). Core, shapley value, nucleolus and nash bargaining solution: a survey of recent developments and applications in operations management. *Omega* 110, 102638. doi:10.1016/j.omega.2022.102638

Paudel, A., Chaudhari, K., Long, C., and Gooi, H. B. (2019). Peer-to-peer energy trading in a prosumer-based community microgrid: a game-theoretic model. *IEEE Trans. Industrial Electron.* 66, 6087–6097. doi:10.1109/tie.2018.2874578

Sarker, E., Seyedmahmoudian, M., Jamei, E., Horan, B., and Stojcevski, A. (2020). Optimal management of home loads with renewable energy integration and demand response strategy. *Energy* 210, 118602. doi:10.1016/j.energy.2020.118602

Tushar, W., Saha, T. K., Yuen, C., Morstyn, T., McCulloch, M. D., Poor, H. V., et al. (2019). A motivational game-theoretic approach for peer-to-peer energy trading in the smart grid. *Appl. energy* 243, 10–20. doi:10.1016/j.apenergy.2019.03.111

Tushar, W., Saha, T. K., Yuen, C., Smith, D., and Poor, H. V. (2020). Peer-to-peer trading in electricity networks: an overview. *IEEE Trans. Smart Grid* 11, 3185–3200. doi:10.1109/tsg.2020.2969657

Tushar, W., Yuen, C., Mohsenian-Rad, H., Saha, T., Poor, H. V., and Wood, K. L. (2018). Transforming energy networks via peer-to-peer energy trading: the potential of game-theoretic approaches. *IEEE Signal Process. Mag.* 35, 90–111. doi:10.1109/msp.2018.2818327

Vieira, G., and Zhang, J. (2021). Peer-to-peer energy trading in a microgrid leveraged by smart contracts. *Renew. Sustain. Energy Rev.* 143, 110900. doi:10.1016/j.rser.2021.110900

Wang, H., and Huang, J. (2016). Incentivizing energy trading for interconnected microgrids. *IEEE Trans. Smart Grid* 9, 2647–2657. doi:10.1109/tsg.2016.2614988

Wang, L., Zhang, Y., Song, W., and Li, Q. (2021). Stochastic cooperative bidding strategy for multiple microgrids with peer-to-peer energy trading. *IEEE Trans. industrial Inf.* 18, 1447–1457. doi:10.1109/tii.2021.3094274

Wei, C., Shen, Z., Xiao, D., Wang, L., Bai, X., and Chen, H. (2021). An optimal scheduling strategy for peer-to-peer trading in interconnected microgrids based on ro and nash bargaining. *Appl. Energy* 295, 117024. doi:10.1016/j.apenergy.2021.117024

Zhong, W., Xie, S., Xie, K., Yang, Q., and Xie, L. (2020). Cooperative p2p energy trading in active distribution networks: an milp-based nash bargaining solution. *IEEE Trans. Smart Grid* 12, 1–1276. doi:10.1109/tsg.2020.3031013

Nomenclature

Indices

i	Index of DSAs
t	Index of hours
w	Index of scenarios

Sets

$\mathcal{M}$	Set of DSAs
Ω	Set of price scenarios
$\mathcal{T}$	Set of time intervals

Parameters

$P^{i,\ t}_{load,Pre}$	Predictable load at time slot t (kW)
$P^{i,\ t,\ w}_{Gen}$	Generation output at time slot t (kW)
$P^{\max}_{Pb}, P^{\max}_{Ps}$	Limitation of purchasing/selling power to the main grid (kW)
$P^{\max}_{Ec}, P^{\max}_{Ed}$	Maximum charging/discharging power of the battery in DSA i
$SOC^{\min}_{i}, SOC^{\max}_{i}$	Minimum/maximum limitation of the SOC in DSA i (%)
U^{i}_{min}, U^{i}_{max}	Minimum/maximum limitation of voltage in bus i
$P^{i,j}_{max}, Q^{i,j}_{max}$	Active/reactive power limitation of branch (i,j)
$P^{i}_{g,max}, Q^{i}_{g,max}$	Active/reactive power limitation of the distribution network
Cap^{i}	Capacity of a battery in DSA i (kW)
c^{i}_{E}	Degradation cost of a battery in DSA i (CNY/kW)
$\eta^{i}_{Ec}, \eta^{i}_{Ed}$	Charging/discharging efficiency of a battery in DSA i
SOC^{i}_{exp}	Expected state of a battery at $t = 24$
α_i	Bargaining power of DSA i
α_L	Ratio of load shifting (%)
$\mu^{t,w}_{Pb}, \mu^{t,w}_{Ps}$	Price at which DSA i purchases/sells energy from/to the main grid (CNY/kW)
c_{Load}	Comfortable penalty cost in DSA i

Variables

C^{i}_{Non}	Operation cost of DSA i without energy interaction (CNY)
C^{i}_{Tra}	Operation cost of DSA i with energy interaction (CNY)
Ce^{i}_{Pay}	Net payment of DSA i for energy interaction among DSAs (CNY)
$P^{i,t,w}_{Pb}$	DSA i purchases power from the main grid (kW)
$P^{i,t,w}_{Ps}$	DSA i sells power to the main grid (kW)
$P^{i,t,w}_{Ec}$	Charging power of a battery in DSA i at time slot t (kW)
$P^{i,t,w}_{Ed}$	Discharging power of a battery in DSA i at time slot t (kW)
$SOC^{i,t,w}$	State of charge of a battery in DSA i(%)
$P^{i,t,w}_{Tra}$	DSA i purchases power from neighbors
$p_{i,t,w}, q_{i,t,w}$	Active/reactive power injection on bus i at time t
$P_{i,j,t,w}, Q_{i,j,t,w}$	Active/reactive power flow on branch (i,j)
$P^{i,t,w}_{g}, Q^{i,t,w}_{g}$	Active/reactive power provided by the distribution network
$U_{i,t,w}$	Squared voltage magnitude of bus i at time t
λ_i	Lagrangian multipliers
$P^{i,t,w}_{Tra,i}$	Auxiliary variables of energy interaction

frontiers | Frontiers in Energy Research

TYPE Original Research
PUBLISHED 04 October 2024
DOI 10.3389/fenrg.2024.1428524

OPEN ACCESS

EDITED BY
Chenghong Gu,
University of Bath, United Kingdom

REVIEWED BY
Runze Wu,
North China Electric Power University, China
Fan Chen,
Nanjing Institute of Technology (NJIT), China
Roberto Francisco Coelho,
Federal University of Santa Catarina, Brazil

*CORRESPONDENCE
Qunying Liu,
lqy1206@126.com

RECEIVED 06 May 2024
ACCEPTED 11 September 2024
PUBLISHED 04 October 2024

CITATION
Chen Z, Hao Z, An J, Fan W, Huang Y and Liu Q (2024) Research on a coordinated control strategy of three-phase photovoltaic converters based on a buck–boost DC link. *Front. Energy Res.* 12:1428524. doi: 10.3389/fenrg.2024.1428524

Research on a coordinated control strategy of three-phase photovoltaic converters based on a buck–boost DC link

Zhiyong Chen[1], Zhifang Hao[1], Jiakun An[1], Wenyi Fan[1], Yuan Huang[1] and Qunying Liu[2]*

[1]Economic and Technical Research Institute of State Grid Hebei Electric Power Co., Ltd., Shijiazhuang, China, [2]School of Automation Engineering, University of Electronic Science and Technology of China, Chengdu, China

The high inductance current ripple and the PV voltage fluctuations limitation at the DC (direct current) -DC link have been the unsolved problems in the photovoltaic systems tied in grid. A control strategy with a current hysteresis loop is proposed to address the issues of high inductance current ripple in photovoltaic systems which can achieve real-time duty cycle regulation. Differing from the conventional mode that uses one switch in the buck–boost DC–DC link, two switches have been designed here to separate the buck and boost modes for the coordinated control, which can achieve a wide PV voltage fluctuations range. Based on the conventional fixed-duty cycle determination method, a real-time duty cycle determination method is proposed by introducing changes in inductance current. In order to improve power conversion efficiency, the incremental conductance method is improved by introducing the steepest gradient descent to quickly achieve the maximum power point tracking. This study experimentally verifies the proposed current hysteresis coordinated control method, effectively suppressing the ripple of the inductor current and expand the PV voltage fluctuation in the DC–DC link on the basis of maintaining power conversion efficiency as much as possible.

KEYWORDS

photovoltaic panel, coordinated control strategy, current hysteresis loop control, buck-boost circuit, DC-DC link

1 Introduction

In the last 20 years, many studies have focused on the topology of DC–DC links and converter technology for the DC–AC interface of photovoltaic (PV) cells and the grid. DC–AC interface technology has included voltage source converters (VSIs) adapted for the interface of PV panels with the grid (Teodorescu et al., 2011). To address the constraint of low leakage current for non-isolated grid-tied converters, a series of different converter structures and control schemes have been investigated (Alluhaybi et al., 2020; Khan et al., 2020), some considering stochasticity (Nan et al., 2018). In addition to converter configuration reformation, the topology and control strategy of the DC–DC link is also a key area of improvement for less harmonics and higher transferring efficiency. Liao et al. (2017) proposed a novel PV converter with a PV current decoupling strategy which can achieve maximum power point tracking performance without increasing electrolyte capacitance. The current decoupling tank in the proposed PV converter can buffer the

difference between the DC current generated by the PV panel and the rectified sinusoidal AC of the power grid. Mohammadi et al. (2018) proposed a novel switching frequency modulation method to address the trade-off between voltage gain and voltage harmonics caused by the coupling of the duty cycle and modulation ratio. Ho and Siu (2019) proposed a new converter structure in which high-frequency switches are used to control the inductor current, while low-frequency switches form a filter structure that adapts to different operating conditions. Unfortunately, the designed structure led to more energy loss.

The output voltage of PV panels is often affected by ambient factors such as sunlight intensity, temperature, and shadow. A buck–boost converter is required to adapt to a wide range of DC voltage fluctuations. Callegaro et al. (2019) proposed a single-phase, single-stage buck–boost converter which uses five switches (implemented using MOSFET power with external fast recovery diodes) to provide buck–boost operation for the wide range of changes in PV output voltage while eliminating leakage current. In order to improve power extraction under the ambient condition, a buck–boost single-phase transformer-free grid-connected photovoltaic converter based on coupled inductance has been proposed by Kumar and Singh (2019) and Hafiz et al. (2021) which has the ability to extract maximum power from the series of photovoltaic panels. Dutta and Chatterjee (2018) proposed a day-and-night operational single-phase energy stored quasi-Z-source-cascaded H-bridge (ES-qZS-CHB) converter PV system to solve the active and reactive power control problem. They designed optimal multiple combinations of duty cycle and modulation ratio to achieve the same voltage gain during night operation.

In order to balance the output voltage of input-independent-output series modules, bidirectional buck–boost and LC series power balancing units have been proposed for multiple PV panels by Dutta and Chatterjee (2020). Liang et al. (2021) proposed a multi-PV panel with battery and bidirectional converter interconnected with a three-phase grid. A buck–boost converter is connected to the main VSC with BES is responsible for the load level adjusting and the MPPT voltage. A new solar PV-fed dynamic voltage restorer (DVR) based on a trans-Z-source converter was proposed by Huang et al. (2021) to improve the power quality of on-grid PV systems, in which a hybrid unit vector template with maximum constant boost control method was proposed for transZSI-DVR. Chauhan et al. (2021) outlined an integrated three-phase transformer-less PV converter structure which utilizes an interleaved dual output buck–boost converter to obtain the boosting voltage. From a single PV source, the voltage waveform of the output terminal can be synthesized into three levels; the high-frequency dynamic is completely eliminated when the voltage passes through parasitic capacitors, effectively suppressing current leakage.

On the basis of a buck–boost circuit, coupling inductance has been proposed by Ali et al. (2021) to regulate power output, forming a secondary voltage gain adjustment strategy. In order to reduce the leakage current and number of components and to improve transfer efficiency, a transformer-free converter structure based on MOSFET power switches was proposed by Dhara and Somasekhar (2022); it shares a common ground between the PV source and grid and applies a zero-beat controller instead of a PI controller. In Yari et al. (2022), a three-phase multi-level converter based on three-level neutral point clamp quasi Z-source topology was proposed to implement maximum power tracking. These methods give almost no or very little consideration for energy conversion efficiency.

In order to achieve high efficiency and negligible loss during high-frequency switching, Gao et al. (2022) proposed a buck–boost PV converter structure with six switches which operates at different frequencies under a discontinuous mode with zero current leakage. A new seven-level common ground (CG) switched capacitor (SC)-based grid-tied transformer-less converter was introduced in Husev et al. (2022) which has three times the boosting capability of input voltage. To step up the input PV voltage and facilitate seven steps in output voltage, two SC cells are connected in parallel.

Inspired by the research outlined above, we designed a buck–boost structure and propose an effective coordinated control in DC–DC and DC–AC to improve power conversion efficiency and reduce harmonics. The configuration and operation mechanism of the PV converter with buck–boost DC links is analyzed in the second section. The third section discusses a coordinated control strategy with the current hysteresis loop on the DC–DC link and converter. To validate the superiority of the proposed coordinated control strategy with the current hysteresis loop strategy, a rigorous experimental evaluation was conducted by designing a rapid control prototype (RCP) framework which gives the simulation verification of the designed converter and the proposed coordinated control strategy, detailed in the fourth section. Conclusions are drawn in the fifth section.

2 Analysis of the structure and operating mechanism of photovoltaic converters based on a buck–boost DC link

The circuit structure of a buck–boost converter with a single photovoltaic (PV) panel is shown in Figure 1. The coordinated current hysteresis control proposed in this paper mainly controls the S1 and S2 switches of the DC link to accelerate its dynamic response ability; these are independently controlled with the converter switches S3–S8. The rationality of the switch control design in the DC–DC link directly affects the quality of the voltage output by the converter. Therefore, the focus here is on the switch control of the DC–DC link while ensuring that the converter switch is normally turned on or off.

The current hysteresis control belongs to PWM (pulse width modulation) tracking technology, the basic idea of which is to compare the controlled variable (usually including the output voltage or the inductor current in the DC–DC link) with its given value. If the difference between the controlled variable and its given value is greater than the set upper limit value, the switch state is changed to reduce the controlled variable. If their difference is less than a set lower limit value, the switch state is changed to increase the controlled quantity. If their difference is between the lower and upper limits, the switch will be kept on. Therefore, the current hysteresis control belongs to the closed-loop control, which has the characteristics of real-time control and fast response speed. Moreover, by changing the upper and lower limits of error, tracking accuracy can be easily controlled. In fact, the current hysteresis control is a non-linear control that can significantly improve the non-linear dynamic performance of the converter. Considering that

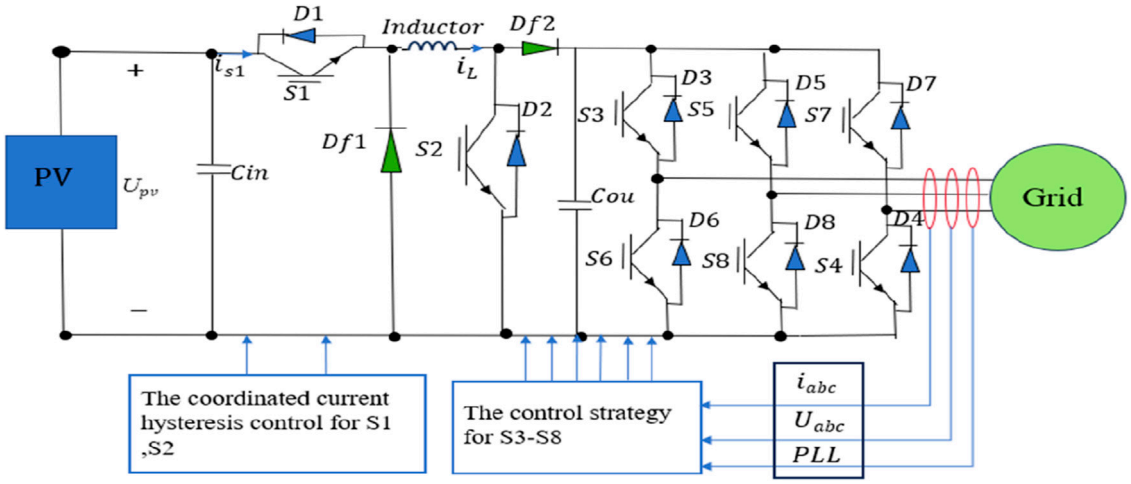

FIGURE 1
Circuit structure of the buck–boost converter with a single photovoltaic panel.

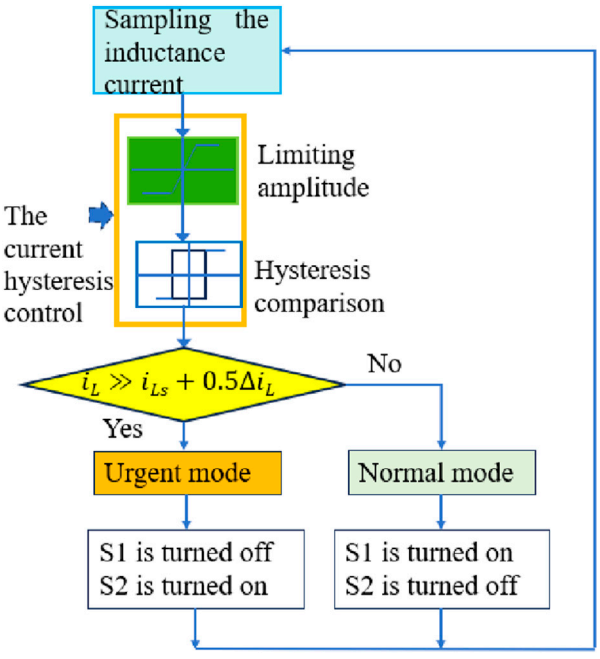

FIGURE 2
Control flow chart of the current hysteresis control.

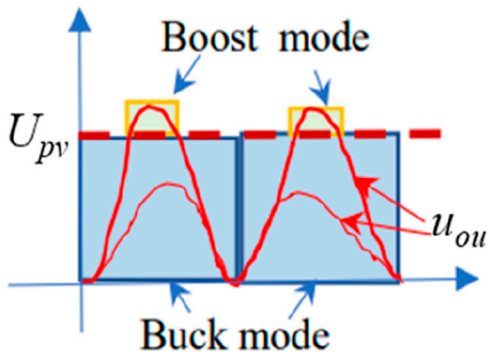

FIGURE 3
Buck and boost mode discrimination.

the PV systems are easily affected by environmental factors such as sunlight, temperature, and cloud cover, the variation range of the output voltage at the PV panel is relatively wide, which can lead to large fluctuations in inductance current. Therefore, the buck–boost converter using inductance current hysteresis control is introduced to adjust the PWM output signal based on the grid current as a reference in hysteresis control, thereby adjusting the duty cycle of the high-frequency switch and adjusting the inductance current in the buck–boost DC link.

In our work, the current hysteresis control of the DC–DC link introduces a current deviation detection loop comprising a limiting loop and a hysteresis comparison loop. Introducing the two loops creates a relationship between output voltage, output current, and inductor current, forming the current hysteresis control strategy based on the changes in output voltage, current, and inductor current to coordinate the on/off modes of S1 and S2 and limit the amplitude of the inductor ripple current. By using the current hysteresis control, sudden changes in input voltage will not have any impact on the average output voltage, only on ripple. Here, current hysteresis control is introduced. The control flow chart of the current hysteresis control is shown as Figure 2. When the transient current of the inductor exceeds a certain range $i_L \geq i_0 + 0.5\Delta i_L$ (i_L is the actual value of the inductor current; i_0 is the reference value of the inductor current; Δi_L is the variation value of the inductor current) in real-time monitoring, the urgent mode current hysteresis control is started to regulate the duty ratio of the S1 and S2 switches to avoid excessive fluctuations in the inductor current. When the inductor current is within the range $i_L \leq i_0 + 0.5\Delta i_L$, it falls in the normal mode, which is the actual processing scope of the PI control.

Figure 3 shows the discrimination in the buck–boost mode. To select this mode, the corresponding switching signal needs to be

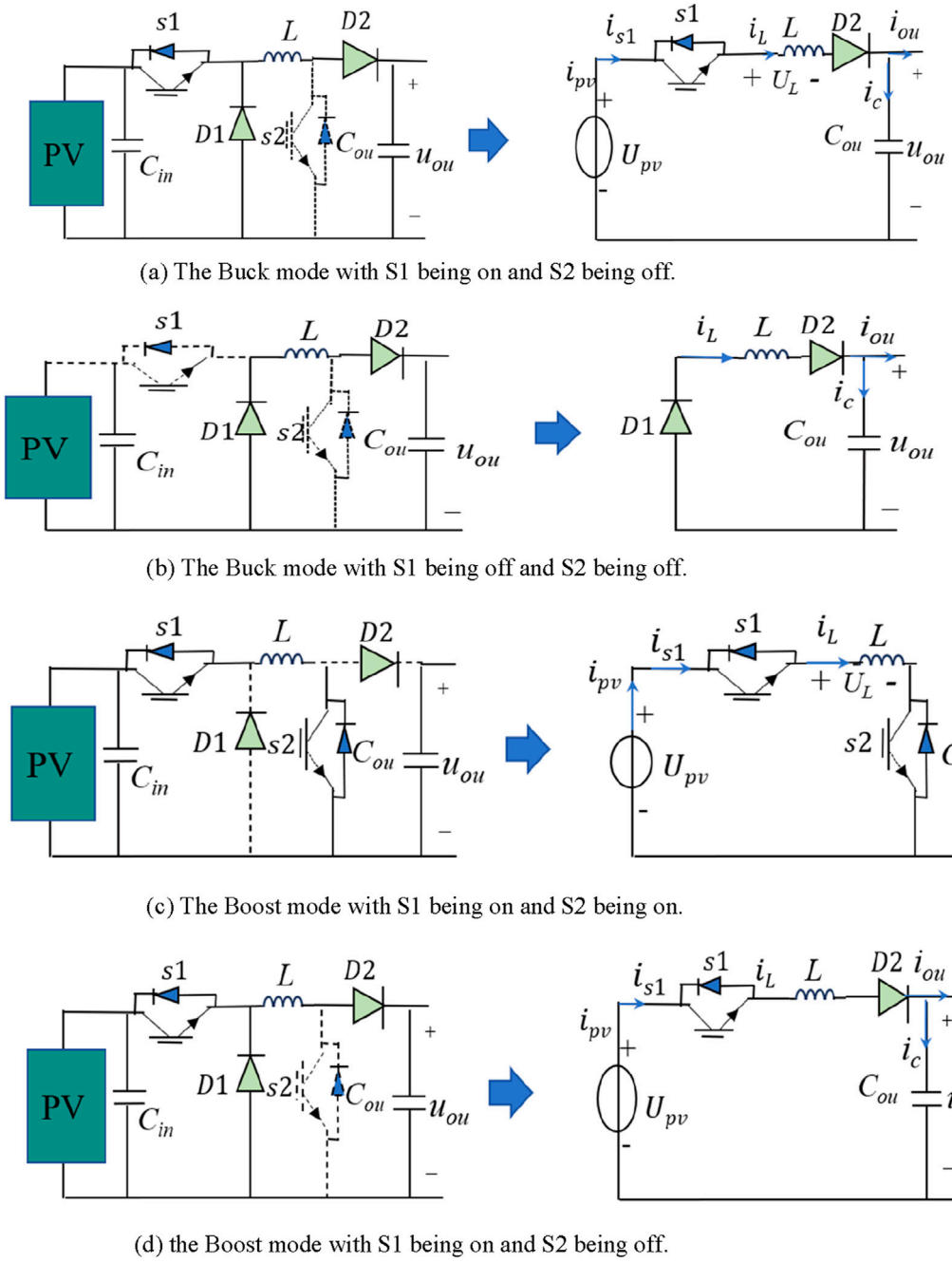

FIGURE 4
Equivalent circuit for buck and boost mode. **(A)** Buck mode with S1 on and S2 off. **(B)** Buck mode with S1 and S2 off. **(C)** Boost mode with S1 and S2 on. **(D)** Boost mode with S1 on and S2 off.

given. Determining the buck or boost mode completely depends on the comparison of the voltage of capacitor u_{cou} and the output voltage U_{PV} of the PV panel. If U_{PV} is lower than u_{cou}, it is in the buck mode, which means that the input voltage in the DC–DC link should be increased. If U_{PV} is higher than u_{cou}, it is in the boost mode, which means that the input voltage in the DC–DC link should be decreased.

According to the operating characteristics of the buck–boost converter under different operating modes, its operating mechanism is elaborated in detail as follows.

2.1 Buck mode: $u_{cou} < U_{PV}$, S1 is on, S2 is off; S1 is off, S2 is off

In Figure 4A, the voltage at the PV panel port is equivalent to the DC source U_{PV}. The voltage at the grid-tied point is assumed to be stable, and the capacitor used for voltage stabilization and connected in parallel with the PV panel is ignored. Hence, the i_{pv} current flowing out from the PV panel is equal to i_{s1}. When S1 is turned on and S2 is off, i_{s1} is also equal to i_L. The inductor is charged, and the current flowing through it not only charges the capacitor but also supplies the grid. The

voltage at both ends of the inductor is positive on the left and negative on the right, resisting the increase in current. In the PV panel, the output voltage is variable; hence, the output current i_{pv} is also variable. To maintain the output voltage of the DC link as a half wave sine, it is necessary for the S1 and S2 switches to be sinusoidal. Therefore, based on the equivalent circuit in the buck mode (Figure 4A), combined with Kirchhoff's voltage and current theorem, the voltage and current relationship of the input and output ports of the PV panel and DC–DC link can be obtained as Equations 1, 2:

$$i_{pv} = i_{s1} = i_L = i_c + i_{ou}, \tag{1}$$

$$U_{pv} = U_L + u_{cou}. \tag{2}$$

According to Equation 2 the relationship between inductance current and voltage can be represented as Equation 3.

$$U_{pv} = L\frac{di_L}{dt} + u_{cou}. \tag{3}$$

According to Equation 3, further deformation can be carried out to obtain Equation 4.

$$\Delta i_L = \frac{U_{pv} - u_{cou}}{L}\Delta t_1, \tag{4}$$

where Δi_L is the inductor current variation value, Δt_1 is the time of switch being on. $\Delta t_1 = d_1 T$, where d_1 is the duty cycle of the sinusoidal variation of S1 and T is the work period. d_1 is expressed as

$$d_1 = \frac{u_{cou}}{U_{pv}}, \tag{5}$$

where d_1 is the ideal duty cycle of S1. The triggering pulse of S1 synchronizes with the phase change of the U_g voltage at the grid-tied point, which not only ensures that the capacitor voltage u_{cou} is consistent with the grid but also ensures that the voltage waveform is a standard sine waveform. Hence, the duty cycle of S1 shown as Equation 5 is modified as

$$d_1 = \frac{u_{cou}}{U_{pv}} + \rho\Delta i_L, \tag{6}$$

where $\rho = \frac{L}{TU_{pv}}$; i_L is the actual value of inductance current. In Equation 6 when ρ remains constant, the increased Δi_L implies that the actual value of the inductance current should be decreased. The maximum power point voltage U_{PV} tracked by MPPT should be decreased, and d_1 should be decreased. If Δi_L decreases, the actual value of the inductor current should be increased. Hence, the maximum power point voltage U_{PV} tracked by MPPT should be increased and d_1 should be increased. Adjusting the duty cycle expression in real-time ensures that the output voltage can still be maintained at a relatively stable level even when the voltage at the PV panel port changes. After obtaining the expression for the duty cycle, Δi_L can be further expressed as

$$\Delta i_L = \frac{U_{pv} - u_{cou}}{L} \cdot d_1 \cdot T. \tag{7}$$

Let setting $\Delta U_{pv} = U_{pv} - u_{cou}$. ΔU_{PV} includes the fluctuation of the PV panel port voltage and its impact on the capacitor output voltage, as the fluctuation of capacitor output voltage is caused by improper control in buck mode. Equation 7 can be further expressed as Equation 8.

$$\Delta i_L = \frac{\Delta U_{pv}}{L} \cdot d_1 \cdot T. \tag{8}$$

The average current passing through S1 in one switching cycle is Equation 9.

$$i_{s1\_T} = d_1 \cdot i_{ou}. \tag{9}$$

When the driving signal of switch S1 is turned to a low level, the switch is turned off, and the inductor L is discharged through the freewheeling diode $D1$. The inductor current gradually decreases, and the inductor voltage reverses to resist the decrease in inductor current. The output voltage is maintained by the discharge of the capacitor C_{ou} and the reduced inductor current. The equivalent circuit is shown in Figure 4B. The output voltage of C_{ou} and the current variation of inductor is expressed as Equations 10, 11.

$$L\frac{di_L}{dt} = u_{cou}, \tag{10}$$

$$\Delta i_L = \frac{u_{cou}}{L}\Delta t. \tag{11}$$

When S1 is turned off, the inductor is discharged until S1 and S2 turn on again.

2.2 Boost mode: $u_{cou} > U_{PV}$, S1 turns on, S2 turns on; S1 turns on, S2 turns off;

According to the equivalent circuit of the boost mode with S1 and S2 both on (Figure 4C) with $u_{cou} > U_{PV}$, inductor L is charged again and the capacitor is discharged to keep the output voltage. The relationship between the port voltage of the PV panel and the inductor current is

$$U_{pv} = L\frac{di_L}{dt}. \tag{12}$$

According to Equation 12, the change of the inductor current is calculated as Equation 13.

$$\Delta i_L = \frac{U_{pv}}{L}\Delta t_2, \tag{13}$$

where Δt_2 is the turning-on time of S2. Considering $\Delta t_2 = T\left(1 - \frac{1}{d_1}\right)$, Δi_L can also be calculated as Equation 14.

$$\Delta i_L = \frac{U_{pv}}{L}T\left(1 - \frac{U_{pv}}{u_{cou}}\right). \tag{14}$$

When S1 turns on and S2 turns off, the equivalent circuit is shown in Figure 4D, which is the same as Figure 4A. The inductor is continuously charged, and the capacitor also starts to be charged after discharging for $d_2 T$. The analysis process is the same as in Figure 4A. Additionally, the voltage and current at the grid-tied point with the converter are set as U_g and I_g, which are both the RMS of u_g and i_g. The amplitude of the output voltage u_{cou} of the capacitor is U_{coum}. The active power generated by the PV panel is expressed as

$$\begin{aligned} P_g &= \frac{1}{\pi}\int_0^{\pi} p_g d(\omega t) \\ &= \frac{2}{\pi}\int_0^{\pi} u_{cou} i_g d(\omega t). \end{aligned} \tag{15}$$

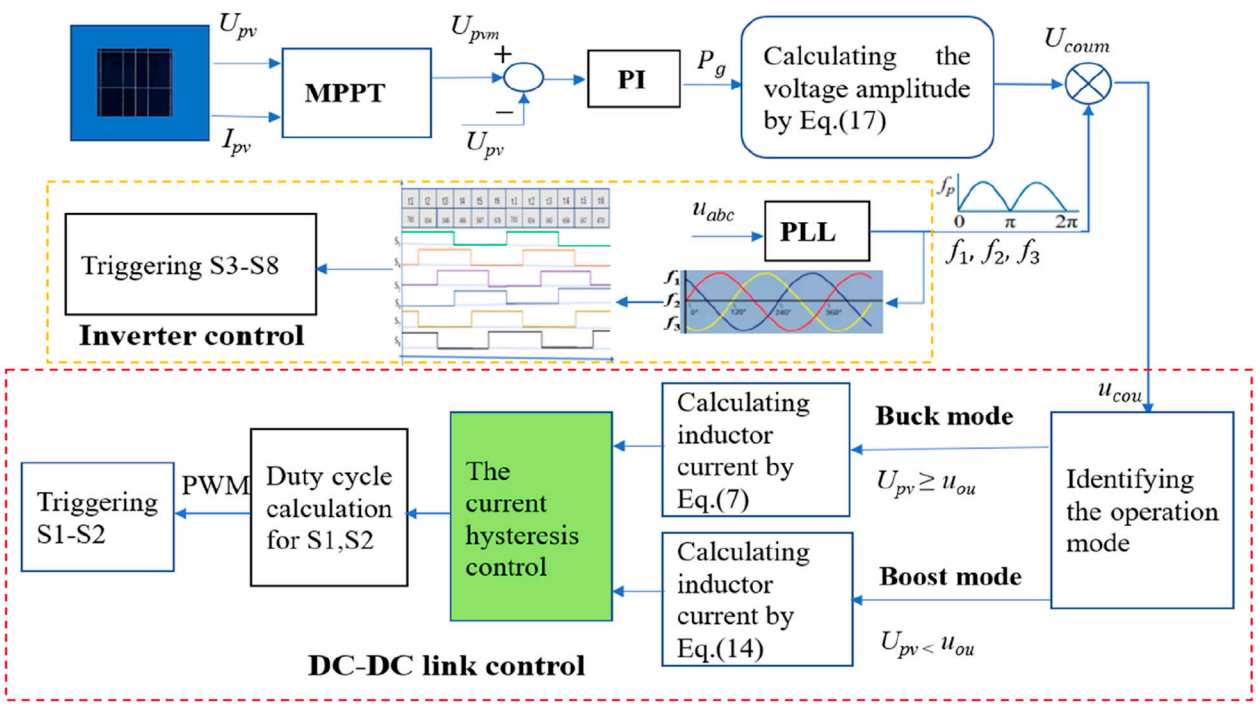

FIGURE 5
Block diagram of the coordinated control method for the whole PV converter.

Because u_{cou} is synchronized with the grid-tied voltage u_g, Equation 15 can be expressed as Equation 16.

$$P_g = \frac{2}{\pi}\int_0^{\pi} U_{coum}\sin(\omega t)\sqrt{2}I_g\sin(\omega t)d(\omega t) = \sqrt{2}U_{coum}I_g. \quad (16)$$

Then, the capacitor voltage amplitude of the DC–DC link can be calculated as Equation 17.

$$U_{oum} = \frac{P_g}{\sqrt{2}I_g}. \quad (17)$$

The voltage amplitude of the capacitor is calculated to perform the operation mode discrimination for buck or boost mode in the coordinated control algorithm with the current hysteresis loop.

3 DC–DC coordinated control strategy with the current hysteresis loop

When the insolation changes, U_{PV} changes correspondingly. If the switch sequence and duty cycles are still operated at the determined mode, the output voltage does not remain constant. To maintain a constant output voltage, the controller must track the voltage changes in the PV panel and adjust the switch sequence and duty cycle in real time based on the changes in voltage changes. Therefore, a coordinated control method for the whole PV converter is proposed; its block diagram is shown in Figure 5.

The whole control diagram includes the converter control and DC–DC link control. In the converter control, the phase-locked loop (PLL) samples the three-phase voltage at the grid side to obtain the three-phase voltage waveform of the grid as f_1, f_2, and f_3, based on the triggering pulse sequences and duty cycles of the S3–S8 switches of the converter. In the DC–DC link control, the MPPT module collects the U_{pv} voltage and I_{pv} current of the PV panel and tracks the maximal power point U_{pvm}. The difference between U_{pvm} and the actual value U_{pv} is processed by the PI controller to generate the active power P_g, which is needed for calculating the voltage amplitude U_{coum} of the expected output voltage of the capacitor. The expected output voltage u_{cou} is then obtained by multiplying the voltage amplitude U_{coum} with the f_p from the PLL, which is obtained by the frequency-based replacement. The expected voltage u_{cou} is compared with U_{PV} in the discriminating operation mode module to determine the buck or boost mode. According to different operation modes, the calculation methods for inductor current changes Δi_L are different. Under the buck mode, the inductor current change is calculated by Equation 7, which is used to modify the duty cycle for S1, while in boost mode, the inductor current change is calculated by Equation 14, which is used to modify the duty cycle for S2. Considering that the changing range of the inductor current is wide, the amplitude limitation and hysteresis comparison loops are used to decrease the inductor current ripple. S1 and S2 are the high frequency switches. The PWM (pulse width modulation) technique is applied to control S1 and S2.

To maintain a constant output voltage, the converter control needs to track the voltage changes in the grid-tied point and adjust the switch sequence of S3–S8. To obtain the three-phase sinusoidal voltage at the terminal of the converter, the S3–S8 switches of the converter must follow a certain triggering sequence and duration to

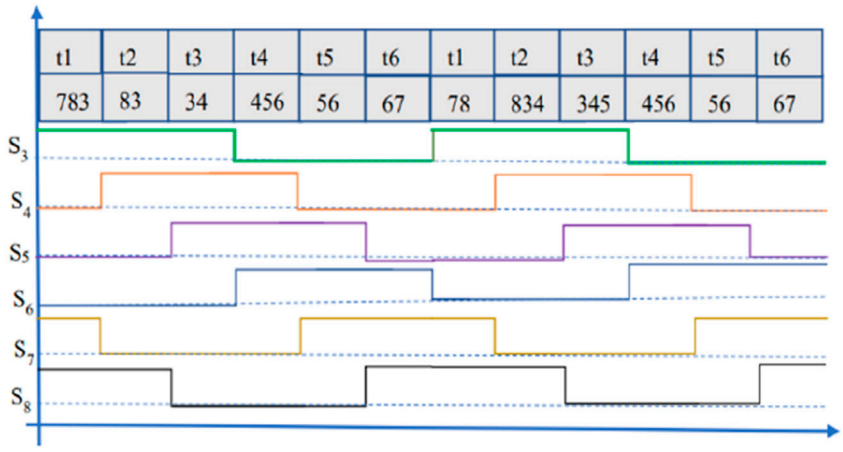

FIGURE 6
Trigger timing sequence and duty cycle length of S3–S8.

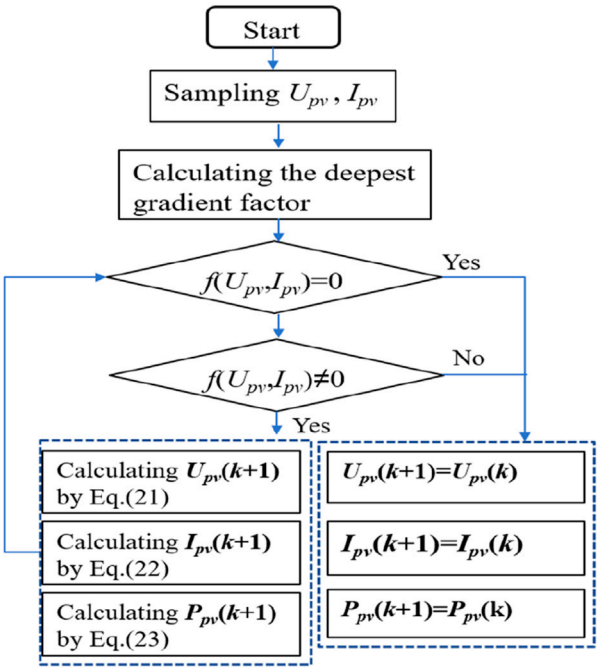

FIGURE 7
Maximum power point search algorithm based on steepest gradient descent.

TABLE 1 Parameter of photovoltaic converter with buck–boost.

Element	Specific parameter
$U_{abc}f_g$	380 V,50 Hz
L,L_g,C_{ou}	0.5 mH,0.4 mH,4 μF
Ground capacitor	0.1 μF
S1–S2 switch frequency	50 kHz
S3–S8 switch frequency	15 kHz
MPPT algorithm	Incremental conductance method based on the fastest gradient
IGBT (s1-s8)	FGA25N120ANTD
Diode (D1-D2)	MBR40250
DSP	TMS320F28335

maintain synchronization with the voltage of the grid-tied point. Figure 6 shows the designed triggering sequence for S3–S8.

The maximal power point tracking algorithm in the MPPT module for the PV system includes the incremental conductance method (INC) and the perturb and observe algorithm (P&O). P&O belongs to the local search algorithms and is susceptible to noise and shadow interference. Compared with P&O, INC shows a fast response but is prone to impact by the step size and sampling frequency.

Therefore, the steepest gradient factor is combined to improve the search speed of the maximal power point. As shown in Figure 7, the first step is to determine the gradient factor, so the steepest gradient factor expression is set as Equation 18.

$$f\left(U_{pv}, I_{pv}\right) = \frac{dI_{pv}}{dU_{pv}} + \frac{I_{pv}}{U_{pv}}. \tag{18}$$

$f\left(U_{pv}, I_{pv}\right)$ will change within the range (-1,+1) with the change of operation point of the PV system, showing the gradient change characteristic. Compared with the traditional INC algorithm, gradient factor $f\left(U_{pv}, I_{pv}\right)$ is actually a direction search factor whose value (negative or positive) shows the searching direction for the maximal power point. In this paper, the gradient factor is introduced into the calculation of U_{PV}, I_{PV}, and P_{PV} at the $(k+1)^{th}$ time. The maximal power point searching equation is shown as

TABLE 2 Changes in voltage, current, and power parameters of photovoltaic panels under different insolations.

Time(s)	0	2	4	6	8	10	12
Insolation on PV	0.15	0.35	0.4	0.5	0.6	0.75	0.9
Temperature of PV (°C)	20	21	23	25	27	29	31
P_{PV}/W	575	1,243	1,425	2,165	2,840	3,678	4,210
I_{gm}/A	1.2	2.8	3.2	4.0	4.9	6.0	7.3
U_{coum}/V	376	385	390	405	416	427	438
i_{Lm}/A	0.06	0.14	0.18	0.20	0.26	0.37	0.45

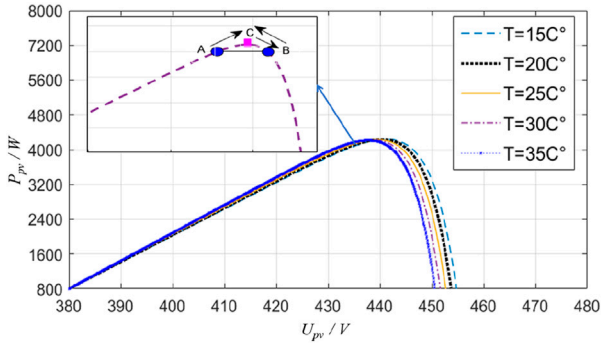

FIGURE 8
Simulated PV curves under different temperatures.

$$U_{pv}(k+1) = U_{pv}(k) + f\left(U_{pv}(k), I_{pv}(k)\right)\frac{U_{pv}(k) + U_{pv}(k-1)}{2}, \tag{19}$$

$$I_{pv}(k+1) = I_{pv}(k) + f\left(U_{pv}(k), I_{pv}(k)\right)\frac{I_{pv}(k) + I_{pv}(k-1)}{2}, \tag{20}$$

$$P_{pv}(k+1) = P_{pv}(k) + f\left(U_{pv}(k), I_{pv}(k)\right)\frac{P_{pv}(k) + P_{pv}(k-1)}{2}, \tag{21}$$

where k+1, k, and k-1 are the sampling time. U_{PV}, I_{pv}, and P_{pv} at the (k+1) time are predicted by the averaging of the k^{th} and $(k+1)^{\text{th}}$ times. Equations 19–21 are the adaptive search process, and the value of the gradient factor determines the search step size. The larger the value of the gradient factor, the shorter the search time. However, if the step size is too large, it will cause the search to exceed the limitation, and *vice versa*, it will affect the extension of the search time. Therefore, the second term in Equations 19–21 is to average the sampling values at k and k-1, and appropriately reduce the search step size.

4 Simulation and experimental verification

To verify the practicability of grid-tied PV system operation for the proposed buck–boost structure and the coordinated control strategy with the current hysteresis loop, the component parameters are set as per Table 1. The HNZL DC power supply has been used to imitate the effect of insolation. In order to emulate simultaneous variation in temperature and in the level of insolation, the MPP parameters are set as follows: U_{PV} = 400 V, I_{pv} = 6.5 A. The effectiveness verification results of the operating characteristics of the proposed converter are shown in Table 2, in which the insolation level is varied on PV. Table 2 provides the estimated mean values of i_L, P_{pv}, u_{cou}, and I_{gm}, as well as the inductance current i_{Lm} during the entire operation period. The calculation results of peak values (i_{Lm}) for P_{pv} and other states I_{gm}, U_{coum} are also presented in Table 2. The estimated values of the above quantities listed in Table 2 are consistent with the values obtained through simulation, ensuring the feasibility of the proposed method.

Figure 8 shows the relationship of the active power output and the voltage changes by the PV curves under different temperatures. When the temperature is lower, the power emitted is greater for the PV panel with the PV panel voltage being improved. When the voltage reaches 438 V, the active power output of the PV panel reaches the maximum point at 30 °C, which is consistent with the estimated value. During the MPPT process of this experiment, the maximum power point search algorithm based on steepest gradient descent takes only 0.22s to reach the maximum power point C, which is shorter than the common incremental conductance method, which is 0.31s to reach point C. This is because the improved maximum power point search algorithm based on the steepest gradient descent only searches the process from points A to C, avoiding the searching process from C to B and B to C, which saves search time. However, the common incremental conductance method tends to search from A to C, C to B, and B to C.

Figures 9A–C show the simulated changes in U_{PV}, i_{pv}, and P_{pv} of the PV panel operation states, which also demonstrate the ability of the proposed converter to operate simultaneously on the MPPT of the PV panel. Figure 10 shows the change caparison of u_{cou}, i_{s1}, i_L, and P_{pv} of the DC–DC link operation at 20 °C and 30 °C. The voltage and current curve at the PV grid-tied points at 20 °C and 30 °C with changed insolation. This shows that when the insulation varies, the voltage and current from the converter output stabilize the sinusoidal waveform synchronized with the power grid, while the current amplitude injected at the grid-collected point varies with the insolation.

Figure 11 shows the simulated voltage and current curve at the PV grid-collection points at 30 °C with changed insolation. This shows that the insolation will impact the output power of the converter. When the insolation becomes strong, the output

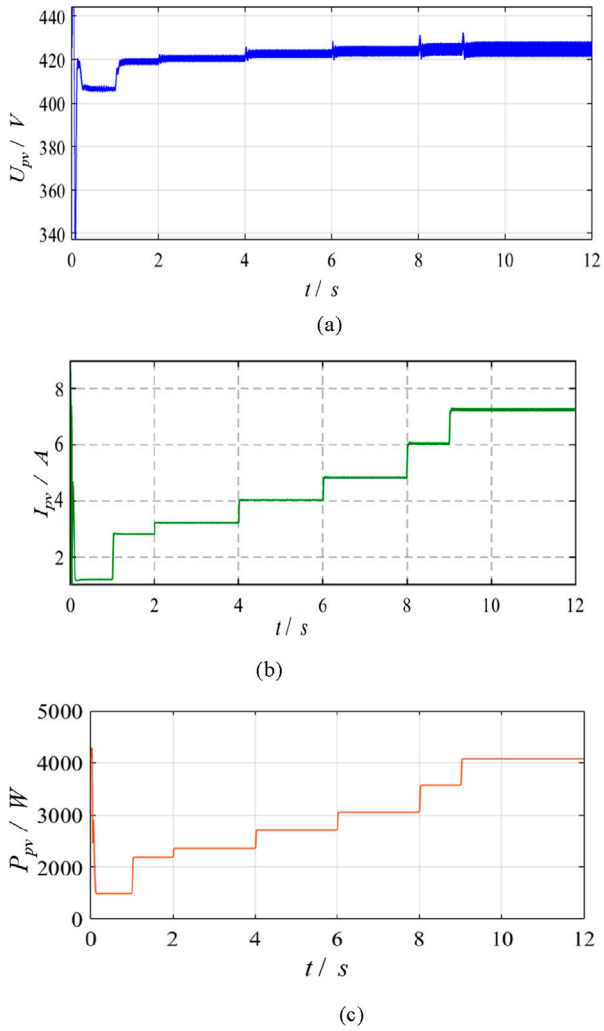

FIGURE 9
Simulated PV panel port states under different insolations: **(A)** voltage U_{PV}; **(B)** current i_{pv}; **(C)** output active power P_{pv}.

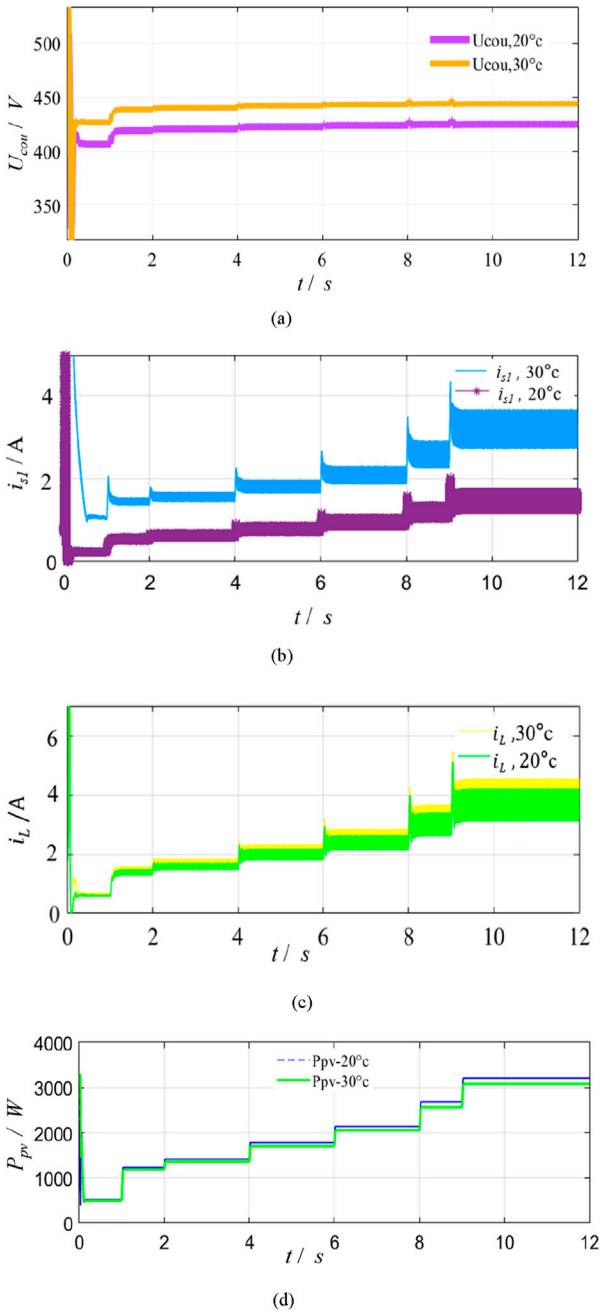

FIGURE 10
Simulated DC–DC link state curves under different temperatures: **(A)** voltage u_{cou}; **(B)** switch S1 current i_{s1}; **(C)** inductor current i_L; **(D)** output active power P_{pv}.

current of the converter increases, while the voltage of the converter remains stable; hence, the output power of the converter increases at the same time. Figure 12 compares the inductor current change when the current hysteresis control is introduced in the coordinated control under the same insolation. During the dynamic process, the ripple current of the inductor is controlled at a relatively satisfactory level, demonstrating the effectiveness of the introduced current hysteresis control. The power conversion efficiency of the PV panel is the percentage of the injected power at the grid-connection point to the output power of the PV panel. The referred voltage and current from the PV panel and grid-tied point are all at the averaging value. Figure 13 is the prototype of the designed buck–boost converter. Under the condition of the converter being off-grid, the experimental waveforms for U_g and i_g are shown in Figure 14, in which, when the input voltage of DC–DC changes from 50 V to 100 V, u_{cou} changes from 100 to 180 V and maintains a stable state. The output voltage amplitude U_g of the converter changes from 150 V to 220 V. During the whole process, the system can effectively ride through situations that arise due to the disturbances in U_g and demonstrates relatively good operation despite it experiencing significant voltage fluctuations.

Figure 15 shows the comparison results between the actual and estimated conversion efficiency of the PV converters, from which it can be inferred that the estimated value tends to consider the ideal situation and ignore the actual ambient condition, resulting in overestimated efficiency. At the maximal power point of 700 W, the actual conversion efficiency is just 97.8%, lower than the

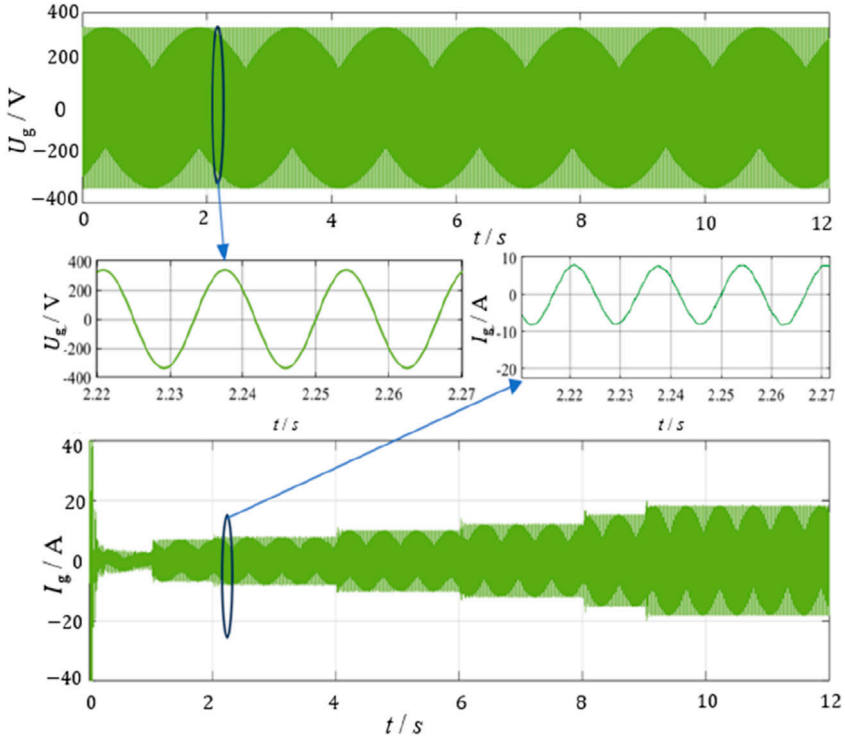

FIGURE 11
Simulated voltage and current curve at photovoltaic grid-collection points at 30 °C with changed insolation.

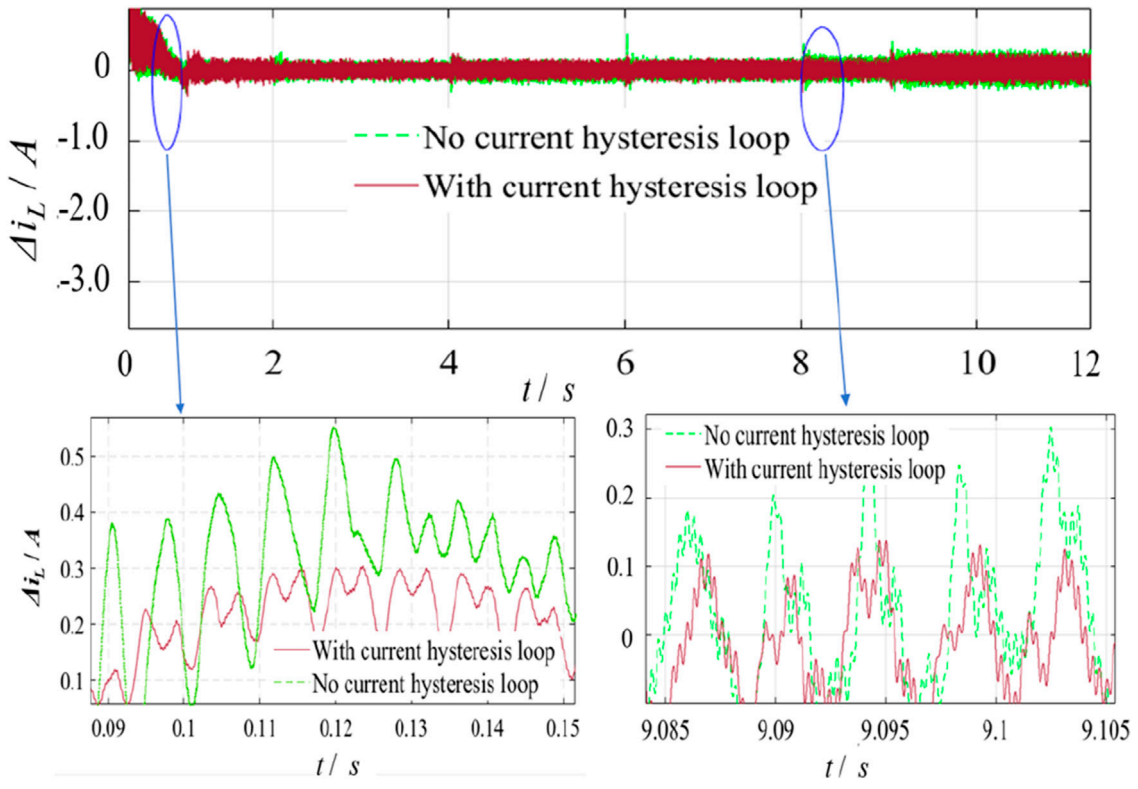

FIGURE 12
Simulated inductor current suppression comparison under same insolation.

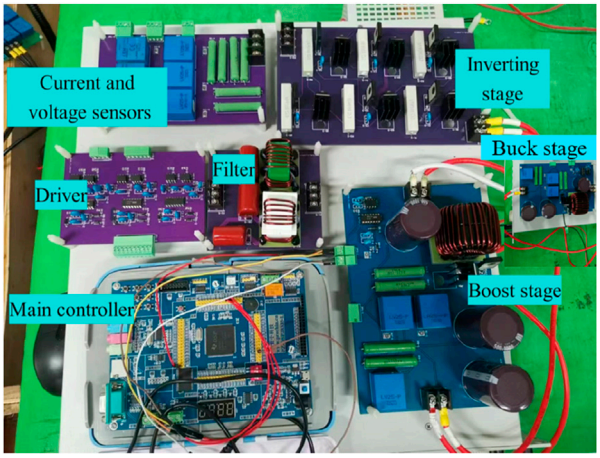

FIGURE 13
Prototype of the designed buck–boost converter.

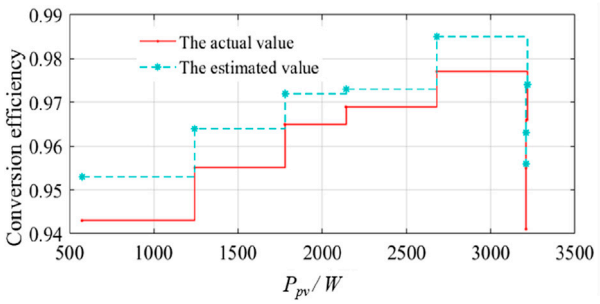

FIGURE 15
Comparison curve between the actual conversion efficiency and estimated conversion efficiency of photovoltaic converters.

estimated value of 98.7%. To further assess the impact of the current hysteresis loop on conversion efficiency, those efficiencies with current hysteresis and without hysteresis are calculated. Figure 16 shows that during the period of low power output, the conversion efficiency with the current hysteresis loop is almost the same as that without current hysteresis loop control. However, with the active power output of the PV panel increasing, the conversion efficiency considering the current hysteresis loop decreases. This means that the increasing active power output corresponds to the increasing inductor current, which is suppressed by the current hysteresis loop at the cost of conversion efficiency. Figure 17 shows the THD comparison curves between the method in Dutta and Chatterjee (2018) and the proposed method here. According to the datum, the changing trend of the THD in the grid-tied point with the output voltage increase of the PV panel remains consistent in the two methods. However, the THD in the proposed method is lower than in Dutta and Chatterjee (2018). Furthermore, the voltage variation range dealt by the method proposed here is 120 V–600 V, with a wider

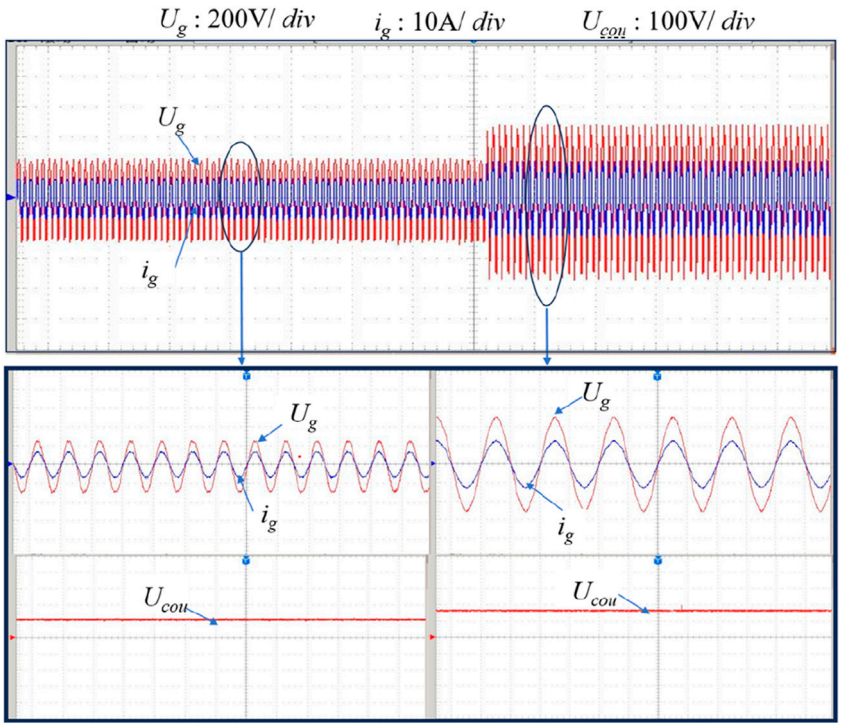

FIGURE 14
Experimental waveforms for U_g, i_g, and u_{cou}.

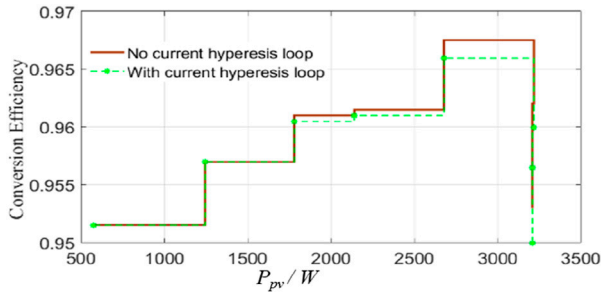

FIGURE 16
Comparison of the conversion efficiency between photovoltaic panels with or without current hysteresis.

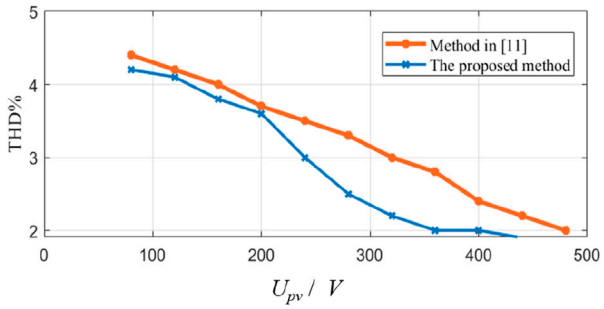

FIGURE 17
Comparison of the THD ratio of the method in Dutta and Chatterjee (2018) and the method proposed here.

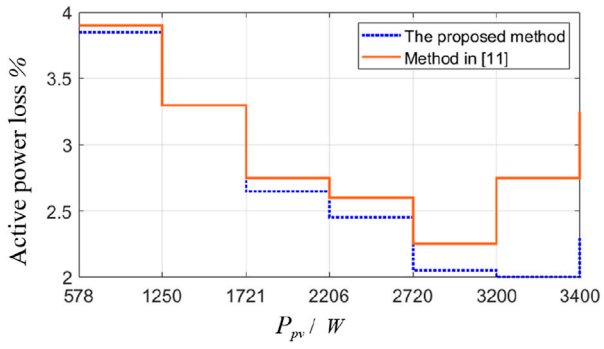

FIGURE 18
Loss distribution at different power levels.

variation range than that in Dutta and Chatterjee (2018). The active power losses at different power levels are also calculated (Figure 18). The comparison results imply that the active power loss values in our method and in Dutta and Chatterjee (2018) are almost the same when the output power of the PV panel is below 1,700 W. Then, with the output power of the PV panel increasing, the active power loss in Dutta and Chatterjee (2018) is higher than the method proposed here, especially when the output power is more than 3,200 W. This shows that the designed converter can adopt higher power production. The above results verify that the designed buck–boost PV converter with the coordinated control strategy has improved operational performance.

5 Conclusion

A buck–boost converter structure and corresponding coordinated control strategy is designed for a grid-tied photovoltaic (PV) panel in this paper. By simulation and experimental verification, the following conclusions are drawn.

(1) To improve the robustness and easing the requirement for PWM dead-times, a wide range buck–boost operation for large fluctuations in PV voltage is provided, and large buck–boost inversions are obtained with relatively smaller duty ratios. Through the operational performance comparison with the classical buck–boost converter, the buck and boost stages in the DC–DC link are decoupled and controlled separately through two switches, which is beneficial for expanding the voltage conversion range of the DC–DC link. However, the designed converter can withstand overlap time in complementary switches without voltage shoot-through problems. At the same time, the incremental conductance method is improved by introducing the deepest gradient factor, which improves the search speed of the maximum power point and enhances the dynamic performance of the converter.

(2) Considering the significant fluctuation of inductor current in the boost stage, a DC–DC coordinated control scheme based on current hysteresis control is here proposed. Based on traditional duty cycle calculation, the influence of the inductor current is introduced, and a duty cycle adjustment based on the current hysteresis control is performed to reduce the ripple of the inductor current at the cost of reducing the conversion efficiency of the PV converter. However, by comparison with the classical buck–boost converter, the designed converter shows noticeable improvement in the THD ratio with the input voltage increase of the DC–DC link. Furthermore, the active power loss caused by the designed converter is also reduced by the coordinated control strategy.

However, under conditions of partial shading, the efficiency of the designed converter is still greatly decreased, the reduction depending on the size of the shading area. The PV ground leakage current is still another unsolved problem in our scheme. Further research should focus on diminishing the leakage current, improving the power conversion efficiency of multiple PV panel series, and suppressing common mode currents under

voltage imbalance caused by different insolation conditions and shadowing.

Data availability statement

The original contributions presented in the study are included in the article/supplementary material; further inquiries can be directed to the corresponding author.

Author contributions

ZC: writing–review and editing, conceptualization, investigation, and methodology. ZH: conceptualization, project administration, resources, and writing–original draft. JA: conceptualization, methodology, visualization, and writing–review and editing. WF: visualization, data curation, investigation, and writing–original draft. YH: visualization, writing–review and editing, and methodology. QL: writing–review and editing, writing–original draft, and conceptualization.

Funding

The authors declare that financial support was received for the research, authorship, and/or publication of this article. This paper is supported by the project of Economic Research Institute of State Grid Hebei Electric Power Co., Ltd., grant number is SGHEJY00GHJS2310078.

Conflict of interest

Authors ZC, ZH, JA, WF and YH were employed by State Grid Hebei Electric Power Co., Ltd.

The remaining author declares that the research was conducted in the absence of any commercial or financial relationships that could be construed as a potential conflict of interest.

The authors declare that this study received funding from Economic and Technical Research Institute of State Grid Hebei Electric Power Co., Ltd. The funder had the following involvement in the study: collection, analysis, interpretation of data.

Publisher's note

References

Ali, M., Padmanaban, S., Ramachandaramurthy, V. K., MitoloO, M., and Benbouzida, M. (2021). A novel solar photovoltaic fed TransZSI-DVR for power quality improvement of grid-connected PV systems. *IEEE Access:Special Sect. Evol. Technol. Energy Storage Syst. Energy Syst. Appl.* 9, 7263–7279. doi:10.1109/access.2020.3048022

Alluhaybi, K., Batarseh, I., Hu, H., and Chen, X. (2020). Comprehensive review and comparison of single-phase grid-tied photovoltaic microinverters. *IEEE J. Emerg. Sel. Top. Power Electron.* 8 (2), 1310–1329. doi:10.1109/jestpe.2019.2900413

Arup, R. P., Bhattacharya, A., and Chatterjee, K. (2023). A single-phase grid-connected boost/buck–boost-derived solar PV micro-inverter topology having power decoupling capability. *IEEE J. Emerg. Sel. Top. Power Electron.* 11 (2), 2340–2349. doi:10.1109/jestpe.2023.3234070

Callegaro, L., Ciobotaru, M., Pagano, D. J., and Fletcher, J. E. (2019). Feedback linearization control in photovoltaic module integrated converters. *IEEE Trans. Power Electron.* 34 (7), 6876–6889. doi:10.1109/tpel.2018.2872677

Chauhan, S., Singh, B., and Singh, B. (2021). Control of three-phase grid integrated multiple solar photovoltaic arrays-BES based MG. *IEEE Trans. Industry Appl.* 57 (6), 6167–6181. doi:10.1109/tia.2021.3109843

Dhara, S., and Somasekhar, V. T. (2022). A three-phase semi-single stage PV inverter with voltage boosting and leakage current minimization. *IEEE Trans. Circuits Systems—II Express Briefs* 69 (1), 169–173. doi:10.1109/tcsii.2021.3082580

Dutta, S., and Chatterjee, K. (2018). A Buck and boost based grid connected PV inverter maximizing power yield from two PV arrays in mismatched environmental conditions. *IEEE Trans. Industrial Electron.* 65 (7), 5561–5571. doi:10.1109/tie.2017.2774768

Dutta, S., and Chatterjee, K. (2020). A coupled inductor-based buck–boost type grid connected transformerless PV inverter having the ability to control two subarrays simultaneously. *IEEE Trans. Industrial Electron.* 67 (7), 5543–5553. doi:10.1109/tie.2019.2931512

Gao, N., Jin, Z., Wang, H., Wu, W., Koutroulis, E., Chung, H.S.-H., et al. (2022). MOSFET-Switch-Based transformerless single-phase grid-tied inverter for PV systems. *IEEE J. Emerg. Sel. Top. Power Electron.* 10 (4), 3830–3839. doi:10.1109/jestpe.2021.3064587

Hafiz, F. A., El Moursi, M. S., Zahawi, B., and Hosani, K.A. (2021). Single-phase photovoltaic inverters with common-ground and wide buck–boost voltage operation. *IEEE Trans. Industrial Inf.* 17 (12), 8275–8287. doi:10.1109/tii.2021.3066511

Ho, C., and Siu, K. (2019). Manitoba inverter—single-phase single-stage buck-boost VSI topology. *IEEE Trans. Power Electron.* 34 (4), 3445–3456. doi:10.1109/tpel.2018.2855560

Huang, Y., Liu, F., Zhuang, Y., Diao, X., Liu, Z., Pan, S., et al. (2021). Bidirectional buck-boost and series LC-based power balancing units for photovoltaic DC collection system. *IEEE J. Emerg. Sel. Top. Power Electron.* 9 (6), 6726–6738. doi:10.1109/jestpe.2021.3074575

Husev, O., Vinnikov, D., Roncero-Clemente, C., Blaabjerg, F., and Strzelecki, R. (2022). MPPT and GMPPT implementation for buck-boost mode control of quasi-Z-source inverter. *IEEE Trans. Power Electron.* 69 (11), 11348–11358. doi:10.1109/tie.2021.3125658

Khan, M. N. H., Forouzesh, M., Siwakoti, Y. P., Li, L., Kerekes, T., and Blaabjerg, F. (2020). Transformerless inverter topologies for single-phase photovoltaic systems: a comparative review. *IEEE J. Emerg. Sel. Top. Power Electron.* 8 (1), 805–835. doi:10.1109/jestpe.2019.2908672

Kumar, S., and Singh, B. (2019). Self-normalized-estimator-based control for power management in residential grid synchronized PV-BES microgrid. *IEEE Trans. Industrial Inf.* 15 (8), 4764–4774. doi:10.1109/tii.2019.2907750

Liang, W., Liu, Y., and Peng, J. (2021). A day and night operational quasi-Z source multilevel grid-tied PV power system to achieve active and reactive power control. *IEEE Trans. Power Electron.* 36 (1), 474–492. doi:10.1109/tpel.2020.3000818

Liao, C.-Y., Lin, W.-S., Chen, Y.-M., and Chou, C.-Y. (2017). A PV micro-inverter with PV current decoupling strategy. *IEEE Trans. Power Electron.* 32 (8), 6544–6557. doi:10.1109/tpel.2016.2616371

Mohammadi, M., Moghani, J. S., and Milimonfared, J. (2018). A novel dual switching frequency modulation for Z-source and quasi-Z-source inverters. *IEEE Trans. Industrial Electron.* 65 (6), 5167–5176. doi:10.1109/tie.2017.2784346

Nan, Y., Di, Y., Zhou, Z., Jiazhan, C., Daojun, C., and Xiaoming, W. (2018). Research on modelling and solution of stochastic SCUC under AC power flow constraints. *IET Generation Transm. and Distribution* 12 (15), 3618–3625. doi:10.1049/iet-gtd.2017.1845

Srivastava, A., and Seshadrinath, J. (2023). A single-phase seven-level triple boost inverter for grid-connected transformerless PV applications. *IEEE Trans. Industrial Electron.* 70 (9), 9004–9015. doi:10.1109/tie.2022.3215815

Teodorescu, R., Liserre, M., and Rodríguez, P. (2011). *Grid converters for photovoltaic and wind power systems*. New York, NY, USA: Wiley.

Yari, K., Mojallali, H., and Hamid Shahalami, S. (2022). A new coupled-inductor-based buck–boost DC–DC converter for PV applications. *IEEE Trans. Power Electron.* 37 (1), 687–699. doi:10.1109/tpel.2021.3101905

frontiers | Frontiers in Energy Research

TYPE Original Research
PUBLISHED 05 November 2024
DOI 10.3389/fenrg.2024.1465301

OPEN ACCESS

EDITED BY
Chenghong Gu,
University of Bath, United Kingdom

REVIEWED BY
Fu Rong,
Nanjing University of Posts and Telecommunications, China
Can Huang,
Pacific Gas and Electric Company, United States
Mrinal Bhowmik,
Durham University, United Kingdom

*CORRESPONDENCE
Li Xia Sun,
lixiasun@hhu.edu.cn

RECEIVED 16 July 2024
ACCEPTED 23 October 2024
PUBLISHED 05 November 2024

CITATION
Zhang S, Ren SY, Zhang B, Feng JZ, Zhang XG, Wu YC and Sun LX (2024) Optimization of emergency frequency control strategy for power systems considering both source and load uncertainties.
Front. Energy Res. 12:1465301.
doi: 10.3389/fenrg.2024.1465301

Optimization of emergency frequency control strategy for power systems considering both source and load uncertainties

Shi Zhang[1], Shao Yi Ren[1], Bo Zhang[1], Jiang Zhe Feng[1], Xin Gang Zhang[1], Yi Chao Wu[2] and Li Xia Sun[3]*

[1]Longyuan (Beijing) Wind Power Engineering Technology Co., Ltd., Beijing, China, [2]State Grid Jiangsu Electric Power Co., Ltd., Ultra High Voltage Branch, Nanjing, China, [3]School of Electrical and Power Engineering, Hohai University, Nanjing, China

With the increasing integration of renewable energy sources and the presence of numerous controllable loads such as electric vehicles and energy storage in the modern power system, higher nonlinearities and uncertainty both sources and loads are introduced. These factors pose challenges in achieving fast and accurate emergency frequency control. Therefore, this paper addresses the issue of dual source-load uncertainties in power system and presents an optimization strategy based on the Soft Actor Critic (SAC) algorithm that involves the participation of controllable loads in emergency frequency control. Firstly, the spatio-temporal uncertainties of wind farm power output on power supply side and power demand on the load side are described using Weibull and normal probability distributions, respectively. Secondly, an improved Markov Decision Process (MDP) model for emergency frequency control is established, which considers the characteristics of the dual source-load uncertainties. Finally, an optimization of the SAC algorithm is conducted based on Deep Reinforcement Learning (DRL), aiming to achieve rapid system frequency recovery and minimize the cost of removing controllable loads. The presented approach in the paper enhances the emergency frequency control strategy for uncertain power systems and effectively addresses the issue of source-load uncertainty compounded by fault power shortages.

KEYWORDS

controllable load, emergency frequency control, deep reinforcement learning, SAC algorithm, source-load dual uncertainties

1 Introduction

The modern power system is continuously evolving and advancing, characterized by sustainability, distribution, dynamism, and intelligent openness. As a result, the control strategy ensuring frequency security and stability in power system has become increasingly complex, leading to greater challenges in emergency frequency control (Zhou et al., 2018; Yi et al., 2019; Li et al., 2020). Meanwhile, the power supply side in power system appears an increasing penetration rate of renewable energy sources. Additionally, there is a significant number of new controllable loads with significant power fluctuations on the load side. These introduce double uncertainties on both the sources and load sides, exacerbating the power shortfalls that occur during system disturbances and further increasing the complexity of

accidents. Hence, it holds immense importance to investigate the emergency frequency control of power system characterized by dual source and load uncertainties.

Considering the nonlinearities and uncertainties at both power supply and load side in modern power systems, various approaches have been proposed to optimize emergency frequency stabilization control, including adaptive and semi-adaptive Under-Frequency Load Shedding (UFLS) methods, event-driven load shedding methods (Xue et al., 2014; Li et al., 2017; Cao et al., 2021), and strategies addressing low inertial (Wu et al., 2015). An emergency frequency control strategy that involves the collaborative participation of renewable energy field stations and conventional units to ensure frequency stabilization while minimizing control costs is conducted (Ke et al., 2022). Reference (Chandra and Pradhan, 2020) addresses an adaptive emergency load shedding method incorporating synchronous generator and photovoltaic plant equivalent models that consider the stochastic variation of solar PV plant power. Frequency characteristics of systems with high penetration of advanced energy technologies is analyzed and proposes a low-frequency load shedding blocking optimization strategy based on df/dt (Sheng et al., 2021). Reference (Masood et al., 2021) presents an emergency frequency stabilization control that simultaneously ensures voltage stability for low-inertia power system containing numerous wind turbines. Reference (Wang et al., 2019) investigates an adaptive emergency frequency control scheme based on inertia estimation from load measurement information of high-percentage renewable energy system. The uncertainty of wind power output and effect of frequency regulation are considered (Zhou and Shi, 2021), an emergency frequency control strategy that combines high-frequency cut-off and low-frequency load-shedding measures are optimized by considering the frequency confidence of power system.

The optimization of emergency frequency control mentioned above primarily adopts model-based methods, including the time-domain simulation method, the dynamic equivalence method, and the linearization analysis method (Zhang et al., 2009; Liu et al., 2014). Among these, the time-domain simulation method is time-consuming and computationally intensive, although it has high accuracy. The dynamic equivalence method is computationally efficient but has low accuracy, which does not meet the requirements of actual power grid. The linearized analysis combines the advantages of the former two methods (Larik et al., 2018), but it does not adapt the topology changes and new elements of power grid. Due to the limitations of physical models, the approaches based on physical models cannot fit with the development of power grid.

In recent years, Machine Learning (ML) methods have been increasingly applied to power system stability control. These methods are based on data for feature mining, do not require accurate mathematical models, and have significant computational performance advantages. Reference (Dai et al., 2012) trained a load shedding prediction model offline using an extreme learning machine and achieved online prediction of actual load shedding. In reference (Bai et al., 2016), an artificial neural network RBF-ANN model was employed to estimate and predict the frequency dynamics process of the power system, contributing to the development of an emergency frequency control scheme. Despite their fast computational speed, traditional ML algorithms are considered shallow learning methods, often relying heavily on expert experience. Their control effectiveness is influenced by the size and quality of the database, resulting in limited adaptability in achieving desired control outcomes. The advancements in deep learning have garnered attention due to their impressive training effectiveness. Consequently, several scholars have explored the application of deep learning methods in optimizing emergency control strategies for power systems (Hu et al., 2019; Lin, 2022). These methods simultaneously enhance control accuracy and reduce decision-making time. In Reference (Qiang et al., 2022), an emergency control model based on an enhanced AlexNet convolutional network is established. This model predicts the system's emergency control sensitivity and identifies alternative control buses, ultimately optimizing to obtain the emergency control strategy. However, deep learning methods require a large number of datasets for model training. In high-dimensional action space problems, a multitude of control scenarios emerge, leading to a significant volume of invalid datasets. This abundance of data presents challenges in model training.

The DRL technique combines the advantages of deep learning and reinforcement learning, which can realize high-dimensional feature extraction and direct learning of complex action space. Hence, to address the highly nonlinear and uncertain nature of emergency frequency stability control problems, some researchers have employed DRL algorithms to optimize strategies that enhance frequency stability while minimizing the total amount of load shedding (Yang et al., 2022). Reference (Chen et al., 2020) optimizes the emergency frequency control strategy using DRL algorithms to reduce frequency stability fluctuations. However, the state space considered in this approach focuses solely on the frequency deviation of the center of inertia. This limitation may lead to inaccurate outcomes since system topology and parameters can significantly vary across different scenarios. In Reference (Ma et al., 2020), a distributed reinforcement learning algorithm is utilized to optimize the emergency frequency control strategy, resulting in improved computational performance and robustness. Reference (Xie and Sun, 2022) considered load variations, measurement noise, and communication delays in real power systems by proposing an emergency frequency control method based on a distributed Soft Actor Critic (SAC) algorithm.

In this paper, a controllable load participation emergency frequency optimization control strategy for source-load dual uncertainty power systems is proposed based on deep reinforcement learning SAC algorithm to address the above problems. Firstly, the source-side output spatio-temporal uncertainty and load-side power uncertainty are described by Weibull and normal probability distribution. Secondly, the action space, state space and reward function of the MDP model are improved according to the characteristics of source-load uncertainty. Then the deep reinforcement learning SAC algorithm with continuous action space is used to train the model to obtain an emergency frequency optimization control strategy for the dual source-load uncertainty power system, which suppresses the depth of the system frequency dip and reduces the stabilized frequency deviation, while minimizing the control cost.

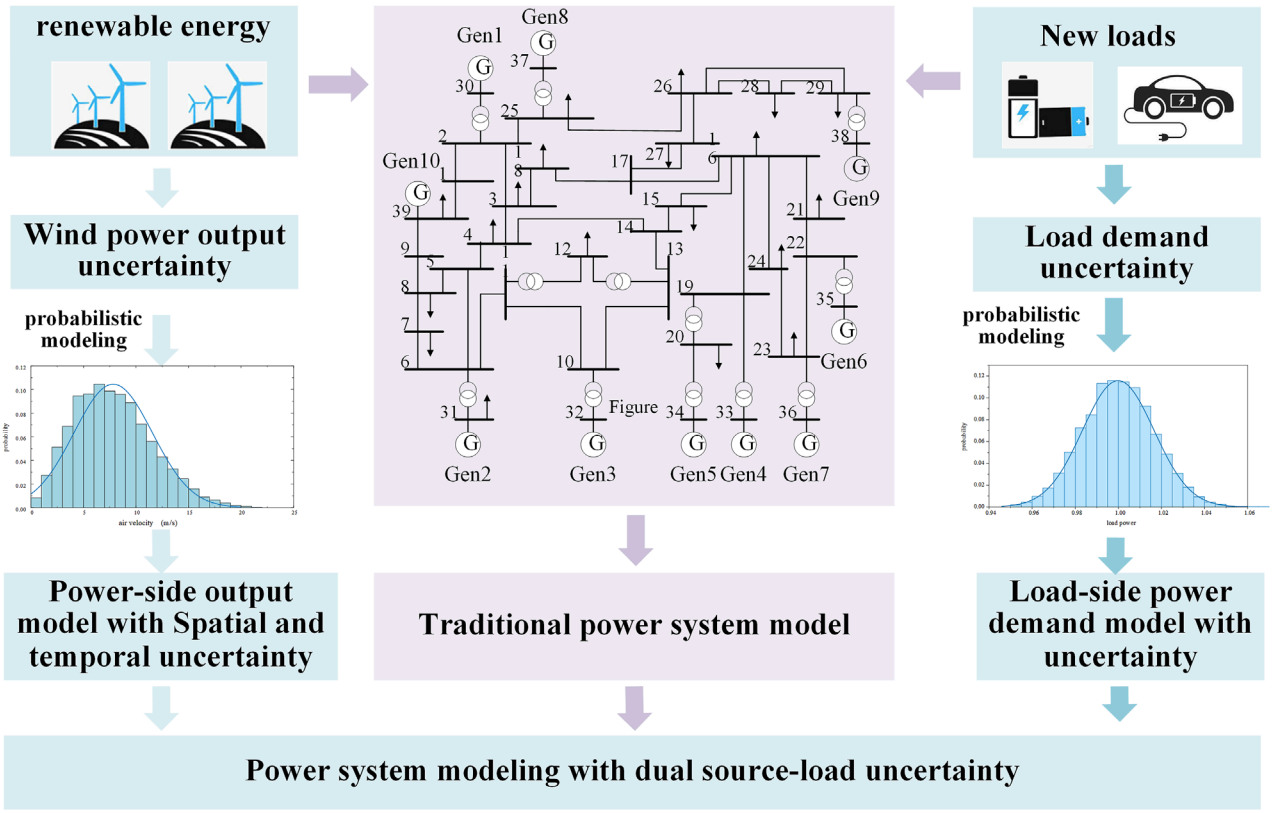

FIGURE 1
Schematic diagram for uncertain source-load power modeling.

2 Modeling of uncertain power on power supply and load

The increasing penetration of renewable energy sources into the power grid impacts its operational characteristics due to various factors, including weather, temperature, and other variables. As a result, the volatility of active power output intensifies, leading to heightened uncertainty in the power-side output of the system. Simultaneously, the grid load is progressively diversifying as numerous new loads, such as electric vehicles and distributed renewable energy sources. These new load types exhibit substantial power fluctuations, further exacerbating the uncertainty in power demand on the load side. The dual uncertainty on both the source and load sides works together to intensify the randomness of the operating conditions. After a power system failure, the power fluctuation resulting from source-load uncertainty and the power deficit caused by failure are superimposed on each other, thereby exacerbating the complexity of the incident, as illustrated in Figure 1.

2.1 Wind power output model on power supply side considering spatial and temporal uncertainty

The uncertainty of wind power output is primarily influenced by wind speed. To more accurately simulate the actual variations in wind speed, it can be represented using probability distributions such as the Weibull distribution, Gaussian distribution, and Pearson distribution. Historical data indicates that the actual wind speed aligns most closely with the Weibull distribution's probability density function. Therefore, this paper employs the Weibull distribution function to characterize the wind speed and establish a probabilistic representation of the uncertainty between the wind turbine's output active power and wind speed. The wind speed probability density function of the Weibull distribution, denoted as $f(v)$, and the cumulative distribution function of the Weibull distribution, denoted as $F(v)$, as shown in Equations 1, 2:

$$f(v) = \frac{K}{C}\left(\frac{v}{C}\right)^{K-1} \exp\left[-\left(\frac{v}{C}\right)^{K}\right] \tag{1}$$

$$F(v) = 1 - \exp\left[-\left(\frac{v}{C}\right)^{K}\right] \tag{2}$$

Where v is the wind speed; K is the shape parameter of the Weibull distribution; C is the scale parameter of the Weibull distribution.

The characteristic curve of wind power output defines the relationship between wind power output and wind speed, where the intensity of wind speed directly influences the magnitude of the output. The relationship between wind power and wind speed can be described by a linear function, quadratic function, or cubic function, leading to distinct wind turbine power curves. Taking into

account the actual statistical wind power data, wind power output is typically modeled using a cubic segmented function, which can be expressed as Equation 3:

$$P_{\mathrm{W}}=\begin{cases}0 & v<v_{\mathrm{in}}\ \text{ or }\ v>v_{\mathrm{out}}\\ P_{\mathrm{r}}\dfrac{v^3-v_{\mathrm{in}}^3}{v_{\mathrm{r}}^3-v_{\mathrm{in}}^3} & v_{\mathrm{in}}\le v<v_{\mathrm{r}}\\ P_{\mathrm{r}} & v_{\mathrm{r}}\le v\le v_{\mathrm{out}}\end{cases} \tag{3}$$

Where v_{r}, v_{in}, v_{out} are the rated wind speed, cut-in wind speed and cut-out wind speed of the wind farm turbine respectively; P_r is the rated power of the turbine.

Apart from temporal uncertainty, wind power output exhibits spatial correlation as well. Due to the close proximity of various wind farms within the same region and their placement in similar wind speed bands, a robust correlation exists between the outputs of different wind farms, consequently impacting the overall uncertainty of wind power. Hence, this section considers the spatial correlation among distinct wind farms and employs the Nataf inverse transformation principle to generate wind turbine output uncertainty data with predetermined correlation coefficients.

The theory of Nataf transform can transform random distribution variables with correlation into standard normal distribution variables that are independent of each other. The Nataf inverse transform serves as the reverse procedure to the Nataf transform, allowing the generation of distribution variables with desired correlation coefficients using independent standard normal distribution variables. This process facilitates the sampling of a significant amount of specified sample data.

Let the vector $P_{\mathrm{W}.i}\,(i=1,2,\ldots,n)$ represent the active outputs of n Weibull-distributed wind farms in the original correlation variable space. Similarly, let the vector $z_i\,(i=1,2,\ldots,n)$ denote the n standard normally distributed random variables in the correlation standard normal space. Subsequently, assume that the linear correlation coefficient matrices for Z and P_{W} are denoted by ρ_0 and ρ, respectively. Here, ρ is a predetermined value, and the relationship equation between the elements of the ρ_0 and ρ matrices is given as:

$$\rho_{0ij}=R_{ij}\rho_{ij} \tag{4}$$

$$R_{ij}=1.063-0.004\rho_{ij}-0.200\left(\gamma_i+\gamma_j\right)-0.001\rho_{ij}^2+0.337\left(\gamma_i^2+\gamma_j^2\right)-0.007\gamma_i\gamma_j \tag{5}$$

Where γ_i and γ_j represent the computational parameters of the random variables P_i and P_j, respectively. The expressions for these parameters are given as follows Equation 6:

$$\begin{cases}\gamma_i=\sigma_i/\mu_i\\ \gamma_j=\sigma_j/\mu_j\end{cases} \tag{6}$$

The positive definite symmetric matrix of correlation coefficients ρ_0 can be obtained through Equations 4, 5, and it can be decomposed into the lower triangular matrix B using the following expression Equation 7:

$$\rho_0=BB^{\mathrm{T}} \tag{7}$$

A standard normal distribution vector Z with specified correlation coefficients can be generated from the pre-obtained independent standard normal distribution vector X. The transformation is shown as Equation 8:

$$Z=BX \tag{8}$$

Based on the equal probability transformation criterion, the standard normal distribution space with correlation is converted into correlated input vectors, i.e., wind power output variables that follow the Weibull distribution. The output power of each wind power node is given by Equation 9:

$$P_{\mathrm{W}.i}=F_i^{-1}\left(\Phi\left(z_i\right)\right) \tag{9}$$

Where $P_{\mathrm{W}.i}$ represents the correlated active power output of wind power node i; $F_i^{-1}(\cdot)$ is the inverse cumulative distribution function of the active power output of wind power node i; $\Phi(z_i)$ denotes the cumulative distribution function of z_i.

2.2 Load-side power demand modeling with uncertainties

The optimization strategy presented in this paper encompasses various novel controllable load types like electric vehicles, energy storage systems, commercial buildings, 5G base stations, and distributed photovoltaics. These loads can be directly enlisted by the emergency control system for urgent load shedding and contribute to the emergency frequency control of the power system. Unlike traditional methods that directly cut the load line during emergency frequency control, these controllable loads have a reduced impact on users when temporarily removed, resulting in lower load shedding costs. Furthermore, the power of these controllable loads can be precisely regulated by power electronic devices, enabling more flexible engagement in the power system's emergency frequency control. The diverse characteristics of controllable loads introduce a complex influence on emergency frequency control, posing challenges in integrating them for considerations such as control continuity and data reliability. Consequently, the load side fluctuation range in modern power systems has expanded, while the time scale has diminished. This, in turn, has led to an escalation in power demand uncertainty, necessitating the characterization of load power uncertainty.

The probability of load power uncertainty is modeled using a normal distribution, which is expressed through a probability density function, as shown in Equation 10:

$$\begin{cases}f(P_{\mathrm{L}})=\dfrac{1}{\sqrt{2\pi}\sigma_{P_{\mathrm{L}}}}\exp\left(-\dfrac{\left(P_{\mathrm{L}}-\mu_{P_{\mathrm{L}}}\right)^2}{2\sigma_{P_{\mathrm{L}}}^2}\right)\\ f(Q_{\mathrm{L}})=\dfrac{1}{\sqrt{2\pi}\sigma_{Q_{\mathrm{L}}}}\exp\left(-\dfrac{\left(Q_{\mathrm{L}}-\mu_{Q_{\mathrm{L}}}\right)^2}{2\sigma_{Q_{\mathrm{L}}}^2}\right)\end{cases} \tag{10}$$

Where P_{L} and Q_{L} represent the active and reactive power of the load, respectively; μ_{PL} and μ_{QL} denote the expected values of the active and reactive power of the load, respectively; σ_{PL} and σ_{QL} indicate the standard deviation of the active and reactive power of the load, respectively.

Additionally, the presence of various new controllable loads on the load side, such as electric vehicles and energy storage, introduces

variability and diversity in load characteristics. The complexity of these controllable load components further contributes to the uncertainty of overall load characteristics. Determining the controllable load characteristics directly becomes infeasible when the power system's operating state changes, necessitating the expression of uncertainty through a probability distribution. Consequently, a novel static load model should be established utilizing frequency and voltage indices that adhere to the probability distribution, as Equation 11.

$$\begin{aligned} P'_{\mathrm{L.new}} &= P_{\mathrm{L}}(U/U_{\mathrm{N}})^{k_{pu.\mathrm{new}}}\left(1+k_{pf.\mathrm{new}}(f-f_{\mathrm{N}})\right) \\ Q'_{\mathrm{L.new}} &= Q_{\mathrm{L}}(U/U_{\mathrm{N}})^{k_{qu.\mathrm{new}}}\left(1+k_{qf.\mathrm{new}}(f-f_{\mathrm{N}})\right) \end{aligned} \tag{11}$$

Where $k_{pu.\,\mathrm{new}}$ and $k_{qu.\,\mathrm{new}}$ represent voltage indices of active and reactive power of the new controllable loads, respectively; $k_{pf.\,\mathrm{new}}$ and $k_{qf.\,\mathrm{new}}$ denote frequency indices of active and reactive power of the loads, respectively.

These parameters, $k_{pu.\,\mathrm{new}}$, $k_{qu.\,\mathrm{new}}$, $k_{pf.\,\mathrm{new}}$ and $k_{qf.\,\mathrm{new}}$, are subject to uncertainty and are characterized by probability distributions that follow a normal distribution.

In summary, considering the uncertainty of load size, which is represented by P_{L} and Q_{L} that conform to normal distribution, and considering the uncertainty of load characteristics, which is represented by $P'_{\mathrm{L.new}}$ and $Q'_{\mathrm{L.new}}$ that contain time-varying load coefficients, a power demand uncertainty model that integrally considers fluctuations in load quantity and fluctuations in load characteristics is thus established.

3 Improvement of the MDP model for emergency frequency control problem in source-load dual uncertainty power system

Reinforcement learning can be formulated through MDP, which performs policy search through the set (S, A, P, R, y). Where S is the state space and A is the action space, which can be either continuous or discrete. P is the state transfer probability, which represents the probability density of the next state s_{t+1} given the current state $s_t \in S$ and the current action $a_t \in A$. R is the reward function and y is the discount factor. Most of the classical MDP theories and RL algorithms are based on discrete-time leapfrog actions, but many power system control problems follow continuous-time dynamics actions, which can only be discretized by using appropriate time intervals to cut the continuous-time dynamics. Therefore, this paper addresses this drawback by using an MDP model for improving the emergency frequency control of the system and optimizing the emergency frequency control strategy using the deep reinforcement learning SAC algorithm with continuous action space.

3.1 State space

Power system emergency frequency stabilization is closely related to generator active power, load power, system frequency, and the rate of frequency change. Considering the dual source-load uncertainty in power-side active output and demand-side active load, it is necessary to incorporate all generator active output and load node power with uncertainty into the state space, defining the state space s_t as Equation 12:

$$\begin{aligned} &s_t = s_1^t \cup s_2^t \cup s_3^t \cup s_4^t \\ &\begin{cases} s_1^t = \{f_1^{\mathrm{t}}\ f_2^{\mathrm{t}}\ \cdots\ f_m^{\mathrm{t}}\} \\ s_2^t = \{(\mathrm{d}f/\mathrm{d}t)_1^t\ (\mathrm{d}f/\mathrm{d}t)_2^t\ \cdots\ (\mathrm{d}f/\mathrm{d}t)_m^t\} \\ s_3^t = \{P_{\mathrm{e}.1}^t\ P_{\mathrm{e}.2}^t\ \cdots\ P_{\mathrm{e}.m}^t\} \\ s_4^t = \{P_{\mathrm{l}.1}^t\ P_{\mathrm{l}.2}^t\ \cdots\ P_{\mathrm{l}.n}^t\} \end{cases} \end{aligned} \tag{12}$$

Where f_i^t is the frequency of generator node i at moment t; $(\mathrm{d}f/\mathrm{d}t)_i^t$ is the frequency change rate of generator node i at moment t; $P_{\mathrm{e}.i}^t$ is the electromagnetic power of generator node i at moment t; $P_{\mathrm{l}.j}^t$ is the active load of load node j at moment t.

3.2 Action space

The control action of each controllable load at moment t should be to reduce a part of the total controllable load at that node. Due to the uncertainty of load demand power, the total controllable load needs to be updated in real time. However, for uniformity of the control action, the action space must be fixed. Therefore, the action space is set as the proportion of the controllable load removed at each node. The actual load reduction is the value of the action at each node multiplied by the total controllable load at that node. Consequently, each controllable load action is defined as a continuous value within [-1, 0], and the total action space is shown as Equation 13:

$$a_t = \{\Delta P_1^t \quad \Delta P_2^t \quad \cdots \quad \Delta P_n^t\} \tag{13}$$

Where $\Delta P_m^{\ t}$ is the load removal of controllable load node m at time t and $\Delta P_m^{\ t} \in [-1,0]$; n is the number of controllable load nodes.

3.3 Reward functions

The goal of the emergency frequency control problem is to restore the frequency to within the stabilization range quickly while minimizing load shedding. For source-load dual uncertainty power systems, the effectiveness of emergency frequency control is primarily evaluated in terms of frequency deviation and load shedding amount.

Therefore, the reward function consists of three parts: 1) the average value of steady-state frequency deviation over a specific time period at the end of the simulation; 2) a penalty term calculated based on controllable load importance and load shedding; and 3) a penalty term for exceeding the lowest point of the system's dynamic frequency. The expression is shown as Equation 14:

$$\begin{aligned} r_t &= \lambda_1 \left|\Delta f_{T_{\mathrm{tem}}}\right| - \lambda_2 \sum_{j=1}^{n} C_j P_{\mathrm{sl}.j} - H_1 \\ H_1 &= \begin{cases} -100, & \mathrm{if}\left(f_{\min} < f_{\min\ .\mathrm{set}}\right) \\ 0, & \mathrm{therwise} \end{cases} \end{aligned} \tag{14}$$

Where T_{tem} is a certain time period before the end of the simulation process; $\Delta f_{T\mathrm{tem}}$ is the average value of the

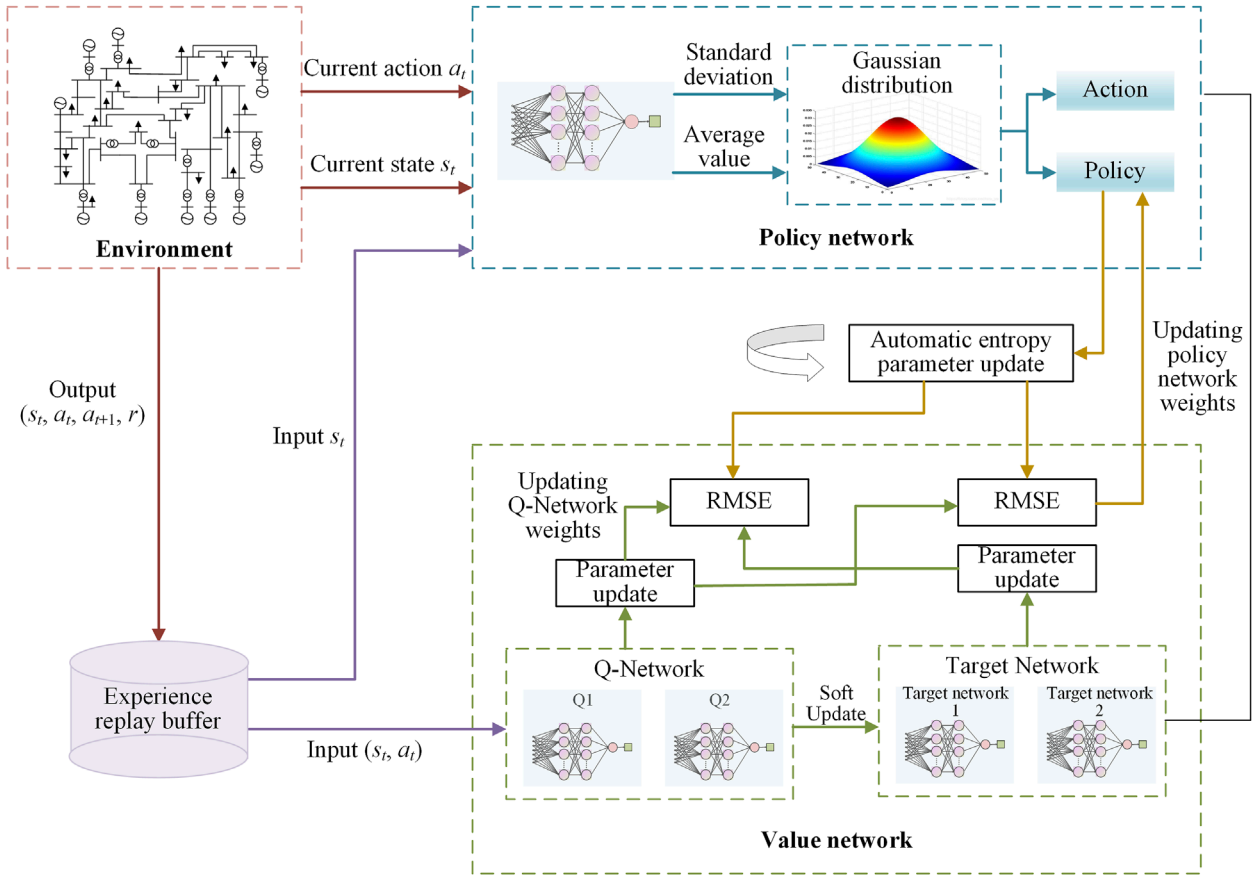

FIGURE 2
Structure of SAC algorithm.

deviation of the center of frequency inertia during T_{tem}; C_j is the importance index of load node j; $P_{sl.j}$ is the amount of load shedding at node j; H_1 is the penalty for the system's center of frequency inertia when the minimum value is less than the integrating value; λ_1 and λ_2 are coefficients for each part of the reward function.

4 Optimization of emergency frequency control strategy considering dual source-load uncertainties

Emergency frequency control is a kind of multi-constraint multi-objective optimization problem, which needs to consider two conflicting objectives of fast frequency recovery and minimizing control cost at the same time. Moreover, it often exhibits a propensity to favor one objective over the other, leading to convergence on local optimal solutions. The SAC algorithm introduces the action entropy value to balance the probability of the various action strategies in the action space, to avoid learning the same action repeatedly and falling into the sub-optimal solution, and it has a stronger exploratory ability, and is more suitable for the studying the emergency frequency control problem with multiple objectives.

Following a failure in a power system that considers dual source-load uncertainty, the power deficit resulting from the disturbance combines with the source-load uncertainty, resulting in increased random volatility in the collected grid state data and causing ongoing oscillations in the training process. Faced with this high level of uncertainty, some DRL algorithms based on strategy gradient exhibit weak generalization abilities, leading to unstable emergency frequency control effects. In contrast, the SAC algorithm incorporates action entropy, enhancing robustness and resistance to disturbances, and demonstrating stronger learning generalization capabilities, rendering it more suitable for the dual source-load uncertainty power system discussed in this chapter.

Moreover, the SAC algorithm features a continuous action space, eliminating the need for discretizing load removal actions. This allows for the removal of the required load amount at once, thereby preventing exacerbation of frequency drop depth resulting from multiple actions. Additionally, continuous action space control enhances precision and reduces the likelihood of excessive or inadequate load removal during emergency frequency control. This ensures a smaller steady-state frequency deviation post-control while minimizing the amount of load removed.

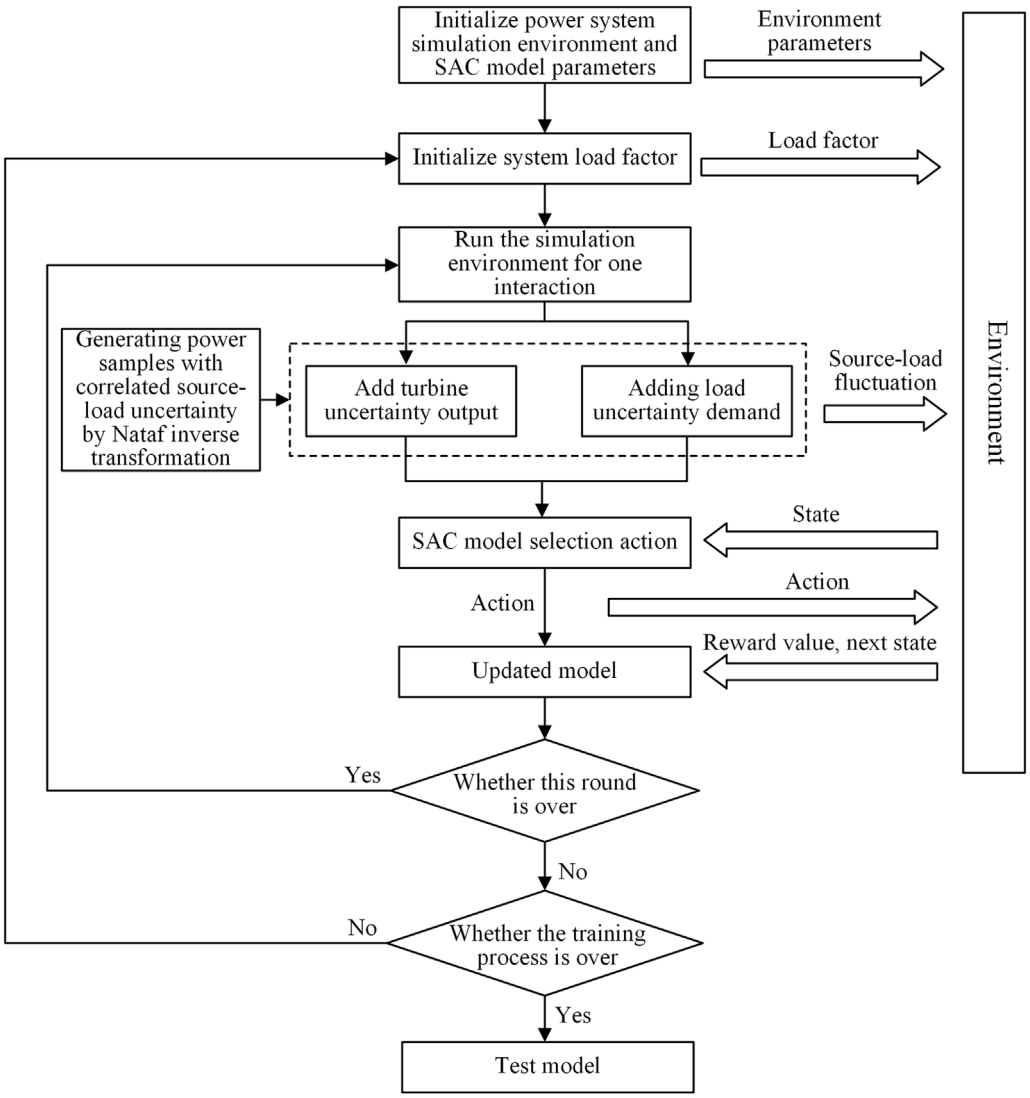

FIGURE 3
Flow chart of emergency frequency control based on SAC algorithm.

The SAC algorithm offers higher exploration capability, improved robustness, and a continuous action space compared to other DRL algorithms. Consequently, the SAC algorithm is employed in this section to optimize the emergency frequency control strategy for source-load dual uncertainty power systems.

4.1 Principle of SAC algorithm and network structure

The SAC algorithm belongs to the deep reinforcement learning algorithms based on the value function, which incorporates a mechanism that encourages exploration through action strategy entropy values. This enhances the algorithm's robustness compared to other strategy gradient-based DRL algorithms like PPO, A3C, and DDPG. The entropy value, defined as the expectation of information quantity, quantifies the uncertainty of a variable. It increases with the uncertainty of an event and can be quantified by the event's probability. The entropy value is defined as Equation 15:

$$H(X) = -\sum_{x_i \in X} l(x_i) \ln l(x_i) \tag{15}$$

Where $H(X)$ is the entropy value; $l(x_i)$ is the event probability.

The DRL algorithm should continuously explore the interaction environment to accumulate experience and avoid selecting too many actions solely based on immediate rewards, as this may lead to convergence on local optimal solutions. The SAC algorithm considers the maximum entropy value of actions. If the entropy value decreases due to repeated selection of a certain action, the maximum entropy mechanism encourages the agent to explore other actions, thus broadening the exploration range and increasing the algorithm's robustness.

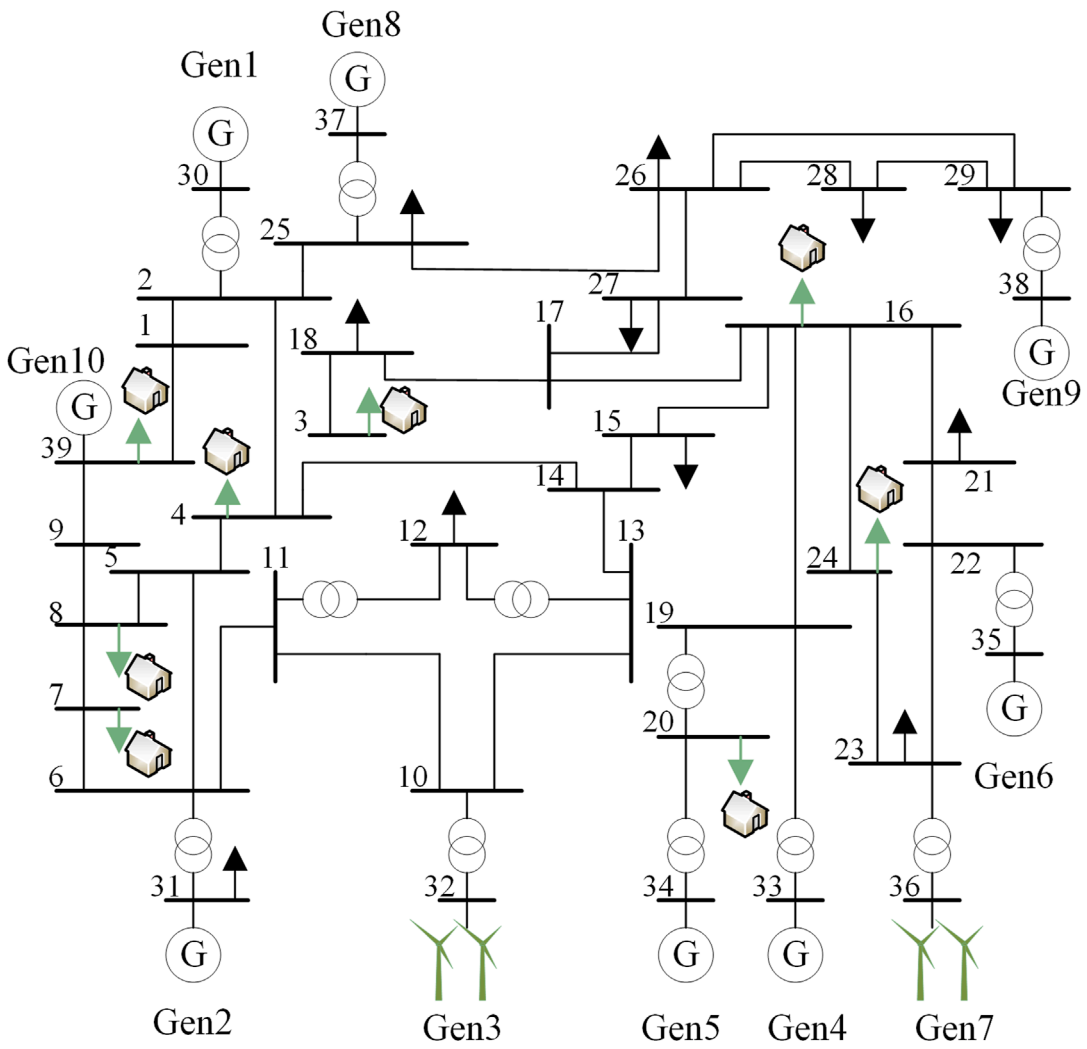

FIGURE 4
Improved topology of IEEE39 nodes.

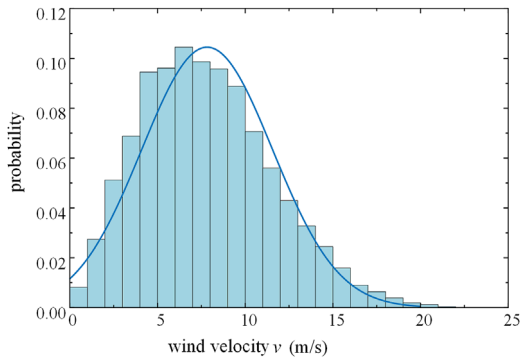

FIGURE 5
Weibull distribution of wind speed.

In other deep reinforcement learning algorithms with stochastic policies, the objective of model learning is clear: to derive an optimal action policy that maximizes the expected cumulative reward through straightforward training. The optimal policy expression is shown as Equation 16:

$$\pi = \mathrm{argmax}_{\pi} E_{(s_t,a_t)\sim\rho_{\pi}}\left[\sum tr(s_t,a_t)\right] \tag{16}$$

The SAC algorithm necessitates maximizing the entropy value of the output action to enhance exploration capability. In other words, an additional term regarding the entropy value is incorporated into the policy expression, resulting in the expression of the improved optimal policy as shown in Equation 17:

$$\pi = \mathrm{argmax}_{\pi} E_{(s_t,a_t)\sim P_{\pi}}\left[\sum_{t} \underbrace{r(s_t,a_t)}_{\text{reward}} + \alpha \underbrace{H(\pi(\cdot \mid s_t))}_{\text{entropy}}\right] \tag{17}$$

Where $E\ (s_t,\ a_t)$ denotes the expectation function; π represents the strategy; s_t and a_t signify the state space and action space at moment t; $r\ (s_t,\ a_t)$ denotes the reward function at moment t $(s_t,\ a_t)\sim P_{\pi}$ signifies the trajectory of state-action under strategy π; + is the automatic entropy temperature parameter, which adjusts the entropy value affecting the degree of rewards; and $H\ (\pi(\cdot|s_t))$

TABLE 1 The proportion of load with different time delay levels.

Load node number	Total share of controllable load	Percentage of class 1 controllable loads	Percentage of class 2 controllable loads	Percentage of class 3 controllable loads
3	0.41	0.5	0.3	0.2
4	0.34	0.3	0.4	0.3
7	0.38	0.4	0.5	0.1
8	0.46	0.3	0.3	0.4
16	0.22	0.6	0.2	0.2
20	0.54	0.6	0.3	0.1
24	0.34	0.5	0.2	0.3
39	0.38	0.4	0.3	0.3

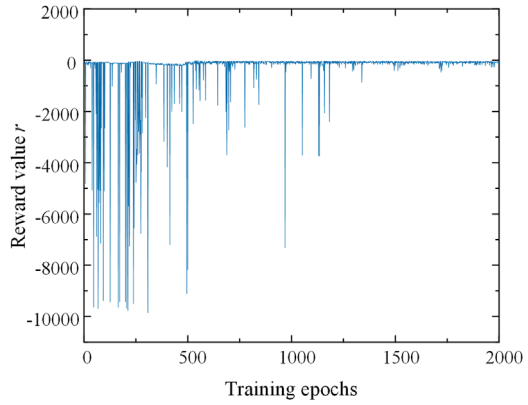

FIGURE 6
Changes in reward values during training.

signifies the entropy of the output action of the strategyπ under the state s_t, as expressed below in Equation 18:

$$H(\pi(\cdot \mid s_t)) = -\sum \pi(\cdot \mid s_t)\log(\pi(\cdot \mid s_t)) = -\int_{a_t} P(\pi(a_t \mid s_t))\ln P(\pi(a_t \mid s_t))\mathrm{d}a_t \tag{18}$$

Where $P(\pi(a_t|s_t))$ denotes the probability that the action value at the time of t is a_t.

In the SAC algorithm for strategy value evaluation, the expression for updating the strategy using the Bellman operator is expressed as Equation 19:

$$Q^{\pi}(s_t,a_t) = r_t + E\left[\sum_{t=1}^{\infty}\gamma^t[r(s_t,a_t) - \alpha\log\pi(a_t \mid s_t)]\right] \tag{19}$$

Where γ denotes the discount factor at the time of strategy update.

The optimal policy can be continuously learned and refined through policy iteration, comprising two steps: soft policy evaluation and soft policy improvement. Firstly, in the strategy evaluation step, the soft value update function of a given strategy π can be obtained using the soft Bellman operator, as shown in Equation 20:

$$\mathcal{T}^{\pi}Q^{\pi}(s,a) = r + \gamma E_{s'}[Q^{\pi}(s',a') - \alpha\log\pi(a' \mid s')] \tag{20}$$

The SAC algorithm belongs to the Actor-Critic class of algorithms, where the Actor is employed for policy modeling and the Critic for Q-value function modeling. Different deep neural networks are utilized to fit the Q-value function and the policy function, respectively, as shown in Equation 21:

$$J_Q(\theta) = E\left[\frac{1}{2}(Q(s_t,a_t) - (r(s_t,a_t) + \gamma V_{\bar{\theta}}(s_{t+1}))^2\right] \tag{21}$$

Where θ denotes the parameters of the policy network; $V_{\bar{\theta}}$ represents the updated value function value.

Both networks are optimized using independent gradients $\hat{\nabla}_{\theta}J_Q(\theta)$, as expressed in Equation 22:

$$\hat{\nabla}_{\theta}J_Q(\theta) = \nabla_{\theta}Q_{\theta}(s_t,a_t)\cdot(\Delta Q_{\theta}) \tag{22}$$

Where the expression of ΔQ_{θ} is expressed as Equation 23:

$$\Delta Q_{\theta} = Q_{\theta}(s_t,a_t) - r(s_t,a_t) + \gamma\left(Q_{\bar{\theta}}(s_{t+1},a_{t+1}) - \alpha\log\left(\pi_{\phi}(a_{t+1} \mid s_{t+1})\right)\right) \tag{23}$$

The outputs of the policy network are the mean and standard deviation values following a Gaussian distribution. The network with the smaller Q value is selected to reduce bias in updating the parameters of the policy network. The approximate gradient of the parameter update is expressed as Equation 24:

$$\hat{\nabla}_{\phi}J_{\pi}(\phi) = \nabla_{\phi}\alpha\log\left(\pi_{\phi}(a_t \mid s_t)\right) + \left(\nabla_{a_t}\alpha\log\left(\pi_{\phi}(a_t \mid s_t)\right) - \nabla_{a_t}Q(s_t,a_t)\right)\nabla_{\phi}f_{\phi}(\varepsilon_t;s_t) \tag{24}$$

At the same time, the action entropy value is also updated in the policy network, making it crucial to choose the appropriate temperature parameter, α. As the reward value varies during the training process, fixing the temperature coefficient reduces the

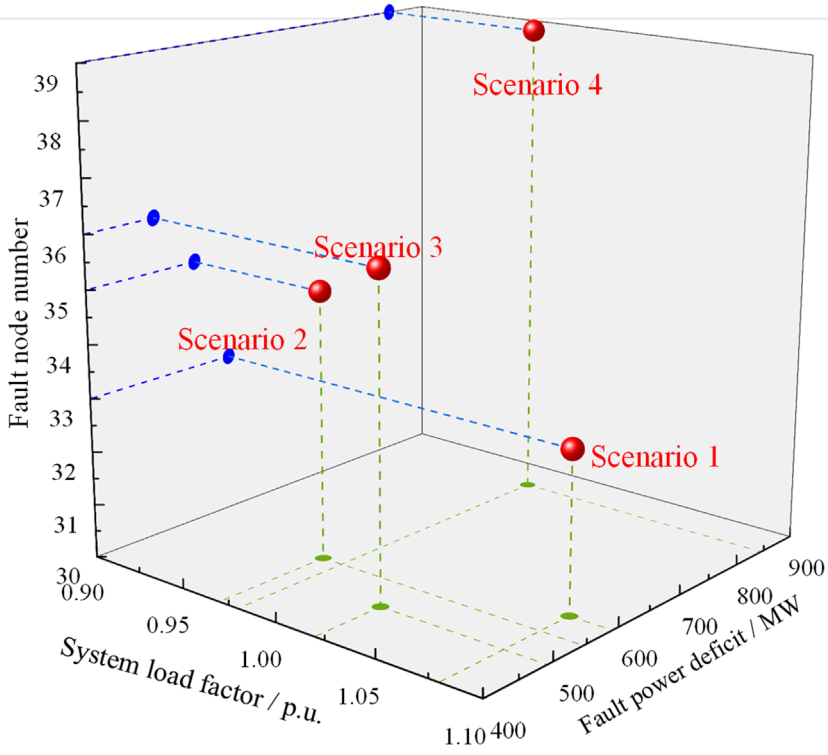

FIGURE 7
Number of excision maneuvers during each training round.

stability of model training. Therefore, the temperature coefficient α is generally updated automatically by minimizing $J(\alpha)$, as expressed in Equation 25:

$$J(\alpha) = E_{a_t \sim \pi_i}\left[-\alpha \log\left(\pi_t(a_t \mid s_t)\right) - \alpha M\right] \tag{25}$$

Where M represents the dimension of the action matrix, specifically denoted as $M = \dim(a)$.

The SAC algorithm for deep reinforcement learning comprises four crucial components: the experience replay buffer, the automatic entropy parameter, the policy network, and the value network. The experience replay buffer stores historical exploration experience, while the automatic entropy parameter stabilizes and adjusts the exploration strategy. The policy network is responsible for action selection, and the value network estimates state-action values. The overall structure of the algorithm is depicted in Figure 2.

4.2 Optimization of emergency frequency control strategy based on SAC algorithm

When utilizing the SAC algorithm to optimize the emergency frequency control strategy, each iterative training process can be summarized into three main steps: firstly, collecting and inputting the operating state data of the power system after the fault into the SAC model; then, the SAC model selects the emergency frequency control action based on the state data; finally, executing the control action on the power system simulation environment to achieve the objective. Additionally, due to the uncertain nature of source-load power systems, it is necessary to incorporate an uncertainty model for wind power output and load demand in each interaction process. The overall process of emergency frequency control for a source-load dual uncertainty system based on the SAC algorithm is illustrated in Figure 3.

Prior to model training, the simulation environment and SAC model parameters are initialized. The power system load factor is randomly initialized, and the model incorporates uncertainty in wind power output and load demand. The Nataf inversion theory is employed to generate source-load dual uncertainty power samples with correlation. Before each interactive training step, uncertainty power samples are randomly assigned to wind turbine nodes, and uncertainty load demand samples are added to load nodes to simulate real-world source-load uncertainty power system conditions. Subsequently, the SAC model obtains the current system state data from the simulation environment, selects an action based on an environmental state update policy, and delivers it to the simulation environment. After receiving the emergency frequency control action from the SAC model, the simulated power system environment executes the load adjustment action, advances to the next state, and sends the updated state data and immediate reward value to the SAC model. This training process continues until the end of a round, marked by maintaining stable system frequency. At this point, the system simulation environment is reinitialized, and the next round begins. Upon completing the training process, the SAC model can be applied to various fault test scenarios to validate its effectiveness and superiority.

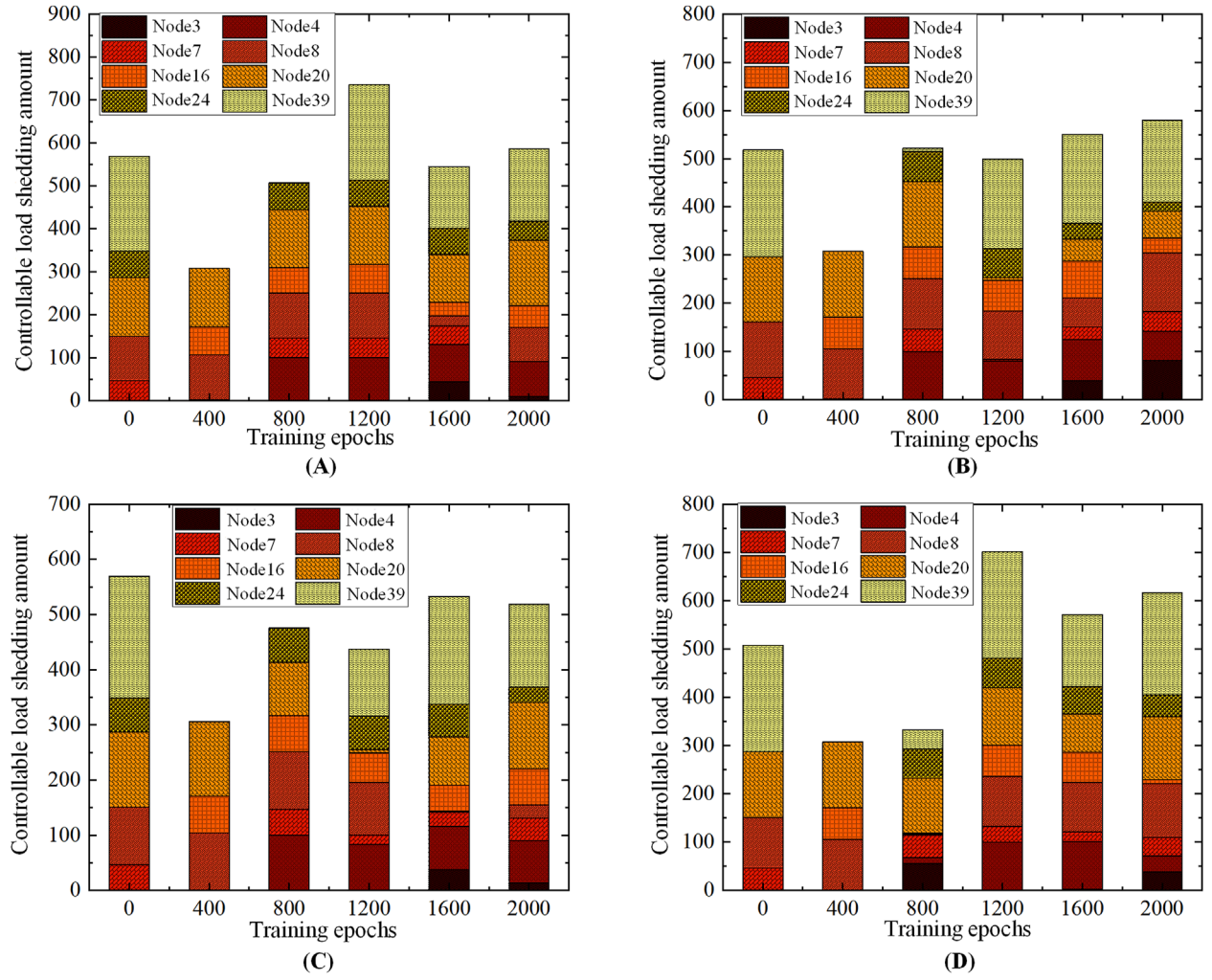

FIGURE 8
Change process of load shedding strategy in scenario **(A–D)** training.

TABLE 2 **Controllable load shedding and dynamic frequency metrics for various test scenarios.**

Scenario	Controllable load shedding/MW	Steady state frequency/Hz	Frequency drop minimum/Hz
1	592	50.01	49.78
2	545	50.05	49.76
3	517	49.98	49.76
4	615	49.91	49.51

5 Simulation analysis

To evaluate the effectiveness of the proposed method in this paper, a deep reinforcement learning environment is constructed to enhance the IEEE10 machine with 39 nodes. This environment is developed using Python and BPA simulation software. The SAC algorithm is employed to solve the specified test cases. The deep neural network is implemented in Python using TensorFlow 1.15. The experiments are conducted on an Intel Core i5-11400H CPU with 16.00 GB RAM and an RTX 3050 GPU.

5.1 Data of the test case

The BPA software is utilized in this paper to generate a fault scenario for the IEEE10 machine with 39 nodes. The generator

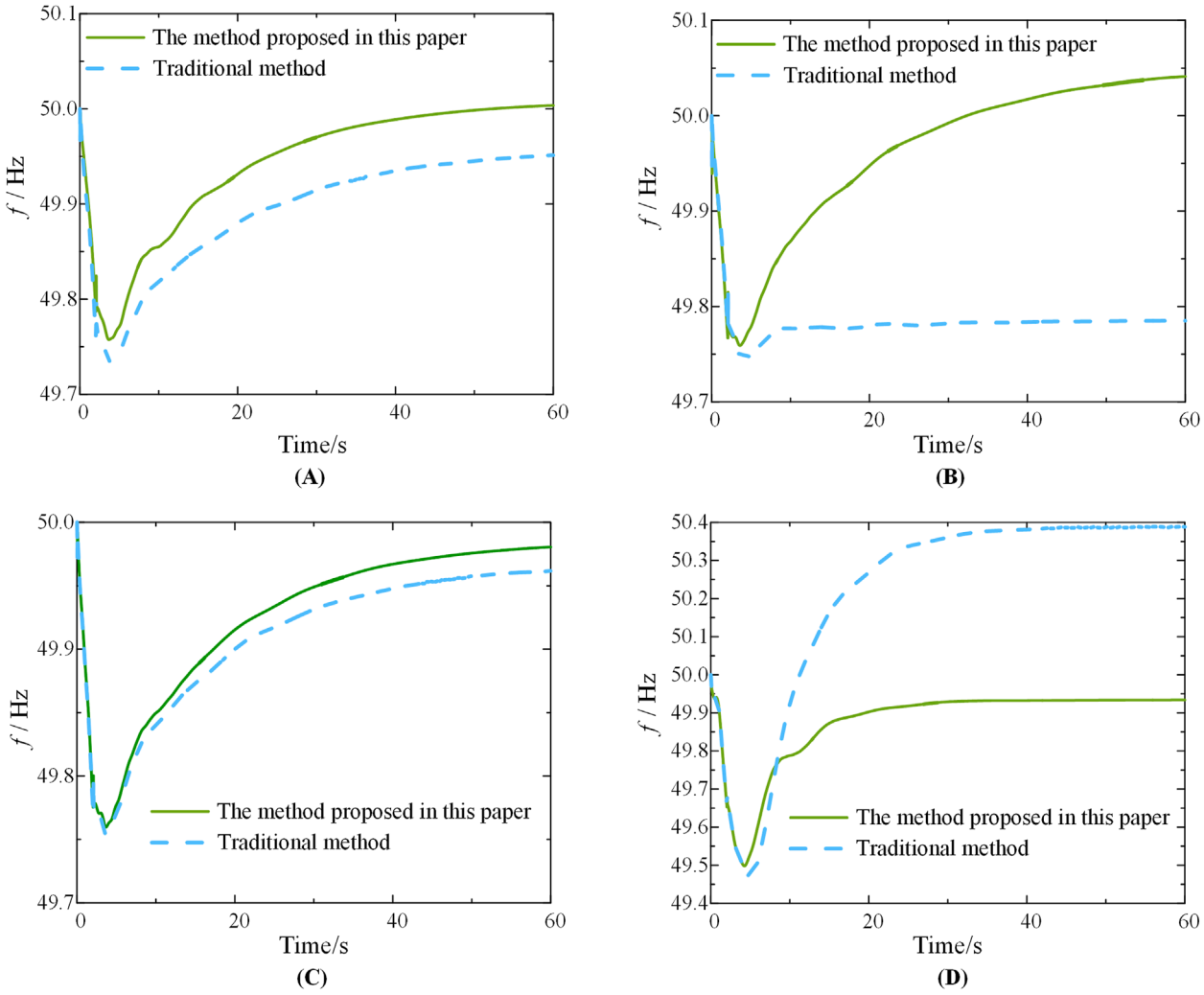

FIGURE 9
Comparison of the dynamic frequency process of scenario **(A–D)** after the execution of the two strategies.

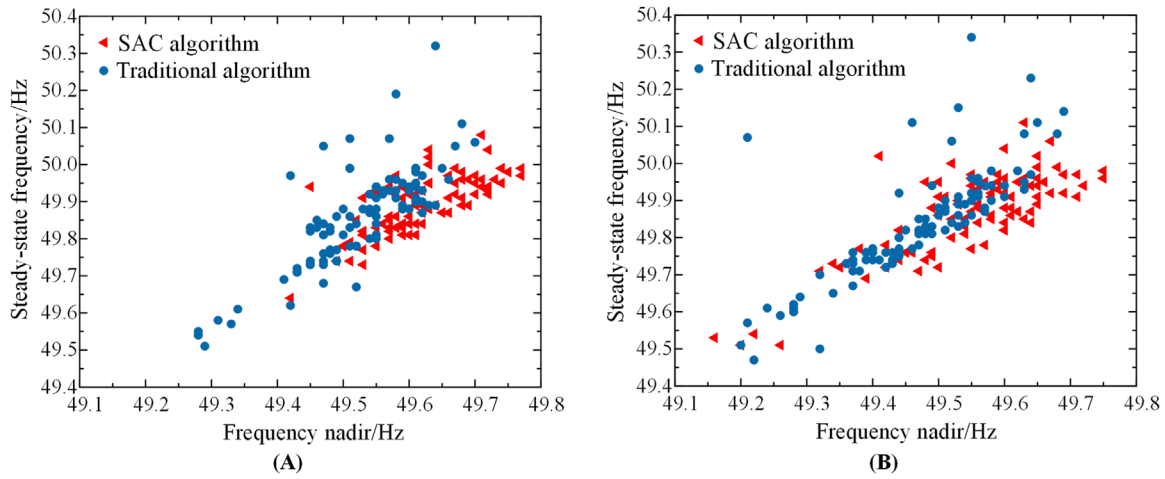

FIGURE 10
(A) Comparison of stochastic test results for source-load deterministic systems **(B)**. Comparison of stochastic test results for the source-load uncertainty system.

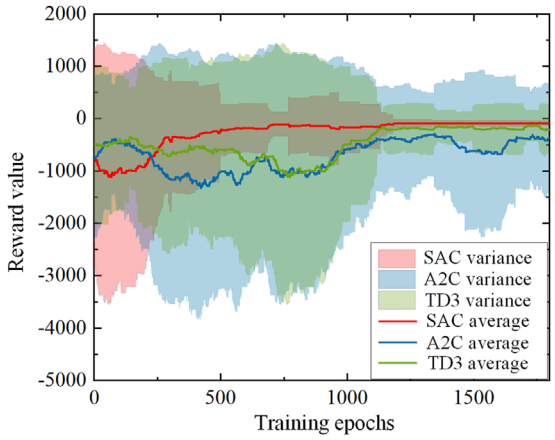

FIGURE 11
Comparison of reward values of different DRL algorithms.

model is based on the sixth order model, while the load model consists of a constant impedance model and a mixed load model incorporating induction motors, with a 50% ratio between the two. The fault scenario involves a generator experiencing a partial power loss, resulting in a power difference within the power system. The total simulation time is 40 s, with each cycle of the waveform serving as a sampling point. To simulate various system fault states and obtain sufficient samples, one of the ten generators is randomly selected at the start of the simulation to experience a loss of active output ranging from 0.5 p. u. to one p. u.

This paper utilizes a modified version of the IEEE10 machine with 39 nodes to validate the proposed methodology in this section. The modification involves replacing nodes 32 and 36 with turbines having rated capacities of 684 MW and 576 MW, respectively. Additionally, nodes 3, 4, 7, 8, 16, 20, 24, and 39 are designated as controllable load nodes participating in frequency emergency control. The system's topology is illustrated in Figure 4.

The power fluctuations at the load nodes follow a normal distribution with a mean and standard deviation equal to 5% of the rated value. Similarly, the load static model voltage and frequency indices also have a mean and standard deviation of 5% of the rated value.

The wind speeds of the wind nodes are modeled by a Weibull distribution with the shape parameter K set to 2.26, the scale parameter C set to 7.55, the cut-in wind speed at 3.5 m/s, the cut-out wind speed at 25 m/s, and the rated wind speed at 7.3 m/s.

To account for the correlation between the wind turbine nodes, 1,000 sets of wind turbine output samples are generated using the Nataf inverse transformations, with correlation coefficients of 0.8. Figure 5 illustrates the Weibull distribution of wind speed.

The deep reinforcement learning state space in this system comprises frequency deviation, frequency rate of change, active output, and load of each node, resulting in a 47-dimensional space. The action space consists of eight load shedding actions for controllable loads. Each action is represented as an 8-dimensional vector, where each element is a continuous value within the range of [-1, 0]. Furthermore, as the Soft Actor Critic (SAC) algorithm can handle continuous action spaces, the emergency frequency control directly determines the necessary load shedding amount and sets the action time for emergency frequency control as 2 s after fault detection. The delay characteristics of controllable loads are categorized into three levels. For loads of the same delay level, the actual control delay is calculated based on the maximum value to ensure that the actual frequency drop depth is less than or equal to the ideal frequency drop depth, thereby avoiding frequency instability. Consequently, after aggregation, it is assumed that the control delay for all level 1 controllable loads is 100 ms, for level 2 controllable loads is 200 ms, and for level 3 controllable loads is 300 ms. The controllable loads are then removed within each node in order of delay from low to high. Table 1 provides the proportions of controllable loads at each node and the distribution of loads across different control delay levels after aggregated modeling.

5.2 Analysis of model training and testing results

The policy network and value network of the SAC model both consist of two hidden layers with 64 neurons each. The activation function is set to ReLU, the learning rate is 0.005, the initial temperature coefficient is 0.1, the self-updating learning rate is 0.0001, and the updating algorithms utilize the alternating multiplier method. The experience replay unit has a capacity of 2,500, and 64 samples are drawn for each training iteration. The convergence criterion for each training round is that the absolute value of the steady-state frequency deviation is less than 0.1 Hz.

The SAC algorithm is employed to learn and train the aforementioned arithmetic model. Figure 6 depict the curves illustrating the changes in reward values during the training process.

Figure 6 demonstrate that, initially, the model struggles to find a control strategy that effectively stabilizes the system frequency, resulting in frequent movements per round and consequently low reward values. Additionally, the maximum number of action steps per round often reaches 50. However, as training progresses, the model gradually discovers more efficient control strategies with shorter action sequences, although the reward value remains suboptimal due to excessive load removal. It is only after 1,200 rounds of training that both the reward value and the number of training rounds stabilize, indicating the completion of the model training process.

To evaluate and compare the frequency recovery process of the proposed emergency frequency control scheme, it is essential to conduct tests using various fault scenarios. These scenarios are characterized by four attributes: the number of faulty nodes, the extent of power shortage in the faulty nodes, the system load factor, and the magnitude of source load fluctuations. For this purpose, four representative fault scenarios are selected, as illustrated in Figure 7.

During the model training process, the emergency frequency control policies for the four representative scenarios are derived

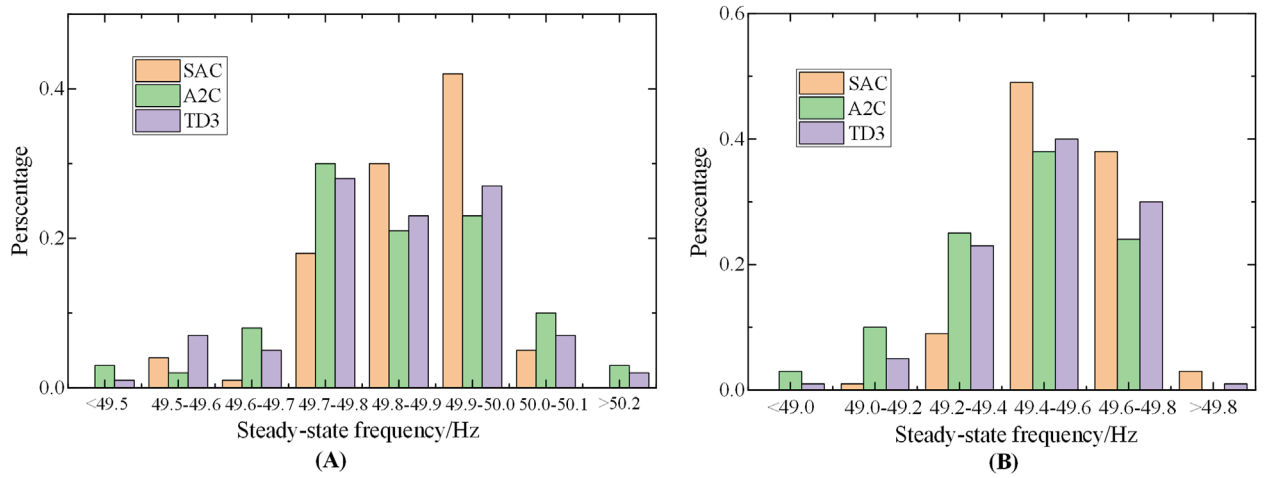

FIGURE 12
(A) Comparison of steady-state frequency deviation distribution of different DRL algorithms for random testing **(B)**. Comparison of frequency drop nadir distribution of different DRL algorithms for random testing.

through testing at intervals of 400 rounds until the completion of 2000 rounds, leading to the acquisition of the optimal control policy, as depicted in Figure 8.

Figure 8 clearly demonstrate significant fluctuations in the emergency frequency control strategies during rounds 0, 400, 800, and 1,200, indicating the model's continuous search for an improved control strategy. In contrast, the control strategies for rounds 1,600 and 2000 exhibit reduced fluctuations, indicating that the model has undergone substantial training. Initially, the emergency frequency control strategy is more random, but through continuous training, the model takes into account factors such as the amount of controllable loads at each node and load removal sensitivity. Consequently, it selects an optimal node for load shedding, resulting in a final strategy with total load removal close to the power deficit.

Table 2 presents the controllable load shedding quantities for the optimal policy in the four representative test scenarios, along with the steady-state frequency values achieved post-policy implementation and the minimum value of dynamic frequency drop.

Table 2 reveals that in the four test scenarios, characterized by diverse fault locations, fault sizes, system loading rates, and source-load uncertainties, the trained model successfully maintains the system within 0.1 Hz of the steady-state frequency deviation. Additionally, the lowest point of the dynamic frequency drop remains above 49.5 Hz. These results substantiate the effectiveness of the emergency control strategy based on the SAC algorithm, particularly for systems affected by source-load uncertainties.

To further ascertain the superiority of the proposed method, a comparative analysis is conducted between the emergency frequency control strategy derived from the traditional adaptive UFLS algorithm and the strategy proposed in this paper. The dynamic frequency recovery process of the system is evaluated for both strategies across the four scenarios, as depicted in Figure 9.

Figure 9 demonstrates that the emergency frequency control strategies optimized by the proposed scheme in this paper effectively maintain the steady-state frequency deviation of the system within 0.1 Hz, with the lowest frequency point exceeding 49.5 Hz across the four different scenarios. In contrast, the adaptive UFLS scheme in Scenarios 1, 2, and three suffers from the issue of insufficient load shedding, resulting in a greater depth of frequency drop and steady-state frequency deviation. Additionally, the conventional scheme in Scenario four exhibits excessive load shedding, leading to a steady-state frequency close to 50.4 Hz. Consequently, the method presented in this chapter proves its superiority in reducing the depth of frequency drop and steady-state frequency deviation, highlighting the effectiveness of the deep reinforcement learning algorithm.

To compare the disparities between source-load uncertainty and deterministic power systems, both the conventional method and the SAC algorithm proposed in this chapter are employed in both systems for 100 tests. The emergency frequency control outcomes are then compared, and the results are illustrated in Figure 10.

Figures 10A, B reveal that the median frequency nadir achieved by the SAC algorithm in the source-load deterministic system and the uncertain system is approximately 49.65 Hz and 49.6 Hz, respectively, whereas the median values obtained by the traditional method are around 49.55 Hz and 49.45 Hz, respectively. Notably, the frequency nadir resulting from the traditional method is significantly lower than that achieved by the deep reinforcement learning method, making it nearly impossible to maintain system frequency stability in numerous scenarios. By contrast, the SAC algorithm effectively improves the steady-state frequency deviation and frequency nadir in both deterministic and uncertain systems, demonstrating its superiority over the traditional method for addressing the emergency frequency control problem in source-load uncertain systems.

To validate the suitability of the SAC algorithm over other reinforcement learning algorithms for addressing the emergency

frequency control problem in the source-load double uncertainty system, the model developed based on the SAC algorithm in this paper is compared with models employing the A2C algorithm and the TD3 algorithm. Figure 11 presents a comparison of the reward value's increasing trend throughout the training process. The solid line represents the smoothed reward value, while the shaded area denotes the variance fluctuation of the reward value.

Figure 11 illustrates that after approximately 500 rounds, the smoothed reward value of the model based on the SAC algorithm surpasses that of the other algorithm models, exhibiting a gradual increase until it stabilizes at the desired value. Furthermore, in terms of variance, the reward value's variance for the SAC algorithm is higher during the initial 300 training rounds and subsequently becomes smaller than that of the other two algorithms. This observation indicates the robustness of the SAC algorithm, its ability to swiftly enhance the reward value through learning, and its reduced oscillation.

The SAC algorithm effectively decreases the minimum system frequency drop compared to other DRL algorithms, while also reducing the steady-state frequency deviation. To visually demonstrate the test's improvement more intuitively, Figure 12A and (B) present the distribution of frequency drop nadir and steady-state frequency deviations resulting from the tests conducted with various algorithms under random scenarios.

As can be seen from Figure 12, the test results of the emergency frequency control strategy using the SAC algorithm show that the probability of the system's steady-state frequency stabilizing at 49.8Hz–50 Hz is more than 50%, which is much higher than that of the test results using the A2C and TD3 algorithms, and the probability of the frequency dip nadir of the SAC algorithm being higher than 49.4 Hz is much higher than that of the other two algorithms. Therefore, the model based on SAC algorithm in this chapter can effectively improve the dynamic frequency nadir and steady-state frequency of the system after emergency frequency control compared to other DRL algorithms.

6 Conclusion

The emerging power systems exhibit dual source-load uncertainty, contributing to the increasing nonlinearity and complexity of the emergency frequency stabilization problem. Consequently, this paper proposes an optimization method based on the SAC algorithm for the emergency frequency control strategy of power systems with dual source-load uncertainty. Experimental verification is conducted through the design of various operational scenarios, yielding the following conclusions.

1) The dual uncertainty in the new power system, stemming from both source and load, is analyzed. This includes the spatio-temporal uncertainty of wind power output on the power source side and the uncertainty in power demand on the load side. This analysis aims to prevent errors caused by the superposition of uncertain power from both sources and the fault power deficit.
2) Enhance the state space, action space, and reward function of the emergency frequency control MDP model to accommodate the characteristics of source-load double uncertainty;
3) Finally, the proposed method is validated in a modified IEEE10 machine 39-node system incorporating source-load uncertainty. The results demonstrate that the proposed model accounts for the superposition of source-load uncertainty power and fault power, leading to a reduction in steady-state frequency deviation after emergency frequency control. Moreover, compared with the traditional UFLS method and other DRL algorithms, the SAC algorithm with continuous action space accurately removes the load in a single pass, thereby enhancing the frequency restoration speed and minimizing the cost of controllable load removal.

Data availability statement

The raw data supporting the conclusions of this article will be made available by the authors, without undue reservation.

Author contributions

SZ: Conceptualization, Funding acquisition, Writing–original draft, Writing–review and editing. SR: Project administration, Writing–review and editing. BZ: Formal Analysis, Writing–review and editing. JF: Validation, Writing–original draft, Supervision. XZ: Validation, Writing–review and editing. YW: Writing–original draft, Writing–review and editing, Supervision. LS: Funding acquisition, Writing–original draft, Writing–review and editing, Methodology, Software.

Funding

The author(s) declare that financial support was received for the research, authorship, and/or publication of this article. This work was supported by the National Natural Science Foundation of China (52077059).

Conflict of interest

Authors SZ, SR, BZ, JF, XZ was employed by Longyuan(Beijing)Wind Power Engineering Technology Co., Ltd. Author YW was employed by State Grid Jiangsu Electric Power Co., Ltd.

The remaining author declares that the research was conducted in the absence of any commercial or financial relationships that could be construed as a potential conflict of interest.

Publisher's note

References

Bai, F., Wang, X., Liu, Y., Liu, X., Xiang, Y., and Liu, Y. (2016). Measurement-based frequency dynamic response estimation using geometric template matching and recurrent artificial neural network. *CSEE J. Power Energy Syst.* 2, 10–18. doi:10.17775/cseejpes.2016.00030JPES.2016.00030

Cao, Y., Zhang, H., Zhang, Y., and Li, C. (2021). Event-driven fast frequency response control method for generator unit. *Automation Electr. Power Syst.* 45, 148–154. doi:10.7500/AEPS20210210001

Chandra, A., and Pradhan, A. K. (2020). An adaptive underfrequency load shedding scheme in the presence of solar photovoltaic plants. *IEEE Syst. J.*, 1–10.

Chen, C., Cui, M., Li, F., Yin, S., and Wang, X. (2020). Model-free emergency frequency control based on reinforcement learning. *IEEE Trans. Industrial Inf.* 17, 2336–2346. doi:10.1109/tii.2020.3001095

Dai, Y., Xu, Y., Dong, Z. Y., Wong, K. P., and Zhuang, L. (2012). Real-time prediction of event-driven load shedding for frequency stability enhancement of power systems. *IET Generation, Transm. and Distribution.* 6, 914–921. doi:10.1049/iet-gtd.2011.0810

Hu, Yi, Wang, X., Teng, Y., Ai, P., and Che, Y. (2019). Frequency stability control method of AC/DC power system based on multi-layer support vector machine. *Proc. CSEE* 39, 4104–4118. doi:10.13334/j.0258-8013.pcsee.181496

Ke, D., Feng, S., Liu, F., Chang, H., and Sun, Y. (2022). Rapid optimization for emergent frequency control strategy with the power regulation of renewable energy during the loss of DC connection. *Trans. China Electrotech. Soc.* 37, 1204–1218. doi:10.19595/j.cnki.1000-6753.tces.210279

Larik, R. M., Mustafa, M. W., Aman, M. N., Jumani, T. A., Sajid, S., and Panjwani, M. K. (2018). An improved algorithm for optimal load shedding in power systems. *Energies* 11, 1808. doi:10.3390/en11071808

Li, C., Wu, Y., Sun, Y., Zhang, H., Liu, Y., Liu, Y., et al. (2020). Continuous under-frequency load shedding scheme for power system adaptive frequency control. *IEEE Trans. Power Syst.* 35, 950–961. doi:10.1109/TPWRS.2019.2943150

Li, S., Liao, Q., Tang, F., Zhao, H., and Shao, Y. (2017). Adaptive underfrequency load shedding strategy considering high wind power penetration. *Power Syst. Technol.* 41, 1084Y1090. doi:10.13335/j.1000-3673.pst.2016.3029

Lin, H. (2022). *Transient stability analysis and control of AC-DC hybrid power grid under topology changes based on deep learning*. Beijing, China: North China Electric Power University.

Liu, K., Wang, X., and Bo, Q. (2014). Minimum frequency prediction of power system after disturbance based on the WAMS data. *Proc. CSEE* 34, 2188–2195. doi:10.13334/j.0258-8013.pcsee.2014.13.021

Ma, Q., Zhang, H., He, X., Tang, J., Yuan, X., and Wang, G. (2020). "Emergency frequency control strategy using demand response based on deep reinforcement learning," in *2020 12th IEEE PES asia-pacific power and energy engineering conference* (Nanjing, China: APPEEC), 1–5. doi:10.1109/APPEEC48164.2020.9220600

Masood, N. A., Haque, S. M. N., Rahman, D. S., and Rani, M. S. (2021). A frequency and voltage stability-based load shedding technique for low inertia power systems. *IEEE ACCESS* 9, 78947–78961. doi:10.1109/ACCESS.2021.3084457

Qiang, Z., Wu, J., Li, B., Zhang, R., Tan, L., and Hao, L. (2022). Emergency Control Strategy for Transient angle instability of power system based on improved AlexNet. *High. Volt. Eng.* 48, 2794–2804. doi:10.13336/j.1003-6520.hve.20210114

Sheng, S., Fan, M., Zhang, W., Pan, X., Li, P., and Zhang, L. (2021). Optimization method of under frequency load shedding for high new energy proportion system. *Acta Energiae Solaris Sin.* 42, 365–369. doi:10.19912/j.0254-0096.tynxb.2018-0978

Wang, H., He, P., Jiang, Y., and others (2019). Under-frequency load shedding scheme based on estimated inertia. *Electr. Power Autom. Equip.* 39, 51–56. doi:10.16081/j.issn.1006-6047.2019.07.008

Wu, D., Javadi, M., and Jiang, J. N. (2015). A preliminary study of impact of reduced system inertia in a low-carbon power system. *J. Mod. Power Syst. Clean. Energy.* 3, 82–92. doi:10.1007/s40565-014-0093-8

Xie, J., and Sun, W. (2022). Distributional deep reinforcement learning-based emergency frequency control. *IEEE Trans. Power Syst.* 37, 2720–2730. doi:10.1109/TPWRS.2021.3130413

Xue, Y., Lei, X., Xue, F., Yu, C., Dong, Z., Wen, F., et al. (2014). A review on impacts of wind power uncertainties on power systems. *Proc. CSEE* 34, 5029–5040. doi:10.13334/j.0258-8013.pcsee.2014.29.004

Yang, B., Chen, Y., Yao, W., Shi, Z., and Shu, H. (2022). Review on stability assessment and decision for power systems based on new-generation artificial intelligence technology. *Autom. Electr. Power Syst.* 46, 200–223. doi:10.7500/AEPS20220114001

Yi, J., Bu, G., Guo, Q., Xi, G., Zhang, J., and Tu, J. (2019). Analysis on blackout in Brazilian power grid on March 21,2018 and its enlightenment to power grid in China. *Automation Electr. Power Syst.* 43, 1–6. doi:10.7500/AEPS20180812003

Zhang, W., Wang, X., and Liao, G. (2009). Automatic load shedding emergency control algorithm of power system based on wide-area measurement data. *Power Syst. Technol.* 33, 69–73.

Zhou, X., Chen, S., Lu, Z., Huang, Y., Ma, S., and Zhao, Q. (2018). Technology features of the new generation power system in China. *Proc. CSEE* 38, 1893–1904. doi:10.13334/j.0258-8013.pcsee.180067

Zhou, Z., and Shi, L. (2021). Risk assessment of power system cascading failure considering wind power uncertainty and system frequency modulation. *Proc. CSEE* 41, 3305–3316. doi:10.13334/j.0258-8013.pcsee.202352

frontiers | Frontiers in Energy Research

TYPE Original Research
PUBLISHED 17 December 2024
DOI 10.3389/fenrg.2024.1510259

OPEN ACCESS

EDITED BY
Zixuan Wang,
North China Electric Power University, China

REVIEWED BY
Chutong Wang,
North China Electric Power University, China
Yue Zhou,
Cardiff University, United Kingdom

*CORRESPONDENCE
Wendi Wang,
sy584278874@163.com

RECEIVED 12 October 2024
ACCEPTED 26 November 2024
PUBLISHED 17 December 2024

CITATION
Wang W, Wang H, Sun S, Cao G, Wang S and Ji Y (2024) Optimal configuration of shared energy storage for industrial users considering lifetime and charge-discharge strategy coupling. *Front. Energy Res.* 12:1510259. doi: 10.3389/fenrg.2024.1510259

Optimal configuration of shared energy storage for industrial users considering lifetime and charge-discharge strategy coupling

Wendi Wang*, Hongyan Wang, Shaobin Sun, Gang Cao, Shufan Wang and Ye Ji

Science and Technology Information Network Branch, Nanjing Suyi Industrial Co., Ltd., Nanjing, China

With the development of renewable energy, energy storage has become one of the key technologies to solve the uncertainty of power generation and the disorder of power consumption and shared energy storage has become the focus of attention for its cost-effective characteristics. However, it is always difficult to quantify the coupling relationship between charge and discharge strategy and life expectancy in energy storage configuration. Based on this, this paper proposes an industrial user-side shared energy storage optimal configuration model, which takes into account the coupling characteristics of life and charge and discharge strategy. Firstly, the life loss model of lithium iron phosphate battery is constructed by using the rain-flow counting method. In order to further optimize the user-side shared energy storage configuration in the multi-user scenario, a two-layer model of energy storage configuration is built, and the Big M method and the Karush-Kuhn-Tucker (KKT) conditions are used to equivalently transform the constraints. Based on the predicted life of energy storage and the dichotomy method, the optimal energy storage configuration results are obtained. Comparing the energy cost of users under the three scenarios of no storage configuration, storage configuration according to fixed storage life, and storage configuration according to the model proposed in this paper, the results show that the proposed method can help accurately describe the energy storage model, increase the utilization rate of the power station, and improve the electricity economy of users.

KEYWORDS

shared energy storage configuration, rain-flow counting, life expectancy of energy storage, Shapley value method, bi-layer model

1 Introduction

Since the 21st century, establishing low-carbon or even zero-carbon energy systems has become a global focus. Consequently, the application and proportion of renewable energy sources like wind, solar, and hydropower in the grid have gradually expanded. However, renewable energy production inherently exhibits intermittency, volatility, and randomness. When integrated on a large scale with power systems, these characteristics exacerbate the imbalance between supply and demand in generation and load, posing a threat to the safe and stable operation of power systems (Azhgaliyeva, 2019).

Energy storage, as a device capable of altering the spatial and temporal distribution of energy, is a key technology supporting the large-scale integration of renewable energy into the grid and promoting the green transition of energy. It can effectively mitigate the instability of renewable energy generation. With the development and application of energy storage, effective demand-side management can be realized, promoting the application of renewable energy and enhancing system operational stability, which will bring significant changes to power system planning, scheduling, and control (Deguenon et al., 2023). The application of energy storage technology will permeate all aspects of power generation, transmission, distribution, and consumption, alleviating peak load power supply demands and improving the utilization rate of existing grid equipment and the operational efficiency of the grid. Zeng et al. (2024) considering shared energy storage and demand response, a power system interval optimization model based on shared energy storage and refined demand response is proposed. This model effectively enhances the utilization of energy storage and the economic operation of the system, achieving coordinated interaction among "source-grid-load-storage." As a flexible resource, energy storage can be applied on the generation side (Wang et al., 2023; Song et al., 2023), grid side (Xie et al., 2022a), and user side (Qian et al., 2023), thereby achieving a coordinated unity of "source-grid-load-storage."

As significant energy consumers, commercial and industrial (C&I) consumers can play a crucial role by enhancing their flexibility and participating in demand response initiatives. On-site renewable energy generation can reduce grid consumption, while energy storage systems (ESS) can store energy for later use, supporting variable generation and shifting demand. Both technologies, when integrated with demand response, can enhance flexibility and benefits (Yasmin et al., 2024). Installing energy storage systems effectively addresses uncertainties in renewable energy sources (RES) and load demands, ensuring the stable and efficient operation of industrial power systems (Jianwei et al., 2022). Kwon et al. (2017) proposed a demand-side electricity procurement approach to minimize energy costs for consumers. Krishnamurthy et al. (2018) introduced a stochastic optimization model to maximize user energy arbitrage, considering uncertainties in day-ahead loads and real-time prices. However, these models focus on optimizing standalone energy storage for single users.

The low cost and inefficiency of standalone systems hinder the development of energy storage (Tahir et al., 2022). This has led to the emergence of shared energy storage solutions (Zhu and Ouahada, 2021). Wang et al. (2024a) developed a new business model that allows multiple users within an industrial park to share leased energy storage, proposing a robust optimization framework. Their results show that shared leasing is significantly more economical than self-built storage. Aminlou et al. (2022) established a peer-to-peer (P2P) energy trading model in the context of shared battery energy storage systems (SBESS), which can save substantial costs for industrial towns.

Regarding the business models and pricing mechanisms of shared energy storage, Zhu et al. (2022) proposed a peer-to-peer (P2P) energy trading system, which integrates energy trading with energy management, enabling each prosumer to jointly manage its energy consumption, storage scheduling, and energy trading in a dynamic manner for smart communities consisting of a group of grid-connected prosumers with controllable loads, renewable generations and energy storage systems. Xu et al. (2023) designed a business model for shared energy storage operators providing deviation insurance services from the perspective of commercial insurance; Yang et al. (2023) considered the regulation demands from the power side and grid side, proposing a distributed shared energy storage operational model; Lai et al. (2022) presented a two-stage pricing mechanism between the coordinator operating the shared energy storage and the prosumers borrowing the shared capacity from the coordinator; Zhang et al. (2022) studied the equilibrium state of supply-demand flow in a peer-to-peer market model for residential shared energy storage units and proposes a method for service pricing and load dispatching. Zhang et al. (2024) addressed the interests of different entities in the operation of Energy Storage Systems and Integrated Energy Multi-Microgrid Alliances by proposing an optimization method based on Stackelberg game theory.

For the configuration and optimization of shared energy storage, Wang C. et al. (2022) categorized residential flexible loads based on different demand response patterns and establishes demand response models for various load types. Xie et al. (2022c) first proposed a community energy storage collaborative sharing model that includes multiple transaction types, then established a community shared energy storage scale and configuration model based on the cooperative game between community users and energy storage operators; based on this, the bilateral Shapley method (Yang et al., 2021) is applied, allocating the annual total cost based on the marginal expected costs brought by each user. For the profit distribution using the Shapley value method, Cremers et al. (2023) conducted a systematic review of the use of Shapley values in energy-related applications, as well as the literature on calculating or approximating them. They developed a new method for accurately calculating Shapley values by clustering producers and consumers into fewer demand profiles, making it applicable to communities with hundreds of agents. Wu et al. (2023) proposed a new profit distribution method based on Shapley values, focusing on cooperative fairness and encouraging alliance improvements. Pedrero et al. (2024) introduced Nested Shapley values as a new sharing mechanism that fairly allocates profits among members of large alliances, addressing the trade-off between fairness and scalability. In the area of energy storage scheduling, Yang et al. (2024) proposed a scheduling method based on multi-stage robust optimization to address the scheduling problems of energy storage systems and uncertain energy. Qian et al. (2024) considered the demand response of electric magnesium loads, an improved scenario-based typically distributed robust energy and reserve renewable energy system that significantly reduces the costs of day-ahead scheduling and rescheduling while enhancing operational economy without compromising the high reliability and safety of the Renewable Portfolio Standard (RPS). Wang K. Y. et al. (2022) presented a dual-layer optimization model for the configuration and scheduling of integrated energy systems in multi-microgrids, considering energy storage and demand response, to enhance renewable energy consumption and reduce carbon emissions.

However, the aforementioned literature focuses on using game theory to achieve the configuration of user/park shared energy storage, neglecting the impact of energy storage losses on

configuration results (Xie et al., 2022b). In integrated configuration and scheduling models, the lifespan of energy storage and optimized charge/discharge strategies are highly coupled, significantly affecting the economic evaluation of energy storage over its entire lifecycle. Scholars have conducted relevant research on these issues. In literature (Wang et al., 2024b), the Rain-flow counting method (Pan et al., 2021) and iterative methods are used to quantify the impact of capacity loss on configuration. By offline calculating the health status of energy storage during each iteration, it is concluded that when the initial health status value reaches consistency at the beginning of each year, the iteration converges, resulting in optimal configuration outcomes. Although the above methods address some issues and make the economic configuration model of shared energy storage more precise, the physical significance of the iterative process is unclear, and the impact of charge/discharge strategies on expected lifespan and corresponding optimal configuration results is overlooked.

Therefore, this paper proposes an optimal configuration model for industrial user-side shared energy storage that considers the coupling characteristics of lifespan and charge/discharge strategies, based on cooperative game theory (Mao et al., 2022) and a business model for users to jointly configure energy storage. First, the Rain-flow counting method is used to solve the equivalent cycle count of the energy storage battery, obtaining a relevant model for calculating battery lifespan loss. Second, a bi-level model is constructed, with the upper-level objective of minimizing the total cost for the user group and the lower-level objective of minimizing the cost of purchasing electricity from the grid for the user group. Finally, the KKT conditions and Big-M method are used to transform the bi-level model, combined with a bisection method to iterate the expected lifespan of energy storage. Shapley value allocation model is applied to allocate the cost of multi-user alliance.

2 Equivalent life model of ESS

2.1 Rain-flow counting method

The Rain-flow counting method was proposed by two British engineers in the 1950s. Its core idea is to decompose complex load curves into multiple load cycles, which are then used for fatigue life estimation. The Rain-flow counting method is a dual-parameter cycle memory model with clear physical significance. Therefore, it can also be used to predict the equivalent cycle life of batteries. The cycle life of a battery varies with different depths of discharge. By using the Rain-flow counting method, the number of charge-discharge cycles and their depths within a typical day for an energy storage battery can be calculated, which is then used for battery life estimation.

The rain-flow counting method is widely used in fatigue life analysis across various fields, such as materials science, and in recent years, it has also been applied to assess battery life (Xu et al., 2021). Figure 1 shows the SOC image after rotation, and the process for obtaining this image is as follows. First, the capacity change data is collected and plotted to create a curve. This curve is then rotated 90 degrees counterclockwise to fit the requirements of the Rain-flow counting method. The starting point on the curve is marked as the origin for simulating "raindrops." As the simulation progresses,

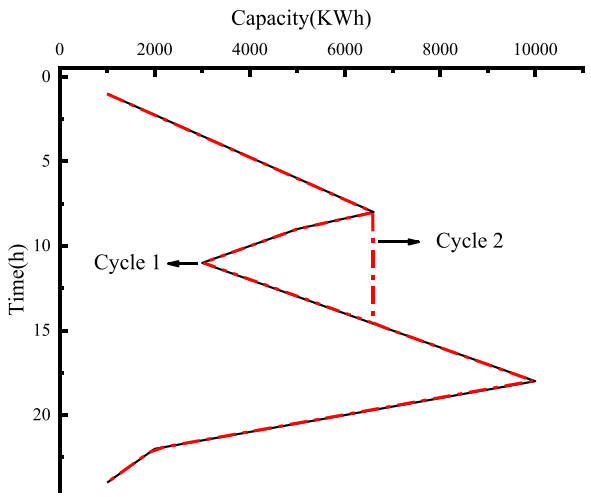

FIGURE 1
Example of calculating the number of cycles of the rain-flow counting method.

"raindrops" flow along the curve, and each time they reach a peak (or "eave"), it is checked whether they can fall. If a "raindrop" falls and is intercepted by another part of the curve, it continues to fall until it reaches either the maximum or minimum value of the curve, at which point it reverses direction. If the value at the endpoint differs from the starting point when the raindrop reaches the endpoint, it is considered that the cycle is divided into two half-cycles, with the division point at the maximum or minimum value of the complete curve. Figure 1 provides an example of calculating the number of cycles using the Rain-flow counting method.

Figure 1 shows the capacity change curve of a battery within 24 h. The State of Charge (SOC) of the battery refers to the ratio of the remaining charge in the battery to the nominal capacity of the battery, usually expressed as a percentage. The Depth of Discharge (DOD) of period one is 0.3366, and period two is 0.8415.

2.2 Battery life loss model

It is generally considered that energy storage batteries are scrapped when their capacity drops below 80% of the initial capacity. The relationship between the cycle life of lithium iron phosphate batteries and the DOD is fitted based on the number of cycles N_{ctf} at different DOD levels.

$$N_{ctf} = 1 + An_k + Bn_k^2 + Cn_k^3 \tag{1}$$

In Formula 1 (Gao et al., 2013), A, B, and C are parameters related to the discharge depth DOD of the Shared Energy Station (SES); n_k represents the number of cycles of the SES at a certain discharge depth $D_{OD,i}$.

If the DOD for the i-th charge-discharge cycle is $D_{OD,i}$, the equivalent cycle life can be expressed by Equation 2 as:

$$N(D_{OD,i}) = \frac{N_{ctf}(D_{OD,1})}{N_{ctf}(D_{OD,i})} \tag{2}$$

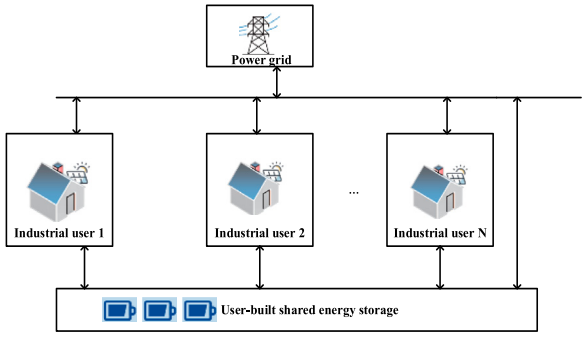

FIGURE 2
User-built shared energy storage system structure diagram.

T_{life} of the battery in the working cycle of the energy storage power station is:

$$T_{life} = \sum_{D_{OD}=0.01}^{D_{OD}=1} \frac{N_{ctf}(D_{OD,1})}{N_{ctf}(D_{OD,i})} \tag{3}$$

In the Equation 3, T_{life} represents the equivalent cycle life.

Therefore, it is considered that the life loss of the energy storage battery is:

$$T = \frac{N_{ctf}(D_{OD,1})}{T_{life}} \tag{4}$$

In the Equation 4, when $T = 1$, the battery is considered to be exhausted and needs to be scrapped.

When the calculation period is year, the equivalent cycle life of shared energy storage in 1 year is the sum of days d:

$$T_{life,year} = \sum_{d=1}^{365} T_{life,d} \tag{5}$$

In Equation 5, $T_{life,\ year}$ represents the equivalent cycle life of shared energy storage in 1 year.

The estimated service life of shared energy storage is:

$$T_{base} = \frac{N_{ctf}(D_{OD,1})}{T_{life,year}} \tag{6}$$

In the Equation 6, T_{base} represents the cycle life of the energy storage battery under the typical day (in years).

3 User-side SES configuration model

When users build their own energy storage stations under this business model, the system structure is shown in Figure 2 (Yan and Chen, 2022) The objective function of the user-side shared energy storage model focuses on the cost of electricity purchase and the construction and operation costs of the energy storage station. The model aims to minimize the total cost of user investment in the station and electricity purchase while achieving the lowest electricity purchase cost for the user.

Therefore, a Bi-level model is established. The upper level aims to minimize the sum of user investment and electricity purchase costs, while the lower level aims to minimize the user's cost of purchasing electricity from the grid. Based on this, this section will establish a cost conversion model for the energy storage station using the Net Present Value (NPV) method and a bilevel model with the objective of minimizing user costs.

3.1 Upper layer model

3.1.1 Upper objective function

In the upper-level model, users need to consider the costs of constructing and operating the energy storage station. Since the construction investment cost of the energy storage station is a one-time investment, the time value of money must be taken into account.

$$min C = \sum_{w=1}^{W} T_w \left(C_{inv,w} + C_{grid,w} + C_{protect,w}\right) + 12 C_{grid,zd,w} \tag{7}$$

In Equation 7, W represents the number of typical days; T_w denotes the number of days corresponding to the w-th typical day; $C_{inv,w}$ is the daily average investment and maintenance cost of the energy storage station; $C_{grid,w}$ is the electricity cost for users from the grid on a typical day; $C_{grid,zd,w}$ is the monthly demand charge for users from the grid.

The daily average investment cost of the energy storage station is given by Equation 8:

$$C_{inv,w} = M_y \frac{\eta_P P_{ess}^{max} + \eta_S E_{ess}^{max}}{N_w T_w T_k} \tag{8}$$

where M_y represents the present value annuity factor; η_P is the power cost of the energy storage station; η_S is the capacity cost of the energy storage station; $P_{ess}{}^{max}$ and $E_{ess}{}^{max}$ are the maximum charge/discharge power and maximum capacity of the energy storage station, respectively; N_w is the number of typical days representing different electricity usage patterns within a year; T_w is the number of days corresponding to the typical day; T_k is the lifespan of the energy storage station in years; $k, k = 0, 1, 2...n (n \in N)$ denotes the iteration count; T_0 is the initial expected lifespan, set to 5 years.

The present value annuity factor is given by:

$$M_y = \frac{[(1+r)^y - 1]}{r(1+r)^y} \tag{9}$$

In Equation 9, r is the annual interest rate of funds; y is the life cycle of the device.

Daily maintenance cost of energy storage power station:

$$C_{protect,w} = \sum_{i=1}^{N} \sum_{t=1}^{N_T} \left(P_{ess,c,w,i}(t) + P_{ess,d,w,i}(t)\right) \delta_{protect} \tag{10}$$

In Equation 10, N represents the number of users; N_T represents the number of time periods; $P_{ess,d,w,i}(t)$ is the power drawn by the i-th user from the energy storage station during period t on a typical day; $P_{ess,c,w,i}(t)$ is the power charged by the i-th user to the energy storage station during period t on a typical day; $\delta_{protect}$ is the operation and maintenance cost paid by users when storing and retrieving electricity from the energy storage station.

The electricity cost for users purchasing electricity from the grid is given by:

$$C_{grid,w} = \sum_{i=1}^{N}\sum_{t=1}^{N_T} \tau(t) \cdot P_{grid,w,i}(t) \cdot t \tag{11}$$

In Equation 11, $\tau(t)$ represents the electricity cost for users purchasing electricity from the grid; $P_{grid,w,i}(t)$ is the power purchased from the grid by the i-th user during period t on a typical day.

The demand charge for users purchasing electricity from the grid is given by Equation 12:

$$C_{grid,zd,w} = \sum_{i=1}^{N} \tau_{zd} \cdot P_{grid,zd,w}(i) \tag{12}$$

where τ_{zd} represents the demand charge for users purchasing electricity from the grid; $P_{grid,zd,w}(t)$ is the monthly peak power demand for the i-th user on a typical day.

According to the demand charge payment rules, users only need to pay the demand charge based on the maximum load from the grid in that month, in addition to the basic electricity cost. The demand charge rate in China varies depending on the user type and typically ranges from 30 to 50 ¥/kW.

3.1.2 Upper constraint

In configuring the energy storage station, constraints on user electricity purchases, station charge/discharge operations, and grid power flow need to be imposed to achieve a rational planning of the user-owned energy storage station business model.

Constraints on the charging and discharging power of the energy storage battery:

$$0 \le P_{ess,abs}(t) \le U_{abs}(t) P_{ess}^{max} \tag{13}$$

$$0 \le P_{ess,relea}(t) \le U_{relea}(t) P_{ess}^{max} \tag{14}$$

$$U_{abs}(t) + U_{relea}(t) \le 1 \tag{15}$$

$$U_{abs}(t) \in \{0, 1\} \tag{16}$$

$$U_{relea}(t) \in \{0, 1\} \tag{17}$$

$$\sum_{t=1}^{N_T} \left(P_{ess,abs}(t) + P_{ess,relea}(t)\right) \le N_{DoD} D_{ideal} E_{ess}^{max} \tag{18}$$

In the above equations, $P_{ess,abs}(t)$ represents the charging power of the energy storage station, $P_{ess,relea}(t)$ represents the discharging power of the energy storage station, $U_{abs}(t)$ represents the charging status of the energy storage station as a binary variable (0 or 1), $U_{relea}(t)$ represents the discharging status of the energy storage station as a binary variable (0 or 1). Equation 15 signifies that either $U_{abs}(t)$ or $U_{relea}(t)$ cannot be 1 at a given time, indicating that the battery cannot be charged and discharged simultaneously. N_{DoD} represents the estimated daily charging and discharging cycles of the energy storage battery, D_{ideal} represents the ideal maximum depth of discharge for the battery. Equation 18 imposes constraints on the daily depth of discharge and the number of cycles for economic reasons, which ensures that the energy storage will not over-charge or over-discharge within a day.

Constraints on the upper and lower limits of energy storage battery capacity:

$$10\% E_{ess}^{max} \le E_{ess}(t) \le 90\% E_{ess}^{max} \tag{19}$$

In Formula 19, $E_{ess}(t)$ indicates the energy stored in the energy storage system at time t. This constraint implies that the maximum energy within the storage system at any given time cannot exceed 90% of the total capacity, and the minimum energy cannot fall below 10% of the total capacity.

The energy storage state constraint for t ESS is shown in Equation 20.

$$E_{ess}(t) = E_{ess}(t-1) + \left[\eta^{abs} P_{ess,abs}(t) - \frac{1}{\eta^{relea}} P_{ess,relea}(t)\right] \Delta t \tag{20}$$

In the above equation, η^{abs} and η^{relea} represent the charging and discharging efficiencies, respectively.

The constraint on the electricity flow between each user and SES:

$$0 \le P_{ess,c,w,i}(t) \le P_{ess}^{max} \cdot U_{cha,w,i}(t) \tag{21}$$

$$0 \le P_{ess,d,w,i}(t) \le P_{ess}^{max} \cdot U_{dis,w,i}(t) \tag{22}$$

$$U_{cha,w,i}(t) + U_{dis,w,i}(t) \le 1 \tag{23}$$

$$U_{cha,w,i}(t) \in \{0, 1\} \tag{24}$$

$$U_{dis,w,i}(t) \in \{0, 1\} \tag{25}$$

where $U_{cha,w,i}(t)$ represents the energy storage status of the i-th user, indicating whether the user is charging the energy storage station (taking values of binary), while $U_{dis,w,i}(t)$ represents the status of the i-th user drawing energy from the energy storage station (also taking values of binary). Equation 23 signifies that $U_{cha,w,i}(t)$ and $U_{dis,w,i}(t)$ cannot both be 1 simultaneously, meaning the i-th user cannot both charge from and discharge to the energy storage station at the same time.

The energy storage power balance constraint is shown in Equation 26.

$$\sum_{i=1}^{N} \left[P_{ess,d,w,i}(t) - P_{ess,c,w,i}(t)\right] = P_{ess,relea}(t) - P_{ess,abs}(t) \tag{26}$$

This constraint signifies that the total sum of the difference in energy exchange values between each user and the energy storage station must equal the change in energy stored in the battery during that time period.

The unidirectional power transmission constraint within the power grid:

$$0 \le P_{grid,w,i}(t) \le P_{grid,zd,w}(i) \tag{27}$$

In Formula 27, the power transmitted through the power grid should be a positive value and less than the maximum transmission capacity.

3.2 Lower layer model

3.2.1 Upper objective function

The lower objective considers the lowest cost of electricity for users and is expressed by Equation 28 as:

$$min\, C = \sum_{w=1}^{W} \left[T_w \cdot C_{grid,w} + 12 C_{grid,zd,w}\right] \tag{28}$$

3.2.2 Lower constraint

User power balance constraints:

$$P_{grid,w,i}(t) + P_{PV,w,i}(t) + P_{ess,d,w,i}(t) - P_{ess,c,w,i}(t) - P_{load,w,i}(t) = 0, \lambda_{1,i,t,w} \quad (29)$$

In Equation 29, $P_{PV,w,i}(t)$ represents the solar power generation of the i-th user during time period t on a typical day, while $P_{load,w,i}(t)$ represents the power load of the i-th user during time period t on a typical day. The purchased electricity by the user needs to balance with their own load, self-generated power, and the energy exchange with the station. $\lambda_{1,i,t,w}$ is the Lagrange multiplier corresponding to this constraint in the subsequent solving process.

The user's power purchasing constraint:

$$0 \le P_{\text{grid},w,i}(t) \le P_{grid,zd,w}(i): u^{min}_{1,i,t,w}, u^{max}_{1,i,t,w} \quad (30)$$

In Equation 30, $u^{min}_{1,i,t,w}, u^{max}_{1,i,t,w}$ represents the Lagrange multiplier corresponding to this inequality constraint in the subsequent solving process. This constraint implies that the power purchased by the i-th user during time period t on a typical day should not exceed the maximum power purchased from the grid for that typical day.

The peak shaving load constraint:

$$P_{load,w,i}(t) - P_{PV,w,i}(t) + \left[P_{ess,d,w,i}(t) - P_{ess,c,w,i}(t)\right] \le (1-\mu)P_{load,max,w}(i), u^{max}_{2,i,t,w} \quad (31)$$

In Equation 31, μ represents the peak shaving rate, and ${u_{2,i,t,w}}^{max}$ represents the Lagrange multiplier corresponding to this inequality constraint.

3.3 The cost allocation model based on the Shapley value method

The revenue distribution model uses the Shapley value method to fairly consider each member's contributions. This helps allocate assets appropriately. Specifically, this model utilizes the Shapley value method to distribute revenues among a coalition composed of n industrial users.

In the calculation process, the marginal contributions made by each member are taken into account, and the revenues are allocated to each member in a reasonable manner, allowing each member to receive corresponding benefits. For a coalition of n industrial users, the allocated revenue for user i, denoted as X_i, is given by:

$$\chi_i = \sum_{Q \subset n_n - \{i\}} \frac{|Q|!(|n_n| - |Q| - 1)!}{|n_n|!}\left(v(Q \cup \{i\}) - v(Q)\right) \quad (32)$$

In Equation 32: X_i represents the allocated revenue for user i; Q is any sub-coalition formed by the total coalition excluding user i; n_n is the total coalition; $\{i\}$ is the individual coalition formed independently by user i; $|Q|$ is the number of users in the sub-coalition; $|n_n|$ is the number of users in the total coalition; and v is the total revenue. The revenue distribution must satisfy the condition that the total revenue of the coalition remains unchanged before and after the distribution, as shown in Equation 33:

$$\sum_{i=1}^{n} \chi_i = v(n_n) \quad (33)$$

4 The solution process of the configuration model

4.1 Upper layer model processing

In the upper-level model, the non-linear constraints arising from the multiplication of binary (0–1) variables and linear variables are handled using the Big-M method for Equations 13–17 and Equations 21–25 (Ding et al., 2020). The processed equations are shown in Equations 34–41.

$$0 \le P_{ess,abs}(t) \le P^{max}_{ess} \quad (34)$$

$$0 \le P_{ess,abs}(t) \le U_{abs}(t)M \quad (35)$$

$$0 \le P_{ess,relea}(t) \le P^{max}_{ess} \quad (36)$$

$$0 \le P_{ess,relea}(t) \le U_{relea}(t)M \quad (37)$$

$$0 \le P_{ess,c,w,i}(t) \le P^{max}_{ess} \quad (38)$$

$$0 \le P_{ess,c,w,i}(t) \le U_{cha,w,i}(t)M \quad (39)$$

$$0 \le P_{ess,d,w,i}(t) \le P^{max}_{ess} \quad (40)$$

$$0 \le P_{ess,d,w,i}(t) \le U_{dis,w,i}(t)M \quad (41)$$

4.2 Lower layer model processing

Due to the dual-level structure of the model under study, it is necessary to appropriately handle the lower-level model to ensure it serves as a constraint for the upper-level model. In this process, we employ the KKT conditions, which are crucial for obtaining the optimal solution in nonlinear programming. By introducing the KKT conditions, even in the face of optimization problems with inequality constraints, we can still utilize the Lagrange multiplier method to continue the solution process, thereby ensuring the accuracy and effectiveness of the model.

The specific steps are as follows:

The lower-level objective function and constraints, along with their Lagrange multipliers, are multiplied to form the Lagrange function, as shown in Equation 42:

$$\begin{aligned} L = &\sum_{w=1}^{W}\sum_{i=1}^{N}\sum_{t=1}^{N_T}\left\{T_w \Delta t\left[\tau(t)P_{grid,w,i}(t)\right] + 12\tau_{zd}P_{grid,zd,w}(i)\right\} \\ &+ \lambda_{1,i,t,w}\left[\begin{array}{l} P_{grid,w,i}(t) - P_{load,w,i}(t) - \\ P_{ess,c,w,i}(t) + P_{ess,d,w,i}(t) \end{array}\right] - u^{min}_{1,i,t,w}P_{grid,w,i}(t) \\ &+ u^{max}_{1,i,t,w}\left[P_{grid,w,i}(t) - P_{grid,zd,w}(i)\right] \\ &+ u^{max}_{2,i,t,w}\left\{\left[\begin{array}{l} P_{load,w,i}(t) + P_{ess,abs}(t) - \\ P_{ess,relea}(t) \end{array}\right] - \right. \\ &\left.\left. (1-\mu)P_{load,max,w}(i) \right\}\right. \end{aligned} \quad (42)$$

The variables present in the lower-level objective function are differentiated to create new equality constraint conditions, which is shown in Equation 43:

$$T_w \cdot \tau(t) + 12 \cdot \tau_{zd} \cdot P_{grid,zd,w}(i) + \lambda_{1,i,t,w} + u^{max}_{1,i,t,w} - u^{min}_{1,i,t,w} - u^{max}_{5,i,t,w} \cdot (1-\mu) \cdot P_{load,max,w}(i) = 0 \quad (43)$$

The modified inequality constraint conditions from the original lower-level model are retained and become the new constraint

conditions of the transformed single-level model, as shown in Equations 44–46:

$$0 \le u_{1,i,t,w}^{min} \perp P_{\text{grid},w,i}(t) \ge 0 \tag{44}$$

$$0 \le u_{1,i,t,w}^{max} \perp \left(P_{grid,zd,w}(i) - P_{\text{grid},w,i}(t)\right) \ge 0 \tag{45}$$

$$0 \le u_{2,i,t,w}^{max} \perp \left((1-\mu)P_{load,max,w}(i) - P_{load,w,i}(t) + P_{PV,w,i}(t) - \left[P_{ess,d,w,i}(t) - P_{ess,c,w,i}(t)\right]\right) \ge 0 \tag{46}$$

The rewritten inequality constraint conditions from the previous step need to be processed using the Big-M method, $M_j^{min}, j = 1, 2...n(n \in N)$ is sufficiently large constants, $v_{j,i,t,w}^{min}, v_{j,i,t,w}^{max}, j = 1, 2...n(n \in N)$ are binary (0–1) variables. The resulting processed constraint conditions are given by Equations 47–52:

$$0 \le u_{1,i,t,w}^{min} \le M_1^{min} \quad v_{1,i,t,w}^{min} \tag{47}$$

$$0 \le P_{\text{grid},w,i}(t) \le M_1^{min}\left(1 - v_{1,i,t,w}^{min}\right) \tag{48}$$

$$0 \le u_{1,i,t,w}^{max} \le M_1^{max} v_{1,i,t,w}^{max} \tag{49}$$

$$0 \le P_{grid,zd,w}(i) - P_{\text{grid},w,i}(t) \le M_1{}^{max}\left(1 - v_{1,i,t,w}^{max}\right) \tag{50}$$

$$0 \le u_{2,i,t,w}^{max} \le M_2^{max} v_{2,i,t,w}^{max} \tag{51}$$

$$0 \le (1-\mu)P_{load,max,w}(i) - P_{load,w,i}(t) + P_{PV,w,i}(t) - \left[P_{ess,d,w,i}(t) - P_{ess,c,w,i}(t)\right] \le M_2{}^{max}\left(1 - v_{2,i,t,w}^{max}\right) \tag{52}$$

4.3 The solution process for SES configuration considering the coupling of lifespan and charge-discharge

In MATLAB simulation software, a dual-layer model for shared energy storage configuration, composed of minimizing total user cost and minimizing user electricity cost, is constructed. The CPLEX 12.10.0 solver is employed for optimization. To determine the optimal battery life, binary search can be used to repeatedly test midpoints within a known range. This approach allows for quick identification of the best lifespan. The ultimate goal of this method is to reduce the number of tests and increase efficiency (Ding et al., 2023). The solution process, as illustrated in Figure 3, is detailed as follows:

Step 1: Users intending to participate in the shared energy storage project are identified. Historical load data for each user is analyzed, and the load profiles for typical days within a year are extracted.

Step 2: A dual-layer model for energy storage optimization is established to optimize the capacity and maximum charge-discharge power of the energy storage system. The total annual operational cost for all users throughout the lifespan of the energy storage system is calculated.

Step 3: Using the energy storage data configured in Step 2, the equivalent cycle life of the battery in the energy storage station is calculated by applying the Rain-flow counting method. The calculated results are compared with the expected battery life under the configuration model in Step 2, and if the condition for iterative convergence is met and the configuration is accepted by all users, the shared energy storage is configured accordingly. Otherwise, proceed to Step 4.

Step 4: Due to the irrationality of the configuration model, the configured result is not feasible. Employing the bisection method, the expected battery life is adjusted towards the result obtained from the Rain-flow counting method in Step 3 to obtain a new expected lifespan. Based on this new expected lifespan, Step 2 is repeated to obtain a new optimal configuration result. The comparative process is repeated until the final configuration result is obtained.

The specific solution flow chart is shown in Figure 3.

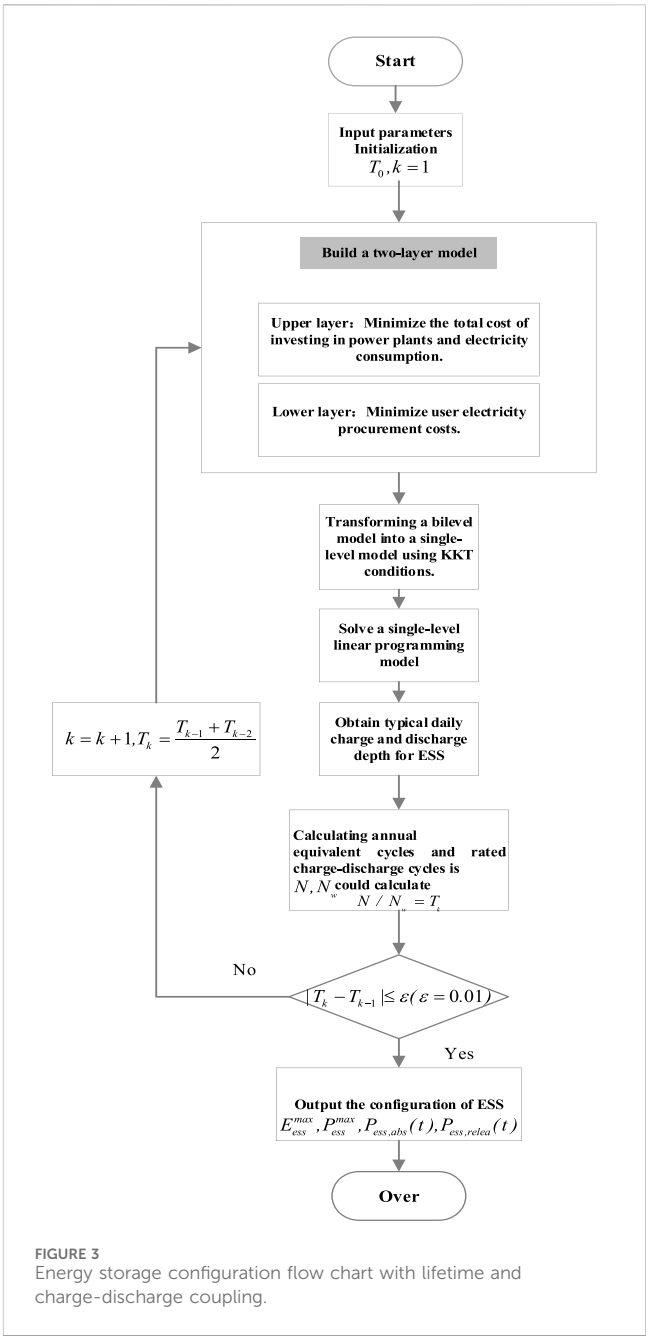

FIGURE 3
Energy storage configuration flow chart with lifetime and charge-discharge coupling.

TABLE 1 Cycle life of lithium iron phosphate battery at different DOD.

DOD	Number of battery cycles
100%	3669.064
80%	4406.474
60%	5080.935
40%	5953.237

TABLE 2 TOU prices for industrial and commercial users.

Period	Time	Electricity price (¥/kWh)
Peak hour	12:00–13:00	1.4028
Peak period	9:00–11:00	0.9644
	14:00–16:00	
Valley period	1:00–8:00	0.4145
	17:00–19:00	
	19:00–24:00	

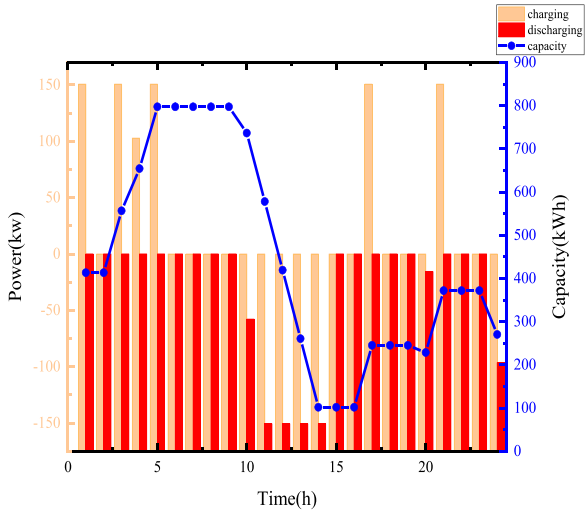

FIGURE 4
Charge and discharge of the energy storage station with a battery life of 5 years.

5 Case studies

5.1 Parameters Setting

The case study is oriented towards a multi-user energy storage project consisting of three users. The industrial time-of-use electricity prices, as shown in Table 1, are based on the price list for commercial users represented by State Grid Zhejiang Electric Power Company. The demand charge is 48 ¥/kWh, collected on a monthly basis. The number of battery cycles at different DODs is referenced in Table 1. The energy storage battery selected is a lithium iron phosphate battery, and the number of battery cycles at different DODs is referenced in Table 1 (Gao et al., 2013). Time-of-Use (Tou) Prices for industrial and commercial users is referenced in Table 2. The unit cost for user investment in energy storage station construction and unit capacity cost are referenced from the literature (Liu et al., 2021), with values of 1,000 ¥/kW and 1,200 ¥/kWh, respectively. Considering the time value of money, the annual interest rate is 4%. Users are responsible for the operation and maintenance costs of their self-built power stations, calculated as follows: each time there is an electricity flow between a user and the station, the user is required to pay an operational fee of 0.05 ¥/kWh. The expected lifespan of the station is initialized to 5 years. The lower limit for the state of charge of the energy storage is 0.1, and the upper limit is 0.9. The initial state of charge and the state of charge at the final time period satisfy the continuity constraint of the energy storage device state. The number of typical days is 1.

5.2 Configuration result analysis

5.2.1 Initial configuration result

When the expected service life of the battery is initialized to 5 years, the model yields the following results: The optimal capacity of the energy storage station is 1018.2328 kWh, with a maximum charge and discharge power of 150.71 kW. The total cost for the user group is ¥66209617.2443, and the total cost for electricity purchase by the user group is ¥65916347.7008.

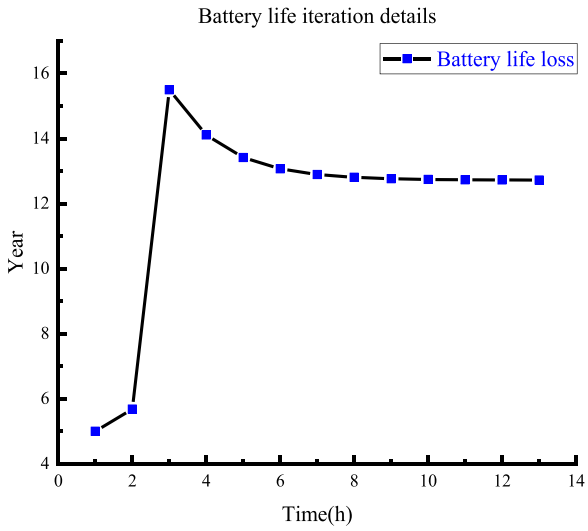

FIGURE 5
Battery life iteration details.

The charge and discharge status of the energy storage station at this time is shown in Figure 4. Energy storage tends to charge during off-peak hours, such as from midnight to 8 a.m., and then discharge during peak demand periods to reduce user load and engage in peak-valley arbitrage. However, it has also been observed that users are not very willing to participate in peak shaving with energy storage. This is due to the relatively short lifespan of energy storage systems and the significant daily investment required.

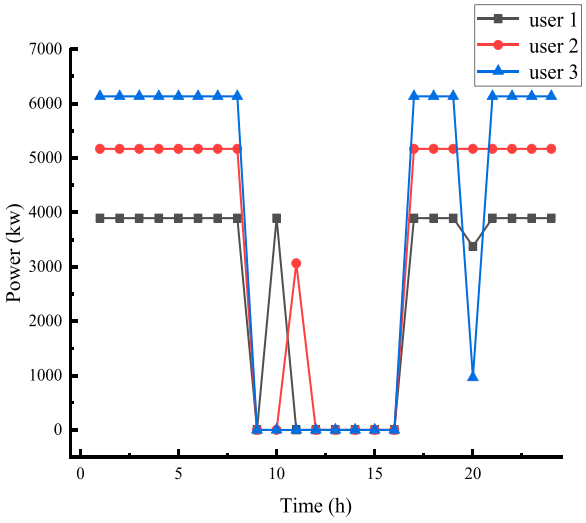

FIGURE 6
Power purchase of users after battery life renewal.

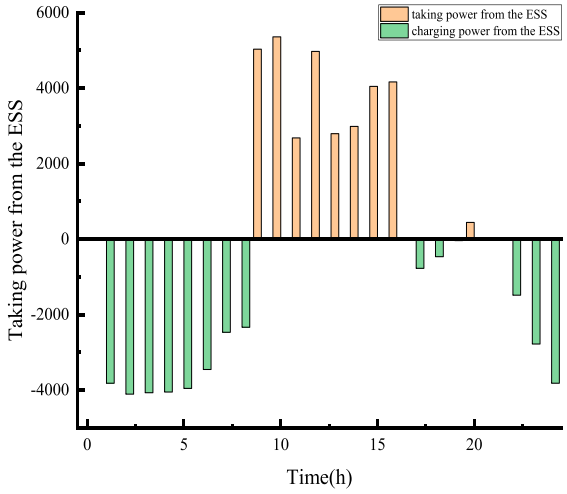

FIGURE 8
User 2's power access after battery life renewal.

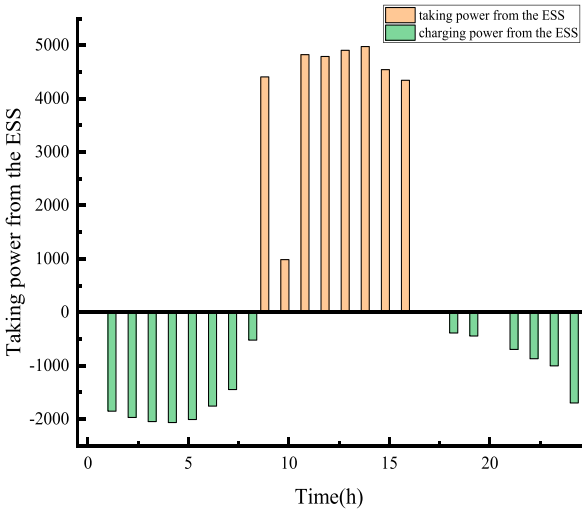

FIGURE 7
User 1's power access after battery life renewal.

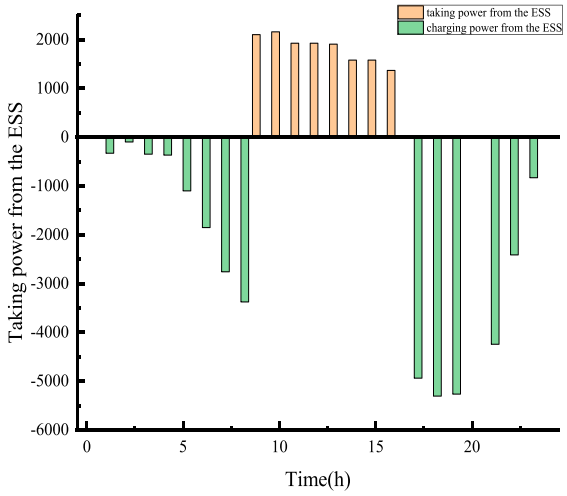

FIGURE 9
User 3's power access after battery life renewal.

5.2.2 Life iteration process

Based on the preset battery life, the battery charge and discharge status are shown in Figure 4, and it is input into the battery life degradation model for calculation. The battery cycling within a typical day consists of two full cycles and one-half cycle, with the battery's charge and discharge depth being:

$$D_{OD,1} = 0.0162$$
$$D_{OD,2} = 0.0997$$
$$D_{OD,3} = 0.6830$$

The calculated equivalent cycle life of the battery is 6.362 years. Using the bisection method, the preset battery life is updated to obtain the new battery life:

$$T_1 = \frac{T_0 + T_{base}}{2} = 5.681$$

The optimization model configuration process for the energy storage system is repeated. The total number of iterations is 13, and the iteration data for the battery life is shown in Figure 5.

5.2.3 Analysis and comparison of optimal configuration results

When the battery service life is 12.72 years, the operational results of the multi-user shared energy storage dual-layer model are as follows: The optimal capacity for the energy storage station for this year is 106507.5029 kWh, and the optimal maximum charge and discharge power for the energy storage station is 11694.06 kW. The total cost for the user group's annual grid

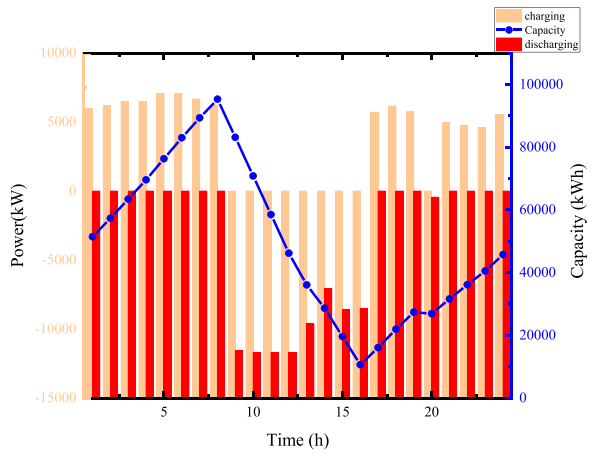

FIGURE 10
Charging and discharging of the power station after battery life renewal.

electricity purchases is ¥47134790.454, and the total annual electricity cost for the user group is ¥60772021.6139. Figure 6 depict the grid electricity purchases by the typical daily users after updating the battery service life.

Figures 7–9 illustrate the charge and discharge status of electricity between the user group and ESS.

Compared with the initial configuration results, it is evident that there has been no change in the overall electricity purchasing strategy within the user group. In contrast, the capacity and power of the energy storage system have increased significantly. This is due to the extended lifespan, which has been raised from 5 years to 12.72 years after iteration, resulting in a substantial reduction in the daily investment for the energy storage system. Consequently, users are more inclined to deploy larger capacity and power storage devices. Furthermore, thanks to the increased capacity and power, the current monthly demand charges are lower compared to the initial configuration results. The most notable changes are as follows:

In the optimal configuration results, User 1 purchases less electricity during the 9:00–16:00 period, with a purchase of 3375.4 kW at 11:00, compared to 3896.1 kW at other times. In the initial configuration, User 2 does not purchase electricity at 10:00, buying 5362 kW from 11:00 to 12:00, while in the optimal configuration, User 2 purchases 810.1 kW at 10:00 and nothing at 11:00. Additionally, User 2 does not purchase electricity from 11:00 to 16:00, but increases purchases during off-peak hours to 5169.14kW, except for a purchase of 443.62 kW at 20:00, storing the excess electricity in the station from 1:00 to 8:00 and 17:00 to 24:00. User 3 purchases less electricity during the 9:00–16:00 period and at 20:00, with all other periods at 6133.53 kW.

Under a reasonable electricity management strategy among users, User 2's cost reduction measure of not purchasing electricity during peak and high-demand periods has been more thoroughly implemented. This strategy not only ensures that User 2 does not incur high electricity purchase costs during peak demand periods but also optimizes the overall electricity usage pattern, further reducing the collective electricity costs for the entire user community. The charge and discharge situation of the station after updating the battery life is shown in Figure 10 Overall, compared to the initial configuration, the energy storage station shows a stronger desire to participate in load regulation. It has greater capacity and power, significantly enhancing its ability to shave peaks and fill valleys, as well as its capability for demand reduction, resulting in more noticeable benefits.

Compared to the configuration results with the preset 5-year battery life, the updated battery exhibits a reduced number of charge and discharge cycles, with the cycling period consisting of two cycles.

$$D_{OD,1} = 0.0044$$
$$D_{OD,2} = 0.7946$$

Overall, the energy storage station's charging activity from 1:00 to 8:00 and 17:00 to 24:00 prepares for load reduction from 9:00 to 16:00.

Table 3 provides a comparison between the initial configuration results and the optimal configuration results.

From the data in the table, it is evident that both before and after updating the battery life in the configuration of the shared energy storage station, the electricity costs for users have decreased compared to when the system was not configured.

Considering the energy losses in the station's batteries, the required station capacity should increase. With the station's service

TABLE 3 Comparison of configuration results.

Optimization index	Initial configuration result	Optimal configuration result	No ESS configured
Rated power/kW	150.71	11694.06	0
Optimal capacity/kWh	1,018.2328	106507.5029	0
User purchase cost/¥	6.59 × 107	4.71 × 107	6.63 × 107
Total user cost/¥	6.62 × 107	6.08 × 107	6.63 × 107

TABLE 4 Cost allocation based on the Shapley value method.

Energy storage Configuration type	Cost for User 1. (¥ × 10^5)	Cost for User 2. (¥ × 10^5)	Cost for User 3. (¥ × 10^5)
Unconfigured storage	2,419	2,381	1,831
Independent Storage	2,192	2,179	1,738
Shared Storage	2,190	2,168	1,719

life updated to 12.72 years, the annual construction cost per year decreases. The increase in the station's charge and discharge power signifies an improved utilization rate, leading to a further reduction in users' electricity costs compared to the initial configuration results, resulting in a significant overall cost reduction for the users.

Based on Table 3, the total costs of cooperative energy storage configurations for the three industrial user types in different combinations all satisfy the Super additivity condition. This indicates that by forming a cooperative alliance, the three industrial user types achieve cost reductions, resulting in cooperative surplus and consequently, excess profits.

According to Table 4, it is evident that the total costs for the three industrial user types through cooperative energy storage configuration are lower than the total costs without energy storage and those of individual energy storage configurations. Compared to not having energy storage, the total cost for Industrial User 1 decreases by approximately 2.39 million yuan, for Flat User 2 by approximately 2.13 million yuan, and for Industrial User 3 by approximately 1.12 million yuan, indicating a significant reduction in total costs for each user. It is apparent that this distribution result satisfies both collective rationality and individual rationality.

Based on the above, it can be concluded that the possibility and stability of forming a cooperative alliance among the three industrial user types are ensured.

6 Conclusion

The configuration of shared energy storage needs to be adjusted according to the actual situation of the construction project in the region. Therefore, there is a necessity to discuss the issue of energy storage station configuration considering the capacity loss of the energy storage system. This paper optimizes the configuration of shared energy storage for multiple users, taking into account the factor of battery capacity loss during the configuration process. The calculation of battery degradation can iteratively update the device's life cycle for energy storage projects, thereby obtaining the most economical, environmentally friendly, reasonable, and practical optimal energy storage station configuration.

1) The Rain-flow counting method is utilized to decompose the battery capacity change curve, and the decomposed important parameters are used for life cycle calculation. A battery life degradation calculation model is established using specified parameters of lithium iron phosphate batteries.
2) The objective is to minimize the total cost of energy storage project construction and electricity usage for all users within a year, considering both the optimal electricity cost for all users and the overall optimal cost of energy storage project construction and electricity usage. A bi-level model is established to achieve the lowest total cost under the condition of optimal electricity cost. In the solution process, the Big-M method and KKT conditions are used to handle the model, ultimately transforming the nonlinear programming problem into a mixed-integer linear programming problem.
3) The results of the bi-level model configuration are updated with the battery life degradation model. Through multiple iterations of optimizing the shared energy storage configuration, the charging and discharging of the shared energy storage device becomes more reasonable. The extension of the shared energy storage device's lifespan not only reduces the waste of power resources and construction materials but also creates more collective economic benefits for multiple users.
4) For the alliance cost of multiple users, a Shapley value allocation model is established for fair distribution. By analyzing and comparing the costs of different users without energy storage configuration and with independent energy storage configuration, the superiority of multiple-user cooperative configuration of shared energy storage is verified, providing assurance for the maintenance and long-term stability of the cooperative alliance.

Data availability statement

The original contributions presented in the study are included in the article/supplementary material, further inquiries can be directed to the corresponding author.

Author contributions

WW: Conceptualization, Methodology, Writing–review and editing, Writing–original draft. HW: Writing–review and editing. SS: Writing–review and editing. GC: Writing–original draft. SW: Writing–original draft. YJ: Writing–original draft.

Funding

The author(s) declare that financial support was received for the research, authorship, and/or publication of this article. Financially supported by the Science and Technology Project of Provincial Management Industry Unit of State Grid Jiangsu Electric Power Co., Ltd. (Project No. JC2024003). The funder was not involved in the study design, collection, analysis, interpretation of data, the writing of this article, or the decision to submit it for publication.

Conflict of interest

Authors WW, HW, SS, GC, SW, and YJ were employed by Nanjing Suyi Industrial Co., Ltd.

Generative AI statement

The author(s) declare that no Generative AI was used in the creation of this manuscript.

Publisher's note

References

Aminlou, A., Mohammadi-Ivatloo, B., Zare, K., Razzaghi, R., and Anvari-Moghaddam, A. (2022). Peer-to-peer decentralized energy trading in industrial town considering central shared energy storage using alternating direction method of multipliers algorithm. *IET Renew. Power Gener.* 16, 2579–2589. doi:10.1049/rpg2.12490

Azhgaliyeva, D. (2019). Energy storage and renewable energy deployment: empirical evidence from OECD countries. *Innov. Solutions Energy Transitions* 158, 3647–3651. doi:10.1016/j.egypro.2019.01.897

Cremers, S., Robu, V., Zhang, P., Andoni, M., Norbu, S., and Flynn, D. (2023). Efficient methods for approximating the Shapley value for asset sharing in energy communities. *Appl. Energy* 331, 120328. doi:10.1016/j.apenergy.2022.120328

Deguenon, L., Yamegueu, D., Kadri, S. M., and Gomna, A. (2023). Overcoming the challenges of integrating variable renewable energy to the grid: a comprehensive review of electrochemical battery storage systems. *J. Power Sources* 580, 233343. doi:10.1016/j.jpowsour.2023.233343

Ding, Y., Xu, Q., Hao, L., and Xia, Y. (2023). A Stackelberg Game-based robust optimization for user-side energy storage configuration and power pricing. *Energy* 283, 128429. doi:10.1016/j.energy.2023.128429

Ding, Y., Xu, Q., and Yang, B. (2020). Optimal configuration of hybrid energy storage in integrated energy system. *Energy Rep.* 6, 739–744. doi:10.1016/j.egyr.2020.11.137

Gao, F., Yang, K., Hui, D., and Li, D. (2013). Energy analysis of cycle life for lithium iron phosphate batteries used in energy storage. *China Electr. Power Eng. J.* 33, 41–45. doi:10.13334/j.0258-8013.pcsee.2013.05.016

Jianwei, G., Fangjie, G., Yu, Y., Haoyu, W., Yi, Z., and Pengcheng, L. (2022). Configuration optimization and benefit allocation model of multi-park integrated energy systems considering electric vehicle charging station to assist services of shared energy storage power station. *J. Clean. Prod.* 336, 130381. doi:10.1016/j.jclepro.2022.130381

Krishnamurthy, D., Uckun, C., Zhou, Z., Thimmapuram, P., and Botterud, A. (2018). Energy storage arbitrage under day-ahead and real-time price uncertainty. *IEEE Trans. Power Syst.* 33, 84–93. doi:10.1109/TPWRS.2017.2685347

Kwon, S., Ntaimo, L., and Gautam, N. (2017). Optimal day-ahead power procurement with renewable energy and demand response. *IEEE Trans. Power Syst.* 32, 3924–3933. doi:10.1109/TPWRS.2016.2643624

Lai, S. Y., Qiu, J., and Tao, Y. C. (2022). Individualized pricing of energy storage sharing based on discount sensitivity. *IEEE Trans. Industrial Inf.* 18, 4642–4653. doi:10.1109/TII.2021.3119953

Liu, Y., Dai, H., and Liu, Z. (2021). Configuration and investment benefit analysis of decentralized shared energy storage for multiple types of industrial users. *Electr. Power Autom. Equip.* 21, 256–264. doi:10.16081/j.epae.202110004

Mao, J., Xiaotong, Z., Chunyun, Y., Aihua, W., and Xudong, Z. (2022). Multivariable coordinated nonlinear gain droop control for PV-battery hybrid DC microgrid access system via a T-S fuzzy decision approach. *IEEE Access* 10, 89414–89427. doi:10.1109/ACCESS.2022.3201149

Pan, C. Y., Tao, S. Y., Fan, H. T., Shu, M. Y., Zhang, Y., and Sun, Y. J. (2021). Multi-objective optimization of a battery-supercapacitor hybrid energy storage system based on the concept of cyber-physical system. *Electronics* 10, 1801. doi:10.3390/electronics10151801

Pedrero, R., Pisciella, P., and Granado, P. (2024). Fair investment strategies in large energy communities: a scalable Shapley value approach. *Energy* 295, 131033. doi:10.1016/j.energy.2024.131033

Qian, J., Cai, J., Hao, L., and Meng, Z. (2024). Improved typical scenario-based distributionally robust co-dispatch of energy and reserve for renewable power systems considering the demand response of fused magnesium load. *Front. Energy Res.* 12. doi:10.3389/fenrg.2024.1401080

Qian, W., Chen, C., Gong, L., and Zhang, W. (2023). Research on nash game model for user side shared energy storage pricing. *Sci. Rep.* 13, 16099. doi:10.1038/s41598-023-43254-z

Song, X. L., Zhang, H. Q., Fan, L. R., Zhang, Z., and Peña-Mora, F. (2023). Planning shared energy storage systems for the spatio-temporal coordination of multi-site renewable energy sources on the power generation side. *Energy* 282, 128976. doi:10.1016/j.energy.2023.128976

Tahir, H., Park, D.-H., Park, S.-S., and Kim, R.-Y. (2022). Optimal ESS size calculation for ramp rate control of grid-connected microgrid based on the selection of accurate representative days. *Int. J. Electr. Power and Energy Syst.* 139, 108000. doi:10.1016/j.ijepes.2022.108000

Wang, C., Ge, P., Sun, L., and Wang, F. (2022). Research on user-side flexible load scheduling method based on greedy algorithm. *Energy Rep.* 8, 192–201. doi:10.1016/j.egyr.2022.10.352

Wang, C., Zhang, X., Xiong, H., and Guo, C. (2023). Distributed shared energy storage scheduling based on optimal operating interval in generation-side. *Sustain. Energy Grids and Netw.* 34, 101026. doi:10.1016/j.segan.2023.101026

Wang, K. Y., Liang, Y., Jia, R., Wang, X. Y., Du, H. D., and Ma, X. P. (2022). Configuration-dispatch dual-layer optimization of multi-microgrid-integrated energy systems considering energy storage and demand response. *Front. Energy Res.* 10. doi:10.3389/fenrg.2022.953602

Wang, Y., Chen, J., Zhao, Y., and Xu, B. (2024a). Incorporate robust optimization and demand defense for optimal planning of shared rental energy storage in multi-user industrial park. *Energy* 301, 131721. doi:10.1016/j.energy.2024.131721

Wang, Y., Huang, C., Wang, C., Li, K., Fang, X., and Yan, G. (2024b). Optimal configuration of shared energy storage in industrial park considering full-cycle economic benefits in electricity market environment. *Automation Electr. Power Syst.* 48, 129–138. doi:10.7500/AEPS20230717009

Wu, W., Zhu, J., Chen, Y., Luo, T., Shi, P., Guo, W., et al. (2023). Modified Shapley value-based profit allocation method for wind power accommodation and deep peak regulation of thermal power. *IEEE Trans. Industry Appl.* 59, 276–288. doi:10.1109/TIA.2022.3208866

Xie, Y., Chang, X., Yin, X., and Zheng, H. (2022a). Research on the transaction mode and mechanism of grid-side shared energy storage market based on blockchain. *Energy Rep.* 8, 224–229. doi:10.1016/j.egyr.2021.11.044

Xie, Y., Yao, Y., Wang, Y., Cha, W., Zhou, S., Wu, Y., et al. (2022c). A cooperative game-based sizing and configuration of community-shared energy storage. *Energies* 15, 8626. doi:10.3390/en15228626

Xie, Y. L., Li, L., and Yang, K. (2022b). Research on shared energy storage configuration considering energy storage battery capacity attenuation. *Guangdong Electr. Power* 35, 25–32. doi:10.3969/j.issn.1007-290X.2022.005.003

Xu, X., Hu, W., Liu, W., Wang, D., Huang, Q., and Chen, Z. (2021). Study on the economic benefits of retired electric vehicle batteries participating in the electricity markets. *J. Clean. Prod.* 286, 125414. doi:10.1016/j.jclepro.2020.125414

Xu, X., Li, G., Yang, H., Liu, D., Wang, J., and Zhang, Z. (2023). Pricing method of shared energy storage bias insurance service based on large number theorem. *J. Energy Storage* 69, 107726. doi:10.1016/j.est.2023.107726

Yan, D., and Chen, Y. (2022). Review on business mode and pricing mechanism for shared energy storage. *Autom. Electr. Power Syst.* 46, 178–191. doi:10.7500/AEPS20220219003

Yang, M., Zhang, Y. H., Liu, J. H., Yin, S., Chen, X., She, L. H., et al. (2023). Distributed shared energy storage double-layer optimal configuration for source-grid Co-optimization. *PROCESSES* 11, 2194. doi:10.3390/pr11072194

Yang, Y., Hu, G. Q., and Spanos, C. J. (2021). Optimal sharing and fair cost allocation of community energy storage. *IEEE Trans. Smart Grid* 12, 4185–4194. doi:10.1109/TSG.2021.3083882

Yang, Z., Wang, S., Zhu, R., Cui, J., Su, J., and Chen, L. (2024). Research on regulation method of energy storage system based on multi-stage robust optimization. *Energy* 121, 807–820. doi:10.32604/ee.2023.028167

Yasmin, R., Amin, B., Shah, R., and Barton, A. (2024). A survey of commercial and industrial demand response flexibility with energy storage systems and renewable energy. *Sustain.* 16, 731. doi:10.3390/su16020731

Zeng, L., Gong, Y., Xiao, H., Chen, T., Gao, W., Liang, J., et al. (2024). Research on interval optimization of power system considering shared energy storage and demand response. *J. Energy Storage* 86, 111273. doi:10.1016/j.est.2024.111273

Zhang, W. Y., Zheng, B. S., Wei, W., Chen, L. J., and Mei, S. W. (2022). Peer-to-peer transactive mechanism for residential shared energy storage. *Energy* 246, 123204. doi:10.1016/j.energy.2022.123204

Zhang, Y., Li, L., Liu, Z., and Wu, Y. (2024). Research on operation optimization of energy storage power station and integrated energy microgrid alliance based on Stackelberg game. *Energy* 121, 1209–1221. doi:10.32604/ee.2024.046141

Zhu, H., and Ouahada, K. (2021). A distributed real-time control algorithm for energy storage sharing. *Energy Build.* 230, 110478. doi:10.1016/j.enbuild.2020.110478

Zhu, H., Ouahada, K., and Abu-Mahfouz, A. M. (2022). Peer-to-peer energy trading in smart energy communities: a lyapunov-based energy control and trading system. *IEEE access* 10, 42916–42932. doi:10.1109/access.2022.3167828

frontiers | Frontiers in Energy Research

TYPE Original Research
PUBLISHED 30 January 2025
DOI 10.3389/fenrg.2025.1536668

OPEN ACCESS

EDITED BY
Yue Xiang,
Sichuan University, China

REVIEWED BY
Xiaoyuan Chen,
Sichuan Normal University, China
Ruohuan Yang,
China Electric Power Research Institute (CEPRI), China

*CORRESPONDENCE
Xiaoming Liu,
xzliuxm2023@163.com

RECEIVED 29 November 2024
ACCEPTED 07 January 2025
PUBLISHED 30 January 2025

CITATION
Yixi C, Liu X, Li Y, Tan J, Liu Z, Danzeng B and Wang L (2025) Optimal configuration strategy of energy storage considering flexible response of high energy-consuming industrial and mining loads in independent microgrid. *Front. Energy Res.* 13:1536668. doi: 10.3389/fenrg.2025.1536668

Optimal configuration strategy of energy storage considering flexible response of high energy-consuming industrial and mining loads in independent microgrid

Cuomu Yixi[1], Xiaoming Liu[1]*, Yu Li[2], Jingming Tan[2], Zhihong Liu[1], Basang Danzeng[1] and Lei Wang[1]

[1]Economic and Technical Research Institute of State Grid Tibet Electric Power Co., Ltd., Lhasa, China, [2]State Grid Tibet Electric Power Co., Ltd., Lhasa, China

The coordinated optimization of industrial and mining loads with energy storage (ES) is a critical approach to achieving power and energy balance in microgrids while promoting the new energy accommodation. Addressing the issue of insufficient flexibility in demand response from high-energy-consuming lithium mining loads, which may lead to conservative ES capacity allocation and underutilization of complementary flexibility potential, this paper proposes an ES optimization strategy for microgrids considering the participation of high-energy-consuming lithium mining loads in demand response. Firstly, considering the production process of extracting lithium from salt lakes brine and the electricity consumption characteristics of major energy-consuming equipment, a mathematical model is developed to quantify the flexibility adjustment potential of lithium mining loads under production behavior constraints. Based on this, incorporating the regulation boundaries of photovoltaic (PV) units, gas turbine units, concentrated solar power (CSP), ES system, and flexible lithium mining loads, an ES capacity optimization model is constructed to minimize the comprehensive system capital and operation costs in independent microgrid. The model is then linearized into a mixed-integer programming problem. Finally, through case study simulations of an actual microgrid in Southwest China, the feasibility and effectiveness of the proposed ES optimization strategy are verified. The results demonstrate that the proposed strategy can economically and effectively meet the power and energy balance of the independent microgrid and the electricity demands of high-energy-consuming loads, while promoting the improvement of new energy accommodation capacity.

KEYWORDS

industrial and mining loads, demand response, energy storage configuration, independent microgrid, mixed integer linear programming

1 Introduction

With the rapid development of new energy vehicles and lithium-ion ES, the demand for battery-grade lithium carbonate preparation continues to grow. However, the salt lakes lithium mines as a crucial raw material source are often located in remote areas, making it challenging to extend power transmission networks to meet the high energy demands of lithium mining operations. Therefore, it is necessary to develop localized microgrids for on-site power supply (Zhang et al., 2024)- (Wu et al., 2024). Under the dual-carbon goals and the new power system construction, the penetration of new energy in microgrids is increasing. However, the inherent seasonality, volatility, and uncertainty of new energy reduce the dispatchable capacity of traditional regulatory resources, making it difficult to ensure the balance of power and energy in microgrids. This highlights the urgent need to expand grid regulation resources and transition from the conventional "source-grid-load" model to the coordinated "source-grid-load-storage" interactive model (Liu et al., 2020). On one hand, high-energy-consuming lithium mining loads are characterized by high flexibility, fast dispatch response, and significant scalability potential. Leveraging their regulatory flexibility for demand response can alleviate the power supply pressure of microgrids (Nie et al., 2023). On the other hand, as an excellent regulatory resource for power and energy balance, the optimal configuration and coordinated operation of ES system are closely related to the operational performance and economic benefits of microgrids. Therefore, studying collaborative configuration strategies for ES under flexible lithium mining load responses is of great significance for maintaining power and energy balance in microgrids and meeting load power demands.

In recent years, some scholars have conducted research on the participation of high-energy-consuming industrial loads in optimizing grid operations, achieving notable results. For instance, Reference (Philipo et al., 2022) proposes a demand-side management strategy based on artificial neural networks that accounts for load-shifting behavior, effectively reducing load demand in standalone PV battery microgrids in East Africa. A novel flexible low-carbon optimal dispatch model is proposed for the distribution network, which coordinates the participation of heat storage industrial loads in demand response (Wang W. D. et al., 2024). In Reference (Xu et al., 2020), a method is proposed to involve the steam systems of industrial loads, such as paper mills and steel plants, as flexible loads in demand response. This approach approximated the flexibility boundaries under the influence of steam uncertainty. Furthermore, Reference (Cui and Zhou, 2018) summarizes the main methods for industrial load demand response, pointing out that modeling industrial processes using a production-buffer approach could yield more reasonable optimization results. Ramesh and Sofana utilize a resource-task network to represent refinery processes and implemented stochastic dynamic programming to shift the electricity usage of refineries, reducing energy costs (Reka and Ramesh, 2016). Additionally, Reference (Liao et al., 2024) analyzes production characteristics and regulation constraints to construct a demand response capability boundary, enhancing the flexibility of large-capacity electrolytic aluminum loads to interact bidirectionally with the grid. Reference (Golmohamadi et al., 2019) aggregates the flexibility of cement manufacturing, metal smelting, and residential loads using load aggregators, leveraging complementary characteristics among different loads to participate in demand response. These studies effectively improved the economic benefits of industrial enterprises and enhanced grid stability by tapping into the flexibility of industrial production processes. However, under the context of new energy standalone microgrids, the quantification and integration of lithium mining load flexibility in demand response remain insufficiently addressed, highlighting a gap in the current research landscape.

Relying solely on industrial and mining loads constrained by production processes is insufficient to effectively maintain the power and energy balance of the grid. Coordinated optimization of flexible loads and ES is a crucial solution. In Reference (Huang et al., 2021), A two-stage optimal scheduling method based on model predictive control is proposed for the energy management of the actual microgrid system containing ES and flexible loads, with improving the optimization control accuracy. Reference (Zeng et al., 2024) develops a refined demand response mechanism and shared ES optimization model for various building loads to achieve source-grid-load-storage synergistic interaction. In Reference (Wang D. et al., 2024), a joint optimization mechanism integrating electric and thermal energy storage with demand response is proposed, aiming to enhance the economic benefits of market participants while improving supply-demand coordination through interregional energy complementarity. Moreover, Reference (Karimianfard et al., 2022) proposes a large-scale ES coordination capacity and optimization strategy that considers load-side response behavior, improving the operational flexibility of smart grids and increasing economic returns for loads. Reference (Sun et al., 2022) treats flexible demand-side resources as virtual ES while employing conventional ES to mitigate load uncertainties. Additionally, Reference (Shen et al., 2022) proposes a multi-objective optimization model for multi-ES capacity planning in industrial park microgrids based on electricity-heat-gas coupled demand response, aiming to minimize economic costs and carbon emissions while enhancing energy supply reliability and economic performance. These studies construct models for load demand response and ES optimization from various perspectives, effectively maintaining grid power balance and ensuring reliable and economic system operation. However, research focusing on the coordinated optimization of ES and demand response for industrial and mining loads remains relatively scarce, leaving room for further exploration in this area.

This study addresses the power supply demands and flexibility regulation of high-energy-consuming lithium mining loads, focusing on independent industrial microgrid scenarios in remote areas. It proposes an optimized ES configuration and operational strategy for independent microgrids, incorporating the potential of mining load regulation to enhance system performance. The main contributions of this paper are summarized as follows:

- A flexibility regulation analysis and quantification model for lithium mining loads is developed, considering the specific production characteristics of lithium extraction. This model effectively enhances the bidirectional flexibility interaction capabilities with the microgrid.

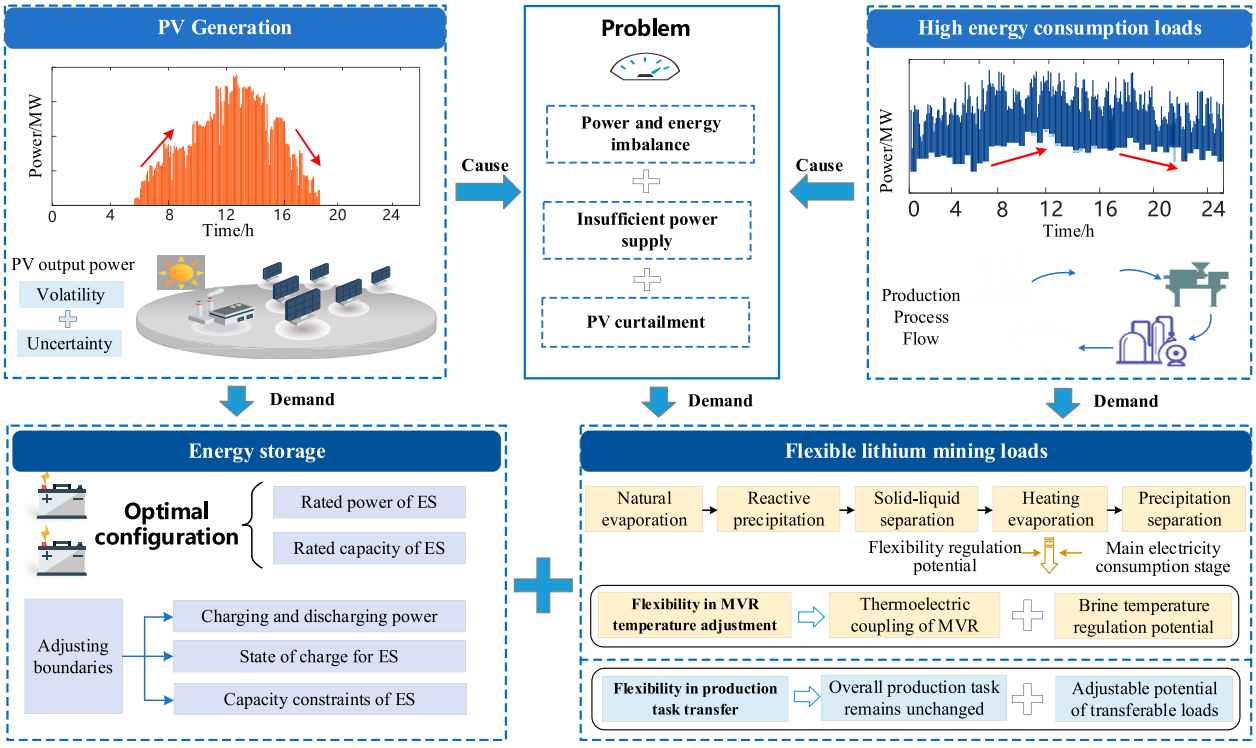

FIGURE 1
Coordinated operation framework of lithium mining loads and ES in microgrid.

- By considering the operational boundaries of PV units, CSP units, ES system, and lithium mining load regulation, an optimized ES configuration model is constructed to minimize the comprehensive construction and operational costs of the independent microgrid. Economically, this approach reduces the operating costs of the microgrid system, while technically, it enhances the renewable energy utilization rate and ensures reliable power supply for lithium mining loads.

The rest of the paper is organized as follows. In Section 2, the regulation potential of industrial and mining load is analyzed and modeled. In Section 3, the coordinated operation strategy of industrial and mining loads with ES is proposed, and the main objectives and constraints of the de-aggregation strategy are provided. Then, Section 4 presents results and discussion based on case studies. The conclusion and future work are drawn in Section 5.

2 Modeling of industrial and mining load regulation potential

Due to the volatility and uncertainty of its output, PV power generation is difficult to match the electricity demand of high-energy-consuming loads, which further leads to the imbalance of power and electricity in the microgrid and the lack of new energy accommodation capacity. By tapping the potential of flexible adjustment on the load side and cooperating with ES resources to participate in the optimal operation of the microgrid, it is helpful to alleviate the above problems, as shown in Figure 1. However, the load regulation potential of lithium ore is affected by its process production characteristics. How to consider this key factor and quantify modeling is an important difficulty and key point in the mining of industrial and mining load flexibility.

The technologies for extracting lithium resources from salt lakes brine have reached a relatively mature stage both domestically and internationally. The primary methods include precipitation, solvent extraction, adsorption, calcination, and electrodialysis. Among these, the precipitation method has become the mainstream technology due to its mature process and wide application (Kong et al., 2024). The typical process flow involves natural evaporation and crystallization of the salt lakes, reaction precipitation, solid-liquid separation, heating and evaporative concentration, and precipitation separation. The heating and evaporative concentration stage primarily relies on MVR technology, which is also the most energy-intensive phase of the entire process (Xiao, 2014).

The flexibility potential of lithium mining loads is mainly reflected in two aspects: 1) Adjustability of the MVR system temperature (Zhou et al., 2022): The MVR evaporative concentration process operates within a temperature-adjustable range, where temperature regulation directly affects electricity consumption. 2) Flexibility in scheduling production tasks over time: The production process allows for adjustments in task timing to accommodate demand response requirements. Specifically, the MVR system provides an adjustable temperature range during the

evaporative concentration stage. Temperature adjustments result in corresponding changes in power consumption. To evaluate the load regulation potential, a mathematical model based on thermal inertia can be developed. This model considers key factors such as the specific heat capacity of brine, the temperature range required to maintain process stability, heat transfer between the compression process and the environment, and the efficiency of heating loads, which contributes to offer theoretical support for assessing the flexibility potential of thermostatically-controlled lithium mining loads (TLMLs).

2.1 MVR temperature adjustable flexibility

2.1.1 Brine heating model

The heat required for heating and evaporating salt lakes brine is related to its mass, specific heat capacity, and temperature changes.

$$Q = mC_b\Delta T \tag{1}$$

where Q represents the heat variation of brine heating; m is quality of brine; C_b represents the specific heat capacity of the brine; ΔT represents the temperature change of the brine.

2.1.2 Heat loss model

Due to the interaction between MVR and the external environment, a certain amount of heat loss is caused.

$$Q_{loss}(t) = hA[T_{bri}(t) - T_{env}(t)] \tag{2}$$

where $Q_{loss}(t)$ represents heat loss due to environmental interaction at time t; h represents the heat transfer coefficient of environment and MVR; A represents the surface area of the MVR in contact with the external environment; $T_{bri}(t)$ is brine temperature; $T_{env}(t)$ is ambient temperature.

2.1.3 Regulation potential for lithium extraction from salt lakes

The process of isobaric evaporation to isobaric condensation of salt lakes brine meets the temperature, power and capacity adjustable range:

$$T_{\min} \le T_{bri}(t) \le T_{\max} \tag{3}$$

$$P_{Li}^{\min}(t) \le P_{Li}(t) \le P_{Li}^{\max}(t) \tag{4}$$

$$Q_{\min} \le Q_{i,0} + \left[\int_0^T P_{Li}(t)dt - Q_{loss}(t)\right] \le Q_{\max} \tag{5}$$

where $T_{\max}$ represents the upper limit of brine temperature; $T_{\min}$ represents the lower limit of brine temperature; $P_{Li}(t)$ is the operating power of TLMLs; $P_{Li}^{\max}(t)$ and $P_{Li}^{\min}(t)$ are the upper and lower limits of adjusted load power at time t, respectively; $Q_{\min}$ and $Q_{\max}$ are the upper and lower limits of thermal storage capacity, respectively.

2.1.4 Thermoelectric coupling characteristics

Considering environmental heat loss, there is a thermoelectric coupling characteristic between power consumption changes and MVR temperature variations.

$$mC_b[T_{bri}(t+1) - T_{bri}(t)] = \eta P_{Li}(t) - Q_{loss}(t) \tag{6}$$

where η is coefficient of thermal efficiency.

2.1.5 MVR continuous regulation limits

The continuous adjustment of MVR will cause frequent fluctuations in evaporator temperature. To maintain production stability to the greatest extent possible, the continuous adjustment limit of lithium mining load power consumption is as follows:

$$\begin{cases} \mu_{lu}^{dw}(t)v_{Li}^{-} \le P_{Li}(t) - P_{Li}(t-1) \le \mu_{lu}^{up}(t)v_{Li}^{+} \\ \mu_{lu}^{dw}(t) + \mu_{lu}^{up}(t) = 1 \\ \left[\mu_{lu}^{dw}(t) + \mu_{lu}^{up}(t)\right] + \left[\mu_{lu}^{dw}(t-1) + \mu_{lu}^{up}(t-1)\right] \le 1 \end{cases} \tag{7}$$

where v- Li and $v + Li$ are the lower and upper limits of the lithium mining load regulation rate; $\mu dw\ lu$ and $\mu up\ lu$are 0–1 state variables that characterize the downward and upward adjustment of the adjustment power.

2.1.6 Economic compensation for industrial and mining load regulation

The benefits of lithium mine load mainly come from two indicators: economic compensation and heat demand. The impact degree of heat demand is transformed into economic index, and the two are linearly summed:

$$C_{Li} = c_{Li}\left|P_{Li}^{fr} - P_{Li}(t)\right| + c_{MVR}\left(\frac{T_{bri}(t) - T_{\min}}{T_{\max} - T_{\min}}\right) \tag{8}$$

where C_{Li} is the economic compensation for the temperature control adjustment of TLMLs; c_{Li} is the economic compensation cost per unit power for temperature regulation of TLMLs; P_{Li}^{fr} is the planned power consumption curve of TLMLs; c_{MVR} is the influence coefficient of temperature changes on the production efficiency of lithium mining loads.

2.2 Transferable flexibility of sequential production

The time-series transfer characteristics of production tasks can be equivalent to the modeling of transferable lithium mining loads. The specific mathematical modeling is as follows:

2.2.1 Load transferability feature

Ensuring the overall production task remains unchanged throughout the entire scheduling cycle, with only timing adjustments.

$$\sum_{t=1}^{T}\left[P_{tr}^{fr}(t) - P_{tr}(t)\right] = 0 \tag{9}$$

where $P_{tr}^{fr}(t)$ and $P_{tr}(t)$ are the power of transferable lithium mining loads before and after scheduling at time t, respectively; T is the scheduling period.

2.2.2 Adjustable potential of transferable loads

$$P_{tr\_\min}(t) \le P_{tr}(t) \le P_{tr\_\max}(t) \tag{10}$$

where $P_{tr\_\max}(t)$ and $P_{tr\_\min}(t)$ are the upper and lower limits of power after lithium mining load transfer, respectively.

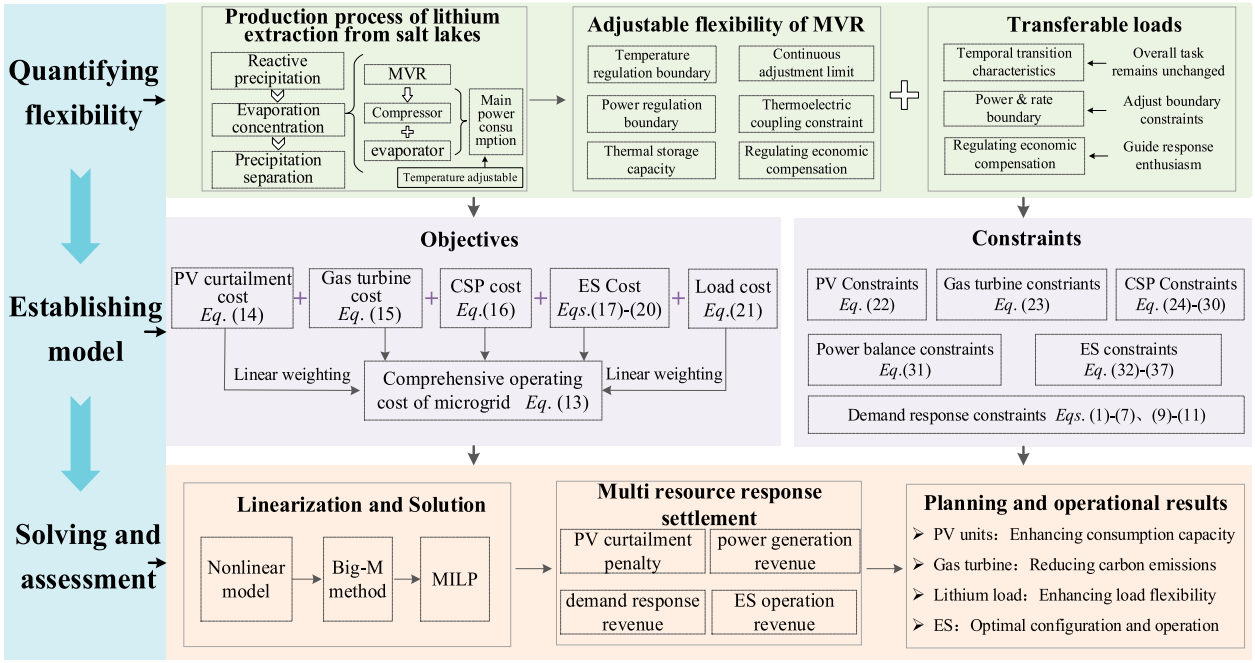

FIGURE 2
Block diagram of optimization configuration and operation model for ES in independent microgrid.

2.2.3 Transferable loads regulation rate

$$v_{tr}^{-} \le P_{tr}(t) - P_{tr}(t-1) \le v_{tr}^{+} \tag{11}$$

where *v-tr* and *v* + tr are lower and upper limit on regulation rate of lithium mining transferable loads.

2.2.4 Economic compensation of transferable loads

When load power is transferred, appropriate economic compensation should be provided to the lithium mining enterprises, which is as Equation 12.

$$C_{tr} = \sum_{t=1}^{T} c_{tr} \left| P_{tr}^{fr}(t) - P_{tr}(t) \right| \tag{12}$$

where C_{tr} is economic compensation of lithium mining transferable loads; c_{tr} is the unit power compensation cost of lithium mining transferable loads.

3 Optimization model for coordinated operation of industrial and mining loads with ES

To fully exploit the flexibility potential of lithium mining loads and the adjustment capabilities of ES system, this study develops a coordinated optimization model for flexible lithium mining loads and ES configurations, as illustrated in Figure 2. The optimization model is implemented in MATLAB, utilizing the YALMIP toolbox to interface with the Gurobi solver for solution computation. Based on the mathematical model of lithium mining load flexibility and its regulatory boundaries, the optimization considers constraints from the grid side, generation side, load side, and storage side. The objective function is to minimize the operational cost of the microgrid system. This problem is formulated as a mixed-integer linear programming (MILP) problem and solved to derive the optimal ES configuration scheme for independent microgrids. This approach integrates flexibility from the lithium mining load and ES to enhance the operational efficiency and economic performance of microgrids, contributing to improved renewable energy utilization and reliable power supply.

3.1 Objective function

Considering the new energy curtailment cost, gas turbine power generation and carbon reduction cost, CSP units cost, ES cost, industrial and mining load adjustment cost, the multi-objective is converted into single-objective comprehensive operation cost of microgrid by linear weighting method, which is as Equation 13.

$$obj = obj_{PV} + obj_{GT} + obj_{CSP} + obj_{ES} + obj_{load} \tag{13}$$

where *obj* is the comprehensive operating cost of microgrid; obj_{PV} is the penalty cost of PV curtailment; obj_{GT} is power generation and carbon emission penalty cost of gas turbine; obj_{CSP} is the operating cost of CSP units; obj_{ES} is the capital and operating cost of ES; obj_{load} is the adjustment cost of the flexible lithium mining loads.

3.1.1 PV curtailment penalty cost

The output power of PV units is used to supply load demand. To enhance the PV utilization rate, the PV curtailment is incorporated

into the optimization objective and transformed into an economic objective of curtailment cost, which is as Equation 14.

$$obj_{PV} = \sum_t c_{PV}\left[P_{PV}^{fr}(t) - P_{PV}(t)\right] \tag{14}$$

where c_{PV} is the penalty cost per unit of curtailed PV power; $P_{PV}^{fr}(t)$ is the predicted PV output power for the typical day; $P_{PV}(t)$ indicates the PV actual operating power.

3.1.2 Gas turbine operating cost

Gas turbine operating costs include power generation costs and carbon emission penalty costs, which is as Equation 15.

$$obj_{GT} = \sum_t (c_{GT} + c_{ca})P_{GT}(t) \tag{15}$$

where c_{GT} and c_{ca} are the power generation cost and carbon emission penalty cost per unit power of gas turbine.; $P_{GT}(t)$is the operating power of the gas turbine.

3.1.3 CSP units operating cost

$$obj_{CSP} = \sum_t c_{CSP}|P_{CSP}(t)| \tag{16}$$

where c_{CSP} is the operating cost per unit power of CSP; $P_{CSP}(t)$ is the output power of the CSP unit at time t.

3.1.4 ES costs

The ES cost includes both capital and operation cost. The capital cost refers to the total investment cost of ES system, amortized into a fixed daily cost. The operation and maintenance cost covers the expenses required to keep the ES system in optimal standby condition, which is as Equations 17–20.

$$obj_{ES} = C_{inv}^{day} + C_{op} \tag{17}$$

$$C_{inv}^{day} = \frac{R_{ES}}{365} c_E E_N \tag{18}$$

$$R_{ES} = \frac{r(1+r)^{T_{ES}}}{(1+\mathrm{r})^{T_{ES}} - 1} \tag{19}$$

$$C_{op} = \sum_t c_{op}|P_{ES}(t)| \tag{20}$$

where *Cday inv* represents the capital cost converted on a typical day.; C_{op} is the operating cost of ES; R_{ES} is the annual investment recovery coefficient of ES; T_{ES} is the life of ES; r is the discount rate; c_E is the life-cycle capital cost of ES; E_N is the rated capacity of ES; $P_{ES}(t)$ is the operating power of the ES at time t; c_{op} is the operation and maintenance cost factor of ES.

3.1.5 Lithium mining loads cost

$$obj_{laod} = C_{Li} + C_{tr} \tag{21}$$

3.2 Constraints

The optimal operation conditions of industrial microgrids include constraints on PV unit output, gas turbine output, CSP unit output, ES operation, and lithium mining load operation.

3.2.1 Power supply constraints

3.2.1.1 PV units constraint

PV output within the predicted output range to participate in the optimization of microgrid operation, which is as Equation 22.

$$0 \le P_{PV}(t) \le P_{PV}^{fr}(t) \tag{22}$$

3.2.1.2 Gas turbine constraint

$$\mu_{GT} P_{GT}^{N} \le P_{GT}(t) \le P_{GT}^{N} \tag{23}$$

where μ_{GT} is the minimum technical output coefficient of gas turbine; P_{GT}^{N} is rated power of gas turbine.

3.2.1.3 CSP units constraints

CSP utilizes photovoltaic power generation to heat molten salt, achieving the conversion of electrical energy into thermal energy, and stores the heat in high-temperature molten salt tanks. The process is subject to the following constraints.

The constraints on power generation output are as Equation 24:

$$\begin{cases} P_{s,\min} * I_{CSP}(t) \le P_{CSP}(t) \le P_{s,\max} * I_{CSP}(t) \\ I_{CSP}(t) \in \{0,1\} \end{cases} \tag{24}$$

where $I_{CSP}(t)$ represents the on/off status of the CSP units at time t, expressed as a binary variable; $P_{CSP}(t)$ is the power output of the CSP at the time t; $P_{s,\min}$, $P_{s,\max}$ are the lower and upper limit of the power output of CSP units, respectively.

The constraints on minimum on/off time period are as Equation 25:

$$\begin{cases} [I_{CSP}(t-1) - I_{CSP}(t)]T_{s,off} + \sum_{j=t-T_{s,on}}^{t-1} \left(1 - I_{j,s}\right) \ge 0 \\ [I_{CSP}(t) - I_{t-1,s}]T_{s,on} + \sum_{j=t-T_{s,on}}^{t-1} I_{j,s} \ge 0 \end{cases} \tag{25}$$

where $T_{s,off}$ indicates the shutdown period of CSP units; $T_{s,on}$ indicates the start period of the CSP units.

The constraints on output power are as Equations 26, 27:

$$0 \le P_{CHP}^{cha}(t) \le \lambda_{cha} P_{CSP}^{solar}(t) \tag{26}$$

$$0 \le P_{CSP}^{dis}(t) \le \lambda_{dis} P_{CSP}^{N} \Big/ \eta_{N,dis} \tag{27}$$

$$\lambda_{cha} + \lambda_{dis} \le 1 \tag{28}$$

where $P_{CHP}^{cha}(t)$ is the heat storage power of CSP at time t; $P_{CSP}^{dis}(t)$ indicates the heat release power of CSP in time t; $P_{CSP}^{solar}(t)$ is available solar thermal power at time t; P_{CSP}^{N} is the rated power of the CSP; $\eta_{N,dis}$ is the efficiency of converting thermal power into electrical power; λ_{cha} and λ_{dis} represents the 0–1 state variable of the CSP thermal storage system, indicating whether it is in charging (heat storage) or discharging (heat release) mode at time t.

The constraints on the state of charge for thermal storage is as Equation 29:

$$E_{CSP}(t) = E_{CSP}(t-1) + \eta_{CSP} P_{CHP}^{cha}(t) - P_{CSP}^{dis}(t) \Big/ \eta_{CSP} \tag{29}$$

where $E_{CSP}(t)$ is the thermal energy stored in the CSP units at the time t; η_{CSP} is the efficiency coefficient of the thermal storage system.

The constraint on thermal storage capacity is as Equation 30:

$$E_{s,\min} \le E_{CSP}(t) \le E_{s,\max} \tag{30}$$

where $E_{s,\min}$, $E_{s,\max}$ are the lower and upper limit of the thermal ES capacity in the CSP untis, respectively.

3.2.2 Power balance constraint

The power on the supply side equals the power on the demand side, which is as Equation 31:

$$\begin{aligned} &P_{PV}(t) + P_{GT}(t) + P_{CSP}(t) + P_{ES}(t) \\ &= P_{Li}^{fr}(t) + P_{Li}(t) + P_{tr}^{fr}P(t) + P_{tr}(t) + P_{Net}(t) \end{aligned} \tag{31}$$

where $P_{Net}(t)$ is unbalanced power that cannot be fully absorbed at time t.

3.2.3 ES constraints

The constraints on capacity configuration and operation are as follows:

$$\begin{cases} P_{ES,\min} \le \lambda_{ES} P_{ES,N} \le P_{ES,\max} \\ E_{ES,\min} \le \lambda_{ES} E_{ES,N} \le E_{ES,\max} \end{cases} \tag{32}$$

where $P_{ES,N}$ is rated power of ES; $E_{ES,N}$ is the rated capacity of ES; λ_{ES} is the 0–1 variable configured for ES; $P_{ES,\min}$ and $P_{ES,\max}$ are the minimum and maximum rated power of ES, respectively; $E_{ES,\min}$ and $E_{ES,\max}$ are the minimum and maximum rated capacity of ES respectively.

The constraint on ES operating is as Equation 33:

$$-\alpha_{ch} P_{ES,N} \le P_{ES}(t) \le \alpha_{dis} P_{ES,N} \tag{33}$$

where $P_{ES}(t)$is the operating power of ES at time t; α_{ch} and α_{dis} are the maximum charging efficiency and the maximum discharge efficiency, respectively.

The constraints on response rate and time of ES are as Equation 34:

$$\begin{cases} v_{ES}^{-} \le P_{ES}(t) - P_{ES}(t-1) \le v_{ES}^{+} \\ D \le \Delta t \end{cases} \tag{34}$$

where v- ES, v + ES are the upper limits of the downregulation and upregulation response rates of ES participating in microgrid regulation at time t, respectively; D is the minimum time period for ES to participate in microgrid regulation; Δt is the time period with ES actually participating in microgrid regulation.

The constraints on state of charge (SOC) for ES are as Equation 35:

$$\begin{cases} SOC_{\min} \le SOC_0 + \left[\int_{t_0}^{t_1} P_{ES}(t)dt\right] \Big/ E_{ES,N} \le SOC_{\max} \\ \forall t_1 \in [t_0, t_{end}] \end{cases} \tag{35}$$

where $SOC_{\min}$, $SOC_{\max}$ represents the ratio of the minimum and maximum capacity of ES; SOC_0 indicates the initial SOC of the ES; t_0, t_{end} represents the start time and end time of ES participation in microgrid regulation, respectively; t_1 represents any moment within the start time and end time of ES participation in microgrid regulation.

3.2.4 Load constraints

The load side constraints are shown in Equations 1–7 and Equations 8–11.

3.3 Model linearization based on Big-M method

Since the multiplication of 0–1 variable and continuous variable is non-linear, the Big-M method is used to linearize Equation 32, making it easy to solve using mature commercial optimization software Gurobi, which is as Equations 36, 37:

$$\begin{cases} P_{MV} = \lambda_{ES} P_{ES,N} \\ P_{MV} \le P_{ES,N} \\ P_{MV} \le P_{ES,N} - M(1-\lambda_{ES}) \\ \lambda_{ES} P_{ES,\min} \le P_{ES,N} \le \lambda_{ES} P_{ES,\max} \end{cases} \tag{36}$$

$$\begin{cases} E_{MV} = \lambda_{ES} E_{ES,N} \\ E_{MV} \le E_{ES,N} \\ E_{MV} \le E_{ES,N} - M(1-\lambda_{ES}) \\ \lambda_{ES} E_{ES,\min} \le E_{ES,N} \le \lambda_{ES} E_{ES,\max} \end{cases} \tag{37}$$

where P_{MV} and E_{MV} are the auxiliary variable that characterizes the ES state; M is relatively large constants.

4 Case study

4.1 Scene setting

To validate the feasibility and effectiveness of the proposed strategy, this section conducts a simulation analysis based on an independent microgrid located in a remote area of Southwest China. The proposed optimization configuration model is solved using the linear solver Gurobi, with the simulation scheduling set for a 24-h period and a scheduling step size of 1 h. The predicted output of the PV unit and the planned load consumption curve are shown in Figure 3, and the basic operational parameters of the independent microgrid are listed in Table 1. Additionally, four cases are set up for comparative analysis, as detailed below. It should be noted that, for the sake of simplicity, other regulation resources below mainly include PV units, CSP units, gas turbines and transferable lithium mining loads.

Case 1: The regulation potential of TLMLs and ES is not considered. The power and energy balance of microgrid is managed solely by other regulation resources.

Case 2: The regulation potential of TLMLs is considered, but ES is not included. The power and energy balance of the microgrid is achieved through the participation of TLMLs and other regulation resources.

Case 3: The regulation potential of TLMLs is not considered, but ES is optimized. The power and energy balance of microgrid is managed through ES and other regulation resources.

Case 4: Both the regulation potential of TLMLs and the optimal configuration of ES are considered. The power and energy balance of the microgrid is achieved through the joint participation of TLMLs, ES, and other regulation resources.

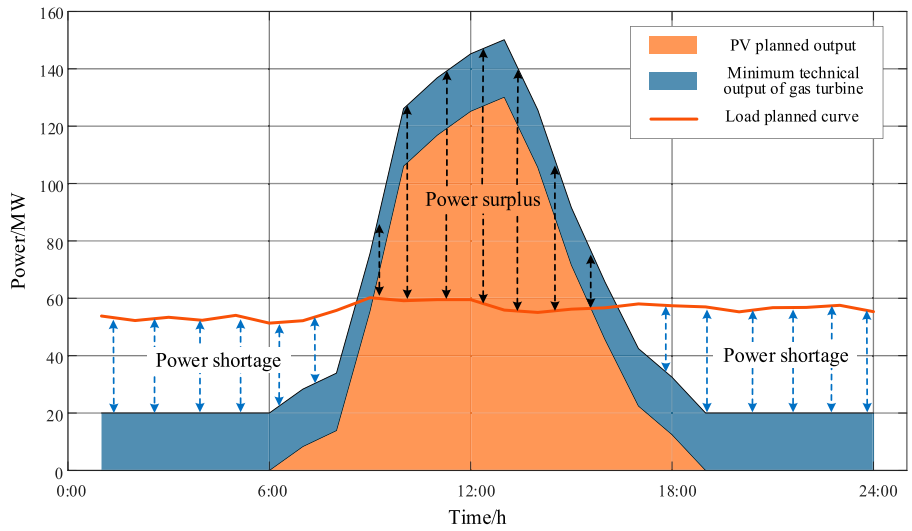

FIGURE 3
Schematic diagram of operation baseline for independent microgrid.

TABLE 1 Basic parameters of independent microgrid.

	Index	Value
Generation	Rated capacity of PV	190 MW
	Rated capacity of CSP	12 MW
ES	Rated power lower limit	20 MW
	Rated power upper limit	200 MW
Lithium mining load	Upper temperature limit	55°C (Ma et al., 2020)
	Lower limit of temperature	65°C (Ma et al., 2020)
	Specific heat capacity of brine	3kJ/(kg °C)
	Heat transfer coefficient	5

TABLE 2 Different operating scenarios in the microgrid.

	ES	TLMLs	Other regulation resources
Case 1	×	×	✓
Case 2	×	✓	✓
Case 3	✓	×	✓
Case 4	✓	✓	✓

4.2 Analysis of ES optimization configuration results

Considering the planned PV output, the minimum technical output of gas turbines, and the planned load consumption curve, the operational status of the independent microgrid is shown in Figure 3. The system exhibits a power surplus during the scheduling period of 9:00–16:00, while power deficits occur during 1:00–8:00 and 17:00–24:00. These highlight significant challenges in achieving system power balance. To address these challenges, the excellent characteristics of ES for power support and energy shifting are fully utilized. Combined with the proposed ES optimization strategy, ES system participates in the power and energy balance control of the microgrid. Furthermore, to effectively compare the impact of demand-side flexibility from lithium mining load regulation on microgrid ES configuration and operation, simulation analyses are conducted for Case 3 and Case 4 in Table 2, with the ES optimization results presented in Table 3. As shown in Table 3, when the flexibility of TLMLs is not considered in the grid optimization, the configured ES capacity is 104.92 MW/419.68 MWh. In contrast, when the flexibility of TLMLs is included in the optimization, the rated power and capacity of the optimized ES configuration are reduced by 26.06% and 22.17%, respectively, compared to Case 3.

TABLE 3 Optimal configuration results of ES in independent microgrid.

Case	Rated power	Rated capacity
Case 3	104.92 MW	398.70 MWh
Case 4	77.58 MW	310.32 MWh

By exploiting the temperature adjustability of the MVR system, the electricity flexibility of TLMLs can be effectively unlocked, achieving the following:

- During peak electricity demand periods when power supply is insufficient, the electricity demand of TLMLs is reduced to alleviate pressure on the power supply of microgrid.
- During low electricity demand periods and high PV generation periods, the electricity demand of TLMLs is increased to enhance the renewable energy utilization of the microgrid.

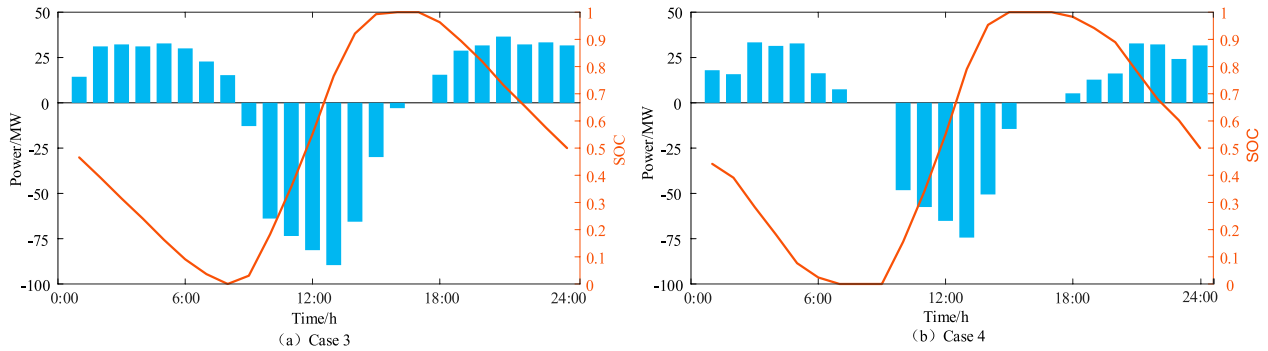

FIGURE 4
Operating power and SOC operation curve of configured ES.

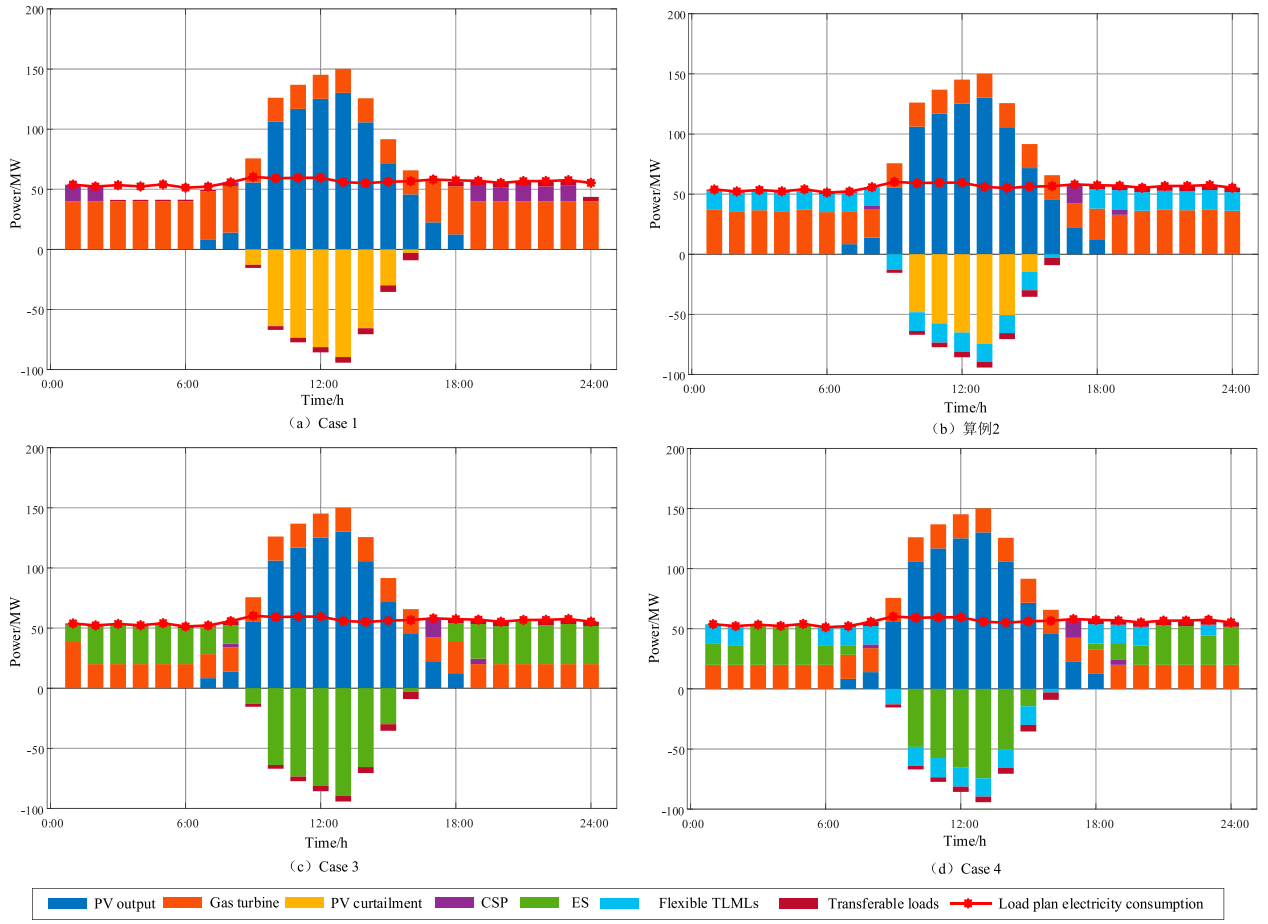

FIGURE 5
Coordinated optimization operation diagram of independent microgrid in cases 1–4. **(A)** Case 1. **(B)** Case 2. **(C)** Case 3. **(D)** Case 4.

These results demonstrate that the flexible regulation capability of TLMLs effectively eliminates part of the system's power imbalance, thereby reducing the ES configuration requirements.

The operating power and SOC curves of the ES system configured in Cases 3 and 4 are shown in Figure 4. It can be observed that the ES system in both cases discharge during power deficit periods to meet load demands and charge during power surplus periods to absorb excess PV generation. This ensures sufficient energy is available for discharge during power deficit periods. Additionally, in Case 3, the configured ES system undergoes charge and discharge actions during all 24 scheduling periods of a typical day. In contrast, the number of charge-discharge

cycles in Case 4 is reduced, which helps to minimize ES losses from frequent cycling and further extends the lifespan of the ES system.

4.3 Technical analysis of optimal operation in independent microgrid

This section focuses on analyzing the optimal operation of different regulation resources in maintaining the power and energy balance of the microgrid. Figure 5 illustrates the optimized operation of the independent microgrid in Cases 1–4. In Case 1, the PV units, CSP units, gas turbines, and transferable loads collectively participate in system regulation. As shown in Figure 5A, some scheduling periods still experience power shortages, resulting in an unbalanced energy volume of 62.16 MWh. During periods of high PV generation, a significant amount of electricity is curtailed due to the limited accommodation capacity of the system, leading to a curtailment rate of 51.53%. This highlights the severe challenge to the microgrid's renewable energy utilization capability. Compared with the regulation resources involved in Case 1, Case two incorporates flexible TLMLs by exploiting the temperature adjustability of MVR system to participate in the power and energy balance control of the microgrid. This approach further alleviates system imbalances and reduces the PV curtailment rate by 48.9% and 26.06%, respectively. However, due to the adjustment boundaries of lithium mining load power under the constraints of lithium extraction production efficiency, solely relying on the inclusion of flexible TLMLs is insufficient to both reduce the curtailment rate and improve the power and energy balance of the system.

Case 3 builds on Case 1 by considering ES configuration to enhance the stable operation of the microgrid. The results of ES optimization and charge-discharge operations were analyzed in detail in Section 4.2 and will not be repeated here. From the optimized operation of the microgrid in Case 3 shown in Figure 5C, it is evident that the PV output power is fully utilized by the microgrid.

Additionally, imbalanced power and gas turbine output power are reduced by 76.45% and 36.51%, respectively, compared with Case 1. Furthermore, despite achieving load demand satisfaction and significantly lowering the PV curtailment rate, the system incurs a high ES capacity cost—nearly twice the average load demand capacity. This highlights the need for further improvement in resource configuration and system flexibility. To address these issues, Case 4 integrates the flexible TLMLs from Case 2 and the ES system from Case 3 for joint participation in the power and energy balance control of the microgrid. The regulation resources in this case include PV units, CSP units, gas turbines, ES, and flexible TLMLs. Similarly, the ES configuration and operational performance, as well as a comparison with Case 3, were elaborated in Section 4.2 and are not repeated here. It is worth noting that, based on the ES capacity configuration in Case 4 and the optimized operation shown in Figure 5D, the microgrid achieves a significant improvement in stability by reducing system imbalances and PV curtailment to 2.12 MWh and 0 MWh, respectively, using only 74% of the ES capacity configured in Case 3.

As indicated by the previous analysis, both Case 2 and Case 4 include flexible TLMLs as key regulation resources in microgrid operations. The main difference lies in the addition of ES regulation in Case 4 compared to Case 2. To compare the impact of ES on the temperature of the primary power-consuming equipment (MVR) in the lithium extraction process, the temperature regulation variation curves of TLMLs are shown in Figure 6. The MVR temperature represents the physical characteristics of lithium extraction from brine, while power quantifies its electricity consumption. These two parameters exhibit a thermo-electric coupling relationship. By analyzing temperature variations, the effect of power regulation on the production efficiency of TLMLs can be effectively reflected. The temperature variations shown in Figure 6 directly correspond to the power flexibility regulation of TLMLs in Figure 5. As observed in Figure 6, the MVR temperature fluctuates within the temperature control boundaries of 55°C–65°C in both Case 2 and Case 4, with similar trends. Specifically, as shown in Figures 3, 5, during power deficit periods (1:00–8:00 and 17:00–24:00), lowering the MVR temperature reduces the electricity demand of lithium mining loads to alleviate the supply pressure on the microgrid. Conversely, during power surplus periods (9:00–16:00), increasing the MVR temperature raises the electricity demand of lithium mining loads to absorb excess power. This effectively enables bidirectional flexible interaction between power supply and demand.

However, whether ES participates in microgrid operations significantly impacts the temperature variations of TLMLs, as evidenced by notable differences between Cases 2 and 4. Specifically, in Case 2, the temperature adjustment range is [56°C, 64°C], with a temperature difference of 8°C and a variance of 9.52°C^2. In comparison, Case 4 demonstrates a narrower temperature adjustment range of [57.8°C, 62°C], with the temperature difference and variance reduced by 47.5% and 25.87%, respectively. Combining Figures 5, 6, the collaboration of ES with flexible TLMLs in microgrid regulation effectively alleviates the pressure on flexible regulation, minimizing the impact of temperature variations on the production efficiency of the lithium extraction process.

4.4 Economic analysis of optimal operation in independent microgrid

This section analyzes the economic costs of microgrid optimized operation. Based on the solution of the objective function in the optimization strategy for independent microgrids discussed in Section 3.1, the economic operation costs for Cases 1–4 are presented in Figure 7.

Specifically, the costs of thermal power generation and carbon emission penalties show a decreasing trend from Case 1 to Case 4, aligning with the technical analysis in Section 4.3. This is mainly due to the gradual inclusion of more flexible regulation resources in microgrid control, which reduces the reliance on costly thermal power generation, contributing to the achievement of "dual carbon" goals. The PV curtailment penalty cost in Case 2 decreases by 21.53% compared to Case 1, while Cases 3 and 4 fully utilize the PV output. This demonstrates that the participation of flexible TLMLs and ES in microgrid regulation continuously enhances the system's renewable energy utilization capability. However, the regulation capacity of TLMLs is limited by the adjustment capacity and the production characteristics of lithium extraction processes, making their regulation capability less effective than that of ES.

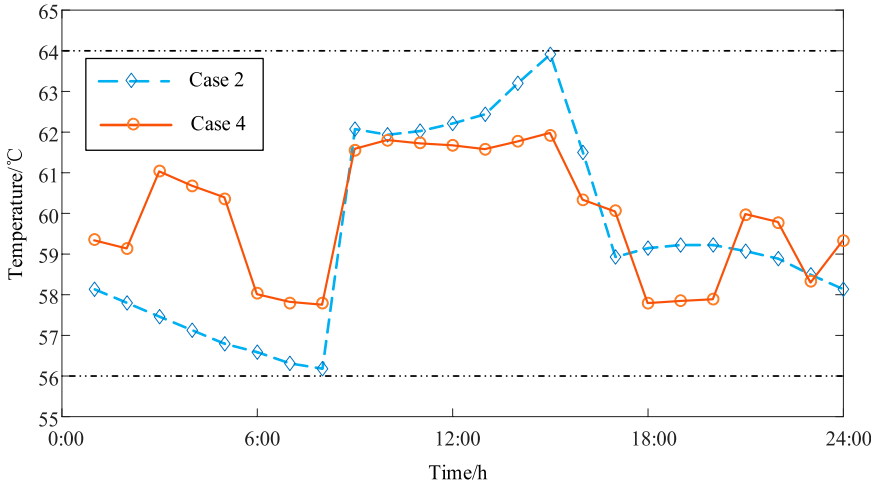

FIGURE 6
Temperature regulation diagram of TLMLs for Cases 2 and 4.

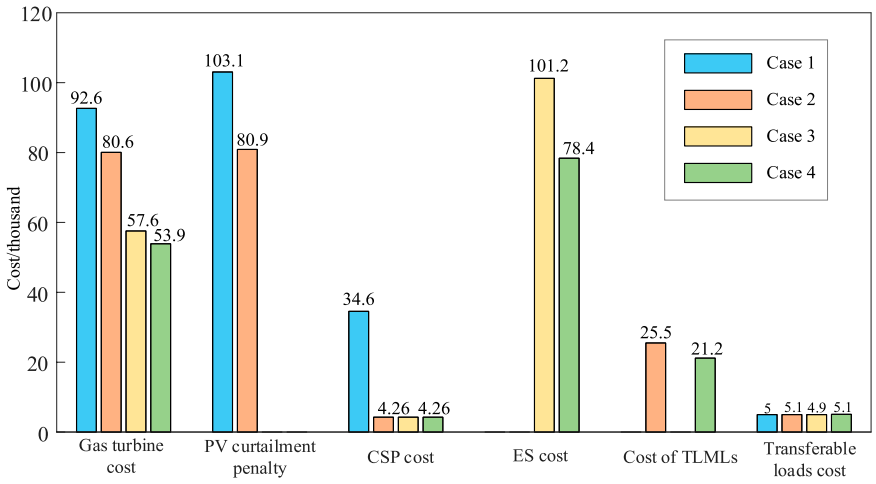

FIGURE 7
The comparison diagram of comprehensive operation cost in cases 1–4.

Nevertheless, the participation of flexible TLMLs in power and energy balance can further alleviate the need for conservative ES capacity configurations, effectively reducing the economic cost of ES. This conclusion is supported by the comparison of ES costs between Cases 3 and 4, where the total capital and operational cost of ES in Case 4 is 22.53% lower than in Case 3. Similarly, the regulation cost of TLMLs in Case 4 decreases from ¥25,500 in Case 2 to ¥21,200. The involvement of ES in power and energy balance also reduces the flexible regulation pressure on TLMLs, thereby mitigating the impact on lithium extraction production efficiency.

In addition, the total operating costs for Cases 1, 2, 3, and four are ¥359,600, ¥259,300, ¥197,300, and ¥167,000, respectively, showing a progressively decreasing trend. This demonstrates that, compared to considering the participation of flexible TLMLs or ES individually in microgrid optimization, their coordinated participation significantly reduces the overall operating costs of the system. ES participation in system regulation effectively reduces the temperature variation of TLMLs, thereby lowering the regulation costs of flexible TLMLs. Simultaneously, the participation of flexible TLMLs in system regulation further reduces the required ES capacity and charge-discharge power, effectively decreasing the capital and operating costs of ES. Therefore, combined with the previous technical analysis, the coordinated participation of flexible TLMLs and ES in microgrid regulation balances the technical and economic benefits of microgrid operation.

5 Conclusion

This study focuses on the power supply needs of high-energy-consuming industrial mining loads and the integration of new

energy in an independent microgrid in a remote area of Southwest China. By analyzing the lithium extraction process from brine and exploring the regulation potential of lithium mining loads, it proposes an ES optimization configuration and operation strategy for independent microgrids, incorporating the flexible response of high-energy loads to jointly participate in the system's power and energy balance regulation. The following conclusions are drawn:

1) Considering the flexibility of lithium mining loads is constrained by the production characteristics of the lithium extraction process, a mathematical model for the flexible regulation of lithium mining loads was developed. This model incorporates the adjustability of the MVR temperature of key power-consuming equipment and includes production behavior constraints.
2) By incorporating the regulation capacity boundaries of various resources in the microgrid, an optimal ES configuration model was developed to minimize the comprehensive operational cost of the system. The participation of ES in microgrid optimization reduced the system imbalance power and comprehensive operational cost by 93.32% and 35.6%, respectively, while effectively decreasing the temperature regulation variation of lithium mining loads by 47.5%.
3) By leveraging their demand-side regulation potential, the flexible lithium mining loads contribute to reducing the required ES capacity by 26.06%. Additionally, this approach effectively alleviates the power supply pressure on generation units, significantly enhancing the technical and economic performance of the microgrid.

This study aims to address the electricity challenges faced by high-energy-consuming loads in high-renewable-energy microgrids, providing valuable insights for the development of demand response. Future research will focus on characterizing the uncertainty in the response of flexible lithium mining loads and exploring multi-stakeholder benefit allocation within microgrid.

Data availability statement

The original contributions presented in the study are included in the article/supplementary material, further inquiries can be directed to the corresponding author.

Author contributions

CY: Conceptualization, Data curation, Funding acquisition, Investigation, Methodology, Project administration, Resources, Software, Supervision, Validation, Visualization, Writing–original draft, Writing–review and editing. XL: Conceptualization, Funding acquisition, Investigation, Methodology, Project administration, Resources, Supervision, Validation, Writing–original draft, Writing–review and editing. YL: Conceptualization, Data curation, Funding acquisition, Investigation, Project administration, Resources, Supervision, Validation, Writing–original draft, Writing–review and editing. JT: Conceptualization, Data curation, Formal Analysis, Investigation, Resources, Supervision, Validation, Visualization, Writing–original draft, Writing–review and editing. ZL: Conceptualization, Formal Analysis, Methodology, Resources, Software, Validation, Visualization, Writing–original draft, Writing–review and editing. BD: Formal Analysis, Supervision, Writing–original draft, Writing–review and editing. LW: Formal Analysis, Methodology, Resources, Supervision, Writing–original draft, Writing–review and editing.

Funding

The author(s) declare that financial support was received for the research, authorship, and/or publication of this article. This work was supported in part by the Science and Technology Major Project of Tibetan Autonomous Region of China (No. XZ202201ZD0003G).

Acknowledgments

The authors wish to thank the project funding from the Science and Technology Major Project of Tibetan Autonomous Region of China (NO. XZ202201ZD0003G).

Conflict of interest

Authors CY, XL, ZL, BD, and LW were employed by Economic and Technical Research Institute of State Grid Tibet Electric Power Co., Ltd. Authors YL and JT were employed by State Grid Tibet Electric Power Co., Ltd.

Generative AI statement

The author(s) declare that no Generative AI was used in the creation of this manuscript.

Publisher's note

References

Cui, H. B., and Zhou, K. L. (2018). Industrial power load scheduling considering demand response. *J. Clean. Prod.* 204, 447–460. doi:10.1016/j.jclepro.2018.08.270

Golmohamadi, H., Keypour, R., Bak-Jensen, B., and Pillai, J. R. (2019). A multi-agent based optimization of residential and industrial demand response aggregators. *Int. J. Electr. Power Energy Syst.* 107, 472–485. doi:10.1016/j.ijepes.2018.12.020

Huang, X. R., Yang, B., Yu, F. Y., Pan, J., Xu, Q., and Xu, W. X. (2021). Optimal dispatch of multi-energy integrated micro-energy grid: a model predictive control method. *Front. Energy Res.* 9, 2021. doi:10.3389/fenrg.2021.766012

Karimianfard, H., Salehizadeh, M. R., and Siano, P. (2022). Economic profit enhancement of a demand response aggregator through investment of large-scale energy storage systems. *CSEE J. Power Energy Syst.* 8 (5), 1468–1476. doi:10.17775/CSEEJPES.2021.02650

Kong, L. J., Li, G. B., Xie, J. H., Yang, X. H., and Bai, X. Q. (2024). Research progress of lithium extraction technology from salt lake brine. *Inorg. Salt Ind.*, 1–15. doi:10.19964/j.issn.1006-4990.2024-0144

Liao, S. Y., Bian, S. Q., Xu, J., Ke, D. P., and Sun, Y. Z. (2024). Evaluation of interactive adjustable capacity of electrolytic aluminum load grid considering energy flow optimization. *Proc. CSEE*, 1–12.

Liu, C., Zhuo, J., and Zhao, D. (2020). A review on the utilization of ES system for the flexible and safe operation of renewable energy microgrids. *Proc. CSEE* 54 (10), 1–12. doi:10.1002/2050-7038.12934

Ma, Y. H., Luo, Y. T., and Zhao, S. B. (2020). Process for preparing battery-grade lithium carbonate from salt lake brine Research on influencing factors. *Yunnan Chem. Technol.* 47 (6), 51–52. doi:10.3969/j.issn.1004-275X.2020.06.018

Nie, Z., Wu, Q., Ding, T., Bu, L. Z., Wang, Y. S., Yu, J. J., et al. (2023). Research progress on industrialization technology of lithium extraction from salt lake brine in China. *Inorg. Chem. Ind.* 54 (10), 1–12. doi:10.19964/j.issn.1006-4990.2022-0542

Philipo, G., Kakande, J., and Krauter, S. (2022). Neural network-based demand-side management in a stand-alone solar PV-battery microgrid using load-shifting and peak-clipping. *Energies* 15 (14), 5215. doi:10.3390/en15145215

Reka, S. S., and Ramesh, V. (2016). Industrial demand side response modelling in smart grid using stochastic optimisation considering refinery process. *Energy Build.* 127, 84–94. doi:10.1016/j.enbuild.2016.05.070

Shen, Y., Hu, W., Liu, M., Yang, M., Yang, F., and Kong, X. Y. (2022). Energy storage optimization method for microgrid considering multi-energy coupling demand response. *J. Energy Storage* 45, 103521. doi:10.10.1016/j.est.2021.103521

Sun, W. Q., Liu, W., Xiang, W., and Zhang, J. (2022). Generalized energy storage allocation strategies for load aggregator in hierarchical electricity markets. *J. Mod. Power Syst. Clean. Energy* 10 (4), 1021–1031. doi:10.35833/MPCE.2020.000737

Wang, D., Huang, D. Y., Hu, Q. E., Jia, H. J., Liu, B., and Yang, L. (2024b). Electricity-heat-based integrated demand response considering double auction energy market with multi-energy storage for interconnected areas. *CSEE J. Power Energy Syst.* 10 (4), 1688–1700. doi:10.17775/CSEEJPES.2022.02140

Wang, W. D., Huang, H., Zhang, X. S., Tan, J., and Sun, S. B. (2024a). Flexible low carbon optimal dispatch of distribution networks considering the demand response of heat storage industrial loads. *Front. Energy Res.* 12. doi:10.3389/fenrg.2024.1507604

Wu, M., Zhang, N. C., Liang, Y., Liu, H. T., and Ji, Y. (2024). Research and development of micropower system technology under the background of new power system. *New Power Syst.* 2 (03), 251–271. doi:10.20121/j.2097-2784.ntps.240049

Xiao, L. H. (2014). *Study on isothermal evaporation crystallization and ultrasonic heating crystallization process of brine in Zabye Salt Lake*. Central South University.

Xu, X. D., Sun, W. Q., Abeysekera, M., and Qadrdan, M. (2020). Quantifying the flexibility from industrial steam systems for supporting the power grid. *IEEE Trans. Power Syst.* 36 (1), 313–322. doi:10.1109/TPWRS.2020.3007720

Zeng, L., Gong, Y. G., Xiao, H., Chen, T. J., Gao, W., Liang, J., et al. (2024). Research on interval optimization of power system considering shared energy storage and demand response. *J. Energy Storage* 86, 111273. doi:10.1016/j.est.2024.111273

Zhang, Z. Z., Pan, Z. S., and Che, D. (2024). Analysis of lithium supply and demand situation based on lithium deposits and resources characteristics from 2024 to 2035, China. *Chin. Min. Ind.* 33 (06), 26–44. doi:10.12075/j.issn.1004-4051.20241183

Zhou, D., Wen, X., Wang, J., Xiong, T., Sun, D. T., Dan, G. J., et al. (2022). Research on matching characteristics of centrifugal steam compressor and evaporator in MVR system. *Chin. J. Eng. Des.* 29 (05), 595–606. doi:10.3785/j.issn.1006-754X.2022.00.071

frontiers | Frontiers in Energy Research

TYPE Original Research
PUBLISHED 22 April 2025
DOI 10.3389/fenrg.2025.1574188

OPEN ACCESS

EDITED BY
Yingjun Wu,
Hohai University, China

REVIEWED BY
Yanbo Wang,
Aalborg University, Denmark
Qiang Fu,
Sichuan University, China
Liwei Zhang,
Northeast Electric Power University, China

*CORRESPONDENCE
Yabo Cao,
caoyabo_2000@163.com

RECEIVED 10 February 2025
ACCEPTED 24 March 2025
PUBLISHED 22 April 2025

CITATION
Yang Z, Wang Y, Wei J and Cao Y (2025) Cooperative control of virtual energy storage devices for energy regulation and rapid frequency support.
Front. Energy Res. 13:1574188.
doi: 10.3389/fenrg.2025.1574188

Cooperative control of virtual energy storage devices for energy regulation and rapid frequency support

Zheng Yang[1,2], Yi Wang[1], Jiahui Wei[1] and Yabo Cao[1]*

[1]Hebei Key Laboratory of Distributed Energy Storage and Microgrid, North China Electric Power University, Baoding, China, [2]State Grid Jibei Integrated Energy Service Co., Ltd., Beijing, China

Various controllable resources contribute to energy regulation and rapid support in the form of virtual energy storage (VES), which can significantly simplify control parameters and facilitate the evaluation of a microgrid's economic and secure operational reserves. This paper establishes a power density virtual energy storage (PDVES) model and an energy density virtual energy storage (EDVES) model. Wind turbines, photovoltaics (PVs), controllable loads, and electric vehicles (EVs) are equated to EDVES and PDVES, respectively. Furthermore, an economic calculation model for microgrids that incorporates VES is developed, and an energy regulation framework for microgrids is constructed with virtual current (VCU) and virtual capacitor (VCA) as scheduling parameters. With the frequency security of island microgrids as a constraint, a rapid support coordinated control strategy for PDVES and EDVES is proposed to ensure the economic and secure operation of microgrids across multiple time scales. Finally, a high-proportion renewable energy test system with VES is established. The test results demonstrate that under the proposed VES control, the energy regulation and dynamic stability control performance of microgrids can be significantly improved.

KEYWORDS

virtual battery, virtual capacitor, energy regulation, frequency support, dynamic stability

1 Introduction

With the rapid increase in the proportion of distributed wind power, photovoltaic (PV), electric vehicles (EVs), seawater desalination loads (SDLs), and other flexible resources (FRs) connected to the power system, both the power supply and load sides present a power challenge potential (Thomas et al., 2018). Microgrids are in urgent need of a feasible solution in order for new energy and controllable loads to be integrated into the system's energy regulation and rapid support control system, realizing the collaborative participation of power sources and loads in system regulation (Mateus et al., 2025; Lin et al., 2025). However, the power output of wind power and PV on the power supply side is intermittent, and controllable loads such as EVs and SDLs have heterogeneous control parameters. Due to the complexity of the operating parameters, microgrids lack a means of evaluation for the system energy and dynamic stability reserves, which not only makes it difficult to

optimize economic operation but also makes it hard to cope with disturbances and guarantee the safe operation of the system. Therefore, microgrids need to integrate FRs, simplify operating parameters, and collaborate to accomplish energy regulation and rapid support control objectives, which will be key to improving the economic and safe operation of the system.

Enhancing the economy of microgrid operation through the cooperative operation of new energy sources, energy storage, and loads is a key research direction for microgrids. Multilevel optimal scheduling models of microgrids have been constructed, which provide a feasible solution for optimizing the energy regulation mode of power source, load and energy storage (Huang et al., 2024; Cao et al., 2025; Li et al., 2025; Morais et al., 2012; Sun et al., 2023) Yang et al. (2025), and Shui et al. (2024) assembled air conditioners, EVs, and smart buildings in a microgrid; considered the interest demands of power, load, and energy storage; and proposed a master–slave co-optimization method to save system investment costs by reducing the peak–valley difference of the operation of the microgrid. However, while the introduction of a demand-side response in microgrids is beneficial for increasing revenue, there is still a lack of coordinated methods for controllable loads, and the resource flexibility potential needs to be further developed. Simplifying system operating parameters reduces the difficulty of energy regulation and coordination between the power supply and load sides, which is essential for unlocking the regulation potential of various FRs. The VES technology, which equates FRs to energy storage and operates jointly with real energy storage, has become a popular topic of research. For example, on the load side, the energy conversion relationship between FRs such as EVs (Westermann and Schlegel, 2013; Zhu and Zhang, 2025), smart air conditioners (Wang et al., 2021; Pahasa et al., 2022), and SDLs (Zhou et al., 2020; Liu et al., 2021), and energy storage is established, and the controllable load can simulate the charging and discharging characteristics of energy storage. Lv et al. (2024) and Wang et al. (2020) established the dynamic relationship between thermal inertia and the charging and discharging characteristics of the VES for the cold\heat load in buildings and improved the economy of a building's energy system through the VES to regulate the load's cold and heat characteristics. However, microgrids that rely solely on a single device for power regulation struggle to meet system energy demands. To further explore the potential of VES, Lv et al. (2024) and Wang et al. (2020) established a combined VES system that incorporated air-conditioning loads and EVs based on their operational characteristics. This system, while balancing the interests of multiple stakeholders, can effectively reduce peak–valley difference, decrease the dependence of the regional power system on traditional energy storage devices, and thus save investment costs. Wang et al. (2024) and Du et al. (2019) proposed realizing the potential of VES by transferring energy across time periods using EVs and smart buildings. By utilizing these in the form of VES, system power fluctuations can be further mitigated. However, due to the different control parameters for electrical and thermal loads, there is still room for improvement in the power coordination between the two. In summary, regarding microgrids, although new energy, energy storage, and load have the potential for energy regulation, the control parameters of each type of equipment are not uniform. Although the charging and discharging characteristics of the VES are involved in system energy regulation, the control process is complicated, and it is difficult to assess the system energy reserve. In microgrids, the joint dispatching strategy of VES and real energy storage needs further improvement.

The rapid responses of FRs to short-term frequency changes to ensure system dynamic stability and alleviate the pressure on power support of the energy storage is another technical bottleneck that urgently needs to be resolved (Chen et al., 2024; Yang et al., 2022). To guarantee the stability of the DC distribution network, Fu et al. (2022) and Tanaka et al. (2011) proposed a coordinated control strategy of controllable loads and batteries to reduce DC voltage fluctuation after disturbances and to avoid the deep charging and discharging of the battery. However, due to the large number of control parameters, the current research does not discuss in detail the control methods for new energy to join the system stability support. Alyami (2024) constructed a hybrid energy storage system containing gas storage, air conditioning, and battery, taking into account time-of-use tariffs, and proposed a coordinated control strategy for PV and hybrid energy storage in an isolated island microgrid. However, while it is suitable for longer time-scale power dispatch, how to respond quickly to short-term frequency changes still needs further research. Gabriele et al. (2023) and Tang et al. (2021) proposed a multi-time-scale coordinated control method for microgrids which can issue control commands for all devices within the day-ahead stage at one time. However, due to the lack of controllable parameters suitable for sensing the power and operating status of controllable devices, the current ability of the microgrid control system to cope with sudden disturbances remains insufficient. In Tangqing et al. (2014) and Honarmand et al. (2014), the energy storage and SDLs coordinate to participate in the primary and secondary frequency regulation of the system. Although existing studies have proposed short-time coordinated control methods for FRs—such as natural gas, smart air conditioners, and SDLs—they have three shortcomings. First, the system power reserve is difficult to assess, and whether the controllable resources can realize continuous regulation needs verification. Second, the operating parameters of the controllable equipment are not uniform, and the design methods of inertia and frequency regulation coefficients are unknown in the short-time frequency response process. Third, whether the FRs in microgrids can take into account energy regulation and short-time frequency support on a long time scale has to be explored. In summary, a VES model urgently needs to be established for microgrids to simplify the operating parameters of each type of FR and to combine the charging and discharging characteristics of PDVES and EDVES. This will realize energy regulation and rapid support control in multiple time scales, give full play to the control potential of the new type of power system, and improve the system operation level.

To optimize the energy regulation effect of microgrids and realize the rapid frequency support control of each type of FR, the PDVES and the EDVES models were respectively established, and a novel cooperative control of VES for energy regulation and rapid frequency support is further proposed. This study is structured as follows. Section 1 establishes VES models for controllable loads, wind turbines (WTs), hydrogen energy storage (HES), and EVs, simplifies the operating parameters of various types of FRs, and proposes the operation mode of a microgrid with VES. Section 2 establishes the economic calculation model of microgrids with VES and proposes a dispatching method of microgrids with VCU and

VCA value as unified instructions and VSOC to assess system energy storage. Section 3 proposes a frequency cooperative control adapted to PDVES, EDVES, and real energy storage devices in microgrids, taking into account both the economic and safe operation of microgrids. Section 4 builds a new energy high-proportion test system with multi-type VES and verifies the effectiveness of the proposed control strategies. The study ends with conclusions.

2 Operation mode of microgrids with VES

2.1 PDVES model

In microgrids, distributed energy resources, controllable loads, HES, and EVs can all be considered typical FRs. Distributed energy resources (such as WTs) and controllable loads possess rapid power response characteristics and can be categorized as PDVES devices. EV and HES systems have the capability to provide sustained power support and can be classified as EDVES. Moreover, to ensure the stable operation of microgrids in island mode, the system requires the configuration of a hybrid energy storage system composed of batteries and supercapacitors. In terms of microgrid control structure, the PV units and permanent magnet direct-drive WTs in the distributed energy resources are connected to the microgrid through inverters. The controllable load, exemplified by SDLs, produces fresh water through reverse osmosis. EVs are charged at a constant voltage and slow charging rate and are connected to the microgrid through a bidirectional inverter. HES is integrated into the microgrid through inverters equipped with electrolyzers and fuel cells; it consumes surplus power from the microgrid by producing hydrogen and supplies power to the microgrid by burning hydrogen. The hybrid energy storage system operates in power control mode.

To flexibly regulate various types of FRs in a microgrid, the operational information on distributed energy resources, controllable loads, and other FRs should be collected by the dispatch control center. In addition, hybrid energy storage should rapidly participate in system regulation. The operation mode of a microgrid is depicted in Figure 1. The microgrid's dispatch center monitors the rotational speed of WTs, the power consumption of controllable loads, and the state-of-charge of EVs, batteries, and supercapacitors. The microgrid needs to process this operational data to generate dispatch commands that facilitate the management and control of multiple types of devices. It also perceives the overall system energy and power reserves, evaluates the reserve status of adjustable system resources, and achieves optimized energy regulation and rapid coordinated control that accounts for various FRs, thereby ensuring the economic operation and dynamic stability of the system.

To simplify the operational parameters involved in the regulation of FRs in microgrids, this paper will establish models for PDVES represented by new energy sources and controllable loads, as well as EDVES represented by HES and EVs. Through unified scheduling by the microgrid, the complexity of coordinated regulation between FRs and real energy storage devices will be mitigated.

i) Controllable load: SDLs are currently recognized as typical controllable loads in microgrids. The high-pressure pumps in SDLs usually possess variable frequency speed regulation capabilities and can be equated with asynchronous motors for simulation purposes. By mimicking the charging and discharging characteristics of power density supercapacitors, an energy conversion relationship can be established between the energy of the capacitor and the kinetic energy of the rotor in the asynchronous motor. This can be expressed as follows:

$$E_{\mathrm{l}} = \int \frac{J_{\mathrm{s}}\omega_{\mathrm{r}}}{p_{\mathrm{n}}^2}\frac{\mathrm{d}\omega_{\mathrm{r}}}{\mathrm{d}t}\mathrm{d}t = \int U_{\mathrm{C}}\frac{\frac{J_{\mathrm{s}}\omega_{\mathrm{r}}\mathrm{d}\omega_{\mathrm{r}}}{\mathrm{d}t}}{\frac{p_{\mathrm{n}}^2 U_{\mathrm{C}}\mathrm{d}U_{\mathrm{C}}}{\mathrm{d}t}}\frac{\mathrm{d}U_{\mathrm{C}}}{\mathrm{d}t}\mathrm{d}t = \int U_{\mathrm{C}}C_{\mathrm{l}}\frac{\mathrm{d}U_{\mathrm{C}}}{\mathrm{d}t}\mathrm{d}t, \quad (1)$$

where E_{l}, J_{s}, ω_{r}, and p_{n} are the rotor kinetic energy, inherent inertia, and angular velocity of the motor, respectively, and Uc is the voltage of the supercapacitor.

It can be seen from Equation 1 that the VCA C_{l} of the SDL is expressed as

$$C_{\mathrm{l}} = \frac{J_{\mathrm{s}}}{p_{\mathrm{n}}^2} \times \frac{\Delta\left(w_r^2\right)}{\Delta\left(U_C^2\right)} \approx \frac{J_{\mathrm{s}}}{p_{\mathrm{n}}^2} \times \frac{(\omega_{\mathrm{r}}^*)^2 - \omega_{\mathrm{r}}^2}{\Delta U_C^2}, \quad (2)$$

In Equation 2, where ω^* r represents the reference value of the electrical angular velocity of the motor.

To facilitate the coordinated control of VES and supercapacitors, this paper introduces the concept of virtual state of charge (VSOC) for the SDL, which is defined as:

$$SOC_{\mathrm{l}} = \frac{J_{\mathrm{s}}\omega_{\mathrm{r}}^2}{2p_{\mathrm{n}}^2} \Big/ \frac{J_{\mathrm{s}}\omega_{\mathrm{rn}}^2}{2p_{\mathrm{n}}^2} = \frac{\omega_{\mathrm{r}}^2}{\omega_{\mathrm{rn}}^2}, \quad (3)$$

In Equation 3, where ω_{rn} represents the rated electrical angular speed of the motor.

ii) Variable speed WT: the variable-speed constant-frequency WT connected to the grid through a power electronic converter has a rapid power response characteristic. The WT simulates the charging and discharging characteristics of a power density supercapacitor, establishing an energy conversion relationship between the capacitor energy and the rotor kinetic energy of the WT. This can be expressed as

$$E_{\mathrm{w}} = \int k_{\mathrm{opt}}\omega_{\mathrm{opt}}^3\mathrm{d}t = U_{\mathrm{C}}\int \frac{\frac{3k_{\mathrm{opt}}\omega_{\mathrm{opt}}^2\mathrm{d}\omega_{\mathrm{opt}}}{\mathrm{d}t}}{\frac{U_{\mathrm{C}}\mathrm{d}U_{\mathrm{C}}}{\mathrm{d}t}}\frac{\mathrm{d}U_{\mathrm{C}}}{\mathrm{d}t}\mathrm{d}t = \int U_{\mathrm{C}}C_{\mathrm{w}}\frac{\mathrm{d}U_{\mathrm{C}}}{\mathrm{d}t}\mathrm{d}t. \quad (4)$$

It is evident from Equation 4 that after equating the variable-speed WT to VES, the VCA value C_{w} of the WT can be expressed as

$$C_{\mathrm{w}} = \frac{2k_{\mathrm{opt}}\Delta\omega_{\mathrm{opt}}^3}{\Delta U_C^2} \approx 2k_{\mathrm{opt}}\frac{\left(\omega_{\mathrm{opt}}^*\right)^3 - \omega_{\mathrm{opt,}}^3}{\Delta U_C^2} \quad (5)$$

In Equation 5, where ω^* opt represents the reference value of the electrical angular speed of the WT rotor.

The VSOC for a variable-speed WT system can be expressed as

$$SOC_{\mathrm{w}} = \frac{E_{\mathrm{w}}}{E_{\mathrm{wn}}} = \frac{\frac{J_{\mathrm{s}}\omega_{\mathrm{opt}}^2}{2p_{\mathrm{n}}^2}}{\frac{J_{\mathrm{s}}\omega_{\mathrm{optn}}^2}{2p_{\mathrm{n}}^2}} = \frac{\omega_{\mathrm{opt}}^2}{\omega_{\mathrm{optn}}^2}, \quad (6)$$

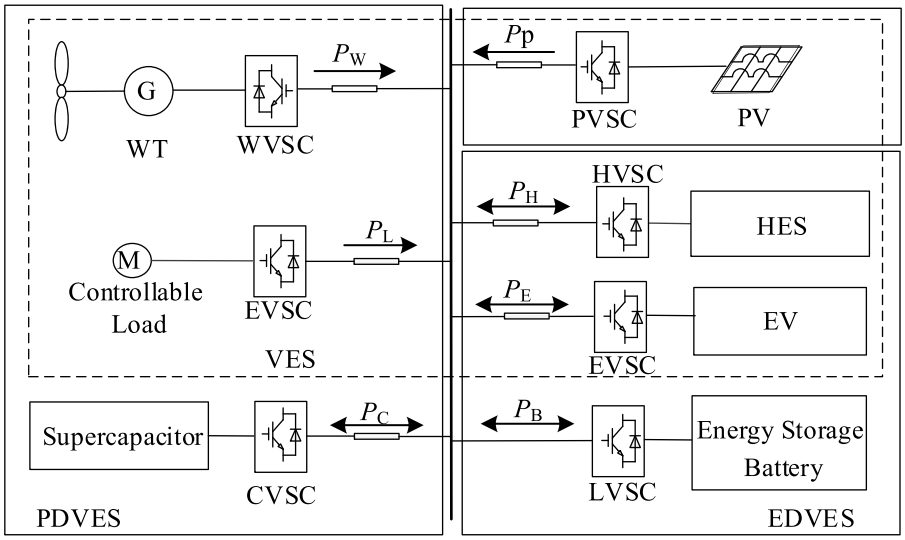

FIGURE 1
Structure of the microgrid with VES.

In Equation 6, where ω_{optn} represents the rated value of the electrical angular speed of the WT rotor.

By equating the SDL and the variable-speed WT to VCAs and introducing the VSOC, the microgrid can regulate FRs with rapid power response capabilities. In conjunction with supercapacitors, this facilitates the evaluation of the energy storage and operational status of the VCAs compared to real energy storage, achieving coordinated regulation between distributed energy resources, controllable loads, and supercapacitors.

2.2 EDVES model

i) HES systems exhibit continuous power regulation characteristics during the electricity-to-hydrogen energy conversion process and can participate in power regulation over extended periods. By simulating the charging and discharging characteristics of energy-density batteries, the HES system can establish an equivalent relationship between the hydrogen production process and the battery charging and discharging process, constructing a connection between the energy conversion of battery charging and discharging and the HES system. The rates of hydrogen production via electrolysis and the combustion of hydrogen can be represented respectively as:

$$\begin{aligned} N_{EL,H2} &= \frac{\eta_{EL} U_{EL} I_{EL} \eta_{in} h_{EL}}{LHV_{H2}} \\ N_{FC,H2} &= \frac{U_{FC} I_{FC} h_{FC}}{\eta_{FC} LHV_{H2} \eta_{out}} \end{aligned}, \tag{7}$$

In Equation 7, where U_{EL} and U_{FC} represent the input and output voltage of the VES, respectively, I_{EL} and I_{FC} represent the input current and output current of the VES, respectively, η_{EL} and η_{EL} represent the electrolysis efficiency and hydrogen combustion efficiency of the HES with values of 0.7 and 0.95, respectively, η_{in} and η_{out} represent the power conversion efficiency of the inverter with a value of 0.95, h_{EL} and h_{FC} represent the working states of the electrolysis hydrogen and fuel cell, respectively, and LHV_{H2} represents the lowest heating value of hydrogen.

After equating the HES device to a virtual battery, the VCU parameter I_{H2V} of the HES can be expressed as:

$$I_{H2V} = \frac{U_{EL} I_{EL} \eta_{in} h_{EL} + U_{FC} I_{FC} h_{FC}}{U_{H2V}}, \tag{8}$$

In Equation 8, where U_{H2V} represents the terminal voltage of the virtual battery.

The VSOC of the HES system, $SOC_{H2}(t)$, can be expressed as follows:

$$SOC_{H2}(t) = SOC_{H2}(t-1) + \frac{N_{EL,H2}(t) - N_{FC,H2}(t),}{M_{H2\,max}} \tag{9}$$

In Equation 9, where M_{H2max} represents the maximum hydrogen mass limit within the hydrogen storage tank.

ii) EVs can adopt time-of-use electricity pricing to guide their charging behavior, achieving orderly load management. By controlling the scaled and orderly charging and discharging of EVs, a controllable virtual battery can be formed to coordinate and solve the problem of unordered charging after EVs are connected to the grid.

EV charging and discharging both occur in a conventionally slow manner. The Monte Carlo simulation method is used to model the daily charging load of EVs. The return time of EVs follows a normal distribution (Zhang et al., 2018) $t_f \sim N$ (17.47, 3.41), and the daily driving distance of EVs follows a log-normal distribution—$S \sim N$ (3.24, 0.88). Based on the Monte Carlo simulation method and by comparing the return time t_f of the i^{th} EV with the end time T_{ms} of the early morning low electricity price period and the start time

T_{ns} of the evening peak electricity price period, the VES of EVs can be charged before the end of the early morning low price period to absorb redundant power. After the evening peak price period, the VES of EVs can be discharged to reduce the impact of the original load power. Reasonably arranging the start time T_c for charging the VES of EVs and the start time T_d for discharging the VES of EVs is as follows:

$$T_c(i) = \begin{cases} t_f(i) & \left(0 \le t_f(i) < T_{ms}\right) \\ t_f(i) & \left(T_{ms} \le t_f(i) \le T_{ns}\right) \\ 0 & \left(T_{ms} \le t_f(i) \le T_{ns}\right), \\ t_f(i) & \left(T_{ns} < t_f(i) \le 24\right) \\ 0 & \left(T_{ns} < t_f(i) \le 24\right) \end{cases} \tag{10}$$

$$T_d(i) = t_f(i) \quad \left(T_{ns} < t_f(i) \le 24\right), \tag{11}$$

In Equations 10, 11, where, T_{ms} represents the end time of the low electricity price period, and T_{ns} represents the start time of the peak electricity price period.

The charging and discharging of the virtual battery require the EV charging pile to obtain the EV battery capacity C_i and the state of charge *SOC*A *I* of the battery. The charging pile management system collects EV users' charging decision behavior, including the expected parking time t_i and the desired state of charge level *SOC*B *I* when leaving, which is set to 0.8. The charging and discharging duration and the amount of electricity for a single EV are, respectively:

$$\begin{aligned} E_{dchar}(i) &= \min\left\{P_C t_C + \left(SOC_i^A - SOC_i^{min}\right)C_i - S(i)w, rC_i\right\} \\ T_{dchar}(i) &= t_i - t_C - \frac{\left(SOC_i^B - SOC_i^{min}\right)C_i}{P_C} - \frac{S(i)w}{P_C} \end{aligned}, \tag{12}$$

In Equation 12, where, P_C is the charging and discharging power of the EV under conventional slow-speed mode, with a value of 1.8 kW, t_c is the charging duration of the EV, *SOC*min *i* is the minimum state of charge of the EV, with a value of 0.1, $S(i)$ is the driving distance of the EV, and w is the battery consumption per kilometer of the EV, with a value of 0.15.

The orderly charging and discharging scheduling process of EVs is shown in Figure 2.

The entire charging duration of the EV is determined by the discharge amount of its virtual battery and the state of charge at the time of return. By guiding the EV to selectively participate in the energy flow in the microgrid during electricity price valleys and peaks, the start time of the EV's virtual battery charging and discharging can be expressed thus:

$$\begin{cases} T_{dchare}(i) = T_{dchar}(i) + T_{dchare}(i) \\ T_{chare}(i) = T_{chare}(i) + \dfrac{\left[\sum_{t=T_{dchare}(i)}^{T_{dchare}(i)} P_C + S(i)w\right]}{P_C}, \end{cases} \tag{13}$$

In Equation 13, where T_{chare} and T_{dchare} represent the end times of charging and discharging, respectively.

The charging and discharging of the electricity $E_{ev}(t)$ of the EV's virtual battery at each moment, as determined by Equation 13, can be expressed as follows Equation 14:

$$E_{ev}(t) = \sum_{t=T_1}^{T_2} P_E = \begin{cases} T_1 = T_{chars}, T_2 = T_{chare} & \text{charging} \\ T_1 = T_{dchars}, T_2 = T_{dchare} & \text{discharging} \end{cases}. \tag{14}$$

After equating the EV to VES, a VCU $I_{ev}(t)$ can be introduced to simulate the battery's charging and discharging characteristics, which can be expressed as

$$I_{ev}(t) = \frac{E_{ev}(t)}{U_{ev}(t)}, \tag{15}$$

In Equation 15, where $U_{ev}(t)$ represents the voltage at the busbar of the EV charging station.

The VSOC of the EV can be expressed as

$$SOC_{ev}(t) = SOC_{ev}(t-1) + \frac{E_{ev}(t)\eta_{ev}}{C}, \tag{16}$$

In Equation 16, where η_{ev} represents the charging and discharging efficiency of the EV.

In the microgrid, HES and EVs can introduce VCU and VSOC as control variables, which have the same operating parameters as real batteries and participate in system power regulation, simplifying the control mode of energy density energy storage devices.

3 Cooperative control of VES for energy regulation and frequency support

3.1 Multi-time scale dispatching system of VES

After introducing VES, the multi-time scale scheduling system structure of the microgrid is shown in Figure 3, where the microgrid's dispatch center is equipped with an energy regulation system for long-time-scale economic optimization operations. After introducing VES, both the EDVES and the battery participate in system regulation and status monitoring through VCU and VSOC, while the PDVES and the supercapacitor participate through VCA and VSOC.

In the energy regulation system, the economic optimization model of the microgrid with VES is solved to complete the dispatch command allocation with the goal of reducing economic operation costs. In the short-term rapid support control system, the microgrid prioritizes the use of PDVES devices to provide inertial support at the initial stage of frequency changes, while the EDVES takes on the task of primary frequency regulation. Because VES actively participates in power regulation at different time scales of the system, it not only reduces the capacity of configuring real energy storage devices but also helps reduce the number of charge and discharge cycles of the energy storage devices, thereby extending the service life of those devices.

3.2 Cooperative energy regulation of VES

3.2.1 Objective function

The energy regulation system of the microgrid utilizes the charging and discharging of VES and adjusts the power output of various FRs. The objective function of the microgrid's energy regulation takes into account the daily revenue R of the load and the operating cost C_{mic}, and can be expressed as:

$$\max \sum_{t=1}^{24}\left[R_{H2} + R_{ev} + R_w - \left(C_{H2} + C_{ev} + C_{wf} + C_{wi} + C_{hy}\right)\right], \tag{17}$$

10.3389/fenrg.2025.1574188

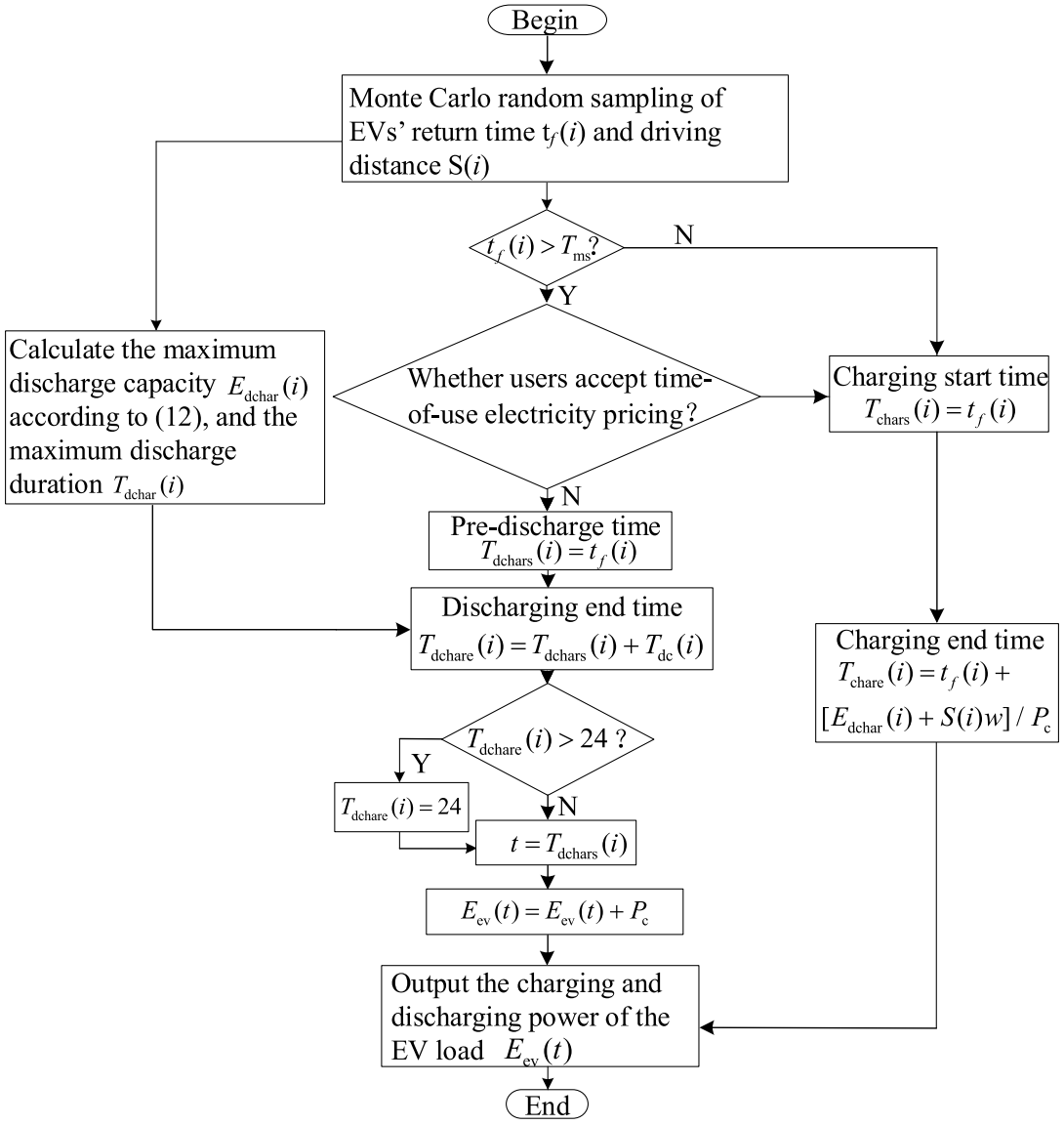

FIGURE 2
Flowchart of virtual battery emulated by EV.

In Equation 17, where R_{H2} represents the revenue from hydrogen production, R_{ev} represents the revenue from EV charging, R_w represents the revenue from the purified water in SDLs, C_{H2} represents the maintenance cost of HES, C_{ev} represents the compensation cost of EVs, C_{wf} represents the cost of WTs participating in system regulation, C_{wi} represents the operation and maintenance cost of WTs, and C_{hy} represents the operation and maintenance cost of energy storage.

3.2.1.1 Revenue of microgrids

As is evident from Equation 17, the revenue of the microgrid is derived from the load revenue, including the revenue from hydrogen production, the revenue from EV charging, and the by-product revenue, which can be expressed as

$$\sum R = \sum_{t=1}^{24} N_{EL,H2}(t) K_{fu} + M_{H2}(t) \Delta SOC_{H2,TK} p_{h2} + \sum_{t=1}^{24} \sum_{j=1}^{N_{ev}} p_t(t) E_{ev}(t) + \sum_{t=1}^{24} K_l Q(t), \tag{18}$$

In Equation 18, where K_{fu} represents the revenue from products obtained by hydrogen production, $\Delta SOC_{H2,TK}$ represents the daily surplus hydrogen mass, p_{h2} represents the hydrogen selling price, $p_t(t)$ represents the electricity purchase price sold by LA to EV users in the time period, $E_{ev}(t)$ represents the charging amount of the virtual battery, N_{ev} represents the number of virtual batteries, and K_l represents the revenue from purified water.

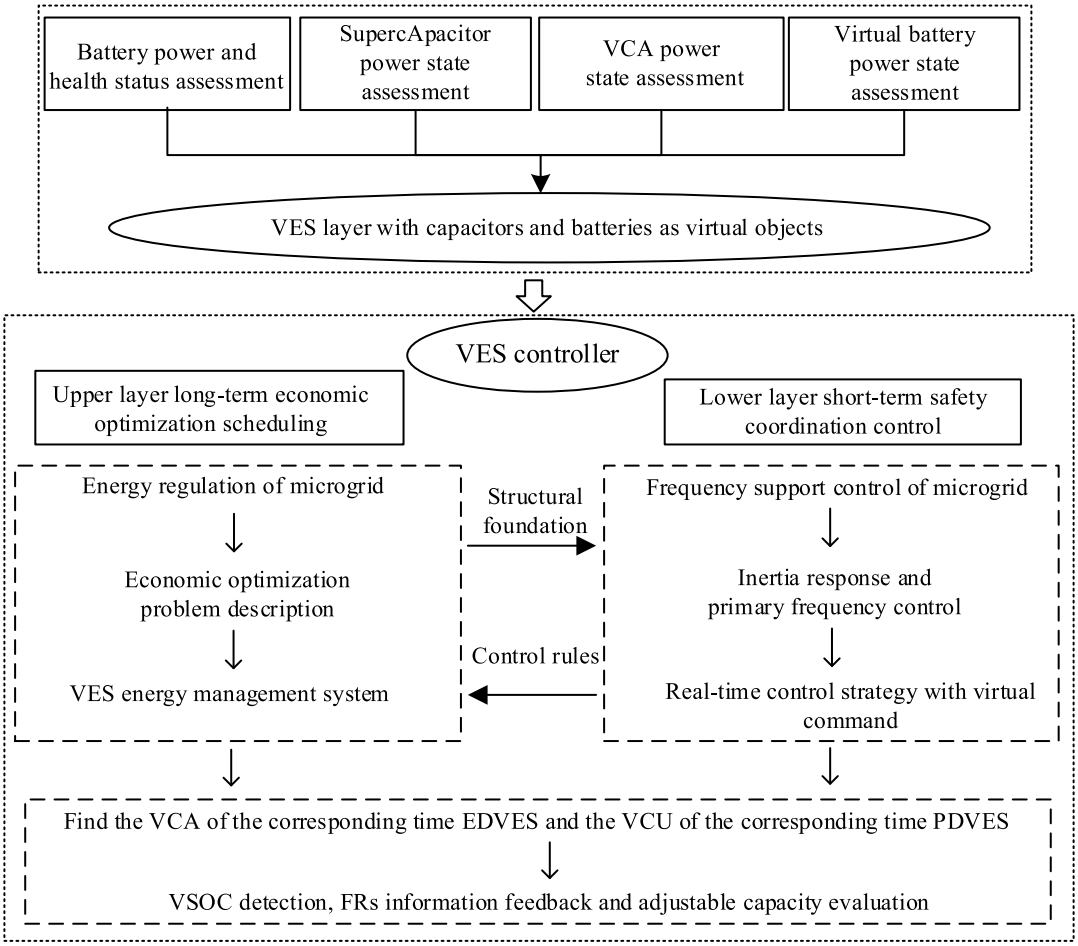

FIGURE 3
Structure of a multi-time scale dispatching system for microgrids with VES.

The controllable load participates in power regulation in the form of a VCA. Referring to the speed change of an asynchronous motor, the relationship between the load power $P_L(t)$ and the output power of the VCA is can be expressed as Equation 19

$$P_L(t) = P_L(t-1) + \frac{J_s[\omega_r^2(t) - \omega_r^2(t-1)].}{2p_n^2\Delta t} \tag{19}$$

Taking the SDL as an example, the relationship between the purified water flow rate and the load output power can be fitted (Wang et al., 2021). The purified water flow rate of the SDL can be expressed as Equation 20

$$Q(t) = 2.741 - 2.408\cos[0.1216P_L(t)] + 1.324\sin[0.1216P_L(t)]. \tag{20}$$

The microgrid scheduling center can output the VCA value according to the revenue optimization result and use the VCA to complete load regulation. The controllable load uses the motor frequency conversion speed regulation system to change the load power so that the PDVES has a variable capacitance value.

3.2.1.2 Cost of microgrids

The operating cost C_{mic} of the microgrid needs to consider the operation and maintenance cost C_{H2} of HES, the peak shaving cost C_{ev} of EV users, the regulation cost C_{wf} of WTs, the operation and maintenance cost C_{wi}, and the operation and maintenance cost C_{hy} of energy storage, which can be expressed as Equation 21

$$\begin{aligned}\sum C_{mic} = {} & U_{EL}I_{EL}h_{EL}p_{EL} + U_{FC}I_{FC}h_{FC}p_{FC} + \sum_{t=1}^{24} K_m P_w(t) \\ & + \sum_{t=1}^{24}\sum_{j=1}^{M} \Delta p(t)E_{evd}(t) + \sum_{t=1}^{24} K_w[P_{wo}(t) - P_w(t)] \\ & + C_{hy},\end{aligned} \tag{21}$$

where, p_{EL} and p_{FC} represent the operation and maintenance costs per unit of electricity of AC and PEMFC, respectively, K_m represents the operation and maintenance cost per unit of electricity of WTs, M and E_{evd} represent the number and discharge amount of virtual batteries, respectively, $\Delta p(t)$ represents the compensation electricity price per unit of discharge amount of EV connected to the grid, $P_{wo}(t)$ represents the output power of WTs under maximum power tracking control, $P_w(t)$ represents the output power of WTs under VES control, and K_w represents the unit wind curtailment cost of WTs.

In actual operation, the charging and discharging of the battery will reduce its service life. Therefore, the operation and maintenance

cost C_{hy} of the hybrid energy storage includes the operation and maintenance cost C_b and the life loss C_B, and can be expressed as Equations 22, 23

$$C_{hy} = C_B + C_b = \sum_{t=1}^{24} C_B(t) + \sum_{t=1}^{24} K_{hy}\left(\left|P_{hyc}(t)\right| + \left|P_{hyd}(t)\right|\right), \quad (22)$$

$$C_B(t) = \frac{W_{total}A}{1 - SOH_{min}}\left|SOC_B(t-1) - SOC_B(t)\right|, \quad (23)$$

where, K_{hy} represents the operation and maintenance cost of energy storage, P_{hyc}(t) and P_{hyd}(t) represent the power output of the energy storage in time period t, respectively, W_{total} represents the purchase cost of the battery, A represents the aging coefficient of the battery, SOH_{min} represents the critical life of battery scrapping, with a value of 0.8, and $SOC_B(t)$ represents the SOC of the battery in time period t.

3.2.2 Constraint conditions

During the microgrid's operation, it is necessary to ensure the power balance of the power source and the load. Therefore, the power balance constraint of the system can be expressed as Equation 24

$$P_w(t) + P_{pv}(t) + P_{hyd}(t) - P_{hyc}(t) = P_L(t) + \sum_{i=1}^{N} E_{ev}(t) + P_{H2}. \quad (24)$$

To avoid overcharging and over-discharging of the real energy storage device, the state of charge constraints of the supercapacitor and the battery are, respectively, expressed as Equation 25

$$\begin{cases} 20\% \le SOC_B(t) \le 80\% \\ 20\% \le SOC_C(t) \le 80\% \\ 40\% \le SOC_B(24) \le 60\% \\ 40\% \le SOC_C(24) \le 60\% \end{cases}. \quad (25)$$

To ensure the continuous operation of the system during the day, the state of charge at the end of the hybrid energy storage device is constrained to meet the energy regulation needs of the system the next day.

During the operation of the EDVES, the operation limits of the electrical equipment need to be considered. For example, the state of charge constraints of HES and EVs are respectively expressed as Equation 26

$$\begin{cases} 30\% \le SOC_{ev}(t) \le 90\% \\ 10\% \le SOC_{H2}(t) \le 90\% \end{cases}. \quad (26)$$

The PDVES also needs to consider the allowable operation range of electrical equipment. For controllable loads such as SDLs and WTs, the VSOC constraints can be respectively expressed as

$$\begin{cases} 21.78\% \le SOC_{vir1}(t) \le 100\% \\ 16\% \le SOC_{virg}(t) \le 100\% \end{cases}. \quad (27)$$

In Equation 27, 46% of the rated speed of the controllable load is set as the minimum rotor speed, which is 1400r/min—the VSOC operation threshold of the controllable load is 21.78%—and 40% of the rated speed of the WT is set as the minimum speed—the VSOC operation threshold of the WT is 16%.

When the HES system is operating, it is necessary to ensure that it works accurately in the AE or PEMFC state. The state constraint of the HES system is expressed as Equation 28

$$h^{EL} + h^{FC} \le 1. \quad (28)$$

3.3 Cooperative control of VES for frequency support

When the system frequency f remains within the safe range, the microgrid maintains economic operation through the energy regulation system. The system collects the operation states of the VES and the real energy storage device and sends them to the microgrid dispatch control center to complete the long-term scale economic optimization. However, if the microgrid encounters a disturbance and the system frequency exceeds the safe operation range, the microgrid should have the ability to coordinate various FRs to participate in the system frequency regulation and reduce the frequency regulation task of the energy storage. The collaborative operation strategy process of the PDVES and the EDVES in the microgrid is shown in Figure 4.

As seen in Figure 4, within the frequency safety range, the microgrid is in the economic dispatching operation mode. When the frequency exceeds the safe range, the controllable electrical equipment with short-term frequency response in the microgrid includes WTs, controllable loads, EVs, and HES. At this time, the WTs and controllable loads deploy their power rapid response capabilities and provide inertia support in the initial stage of frequency change. EVs and HES participate in the primary frequency regulation of the system.

As shown in Figure 4, the PDVES mainly undertakes the rapid power regulation in the initial inertia response stage ($df/dt < 0$). In this stage, the PDVES adjusts ω^* r and ω^* opt respectively through the VCA C_l and C_w to further adjust its power output, share the inertia support task of the supercapacitor, and reduce the rate of change of the system frequency. In the frequency recovery stage ($df/dt > 0$), the PDVES and the EDVES jointly undertake the frequency regulation task. In this stage, the EDVES outputs I_{H2} and I_{ev} through the VCU instruction, simulates the charging and discharging characteristics of the battery, adjusts the hydrogen storage electrolysis rate N_{EL} or the hydrogen combustion rate N_{FC} and the EV charging amount $E_{ev}(t)$, respectively, relieves the frequency regulation pressure of the battery, and accelerates the system frequency recovery speed. Under the multi-terminal regulation of the source, storage, and load, the system frequency gradually recovers until ($df/dt > 0$), when the system frequency returns to the steady-state value, the system frequency no longer changes, an inertia response link exits, and the primary frequency regulation link continues to maintain the safe operation of the system frequency in the new operating state.

In Figure 5, the red lines represent the data flow of the microgrid. The microgrid uses the communication network to obtain information on the output and response of sources, loads, and energy storage. After analysis and processing, this information is converted into coordinated operation commands represented by VCA and VCU parameters. These virtual commands are then

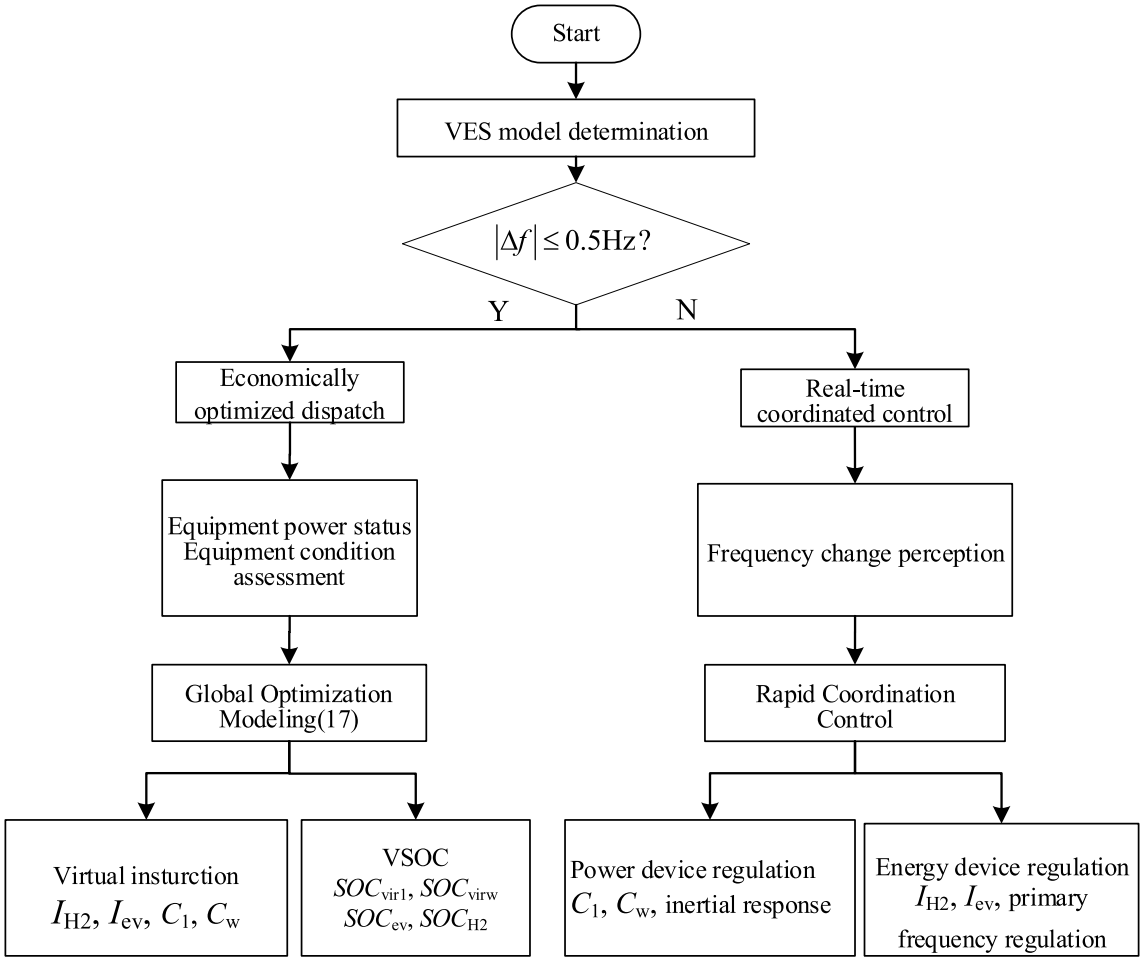

FIGURE 4
Cooperative control of the microgrid for energy regulation and frequency response.

transmitted to the FR device terminals through the data flow. The blue lines indicate the power flow of the microgrid, which is the control structure for the FR device to participate in energy regulation. Upon receiving the virtual commands, the FR device terminals switch to the corresponding working modes and adjust the actual parameters. By responding to power changes, they provide rapid frequency support, thereby ensuring the stability of the microgrid operation.

The VCA value C_{vir} set by the PDVES has the following relationship with the capacitance value C of the real supercapacitor:

$$C_{vir} = k_{virc} C. \tag{29}$$

In Equation 29, k_{virc} represents the VCA adjustment coefficient.

The state of charge of the supercapacitor is closely related to the terminal voltage and can be expressed as

$$SOC_{CP} = \frac{U_C - U_{Cmin}}{U_{Cmax} - U_{Cmin}}. \tag{30}$$

In Equation 30, U_C represents the voltage of the supercapacitor, and U_{Cmax} and U_{Cmin} represent the allowable upper and lower limits of the voltage of the supercapacitor, respectively.

If the system frequency change is $\Delta\omega_e$, the PDVES needs to provide inertia support, and the change in virtual rotational kinetic energy is

$$\Delta E_{LG} = \frac{1}{2} J_{vB} \omega_e \Delta\omega_e, \tag{31}$$

$$H_{vB} = \frac{J_{vB}\omega_e^2}{2S_{NB}}, \tag{32}$$

where, J_{vB} represents the moment of inertia of the PDVES, ω_e is the angular velocity of the virtual synchronous generator, and S_{NB} is the capacity of the virtual synchronous generator.

Substituting Equation 32 into Equation 31 yields

$$\Delta E_{LG} = 2H_{vB} S_{NB} \Delta\overline{\omega}_e. \tag{33}$$

In Equation 33, $\Delta\overline{\omega}_e$ represents the per-unit value of the angular frequency variation.

Writing it in the form of frequency gives

$$\Delta E_{LG} = 4\pi H_{vB} S_{NB} \Delta\overline{f}, \tag{34}$$

where $\Delta\overline{f}$ represents the per-unit value of the frequency variation.

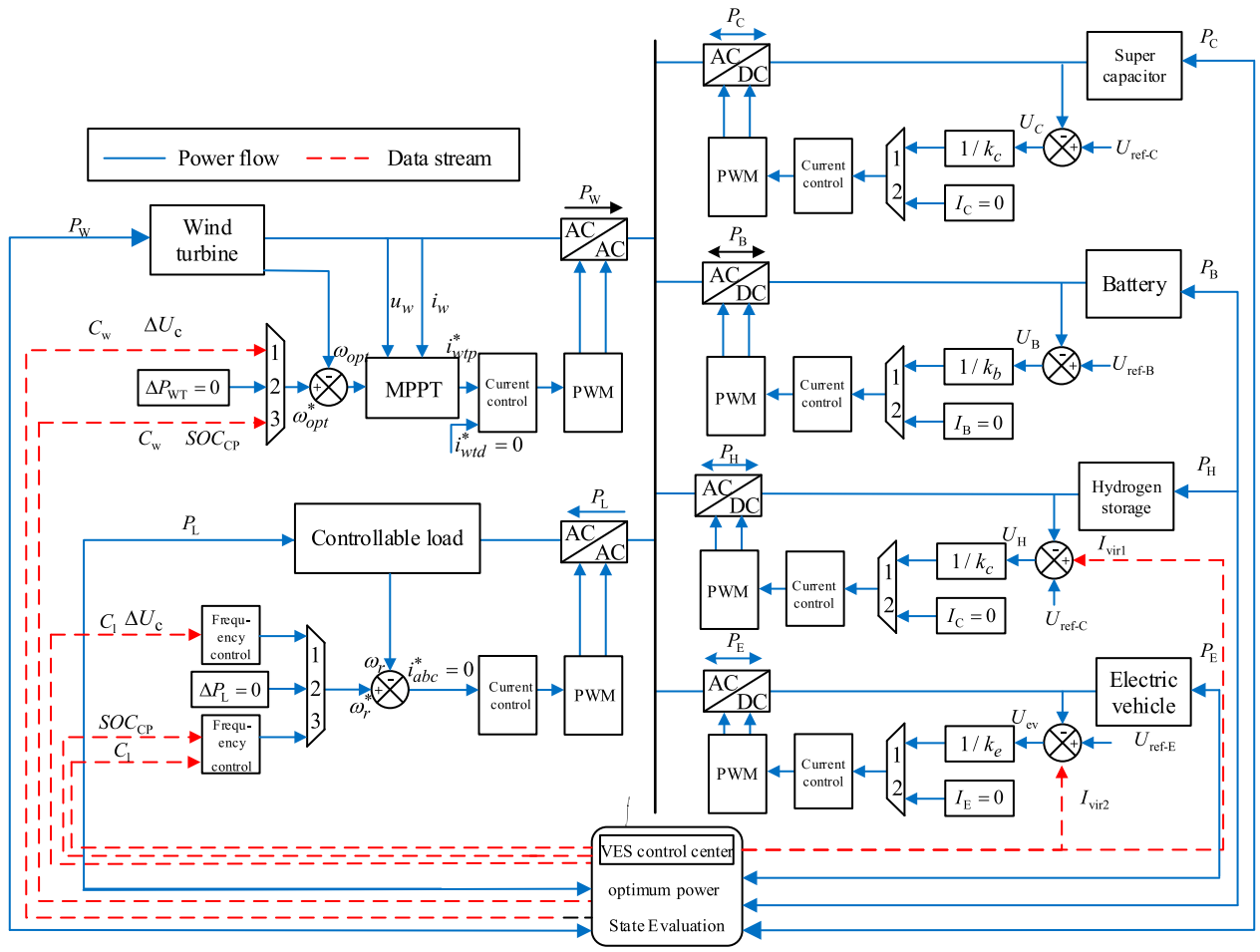

FIGURE 5
Cooperative control structure diagram of the microgrid with VES.

Assuming that all the unbalanced energy of the system during the frequency change is provided by the VCA, the energy change of the VCA is expressed as

$$\Delta E = \frac{1}{2}C(U_c^2 - U_{c0}^2), \tag{35}$$

where U_c and U_{c0} are the steady-state DC voltage of the VCA and the voltage value of the VCA after participating in frequency regulation, respectively.

According to Equations 34 and 35, the system frequency change can be reflected as the DC voltage fluctuation of the PDVES so as to adjust the output power of the VCA in Equation 36:

$$\Delta \bar{f} = \frac{C(U_c^2 - U_{c0}^2)}{8\pi H_{vB} S_{NB}}. \tag{36}$$

After introducing VES, the relationship between the capacitor voltage and the virtual amplification factor is expressed as

$$k_{virc} = \frac{U_C^2(t) - U_C^2(t_{set})}{U_C^2(t) - U_C^2(t_{res})}, \tag{37}$$

where $U_C(t_{set})$ is the terminal voltage of the capacitor when the set SOC_{CP} value is reached, and $U_C(t_{res})$ is the voltage of the supercapacitor when the SOC_{CP} reaches the limit value.

From Equations 2, 5, and 37, the reference values of the electrical angular velocity of the SDL and the WT are respectively expressed as

$$\omega_r^* = \begin{cases} \omega_{rmin} & \omega_r \le \omega_{rmin} \\ \omega_{rn}\left(K_1 \Delta SOC + SOC_1^{\frac{3}{2}}\right)^{\frac{3}{2}} & \omega_{rmin} \le \omega_r \le \omega_{rn} \\ \omega_{rn} & \omega_{rn} \le \omega_r \end{cases}, \tag{38}$$

$$\omega_{opt}^* = \begin{cases} \omega_{optmin} & \omega_{opt} \le \omega_{optmin} \\ \omega_{optn}\left(K_2 \Delta SOC + SOC_w^{\frac{3}{2}}\right)^{\frac{3}{2}} & \omega_{optmin} \le \omega_{opt} \le \omega_{optn}, \\ \omega_{optn} & \omega_{optn} \le \omega_{opt} \end{cases} \tag{39}$$

In Equations 38, 39, where, $K_1 = 2{p_n}^2 U_C C_1 (U_{Cmax}\text{-}U_{Cmin})/(J_s {\omega_m}^2)$, $\Delta SOC = SOC_{CP}\text{-}SOC_{Cres}$; SOC_{Cres} represents the limit value of the VSOC SOC_{CP} of the SDL, $K_2 = U_C C_w (U_{Cmax}\text{-}U_{Cmin})/(k_{opt} {\omega_{optn}}^3)$, SOC_{Cgres} represents the limit value of the VSOC SOC_{CP} of the WT, and ω_{rmin} and ω_{optmin} represent the minimum angular velocities of the motor and the WT, respectively.

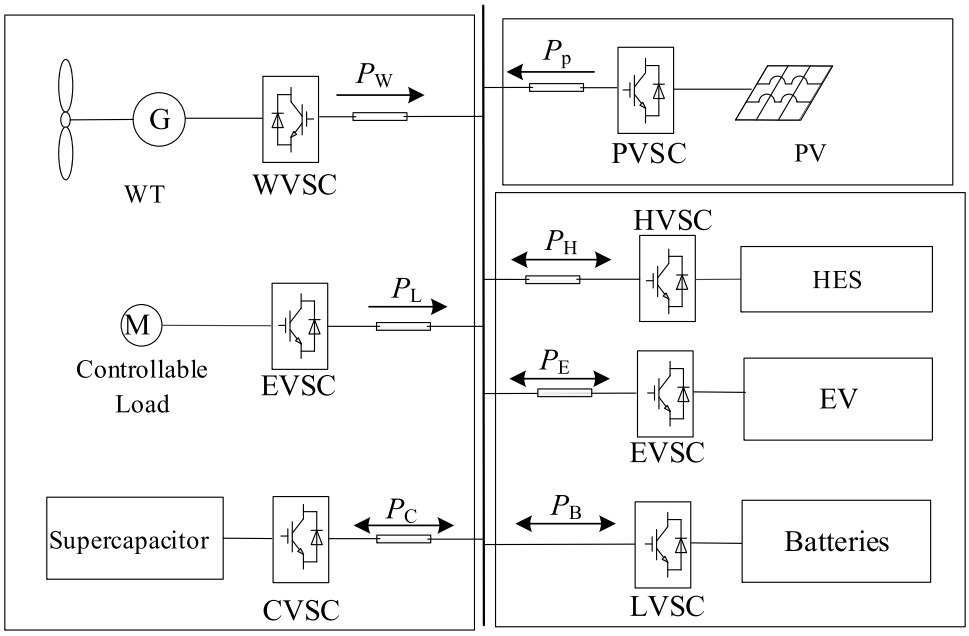

FIGURE 6
Structure of the test system.

TABLE 1 Simulation system parameters.

Component	Parameters
WTs	P_N = 3000 kW, ω_N = 1500 rad/min
Supercapacitors	C = 1000 mF, V_{cN} = 30 kV
Batteries	Q_N = 10000 A h, V_{batN} = 12 kV
SDLs	n_N = 3000 rad/min, n_{min} = 1400 rad/min
EVs	N = 500,SOC_e: 30%–90%
HES	Maximum inlet volume 2380Nm^3/h, maximum outlet volume 1770Nm^3/h

The VCU value I_{vir} of the EDVES can be set as

$$I_{vir} = k_{viri} I_B, \tag{40}$$

In Equation 40, where k_{viri} is the VCU adjustment coefficient, and I_B is the output current of the real battery.

The frequency response model of the microgrid after introducing VES is

$$\left(2H_g p + D_{sys}\right)\Delta f(t) = \Delta P_{LG} + \Delta P_{LN} - \Delta P_d, \tag{41}$$

where H_g is the system inertia when the new energy penetration rate is r, D_{sys} is the damping coefficient of the system, ΔP_{LG} is the power output of the PDVES, ΔP_{LN} is the power output of the EDVES, and ΔP_d is the disturbance power.

Combining Equations 8, 15, and 41, the VCU values of the two EDVES can be obtained respectively as Equations 42, 43

$$I_{vir1} = \frac{\Delta P_{LG1}}{U_{H2V}}, \tag{42}$$

$$I_{vir2} = \frac{\Delta P_{LG2}}{U_{ev}}, \tag{43}$$

where, I_{vir1} and ΔP_{LG1} are the VCU and output power of the HES, respectively, and I_{vir2} and ΔP_{LG2} are the VCU and output power of the EV, respectively.

By calculating the reference value of the electrical angular velocity and the VCU command value through the VCA and the virtual battery, respectively, the output power of the EDVES and the PDVES can be adjusted to provide rapid power support and improve the frequency stability. In addition, the operation state of the VES can be directly monitored through the VSOC and combined with the energy regulation system, taking both the economy and safety of the microgrid into account.

4 Simulation analysis

4.1 Introduction of the test system

In order to verify the enhancement effect of the proposed VES on the energy regulation and rapid power support of the microgrid, a test system was built (Figure 6). This paper compares two scenarios: one without additional control and one with VES control. In the scenario without additional control, only the batteries and supercapacitors participate in power regulation, and the FR in the microgrid consumes electrical energy as loads. In the scenario with VES control, in addition to the batteries and supercapacitors

TABLE 2 Time-of-day tariffs.

Time period	08:00–11:00 18:00–21:00	22:00–06:00	06:00–08:00 11:00–18:00 21:00–22:00
Electricity price/CNY/(kW·h)	1.197	0.356	0.744

TABLE 3 Benefit/cost factor for economic operation of the system (Wang et al., 2023).

Parameters	Value	Parameters	Value
k	5.4 CNY/Ton	$\Delta p(t)$	0.42 CNY/(kW·h)
p_{h2}	10.3 CNY/m^3	K_w	0.35 CNY/(kW·h)
p_{EL}	0.148 CNY/(kW·h)	K_m	0.0296 CNY/(kW·h)
p_{FC}	0.263 CNY/(kW·h)	K_{hy}	0.9 CNY/(kW·h)

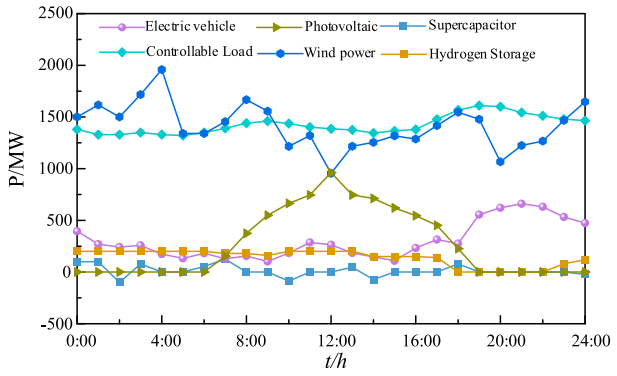

FIGURE 7
Power dynamic responses of the test system without additional control.

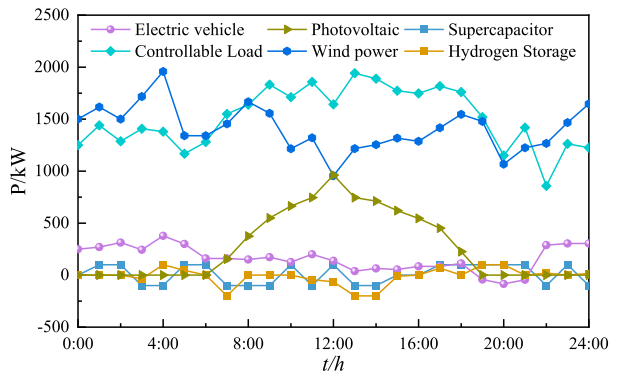

FIGURE 8
Power dynamic responses of the test system under VES control.

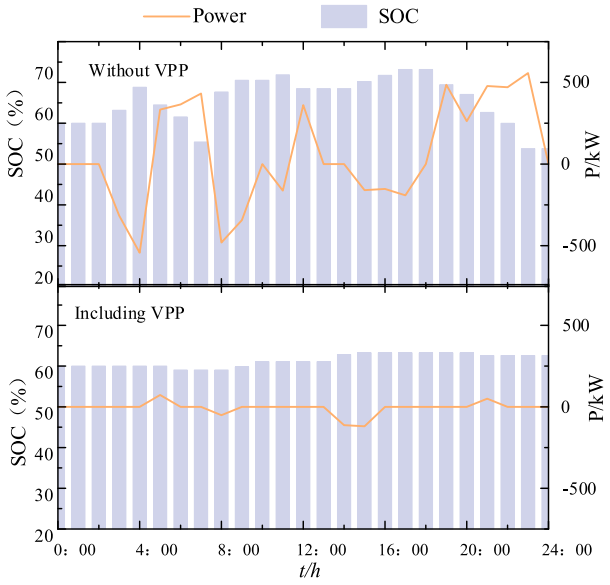

FIGURE 9
State of charge and power responses of the battery under two scenarios.

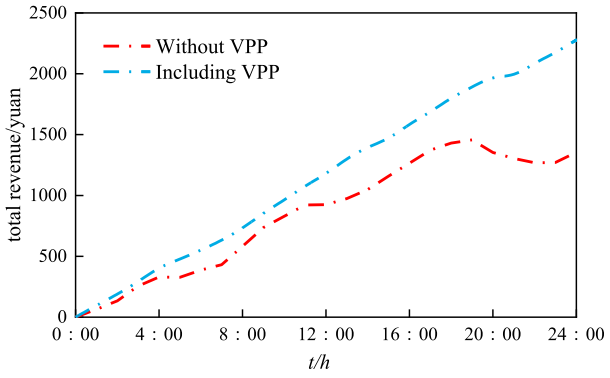

FIGURE 10
System gain results under two scenarios.

participating in power regulation, the FR in the microgrid also participates in system energy management and rapid power support through VES.

The operating parameters of WTs, supercapacitors, batteries, SDL, EVs, and HES in the test system are shown in Table 1, the EV time-of-use tariffs are shown in Table 2, and the economic

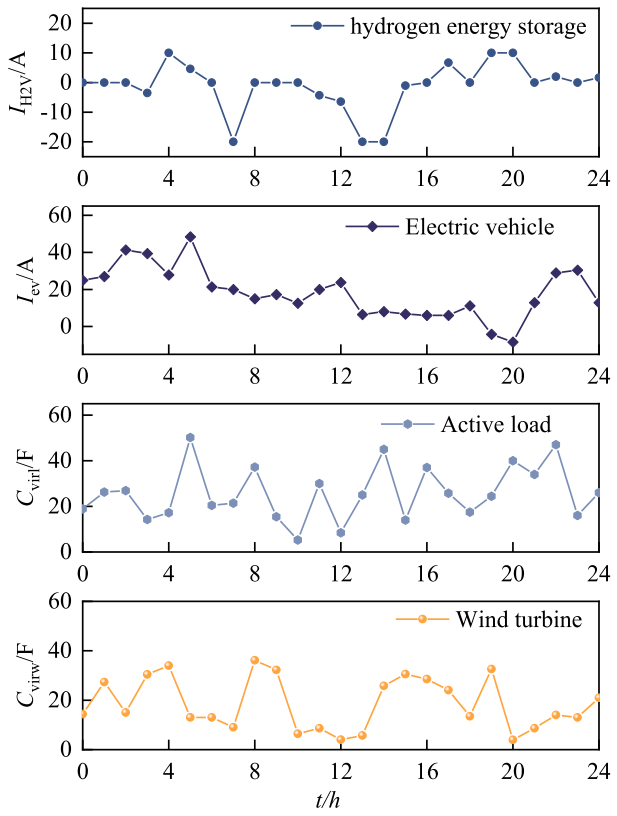

FIGURE 11
VCU and VCA command values.

operating parameters of the system are shown in Table 3 (Wang et al., 2021; Wang et al., 2023). The test system solves the energy regulation model by invoking the CPLEX solver.

4.2 Analysis of energy regulation

The comparison of the test results with and without the economic optimization dispatch under the no-attachment control and VES control are shown in Figures 7–11.

After the introduction of VES, the energy regulation system of the microgrid scheduling and control center will generate VCA value and VCU value commands to cooperate the resources to respond to the system (Figure 11). During the economic operation scheduling process, based on the VSOC of the VES device (Figure 12), the microgrid can intuitively perceive the energy reserve state of the system.

Looking at Figures 7 and 9, it can be seen that in the traditional mode without additional control—between 0:00 and 4:00—the output power of the WT increases, and the EV charging load demand is less, failing to respond to the wind power disturbance; this achieves wind power dissipation by charging the supercapacitor. In addition, at 2:00–4:00, when the supercapacitor charging reaches the limit—after the state of charge rises to the maximum value—it is handed over to the battery charging to smooth out the wind power disturbance, which makes the SOC of the battery rise to 67.4% at 4:00.

At 5:00, the wind power decreases significantly. To respond to the system power disturbance in time, the supercapacitor and the battery participate in power regulation to maintain the system power balance. At 8:00–18:00, on the one hand, the PV modules begin to generate electricity. On the other hand, the wind power plummets at 12:00, and under the pressure of this double disturbance, coupled with the limited range of supercapacitor regulation, the controllable loads as well as other controllable FRs fail to participate in the response. They mainly rely only on the hybrid energy storage system of the battery to respond to the system disturbance, leading to an increase in the depth of discharge of the battery and also putting the battery in a state of frequent charging and discharging; this causes the SOC of the battery to show a rising–declining–rising trend.

After 18:00, the EV is in a centralized charging state, and a load peak occurs, its maximum load reaching 620 kW. In addition, the PV is unable to output power at night, resulting in an increase in the system's peak–valley difference. The batteries will be deeply discharged, and the lowest value of its SOC reaches 53.79%.

In this model, some controllable FRs (EVs, controllable loads, HES) fail to exploit their adjustable potential or fully mobilize their response. The hybrid energy storage system consisting only of supercapacitors and batteries supports the unbalanced net load caused by wind and PV power disturbances. In addition, combining Table 4 and Figure 10 shows that the net gain of the system in 24 h is ¥ 1,354.72. It is worth noting that during the dispatch cycle, the battery is in a frequent charging and discharging state; especially after 18:00, the battery is deeply discharged, which leads to an increase in the cost of operation and maintenance and aging, and the system revenue is significantly reduced.

After the introduction of VES, the microgrid uses the VCU and VCA values in Figure 6 to regulate the FRs and simulate the charging and discharging characteristics of energy storage devices.

As shown in Figure 11, from 0:00 to 4:00, in order to fully stimulate the responsiveness of controllable FRs and under the constraint of meeting customer charging demand, the microgrid adopts time-of-use tariffs so that EVs are charged when the price is low and discharged when the price is high, forming a phenomenon of "low storage and high generation." In order to flexibly dispatch EVs, the microgrid generates VCU values to regulate EVs for VES. In addition, in order to tap its adjustable potential, the microgrid treats the SDL as VES and regulates the load power through the VCA value.

At 3:00, the WT sets the VCA to 37.1 F through the VES technology, which responds quickly to the power change and balances the system power. During this period, battery charging and discharging power is significantly reduced, and the microgrid effectively consumes the significantly increased wind power. At 5:00, the wind power is reduced, and the WTs are constrained by the rotational speed and wind speed. At this time, the controllable loads mainly carry out the rapid power response, and the HES and EV clusters carry out the supplemental regulation to satisfy the system power demand, fully mobilizing the enthusiasm of the VES in responding to the power change.

At 8:00–18:00, the PV begins generating power, system power redundancy, and controllable load through the VES technology to set the VCA to 22.4 F to increase the rotor speed to dissipate the redundant power. At 12:00, when the wind power

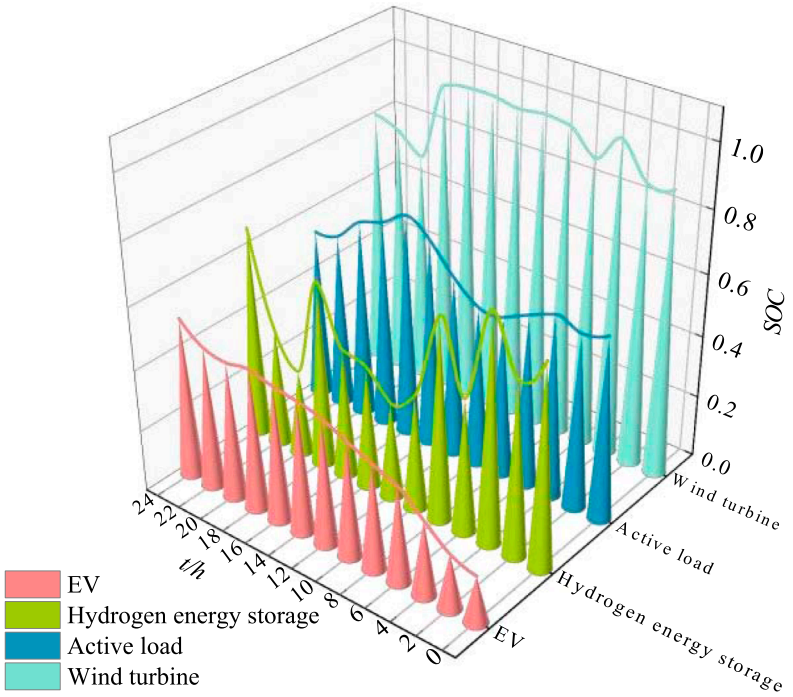

FIGURE 12
VSOCv of VES.

TABLE 4 Economy results under different cases.

Case benefits/costs/CNY	No additional controls	VES control
Revenue from water production	2,704.07	2,575.48
Revenue from EV sales	221.03	129.43
Hydrogen production	330	80.67
Comprehensive O&M Costs	1900.38	215.6
Peaking costs	0	51
EV Dispatch compensation	0	240.43

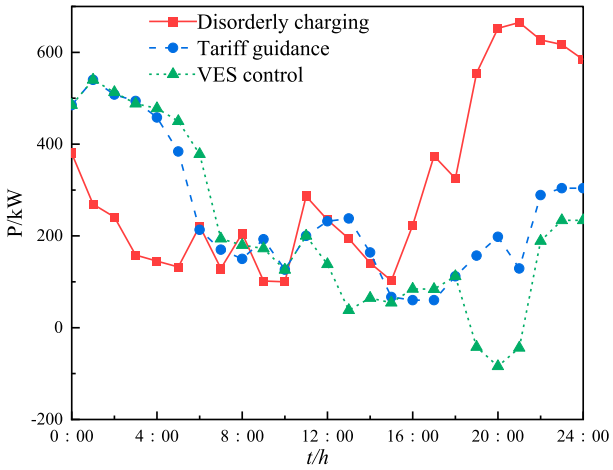

FIGURE 13
Load profile of EV in multiple modes.

plummeted—limiting the WT VES adjustable potential—the controllable load actively participated in the system regulation, reduced its own operating power, and reduced the output power to 1,642 kW. The energy regulation system generates a negative VCU value, and the HES works in the fuel cell state, increasing the output power by burning hydrogen; this reduces the number and depth of battery discharges.

After 18:00, unlike the EV as a load in the no-attachment control, the EV has already shifted the peak power consumption to other times to dissipate the wind–PV disturbances through the complementary response of the power on different periods. Therefore, at this time, the dispatch center of the microgrid sends a command to the EV with a negative value for the VCU to supply power to the system and maintain the power balance. At 24: 00, the battery SOC is controlled to be at 62.57%. At this time, compared with no additional control, the battery SOC in the VES mode is improved by 8.78%.

The test results indicated that after the introduction of VES, the maximum change of battery SOC without additional control is 12.4%, and the battery starts charging and discharging 17 times; the maximum change of battery SOC in the VES mode is 3.7%, and the battery starts charging and discharging five times. The change

10.3389/fenrg.2025.1574188

of battery SOC decreases in amplitude, and the fluctuation number is significantly reduced, which alleviates the depth of charging and discharging of batteries, reduces the number of times for their charging, and reduces system operation cost.

Combined with Table 4 and Figure 10, the cumulative net gain of the system in 24 h is ¥ 2,278.55. Compared to the scenario without additional control, the system's revenue has increased by a factor of 1.68. The main reason is that after the VES participates in power regulation, although the microgrid revenue is reduced, the battery operation and maintenance costs are significantly reduced.

To test the effectiveness of the VES of EVs, this paper established three scenarios: uncontrolled charging, price-guided charging, and VES control. The comparison of the charging load curves of EVs under these three scenarios is shown in Figure 13.

By comparing the three scenarios, it can be seen that under the uncontrolled charging scenario, the charging behavior of EVs exhibits significant spatiotemporal clustering characteristics. The charging load of EVs surges in the evening, exacerbating the system's peak–valley difference. The maximum charging load reaches 650 kW at 21:00, which poses a threat to the safe and stable operation of the system. Under the price-guided scenario, EVs are guided to charge in an orderly manner, concentrating their charging during the low-price period from 0:00 to 6:00, achieving a redistribution of charging load in time and space. Under the VES control scenario, EVs are centrally scheduled to supply power to the microgrid between 19:00 and 21:00, providing 194 kW of power. The results show that the participation of FRs in the coordinated operation of the microgrid can effectively regulate the resources within the grid, achieving the "peak shaving and valley filling" of the microgrid.

To validate the effectiveness of the solution proposed in this paper, its optimization results obtained are compared with those obtained from the particle swarm optimization (PSO) algorithm under the described VES control scenario. After solving with PSO, the best result among ten runs is selected and set as the VCA and VCU values to participate in the system's energy management. The specific economic indicators obtained from solving with CPLEX and PSO are compared in Table 5.

The differences in the economic indicators obtained from the two solution methods are relatively small. The CPLEX solution increased the microgrid revenue by 0.81% compared to the PSO solution. This situation may be caused by the parameters set for the PSO algorithm, which may still converge to a local optimum even after multiple iterations. In contrast, the CPLEX solution method can effectively avoid the issue of falling into a local optimum and has demonstrated reproducibility through repeated validation. The comparison confirms the rationality of the solution results in this paper and indicates that using CPLEX can significantly improve the efficiency of solving the optimization model.

TABLE 5 Comparison of results from different solution methods.

Solution method	Net revenue/¥	Operating revenue/¥						
		Water production revenue	Electricity sales revenue	Hydrogen production revenue	Operation and maintenance cost	Peak shaving cost	EV compensation
CPLEX	2,278.55	2,278.55	2,575.48	129.43	80.67	215.6	51
PSO	2,260.64	2,265.42	2,270.70	129.62	53.69	137.44	13.27

4.3 Analysis of frequency support effect

After 12:00, the wind power decreases abruptly after 10 s, causing the system frequency to fall and exceed the safety threshold by 0.5 Hz. The FRs in the microgrid need to respond quickly to the frequency change to guarantee the dynamic stability of the system. The system dynamic response before and after the VES is shown in Figure 14.

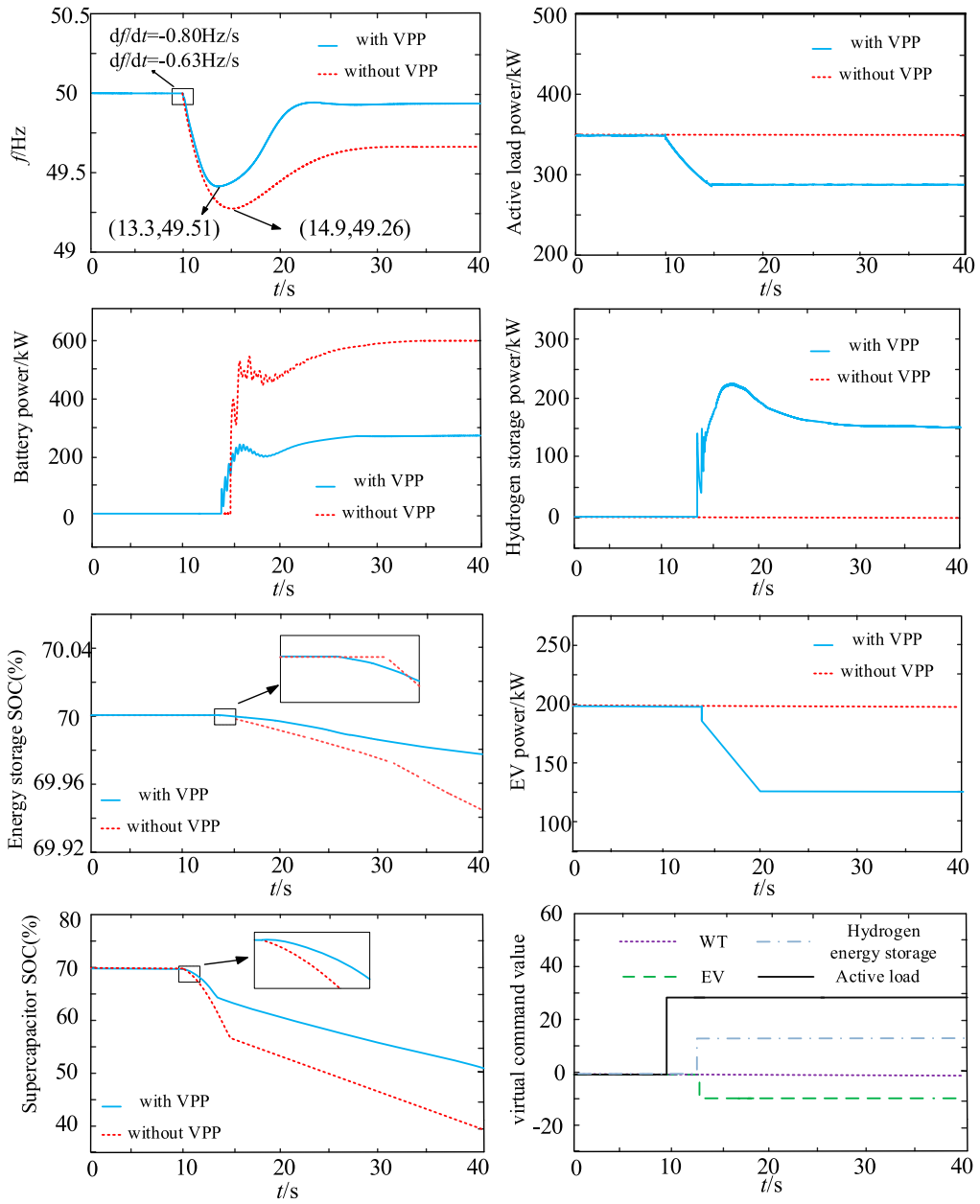

FIGURE 14
Dynamic responses of the system after sudden wind power reduction.

Figure 14 shows that at 10 s, the wind speed decreases suddenly, and when VES is not introduced, the supercapacitor and battery can participate in the system frequency support, but the regulation ability is insufficient, and the inertia response time is 4.9 s. At the early stage of the disturbance, the system frequency drops at a rate of 0.80 Hz/s, and the maximum frequency deviation Δf_h is 0.74 Hz. The supercapacitor SOC falls to 18% in this mode. In the frequency recovery phase, the hybrid energy storage undertakes a frequency regulation task, and the frequency returns to a steady state at 31.2 s. The frequency at steady state is 49.69 Hz.

After the introduction of VES, in the inertial response stage, the system frequency change rate is 0.63 Hz/s, and the maximum frequency deviation Δf_h is 0.49 Hz. The supercapacitor SOC decreases by 7.2%, which satisfies the frequency safety regulation. In this process, the controllable load shares the pressure of the supercapacitor participating in the frequency adjustment with a VCA value of 29.8 F. The supercapacitor's SOC is also reduced by 7%. As shown in Figure 14, the load power is rapidly reduced by 129 kW, the rapid frequency response mode of the FRs is simple, and the control potential is fully released. It should be noted that if the wind power is insufficient to cause the frequency drop, the WT operates at the upper limit of the wind speed under the maximum power tracking control and cannot further increase the wind power, so the WT does not activate the VES control at low wind speeds.

After 13.3 s, the HES and EV clusters in the system frequency recovery phase participate in one frequency regulation with VCU

values of 13.7 A and −7.9 A, respectively, to share the discharge pressure of the batteries. The frequency returns to the steady-state value after 25.5 s, and the frequency in the steady state is 49.92 Hz. Compared with the no-attachment control, the frequency deviation is reduced by 0.23 Hz, the amount of the change in the SOC of the batteries is significantly lower, and the frequency stability of the system is improved.

5 Conclusion

To enhance the coordinated operation performance of renewable energy, energy storage, and controllable loads, a novel cooperative control of VES is proposed to fully release the regulation potential of FRs in the microgrid across multiple time scales. Through a combination of theoretical analysis and testing verification, the following conclusions are drawn.

1) WTs, controllable loads, HES, and EVs participate in system energy regulation in the form of VES, which unifies the control parameters for the scheduling operation of various FRs into VCU and VSOC. This not only facilitates the evaluation of system energy reserves but also makes it easier to integrate with real energy storage devices for joint participation in system energy regulation.
2) With the introduction of VES, the FRs in the microgrid, under the proposed dual-layer optimization scheduling mode, can coordinate power distribution through VCU, and the system's energy reserves can be intuitively reflected in real-time through the VSOC. The test results indicate that under the proposed optimized energy regulation mode, the system operation model is significantly simplified and the daily net revenue is increased 1.48 times, effectively enhancing the economic operation capability of the microgrid.
3) Due to the identical control parameters, EDVES and PDVES can easily cooperate with batteries and supercapacitors. During the frequency support process, they can quickly generate VCU commands, enabling the orderly response of various FRs and real energy storage devices to system frequency changes. The test results demonstrate that with the cooperative support of VES, the maximum system frequency deviation is reduced by 31%, and the frequency recovery time is shortened to 5.7 s. The desired rapid frequency response and the economic operation of the test system are both achieved.

Data availability statement

The original contributions presented in the study are included in the article/supplementary material; further inquiries can be directed to the corresponding author.

Author contributions

ZY: Data curation, Formal analysis, Investigation, Methodology, Software, and Writing – review and editing. YW: Conceptualization, Funding acquisition, Project administration, Resources, and Writing – review and editing. JW: Resources, Software, Supervision, and Writing – original draft. YC: Validation, Visualization, and Writing – review and editing.

Funding

The author(s) declare that financial support was received for the research and/or publication of this article. The work described in this paper was fully supported by a grant from the Science and Technology Project of the State Grid Jibei Integrated Energy Service Co., Ltd. (SGJBZN00AJJS2400078).

Conflict of interest

Author ZY was employed by the State Grid Jibei Integrated Energy Service Co., Ltd.

The remaining authors declare that the research was conducted in the absence of any commercial or financial relationships that could be construed as a potential conflict of interest.

The authors declare that this study received funding from State Grid Jibei Integrated Energy Service co., ltd. The funder had the following involvement in the study, including methodology, software, formal analysis, investigation and data curation.

Generative AI statement

The authors declare that no generative AI was used in the creation of this manuscript.

Publisher's note

References

Alyami, S. (2024). Management of diverse smart homes: coordination among controllable loads, EVs, and PVs. *Energy Rep.* 125, 5221–5233. doi:10.1016/j.egyr.2024.10.030

Cao, J., Xu, C., Zi, S., Yu, M., and Diao, R. (2025). Scenario-driven distributionally robust optimization model for a rural virtual power plant considering flexible energy-carbon-green certificate trading. *Appl. Energy* 379, 124904. doi:10.1016/j.apenergy.2024.124904

Chen, Q., Lyu, R., Guo, H., and Su, X. (2024). Real-time operation strategy of virtual power plants with optimal power disaggregation among heterogeneous resources. *Appl. Energy* 361, 122876. doi:10.1016/j.apenergy.2024.122876

Du, L., Jin, X., and He, W. (2019). A tie-line power smoothing control method for an office building microgrid by scheduling thermal mass of the building and plug-in electric vehicles. *Electr. Power Constr.* 40 (8), 26–33. doi:10.3969/j.issn.1000-7229.2019.08.004

Fu, S., Wang, C., Zhang, L., Chen, X., and Shu, Y. (2022). Optimized control of active loads in DC microgrids with virtual energy storage. *Energy Rep.* 8, 13962–13969. doi:10.1016/j.egyr.2022.10.336

Gabriele, F., Paolo, M., Marco, B., and Dimosthenis, T. (2023). The flexibility of virtual energy storage based on the thermal inertia of buildings in renewable energy communities: a techno-economic analysis and comparison with the electric battery solution. *J. Energy Storage* 73 (PC), 1–12. doi:10.1016/j.jes.2023.103008

Honarmand, M., Zakariazadeh, A., and Jadid, S. (2014). Optimal scheduling of electric vehicles in an intelligent parking lot considering vehicle-to-grid concept and battery condition. *Energy* 65, 572–579. doi:10.1016/j.energy.2013.11.045

Huang, H., Ning, Y., Jiang, Y., Tang, Z., Qian, Y., and Zhang, X. (2024). Corrigendum: dynamic pricing optimization for commercial subcontracting power supplier engaging demand response considering building virtual energy storage. *Front. Energy Res.* 12, 1498767. doi:10.3389/fenrg.2024.1498767

Li, Q., Dong, F., Zhou, G., Mu, C., Wang, Z., Liu, J., et al. (2025). Co-optimization of virtual power plants and distribution grids: emphasizing flexible resource aggregation and battery capacity degradation. *Appl. Energy* 377 (PB), 124519. doi:10.1016/j.apenergy.2024.124519

Lin, M., Liu, J., Tang, Z., Zhou, Y., Jiang, B., Zeng, P., et al. (2025). Coordinated DSO-VPP operation framework with energy and reserve integrated from shared energy storage: a mixed game method. *Appl. Energy* 379, 125006. doi:10.1016/J.APENERGY.2024.125006

Liu, B., Zhou, B., Yang, D., Li, G., Cao, J., Bu, S., et al. (2021). Optimal planning of hybrid renewable energy system considering virtual energy storage of desalination plant based on mixed-integer NSGA-III. *Desalination* 521, 115382. doi:10.1016/j.desal.2021.115382

Lv, G., Ji, Y., Zhang, Y., Wang, W., Chen, J., et al. (2023). Optimization of building microgrid energy system based on virtual energy storage. *Front. Energy Res.* 11, 1053498. doi:10.3389/fenrg.2022.1053498

Lv, R., Wu, E., Lan, L., Fu, C., Guo, M., Chen, F., et al. (2024). Research on virtual energy storage scheduling strategy for air conditioning based on adaptive thermal comfort model. *Energies* 17 (11), 2715. doi:10.3390/en17112670

Mateus, K., Wan, Y., Daniel, G., Clodomiro, U., and Tomislav, D. (2025). Review on virtual power plants/virtual aggregators: concepts, applications, prospects and operation strategies. *Renew. Sustain. Energy Rev.* 211, 115242. doi:10.1016/J.RSER.2024.115242

Morais, H., Pinto, T., Vale, Z., and Praça, I. (2012). Multilevel negotiation in smart grids for VPP management of distributed resources. *IEEE Intell. Syst.* 27 (6), 8–16. doi:10.1109/MIS.2012.105

Pahasa, J., Potejana, P., and Ngamroo, I. (2022). MPC-based virtual energy storage system using PV and air conditioner to emulate virtual inertia and frequency regulation of the low-inertia microgrid. *IEEE Access* 10, 133708–133719. doi:10.1109/ACCESS.2022.3231751

Shui, J., Peng, D., Zeng, H., Song, Y., Yu, Z., Yuan, X., et al. (2024). Optimal scheduling of multiple entities in virtual power plant based on the master-slave game. *Appl. Energy* 376 (PB), 124286. doi:10.1016/j.apenergy.2024.124286

Sun, H., Dou, Y., Hu, S., Gao, Z., Wang, Z., and Yuan, P. (2023). Day-ahead bidding strategy of a virtual power plant with multi-level electric energy interaction in China. *Energies* 16 (19), 6760–6815. doi:10.3390/en16196760

Tanaka, K., Yoza, A., Ogimi, K., Yona, A., Senjyu, T., Funabashi, T., et al. (2011). Optimal operation of DC smart house system by controllable loads based on smart grid topology. *Renew. Energy* 39 (1), 132–139. doi:10.1016/j.renene.2011.07.026

Tang, X., Hu, Y., and Geng, Q. (2021). Optimal energy management of a residential local energy network based on model predictive control. *Automation Electr. Power Syst.* 45 (4), 81–90. doi:10.1109/AEPS.2020.3023503

Tangqing, T., Nian, L., and Jianhua, Z. (2014). Optimal operation method for microgrid with wind/PV/diesel generator/battery and desalination. *J. Appl. Math.* 2014, 1–12. doi:10.1155/2014/857541

Thomas, M., Branislav, H., and Agelidis, V. G. (2018). Control strategies for microgrids with distributed energy storage systems: an overview. *IEEE Trans. Smart Grid* 9 (4), 3652–3666. doi:10.1109/tsg.2016.2637958

Wang, Y., Hu, C., Wu, B., Zhang, j., Zi, Z., and Kang, L. (2020). Matching characteristic research of building renewable energy system based on virtual energy storage of air conditioning load. *Energies* 13 (5), 1269–1314. doi:10.3390/en13051269

Wang, D., Lai, C., Li, X., Vaccaro, A., Gao, X., Lai, L. L., et al. (2021). Smart coordination of virtual energy storage systems for distribution network management. *Int. J. Electr. Power Energy Syst.* 129 (4), 106816. doi:10.1016/j.ijepes.2021.106816

Wang, C., Fu, S., Zhang, L., Jiang, Y., and Shu, Y. (2023). Optimal control of source-load-storage energy in DC microgrid based on the virtual energy storage system. *Energy Rep.* 9, 621–630. doi:10.1016/j.egyr.2022.12.002

Wang, Y., Dong, H., Ma, K., Wang, H., and Zhang, J. (2024). Multi-frequency stability optimization of integrated energy systems considering virtual energy storage characteristics of heating networks. *Appl. Therm. Eng.* 257 (PA), 124254. doi:10.1016/j.applthermaleng.2024.124254

Westermann, D., and Schlegel, S. (2013). Energy storage capability of battery electric vehicles. *IEEE PES General Meet.*, 1–5. doi:10.1109/PESMG.2013.6672507

Yang, L., Guo, H., and Huang, K. (2019). Optimal dispatch for a combined cooling, heating and power micro-grid considering building virtual energy storage. *J. Electr. Eng. Technol.* 14 (2), 581–594. doi:10.1007/s42835-018-00055-z

Yang, W., Wen, Y., Pandi, H., and Zhang, W. (2022). A multi-state control strategy for battery energy storage based on the state-of-charge and frequency disturbance conditions. *Int. J. Electr. Power Energy Syst.* 135, 107600. doi:10.1016/j.ijepes.2021.107600

Yang, J., Yu, T., Zhao, H., Huang, Y., Weng, W., and Li, Y. (2025). Trading incentive mechanism and response model for high-frequency interaction between virtual power plants and main grid under spot markets. *Int. J. High Speed Electron. Syst.* doi:10.1142/S012915642540275X

Zhang, T., Chen, X., Yu, Z., Zhu, X., and Shi, D. (2018). A Monte Carlo simulation approach to evaluate service capacities of EV charging and battery swapping stations. *IEEE Trans. Industrial Inf.* 14, 3914–3923. doi:10.1109/tii.2018.2796498

Zhou, B., Liu, B., Yang, D., Cao, J., and Littler, T. (2020). Multi-objective optimal operation of coastal hydro-electrical energy system with seawater reverse osmosis desalination based on constrained NSGA-III. *Energy Convers. Manag.* 207, 112533. doi:10.1016/j.enconman.2020.112533

Zhu, Z., and Zhang, H. (2025). Real-time coordinated operation of electric vehicle fast charging stations with energy storage: an efficient spatiotemporal decomposition approach. *IEEE Trans. Smart Grid*, 1. doi:10.1109/TSG.2025.3525495

Frontiers in
Energy Research

Advances and innovation in sustainable, reliable and affordable energy

Explores sustainable and environmental developments in energy. It focuses on technological advances supporting Sustainable Development Goal 7: access to affordable, reliable, sustainable and modern energy for all.

Discover the latest Research Topics

See more →

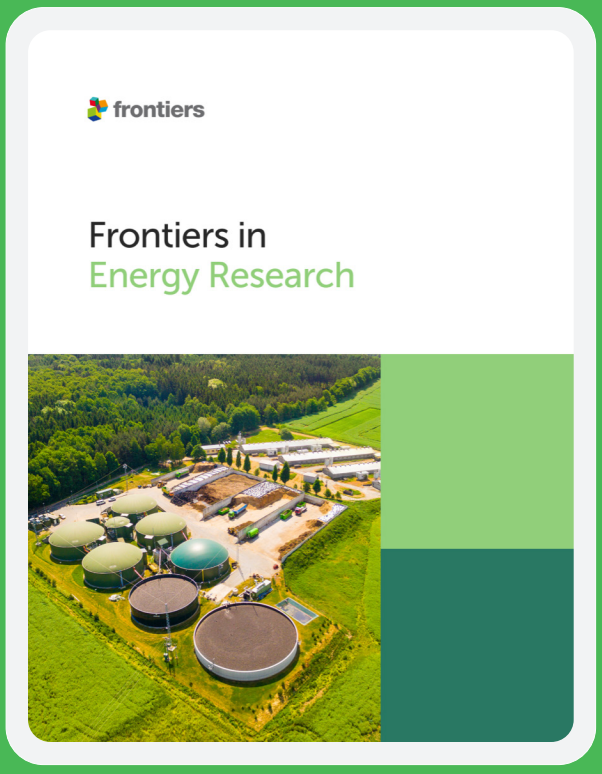

Frontiers

Avenue du Tribunal-Fédéral 34
1005 Lausanne, Switzerland
frontiersin.org

Contact us

+41 (0)21 510 17 00
frontiersin.org/about/contact